INERTIAL CONFINEMENT FUSION

James J. Duderstadt
Department of Nuclear Engineering
The University of Michigan
Ann Arbor, Michigan

INERTIAL CONFINEMENT FUSION

1. INTRODUCTION

   Basic ideas
   History
   Program status
   Outline philosophy of approach (find necessary conditions for ICF, then work backwards to see how these are produced; include a brief scenario here)

2. INERTIALLY CONFINED THERMONUCLEAR FUSION REACTIONS

   Fusion reaction physics
   Thermonuclear fusion reaction criteria (Lawson vs. rho-R)
   ICF driver requirements
   Implosion scenario: compression, pressure, burn
   Pellet gain requirements
   ICF burn physics: uncompressed spheres/ uniform self-heating/ burn propagation

3. THE PHYSICS OF HYDRODYNAMIC COMPRESSION

   Introduction
   Rem edial hydrodynamics
   Shock waves
   Convergent shock waves
   Isentropic compression
   Equations of state
   Ablation-generated pressures

4. ENERGY TRANSPORT IN ICF PLASMAS

   Introduction
   Thermal conduction (Spitzer theory, linear vs. nonlinear, supersonic heat waves, corona-core decoupling, flux limiters, inhibition)
   Radiation transport
   Superthermal particles

5. DRIVER ENERGY DEPOSITION

   Laser light absorption in plasmas (classical-IB, parametric, resonant)
   Energy deposition by charged particles (electrons, light ions, heavy ions)

6. COMPUTER SIMULATION

   Hydrodynamic equations for a plasma
   Eulerian vs Lagrangian
   Numerical methods
   Radiation transport
   Superthermal transport

7. DRIVER DEVELOPMENT I: LASERS

Laser Physics
Solid State Lasers
Gas Lasers
Advanced laser concepts

8. DRIVER DEVELOPMENT II: PARTICLE BEAMS

Electron beams (diode and beam accelerators)
Light ion beams
Heavy ion beams

9. TARGET DESIGN AND FABRICATION

General tools of target design
Laser fusion targets
Particle beam fusion targets
Target fabrication

10. DIAGNOSTIC METHODS IN ICF FUSION EXPERIMENTS

General experimental methods
X-ray measurements
Charged particle measurements
Optical measurements
Neutron measurements

11. APPLICATIONS

Power production reactors
Hybrid fusion-fission reactors
Synthetic fuel production
Propulsion
Other applications

CHAPTER 1

INTRODUCTION

As the limitations of the Earth's resources of conventional fuels have become more apparent, man has begun to look toward the stars for a new source of energy. It has been known for several decades that a major energy source in stars is due to nuclear fusion reactions. In this process the nuclei of light elements are fused together at enormous temperatures to produce more tightly bound, heavier nuclei, releasing energy in the process.

An example of such a reaction is that which occurs between the two heavier isotopes of hydrogen, deuterium and tritium: $D + T \longrightarrow {}^{4}He + n + 17.6$ MeV. This fusion reaction releases energy that is carried off by the reaction products (in this case, the helium nucleus and a neutron). The energy content of such fusion fuels is truly enormous. A thimbleful of deuterium would release as much energy as 20 tons of coal. The natural deuterium occurring in 1 liter of water would produce the fusion energy equivalent of 300 liters of gasoline.

The potential of such reactions for generating large amounts of energy is evident. We need only look at any star to see a massive example of fusion energy release. In a sense, nuclear fusion can be regarded as the most primitive form of solar power, since it is also the energy source of our sun. Hence it was natural for scientists to question whether fusion might be employed as a terrestrial energy source. The awesome potential of this quest was demonstrated by the development of nuclear fusion weapons--the hydrogen bomb--in the early 1950s. Since that time, proponents of fusion power have predicted that someday this nuclear process would provide man with a safe, clean, and abundant source of energy.

Unfortunately, a rather major hurdle must be overcome before fusion reactions can occur. The light nuclei that must fuse together are both positively charged and repel one another quite strongly. To overcome this repulsion, we must slam the two nuclei together at very high velocities. One way of doing this is to take a mixture of deuterium

and tritium and heat it to such high temperatures that the velocities of thermal motion of the nuclei overcome charge repulsion and initiate the fusion reaction. Such a scheme is referred to as a thermonuclear fusion reaction. The temperature required is quite high, roughly 100 million degrees. In fact, the interior of the sun is at just such enormous temperatures. Until quite recently man had imitated the sun in only a rather violent fashion by using a nuclear fission bomb to create temperatures high enough to ignite the fusion reaction in the hydrogen bomb.

But simply heating the fusion fuel to enormous temperatures is not enough to light the fusion reaction. For most of the time, when the nuclei run into each other, they simply bounce off without fusing together. Indeed, such scattering collisions are a million times more probable than fusion reactions. So somehow we have to hold the high temperature fusion fuel together long enough to allow the nuclei to collide the millions and millions of times necessary to induce the fusion reaction.

Therefore to achieve thermonuclear fusion energy release we must solve two problems: (1) produce and heat a plasma fuel to thermonuclear temperatures, and (2) confine it long enough to produce more fusion energy than we have invested in heating the fuel. These twin requirements are usually quantified by a mathematical relation known as the Lawson criterion, which essentially reflects the balance between thermonuclear energy production and heating energy. This criterion can be expressed as a condition on the product of the fuel density n and the time of fusion fuel containment τ . If we express n in units of number of nuclei per cm^3 and τ in seconds, then the Lawson criterion demands that the product $n\tau$ exceed 10^{14} s/cm^3 for a deuterium-tritium fusion reaction.

How are we to accomplish the twin goals of heating and confinement in such a way as to satisfy the Lawson criterion? In a star the enormous mass causes gravitational forces that confine the reacting fuel, compressing it and heating it to the necessary temperatures. Certainly we cannot expect gravity to do that job here on earth.

In thermonuclear weapons no attempt is made to confine the reacting fuel. Rather one merely attempts to heat the fuel to thermonuclear temperatures so fast that an appreciable number of fusion reactions occur before it is blown or explodes apart. This scheme is known as inertial confinement since it is the inertia of the reacting fuel that keeps it from blowing apart prematurely. But to heat an appreciable mass of fuel to such high temperatures requires an extremely large energy source, and the source used in thermonuclear weapons is a fission reaction. That is, an atomic bomb is used to heat the thermonuclear fuel to ignition temperatures. Again, this approach is highly unsuited for a controlled application.

The approach to fusion power that has been studied most extensively works with far smaller quantities of thermonuclear fuel. In particular, it takes advantage of the fact that at the enormous temperatures necessary for fusion to occur, the fuel becomes an ionized or charged gas known as a plasma. Since such charged particles have difficulty moving across magnetic field lines (instead, tending to spiral along them), the primary approach has been to design a "magnetic bottle" to contain the fuel composed of strong magnetic fields. Traditionally these magnetic confinement fusion schemes have worked with very low fuel densities ($\sim 10^{14}$ cm^{-3}) and have attempted to achieve confinement times of the order of a second to satisfy the Lawson criterion. After two decades of intensive research, magnetic fusion research has reached the threshold of achieving the goal of scientific breakeven in which the Lawson criterion is satisfied, and the fusion energy produced by the fuel exceeds the energy necessary to heat and confine it.

Recently, however, scientists have become excited about an alternative approach to controlled thermonuclear fusion based upon inertial confinement. In this approach intense laser or charged particle beams would be used to rapidly compress a tiny pellet of deuterium-tritium fuel to enormous densities and temperatures and ignite a thermonuclear fusion reactor or burn. If the fuel pellet is compressed to sufficient densities, then it will burn so rapidly that appreciable fusion energy will be released before it can blow apart.

More precisely, the intense laser or charged particle beams (the "driver" beams) would strike the pellet surface, ionizing this surface and ablating it off into the vacuum surrounding the pellet. As the outer surface of the pellet blows away, an enormous pressure is generated (much as by a rocket exhaust) which would compress the core of the fuel pellet to densities as high as 1000 to 10,000 times solid state density. This compression would also raise the temperature of the core of the pellet to fusion temperatures so that a thermonuclear burn is ignited. This burn would then propagate outward through the rest of the fuel pellet, resulting in the explosive release of fusion energy. The process of compression and thermonuclear ignition and burn would occur in a time much shorter than the time required for the pellet to blow apart ($\sim 10^{-9}$ seconds). Hence a premium is placed on developing driver beams capable of delivering large quantities of energy onto tiny targets (roughly 1 mm in diameter) in a very short pulse ($\sim 10^{-9}$ seconds).

In a sense, the inertial confinement approach to controlled fusion represents a scaling down of the hydrogen bomb over a million fold to a tiny micro-explosion. For a brief instant, the driver beams compress the fuel pellet in such a way as to produce conditions similar to those found in stars. A tiny sun is produced which bursts in an instant, releasing its fusion energy. If we can capture this energy, then we can convert it to useful purposes.

Inertial confinement fusion can be regarded as essentially the internal combusion approach to fusion. To make the analogy more precise, recall that the internal combustion engine of your car is based on a four-stage combustion cycle: (1) injection of fuel (gas and air) into the cylinder, (2) compression of the fuel mixture by a piston, (3) ignition of the compressed fuel by a spark plug, and (4) combustion of the fuel mixture in a small explosion that drives the piston and hence the crankshaft (converting chemical energy into mechanical energy).

In direct analogy, inertial confinement fusion schemes are based on the following sequence: (1) a tiny pellet of deuterium-tritium isotopes is injected into a blast chamber, (2) the pellet is compressed to very high density with intense laser or charged particle beams, (3) the high density and compression heat induces the ingition of a thermo-

nuclear reaction, (4) the thermonuclear energy carried by the reaction products including neutrons, X rays, and charged particles is deposited as heat in a blanket that then acts as a heat source in a steam thermal cycle that produces electricity (conversion of nuclear energy into electric energy). The laser fusion internal combustion engine would use series of microthermonuclear explosions (from 1 to 100 per second, each generating the energy equivalent of several kilograms of high explosive) to generate power.

The applications of inertial confinement fusion (ICF) fall into several catagories: power production, weapons applications, and fundamental physics studies. Much of the funding for research activities in this area has been stimulated by the recognition that the environment created by the implosion and thermonuclear burn of a tiny fuel pellet is similar in many respects to that of a thermonuclear weapon. Hence there has been considerable interest in using ICF targets to simulate weapons physics and effects on a microscopic scale.

Perhaps the most immediate application of ICF will be in basic physics studies. The imploded ICF pellet produces conditions of temperature and pressure which are quite unusual (at least on a terrestrial scale). ICF implosions can be used to study properties of matter under extreme conditions, the interaction of intense radiation with matter, and aspects of low energy nuclear physics. Indeed, ICF presents us with a unique opportunity to study certain aspects of astrophysics such as steller interiors on a laboratory scale.

But the most significant application of inertial confinement fusion will be to the production of energy which can then be used for a variety of purposes such as the generation of electricity, the production of process heat or synthetic fuels, or propulsion. The importance of this application becomes apparent when it is recognized that there are only three major inexhaustible energy source options available to our civilization: the nuclear fission breeder reactor, solar energy, and nuclear fusion. Serious social and political questions threaten to stall breeder reactor development. Solar energy faces enormous challenges of a technical and economic nature. Hence the importance of

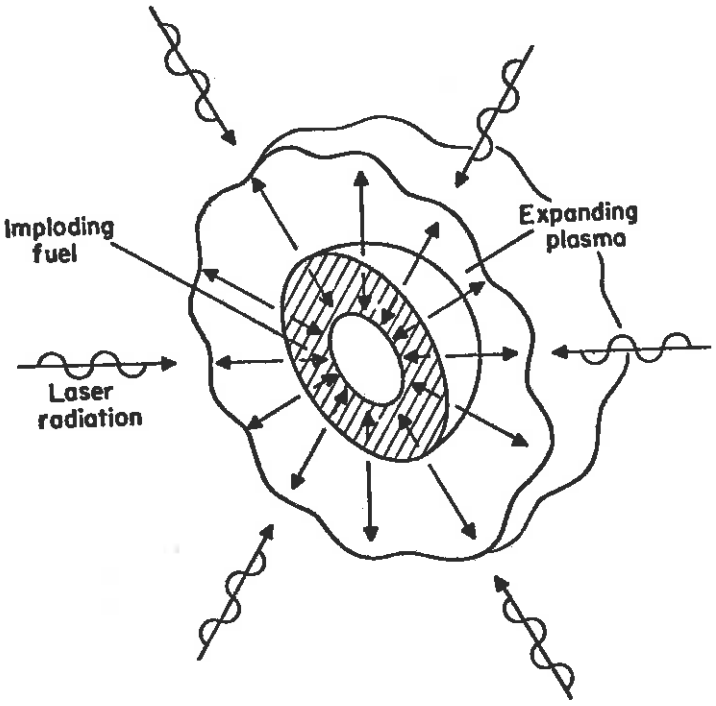

Cut-away view of a DT fuel pellet during laser heating.

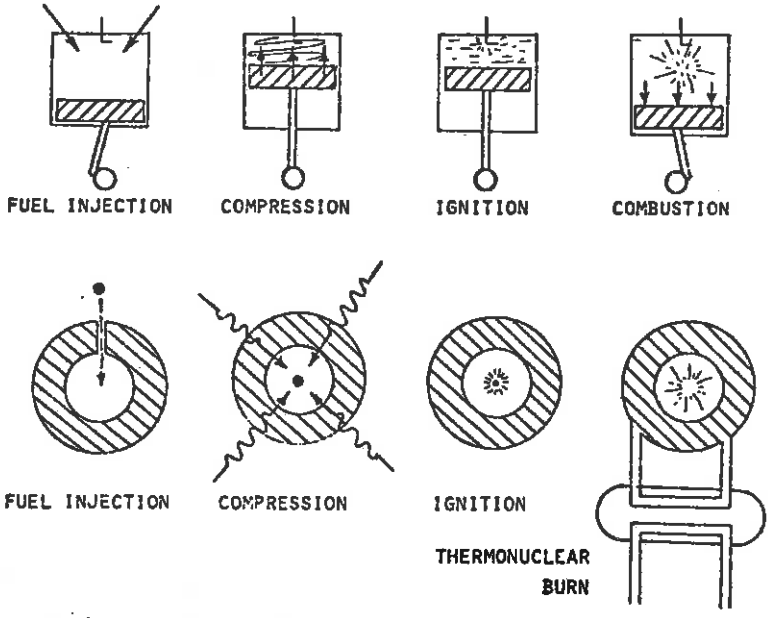

A comparison of internal combustion engines: the top sequence for a gasoline engine of an automobile, the bottom sequence for a laser fusion reactor.

an aggressive nuclear fusion research effort appears evident.

On a more philosophical level, inertial confinement fusion is, in fact, both the present and future source of energy in our universe. All other energy sources, whether they be solar, geothermal, wind, or biomass, are merely derivatives. In truth, only inertial confinement fusion is an unlimited energy source (at least on the time scale of our universe).

Controlled thermonuclear fusion in general, and inertial confinement fusion in particular, present man with a staggering technological challenge. But the potential benefit to mankind of a truly unlimited energy source compels us to address this challenge with a dedicated effort.

1.1. BASIC CONCEPTS

The basic requirements of the fusion game involve heating a plasma fuel (e.g., D-T or D-D) to thermonuclear temperatures (approximately 10 keV) and then confining this high temperature fuel for a sufficiently long time that it produces more fusion energy than the energy invested in its heating and confinement. The scoreboard for this game is the Lawson criterion which demands a certain minimum value of the product of number density n and confinement time τ --for example, the "scientific feasibility" criterion for a D-T fuel is $n\tau > 10^{14}$ s cm^{-3}. As we have noted, the traditional fusion approach has been to attempt to confine a very low density plasma fuel (at $n \sim 10^{14}$ cm^{-3}) for a relatively long time ($\tau \sim 1$ s) in a suitably shaped magnetic field (e.g., toroidal fields such as in the Tokamak).

The inertial confinement scheme takes the opposite approach. One attempts to heat a dense fuel to thermonuclear temperatures extremely rapidly so that an appreciable thermonuclear reaction energy will be generated before the fuel blows itself apart. To see what we are up against, consider a small pellet of radius 1 mm. The "disassembly time" τ_d required for the heated pellet to blow itself apart is roughly just the time required for a sound wave to traverse the pellet. Since

the speed of sound in a 10 keV D-T plasma is roughly 10^8 cm/s, the disassembly time $\tau_d \sim 0.1/10^8 = 10^{-9}$ s = 1 ns. Hence to satisfy the Lawson criterion, we must use a fuel density in excess of $n = 10^{14}/\tau_d = 10^{23}$ cm^{-3}--which is roughly solid state density.

Therefore the new game we must play in inertial confinement schemes is to heat a small, solid-density D-T pellet to thermonuclear temperatures before it has a chance to expand--that is, in 1 ns or 1 billionth of a second. Actually the energy required is not too great--roughly 1 million joules (1 MJ) or about 0.28 kwh--about the energy consumption of one evening's operation of your television set. But when this energy is delivered in 10^{-9} seconds, it corresponds to a power level of $10^6/10^{-9} = 10^{15}$ watts. The staggering demands of such a power level become apparent when it is noted that the present electrical generating capacity of all the power plants in the United States is a shade under 10^{12} watts.

Hence we are faced with generating enormous powers and focusing these down on a tiny pellet, roughly 1 mm in radius. But this is what a laser is good at. For not only can a laser focus large amounts of energy onto very tiny spots, it can also zap this energy in a very short time--easily within 1 ns (indeed, laser pulses as short as 10^{-12}s -- 1 trillionth of a second--have been achieved).

So if we use the laser just like a very big flashlight to zap the fuel pellet to fusion temperatures very rapidly, we can visualize that a laser fusion system might work something as shown below:

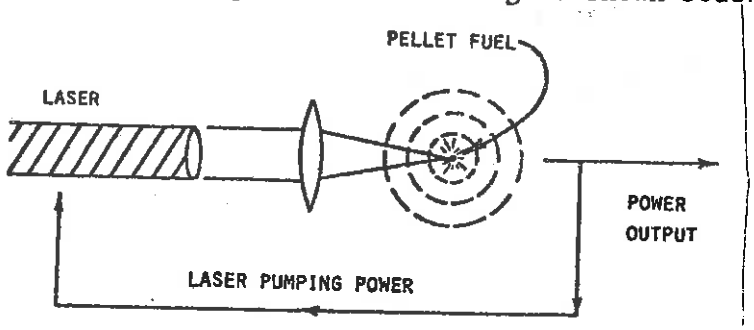

The laser light is focused on the pellet, heating it rapidly to thermonuclear temperatures and thereby inducing a thermonuclear microexplosion. The energy from this explosion is then captured and converted to electricity through a steam thermal cycle. After using part of this energy to re-energize the laser, the remaining energy is then distributed to the electrical power grid.

So far, so good! And this was essentially the "public image" presented by the laser fusion effort in the B,D.C, (before declassification) days prior to 1972, But this simple-minded scheme had a fatal flaw, which became apparent when one tried to estimate the elaser energy required to produce such a microexplosion,

Suppose (because of laser and thermal cycle inefficiencies) we require the thermonuclear energy produced by the pellet to be M times the incident laser energy, Suppose further that only a fraction ϵ_L of the incident laser light would be coupled into the target. Then we can factor these expressions into the Lawson criterion to make an estimate of the required laser energy for ICF as:

$$E_{laser} = \frac{M^3}{\epsilon_L^4}\left(\frac{n_s}{n}\right)^2 \times 10^6 \text{ joules}$$

where n_s is the number density for a solid (4.5×10^{22} cm^{-3} for D-T), let us now apply this estimate to calculate the laser energy required for scientific feasibility, that is, for M = 1, If we take $\epsilon_L = 1$ and $n = n_s$, we find a laser energy requirement of 10^7 joules, To place this number in perspective, the largest laser in the world today, the SHIVA laser at Livermore, produces a pulse of only 20 kJ--a thousand times too small. For a reactor, we would have to require M = 10 which implies a laser energy of 10^9 joules, hopeless large, Viewed in this light, laser fusion is clearly a fool's quest,

Or is it ? We mentioned that this was the "naive" or B,D,C, approach. We must be a bit more sophisticated in our analysis, Let us begin by re-examining the criterion for achieving net fusion energy release in a somewhat different light, We can identify two times of major significance for inertial confinement schemes: the disassembly time which scales as

$$\text{disassembly time} \equiv \tau_d \sim \frac{R}{c_s} \sim \frac{R}{T^{1/2}}$$

and the thermonuclear burn time

$$\text{burn time} \equiv \tau_b \sim \frac{1}{\rho \langle v \sigma_f \rangle} \sim \frac{1}{\rho T^{1/2}}$$

where R is the pellet radius, and ρ is its mass density, while we have noted that the speed of sound c_s and the fusion reaction frequency $\langle v \sigma_f \rangle$ are both proportional to $T^{1/2}$ in the temperature range of interest,

If we regard τ_b as a measure of the time required to burn a pellet of density ρ, and τ_d as the time during which the thermonuclear reaction will occur, then evidently we find that the "thermonuclear burn efficiency" is just the ratio of these two times,

$$\epsilon_b \equiv \text{thermonuclear burn efficiency} \equiv \frac{\tau_d}{\tau_b} \sim \rho R$$

If we reinsert the appropriate numerical constants, we find that an alternative to the Lawson criterion which is far more appropriate for inertial confinement schemes becomes

$$\rho R > 1 \quad g/cm^3$$

(Actually, if we are a bit more careful and take into account fuel depletion, we find that the burn efficiency becomes $\epsilon_b = \rho R/(6 + \rho R)$. Hence for $\rho R = 3$, roughly 1/3 of the pellet fuel would be burned.)

To understand the implications of this result, note that for a 1 mm pellet, $\rho R = 1$ implies a fuel density of $\rho = 10$ g/cm^3. But since the solid state density of D-T is only $\rho_s = 0.2$ g/cm^3, we find that this implies a compression of the pellet to at least 50 times itsinitial density. Hence the key to inertial confinement fusion is apparently high compression. The more we compress the fuel, the larger ρR becomes, and the more efficient the thermonuclear burn becomes. For example, a compression of 1000 would reduce our requirements for scientific breakeven to only 1 J and for a reactor to 1000 J. Actually, these simple scaling arguments are far too naive, but they do illustrate the strong dependence of required laser energy on the inverse square of the compression factor.

So the only remaining question is "how". How do we achieve such enormous compressions? Certainly not by normal mechanical forces. Nor will chemical explosives do the job (they are limited to compressions of roughly 10 by the strength of interatomic forces). Densities as large as 1000 times solid state density are not common even on an astronomical scale and occur only in very dense white dwarf stars.

The trick involves using the laser itself. The intense laser light is focussed by a number of beams onto the pellet surface (see Figure on the next page). As the pellet absorbes this intense light energy, its

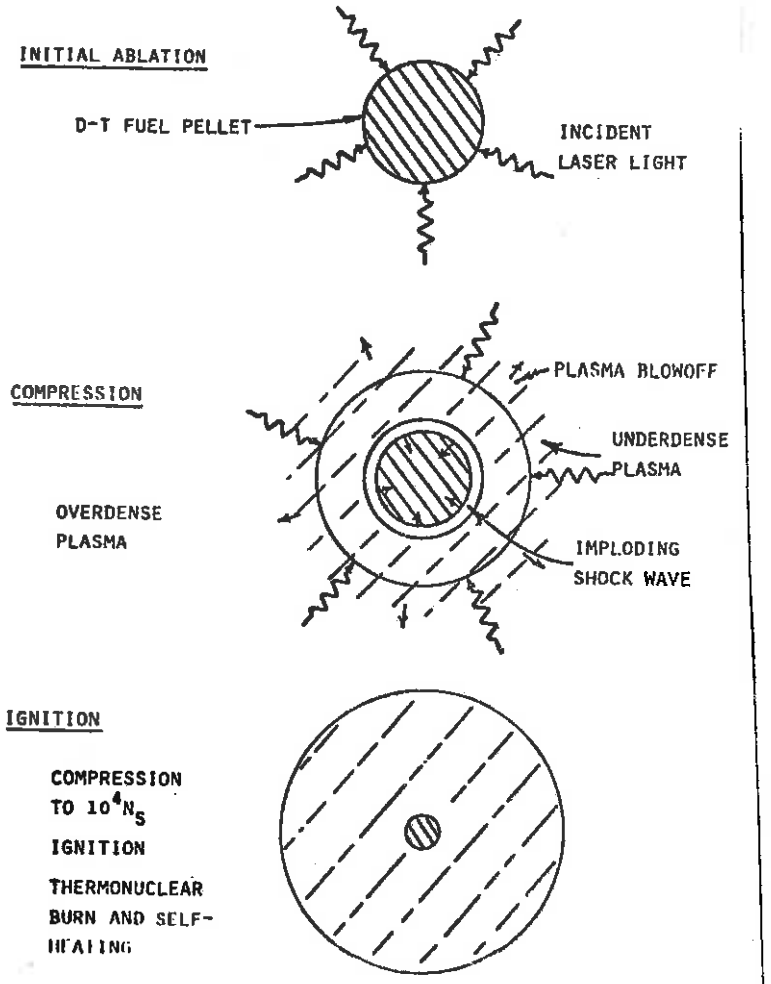

Laser compression of fuel pellet.

surface is rapidly vaporized, ionized, and heated to high temperature, blowing off into the vacuum surrounding the pellet. This blowoff or ablation of the pellet surface drives a shock wave back into the pellet (recall Newton's third law--or better yet, imagine the ablation as being comparable to the thrust from a rocket exhaust). As this shock wave implodes in toward the center of the pellet, it compresses the fuel to high density and thermonuclear temperatures so that ignition occurs. At these very high densities, the energetic alpha particles produced in the D-T fusion reactions are absorbed in the fuel, heating it to still higher temperatures and causing the fuel to burn even more rapidly. The thermonuclear burning propagates outward into the cold, compressed

fuel surrounding the ignited pellet core, consuming the fuel in a very rapid thermonuclear microexplosion. After only a few picoseconds, a significant fraction of the imploded pellet fuel has burned, and the very high energy release blows the pellet apart, thereby terminating the reaction.

Hence the key idea is to use the laser beam to bring the central region of the pellet to ignition densities and temperatures, but in such a way that the rest of the compressed fuel remains cold (so that the required compression energy is minimized). That is, one wishes to adiabatically or isentropically compress the fuel. Only a central "spark" is created in the compressed fuel to light the fusion fire. In this way, one lowers the laser energy requirements to 1000 to 10,000 J.

This simple picture is complicated somewhat by that fact that laser light cannot penetrate into a very dense plasma very far without being reflected. In fact, if the plasma density is above 10^{21} cm^{-3}, the incident laser light (from the Nd glass laser commonly used in ICF experiments) will not penetrate. Hence during the actual laser heating, a low density cloud or atmosphere ablates off and surrounds the pellet core, shielding it from direct laser radiation. The laser energy absorbed in this atmosphere or corona is then transported into the denser regions of the pellet by thermal conduction to drive the imploding shock wave.

Although this scheme sounds rather far-fetched, it has actually been demonstrated in laboratory experiments. In such experiments, laser beams are focused by specially designed mirrors onto the surface of tiny pellets consisting of glass shells (from 50 to 100 μm in diameter and 1-5 μm in thickness) containing D-T gas up to 100 atm in pressure. These glass microballoon targets have been compressed to fuel densities as high as 10 times solid state density. More advanced targets are being studied which utilize multiple layers of materials to provide for the efficient absorption of the incident light and energy matching in the implosion and thermonuclear explosion.

However the success of such experiments should not be interpreted as a demonstration of the scientific feasibility for laser fusion. Indeed, present estimates are that the achievement of $\rho R \gtrsim 1$ g/cm^3 will require

lasers operating at power levels in excess of 100 TW (10^{14} watts). For a laser fusion reactor, the requirements become even more severe, with $\rho R \gtrsim 3$ corresponding to lasers of 1 MJ and 1000 TW. Other laser requirements are tabulated below:

Energy: 1000 joules absorbed for breakeven → 10,000-joule laser 100,000- to 1,000,000-joule laser for a reactor
Focal spot size: 100 microns in diameter
Pulse length: 100 picoseconds (carefully shaped to within 10 picoseconds)
Repetition rate: 10 to 100 per second
Laser efficiency: 10% (or higher, if possible)
Laser wavelength: preferably in the range 0.3 to 0.8 microns (in the visible)

These goals present a very difficult challenge to high-powered laser technology. Such lasers typically consist of a source or oscillator which feeds light beams into a number of trains of successively more powerful laser amplifiers:

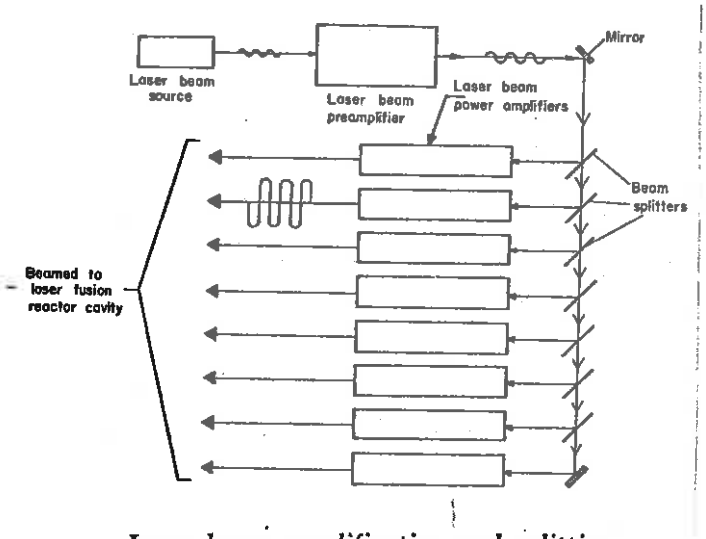

Laser beam amplification and splitting.

Large laser systems may consist of dozens of these beam lines and hundreds of amplifier stages.

Most high energy laser facilities designed for laser fusion research utilize large Nd glass lasers which emit infrared light at a wavelength of 1.06 μm. To date these lasers have been restricted by glass damage considerations to energies less than 1000 J per beam. Several laboratories in the United States and abroad have Nd laser systems operating or under development which approach 10 TW or greater

in power level. However since these lasers must be pumped using flashlamp techniques, they are intrinsically very inefficient (less than 0.1%) and therefore would not be suitable for any reactor design.

To achieve the high efficiencies and power levels required by reactor applications, it will probably be necessary to use gas lasers. For example, CO_2 lasers have been operated at efficiencies of several percent at high power levels. However they produce light at rather long wavelengths for laser fusion applications (10.6 μm) and are more difficult to operate at very short pulse lengths than solid state lasers. Actually, the brand-X type laser which is most suited to laser fusion applications has not been developed yet, although several possible candidates have been identified as shown below:

Laser	Wavelength	Advantages	Disadvantages
CO_2	~ 10 μm	High energy High power Possibly acceptable efficiency Short pulse	Long wavelength High gain
Iodine	1.3 μm	High energy High power Short wavelength Short pulse	Low efficiency High gain
HF	~ 3 μm	High energy High efficiency	Long pulse High gain Poor energy storage
Oxygen, oxides	~ 0.55 μm	Short wavelength High energy High power Short pulse	Low efficiency to date
Excimers (Ar_2, Kr_2, Xe_2, ArF, KrF)	~ 0.20 μm	High power High energy High efficiency	Wavelength possibly too short for optics Long pulse
Excimers (NF, HG_2, HgCd)	~ 0.33-0.80 μm	Short wavelength High power High energy High efficiency	No experience Long pulse

There are several alternatives to using high-powered lasers as the piston to drive the pellet implosion. In particular, accelerator designs have been capable of producing extremely energetic electron or ion beams for some time now. Both electron and ion beams are quite efficient in converting an appreciable fraction of electrical energy

into beam energy (40% or better).

The most common type of charged particle accelerator is based on a pulsed diode. It consists basically of a high-voltage source that stores energy in capacitors and then switches into an insulated pulse-forming line and thence into a diode. Electrons are acclerated to the anode from a dense plasma which forms on the cathode surface. These electrons (or a corresponding beam of ions) can then be passed through a foil and focused onto a target. Such charged particle beams have been used to implode pellets to fusion conditions at Sandia Laboratory. Other accelerator designs which can produce intense beams of heavy ions are also being studied.

Let us leave the questions of just how such thermonuclear micro-explosions can be produced, and turn to a consideration of how such explosions can be used to produce useful energy in some kind of reactor device. In a typical design, the pellet implosion is assumed to yield some 10^8J (about 20 kg of high explosive worth of energy). If such explosions are repeated 30 times per second, then such a reactor would yield 3000 MWt of thermal power corresponding to a steam thermal cycle electricity output of 1000 MWe.

The thermonuclear explosion energy appears as various types of radiation emitted from the exploding pellet. Typically some 75% of the energy will appear as fast, 14 MeV neutrons, 24% as energetic charged particles, and 1% as X-rays. Surprisingly enough, it is relatively easy to design a blast chamber than can withstand the force of such a blast. Rather the principal concern is the damage that the incident radiation can do to the chamber wall. However, by careful design, for example, by wetting the wall surface with a film of lithium to absorb the X-rays and charged particle debris, it should be possible to design a blast chamber to contain such pellet implosions.

Most of the explosion energy would be carried by fast neutrons, and therefore the blast chamber would be surrounded by a blanket--such as lithium--designed to absorb the neutron energy (and produce tritium for further refueling as well). This blanket could then be cooled using conventional techniques, and the heat withdrawn by a coolant would be used to produce steam for a turbogenerator.

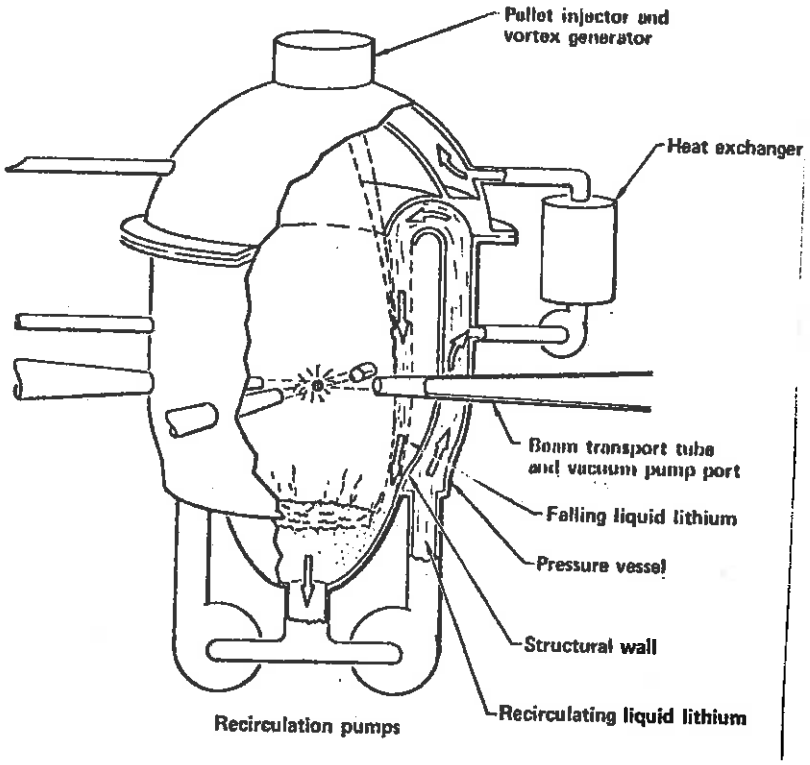

Since ICF systems should be capable of producing large quantities of neutrons, it has been suggested that alternative uses of these devices may be of interest. The neutrons might be used to convert fertile material (e.g., uranium U-238 or thorium) into fissile material (plutonium or U-233). Or perhaps the neutrons could be used to transmute long-lived radioactive waste into shorter-lived or stable isotopes. Yet another application would be to use the neutrons to radiolytically decompose water into hydrogen and oxygen, and then use the hydrogen in chemical processes to produce methant that can supplement our vanishing natural gas reserves.

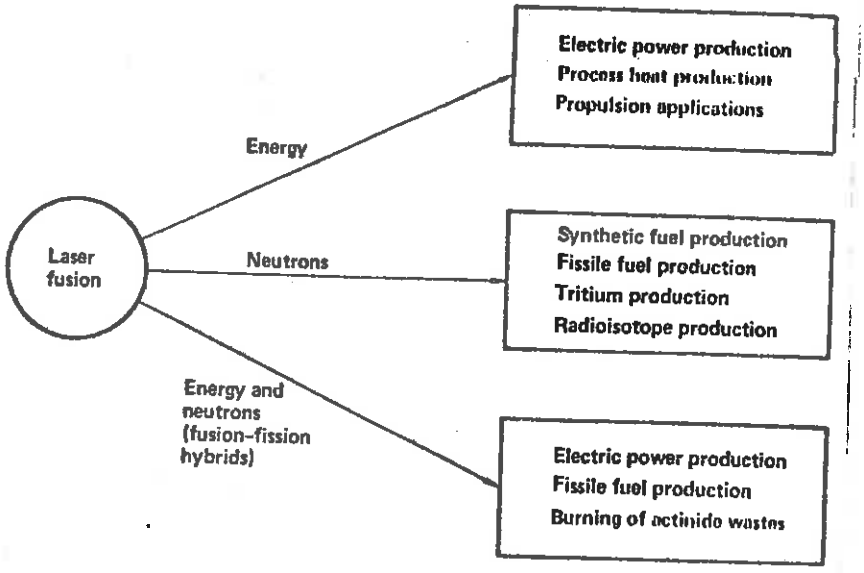

Whatever the application, it should be evident that the successful development of a viable laser (or electron or ion beam) fusion reactor is still many years down the road. Indeed, we are still several years away from the demonstration of scientific feasibility (just as we are with magnetic confinement fusion approaches).

1.2. HISTORICAL DEVELOPMENT

The roots of inertial confinement fusion might be traced back to Bethe's recognition in 1931 that nuclear fusion was a primary energy source in stars or perhaps to the development of the basic theory of thermonuclear fusion reactions by Teller, Fermi, Tuck, and others at Los Alamos during the 1940s. Actually, the foundation for ICF was laid many years earlier by the hydrodynamic analysis of spherical bubble implosions (cavitation) by Besant in 1859 and Rayleigh in 1917. Of particular interest was a self-similar solution to the problem of an imploding shock wave given by Guderley in 1942. These ideas were applied to the design of nuclear fission weapons by Neddemeyer, Von Neumann, Teller, Tuck, Christy, and others at Los Alamos during the days of the Manhattan Project. Moderately high compressions were achieved by using high explosives to drive spherical implosions. However, as we will demonstrate later, the maximum compressions that could be achieved using chemical explosives fall far short of those needed for ICF microexplosions.

As early as 1961, a Livermore scientist, John Nuckolls, realized that the powerful light beam of a pulsed laser could be used to achieve the energy densities necessary to produce very high compressions. His early calculations (based on the laser pellet coupling physics developed by Ray Kidder and Sterling Colgate) suggested that carefully tailored laser light pulses could produce ablatively-driven implosions of D-T pellets to compressions as high as 10,000 solid state density. Similar calculations were performed by others during the mid-1960s, including Kidder and Zabawski at Livermore, Dawson at Princeton, Lubin at the University of Rochester, Hertzberg, Daiber, and Wittliff at the Cornell Aeronautical Laboratory, Brueckner at the University of

California, and by scientists at Los Alamos.

The calculations of Nuckolls and Kidder motivated the initiation of a highly classified experimental laser fusion program at Livermore, By the mid-1960s Kidder and Mead had constructed a twelve-beam ruby laser system to test the implosion calculations.

Experimental and theoretical analysis of laser drive fusion continued to appear, both within the classified weapons program and the open literature. Of particular note was the experimental work of Moshe Lubin at Rochester, Alan Haught at United Aircraft, and Nikoli Basov at the Lebedev Institute in Moscow, The Russian group reported the first indicationof laser produced fusion temperatures and neutrons in the late 1960s. Nuckolls and his colleagues continued to develop the theory of laser driven implosions under the cloak of security classification at Livermore. These calculations suggested that adiabatic implosions might yield scientific breakeven at one kJ of laser energy.

In 1972 the first major declassification of the implosion scheme occurred. Stimulated by references in the Russian literature suggesting ICF implosions to super high density, Brueckner at KMS, Fusion, Nuckolls and colleagues at Livermore, and Clarke, et. al. at Los Alamos simultaneously presented papers detailing the concept of using ablatively driven compression to produce implosions to superhigh density in D-T pellets.

The first major experimental results involve the implosion of a 100 μm diameter CD_2 micro sphere with a few hundred joule, 9 beam laser system by Basov's group at the Levedev Institute. This experiment yielded roughly 3×10^6 neutrons.

A second major milestone was achieve in 1974 when KMS Fusion irradiated D-T gas filled glass targets using a two beam laser system capable of roughly 100 joules and achieved compressions of roughly 100 over gas fill density. The 10^4 neutrons produced in these experiments were verified to be of fusion origin. Although only a few hundred ergs of energy were released in these implosions, a Lawson number of roughly 2×10^{12} and a D-T fuel temperature of 1 keV were achieved. By late 1974 KMS scientists were routinely producing pellet implosions

yielding 10^6 to 10^7 neutrons per shot. In December of that year, Livermore began similar experiments on their JANUS laser system using a single beam at a power level of 0.2 TW. Subsequent experiments on the two beam, 0.4 TW JANUS system increased neutron yields by several orders of magnitude during 1975. The 4 TW, two beam ARGUS laser system increased neutron yields to 10^9 - 10^{10} and ion temperatures to 10 keV by 1976.

These early experiments were performed with DT gas-filled glass microballoons which behaved in an exploding pusher mode. That is, the glass shell was heated and exploded by electron conduction from the laser heated plasma surrounding the target. The inward moving shell or pusher acted as a piston which compressed the DT gas to nearly the original pusher density ($\sim$1 g/cm^3) and produced high ion temperatures. However it rapidly became apparent that this type of target could never achieve the fusion energy gains needed for breakeven performance (see Figure on the next page). Rather, the experiments would have to be redirected toward laser pulses and targets which were suited to the isentropic compression required for very high fuel compressions.

In 1976 the first experiments were begun on the ARGUS system with ablative targets in order to produce high fuel density (although at low fuel temperatures). By 1978 with ARGUS operating at 2 kJ, Livermore had achieved 10 x liquid density and by 1979 had announced compressions of as high as 100 using the 10 kJ SHIVA laser system. The fuel temperatures in these fuel compressions were kept low (approximately 0.5 keV) to maximize fuel compression and provide only sufficient number of thermonuclear reactions for diagnostic purposes.

The CO_2 laser program at Los Alamos experienced a similar success. By early 1977 implosions to fusion conditions were produced using the Two-Beam CO_2 laser system. In 1978 the 10 kJ Helios system came on line, and experiments with ablatively driven targets were begun. Compressions as high as 30 have been reported to date.

Electron and ion beam driven ICF experiments were conducted on the Proto I and Proto II diode accelerators at Sandia Laboratory, and once again fusion neutrons were measured.

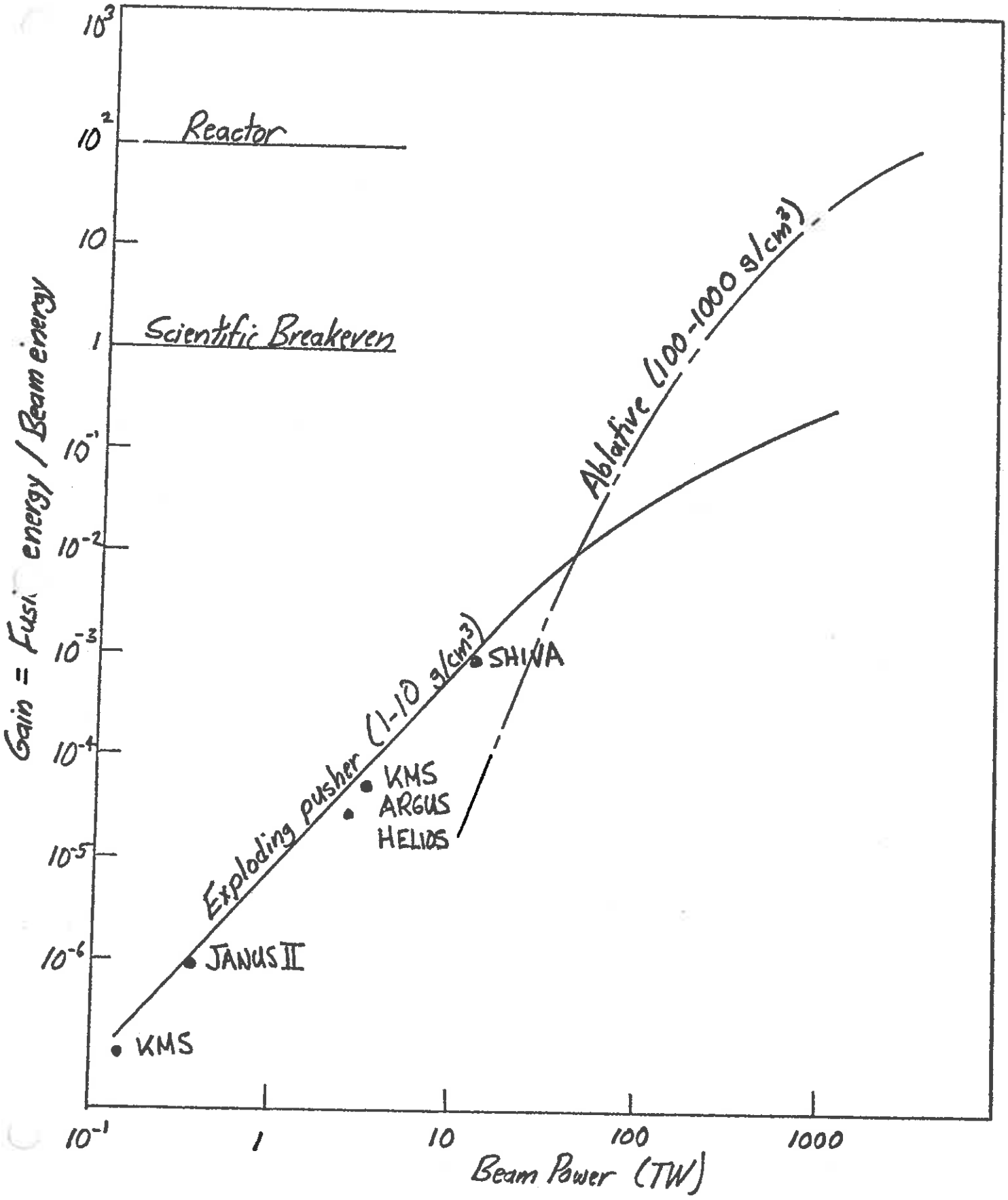
Gain = Fusion energy / Beam energy
10^3
10^2
Reactor
10
1
Scientific Breakeven
10^{-1}
10^{-2}
10^{-3}
10^{-4}
10^{-5}
10^{-6}
Ablative (100-1000 g/cm³)
Exploding pusher (1-10 g/cm³)
SHIVA
KMS
ARGUS
HELIOS
JANUS II
KMS
10^{-1}
1
10
100
1000
Beam Power (TW)

Other large laser systems are now coming on line, both in the United States (University of Rochester Laboratory for Laser Energetics) and elsewhere (Lebedev Institute, Institute for Laser Engineering at Osaka University). Both Livermore and Los Alamos have under development large 100 kJ, 100 TW laser systems (Nova and Antares, respectively). Sandia Laboratory's Particle Beam Fusion Accelerator (PBFA) is also scheduled for operation at the 100 TW level within the next year.

The next step in the experimental programs is to achieve greater than 1000 x liquid density coupled with the production of fusion temperatures to initiate thermonuclear burn. Scientific breakeven experiments are projected for the mid-1980s at several laboratories.

1.3. STATUS

Several laboratories have imploded D-T targets to high density with lasers operating in the 10 kJ, 10 to 20 TW range. Most of these experiments have used exploding pusher pellets based on simple glass microballoons filled with DT gas at high pressure. These targets have the advantage that they can yield relatively large numbers of neutrons (because of the high ion temperatures produced in the nonadiabatic implosion) with moderate scale drivers.

Unfortunately, exploding pusher target experiments do not address the main technical questions of high compression implosions necessary for appreciable gain. While thermonuclear ignition could be obtained with a sufficiently large exploding pusher pellet, the energy required to drive such a pellet is beyond the capabilities of any projected driver. Thus experiments have turned instead to ablative targets in which the fuel is compressed to high density at relatively low temperatures (adiabatic compression). This requires careful driver pulse shaping, minimizing preheat, and extremely symmetric implosions.

Four laboratories in the United States (LLL, LASL, KMS, and LLE) have performedhigh density implosion experiments achieving compressions of from 1 to 100 times liquid DT density (LD), 0,2 g/cm^3. These measurements are compared in the Figure on the next page.

Both the KMS and LLE experiments have been performed with modest

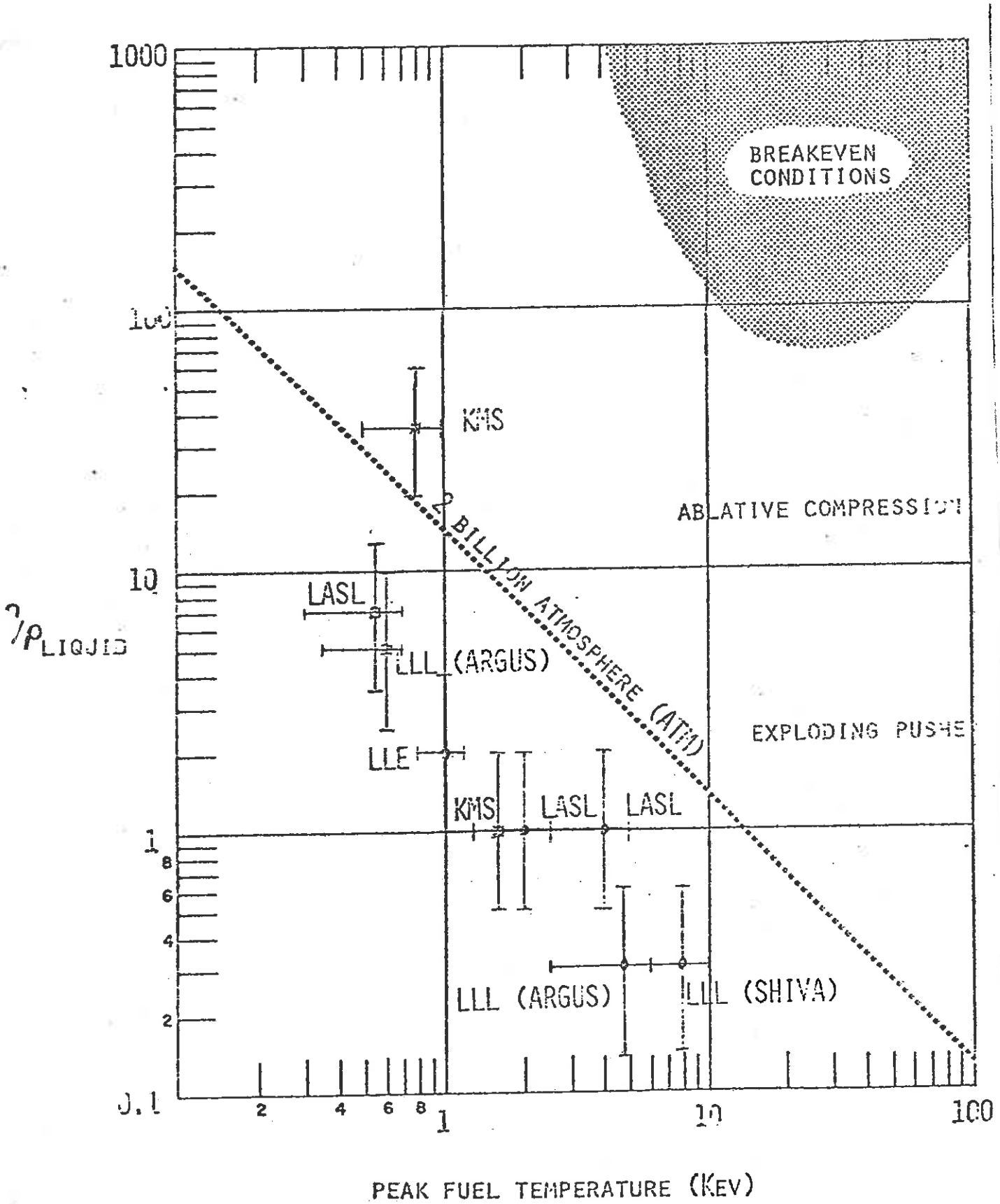
1000
100
10
1
.8
.6
.4
.2
.1
2
4
6
8
1
10
100
BREAKEVEN CONDITIONS
ABLATIVE COMPRESSION
EXPLODING PUSHER
2 BILLION ATMOSPHERE (ATM)
KMS
LASL
LLL (ARGUS)
LLE
KMS
LASL
LASL
LLL (ARGUS)
LLL (SHIVA)
ρ/ρLIQUID
PEAK FUEL TEMPERATURE (KEV)

LASER FUSION — PROGRESS PROJECTIONS

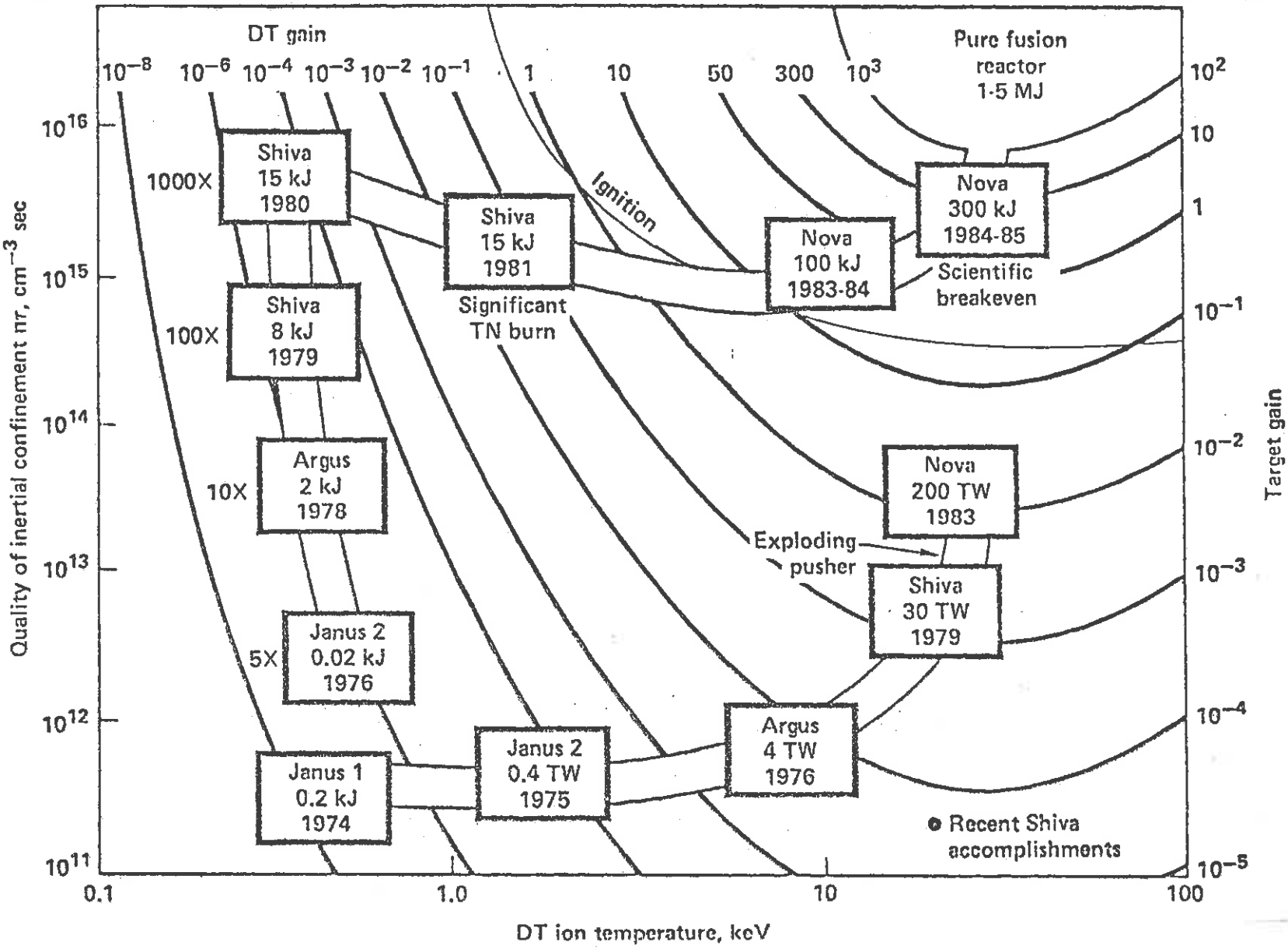

energy (100 J or less), but taking great care to achieve spherically symmetric target illumination. The KMS experiments have used glass microballoon targets filled with DT gas which is then solidified into a thin shell using cryogenic methods. Compressions of up to 35 times LD have been achieved. LLE has also used glass microballoons as targets with their 4-beam DELTA system to obtain compressions of several times LD.

Los Alamos results have been achieved by irradiations of plastic coated glass microballoons using the 8 beam HELIOS CO_2 laser system operating at 2300 joules (1 ns pulse width). Livermore has used both the ARGUS and SHIVA laser systems to irradiate ablative targets (of a classified design) to obtain the compressions noted in the Figure on the next page.

Such experiments demonstrate that spherically symmetric implosions to high density can be achieved and provide confidence for future experiments on larger 100 TW laser systems designed to initiate thermonuclear burn. On a longer range basis, several laser systems are being proposed for the 300-500 TW level felt to be necessary to achieve scientific breakeven by the mid-1980s. Based on these experiments, more detailed plans can be made for the high gain experiments necessary for reactor applications.

1.4. A ROADMAP OF THE LECTURE NOTES

These notes are intended to serve as an introduction to inertial confinement fusion. In any such field which is as yet so far removed from practical applications, there are a great many uncertainties that tend to influence a choice of topics. Primary among these is a choice of ICF driver. Although early investigations have emphasized laser fusion, more recent efforts have shifted some attention to particle beams (relativistic electron beams, light ion beams, and heavy ion beams). We have chosen to deal with the uncertainty surrounding a final choice of driver by keeping the first half of the notes as general as possible, describing inertial confinement fusion physics in

FUEL DENSITY AT BURN TIME VERSUS NEUTRON YIELD

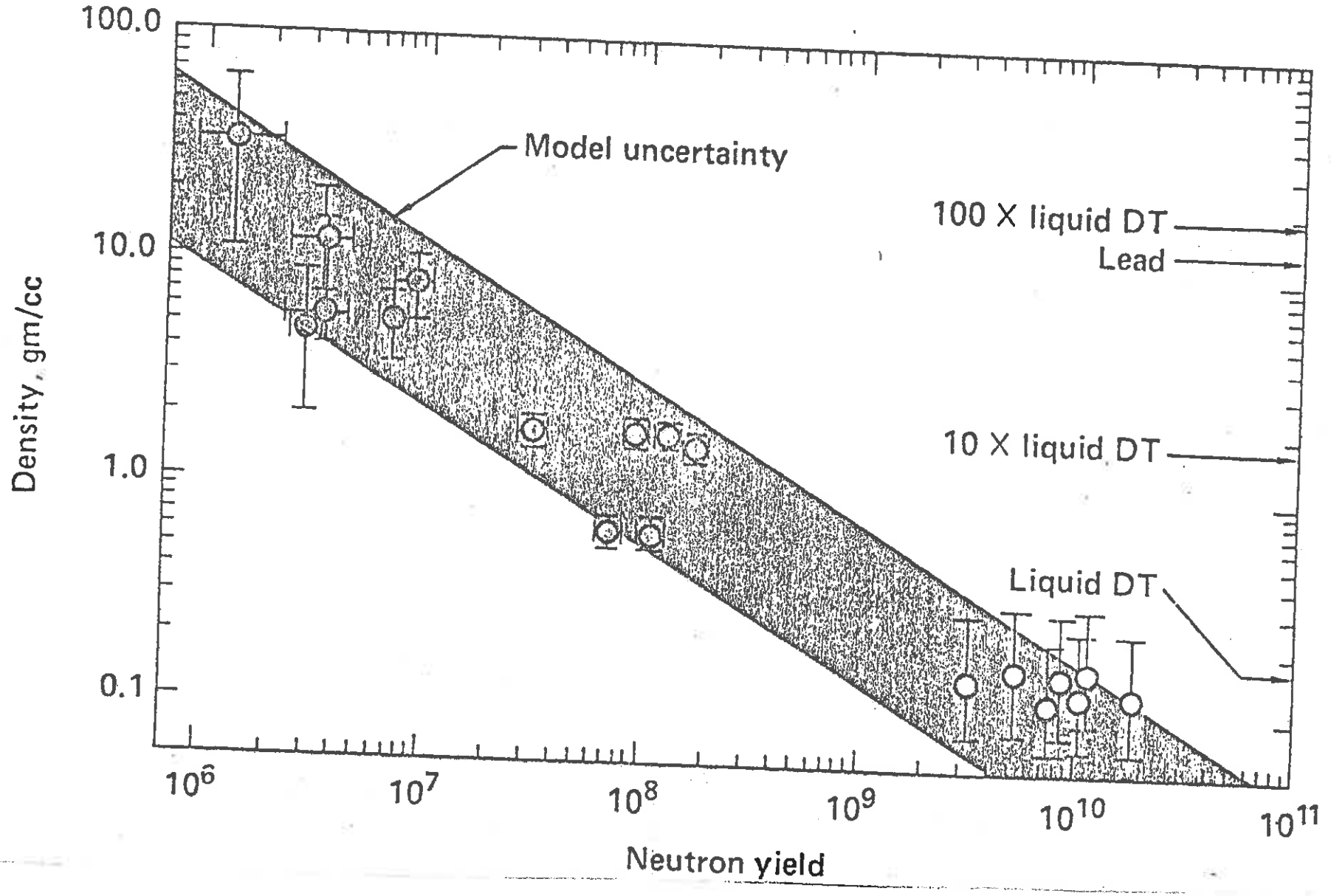

NEAR-TERM PROGRAM MILESTONES

Laser Fusion -

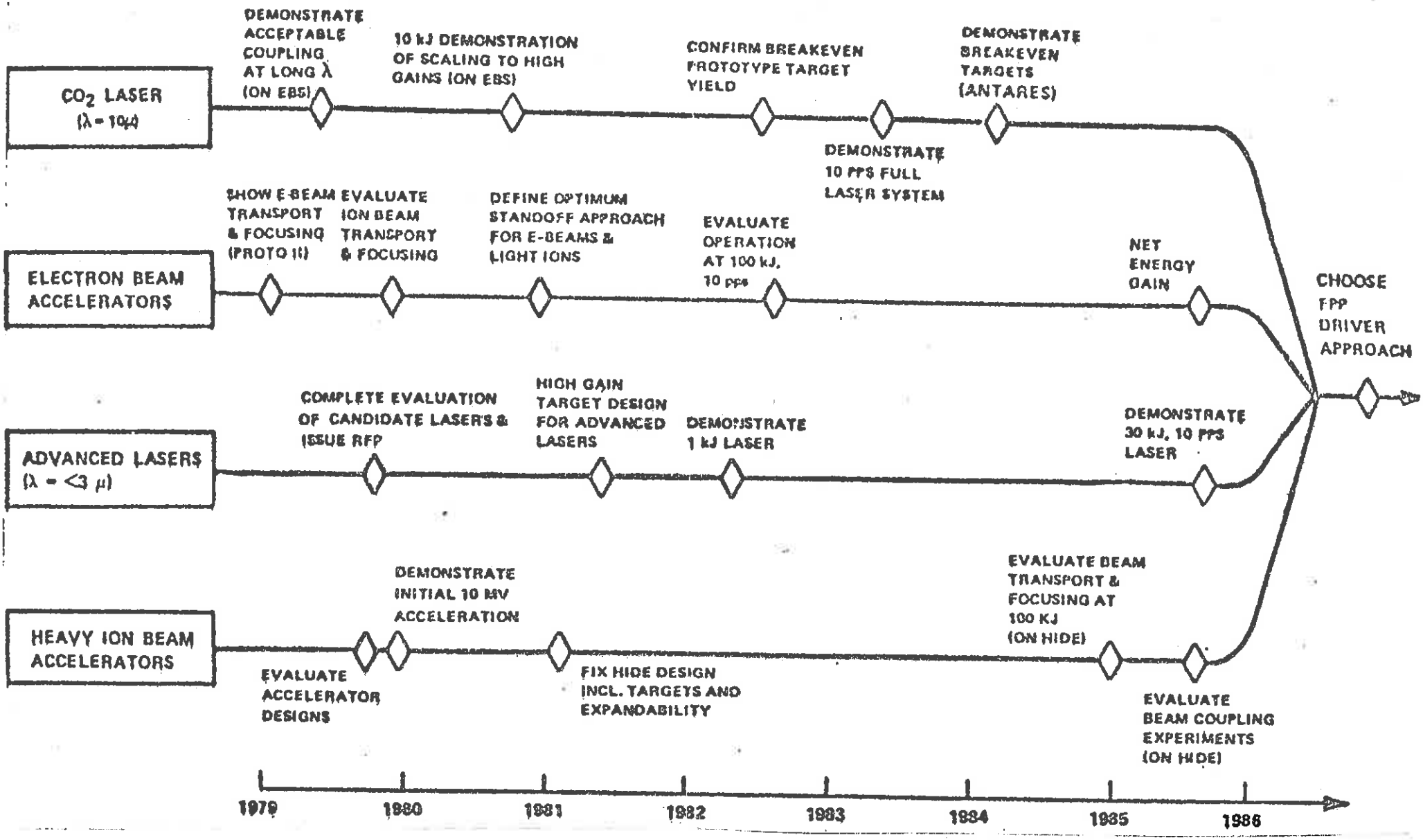

in a manner independent of driver type.

A second uncertainty is somewhat more difficult to deal with. This concerns the mists of security classification which tend to veil certain aspects of ICF physics because of their presumed similarity to nuclear weapons physics. Fortunately, the classification shround is rather narrow and appears to involve only certain aspects of ICF target design. Hence 99% of the physics of inertial confinement fusion, including the details of driver design, driver energy deposition, energy transport and hydrodynamics of ICF targets, and most aspects of ICF target design have appeared in the open literature and will be discussed in these notes.

In line with our effort to keep our development of ICF concepts as independent of driver type as possible, we will adopt a pedagogy of working backwards, from the details of inertially confined thermonuclear burn, to hydrodynamic implosions and compression, to energy transport in dense plasmas, and finally to a detailed consideration of driver energy deposition in the target. It is only at this last stage that we will need to introduce particular details of driver types. We will devote particular attention to the theoretical, computational, and experimental tools used to analyze ICF targets.

We then turn our attention to ICF drivers and consider laser and particle beam drivers in detail. Here we not only discuss present driver types, but attempt to look ahead at possible drivers for various applications.

Our final topic concerns applications of ICF. After a brief discussion of ICF target design, we turn to a detailed discussion of applications, with particular attention devoted to power production (including the production of process heat and synthetic fuels).

CHAPTER 2

INERTIALLY CONFINED THERMONUCLEAR FUSION REACTIONS

2.1. FUSION REACTION PHYSICS

We will be most interested in the D-T fusion reaction

$$D + T \rightarrow \alpha + n + W, \qquad W = 17.6 \text{ MeV}$$

where the reaction energy is partitioned with 3.5 MeV to the α and 14.1 MeV to the neutron. The cross section for this reaction has a resonance near zero energy. When the Coulomb barrier is included, the cross section reaches a peak of 5 b at 125 keV. This yields an appreciable reaction rate at several keV. The cross section can be modeled by the Gamow form:

$$\sigma(E_{rel}) = \frac{A}{E_{rel}} \exp\left[-B/\sqrt{E_{rel}}\right], \quad E_{rel} = \tfrac{1}{2}\mu v_{rel}^2$$

The next most probable reaction is the D-D fusion reaction

$$D + D \xrightarrow{50\%} {}^3He + n + 3.3 \text{ MeV}$$
$$D + D \xrightarrow{50\%} T + p + 4.0 \text{ MeV}$$

This reaction is accompanied by a side reaction among products:

$$D + {}^3He \rightarrow \alpha + p + 18.3 \text{ MeV}$$

The basic structure of the Maxwellian averaged reaction rates for these reactions is provided in Figure 2.1. It should be noted from this figure that the D-T reaction is favored over D-D reactions by almost two orders of magnitude for temperatures below 10 keV.

Figure 2.1

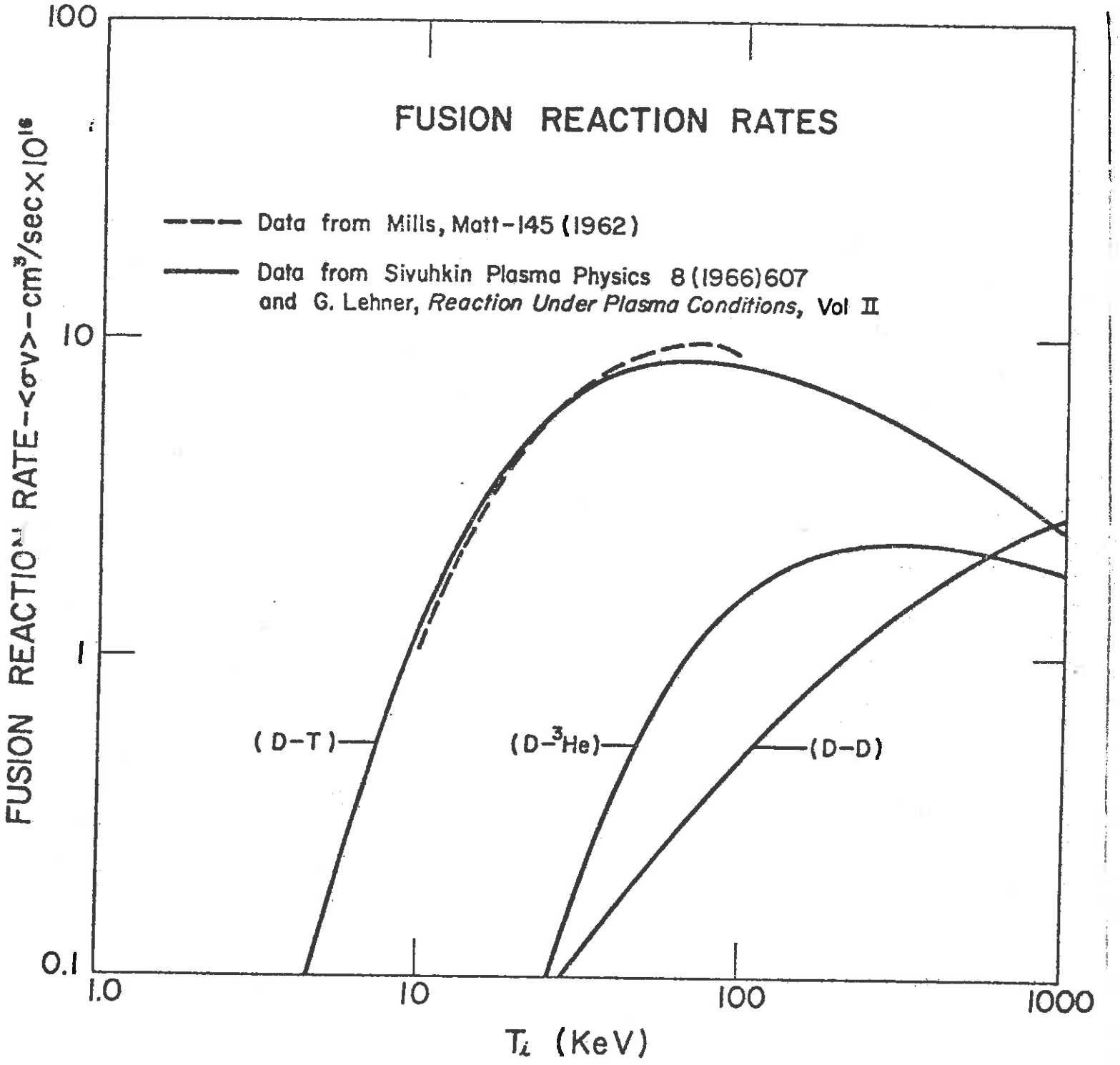
FUSION REACTION RATES
Data from Mills, Matt-145 (1962)
Data from Sivuhkin Plasma Physics 8 (1966)607
and G. Lehner, Reaction Under Plasma Conditions, Vol II
FUSION REACTION RATE-<σv>-cm³/sec×10¹⁶
100
10
1
0.1
(D-T)
(D-³He)
(D-D)
1.0
10
100
1000
Ti (KeV)

We can write down the rate equations for a D-T fuel mixture as

$$\frac{dn_D}{dt} = -n_D n_T \langle v\sigma \rangle_{DT} - n_D n_D \langle v\sigma \rangle_{DD}$$

$$\frac{dn_T}{dt} = -n_D n_T \langle v\sigma \rangle_{DT}$$

Since the D-D reaction produces one T for every two fusion reactions, one might expect that the equation for n_T should also contain a source term of the form $+ n_D\, n_D \langle v\, \sigma \rangle_{DD}$. However here we must remember that the T ion appears with an energy of roughly 1 MeV. Therefore it is not in thermal equilibrium with the tritium fuel, and its contribution to the reaction rate must be treated separately (in effect, as a "beam-plasma" interaction with an enhanced reaction rate).

We should also note that if the fuel can be brought to conditions where the D-D reaction will contribute, then the products D and ^{3}He will react promptly with the D nuclei, yielding an overall energy release per unit burned mass which is the same as that for the D-T reaction, namely 3.5 MeV per nucleon.

2.2. THERMONUCLEAR FUSION REACTION CRITERIA

Lawson Criterion

The usual Lawson criterion for a thermonuclear fuel is given by balancing the fusion energy release against the energy investment in bring the fuel to thermonuclear temperatures and the energy lost through radiation (both bremsstrahlung and cyclotron):

$$E_{fusion} = E_{thermal} + E_{rad}$$

The fusion energy released is given in terms of the fusion reaction rate and the time characterizing the reaction, the confinement time τ:

$$E_{fusion} = n_D n_T \langle v\sigma \rangle W \tau = \frac{n^2}{4} \langle v\sigma \rangle W \tau$$

where we have assumed equi-molar concentrations of D and T so that

$$n_D = n_T = \frac{n}{2}$$

where n is the ion number density. The thermal energy is then

$$E_{thermal} = \frac{3}{2} n k T_i + \frac{3}{2} n k T_e = 3 n k T$$

where we have assumed $T_i = T_e$ for convenience. We will ignore the radiation energy loss for now

$$E_{rad} \sim 0$$

noting that if the fuel temperature is greater than 4 keV, the fusion energy release will exceed the bremsstrahlung radiation loss. In inertial confinement schemes, the thermonuclear burn typically occurs at 20 to 100 keV. Furthermore in such schemes, magnetic field effects can be ignored to first order so that cyclotron radiation is of no concern.

If we now balance the fusion energy release against the thermal energy,

$$\frac{n^2}{4} \langle v\sigma \rangle W \tau = 3 n k T$$

we can solve for a condition on the density times the time of confinement

$$n\tau = \frac{12 kT}{\langle v\sigma \rangle W}$$

When the reaction rate is evaluated at suitable temperatures (10 keV for D-T, 100 keV for D-D), this yields the usual Lawson criteria:

$$n \tau > 10^{14} \quad \text{for D-T reactions}$$

$$n \tau > 10^{16} \quad \text{for D-D reactions}$$

Criteria for Efficient Inertial Confinement Fusion: The "ρR" Criterion

The basic concept of inertial confinement fusion is to implode the fuel to very high densities so that the time characterizing thermonuclear reactions becomes shorter than the inertial confinement time (the fuel pellet disassembly time).

The most meaningful figure of merit for ICF plasmas is the product of the fuel density ρ and radius R, rather than the customary density-confinement time nτ product considered by the Lawson criterion. To understand this, suppose we estimate the fuel dissassembly time as the pellet radius R divided by the speed of sound (essentially the time required for a density disturbance to propagate from the surface of the pellet into the center):

$$\text{fuel dissassembly time} = \tau_d = \frac{R}{c_s}$$

In a similar fashion, we can estimate the thermonuclear reaction time as the inverse of the reaction rate:

$$\text{thermonuclear reaction time} = \tau_b = [(\rho/m_i)\langle v\sigma_f\rangle]^{-1}$$

Thus a crude estimate of the efficiency of thermonuclear burn is given by the ratio of these times:

$$f_b \sim \frac{\tau_d}{\tau_b} = \frac{\langle v\sigma\rangle}{m_i c_s}\rho R = \text{thermonuclear burn fraction}$$

where we have introduce the thermonuclear burn fraction f_b defined as the fraction of the fuel consumed in the reaction. (We will develop a slightly more accurate expression for f_b which accounts for fuel depletion later in this section.)

We now recall that

$$c_s = [kT/m_i]^{1/2} \sim \sqrt{T}$$

Furthermore, for DT fuel at efficient burn temperatures (20 keV),

$$\langle v\sigma\rangle \sim \sqrt{T}$$

In fact, if we plug in the numbers for DT fuel at 20 keV, we find

$$\frac{\langle v\sigma \rangle}{m_i c_s} \sim \text{constant} \sim 1$$

Thus we find that

$$\text{thermonuclear burn efficiency} \equiv f_b \sim \rho R \ \text{g/cm}^2$$

Hence the criterion characterizing efficient inertial confinement fusion is apparently

$$\rho R \sim 1$$

The product of density times radius is important for other reasons. To sustain the thermonuclear burn, some of the fusion energy must be redeposited in the pellet. For the case of DT reactions:

$$D + T \rightarrow \alpha \ (3.5 \text{ MeV}) + n \ (14.1 \text{ MeV})$$

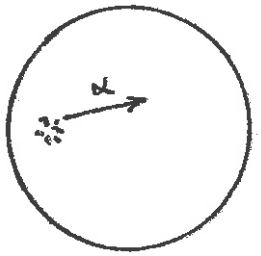

To capture the energy of the 3.5 MeV α, the fuel size must exceed the range of the α. But the range of a 3.5 MeV α in 20 keV DT plasma is about 0.5 g/cm^3. Hence if

$$\rho R > 0.5$$

then the α energy will be deposited in the fuel, and efficient self-heating will occur.

Perhaps a somewhat different perspective of the importance of the ρR product is useful. The most important processes in fusion reactions are binary collisions. Examples include the fusion reactions themselves as well as the collisions which lead to α slowing down and energy deposition (self-heating). Hence if somehow we could increase density by a factor of 10^3, we could increase the collision rate by 10^6.

More precisely, one can scale

$$\left.\begin{array}{l}\text{rate of thermonuclear burn} \\ \text{energy deposition by charged particles} \\ \text{electron-ion energy exchange}\end{array}\right\} \sim \rho$$

But we have found that

$$\text{inertial confinement time} \sim R$$

Hence we can scale

$$\left.\begin{array}{l}\text{thermonuclear burn efficiency}\\ \text{self heating}\\ \text{burn propagation}\end{array}\right\} \sim \rho R$$

We will demonstrate later that the optimum value of R is about 3 g/cm^2 for DT fuels. Hence, for inertial confinement fusion in DT fuel, we replace the usual Lawson criterion

$$n\tau \gtrsim 10^{14} \text{ sec/cm}^3$$

by the new goal

$$\rho R \gtrsim 3 \text{ g/cm}^2$$

Relationship between the ρR and $n\tau$ Criteria

We can easily relate the Lawson criteria and the ICF ρR criteria. First we recall that for a freely expanding sphere of radius R, density

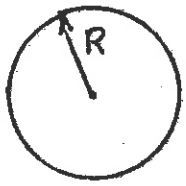

$$\tau \sim \frac{R}{4c_s}, \quad n = \frac{\rho}{m_i}$$

(Here we are using a slightly more accurate estimate of the inertial confinement time τ_d which takes account of the fact that in a sphere, half of the mass is beyond 80% of the radius. Hence we have adjusted the inertial confinement time accordingly:

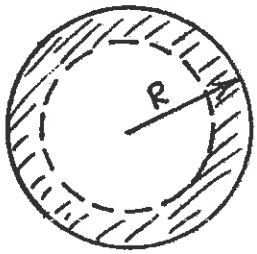

$$\tau_d \sim \frac{R}{c_s} \rightarrow \frac{R}{4c_s}$$

Hence we can compute

$$n\tau = \frac{\rho R}{4 C_s}$$

If we plug in the numbers, we find that

$$\rho R = 3 \text{ g/cm}^2 \quad \Longrightarrow \quad n\tau = 2 \times 10^{15} \text{ s/cm}^3$$

Hence efficient thermonuclear burn demands an $n\tau$ product well in excess of that of the usual Lawson criterion. (It should be noted that magnetic confinement fusion schemes which work close to the Lawson criterion will burn only a small fraction of their thermonuclear fuel.)

We can correct this result slightly for the temperature dependence of the reaction rate and the speed of sound. If we recall that

$$f_b = \left[\frac{\langle \sigma v \rangle}{m_i C_s}\right] \rho R$$

then we can note that $\left[\frac{\langle \sigma v \rangle}{m_i C_s}\right]$ actually has a mild temperature dependence. For DT fuel, this quantity reaches a maximum for temperatures $20 < T < 80$ keV. Now thermonuclear ignition will occur when the fuel deposits its fusion energy rapidly enough to overcome energy loss (due to thermal conduction and radiation) and raise the fuel temperature to 20 keV before disassembly. We can compute the dependence of the ICF "Lawson criterion" on temperature as shown below:

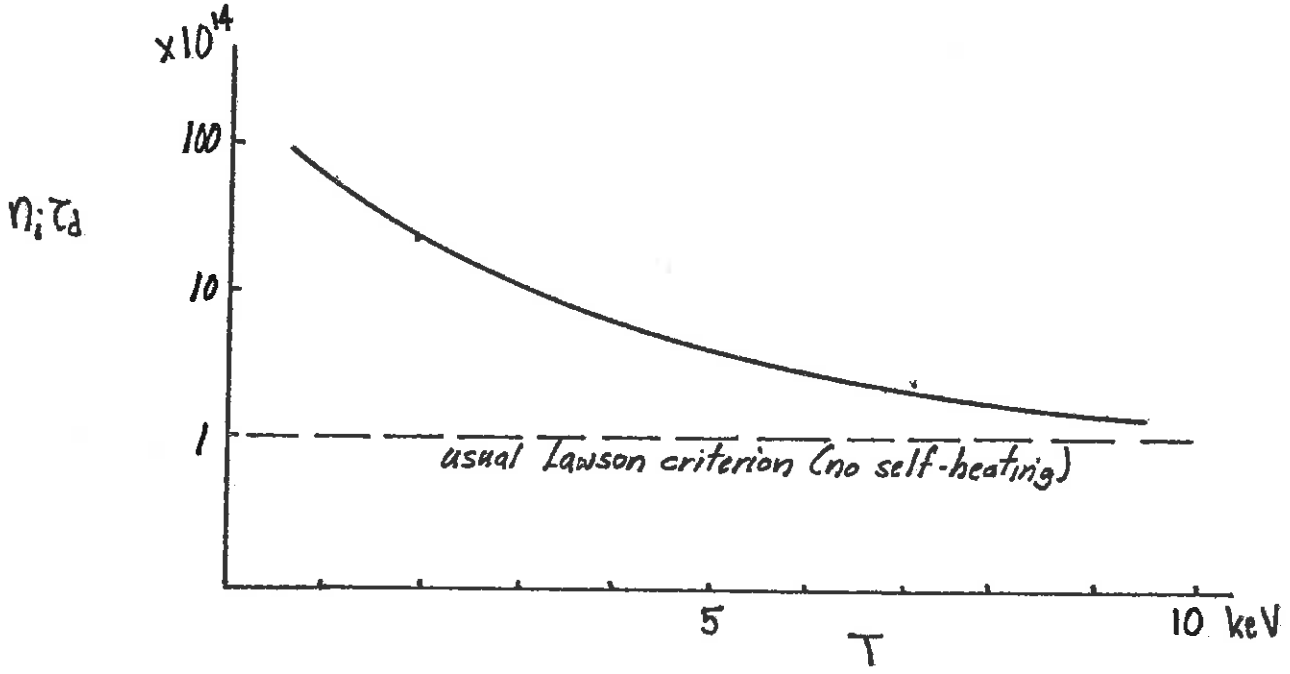

Depletion Effects

We can improve our estimate of the burn fraction f_b by taking account of the depletion of the fuel as the burn proceeds. Recall the rate equation:

$$\frac{dn_T}{dt} = -n_D n_T \langle v\sigma \rangle_{DT}$$

If we take $n_D = n_T = n/2$, then we find

$$\frac{dn}{dt} = -\frac{n^2}{4}\langle v\sigma \rangle$$

We can now integrate this equation as

$$\int_{n_o}^{n} dn' \frac{1}{n'^2} = -\frac{\langle v\sigma \rangle}{4} \int_0^{\tau_d} dt'$$

to find

$$\frac{1}{n} - \frac{1}{n_o} = \frac{1}{2}\langle v\sigma \rangle \tau_d$$

Let us now define the burn fraction f_b as

$$f_b \equiv \frac{n_o - n}{n_o} = 1 - \frac{n}{n_o}$$

where n_0 is the initial fuel density. If we now use

$$\tau_d = \frac{R}{4C_s} \quad , \quad \rho = n m_i$$

we find

$$\rho R = \left[\frac{8 m_i C_s}{\langle v\sigma \rangle}\right] \frac{f_b}{1 - f_b}$$

or rearranging:

$$f_b = \frac{\rho R}{\left[\frac{8 m_i C_s}{\langle v\sigma \rangle}\right] + \rho R}$$

Finally, we can evaluate the bracketed quantity $\left[\frac{8 m_i C_s}{\langle v\sigma \rangle}\right]$ for DT fuel at 20 keV to find

$$\left[\frac{8 m_i C_s}{\langle v\sigma \rangle}\right]_{DT} \sim 7$$

Thus our more accurate expression for the burn fraction in ICF DT fuel is

$$f_b \sim \frac{\rho R}{7 + \rho R}$$

In particular, note that $\rho R \sim 3$ g/cm^2 implies a burn fraction f_b of 0.30, that is, the burn of some 30% of the fuel.

Possible ICF Fuel Candidates

Let us return to our more general expression for the burn fraction f_b

$$f_b = \frac{\rho R}{\left[\frac{8 m_i C_s}{\langle v\sigma \rangle}\right] + \rho R}$$

This provides us with a means to compare the attractiveness of various fusion reactions since we can evaluate their ρR requirements for efficient thermonuclear burn

$$\rho R > \frac{m_i C_s}{\langle v\sigma \rangle}$$

We consider three fuel candidates:

Fuel candidate	ρR requirement
① $D + T \rightarrow {}^4He + n$	2-5 g/cm^2
② $D + D \rightarrow {}^3He + n$ / $T + p$	10-20
③ ${}^{11}B + p \rightarrow 3\ {}^4He$	$\sim$ 200

Hence it is apparent that our initial attention should be focussed on the DT reaction. It is also apparent that we can effectively ignore the DD reaction in a DT fuel mixture (whenever the fuel contains more than a few atomic percent of T).

2.3. A SIMPLE ANALYSIS OF ICF DRIVER REQUIREMENTS

Let us now examine the requirements on a driver (laser or charged particle beam) designed to implode ICF fuel pellets to produce a net energy gain. A crude sketch of an ICF system is given below

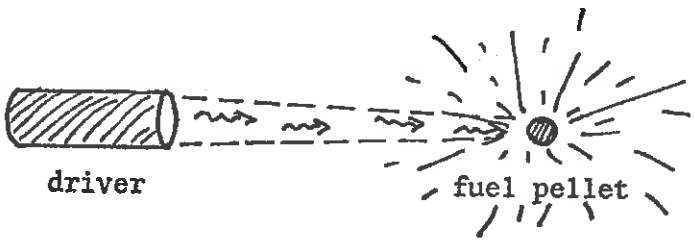

fusion energy E_{fusion}

driver energy E_{driver} fuel energy E_{fuel}

We will define

$$\text{pellet or target energy gain or multiplication} \equiv M = \frac{E_{fusion}}{E_{driver}}$$

$$\text{driver coupling efficiency} \equiv \varepsilon_D = \frac{E_{fuel}}{E_{driver}}$$

The fusion energy can be calculated in terms of the fusion reaction rate as

$$E_{fusion} = \left(\frac{4}{3}\pi R^3\right) n^2 \langle v\sigma \rangle W \tau \beta$$

Here we have introduced a factor β to account for self-heating and thermonuclear burn propagation.

We now recall that the derivation of the familiar Lawson criterion proceeded by balancing

$$E_{fusion} = E_{fuel}$$

to find $n\tau \sim 10^{14}$ s/cm^3. We therefore might proceed by balancing

$$E_{fusion} = M E_{driver} = \frac{M}{\varepsilon_D} E_{fuel} \qquad (*)$$

to find a new Lawson criterion

$$n\tau \sim \frac{M}{\beta \epsilon_D} \times 10^{14}$$

But we are after more information--the driver energy E_{driver} itself.

If we take the electron and ion temperatures to be equal, $T_e = T_i = T$, and at their initial burn temperatures, then

$$E_{fuel} = \text{thermal energy} = \left(\frac{4}{3}\pi R^3\right) 2 \left(\frac{3}{2} nkT\right)$$

We can return to plug this into our balance condition (*), recalling

$$\tau = \tau_d \sim \frac{R}{c_s}$$

to write

$$\left(\frac{4}{3}\pi R^3\right) n^2 \langle v\sigma \rangle W \beta \left(\frac{R}{c_s}\right) = \frac{M}{\epsilon_D} 4\pi R^3 nkT$$

We can now solve for R as

$$R = \left(\frac{M}{\beta \epsilon_D}\right) \frac{kT c_s}{n \langle v\sigma \rangle W}$$

Finally, we use

$$E_{driver} = \frac{1}{\epsilon_D} E_{fuel} = \frac{1}{\epsilon_D} 4\pi R^3 nkT$$

$$= \frac{4\pi}{\epsilon_D} \left(\frac{M}{\beta \epsilon_D}\right)^3 \left(\frac{kT c_s}{n \langle v\sigma \rangle W}\right)^3 nkT$$

We can write this in a more convenient form as

$$E_{driver} = \frac{M^3}{(\epsilon_D \beta)^4} \frac{1}{\eta^2} \times 1.6 \times 10^6 \text{ J}$$

where we have introduced the compression factor

$$\eta = \left(\frac{n}{n_{solid}}\right) \quad \text{, where } n_{solid} = 0.2 \text{ g/cm}^3 \text{ for DT}$$

A couple of examples are illustrative:

EXAMPLE:	Energy breakeven	$M = 1$	
	solid density	$\eta = 1$	$E_{driver} = 1.6$ MJ
		$\varepsilon_B\beta = 1$	
EXAMPLE:	Reactor	$M = 100$	
	solid density	$\eta = 1$	$E_{driver} = 1.6 \times 10^6$ MJ
		$\varepsilon_B\beta = 1$	

Hence the required driver energies are quite large if we are working with solid density fuels. But noti e that the driver energy scales as the inverse square of the compression. Hence suppose we were able to compress the fuel to very high densities:

EXAMPLE:	High compression	$\eta = 10^4$	
	Reactor	$M = 100$	$E_{driver} = 16$ kJ
		$\varepsilon\beta = 1$	

This is beginning to look a bit more hopeful (although actually it is a bit optimistic for reasons that will become apparent in a moment).

As an aside, we should note that most of the incident driver energy will be used to compress the fuel rather than heat it. We will demonstrate later that the driver coupling efficiency is typically about $\varepsilon_D \sim 5\%$. Hence if we are to achieve $\varepsilon\beta \sim 1$, we will need a multiplication due to thermonuclear burn and self-heating of $\beta \sim 20$. These latter processes will therefore play a very important role in any practical ICF scheme.

2.4. ICF IMPLOSION SCENARIO

We have noted that the most important processes in fusion reactions involve binary collisions (fusion reactions, alpha particle energy deposition) and therefore scale as the square of the compression. That is, increasing density by a factor of 10^3 increases the collision rate by 10^6. This is manifested in the dependence of thermonuclear burn efficiency, self-heating, and burn propagation on the product of fuel density times radius, ρR.

In spherical compression, the density (for constant mass) scales as

$$\rho \sim \frac{1}{R^3}$$

Hence we find that

$$\rho R \sim \frac{1}{R^3} R \sim \frac{1}{R^2}$$

Thus compression by 10^3 reduces the mass required to initiate efficient thermonuclear burn by 10^6. (The typical imploded fuel masses in ICF schemes are of the order of 10^{-3} g.)

But how do we achieve such densities. There are several examples on an astronomical level:

(i) In the sun, $\eta = n/n_s \sim 10^3$ with a temperature of 1-2 keV. This corresponds to a pressure of $p \sim 10^{11}$ atm. The fuel confinement is maintained by the enormous mass of the sun, $m_\odot \sim 10^{33}$ g.

(ii) In white dwarf stars, $\eta \sim 10^5 - 10^6$ corresponding to staggering pressures of $p \sim 10^{15}$. At these compressions the electrons become degenerate. That is, their wavelengths become comparable to their separation so that the exclusion principle becomes important and results in an additional repulsive force. The condition for degeneracy can be expressed by comparing the Fermi energy ϵ_F with the thermal energy:

$$\epsilon_F = \frac{h^2}{8m}\left(\frac{3}{\pi} n_e\right)^{2/3} > kT$$

But how can we generate pressures sufficient to compress the fuel to $\eta \sim 10^4$? It is apparent that we need $p \sim 10^{12}$-10^{15}. There are several possibilities:

(i) Chemical explosives? The pressures generated by chemical explosives are limited by the strengths of chemical bonds to

$$p \lesssim 10^6 \text{ atm}$$

These pressures can be increased another order of magnitude ($p \sim 10^7$) by using implosion convergence, but they still fall far short of the required magnitude.

(ii) Light pressure? Suppose we focus the intense beams of high powered lasers on the fuel. Then the ponderomotive pressure exerted by the light on the pellet surface is given by

$$p \sim I/c \sim \frac{10^{17} \text{ w/cm}^2}{3 \times 10^{10}} \sim 10^8 \text{ atm}$$

--still not good enough.

(iii) Ablation pressure? Here the idea is to use the driver energy beam (laser light or charged particle beams) to heat surface material and ablate it off into the vacuum surrounding the pellet. The back reaction to the ablating surface generates a pressure, much as that generated by a rocket exhaust. For the same reason that matter-ejecting rockets have much larger thrust than photon rockets, the pressure is multiplied to

$$p \sim \frac{I}{v} \sim \frac{10^{17}}{10^8} \sim 10^{10} \text{ atm}$$

(iv) We can multiply this pressure further by taking advantage of convergence in an implosion geometry. This increases the pressure by 10^2 or more.

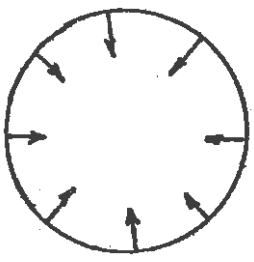

(v) If we compress the fuel isentropically, so that it is not heated to high temperatures, then we can compress it into a Fermi degenerate state where the pressure required for a given fuel density is at a minimum:

$$p \sim \frac{2}{3} n_e \epsilon_F \left[\frac{3}{5} + \frac{\pi^2}{4}\left(\frac{kT}{\epsilon_F}\right)^2 - \frac{3\pi^4}{80}\left(\frac{kT}{\epsilon_F}\right)^4 + \cdots\right]$$

For example, at a compression of $\eta \sim 10^4$ (corresponding to an electron density of $n_e \sim 5 \times 10^{26}$), the minimum pressure is $p \sim 10^{12}$ atm when $\epsilon_F >> kT$. This should be compared with a required pressure of $p \sim 10^{13}$ for a temperature of kT = 5 keV (which corresponds to the ideal ignition temperature).

To illustrate just how this compression is achieved, let us consider a brief scenario of the implosion of a fuel pellet to the required densities using high powered laser beams:

1. We begin by irradiating a 1 mm sphere of liquid DT fuel uniformly about its surface with intense laser light (which will reach a peak intensity of 10^{17} w/cm^2).

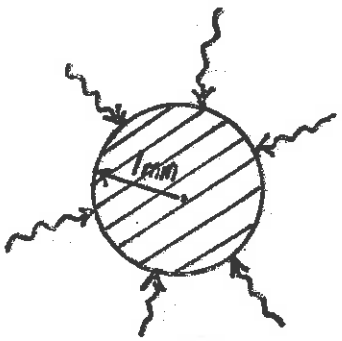

2. The outer surface of the pellet heats, ionizes, and ablates off to surround the pellet in a cloud or "corona" of low density plasma ($n_e \sim 10^{19}$ - 10^{22}).

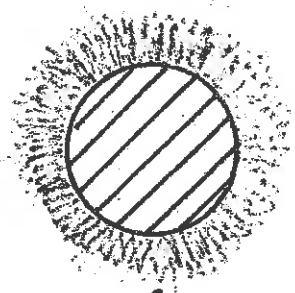

3. The electrons in the corona continue to absorb more energy from the incident laser beams, but now the beam can only penetrate into the critical density where the plasma frequency equals the light frequency--10^{21} for Nd light at 1.06 μm (10^{19} for CO_2 light at 10.6 μm).

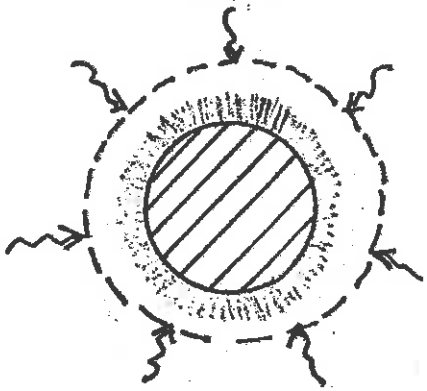

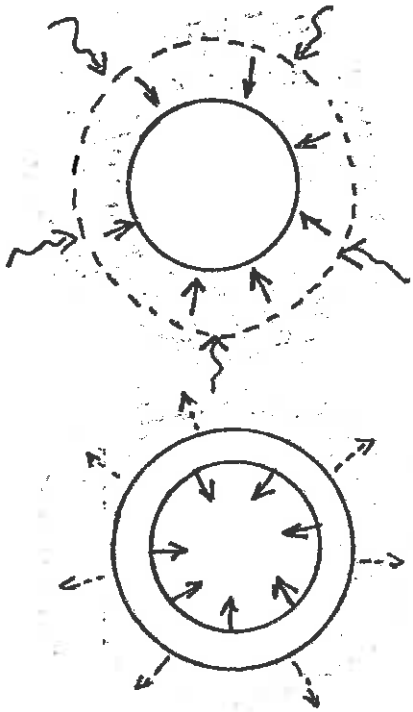

4. The energy deposited by the laser at the critical surface is then transported into the surface of the pellet by electron thermal conduction. This energy then continues the heat the pellet surface and drive the ablation.

5. As the ablation of the surface continues, a shock front is formed that converges (implodes) inward, pushing cold DT fuel ahead of it to higher and higher densities along the "Fermi degenerate adiabat". The dominate energy transport mechanisms are electron thermal conduction and hydrodynamic motion (shock waves).

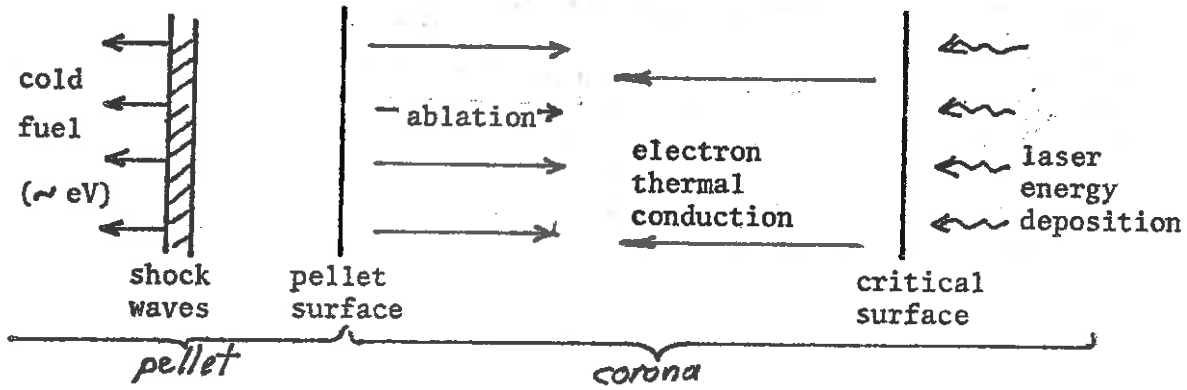

The general idea is to compress the pellet fuel isentropically (without appreciable heating) to bring it to very high density while still leaving it relatively cold.

6. When the shock fronts converge at the center of the highly compressed pellet core, they shock heat a small region at the center of the compressed core to thermonuclear ignition temperatures (1-2 keV). If $\rho R > 0.5$ g/cm^2, alpha particle self-heating will occur and the intense spark at the center of the compressed core will rapidly heat to optimum burn temperatures of 20 to 100 keV.

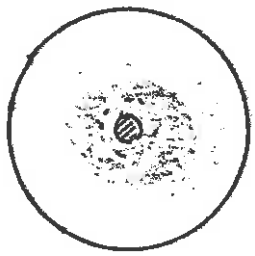

7. As the central spark burns, some alphas are deposited in adjacent cold fuel, bringing it to ignition temperatures. (The tendency of the fuel to become transparent to alphas as it heats up enhances this process.) This process continues, leading to a thermonuclear burn wave which propagates outward, consuming the dense pellet core. If $\rho R > 3$ g/cm^2, this will lead to efficient burn (with some 30% of the fuel in the dense core being consumed).

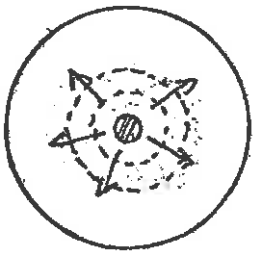

Of course there are a great many physical processes, some of which are only marginally understood, involved in this scenario. These will be the topics covered in this course. A brief roadmap to the physics of ICF pellet implosion (due to R. Kidder) has been provided in the figure on the next page.

2.5. PELLET GAIN REQUIREMENTS

What kind of pellet energy gains are required in ICF applications? Recall that we have defined the pellet or target energy gain as:

$$\text{pellet energy gain} = M = \frac{E_{fusion}}{E_{driver}}$$

Also recall the definition of the driver coupling efficiency:

$$\text{coupling efficiency} = \epsilon_D = \frac{E_{fuel}}{E_{driver}}$$

It is useful to introduce one further efficiency which takes recognition of the fact that the thermonuclear burn will occur only in the highly compressed core of the fuel pellet. We will define the fuel gain G_F by

$$\text{fuel gain} = G_F = \frac{E_{fusion}}{E_{core}}$$

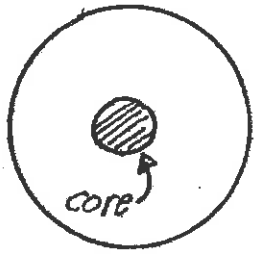

PHYSICS ROADMAP

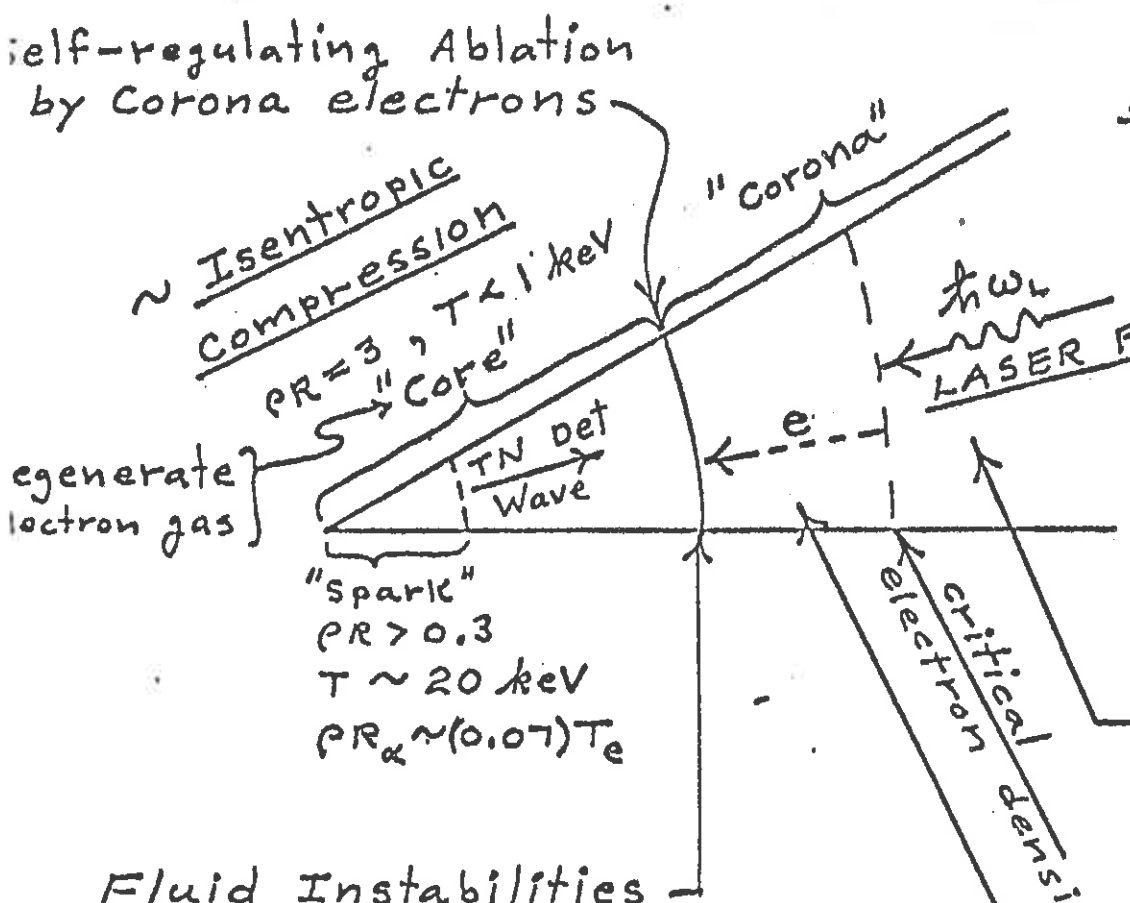

Light-Plasma Interaction

Linear:
- refraction
- free-free absorption (IB)
- resonant absorption
- ponderomotive force (light pressure)
- mag field generation

Nonlinear:
- absorption (decrease) ⇒ transparent
- refraction (increase) ⇒ self-focus
- harmonic generation (generate multiple frequencies)

Light-Plasma Instabilities:

Reflective: Stim Brillouin
" Raman
" Compton

Absorptive: Decay-Osc Two Stream
Two-Plasmon

Energetic Charged Particles (not electron and positron)

Fluid Instabilities

Rayleigh-Taylor modified by ablation, viscosity, heat conduction.

Coupling Interaction

Corona-core decoupling
Two-stream instability
Anomalous Transport Coeff.
Flux Limit

LASER SYSTEM ($<10^{10}$ w/cm^2)

Wavefront Distortion
Self-focusing, Medium Inhomog.
Pulse-shape Distortion
, Self-phase mod, Gain saturation

R.E.K.

The fuel gain and pellet gain are related by:

$$M = \varepsilon_{LF} \; G_F$$

where

ε_{LF} = fraction of absorbed driver energy converted into internal energy of highly compressed fuel core at time of ignition

For example, a high gain pellet with M = 200 would be characterized by a coupling efficiency of $\varepsilon_{LF} = 0.05$ and therefore would require a very large fuel gain of $G_F = 4000$.

To determine the pellet gain requirements for a power reactor, suppose we consider the use of the fusion energy to produce electricity through a thermal cycle as shown schematically below:

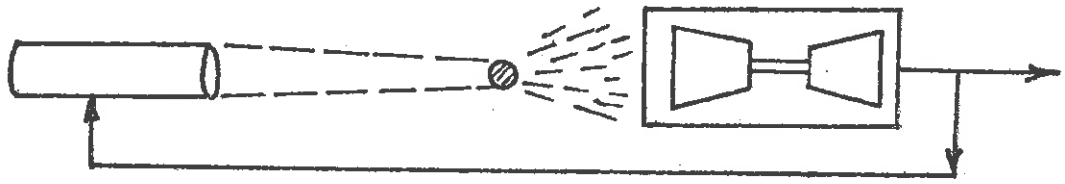

Here we have noted that a certain fraction of the produced electrical energy must be circulated back to power the driver. We can associate an efficiency with each aspect of this scheme as follows:

driver efficiency = η_D = $\dfrac{\text{driver energy output}}{\text{driver elelectrical input}}$

gross plant thermal efficiency = η_{th}

net plant thermal efficiency (taking into account driver power) = η_p

From the definition of the pellet gain we can determine

$$M = \frac{1}{\eta_D(\eta_{th}-\eta_p)} - 1$$

Hence we can solve for the plant efficiency as a function of pellet gain:

$$\eta_P = \eta_{th} - \frac{1}{\eta_D(M+1)}$$

The fraction of the gross electrical power needed for the driver is given by

$$F_D = \frac{1}{\eta_D \eta_{th}(M+1)}$$

With this background, we can now go on to define two criteria for determining pellet gain requirements.

Engineering breakeven: Fusion energy production is just sufficient to balance driver energy needs, i.e., $F_R = 1$

$$M^{EB} = \frac{1-\eta_D}{\eta_D}$$

Scientific breakeven: Fusion energy production is just sufficient to balance driver energy output

$$M^{SB} = 1$$

For typical thermal cycles, $\eta_{th} \lesssim 35\% - 50\%$. Furthermore, most driver designs (lasers, in particular) assume a driver efficiency of $\eta_D \sim 10\%$. Thus we can find that:

$$M^{EB} \sim 10$$

For significant power production it is apparent that we will need

$$M \gtrsim 100$$

In fact, most power plant designs based on ICF schemes assume a pellet gain of $M \sim 150\text{-}200$.

As an aside, it should be noted that pellet gains tend to increase with yield. For example, a pellet with gain M ~ 100 is characterized by a fusion energy release E_{fusion} of about 100 MJ.

EXAMPLE: The Wisconsin SOLASE laser fusion reaction design assumes:

laser efficiency: $\eta_D = 0.07$ (7% efficiency)
fusion energy: $E_{fusion} = 150$ MJ
laser energy output: $E_{driver} = 1$ MJ

This corresponds to a pellet gain of M = 150. We can compute the required fuel mass for these pellets by first calculating the number of fusion reactions required for an energy release of 150 MJ:

$$N = \frac{E_{fusion}\,(MJ)}{W\,(MeV)(1.6\times10^{-19}\,MJ/MeV)} = 5.325\times10^{19}$$

Hence the corresponding mass is

$$\text{Mass} = N\,(m_D + m_T) = 0.4455 \text{ mg}$$

At $\rho R = 3$, the fractional burnup f_b is 0.30. Hence the total mass of the compressed pellet core is 1.437 mg. (Notice that this implies that the compression is $\eta = 1314$.)

We should note that the required pellet gain is very sensitive to the driver efficiency:

$$M^{EB} = \frac{1-\eta_D}{\eta_D}$$

High-powered lasers exhibit a driver efficiency of 1-10% (at best). In sharp contrast, charged particle beams can achieve efficiencies of $\gtrsim$50% or better. Hence the use of charged particle beam drivers greatly reduces the requirements on target designs.

But what kind of fuel gains might we expect from ICF targets? Consider again the DT reaction:

$$D + T \longrightarrow {}^4He\ (3.5\ MeV) + n(14.1\ MeV)$$

The greatest DT reaction rate is in the temperature range of 20 to 100 keV. In conventional thermonuclear fusion schemes, one usually considers the ignition temperature to be 10 keV. Suppose we assume an ion temperature $T_i \sim 10$ keV. Then the energy required for a single DT reaction (including both ions and electrons) is 4 x 10 keV. Hence the energy gain from a single DT reaction is

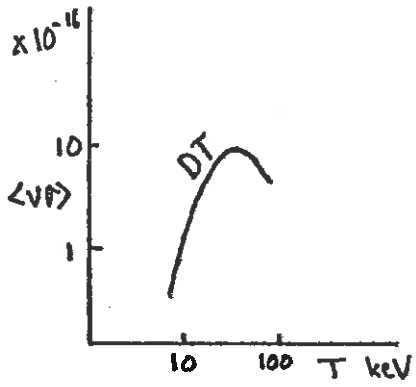

$$\frac{17.6\ MeV}{4 \times 10\ keV} = 440$$

Hence a 100% burn of a uniformly heated pellet core would yield a fuel gain of only

$$G_F = 440$$

But this is not sufficient, since we know that typical burn fractions are $f_b \sim$ 30-50%. Furthermore, the driver coupling efficiency of $\epsilon_D \sim 0.05$ implies that to achieve pellet gains of $M \sim 100$, we are going to need fuel gains of $G_F \sim 2000$ or greater.

But how do we design such high gain targets? Let's look at some order of magnitude estimates. Suppose we have somehow managed to compress the core of a fuel pellet to the desirable condition of $\rho R \sim 3$ g/cm^2. Since this is sufficient to capture the alpha reaction products (with range 0.5 g/cm^3), we need only heat the core to ignition temperatures of 1-2 keV. This corresponds to an ignition energy of

$$E_{ignition} \sim 3 \times 10^7 \text{ J/g}$$

To achieve the necessary ρ R condition requires a compression of $\eta \sim 10^4$. If we manage to compress the pellet into a degenerate state such that

$$k T << \epsilon_F \sim 1 \text{ keV}$$

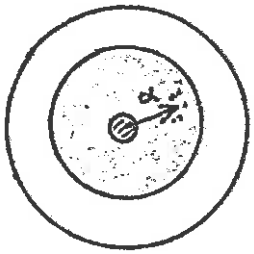

when the compression energy (pdV work) required is

$$E_{compression} \sim 3 \times 10^7 \text{ J/g}$$

Hence the total energy input required is

$$E_{ignition} + E_{compression} \sim 6 \times 10^7 \text{ J/g}$$

For a $\rho R \sim 3$ g/cm^2, the fusion energy release is

$$E_{fusion} \sim 10^{11} \text{ J/g}$$

Hence the fuel gain achievable if the pellet can be ignited is

$$\text{fuel gain } G_F = \frac{E_{fusion}}{E_{core}} = 1500$$

If we recall that roughly 95% of the driver energy goes to ablation required to drive the implosion, that is, $\eta_D = 0.05$, then we find a pellet gain of

$$M = \frac{E_{fusion}}{E_{driver}} = 75$$

Hence it is apparent to achieve such high gain pellets, we must depend on the processes of self-heating and thermonuclear burn propagation to minimize the driver energy that will act as a "match to light the fusion flame".

2.6. INERTIAL CONFINEMENT FUSION BURN PHYSICS

Recall that the driver energy requirement was given approximately by

$$E_{driver} \sim \frac{M^3}{(\beta\epsilon)^4} \times 1.6 \times 10^6 \text{ J}$$

Actually, more detailed studies have indicated that this expression is too low, due primarily because of the time required for the ion temperature T_i to equilibrate with the electron temperature T_e (which absorbs the driver energy).

To present more accurate models and study the detailed physics of ICF burn physics, we will consider a sequence of three models of the burning pellet.

Direct Heating of Uncompressed Spheres

Perhaps the simplest model is to consider the very rapid heating of a simple spherical drop of DT at liquid density $\rho_s = 0.2$ g/cm^3 (particle density $n = 4.5 \times 10^{22}$ cm^{-3}). The essential idea here is to attempt to heat the fuel pellet to thermonuclear temperatures very rapidly so that an appreciable number of DT fusion reactions occur before the pellet disassembles.

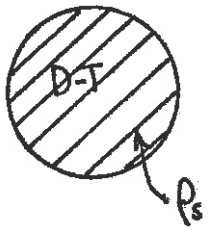

The key to the physics of this problem is to recognize that the driver beam can deposit energy only in the outer layers of the target. For example, laser light will only penetrate into the critical density (10^{21} cm^{-3} for 1.06 μm light). Hence the target must be heated to fusion temperatures by some other mechanism.

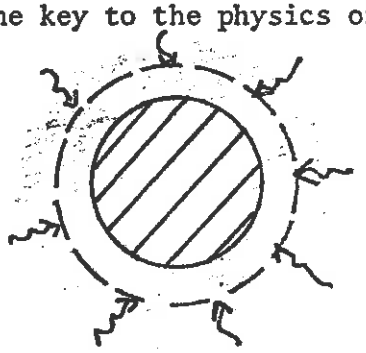

NOTE: If we could develop ultraviolet lasers, say with wavelengths of 0.13 μm, then the light beam could penetrate into even solid density plasma. But for the two principle types of lasers, Nd and CO_2, the critical densities are 10^{21} and 10^{19}, respectively.

The principal heating mechanism is due to electron thermal conduction. Indeed, the mass of the electrons in a plasma is so small, that they make the plasma an excellent conductor of heat. The thermal conductivity is strongly temperature dependent, $\kappa \sim T^{5/2}$. These leads to a number of interesting nonlinear conduction effects which will be considered in detail in Chapter 4. However of most relevance to the present discussion is the formation of a thermal wave that moves into the target to heat the fuel material.

In the actual pellet we find a large variety of physical phenomena, ranging from the absorption of the driver energy, the transport of this energy into the surface of the pellet via electron thermal conduction, the heating and ablation of the target surface, the penetration of both thermal and shock waves into the dense pellet fuel. These processes are illustrated in the Figure on the next page.

For the purposes of our present discussion of the heating of an uncompressed target at solid density, we will consider a simple model in which the driver energy is transported into the surface of a slab (one-dimensional) target in such a way that the temperature at the surface is maintained at a constant magnitude, $\theta_e = k T_e$. The driver energy is assumed to maintain the surface of the target at this temperature.

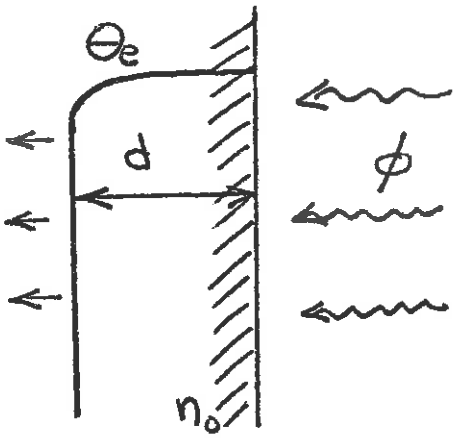

This process will drive a thermal wave into the target which heats the dense fuel material. We can estimate the distance d_{HW} the heat wave will propagate into the target in a time t by a simple energy balance argument. If n_o is the number density of the target, and ϕ is the power intensity (w/cm^2) at its surface, then

$$\begin{matrix}\text{energy incident} \\ \text{on surface}\end{matrix} = \phi t \sim n_o \Theta_e d_{HW} = \begin{matrix}\text{thermal energy per} \\ \text{unit area of target}\end{matrix}$$

We can balance this energy flux against the heat flux conducted into the target by using Fourier's law

$$q = -\kappa \frac{\partial T}{\partial x}$$

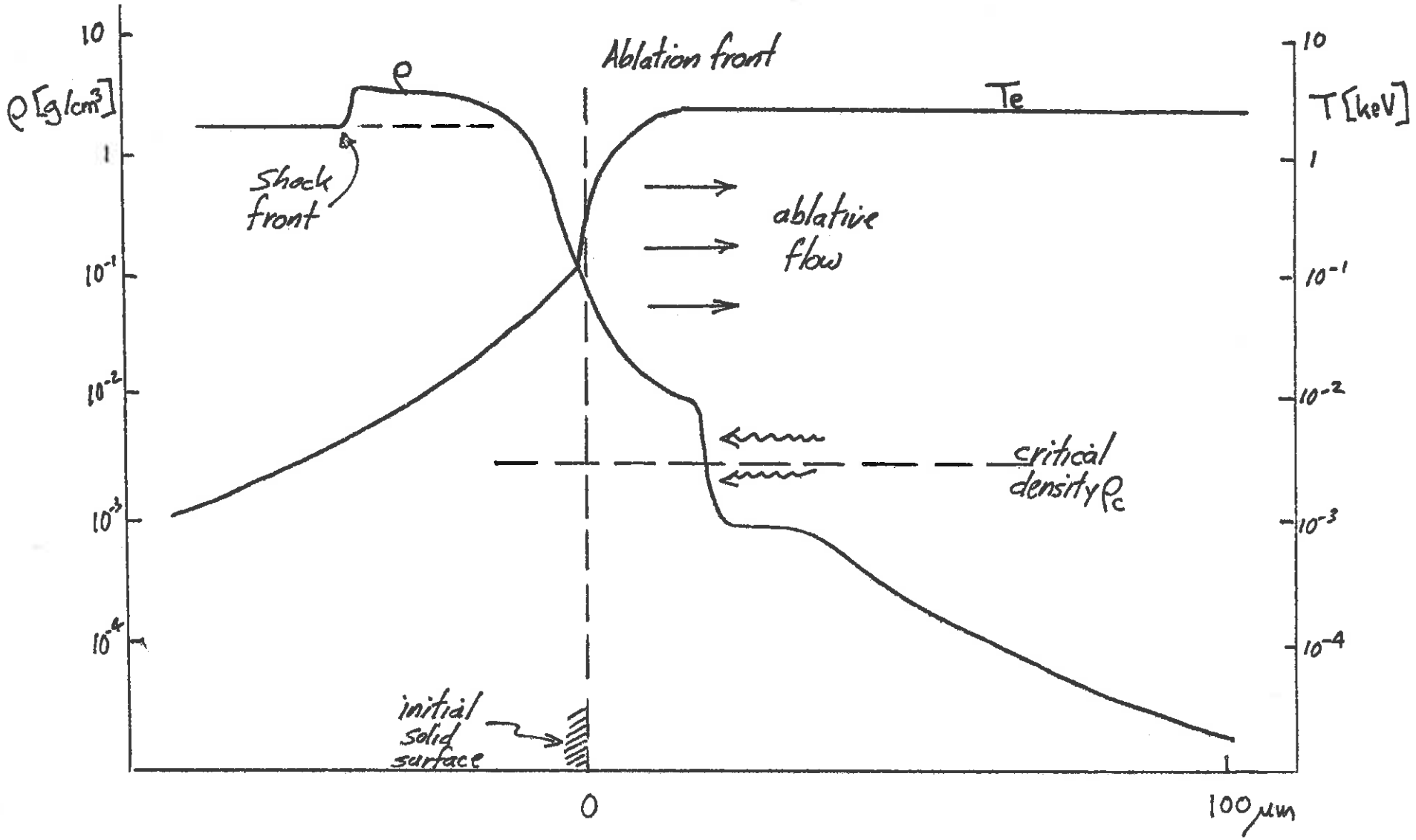
ρ [g/cm³]
10
1
10⁻¹
10⁻²
10⁻³
10⁻⁴
ρ
Ablation front
Te
T [keV]
10
1
10⁻¹
10⁻²
10⁻³
10⁻⁴
Shock front
ablative flow
critical density ρc
initial solid surface
0
100 μm

If we balance this against the incident energy flux ϕ and estimate the temperature gradient $\partial T/\partial x \sim (\theta/k)/d_{HW}$, we find

$$\phi \sim \kappa\left(\frac{\theta_e}{k}\right)\frac{1}{d_{HW}}$$

But for a plasma,

$$\kappa = \kappa_0 \theta_e^{5/2}$$

Hence we can solve for the distance of penetration of the heat wave as

$$d_{HW} \sim \left[\kappa_0 \theta_e^{5/2} t/n_0\right]^{1/2}$$

where $\kappa_0 = 3\times10^{27}\ cm^{-1}s^{-1}(keV)^{-5/2}$, $n_0 = 4\times10^{22}\ cm^{-3}$ $(\rho_0 = \rho_s = 0.2\ g/cm^3)$

[An exact solution of the nonlinear diffusion equation,

$$\frac{\partial \theta_e}{\partial t} = -\kappa_0 \frac{\partial}{\partial x}\theta_e^{5/2}\frac{\partial \theta_e}{\partial x}$$

will give a similar result as we will demonstrate in Chapter 4.]

But this is only part of the story. We must now account for the fact that the pellet will disassemble by the propagation of a rarefaction wave inward at the speed of sound. The depth of penetration of this hydrodynamic disassembly wave is

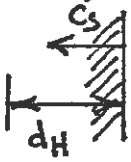

$$d_H = c_s t = v_0\left[(\theta_e + \theta_i)/2\right]^{1/2} t$$

where $v_0 = 3.5 \times 10^7$ cm/s (θ in keV)

Note here that at first the heat wave will propagate into the target more rapidly than the disassembly wave since

$$d_{HW} \sim \sqrt{t} \qquad d_H \sim t$$

The rarefaction wave will catch up with the heat wave when

$$d_{HW} \sim d_H$$

or

$$d_{HW} = \left(\frac{\kappa_0}{2v_0 n_0}\right)\left[\frac{\theta_e^{5/2}}{\left(\frac{\theta_e + \theta_i}{2}\right)^{1/2}}\right]$$

At this point the target density n_o will drop, and the driver beam (e.g., the laser beam) can penetrate into the target and heat the fuel directly.

The thermal energy (per unit area) of the heated region of the target is given by

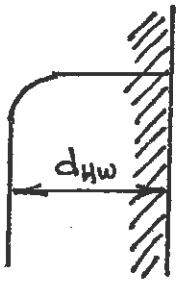

$$E_{thermal} = \frac{3}{2} n_o (\theta_e + \theta_i) d_{HW}$$

If we heat this region to fusion temperatures, the fusion energy produced is given in terms of the reaction rate

$$E_{fusion} = \frac{n_o^2}{4} \langle v\sigma \rangle W \tau_R d_{HW}$$

where the reaction time τ_R can be identified as the disassembly time for the region

$$\tau_R \sim \tau_d \sim \frac{d_{HW}}{c_s} = \frac{\kappa_o \theta_e^{5/2}}{v_o^2 n_o (\theta_e + \theta_i)}$$

What temperature do we evaluate $\langle v\sigma \rangle$ at? The heat wave will heat the electrons first. The ion temperature will then equilibrate with that of the electron according to

$$\frac{d\theta_i}{dt} = \frac{1}{\tau_{ei}} (\theta_e - \theta_i), \quad \tau_{ei} = \frac{3 m_e m_i}{8\sqrt{2\pi}\, n e^4 \ln\Lambda} \left(\frac{\theta_e}{m_e}\right)^{3/2}$$

We can again use simple estimates of the derivative term, $d\theta_i/dt \sim \theta_i/\tau_R$ to find

$$\theta_i \sim \frac{\tau_R}{\tau_{ei}} (\theta_e - \theta_i)$$

If we now use our expression for the disassembly time for τ_R, we can solve for

$$\theta_i = 10^{10} \left[\frac{\kappa_o \theta_e (\theta_e - \theta_i)}{v_o^2 n_o (\theta_e + \theta_i)} \right] = 0.315\, \theta_e$$

Hence the ions will only partially equilibrate with the electrons. The ion temperature in the reaction zone will always be much lower than the electron temperature. (Computer calculations confirm this behavior.)

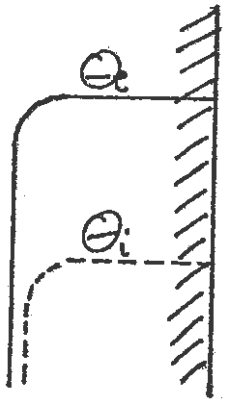

We can now combine these equations to estimate the thermal energy as

$$E_{thermal} = \frac{3}{2}\frac{n_0}{V_0}\Theta_e^{5/2}\left(\frac{\Theta_e+\Theta_i}{2}\right)^{1/2} = 14{,}600\,\Theta_e^3\ J/cm^2$$

Thus we find the final result of interest

$$\frac{E_{fusion}}{E_{thermal}} = \frac{1}{6}\langle v\sigma\rangle W\left[\frac{n_0\Theta_e^{5/2}}{V_0^2(\Theta_e+\Theta_i)^2}\right]$$

$$= 0.646\left[10^{16}\langle v\sigma\rangle\right]\Theta_e^{1/2}$$

We can study the implications of this result by consider two examples:

EXAMPLE 1: Θ_e = 10 keV, Θ_i = 3.15 keV
$\langle v\sigma\rangle = 3.7 \times 10^{-18}\ cm^3/s$
$E_{thermal} = 14.6\ MJ/cm^2$
$d_{HW} = 0.15\ cm$
$\tau_R = 1.02\ ns$
$\Rightarrow \frac{E_{fusion}}{E_{thermal}} = 0.0755$

EXAMPLE 2: Θ_e = 30 keV, Θ_i = 9.45 keV
$\langle v\sigma\rangle = 1 \times 10^{-16}\ cm^3/s$
$E_{thermal} = 395\ MJ/cm^2$
$d_{HW} = 0.95\ cm$
$\tau_R = 5.34\ ns$
$\Rightarrow \frac{E_{fusion}}{E_{thermal}} = 3.54$

To clarify these results, suppose we consider the heated area of the target to be $\pi\, d_{HW}^2$. Then

Θ_e = 10 keV $\Rightarrow$ 505 kJ
Θ_i = 30 keV $\Rightarrow$ 1,120 MJ (breakeven)

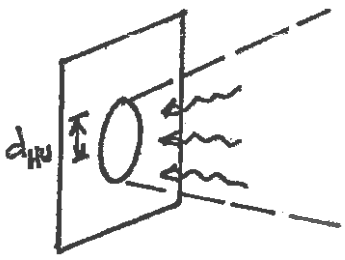

Hence the driver requirements for breakeven are of the order of 10^3 MJ because of the balance between the time required to conduct heat into the target, the time required for the electron and ion temperatures to equilibrate, and the time available before the pellet disassembles. It is apparent from this analysis that the direct heating of an uncompressed pellet looks quite out of the question. (And we still haven't accounded for incomplete driver energy absorption, energy lost to surface ablation, or temperature and density gradients in the heated layer.)

Uniform Sphere with Compression and Self-Heating

We now wish to account for alpha particle self-heating in the fuel. We begin with the rate equation

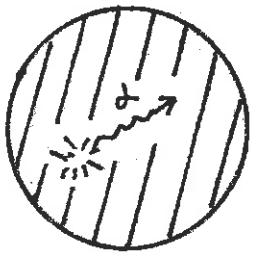

$$\frac{dE_{fusion}}{dt} = \frac{4}{3}\pi R^3 n_D n_T \langle v\sigma\rangle_{(\theta_i)} W$$

$$= \frac{4}{3}\pi R^3 \frac{n^2}{4} \langle v\sigma\rangle_{(\theta_i)} W$$

We will assume temperature equilibration, $\theta_e = \theta_i = \theta$. If W_{dep} is the part of the energy deposited in the fuel, we find

$$\left.\frac{dE}{dt}\right|_{\substack{fusion \\ dep}} = \frac{4}{3}\pi R^3 \frac{n^2}{4} \langle v\sigma\rangle_{(\theta_i)} W_{dep} = \frac{4}{3}\pi R^3 3n \frac{d\theta}{dt}$$

noting that the thermal energy is

$$E_{thermal} = \frac{3}{2} n (\theta_i + \theta_e) \frac{4}{3}\pi R^3$$

Hence we can solve for

$$\frac{1}{12} n = \frac{1}{\langle v\sigma\rangle_{(\theta)} W_{dep}} \frac{d\theta}{dt}$$

Now the time available for heating and fusion is again determined by the disassembly time. If the temperature were uniform, we would just use

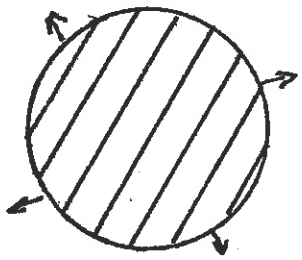

$$\tau_d \sim \frac{R}{c_s}$$

But we recall that the speed of sound scales as

$$c_s = v_0 \theta^{1/2} t$$

If we now note that any radial point r in the pellet expands at the sonic velocity

$$\frac{dr}{dt} = c_s$$

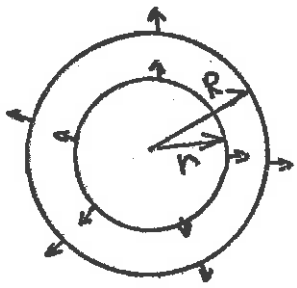

we can make a variable transformation from time to r

$$\frac{d\theta}{dt} = \frac{d\theta}{dr}\frac{dr}{dt} = \frac{d\theta}{dr} v_0 \theta^{1/2} t$$

Hence we can integrate our balance equation (*) to find

$$\frac{1}{12}\int_0^r n\,dr' = \int_{\theta_0}^{\theta_1} \frac{v_0 \theta^{1/2}}{\langle v\sigma\rangle_{(\theta)} W_{dep}}\, d\theta$$

where $_0$ is the initial temperature and $_1$ is the temperature after a time corresponding the the disassembly time (the time required for the sound wave to have traversed the radius of the pellet).

The thermal energy of the pellet just prior to ignition is

$$E_{thermal}(0) = \frac{4}{3}\pi R^3\, 3\, n\, \theta_0$$

We can also integrate the fusion reaction rate equation to find

$$E_{fusion}(t) = \frac{4}{3}\pi R^3 \frac{W}{4}\int_0^t n\langle v\sigma\rangle_{(\theta)}\, dt'$$

Hence we find

$$\frac{E_{fusion}}{E_{thermal}(0)} = \frac{W}{12\theta_0}\int_0^t n\langle v\sigma\rangle_{(\theta)} dt'$$

$$= \frac{W}{\theta_0}\int_{\theta_0}^{\theta_1} \frac{d\theta}{W_{dep}(\theta)} \qquad (**)$$

Our remaining task is to estimate the energy deposited, W_{dep}. If we recall the DT reaction

$$D + T \rightarrow \alpha\ (3.5\ MeV) + n\ (14.1\ MeV)$$

The neutron range is some 50 times that of the alpha range. Hence we can assume that alpha self-heating will dominate (at least for $\rho R < 10$).

To estimate the energy deposition, we can interpolate

$$W_{dep} = W_\alpha \left(\frac{R}{R_\alpha + R}\right)$$

where W_α = 3.5 MeV. Here we estimate the range of the alpha as

$$R_\alpha \sim 2\times10^{21}\,\text{cm}^{-2}\left(\frac{\Theta_e^{3/2}}{n}\right) \equiv \lambda_0\left(\frac{\Theta_e^{3/2}}{n}\right)$$

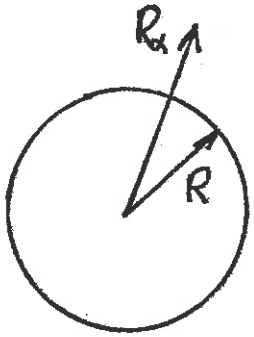

Then we find that (**) becomes

$$\frac{E_{fusion}}{E_{thermal}(0)} = \frac{W}{\Theta_0 W_\alpha}\int_{\Theta_0}^{\Theta_1}\left(\frac{\lambda_0\Theta^{3/2}}{Rn}+1\right)d\Theta$$

For an estimate, we take R = initial radius R_0, n = initial density = n_0 (which neglects hydrodynamic motion and fuel depletion). If we recall our definitions

$$M = \frac{E_{fusion}}{E_{driver}}$$

$$\varepsilon_D = \frac{E_{thermal}}{E_{driver}} \quad \Rightarrow \quad \frac{M}{\varepsilon_D} = \frac{E_{fusion}}{E_{thermal}(0)}$$

We will also take W/W_α = 17/3.5 = 5 to find

$$\frac{M}{\varepsilon_D} = \frac{2\lambda_0}{n_0 r_0 \Theta_0}\left(\Theta_1^{5/2} - \Theta_0^{5/2}\right) + 5\left(\frac{\Theta_1 - \Theta_0}{\Theta_0}\right)$$

We can similarly evaluate (*)

$$\underbrace{\int_{\Theta_0}^{\Theta_1}\frac{v_0\Theta^{1/2}d\Theta}{\langle v\sigma\rangle W_{dep}}} = \frac{1}{12}\underbrace{\int_0^R n\,dr}$$

$$\frac{v_0}{W_\alpha}\left[\int_{\Theta_0}^{\Theta_1}\frac{\Theta^{1/2}d\Theta}{\langle v\sigma\rangle} + \frac{\lambda_0}{n_0 R_0}\int_{\Theta_0}^{\Theta_1}\frac{\Theta^2 d\Theta}{\langle v\sigma\rangle}\right] = \frac{n_0 R_0}{12} \qquad (***)$$

We also recall that

$$E_{driver} = \frac{4\pi R_0^3}{3\varepsilon_D}\,3n_0\Theta_0$$

For weak heating, $\lambda_0 \to \infty$ or $R_\alpha >> R$ so that

$$\Delta\Theta \equiv \Theta_1 - \Theta_0 \sim \frac{12 v_0}{25 W_\alpha \lambda_0} \left(\frac{M}{\epsilon_D}\right)^2 \frac{\Theta_0}{\langle v\sigma \rangle_{(\Theta_0)}}$$

At 10 keV,

$$\Delta\Theta = 0.233 \left(\frac{M}{\epsilon_D}\right) \text{ keV}$$

Hence we find appreciable self-heating does not occur until $M/\epsilon_D >> 1$.

$$\frac{M}{\epsilon_D} = 4 \quad \Rightarrow \quad \Delta\Theta = 4 \text{ keV}$$

For larger M/ϵ_D we must evaluate the integrals in (***). (Of course this is the most interesting case.) Brueckner has done this and the results are presented in the figure below:

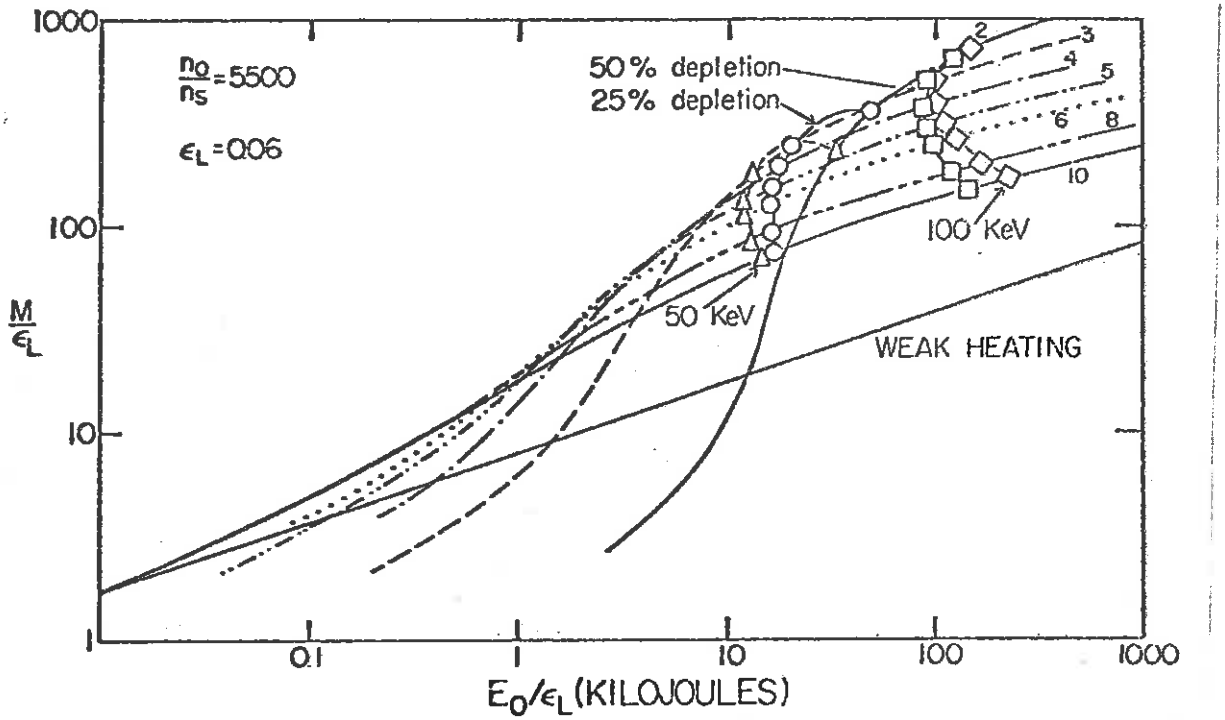

Analytic results for laser energy as a function of M/ϵ_L, based on Eqs. (**) & (***) for a compression ratio of 5500 and a laser coupling efficiency ϵ_L of 0.06. The points of 25% and 50% fuel depletion and of 50 and 100 kev final temperature are indicated. Reproduced from studies at KMSF performed by K. A. Brueckner et al.

For example, $M/\epsilon_D = 100$ yields a self-heating temperature increase $\Delta\theta$ of about 50 keV. This lowers the required driver energy by a factor of 400 over that for an uncompressed pellet, since the driver only has to provide the relatively small energy for ignition.

What is the optimum temperature for ignition, θ_o?

For small M/ϵ_D, $\theta_o \rightarrow$ 10 keV.

For large M/ϵ_D, $\theta_o \rightarrow$ 2 keV.

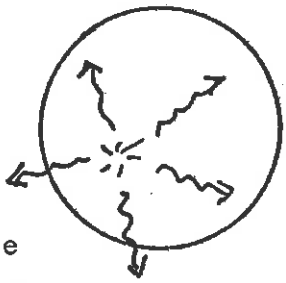

The optimum ignition energy depends on other processes. For example bremsstrahlung radiation is a serious loss mechanism for low temperatures. For example, the bremsstrahlung energy loss rate is some 4 times that of the alpha particle heating rate below 4 keV.

The condition for pellet transparency to bremsstrahlung radiation is

$$R\, n^2 \leq 6.43 \times 10^{47}\, \theta^{7/2}\ \text{cm}^{-5}$$

If we use the disassembly time $\tau_d = R/c_s$, we find this condition becomes

$$\eta = \frac{n}{n_s} \leq 7.75 \times 10^4\ (\epsilon_D/M)$$

Hence for compressions $\eta \sim 10^3$-10^4 and values of $M/\epsilon_D \sim$ 100-1000, the fuel becomes opaque to bremsstrahlung radiation, and ignition can occur for temperatures θ_o less than 4 keV.

Nonuniform Compressed Sphere with Self-Heating and Burn Propagation

Here the general idea is to use shock compression to induce central ignition of the fuel, that is, a "spark" surrounded by cold fuel below the ignition temperature. Then one can ignite a spherically expanding burn wave which propagates outward, leading to complete ignition of the compressed pellet core.

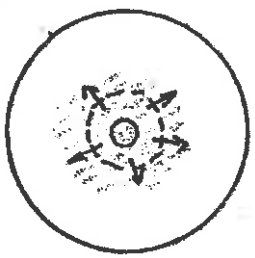

Energy transfer from the burning central region to adjacent cold fuel can occur because of three mechanisms:

(i) hydrodynamic energy transfer (due to rapid pressure buildup in burning region)

(ii) electron thermal conduction from the hot burning region to the cold fuel material

(iii) energy deposition by escaping reaction products (alphas, neutrons, and X-rays)

Usually the propagation of the burn front is highly supersonic, so that hydrodynamic energy transfer (i) is not dominant.

To model the latter two processes, we can ignore hydrodynamic motion and determine the rate of advance of the burn wave based on energy conservation. First note that if the central spark is characterized by a density n_o and radius r, we can write

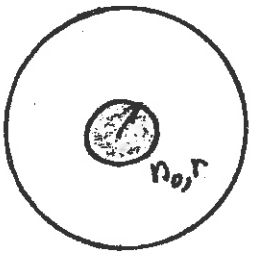

Rate of energy production in uniform region of n_o, r

$$= \left.\frac{dE_{fusion}}{dt}\right|_r = \frac{4}{3}\pi r^3 \langle v\sigma\rangle W_\alpha \frac{n_o^2}{4}$$

(Here we ignore the neutron energy which is only weakly deposited in the burning region.)

Next, compute the rate of change of the internal energy in the expanding region:

$$\frac{d}{dt}\left(\frac{4}{3}\pi r^3 n_o \theta_o\right) = \frac{4}{3}\pi r^3 n_o \dot{\theta} + 4\pi n_o r^2 \theta \dot{r}$$

Hence equating these two energy expressions, we can obtain an equation for the radius of the burning region r:

$$\dot{r} = \frac{n_o \langle v\sigma\rangle W_\alpha}{12\theta_o} r - \frac{1}{3} r\left(\frac{\dot{\theta}_o}{\theta_o}\right)$$

Now the temperature of the burning region, θ_o, will increase until the alpha particle range R_α will become large enough to allow alphas to escape into the surrounding fuel.

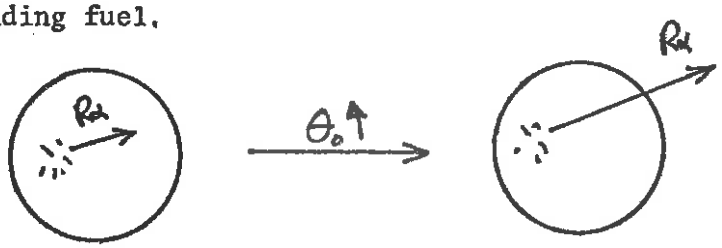

That is, the burn region temperature θ_o will adjust itself so that $R_\alpha \sim r$,

$$r \sim R_\alpha = \lambda_o \frac{\Theta_o^{3/2}}{n_o} \qquad \text{(good for } \Theta_o < 40 \text{ keV)}$$

Hence we can write

$$\frac{\dot{\Theta}_o}{\Theta_o} \sim \frac{2}{3}\frac{\dot{r}}{r}$$

But we recall that the speed of sound is given by

$$c_s = V_o \Theta^{1/2}$$

Hence we can calculate

$$\frac{\text{burning front speed}}{\text{speed of sound}} = \frac{\dot{r}}{c_s} \sim 3\langle v\sigma\rangle W_\alpha \lambda_o / 44 V_o$$

$$= 1.37 \times 10^{16} \langle v\sigma\rangle$$

For $\theta_o > 15$ keV, $\dot{r}/c_s \gtrsim 2$--that is, the propagation of the burn front is supersonic in the cold fuel material.

If we return now to the self-heating equation derived on p. 2-30

$$n_o r = \frac{6V_o}{W_\alpha}\left[I_1 + \left(I_1^2 + \frac{W_\alpha \lambda_o I_2}{3V_o}\right)^{1/2}\right]$$

we can attempt to calculate the required driver energy for ignition. We will take $\theta_o = 4$ keV and $\theta_1 = 2$ keV so that

$$\left(\frac{n_o}{n_s}\right) r = 2.81$$

Hence the initial thermal energy required for central ignition is

$$E_{\text{thermal}} = 4\pi n_o r^2 \Theta_o = 7.99 \times 10^6 \left(\frac{n_s}{n_o}\right)^2 \text{kJ}$$

The minimum energy of the cold fuel is the degeneracy energy (that is, the energy due to the repulsion of the degenerate electrons):

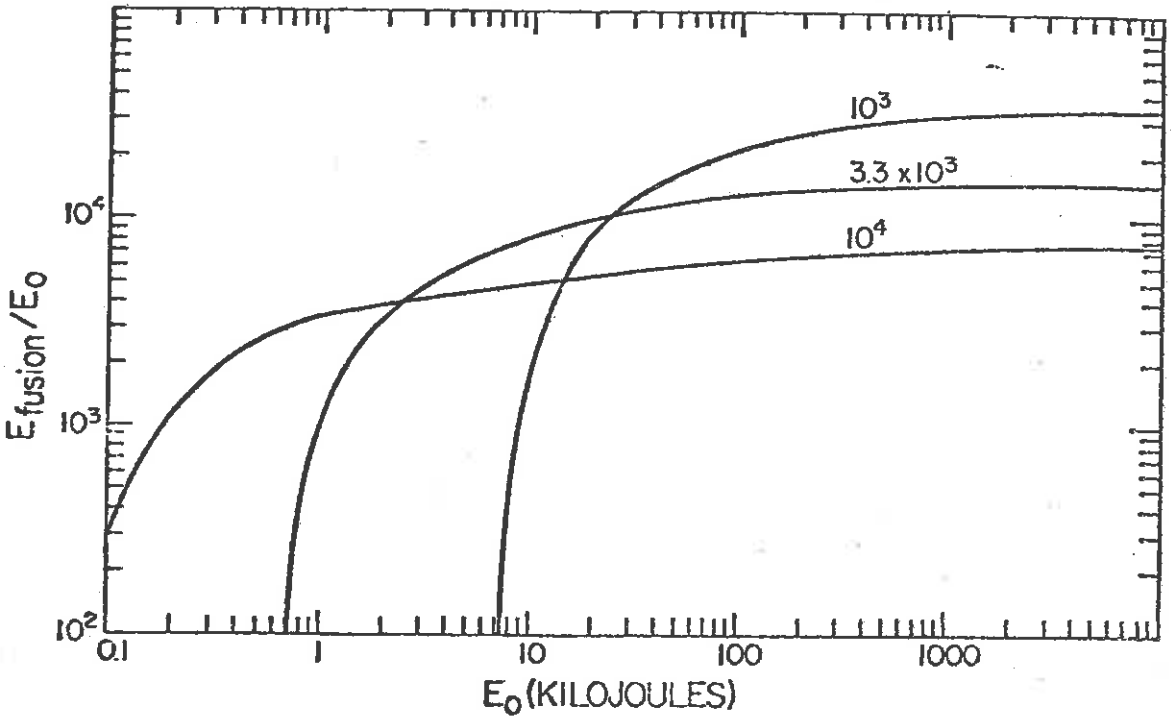

Analytic estimate of fusion-energy production in cold DT fuel ignited by a spherically propagating burning wave. Equation (23.8-43) gives the ignition energy, Eq. (23.8-45) the degeneracy energy, and Eq. (23.8-47) the fusion energy. The initial energy E_0 is the sum of the ignition and degeneracy energy. The laser energy required to give this initial energy depends on the efficiency of laser-energy deposition and of hydrodynamic transfer to the compressed fuel, and typically is a factor of ten to twenty larger than E_0. The curves are labeled by the compression ratio relative to solid DT (0.19 g/cm^3). Reproduced from studies at KMSF performed by K. A. Brueckner et al.

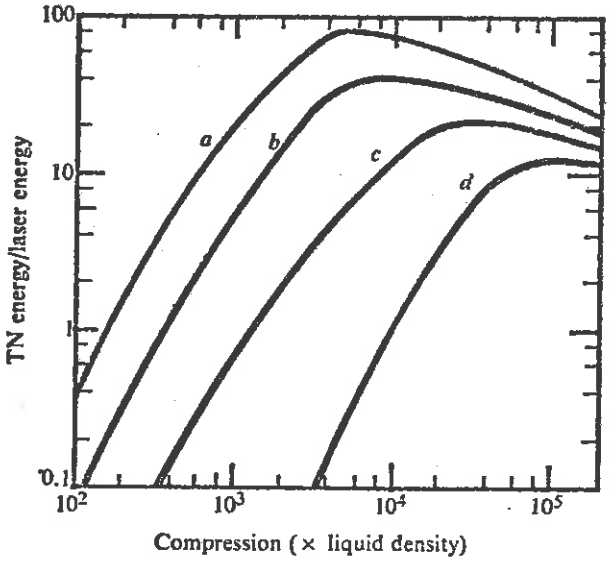

Energy gain plotted against compression: *a*, 10^6 J; *b*, 10^5 J; *c*, 10^4 J; *d*, 10^3 J.

CHAPTER 3

THE PHYSICS OF HYDRODYNAMIC COMPRESSION

The primary objective in inertial confinement fusion schemes is to compress the fuel pellet in such a way that only a central region of the compressed fuel mass is brought to ignition temperatures, leaving the rest of the compressed pellet as cold as possible. In this way, one can ignite a central spark which propagates through the compressed fuel mass as a thermonuclear burn wave.

The essential physics processes involved in this scheme are shown in the Figure below:

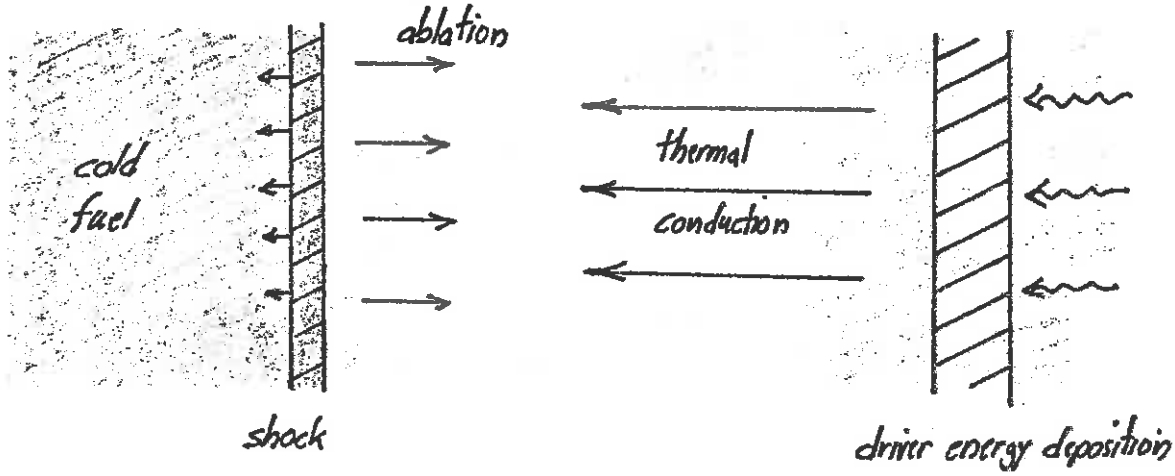

The driver energy is deposited in the outer layers of a plasma cloud or corona surrounding the fuel pellet. This energy is then transported into the pellet surface by electron thermal conduction and heats the surface material, ablating it off into the vacuum surrounding the fuel pellet. This ablation generates shock waves which then implode inward, compressing the fuel to very high temperatures in such as manner as to avoid premature fuel heating (isentropic compression). At peak compression, the central region of the compressed fuel mass is brought to ignition temperature, and a thermonuclear burn wave is produced which propagates outward, consuming the cold compressed fuel material and producing thermonuclear energy.

We will examine each of the important physical processes involved in this approach to inertial confinement fusion, working backwards from the

compression of the fuel material to optimum inertial confinement fusion burn conditions ($\rho R > 1$) to the generation of pressures by ablation to energy transport via thermal conduction and finally to the deposition of the driver energy in the plasma cloud surrounding the pellet. More specifically, our sequence of considerations will be as follows:

(i) Isentropic compression by convergent shock waves
(ii) Equations of state of highly compressed matter
(iii) Ablation-generated pressures
(iv) Energy transfer by electron thermal conduction
(v) Driver energy deposition

We will begin with a discussion of the physics of the hydrodynamic compression of matter.

3.1. SOME REMEDIAL HYDRODYNAMICS

We begin by briefly reviewing the hydrodynamics of a single species fluid such as a gas. We will characterize the state of the fluid by:

mass density: $\rho(\underset{\sim}{r},t) = m\, n(\underset{\sim}{r},t)$

local fluid velocity: $\underset{\sim}{u}(r,t)$

temperature: $T(\underset{\sim}{r},t)$

We can now implement the laws of conservation of mass, momentum, and energy to write

$$\frac{\partial \rho}{\partial t} + \underset{\sim}{\nabla}\cdot\rho\underset{\sim}{u} = 0 \qquad \text{(mass)}$$

$$\rho\left(\frac{\partial}{\partial t} + \underset{\sim}{u}\cdot\underset{\sim}{\nabla}\right)\underset{\sim}{u} - \frac{\rho}{m}\underset{\sim}{F} = -\underset{\sim}{\nabla}\cdot\underset{\approx}{P} \qquad \text{(momentum)}$$

$$\rho c_v\left(\frac{\partial}{\partial t} + \underset{\sim}{u}\cdot\underset{\sim}{\nabla}\right)T = -\underset{\sim}{\nabla}\cdot\underset{\sim}{q} - \underset{\approx}{P} : \underset{\approx}{\Lambda} \qquad \text{(energy)}$$

where

$\underset{\sim}{\underset{\sim}{P}}$ pressure tensor

$$[\underset{\sim}{\underset{\sim}{\Lambda}}]_{ij} \equiv \frac{m}{2}\left(\frac{\partial u_i}{\partial x_j} + \frac{\partial u_j}{\partial x_i}\right)$$

$\underset{\sim}{q}$ heat flux density

These equations can be derived in a number of ways (including control volume arguments, taking moments of the Boltzmann equation). They are exact, However they are incomplete as they stand (the pressure tensor and heat flux are as yet unspecified). To close the equations, it is customary to introduce the usual transport laws (approximations):

Stokes law of viscosity:

$$\underset{\sim}{\underset{\sim}{P}} = p\,\underset{\sim}{\underset{\sim}{I}} - 2\frac{\mu}{m}\left(\underset{\sim}{\underset{\sim}{\Lambda}} - \frac{m}{3}\,\underset{\sim}{\underset{\sim}{I}}\,\underset{\sim}{\nabla}\cdot\underset{\sim}{u}\right)$$

where p is the local hydrostatic pressure, $p = \rho(k/m)\,T$ and μ is the shear viscosity

Fourier's law of thermal conduction:

$$\underset{\sim}{q} = -\kappa\,\underset{\sim}{\nabla}T$$

where κ is the thermal conductivity

The hydrodynamics equations characterizing the fluid then can be written as

$$\frac{\partial \rho}{\partial t} + \underset{\sim}{\nabla}\cdot\rho\underset{\sim}{u} = 0$$

$$\rho\left(\frac{\partial}{\partial t} + \underset{\sim}{u}\cdot\underset{\sim}{\nabla}\right)\underset{\sim}{u} - \rho\underset{\sim}{F}/m = -\underset{\sim}{\nabla}p + \frac{1}{3}\underset{\sim}{\nabla}\mu\,\underset{\sim}{\nabla}\cdot\underset{\sim}{u} + \mu\nabla^2\underset{\sim}{u}$$

$$\rho c_v\left(\frac{\partial}{\partial t} + \underset{\sim}{u}\cdot\underset{\sim}{\nabla}\right)T = -\rho\,(\underset{\sim}{\nabla}\cdot\underset{\sim}{u})T + \underset{\sim}{\nabla}\cdot k\,\underset{\sim}{\nabla}T$$

These are sometimes referred to as the Navier-Stokes equations.

Thus far we have confined our attention to a single species gas. But a plasma can be modeled as a two component fluid, accounting for both ions and electrons, and therefore would be characterized by 6 state variables:

$$\rho_e, \rho_i, u_e, u_i, T_e, T_i$$

Therefore we might expect to need 6 hydrodynamic equations.

Fortunately for most inertial confinement fusion applications, we can collapse the hydrodynamic equations for a plasma somewhat by first recognizing that over the length scales of most concern, there is no charge separation. More precisely, we can ignore charge separation if the ratio of the Debye length to the mean free path is much less than one:

$$\frac{\lambda_D}{\lambda_{ee}} << 1$$

Here

$$\text{Debye length} = \lambda_D = \left[\frac{kT_e}{4\pi n_e e^2}\right]^{1/2}$$

$$\text{electron mean free path} = \lambda_{ee} = \frac{(3kT_e)^2}{8(.714)\pi n_e e^2 \ln\Lambda}$$

In ICF applications, this ratio is typically:

$$10^{-3} < \frac{\lambda_D}{\lambda_{ee}} < 0.036 << 1$$

($n_e \sim 10^{23}$, $\theta_e \sim 1$ keV) ($n_e \sim 10^{27}$, $\theta_e \sim 1$ keV)

Hence we can assume that $n_e \sim n_i$ and $u_e \sim u_i$.

However, in most cases the time scales of interest are much shorter than the electron-ion temperature equilibrium times (although usually larger than the election or ion self-equilibration times). Hence we must characterize each of the components of the plasma fluid by a different temperature: $\theta_e \neq \theta_i$.

Therefore the model most frequently used to describe the hydrodynamics of a ICF plasma is a single fluid, two-temperature description in which

$$n_i = n_e = n, \qquad \rho = n(m_i + m_e)$$

$$u_i = u_e = u, \qquad p = p_i + p_e = n(\theta_e + \theta_i)$$

Several other remarks are useful before we write down the full form of the hydrodynamics equations for an ICF plasma. First we note that because of the large mass difference between the electrons and the ions, $m_i >> m_e$,

the ions are responsible for momentum transport (and hence viscosity)
the electrons are responsible for energy transport (and hence thermal conduction)

In mathematical terms,

$$\mu_i \frac{\partial u_i}{\partial x} >> \mu_e \frac{\partial u_e}{\partial x}$$

$$\kappa_e \frac{\partial \theta_e}{\partial x} >> \kappa_i \frac{\partial \theta_i}{\partial x}$$

Furthermore, the very high thermal conductivity in a plasma leads to a Prandtl number:

$$Pr \equiv \frac{\mu C_p}{\kappa} = 0.065$$

which is very small.

The form of the single-fluid, two temperature hydrodynamic equations used to describe an ICF plasma then becomes:

$$\frac{\partial \rho}{\partial t} + \underset{\sim}{\nabla} \cdot \rho \underset{\sim}{u} = 0$$

$$\rho \left(\frac{\partial}{\partial t} + \underset{\sim}{u} \cdot \underset{\sim}{\nabla} \right) \underset{\sim}{u} - \rho \underset{\sim}{F}_m = -\underset{\sim}{\nabla} p + \frac{1}{3} \underset{\sim}{\nabla} \mu_i \underset{\sim}{\nabla} \cdot \underset{\sim}{u} + \mu_i \nabla^2 \underset{\sim}{u}$$

$$\rho C_v \left(\frac{\partial}{\partial t} + \underset{\sim}{u} \cdot \underset{\sim}{\nabla} \right) T_e = -\rho (\underset{\sim}{\nabla} \cdot \underset{\sim}{u}) T_e + \underset{\sim}{\nabla} \cdot \kappa_e \underset{\sim}{\nabla} T_e - \frac{1}{\tau_{ei}} (T_e - T_i)$$

$$\rho C_v \left(\frac{\partial}{\partial t} + \underset{\sim}{u} \cdot \underset{\sim}{\nabla} \right) T_i = -\rho (\underset{\sim}{\nabla} \cdot \underset{\sim}{u}) T_i + \mu_i (\underset{\sim}{\nabla} \cdot \underset{\sim}{u})^2 + \frac{1}{\tau_{ei}} (T_e - T_i)$$

3.2. SHOCK WAVES

When a large disturbance is suddenly introduced into a gas, say by the rupture of a diaphragm maintaining a pressure differential in the gas or by a rapid local deposition of energy, this disturbance will propagate into the adjacent gas with the local speed of sound c_s. But we have noted that the speed of sound is proportional to the square root of the gas density,

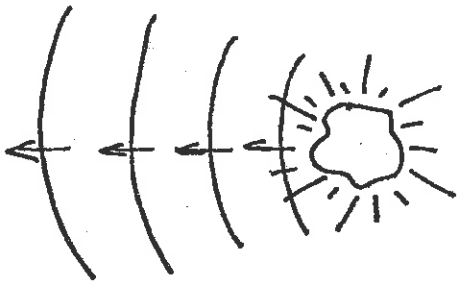

$$c_s \sim \sqrt{\rho}$$

Hence regions of the disturbance with higher densities will tend to propagate faster than those of lower density, thereby causing a density perturbation to steepen into a sharp wave front or "shock wave" propagating faster than the speed of sound in the ambient gas ahead of the wave.

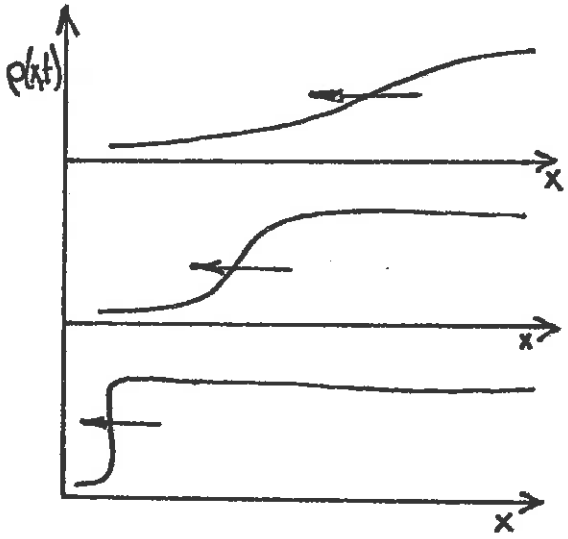

Mathematically, we can define a shock wave as any abrupt disturbance that propagates through the gas, causing a change of state. The Euler equations for an ideal fluid predict that such shock waves will propagate as a discontinuity in ρ, u, and T. But dissipative phenomena such as viscosity and thermal conduction will yield a finite shock wave thickness (although the shock thickness is frequently on the order of a mean free path).

To be more specific, we will consider the propagation of a plane (one-dimensional) shock wave propagating from right to left in a medium with a speed D. We will furthermore assume that the fluid ahead of and behind the shock wave is in a steady-state situation, described by the state variables indicated on the diagram below:

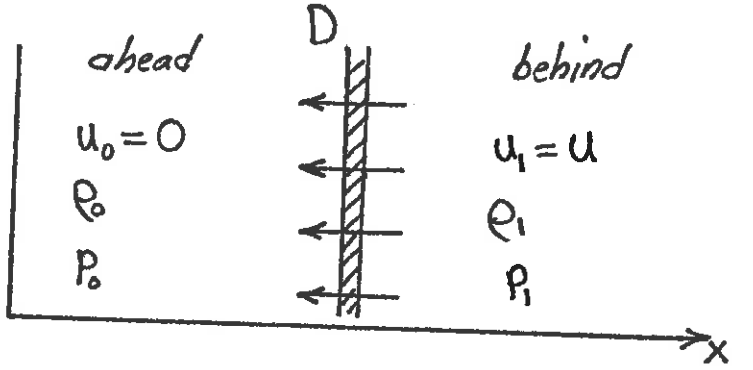

It is customary to take the flow velocity ahead of the shock as zero--that is, the ambient gas ahead of the shock wave is at rest:

$$u_o = 0$$

The gas behind the shock is set into motion with a velocity u_1. We are usually given the density and pressure in the ambient gas ahead of the shock, ρ_o, p_o, along with some measure of the shock wave strength such as its speed D or the driving pressure behind it, p_1. Our goal then is to determine the gas properties after the shock has passed such as the density ρ_1 and the flow velocity v_1. Here is should be noted that one commonly introduces the Mach number characterizing the shock wave which is defined as the ratio of the shock speed and the speed of sound in the ambient gas ahead of the shock;

$$M = \frac{D}{c_{so}} = \text{Mach number}$$

It should be apparent that, by definition, the Mach number characterizing the shock wave is greater than one--the shock wave propagates supersonically into the gas ahead.

To analyze the shock wave, it is convenient to shift to a coordinate frame moving along with the shock. In this frame the gas appears to decelerate from a speed $u_o' = D$ to a slower speed $u_1' = D - u_1$. For that reason, one refers to the gas ahead of and behind the shock wave as the "upstream" and "downstream" shock regions or the "intake" and "exhaust" regions, respectively:

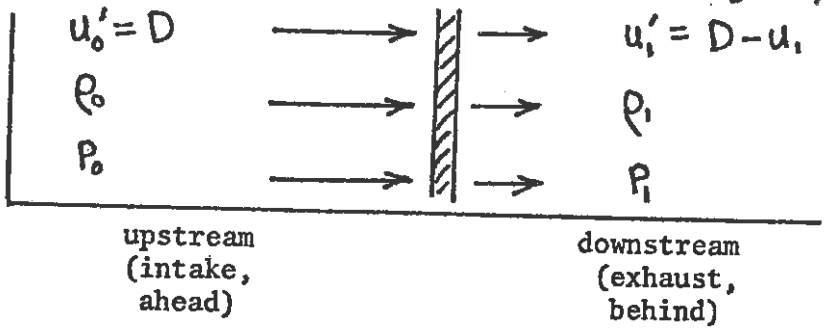

We will drop the primes from the notation for the velocities u_o and u_1 in the coordinate frame moving with the shock wave for convenience.

We can easily determine the downstream variables by using the conservation equations, written in one-dimensional form (and setting viscosity and thermal conductivity equal to zero, for the present at least):

$$\frac{\partial \rho}{\partial t} + \frac{\partial}{\partial x}(\rho u) = 0$$

$$\frac{\partial}{\partial t}(\rho u) + \frac{\partial}{\partial x}(p + \rho u^2) = 0$$

$$\frac{\partial}{\partial t}\left(\rho e + \frac{\rho u^2}{2}\right) + \frac{\partial}{\partial x}\left[\rho u\left(e + \frac{u^2}{2} + p/\rho\right)\right] = 0$$

Here we have found it convenient to introduce:

$$\text{internal energy} = e = c_p\,\theta$$

$$\text{specific enthalpy} = h = e + p/\rho$$

For steady-state flow we can ignore the time derivatives and integrate the conservation equations across the shock from $-\varepsilon$ to $+\varepsilon$ to find:

mass conservation: $\rho_o u_o = \rho_1 u_1$

momentum conservation: $p_o + \rho_o u_o^2 = p_1 + \rho_1 u_1^2$

energy conservation: $h_o + \frac{u_o^2}{2} = h_1 + \frac{u_1^2}{2}$

These equations are known as the Rankine-Hugoniot relations. They are quite general and exact (and can be derived from a number of different perspectives, including simple physical arguments).

The Rankine-Hugoniot relations represent 3 equations for six unknowns: (ρ_o, u_o, p_o) and (ρ_1, u_1, p_1), since the specific enthalpy is presumably given in terms of the density and pressure by an equation of state

$$h_o = h_o(\rho_o, p_o)$$
$$h_1 = h_1(\rho_1, p_1)$$

We are presumably given the density and pressure in the undisturbed gas ahead of the shock, ρ_o and p_o. Furthermore, we are frequently given the "strength" of the shock in terms of the shock speed $D = u_o - u_1$ or the driving pressure p_1 (we will usually assume the latter situation since it most closely approximates the situation of interest in ICF applications). Therefore we have 3 equations in 3 unknowns:

$$\rho_o,\ p_o,\ p_1 \quad \Rightarrow \quad \rho_1,\ u_1,\ u_o$$

To proceed further, we must assume some form of equation of state characterizing the gas. For the moment, we will leave this arbitrary and develop a slightly different perspective of the shock propagation. We begin by solving the Rankine-Hugoniot relations for the upstream and downstream velocities in terms of the specific volumes $V_o = 1/\rho_o$ and $V_1 = 1/\rho_1$:

$$u_o^2 = V_o^2 \frac{p_1 - p_o}{V_o - V_1}$$

$$u_1^2 = V_1^2 \frac{p_1 - p_o}{V_o - V_1}$$

But

$$\frac{1}{2}(u_o^2 - u_1^2) = \frac{1}{2}(p_1 - p_o)(V_o + V_1)$$

so that

$$h_1 - h_o = \frac{1}{2}(p_1 - p_o)(V_o + V_1)$$

When combined with equations of state, this yields the pressure behind the shock as a function of the pressure ahead of the shock and the specific volumes:

$$p_1 = H(V_1,\ p_o,\ V_o)$$

This function relating p_1 to $V_1 = 1/\rho_1$ is known as the shock Hugoniot. It is most convenient to represent this function as a curve on the usual pV diagram familiar from thermodynamics.

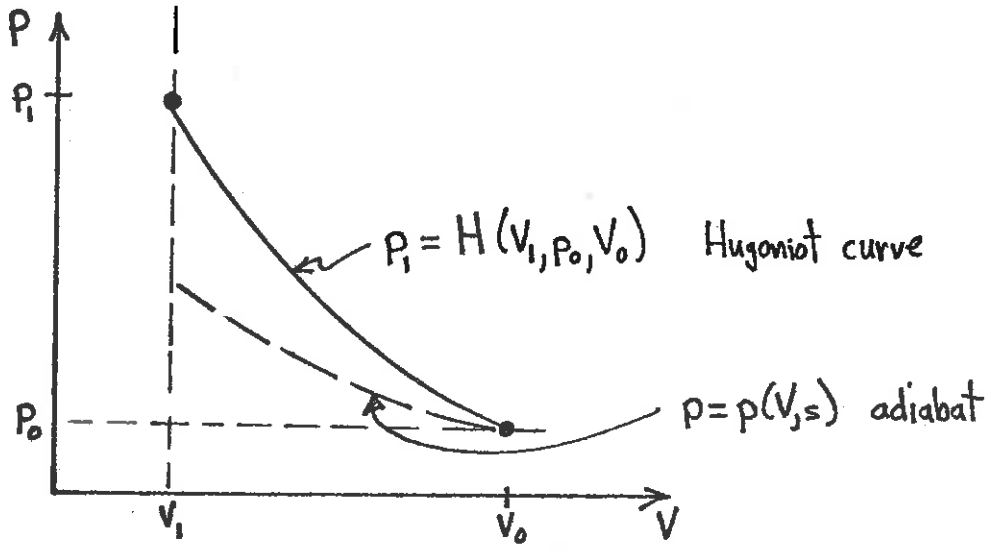

It should be noted at the outset that the shock Hugoniot differs substantially from the pV curve characterizing the reversible, adiabatic (or isentropic) compression of a gas (which we have also sketched on the pV diagram). This latter curve is given for an ideal gas by

$$pV^{\gamma} = \text{constant}$$

(We will demonstrate this later when we discuss the equation of state for compressed matter.) We recall that the area under the p-V curve represents the work required to compress the fluid. Hence the fact that the shock Hugoniot lies above the adiabatic or isentrope for the gas implies that more work is required to compress a material by the passage of a shock than would be required by an isentropic compression (that follows the adiabatic curve). We will note in a moment that this is evidence of the fact that the propagation of a strong shock wave is not isentropic. Irreversible processes such as viscosity and thermal conduction increase the internal energy (i.e., temperature) of the shocked medium beyond the minimum energy necessary to merely compress it. We will also demonstrate that the stronger the shock wave, the more the shock Hugoniot will depart from the adiabat (the more work required for compression by the shock--the more energy dissipated).

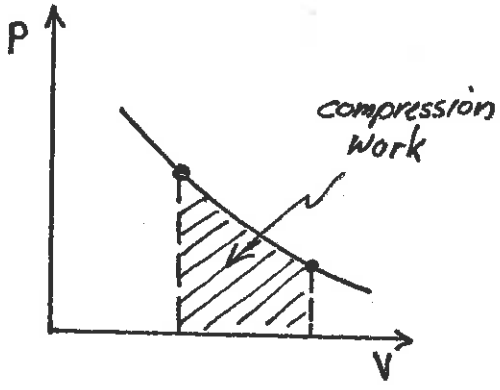

EXAMPLE: Shock wave propagation in an ideal gas

To consider a specific example, let us consider the equation of state of an ideal gas (for details refer ahead to the section on equations of state) which implies

$$e = c_v T = \frac{1}{\gamma - 1} p V$$

$$h = c_p T = \frac{\gamma}{\gamma - 1} p V$$

Hence we can solve for

$$u_0^2 = \frac{V_0}{2}\left[(\gamma-1)p_0 + (\gamma+1)p_1\right]$$

$$u_1^2 = \frac{V_0}{2}\left[\frac{\left[(\gamma+1)p_0 + (\gamma-1)p_1\right]^2}{(\gamma-1)p_0 + (\gamma+1)p_1}\right]$$

In this way we can calculate the relationship between upstream and downstream variables:

$$\frac{\rho_1}{\rho_0} = \frac{(\gamma+1)\rho_1 - (\gamma-1)\rho_0}{(\gamma+1)\rho_0 - (\gamma-1)\rho_1}$$

$$\frac{\rho_1}{\rho_0} = \frac{(\gamma+1)p_1 + (\gamma-1)p_0}{(\gamma-1)p_1 + (\gamma+1)p_0}$$

$$\frac{T_1}{T_0} = 1 + \frac{2\gamma}{(\gamma+1)^2}\,\frac{\gamma M_0^2 + 1}{M_0^2}\,(M_0^2 - 1)$$

Notice that if we substitute in the specific volume into the pressure-density relation, we find an explicit form for the shock Hugoniot in an ideal gas:

$$p_1 = p_0\left[\frac{(\gamma+1)V_0 - (\gamma-1)V_1}{(\gamma+1)V_1 - (\gamma-1)V_0}\right] = H(V_1, p_0, V_0)$$

We can also calculate the upstream and downstream Mach numbers:

$$M_0 = \left[\frac{(\gamma-1)+(\gamma+1)P_1/P_0}{2\gamma}\right]^{1/2} \rightarrow \left(\frac{\gamma+1}{2\gamma}\right)^{1/2}\left(\frac{P_1}{P_0}\right)^{1/2}$$

$$M_1 = \left[\frac{(\gamma-1)+(\gamma+1)(P_0/P_1)}{2\gamma}\right]^{1/2} \rightarrow \left(\frac{\gamma-1}{2\gamma}\right)^{1/2} \longrightarrow 0.45$$

As we might expect, $M_0 > 1$ and $M_1 < 1$ implies that the motion of the shock is supersonic into the material ahead of it and subsonic with respect to the gas behind the shock.

The limiting form of the relations between upstream and downstream variables for very strong shock waves ($p_1/p_0 \to \infty$) is particularly interesting:

$$\frac{P_1}{P_0} \rightarrow 1 + \frac{2\gamma}{\gamma+1}(M_0^2-1) \rightarrow \infty$$

$$\frac{\rho_1}{\rho_0} \rightarrow \frac{(\gamma+1)M_0^2}{(\gamma-1)M_0^2+2} \rightarrow \frac{\gamma+1}{\gamma-1}$$

$$\frac{T_1}{T_0} \rightarrow \left(\frac{\gamma-1}{\gamma+1}\right)\frac{P_1}{P_0} \rightarrow \infty$$

This dependence is shown in the figure below:

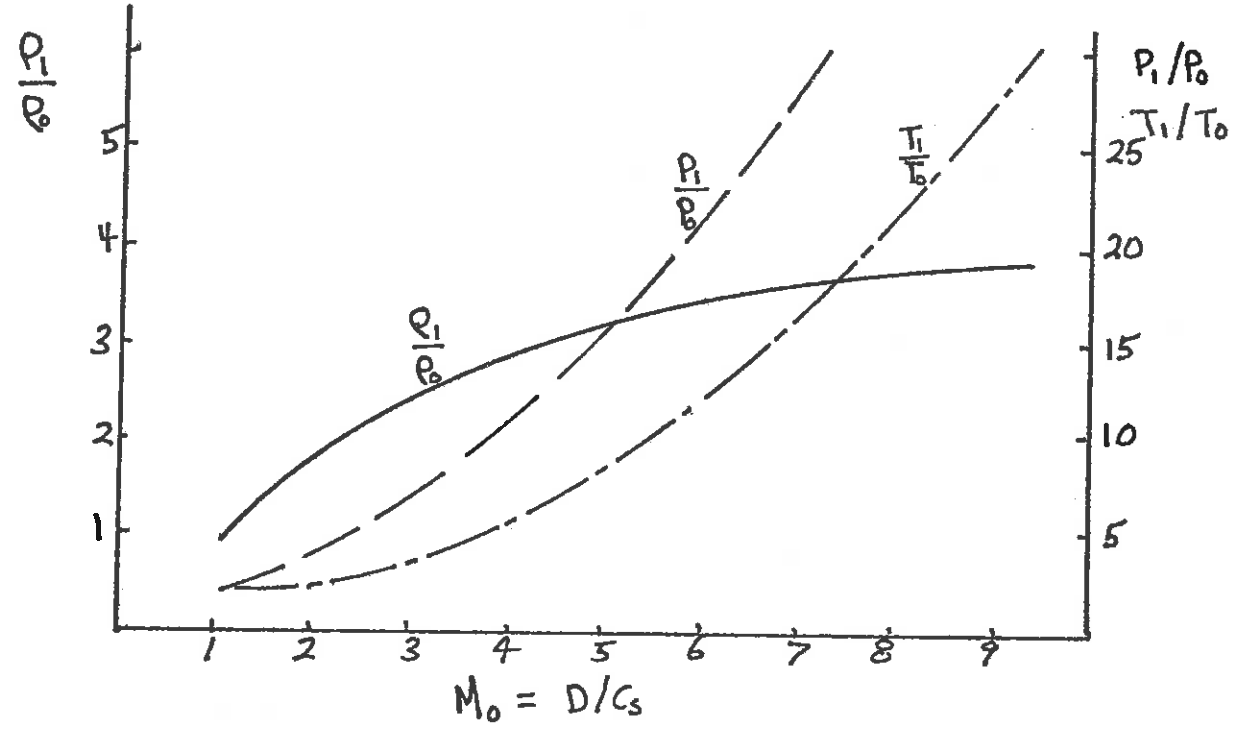

In particular, we note that while the temperature and pressure rise across the shock will increase indefinitely with the strength of the shock, the compression or density change approaches an asymptotic limiting value of

$$\frac{\rho_1}{\rho_0} \rightarrow \frac{\gamma+1}{\gamma-1}$$

For an ideal monatomic gas, $\gamma = 5/3$, Hence we find the important result that the maximum compression that can be achieved by a single plane shock wave in a monatomic gas is 4:

We can also calculate the entropy change across the shock, If we define the specific entropy as

$$s = c_v \ln p\rho^{-\gamma}$$

then the entropy change is

$$\Delta s \equiv s_1 - s_0 = c_v \ln \left\{ \frac{p_1}{p_0} \left[\frac{(\gamma-1)p_1 + (\gamma+1)p_0}{(\gamma+1)p_1 + (\gamma-1)p_0} \right]^{\gamma} \right\}$$

In particular, we note that the entropy increases as the log of the shock strength, p_1/p_0:

$$\Delta s \sim c_v \ln c\left(\frac{p_1}{p_0}\right) \rightarrow \infty$$

(It should be noted that while we have not specifically included the effects of viscosity and heat conduction in our analysis based on the Rankine-Hugoniot, such dissipative behavior is still properly described by calculating the change in the state of the gas as we have done. A specific inclusion of viscous and thermal conduction effects would only facilitate the study of the shock wave structure, not the states of the gas ahead of and behind the shock.)

In particular, we should note that in the limit of weak shock waves,

$$\Delta s \to 0 \qquad \text{as} \qquad \frac{p_1}{p_0} \to 1$$

--that is, the propagating disturbance tends to the limiting case of an isentropic acoustic (sound) wave.

With this background, let us return to our diagram of the shock Hugoniot and address the question of how we might use shock waves to isentropically compress thermonuclear fuel to high density while leaving it relatively cold. Since weak shock waves approach an isentropic sound wave, we might attempt to use a series of many weak shocks to approach isentropic compression. This approach is shown in detail in the p-V diagram, in which a series of multiple shocks is used to approximate the adiabat and isentropically compress the fuel to a much higher density for the same final pressure (and therefore requiring far less pV work than would be required by a single shock wave).

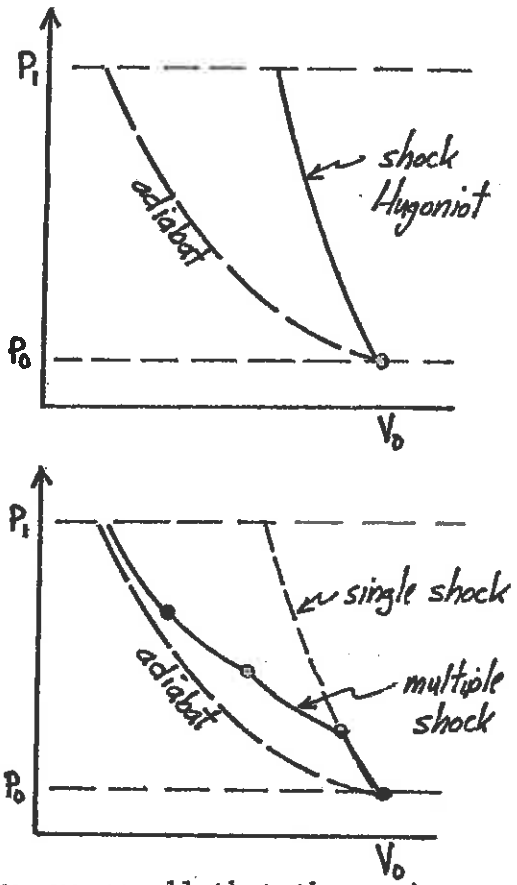

From a somewhat different point of view, we recall that the maximum compression achievable by a single plane shock wave in a monatomic gas is 4. Therefore, by subjecting the shocked gas to a second shock wave, we can increase density by a factor of 4 x 4. We can continue on in this fashion to multiply-shock the fuel to higher and higher density.

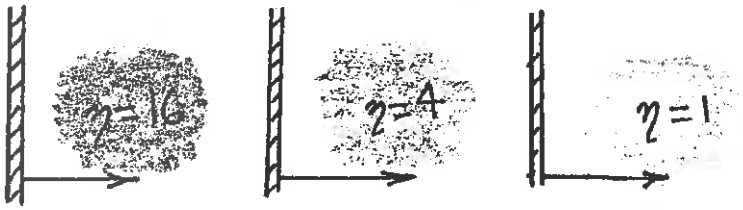

Several comments should be made concerning shock waves in a plasma. Thus far we have analyzed the propagation of a shock wave in a single component gas. However a thermonuclear plasma is in fact a two-component gas with a dramatic difference in the mass of each species (electrons versus ions). This leads to a more complex shock structure.

To be more precise, we have shown below the shock wave structures for a plane shock wave in an ideal gas (described as a sharp discontinuity by the Euler equations), a shock in a real gas (in which viscosity and thermal conductivity broaden out the shock, providing a structure or shock thickness several mean free paths in thickness), and a shock wave in a plasma:

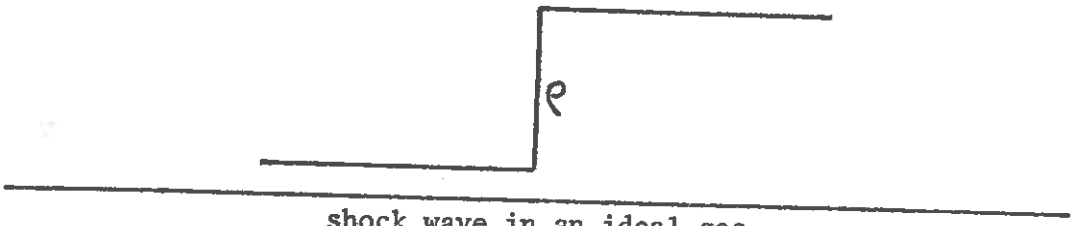

shock wave in an ideal gas

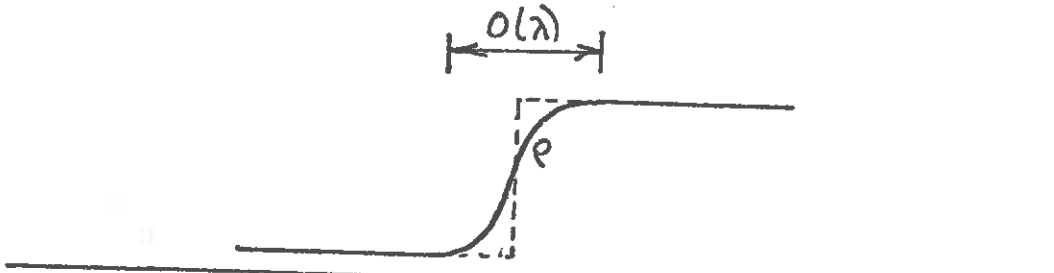

shock wave in a real gas

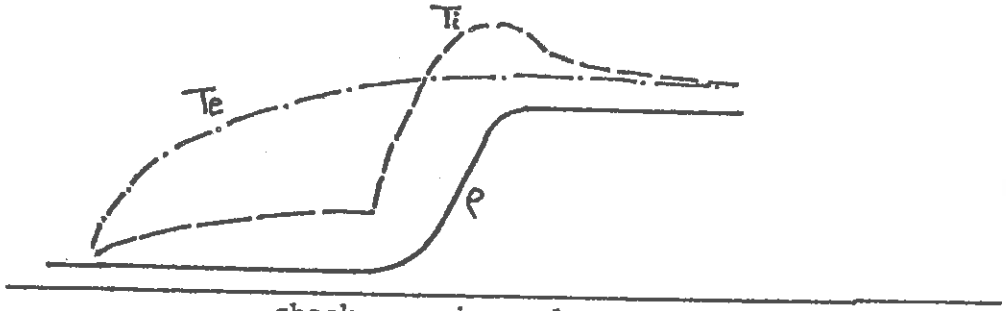

shock wave in a plasma

We can understand the more complex structure of the shock wave in a plasma if we recall that thermal conduction or energy transport is due to electrons, and viscosity or momentum transport is due to the ions. If we assume a single-

fluid, two-temperature model, then the shock structure of the density profile is determined essentially by the ions and therefore a thickness of the order of the ion mean free path.

However the new feature is the role played by electron thermal conduction. In the shock waves typical of ICF plasmas, the driver energy is deposited in the electrons, resulting in an increase of electron temperature behind the shock. But the very large thermal conductivity of the electrons transports this thermal energy in a thermal conduction wave ahead of the shock. This electron conduction wave leads the ion shock structure by the mean free path for electron-ion collisions. This thermal energy in the electrons ahead of the shock is then transferred to the ions by electron-ion collisions, resulting in the preheating of ions ahead of the shock wave. The ion temperature then rises through the shock wave from viscous heating and may overshoot the electron temperature behind the shock. Eventually, far behind the shock, the electron and ion temperatures will equilibrate.

The presence of a preheating "foot" ahead of the shock due to electron thermal conduction is a very important phenomena since it reduces the strength

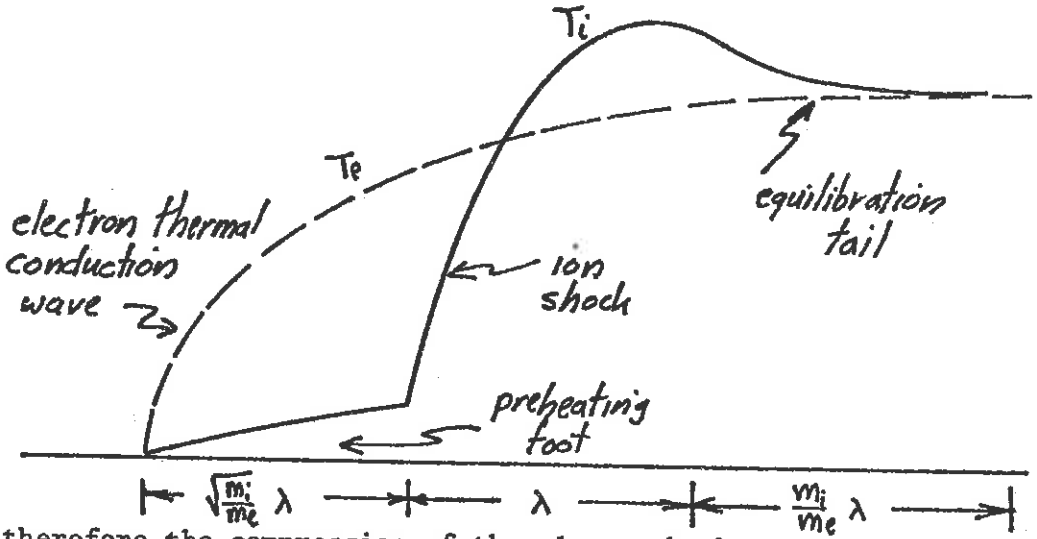

and therefore the compression of the plasma shock wave. Another interesting feature of plasma shock waves is the presence of two Mach numbers, one characterizing ion flow (which is essentially the Mach number of the shock)

$$M = \frac{\frac{1}{2}m_i u_i^2 + \frac{1}{2}m_e u_e^2}{\gamma_i k T_i + \gamma_e k T_e} \sim \frac{m_i u_i^2}{2\gamma_i k T_i}$$

and another Mach number M_e characterizing electron flow

$$M_e = \frac{u}{c_{se}}$$

It should be noted that

$$M = \frac{1}{2}\sqrt{\frac{m_i}{m_e}}\, M_e$$

Therefore the electron flow will remain subsonic in the shock even for very large Mach numbers $M < 30$.

3.3. SPHERICALLY CONVERGENT SHOCK WAVES

A key idea in the use of shock waves to compress ICF fuel pellets is to use the convergence properties of a spherical implosion to multiply the pressure generated and hence the compression. The earliest analysis of this phenomenon was due to Guderly [Luftfahrt-Forshung 9, 302 (1942)] who considered a self-similar solution of the Euler equations for a spherically convergent shock wave in an ideal gas.

DETOUR: In fluid dynamics one frequently finds that the fluid variables $\rho(x,t)$, $u(x,t)$, and $T(x,t)$ become a function of a combination of space and time, say

$$\rho(x,t),\ u(x,t),\ T(x,t) \longrightarrow \text{fcn}(xt^{\alpha})$$

This corresponds in essence to a frozen picture of the flow. That is, all distributions with respect to x change with time without changing form--they remain "similar to themselves".

The type of flow in which the distributions of flow variables remain similar to themselves with time and vary only as a result of changes of scale are called self-similar. The most common case is $\alpha = -1$, that is

$$\rho(x,t),\ u(x,t),\ T(x,t) \longrightarrow \text{fcn}(x/t)$$

The physical reason for this behavior lies in the fact that the Euler equations contain no characteristic length or time scales. (Indeed, the only length and time scales in a gas are the mean free path and the collision time, which are related to viscosity and thermal conductivity). The only dimensional parameter is the speed of sound, c_s. Hence the flow can depend only on the combination x/t.

The mathematical importance of self-similar flow is that it reduces the usual partial differential equations describing hydrodynamics to ordinary differential equations:

PDE ——self-similar solutions ——→ ODE

Guderly obtained a self-similar solution of the Euler equations for a spherically convergent geometry in terms of reduced variables related to the radius-time diagram of the shock front:

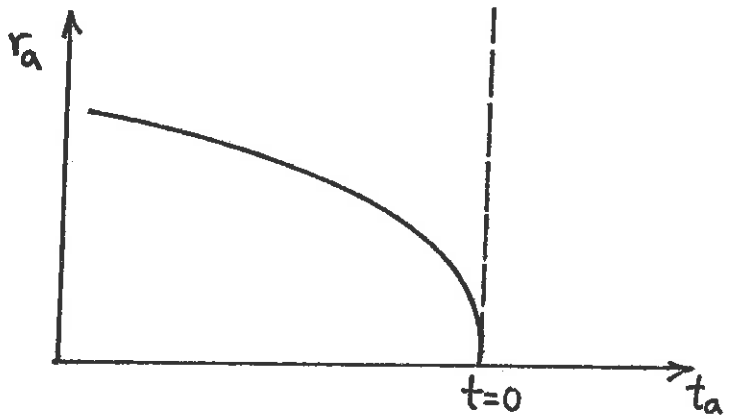

He found a solution for the shock radius

$$r_a = S\,(-t_a)^n$$

where the time $t_a = 0$ corresponded to convergence of the shock at the center. Here, $n = 0.69$ for a monatomic gas ($\gamma = 5/3$) and S is a measure of shock strength.

Of more interest, however, was the state of the gas behind the converging shock wave. Guderly found that the passage of a converging shock gives a density increase or compression of 4 (for a gas with $\gamma = 5/3$), just as

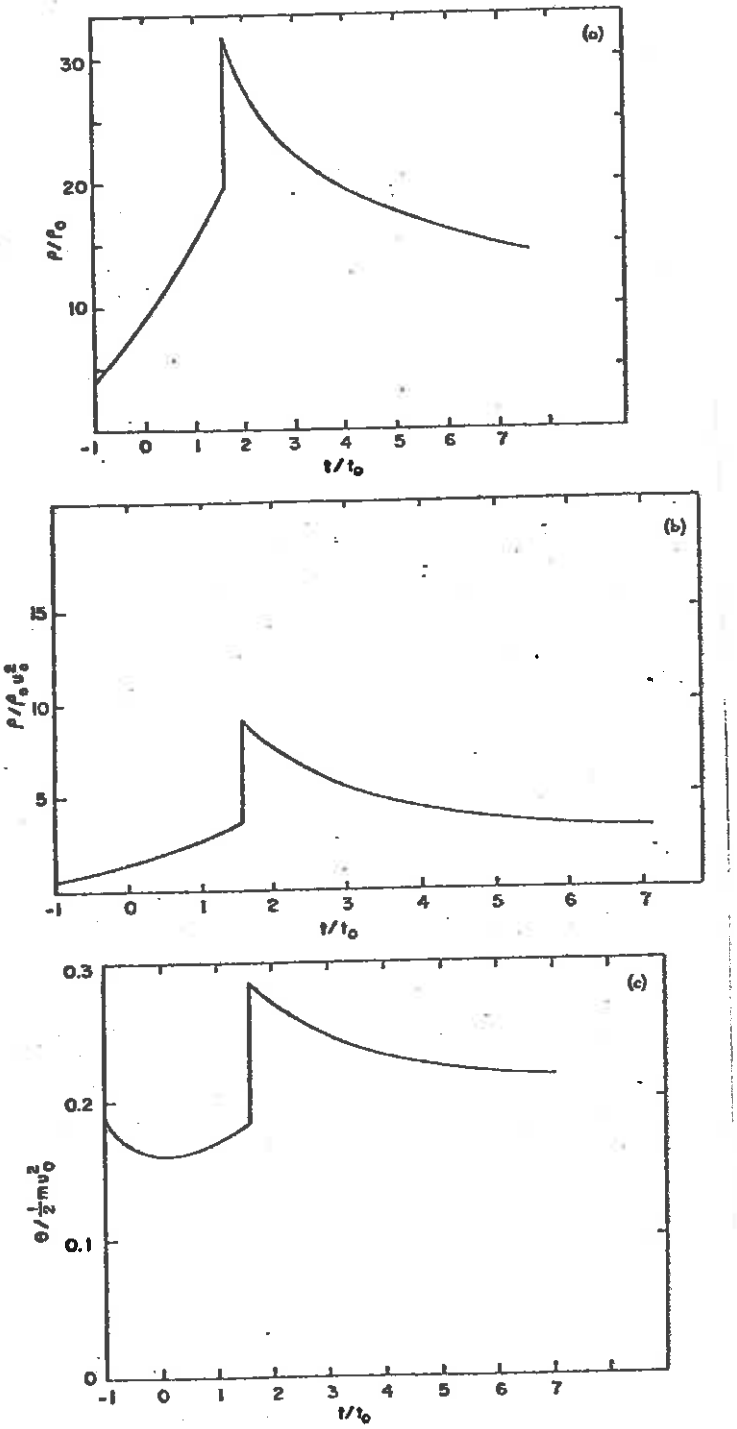

Distributions of density ρ, pressure p, and temperature θ for a converging shock wave (Goldman, 1972).

for a plane shock wave. However this is followed in the spherically convergent case by an adiabatic compression to a compression of about 15. The shock wave is then reflected at the center, and upon returning, gives a further shock compression to 33. That is,

maximum compression from a single convergent shock $\sim$ 33

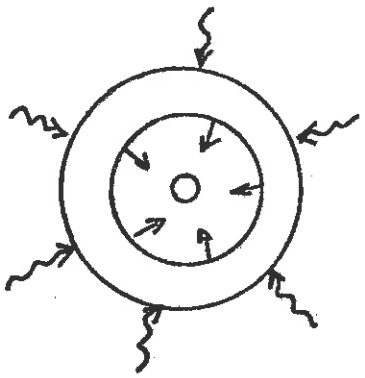

Hence one approach to achieving the conditions necessary for efficient thermonuclear burn would be to deposit energy uniformly on the surface of the fuel pellet in such as way as to produce a strong convergent shock. Brueckner and Jorna have analyzed this situation and predict a driver energy requirement of

$$E_{driver} = 40.9 \frac{M^3}{\epsilon_D^4} \eta^2 \text{ MJ}$$

Hence convergent shock compression does not appreciably reduce the required driver energy. Their analysis indicates that the effect of compression is offset by an inefficient temperature distribution which reduces fusion energy production in most of the fuel. The compressed pellet core which is strongly heated is too small and the compression time is too short to yield an appreciable fusion energy yield. More detailed computer calculations indicate that the required driver energy for breakeven using single shock compression is roughly 500 MJ.

3.4. ISENTROPIC COMPRESSION

The key to achieving the very high fuel densities necessary for efficient thermonuclear burn is to compress the pellet isentropically in such a way that the heating of the dense fuel core is minimized and the minimum compression energy is required. This can be accomplished by producing a sequence of shock waves that approach the adiabatic curve of compression in the p-V diagram of the fuel. Such isentropic compression requires a gradually rising pressure on the surface of the pellet which generate a sequence of shock waves of increasing strength which are adjusted in time so that successive shocks do not overtake each other before arriving at the center of the pellet.

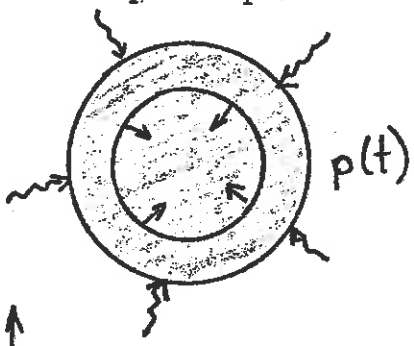

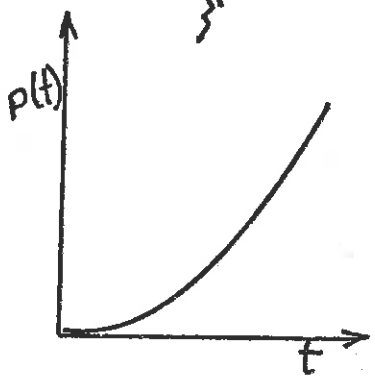

More precisely, the compression and temperature history of the fuel after the passage of the first shock follow (approximately) an adiabat, until the shock reaches the center where its kinetic energy is converted into internal energy and a reflected shock forms.

The final temperature is determined by the initial shock strength. To avoid excessive preheating, we want to reach only the minimum temperature required for ignition. Then the achievable compression is limited only by the degeneracy pressure of the electrons or by the ignition of the fuel before maximum compression has been achieved.

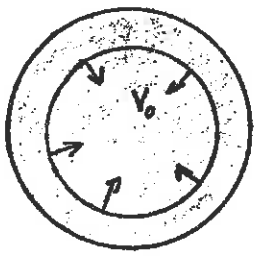

As a model of this process, consider a strong shock wave moving inward at a speed v_o which brings the fuel to a temperature θ_o when it converges to the center of the pellet at time t_o.

The idea is to generate pressure waves after the first shock which overtake the shock at the center. The limiting condition on the pressure wave speed is then:

$$v_s(t)(t_0 - t) = r$$

In this situation the compression is almost adiabatic and

$$\theta = \theta_0 \left(\frac{r_0}{r}\right)^2$$

$$p = p_0 \left(\frac{r_0}{r}\right)^5$$

$$v_s = v_0 \left(\frac{\theta}{\theta_0}\right)^{1/2}$$

so that

$$r^2 = r_0^2 (1 - t/t_0) \quad \text{where} \quad t_0 = r_0/2v_0$$

The compression at the minimum radius is

$$\frac{\rho_m}{\rho_0} = \left(\frac{r_0}{r_m}\right)^3$$

where

$$\theta_m = \theta_0 \left(\frac{r_0}{r_m}\right)^2$$

Here, θ_m is determined by the ignition requirements. One usually takes $\theta_m \sim 2$ keV (corresponding to a local maximum of 5 keV within r_m).

The driver energy profile is then

$$\phi \sim 4\pi r^2 4 v_s p = 16\pi r_0^2 v_0 p_0 \left(\frac{r_0}{r}\right)^4$$

$$= 8\pi \frac{r_0^3 p_0}{t_0} \frac{1}{(1 - t/t_0)^2}$$

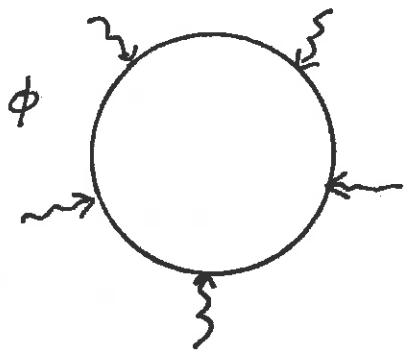

The absorbed driver energy to the implosion maximum is

$$E_{\substack{\text{driver}\\ \text{abs}}} = 8\pi r_o^3 p_o \frac{1}{(1 - t_m/t_o)} = 8\pi r_o^3 p_o \left(\frac{\rho_m}{\rho_o}\right)^{2/3}$$

$2 n_o \theta_o \leftarrow \quad \theta_m = \theta_o (r_o/r_m)^2$

$$= 16\pi r_o^3 n_o \theta_m$$

$$= 4\left[\frac{4}{3}\pi r_m^3 \, 3\theta_m\right]$$

We recognize the quantity in brackets as the energy required to bring the compressed fuel material to a temperature θ_m. Hence it is apparent from this analysis that 75% of the absorbed energy is carried off by ablation products.

EXAMPLE: Consider the pellet conditions:

$$\eta = \frac{\rho_m}{\rho_o} = 10^4, \quad \theta_m = 2\,\text{keV}, \quad r_m = 300\,\mu\text{m}, \quad f_b = 30\%$$

This implies a fusion energy of

$$E_{\text{fusion}} = 3\ \text{MJ}$$

and a driver absorption energy of

$$E_{\text{driver}} = 43.6\ \text{kJ}$$

Hence the pellet gain is

$$M = 75$$

In this case the core temperature is

$$\theta_o = \theta_m (\rho_o/\rho_m)^{2/3} = 4.32\ \text{eV}$$

while the implosion velocity and time are

$$v_o = 1.98 \times 10^6\ \text{cm/s}$$

$$t_o = 15.2 \times 10^{-9}\ \text{s}$$

The maximum driver power is

$$\phi_D\big|_{\max} = \frac{E_{\text{driver abs}}}{t_o}\left(\frac{\rho_m}{\rho_o}\right)^{2/3} = 1.33 \times 10^{15}\ \text{W}$$

Of course, the actual driver energy required will be larger because of the losses due to driver beam reflection and refraction. But this effect can be offset by using shell targets in which the shell stores kinetic energy during the implosion, and then produces the necessary temperatures and pressures in the DT fuel by energy transfer upon convergence. One can also use a shell of DT fuel inside a tamper shell of massive material. We will study these more sophisticated target designs in some detail in Chapter 9.

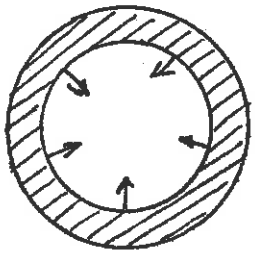

One can develop a more elaborate theory of isentropic compression using self-similarity concepts. Such a theory indicates that it is possible to compress an ideal gas indefinitely to infinite compression with a pressure time profile of

$$\frac{p(\tau)}{p_0} = F(\tau) = \frac{1}{(1-\tau^2)^{5/2}}$$

$$\tau = t/t_c$$

$$t_c = \frac{R_{20}^2 - R_{10}^2}{3C_{20}^2}$$

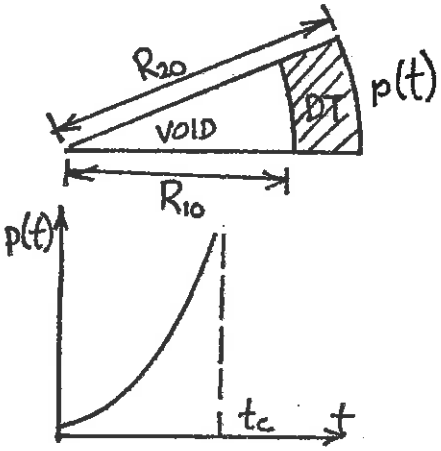

(Kidder develops the theory of isentropic, homogeneous compression to derive this result.)

In practice, we want to bring the fuel to ignition temperatures during the latter stages of compression, so we would vary the pressure profile just prior to shock convergence, for example, by choosing a profile such as

$$\frac{p(\tau)}{p_0} = \begin{cases} F(\tau), & 0 \le \tau \le \tau_a < 1 \\ F(\tau_a)\exp\left[5\tau_a \frac{(\tau-\tau_a)}{(1-\tau_a^2)}\right], & \tau > \tau_a \end{cases}$$

This analysis indicates that roughly 1/6 of the original pellet mass can be compressed by a factor of 10^4.

3.5. EQUATIONS OF STATE

A key ingredient in the study of the compression of matter is the equation of state, commonly written in the form

$$\rho = \rho(p,T)$$

We will first review some simple concepts of equations of state by considering the case of an ideal gas. We then extend these ideas to the description of dense matter.

Ideal Gas

An ideal gas is defined by the equation of state:

$$p\,V = n\,R\,T = n\,k\,T$$

and by the condition that the internal energy of the gas does not depend on the pressure:

$$\left(\frac{\partial e}{\partial p}\right)_T = 0$$

Since one can infer that $\left(\frac{\partial e}{\partial V}\right)_T = 0$, this implies that the internal energy e is a function of temperature only

$$e = e(T)$$

This ignores the dependence of internal energy on pressure which arises from molecular interactions (which are ignored in the ideal gas model).

If we now recall the first law of thermodynamics

$$dQ = de + p\,dV$$

heat addition	change in internal energy	work performed

and the definition of the specific heat at constant volume

$$c_v = \left(\frac{\partial e}{\partial T}\right)_V$$

we can use the ideal gas assumption e = e(T) only to write

$$c_v = \left(\frac{\partial e}{\partial T}\right)_V = \frac{de}{dT}$$

and substitute this into the first law to find

$$dQ = \frac{de}{dT}\,dT + p\,dV = c_v\,dT + p\,dV$$

But we recall the equation of state, $pV = \eta RT$, so that

$$p\,dV + V\,dp = \eta\,R\,dT$$

Hence the first law becomes

$$dQ = (c_v + \eta R)\,dT - V\,dp$$

or

$$\frac{dQ}{dT} = c_v + \eta R - V\frac{dp}{dT}$$

or at constant pressure,

$$c_p = \left.\frac{dQ}{dT}\right|_p = c_v + \eta R = \text{fcn}(T) \text{ only}$$

We can also find

$$dQ = c_p\,dT - V\,dp$$

Let us apply these results to describe the adiabatic, reversible (isentropic) compression of an ideal gas. We begin with our two alternative forms of the first law:

$$dQ = c_v\,dT + p\,dV$$

$$dQ = c_p\,dT - V\,dp$$

In an adiabatic process, by definition dQ = 0 or

$$V\,dp = c_p\,dT$$

$$p\,dV = -c_v\,dT$$

We can take the ratio of these two expressions to find

$$\frac{dp}{p} = -\frac{c_p}{c_v}\frac{dV}{V} = -\gamma\frac{dV}{V}$$

where we have defined

$$\gamma = \frac{c_p}{c_v}$$

If we integrate this equation, we find

$$\ln p = -\gamma \ln V + \text{constant}$$

or

$$p V^{\gamma} = \text{constant}$$

as the usual equation for the adiabat for the isentropic compression of an ideal gas (see p-V diagram).

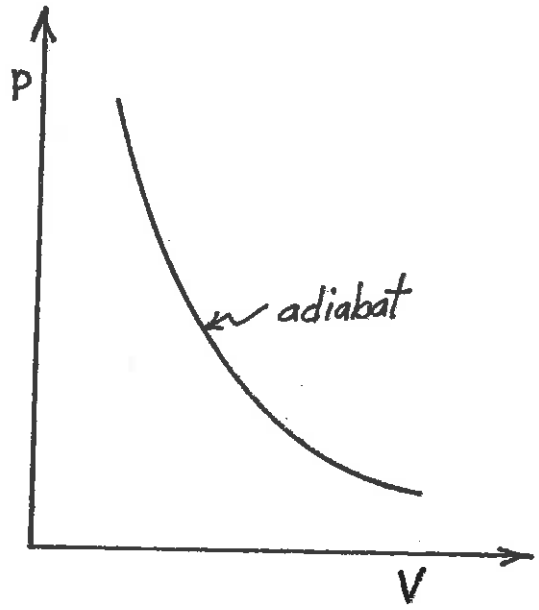

Alternative forms of this result are

$$p\,\rho^{-\gamma} = \text{constant}$$

and

$$T\,\rho^{1-\gamma} = \text{constant}$$

In an ideal gas,

$$e = \frac{1}{\gamma - 1}\frac{p}{\rho} = c_v T$$

$$h = \frac{\gamma}{\gamma - 1}\frac{p}{\rho} = c_p T$$

If the gas is monatomic (3 degrees of freedom, $\frac{1}{2}$ kT per degree), then $\gamma = 5/3$.

It should be apparent that if we want to maximize the final compressed fuel density ρ_F and a given final pressure, p_F, we wish as low an adiabat as possible with a minimum initial p_o for a given ρ_o since

$$\frac{\rho_F}{\rho_0} = \left(\frac{p_F}{p_0}\right)^{1/\gamma}$$

--that is, we must avoid preheating of the fuel.

But here we must be careful, because as the density increases with fixed temperature, we begin to depart from ideal gas behavior. We can identify several stages depending on the pressure and density

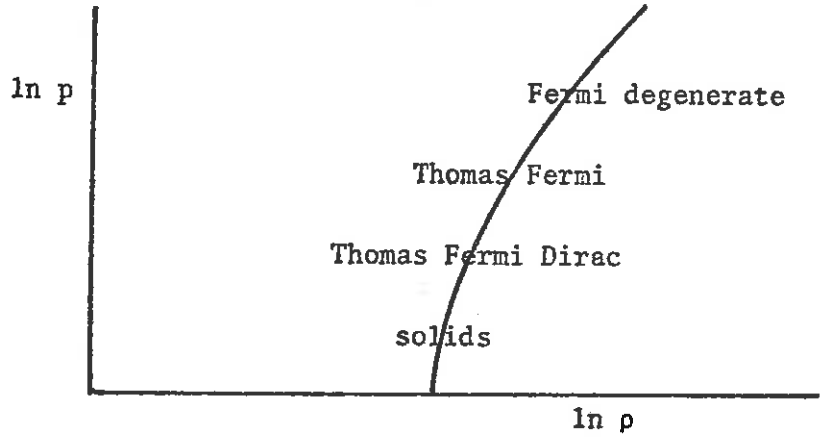

Fermi Degenerate Electron Gas

If the density of the fuel becomes high enough, the electron wavelength will become comparable to the interparticle spacing and the exclusion principle will become important. The electrons become a "degenerate electron gas". If n_e is the electron density, then the maximum momentum state filled in the degenerate gas is given by

$$n_e = \int_0^{p_F} \frac{8\pi p^2}{h^3} dp$$

The corresponding maximum energy ϵ_F is known as the Fermi energy and given by

$$\epsilon_F = \frac{p_F^2}{2m_e} = \frac{1}{8}\left(\frac{3}{\pi}\right)^{2/3} \frac{h^2}{m_e} n_e^{2/3}$$

The corresponding pressure exerted by the degenerate gas is

$$p_F = \frac{1}{20}\left(\frac{3}{\pi}\right)^{2/3} \frac{h^2}{m_e} n_e^{5/3}$$

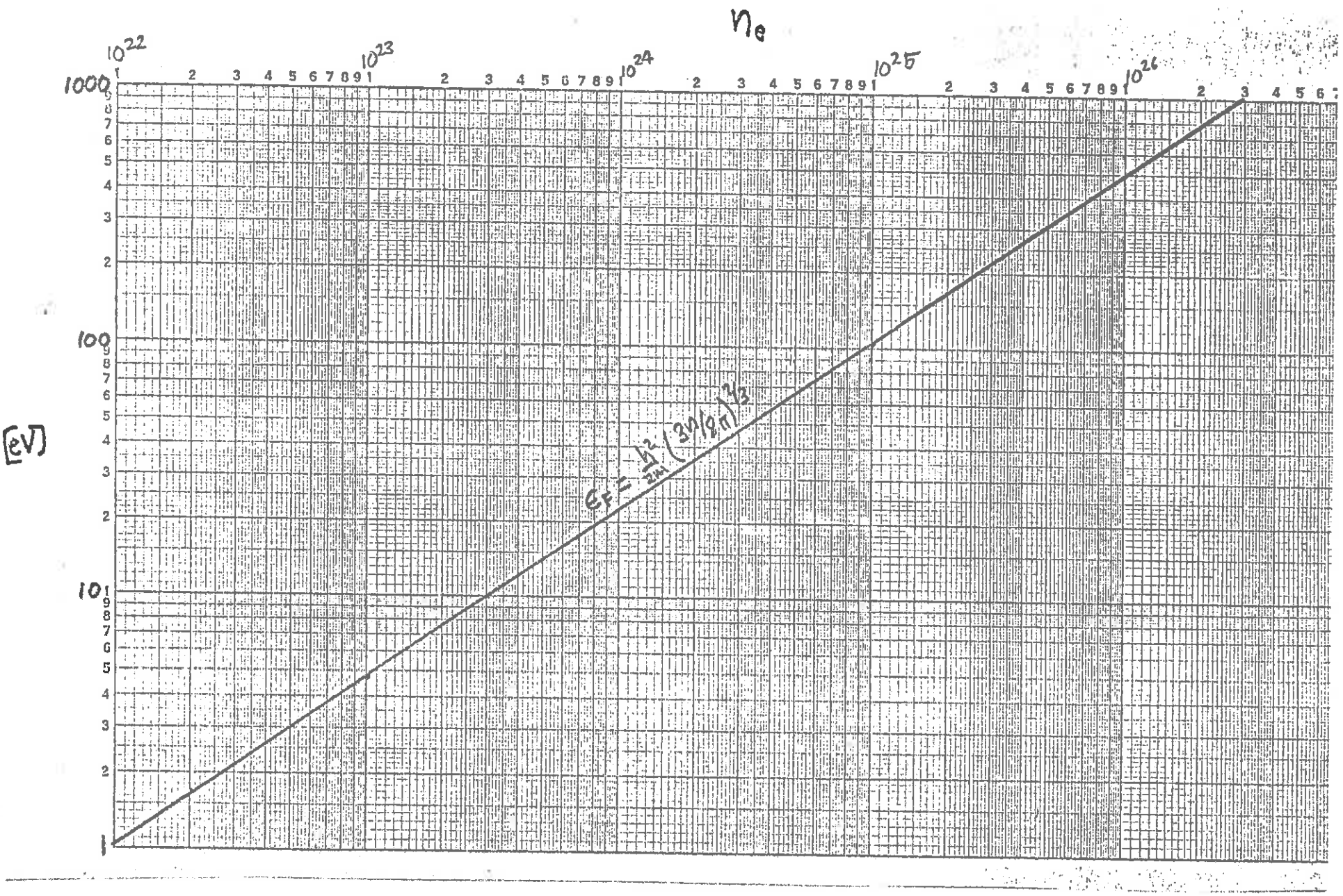
n_e
10^{22}
10^{23}
10^{24}
10^{25}
10^{26}
1000
100
10
1
[eV]
$E_F = \frac{\hbar^2}{2m}(3n/8\pi)^{2/3}$

It is particularly important to note that

$$\varepsilon_F \sim n_e^{2/3}$$

$$p_F \sim n_e^{5/3} \qquad \text{(just as the ideal gas)}$$

The usual condition for Fermi degeneracy can be expressed by comparing the thermal energy kT to the Fermi energy ε_F. For example, at solid state density, $n_e = 4 \times 10^{22}$ and the Fermi energy $\varepsilon_F = 5$ eV. Hence if the thermal energy of the electrons is below 5 eV, the electrons will behave as a degenerate gas. This, of course, is the situation for electrons in a metal.

By way of contrast, in the highly compressed core of a ICF fuel pellet, $n_e \sim 10^{27}$ and $\varepsilon_F \sim 2$ keV. Hence the fuel will be in a degenerate state until it ignites and heats to appreciably higher temperatures.

We have plotted the Fermi energy as a function of density in the Figure on the next page. More specifically,

$$\varepsilon_F = 2.19 \times 10^{-15}\, n^{2/3} \text{ (eV)}$$

$$p_F = 3.3\, \rho(\text{g/cm}^3)^{5/3} \text{ Mbar}$$

Thomas Fermi Model

For dense fuels we must also worry about the Coulomb energy since occasionally

$$\frac{Ze^2}{r_{ei}} > \varepsilon_F$$

where r_{ei} is the electron-ion separation which scales as $\rho^{-1/3}$. For example, for solid state density $n_e = 4.5 \times 10^{22}$, T = 5 eV, Z = 1, the Fermi energy and Coulomb energy are comparable and we must consider Coulomb effects. This is usually accomplished by using the Thomas-Fermi which treats the electron energy as the sum of kinetic and Coulomb terms

$$E_e = \frac{p_e^2}{2m_e} - e\,\phi(\underset{\sim}{r})$$

and then solves Poisson's equation to find the self-consistent electron density $n_e(\underset{\sim}{r})$ and potential $\phi(\underset{\sim}{r})$.

Other Equation of State Models

The Fermi and Thomas-Fermi models consider only repulsive forces. They predict unreasonably large pressures for solids. They are useful only when the pressure is much larger than the binding pressure.

To account for attractive forces, the more complex Thomas-Fermi-Dirac model is used.

One can also use limited experimental data obtained on the shock Hugoniot for solids. Many equations of state are now available in tabulated form.

3.6. ABLATION-GENERATED PRESSURES

Coupling of Driver Energy into Ablation

We will first examine the coupling of the driver energy into the surface ablation process. We recall that the driver energy is absorbed in the outer layers of the target and then conducted into the pellet surface to drive the ablation. We will ignore the details of the driver energy absorption and thermal conduction in this simple analysis, and merely assume that an energy flux ϕ (W/cm^2) is incident on the ablation surface.

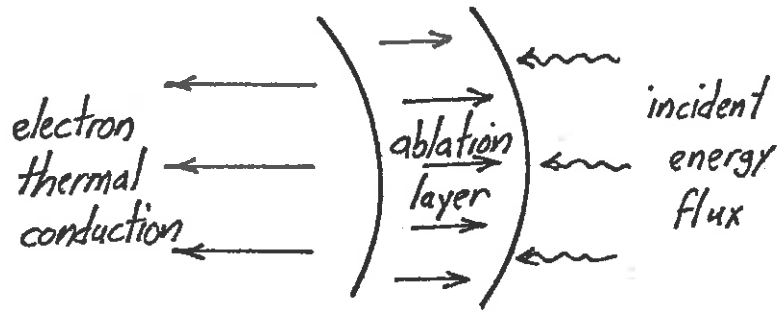

This energy is partitioned among several processes:

(i) thermal energy of absorbing layer

(ii) kinetic energy of ablation layer

(iii) thermal and kinetic energy of dense fuel ahead of ablation layer

We recall here the essential physics of a thermal conduction wave propagating into the dense fuel, followed by a rarefaction wave characterizing the ablation process.

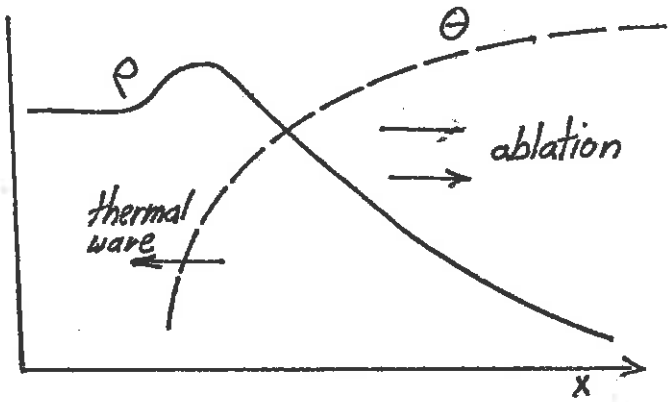

The absorbed energy is markedly depleted by the loss of energy to the ablation and rarefaction wave.

To analyze this, we will assume that electron thermal conduction in the ablating region is so large that isothermal conditions apply,

$$\theta_e = \theta_i = \theta$$

The relevant hydrodynamic equations describing the isothermal flow are then

$$\frac{\partial n}{\partial t} + \frac{\partial}{\partial x}(nu) = 0$$

$$m_i n\left(\frac{\partial}{\partial t} + u\frac{\partial}{\partial x}\right)u = -2\theta\frac{\partial n}{\partial x}$$

We can solve these for

$$n(x,t) = n_o\, e^{-x/c_T t}$$

$$u(x,t) = c_T + x/t$$

where

$$c_T = (2\,\theta/m_i)^{1/2} \qquad \text{isothermal sound velocity}$$

The total energy in the ablation layer (per cm^2) can be obtained by integration

$$E = \int_0^\infty dx \left[\tfrac{1}{2}\rho u^2 + \tfrac{3}{2}(2n\theta)\right]$$

$$= \int_0^\infty dx \left[\tfrac{1}{2} m_i n \left(c_T + \tfrac{x}{t}\right)^2 + 3n\theta\right] = 8 n_o \theta c_T t$$

Hence for energy balance we set

$$\text{driver energy flux } \phi \quad = \quad 8\, n_o\, \theta\, c_T$$

Our task now is to determine the ablation time t. The mass flow in the rarefaction zone can be written as

$$\dot{m} \quad = \quad m_i\, c_T\, n_o$$

while the ablation pressure is

$$p_A \quad = \quad 2\, n_o\, \theta$$

We can now use these equations to determine the acceleration of the ablating layer. If the initial mass is m_o, then

$$m(t) \quad = \quad m_o - \dot{m}\, t$$

But if we apply Newton's law, $m\, d^2r/dt^2 = F$, we find

$$(m_o - \dot{m}\, t)\, \frac{d^2r}{dt^2} \quad = \quad F/A \quad = \quad p_A$$

or integrating

$$v(t) \quad = \quad (p_A/\dot{m})\, \ln\, (m_o/m(t))$$

$$= \quad c_F\, \ln\, [m_o/m(t)]$$

The kinetic energy in the accelerated layer is

$$\tfrac{1}{2}\, m(t)\, v(t)^2 \quad = \quad \tfrac{1}{2}\, m(t)\, c_T^2\, [\ln\, (m_o/m(t))]^2$$

If we solve for the ablation time t as

$$t = \frac{m_o - m(t)}{\dot{m}}$$

we can calculate the driver energy as

$$E_D = \phi t = 8 n_o \theta C_T [(m_o - m(t))/\dot{m}] = 4 C_T^2 [m_o - m(t)]$$

Hence

$$\frac{\text{Energy in accelerated layer}}{\text{Incident driver energy}} = \frac{\frac{1}{2} m(t) v^2(t)}{E_D} = \frac{1}{8} \frac{m(t)}{m_o - m(t)} \left[\ln \frac{m_o}{m(t)}\right]^2$$

From this expression, we can determine that the maximum energy transfer occurs when $m_o/m(t) \sim 5$. Then

$$\left.\frac{\frac{1}{2} m(t) v^2(t)}{E_D}\right|_{max} = 0.081$$

Thus, <u>at best</u>, only about 10% of the incident driver energy can be coupled in to generate the implosion pressure. That is,

$$\epsilon_D\big|_{max} \sim 10\%$$

When other effects are included (spherical geometry, etc.), the coupling efficiency drops to

$$\epsilon_D \sim 5\%$$

Determination of Ablation-Generated Pressures

It is useful to recall once again the essential physics of the ablation driven compression process as shown in the Figure on the next page. The incident driver energy is absorbed in the outer regions of the pellet corona. This energy is conducted into the surface of the pellet, where it generates the high temperatures leading to surface ablation. The ablation produces

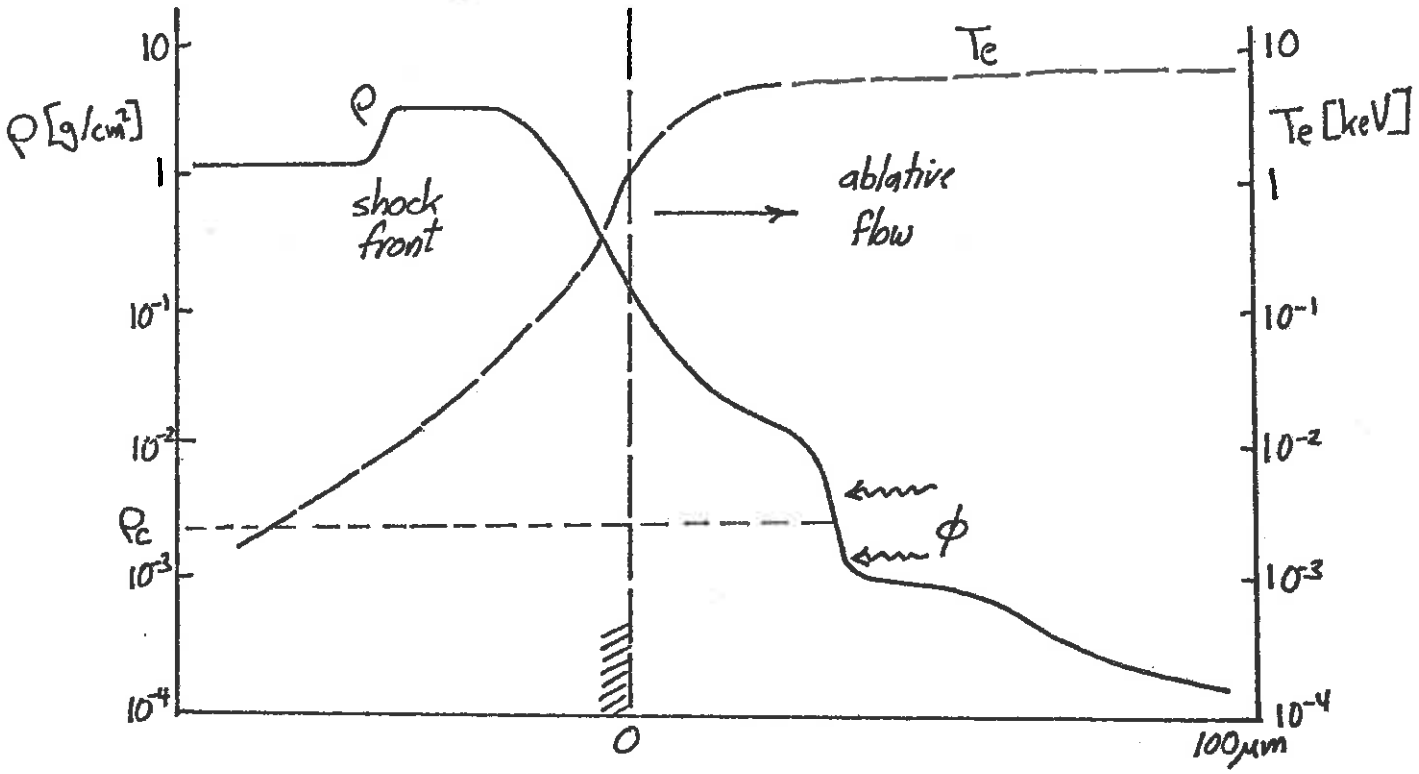

large pressures which drive the shock waves into the pellet to compress the fuel.

There are actually three pressures generated by the driver:

(i) ablation pressure: This pressure is due to the heat transported in from the driver energy deposition region and it is associated with the flow or ablation of heated plasma from the pellet surface. The ablation pressure p_A is greatest where $\rho\ T_e$ is the largest.

(ii) superthermal particle preheat pressure: The driver will also produce very energetic electrons which can stream in to the pellet surface and deposit their energy.

(iii) light pressure: If a laser driver is utilized, the incident light can generate a ponderomotive force or pressure at the critical surface. The magnitude of this light pressure is

$$p_L = I/c \simeq 3\ [\frac{I(W/cm^2)}{10^{16}}]\ \text{Mbar}$$

Although it can affect the blowoff plasma profile, it can not directly drive the pellet compression.

We can treat the ablation front just as we treated the shock wave, that is, as a discontinuity in the plasma properties. If we more to a coordinate frame fixed at the ablation front

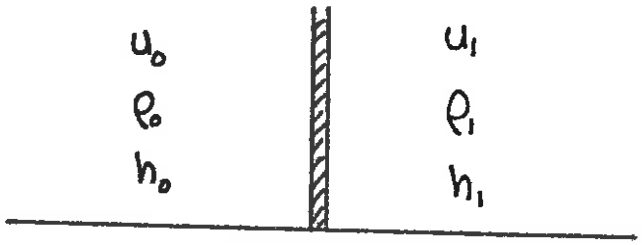

we can again apply the Rankine-Hugoniot equations

$$\rho_0 u_0 = \rho_1 u_1$$

$$p_0 + \rho_0 u_0^2 = p_1 + \rho_1 u_1^2$$

$$h_0 + \frac{1}{2} u_0^2 + \frac{W}{\rho_0 u_0} = h_1 + \frac{1}{2} u_1^2$$

Here we have inserted a new term, W, into the energy equation to represent the heat source due to electron thermal conduction in from the energy deposition region.

There are two characteristic propagation velocities characterizing the ablation process:

heat wave velocity: $v_{HW} \sim W/\rho_0 h_1$

(which can be obtained by equating the absorbed power to the enthalpy flux)

shock wave velocity: $v_{SW} \sim \sqrt{p_1/\rho_0}$

There are three possible cases:

(i) If the shock speed v_{SW} is greater than the heat wave speed v_{HW}, then the shock is driven into the dense pellet medium by the ablation pressure as shown below:

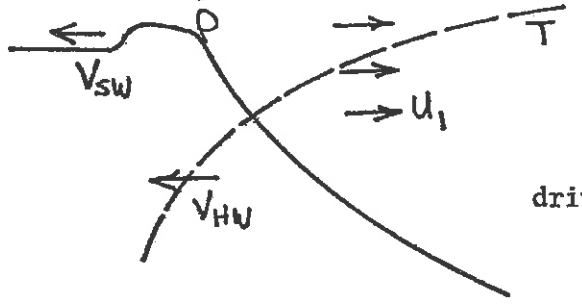

driving pressure $p_1 + \rho_1 u_1^2$

This case in which $v_{SW} > v_{HW}$ is known as subsonic deflagration.

(ii) In the opposite extreme, the heat front velocity v_{HW} is greater than the shock wave velocity v_{SW}, and the heat wave moves into the pellet material ahead of the shock, preheating it and reducing the compression achieved by the following shock. This is known as a supersonic thermal conduction wave. We will consider it in more detail in the next chapter.

(iv) The limiting case of $v_{HW} = v_{SW}$ is known as the Chapman-Jouget deflagration. In the frame moving with the ablation surface, the flow variables look as shown below for this case;

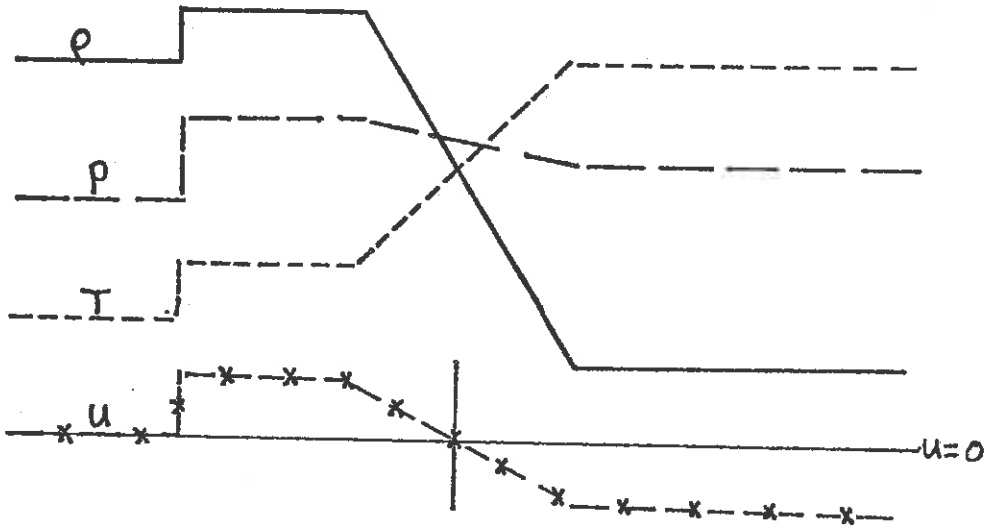

If we again assume an ideal gas with

$$h = \left(\frac{\gamma}{\gamma-1}\right)\frac{p}{\rho}$$

we have 4 equations in 5 unknowns, u_o, u_1, ρ_1, h_1, p_1 for a given ρ_o, h_o, and W. We need one more equation relating the driver energy and the ablation parameters. This latter equation is a "heating law" representing the interaction physics between the driver and the plasma. It allows us to complete the set and solve for the jump relations across the ablation front:

SPECIAL CASE: Chapman-Jouguet deflagration at the critical density (where the driver energy is absorbed):

$M_1 = 1$ (Chapman-Jouguet condition: $v_{SW} = v_{HW}$)

ρ_1 = critical density $= \rho_c$

Then

$$u_1 = \left(\frac{\gamma_1 P_1}{\rho_1}\right)^{1/2}$$

$$\rho_1 = \rho_c$$

If

$$\gamma_0 = \gamma_1, \quad \rho_c << \rho_0, \quad h_0 + \tfrac{1}{2}u_0^2 << \frac{W}{\rho_0 u_0}$$

and we find

$$W = \frac{P_1^{3/2}}{\rho_c^{1/2}} \gamma^{1/2}\left(\frac{\gamma}{2} + \frac{\gamma}{\gamma-1}\right)$$

For laser light of intensity I at wavelength λ and with $\gamma = 5/3$, we find

$$P_1 = 120\,\lambda^{-2/3}\left(\frac{I_0\ W/cm^2}{10^{16}}\right)^{2/3} \text{Mbar}$$

The pressure behind the shock is then

$$P_1 + \rho_1 u_1^2 \sim 2P_1$$

We can obtain the temperature from

$$e = \frac{1}{\gamma-1}\left(P_1/\rho_c\right) = \frac{3}{2}\frac{kT_1}{2m}$$

or

$$kT_1 = 70\,\lambda^{4/3}\left(\frac{I\ w/cm^2}{10^{16}}\right) \text{keV}$$

(Here we should note that this model ignores the thermal conduction into the ablation region.)

SPECIAL CASE: Self-Regulation

For laser light absorption in which inverse bremsstrahlung (IB) is dominant, the plasma flow will adjust to balance absorption:

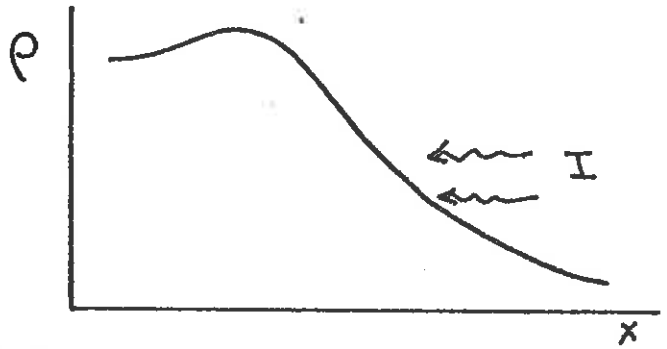

If the ablation rate decreases, the temperature increases. Since absorption is proportional to $T^{-3/2}$, absorption decreases and the plasma becomes more transparent to the light. The light penetrates in and increases ablation.

If we define the scale length ℓ characterizing the blowoff:

$$\ell \sim \left|\frac{n}{\nabla n}\right|$$

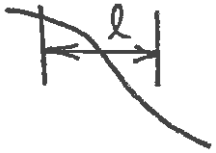

then we can characterize the self-regulation criterion by demanding that

$$\kappa\ell$$

where κ is the absorption coefficient. In this case we find the scaling laws:

$$\rho_1 \sim I^{1/4}\,\lambda^{-3/8}$$

$$T_1 \sim I^{1/2}\,\lambda^{1/4}$$

$$P_1 \sim I^{3/4}\,\lambda^{-1/8}$$

More precisely, for this case the ablation pressure is given by

$$P_A = P_1 = 230\,Z^{-9/16}A^{7/16}\lambda^{-1/4}\left(\frac{I}{10^{16}}\right)^{3/4} \quad \text{Mbar}$$

If the effects of spherical geometry is included, these scaling laws become

$$P_1 \sim I^{1/3}$$

$$T_1 \sim I^{4/9}$$

$$\rho_1 \sim I^{7/9}$$

and the ablation pressure is

$$P_A = 380 Z^{-3/18} A^{-7/18} \lambda^{-2/9} \left(\frac{R(\mu m)}{100}\right)^{-1/9} \left(\frac{I}{10^{16}}\right)^{7/9} \text{ Mbar.}$$

So far, so good. But there is one very important effect we have left out thus far. In all ICF schemes, the driver energy is deposited in the outer layers of the target, far from the ablation surface. This energy must be transported into the surface to drive the ablation and produce the pressures necessary for compression:

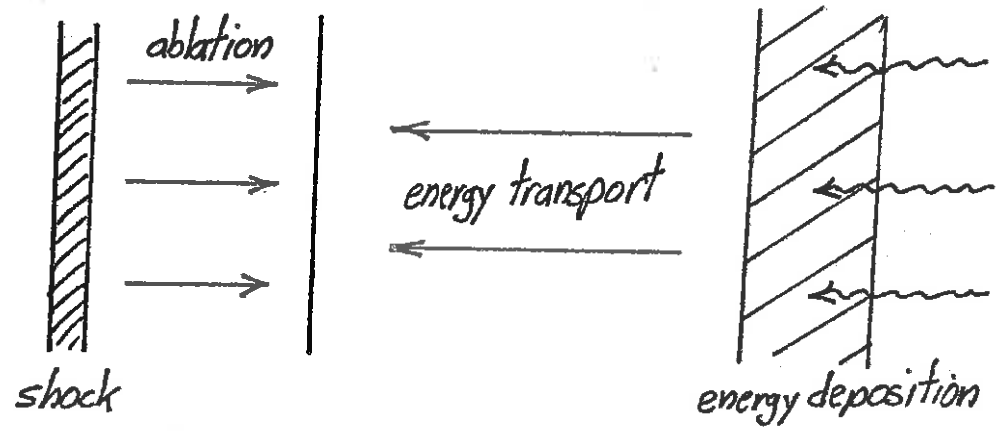

Therefore we must now turn our attention to the next process of critical importance in inertial confinement fusion schemes, energy transport.

CHAPTER 4

ENERGY TRANSPORT IN INERTIAL CONFINEMENT FUSION PLASMAS

By way of review, let us briefly the consider the scenario of ICF pellet implosion as shown in sketches below. A driver beam (laser or charged particle) deposits energy on the surface of the pellet in a very carefully tailored pulse shape I(t). This energy ablates the surface of the pellet off into the surrounding vacuum, producing large pressures which drive a sequence of quasi-adiabatic shock waves into the pellet. This compresses the core of the pellet to densities sufficient to yield efficient thermonuclear burn conditions ($\rho R \sim 3$ g/cm^2). Thermonuclear ignition occurs, and alpha particle self-heating and burn propagation spread the thermonuclear burn throughout the compressed fuel.

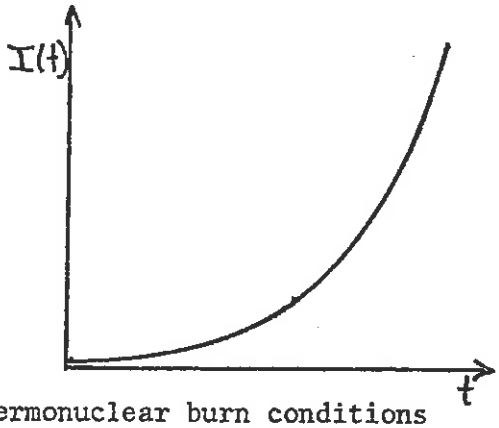

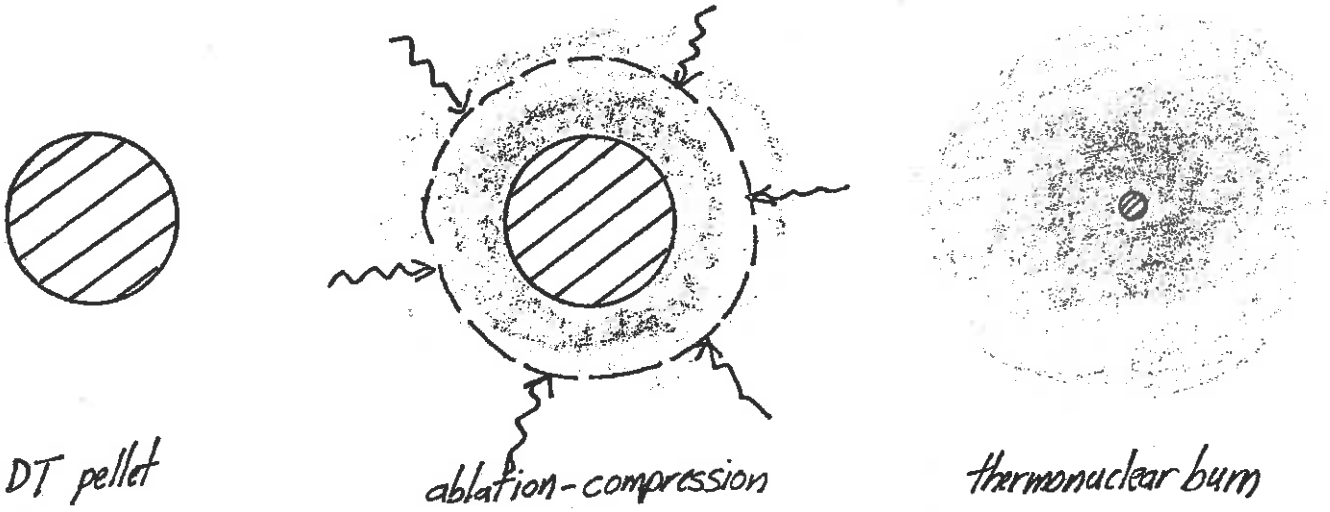

A instantaneous snapshot of the density and temperature profiles in the irradiated pellet are shown below:

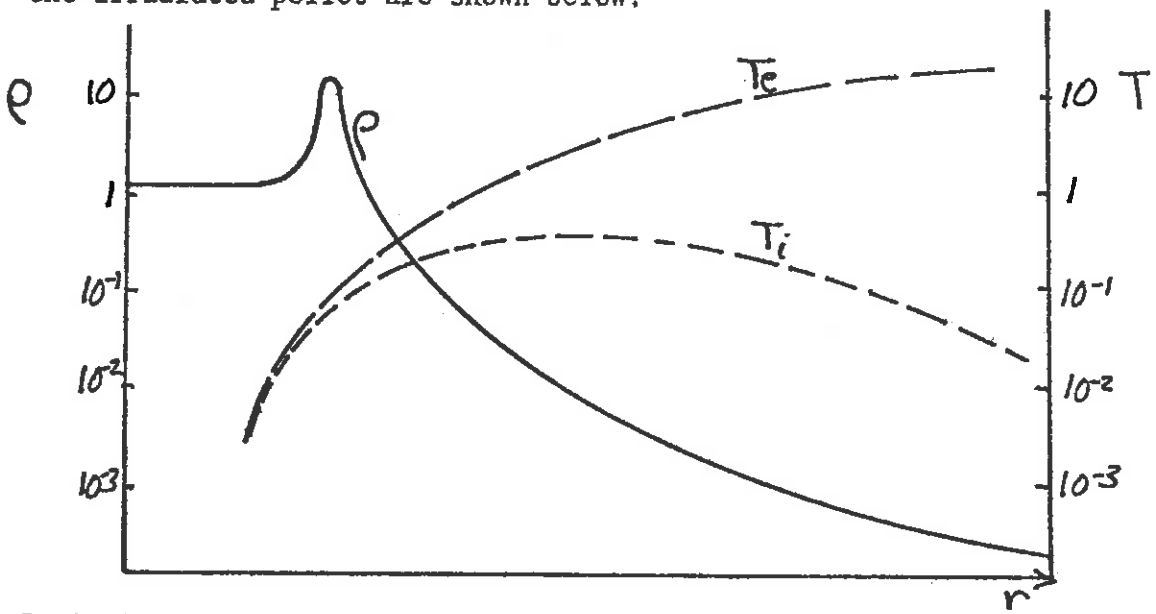

It is important to note that a number of processes are involved in transporting the absorbed driver energy into the compressed fuel core:

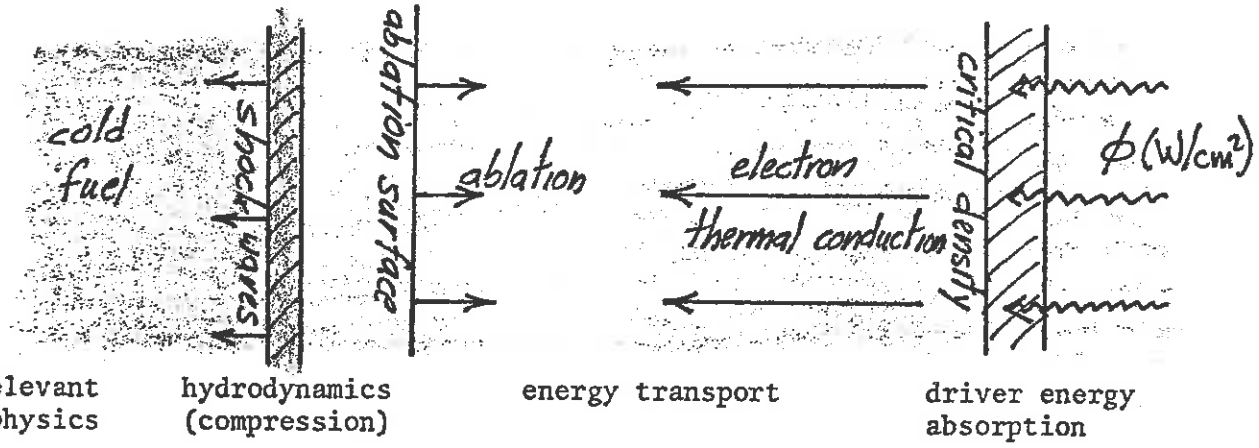

We now turn to a detailed discussion of the various mechanisms which can transport energy from the absorption region into the ablating surface of the fuel pellet.

4.1. ELECTRON THERMAL CONDUCTION

The dominant energy transport mechanism is electron thermal conduction. The small mass of the electrons coupled with the high temperature of the pellet plasma corona or blowoff cloud make its thermal conductivity quite high. Although the process of conventional thermal conduction in plasmas is well understood, there are additional phenomena present in ICF plasmas which complicate the conduction process considerably. The driver energy absorption produces a number of very high energy electrons (so-called superthermal particles since they are not characterized by the usual thermal distribution assumed in the plasma hydrodynamic model). These electrons can stream into the dense pellet fuel, preheating it before the ablation driven shock waves can compress it. The presence of both hot and cold electrons can lead to plasma instabilities which produce a turbulent state in the plasma corona, tending to inhibit the thermal conduction process. Density and temperature gradients can produce large magnetic fields which also inhibit the conduction process. Therefore it should be apparent that the thermal conduction energy transport process is rather complex in ICF plasmas and must be studied in some detail.

Electron Thermal Conductivity

In the classical theory of electron thermal conduction, one assumes that the heat flux is given by Fourier's law of thermal conduction

$$\underset{\sim}{q} = -\kappa \underset{\sim}{\nabla} T$$

where κ is the thermal conductivity. The thermal conduction is dominated by the fast moving electrons (the contribution of the much slower ions can be ignored to first order). The thermal conductivity characterizing non-interacting electrons diffusing through a background of fixed ions (the Lorentz gas model) has been calculated by Spitzer as

$$\kappa = \frac{5 n_e k_B^2 T_e}{m_e \nu_{ei}} = 20 \left(\frac{2}{\pi}\right)^{3/2} \frac{(k_B T_e)^{5/2} k_B}{\sqrt{m_e}\, e^2 Z \ln \Lambda}$$

However, the kinetic theory of gases indicates that heat flow is possible only with a skewed or distorted distribution function:

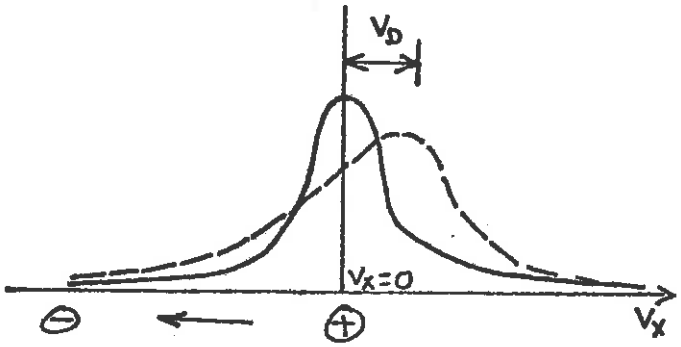

Thus the flow of hot electrons carrying the thermal energy must be compensated by a return drift of cold electrons. An electric field is established by this motion. This field will contribute to the heat flux:

$$\underset{\sim}{q} = -\kappa \underset{\sim}{\nabla} T - \beta \underset{\sim}{E}$$

We can relate the electric field to the temperature gradient by demanding that the net current density be zero:

$$\underset{\sim}{j} = \frac{1}{\eta}\underset{\sim}{E} + \alpha \underset{\sim}{\nabla} T = 0$$

so that

$$\underset{\sim}{E} = -\alpha\eta \underset{\sim}{\nabla} T$$

Hence we find that the heat flux becomes

$$\underset{\sim}{q} = -(\kappa - \beta\alpha\eta)\underset{\sim}{\nabla} T = -\kappa_{eff} \underset{\sim}{\nabla} T$$

where we have defined an effective thermal conductivity which takes account of the induced electric field:

$$\kappa_{eff} \equiv (\kappa - \beta\alpha\eta) = \left(1 - \frac{\beta\alpha\eta}{\kappa}\right)\kappa \equiv \delta\kappa$$

The scaling parameter assumes a value of $\delta = 0.4$ for a Lorentz gas. More generally, $\delta(T,Z)$ is a function of temperature and charge and is tabulated by Spitzer.

The general form of the thermal conductivity can therefore be written as

$$\kappa = \delta(T,Z)\, 20 \left(\frac{2}{\pi}\right)^{3/2} \frac{(kT)^{5/2} k}{m^{1/2} e^4 Z \ln\Lambda}$$

Conventional Theory of Heat Conduction in Plasmas

When energy is locally deposited in a fluid, it gives rise to local perturbations in fluid properties such as density, pressure, and temperature. These disturbances will then propagate away from the source, transporting energy to other regions of the fluid. In most fluids the two principal energy transport modes are:

(i) hydrodynamic motion (sound waves or shock waves)

(ii) thermal conduction

(although in certain types of high temperature phenomena, radiative transfer also becomes quite important).

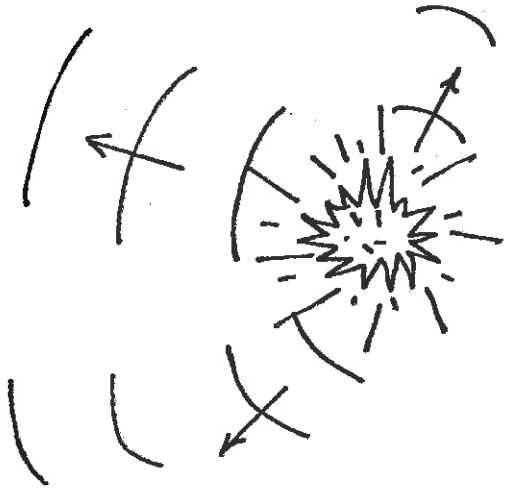

The velocities characterizing energy transport via thermal conduction are usually much smaller than those characterizing hydrodynamic disturbances such as sound waves. Therefore in most fluids, pressure disturbances will propagate out more rapidly and equilibrate before temperature disturbances. In these cases, we can effectively decouple thermal conduction from hydrodynamic motion and consider the energy transport to be governed by the equation of thermal conduction

$$\rho C_p \frac{\partial T}{\partial t} = -\underset{\sim}{\nabla} \cdot \underset{\sim}{q} + W$$

where the heat flux vector q(r,t) is given by Fourier's law:

$$\underset{\sim}{q} = -\kappa \underset{\sim}{\nabla} T$$

In conventional heat conduction problems, one usually assumes that the thermal conductivity is a constant

$$\kappa \sim \text{constant}$$

so that we can write

$$\rho c_p \frac{\partial T}{\partial t} = \kappa \nabla^2 T + W$$

If we divide through by $\rho\ c_p$, then we find the usual diffusion equation

$$\frac{\partial T}{\partial t} = D_T \nabla^2 T + Q$$

where

$$D_T \equiv \frac{\kappa}{\rho c_p} = \text{thermal diffusivity}$$

$$Q = W/\rho c_p$$

Although the thermal diffusivity is the diffusion coefficient for energy transport rather than particle transport, in gases we can estimate

$$D_T \sim D \sim \frac{\lambda}{3} v_{th}$$

where λ is the mean free path and v_{th} is the thermal velocity of the particles. [As an example, in air at STP conditions, $D_T \sim 0.205\ cm^2/s$ while in water, $D_T \sim 1.5 \times 10^{-3}\ cm^2/s$.]

When the thermal conductivity is a function of temperature

$$\kappa = \kappa(T)$$

we are playing a new ball game since the equation of heat condition now becomes nonlinear

$$\rho c_p \frac{\partial T}{\partial t} = \underset{\sim}{\nabla} \cdot \kappa(T) \underset{\sim}{\nabla} T + W$$

A variety of new phenomena arise such as the presence of supersonic thermal conduction waves. The situation in which the thermal conductivity becomes strongly temperature dependent arises in several phenomena:

$\kappa \sim T^{5/2}$ heat conduction in plasmas

$\kappa \sim T^{4}$ radiation heat conduction

The general theory of such nonlinear heat conduction has been considered in detail by Zel'dovich and Raizer (Chapter 10) who assume a general form for the thermal diffusivity of

$$D_T = \frac{\kappa}{\rho c} = a\, T^n$$

We will briefly summarize the results of their analysis with particular applications to heat conduction in plasmas.

Linear Heat Conduction

We begin by considering the classical problem of a pulsed heat source at the origin of an infinite medium (the Green's function problem) in the case that the thermal conductivity is constant:

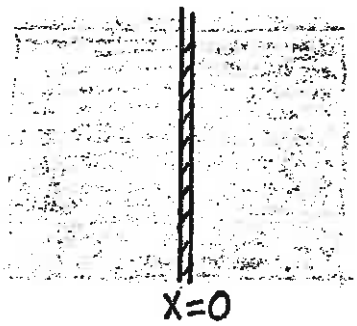

$$\frac{\partial T}{\partial t} = D_T \frac{\partial^2 T}{\partial x^2} + Q\,\delta(x)\,\delta(t)$$

This yields the classical spreading Gaussian shape solutions of the form

$$T(x,t) = \frac{Q}{(4\pi D_T t)^{1/2}} e^{-x^2/4D_T t}$$

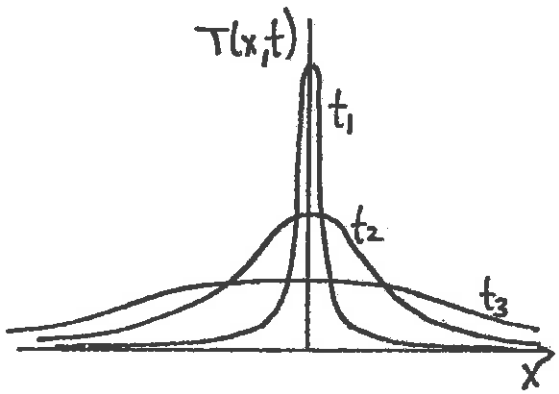

The area under the Gaussian curves is constant and given by

$$\int_{-\infty}^{\infty} dx\, T(x,t) = Q$$

This, of course, is the usual solution to the time-dependent diffusion equation. As such, these solutions are not waves since they exhibit an infinite propagation speed. That is, for any time $t > 0$, there will be some response in the temperature $T(x,t)$, no matter how far one is from the source plane at $x = 0$. There is no true wave-front.

We can nevertheless define a psuedo-wave-front speed by noting that most energy is localized in a zone out to a distance

$$x_F \sim (4\, D_T\, t)^{1/2} \sim (D_T\, t)^{1/2}$$

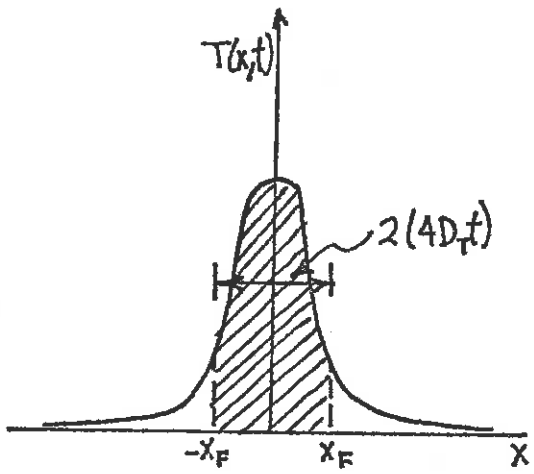

If we characterize the thermal conduction "wave" by a wave-front at position $x_F(t)$, we can then calculate a speed of propagation

$$v_{HW} = \frac{dx_F}{dt} \sim \left(\frac{D_T}{t}\right)^{1/2} \sim \frac{D_T}{x_F} \sim \left(\frac{\lambda}{x_F}\right) v_{th}$$

This is an important result, for it implies that after the heat wave has propagated a distance x_F greater than a mean free path λ, its speed of propagation will be less than the thermal velocity v_{th}. Since v_{th} is of the same order as the speed of sound, c_s, this result implies that as soon as the heat wave has propagated further than a mfp, it will be moving much more slowly than the speed of sound.

$$v_{HW} \sim \left(\frac{\lambda}{x_F}\right) v_{th} \ll v_{th} \sim c_s$$

(Actually, the diffusion equation is only valid for distances greater than a mfp from the source plane anyway.)

Hence we conclude that the diffusion "wave" characterizing a linear heat conduction process always travels much more slowly than do hydrodynamic disturbances (sound waves or shock waves) and will therefore decouple from hydrodynamic motion.

Nonlinear Heat Conduction

The situation changes dramatically when the thermal conductivity becomes a function of temperature. Suppose, for example, that

$$\kappa \sim T^n$$

If we recall that the heat flux is given by

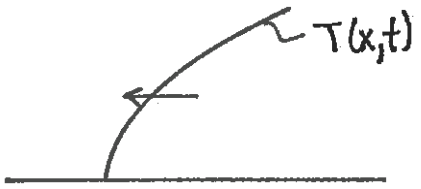

$$q = -\kappa \frac{\partial T}{\partial x} \sim -T^n \frac{\partial T}{\partial x}$$

and assume that ahead of the heat disturbance the temperature is essentially zero, then we find that there can be no heat flux ahead of the heat disturbance:

$$T \sim 0 \Rightarrow \kappa \sim 0 \Rightarrow q \sim 0$$

That is, we find a sharp wave front of the heat disturbance--a heat wave. [In the case of linear heat conduction, the conductivity does not vanish for vanishing temperatures, and hence the heat flux is always non-zero for any x.]

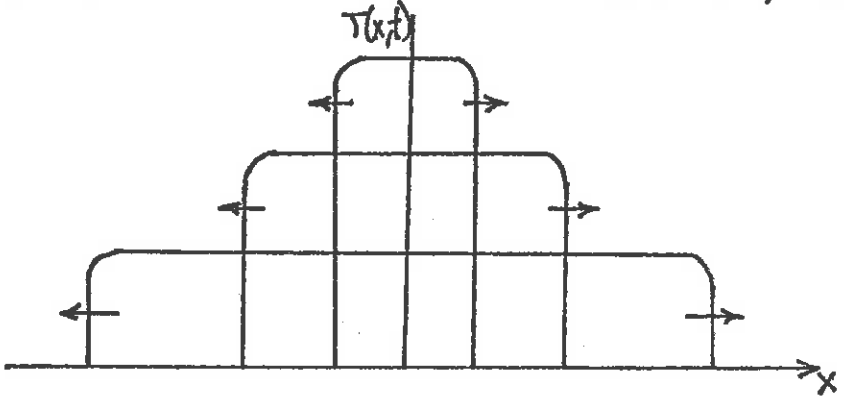

We can estimate the shape of the heat wave front by assuming a wave behavior

$$T(x,t) = T(x - v_{HW}t)$$

where v_{HW} is the velocity of the heat wave. If we substitute this trial solution into the nonlinear diffusion equation written in the form

$$\frac{\partial T}{\partial t} = \frac{\partial}{\partial x}\left[a T^n\right] \frac{\partial T}{\partial x}$$

we find

$$-v\frac{dT}{dx} = a\frac{d}{dx}T^n\frac{dT}{dx}$$

We can integrate this equation twice with respect to x, using the boundary condition that T = 0 at some wave-front $x = x_F(t)$, to find a wave shape

$$T(x,t) = \left[\frac{n v_{HW}}{a}\left|x_F(t) - x\right|\right]^{1/n}$$

Here $x_F(t)$ and $v_{HW} = dx_F/dt$ are as yet undetermined. Although a precise determination of these quantities requires a detailed solution of the nonlinear thermal conduction equation, we can use dimensional analysis to estimate

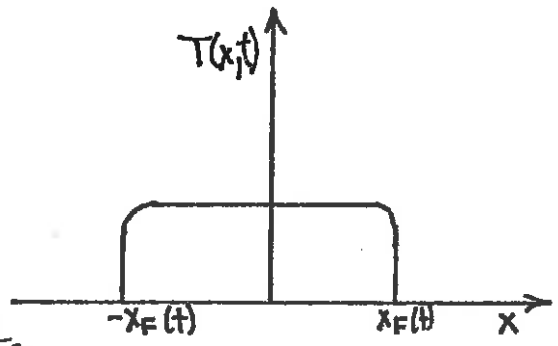

$$x_F(t) \sim (aQ^n t)^{\frac{1}{n+2}} = (aQ^n)^{\frac{1}{n+2}} t^{\frac{1}{n+2}}$$

$$v_{HW}(t) = \frac{dx_F}{dt} \sim (aQ^n)^{\frac{1}{n+2}} t^{\frac{1}{n+2}-1} \sim \frac{x_F}{t} \sim \frac{aQ^n}{x_F^{n+1}}$$

This suggests that the heat wave slows down as it travels away from the source. The stronger the dependence of the thermal conductivity on temperature (the larger the exponent n), the more rapidly the wave slows down.

EXACT SOLUTION: Zel'dovich and Raiser have constructed an exact self-similar solution to the nonlinear heat conduction equation for a pulsed source at the origin:

$$\frac{\partial T}{\partial t} = \frac{\partial}{\partial x}\left[aT^n\right]\frac{\partial T}{\partial x} + Q\delta(x)\delta(t)$$

The only dimensionless combination appearing in this equation is

$$\xi \equiv \frac{x}{(aQ^n t)^{\frac{1}{n+2}}}$$

They seek a solution

$$T(\xi) = \left(\frac{Q^2}{at}\right)^{\frac{1}{n+2}} f(\xi)$$

Then substituting this solution into the nonlinear heat conduction equation, one finds an ordinary differential equation

$$(n+2)\frac{d}{d\xi}\left(f^n \frac{df}{d\xi}\right) + \xi \frac{df}{d\xi} + f = 0$$

$$\text{b.c.:} \quad f(\infty) = 0, \quad \left.\frac{df}{d\xi}\right|_{\xi=0} = 0$$

This equation can be solved for

$$f(\xi) = \left[\frac{n}{2(n+2)}\xi_0^2\right]^{\frac{1}{n}}\left[1 - \left(\frac{\xi}{\xi_0}\right)^2\right]^{1/n}, \quad \xi < \xi_0$$

$$= 0 \qquad \xi > \xi_0$$

If we use the condition that

$$\int_{-\infty}^{\infty} f(\xi)\, d\xi = 1$$

then we find

$$\xi_0 = \left[\frac{(n+2)^{n+1}\, 2^{1-n}}{n\pi^{n/2}}\right]^{\frac{1}{n+2}}\left[\frac{\Gamma\left(\frac{1}{2}+\frac{1}{n}\right)}{\Gamma\left(\frac{1}{n}\right)}\right]^{\frac{n}{n+2}}$$

Note, in particular, that the solution exhibits a wave-front behavior at the point ξ_0, that is, at

$$x_F(t) = \xi_0 (aQ^n t)^{\frac{1}{n+2}}$$

We can then write the general solution as

$$T(x,t) = T_c(t)\left[1 - \frac{x^2}{x_F^2(t)}\right]^{\frac{1}{n}}$$

where

$$T_c(t) \equiv \frac{Q}{2x_F(t)}\left[\frac{\sqrt{\pi}\,\Gamma\left(\frac{1}{n}\right)}{(n+2)\Gamma\left(\frac{1}{n}+\frac{1}{2}\right)}\right]$$

SPECIAL CASE: The case of most interest in plasma physics is n = 5/2.

Then our solution takes the form

$$T(x,t) = T_c(t)\left[1 - \frac{x^2}{x_F^2(t)}\right]^{2/5}$$

where $$x_F(t) = \xi_0 (aQ^{5/2}t)^{2/9}$$

This yields a heat conduction wave velocity of

$$v_{HW}(t) = \frac{dx_F}{dt} = \xi_0 (aQ^{5/2})^{2/9} \frac{1}{t^{7/9}}$$

To be more specific, for a plasma

$$\frac{\partial T_e}{\partial t} = \frac{2m_i}{3k\rho_0}\frac{\partial}{\partial x}\left(\nu_e \frac{\partial T_e}{\partial x}\right)$$

where $$\nu_e = 1.89\left(\frac{2}{\pi}\right)^{3/2}\frac{k^{7/2}}{\sqrt{m_e}e^4 \ln\Lambda} T_e^{5/2} = \nu_e^0 T_e^{5/2}$$

Hence for this case we find

$$T_e(x,t) = \left(\frac{Q^2}{at}\right)^{2/9} f(\xi), \qquad a \equiv \nu_e^0 \frac{2m_i}{3k\rho_0}$$

$$f(\xi) = \left[\frac{5}{18}(\xi_0^2 - \xi^2)\right]^{2/5}$$

$$\xi = \frac{x}{(Q^{5/2}at)^{2/9}}$$

$$\xi_0 = \frac{(9/2)^{7/2}\, 2^{-3/2}}{(5/2)\,\pi^{5/2}}\left[\frac{\Gamma(\frac{9}{10})}{\Gamma(\frac{2}{5})}\right]^{5/2}$$

The structure of the heat conduction wave is compared against that for linear heat conduction in the Figure on the next page.

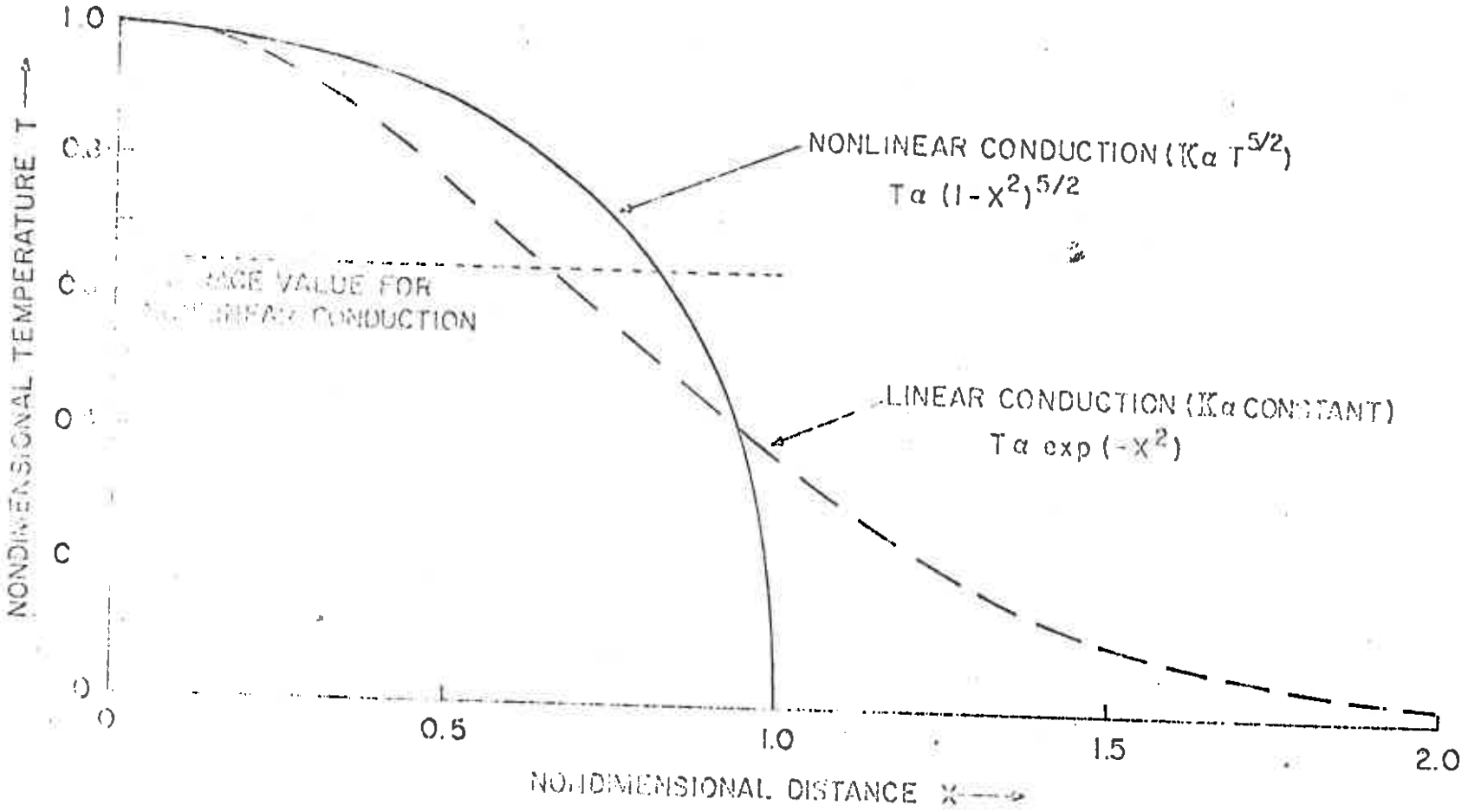

SIONAL PLOT OF THE TEMPERATURE AS A FUNCTION OF DISTANCE FOR THE $K \alpha T^{5/2}$ CONDUCTIVITY SOLUTION. PLOTTED FOR COMPARISON IS THE PROFILE FOR LINEAR CONDUCTION.

CONSTANT HEAT SOURCE: A problem of perhaps more interest is that of a half-space subjected to a constant heat flux S_o on its boundary. That is, one solves the nonlinear heat conduction equation

$$\frac{\partial T}{\partial t} = a \frac{\partial}{\partial x} T^n \frac{\partial T}{\partial x}$$

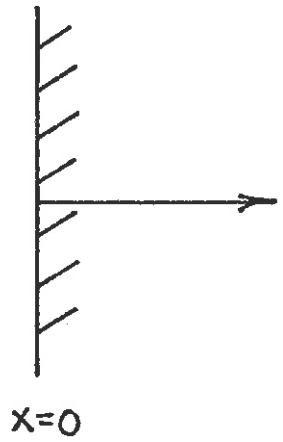

subject to the boundary condition

$$S_o = -\kappa \frac{\partial T}{\partial x}\bigg|_o = -c_v \rho a T^n \frac{\partial T}{\partial x}\bigg|_o$$

Zel'dovich and Raizer have obtained a self-similar solution to this problem. For our purposes, however, it is sufficient to use order of magnitude estimates. The average temperature in the wave must be given by balancing

$$S_o \sim c_v \rho a \frac{T^{n+1}}{x_F}$$

But note

$$\frac{T}{t} \sim \frac{S_o}{x_F}$$

Thus we find

$$x_F(t) \sim (c_v \rho a S_o^n)^{\frac{1}{n+2}} t^{\frac{n+1}{n+2}}$$

$$T(x,t) \sim \left(\frac{S_o^2}{c_v \rho a}\right)^{\frac{1}{n+2}} t^{\frac{1}{n+2}}$$

SPECIAL CASE: Again consider the case of a plasma for which n = 5/2. Then

$$x_F(t) \sim (c \rho a S_o^n)^{2/9} t^{7/9}$$

$$V_{Hw}(t) = \frac{dx_F}{dt} = \frac{7}{9}(c \rho a S_o^n)^{2/9} \frac{1}{t^{2/9}}$$

It is interesting to compare this result with that characterizing a pulsed heat source:

Heat pulse

$V_{HW} \sim \frac{1}{t^{3/9}}$

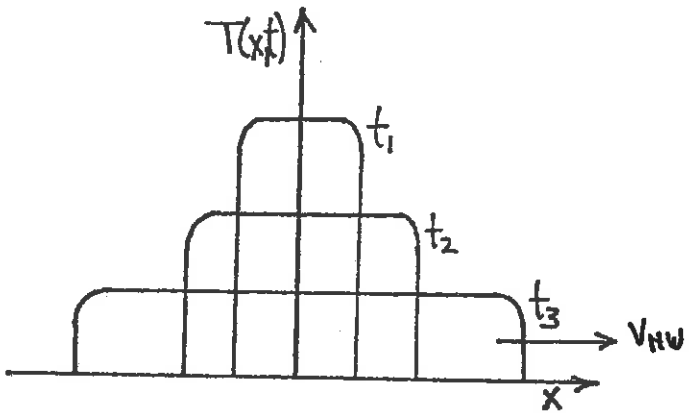

Constant heat source

$V_{HW} \sim \frac{1}{t^{2/9}}$

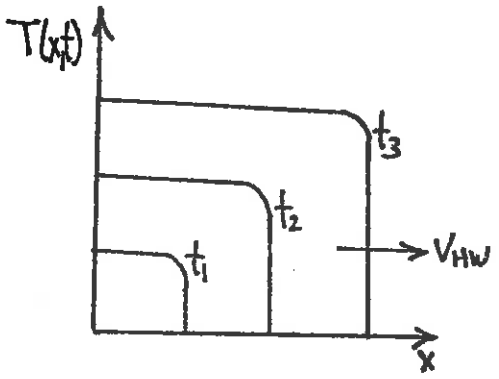

Note that the speed of the heat wave decreases more slowly for the constant heat source. Again we find that in the early stage of the thermal wave, when the temperature is very high, the propagation speed is much higher. In fact, if the heat source is large enough, the heat wave will propagate supersonically, with

$$v_{HW} > v_{SW} \gtrsim c_s$$

In these cases, the fluid simply does not have enough time to get moving before the heat wave moves into it, heating it to high temperatures. Eventually, however, the heat wave slows down to the speed of sound or below (subsonic propagation).

It is an interesting exercise to determine that heat source or temperature time dependence on the boundary which will match the speeds of the heat wave and the shock wave. Let us suppose that the temperature on the boundary is programmed to increase as

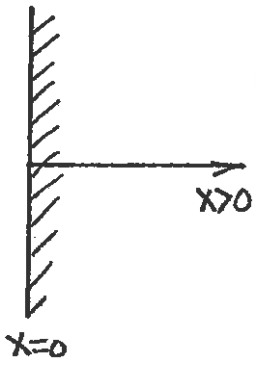

$$T_o(t) = \text{Constant } t^q$$

Then the distance which heat is carried into the medium is

$$x_F \sim \sqrt{D_T t} \sim T^{n/2} t^{1/2} \sim t^{\frac{nq+1}{2}}$$

Hence the speed of the thermal wave is

$$v_{HW} = \frac{dx_F}{dt} \sim \frac{x_F}{t} \sim t^{\frac{nq-1}{2}}$$

Now the shock will travel into the medium with a speed

$$c_s \sim \sqrt{T} \sim t^{q/2}$$

Therefore if

$$\frac{n\,q-1}{2} < \frac{q}{2} \quad \Rightarrow \quad q < \frac{1}{n-1}$$

then $v_{HW} > c_s$ and we have a supersonic thermal wave. For

$$\frac{n\,q-1}{2} > \frac{q}{2} \quad \Rightarrow \quad q > \frac{1}{n-1}$$

the shock will outrun the thermal wave ($c_s > v_{HW}$)

The limiting case is

$$q = \frac{1}{n-1}$$

so that $v_{HW} = c_s$.

SPECIAL CASE: $n = 5/2 \Rightarrow q = 2/3$

Thus to match the heat wave and the shock wave, we would like the temperature on the boundary to rise as

$$T_o = \text{const } t^{2/3}$$

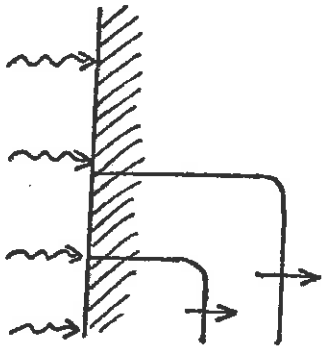

If we assume that all of the incident driver energy is absorbed at x = 0,

$$\rho c_v \left.\frac{dT}{dt}\right|_{x=0} = Q(t)$$

Hence we can infer a driver pulse profile of

$$Q(t) = \text{const}\, \rho c_v \frac{d}{dt}\left(t^{2/3}\right) = \text{const}\, \frac{1}{t^{1/3}}$$

The implications of this analysis are quite important since they imply that if the rate of energy deposition is too rapid, the thermal wave will propagate supersonically into the pellet before it can be compressed by the following shock wave. If we recognize that a 1 keV electron moves with a thermal speed of $v_{th} \sim 2.3 \times 10^9$ cm/s = 23 μm/ps, then it is apparent that these thermal waves can propagate very fast indeed.

We recall also that this nonlinear thermal wave also appears as part of the shock wave structure in a plasma, even when $v_{HW} < v_{SW}$:

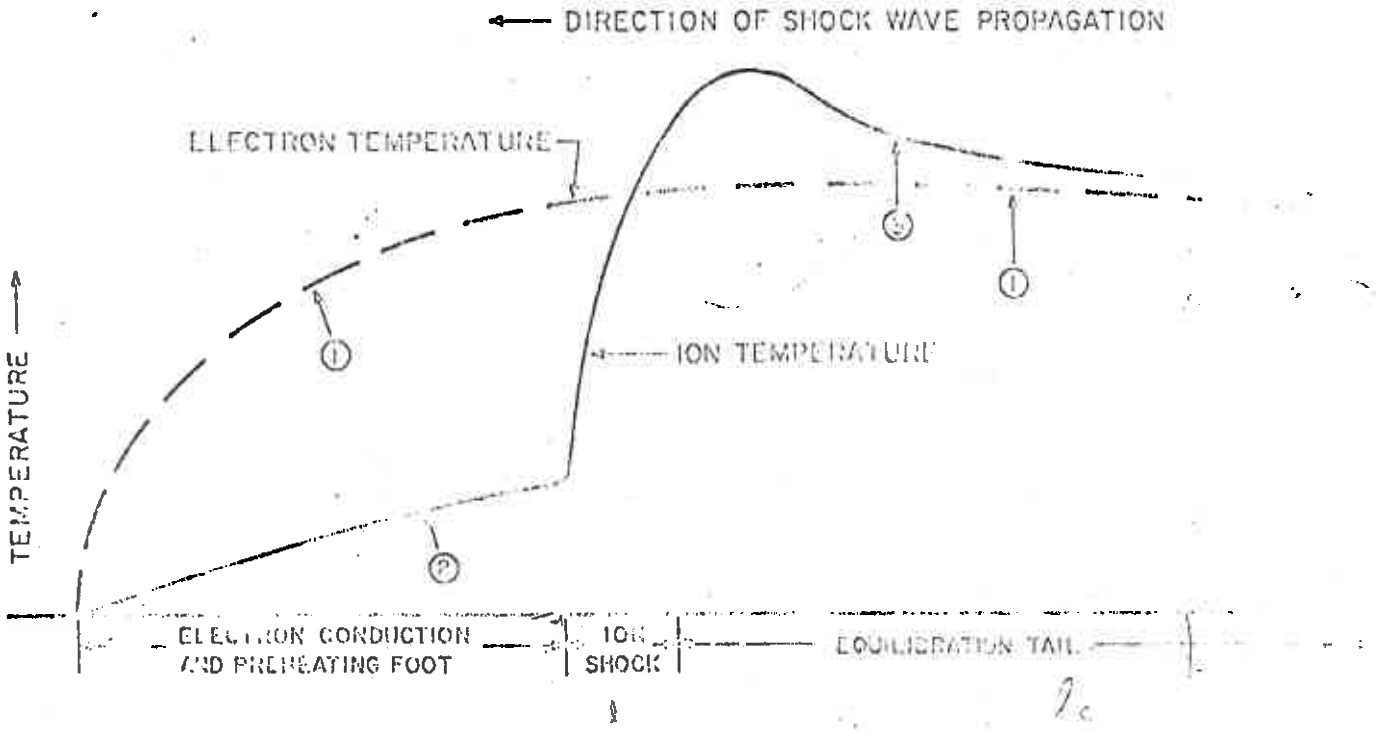

FIG. 3.2 SCHEMATIC DRAWING OF THE ELECTRON AND ION TEMPERATURE PROFILES IN A STRONG SHOCK WAVE (JAFFRIN AND PROBSTEIN[13]). ①, ②, AND ③ ARE THE THREE DIFFERENT MODES OF ENERGY INPUT. ① , ENERGY IS DEPOSITED IN THE ELECTRONS, RESULTING IN AN OVERSHOOT OF THE ELECTRON TEMPERATURE. ② , ENERGY IS PREFERENTIALLY DEPOSITED IN THE ELECTRON CONDUCTION FOOT, RESULTING IN A REDUCTION IN STRENGTH OF THE ION SHOCK. ③ , ENERGY IS PREFERENTIALLY DEPOSITED IN THE IONS LOCATED IN THE EQUILIBRATION TAIL, RESULTING IN AN INCREASE OF THE ION SHOCK STRENGTH.

Corona-Core Decoupling

A particularly important phenomena is the coupling of thermal energy between the pellet core and the plasma corona in which the driver energy deposition occurs. The absorption and transport of energy into the pellet core is governed by several significant time scales:

laser pulse rise time	$\Rightarrow$	rate at which energy is dumped into outer plasma corona of pellet
thermal conduction time	$\Rightarrow$	rate at which energy is conducted into ablation surface
electron-ion and electron-electron equilibration time at ablation surface	$\Rightarrow$	rate at which electrons can transfer energy into pellet core

We can develop a simple model of how these times affect the transfer of energy from the energy deposition region in the corona to the pellet core. If we characterize the corona and core by bulk temperatures T_{corona} and T_{core}, respectively, we can write the balance equations:

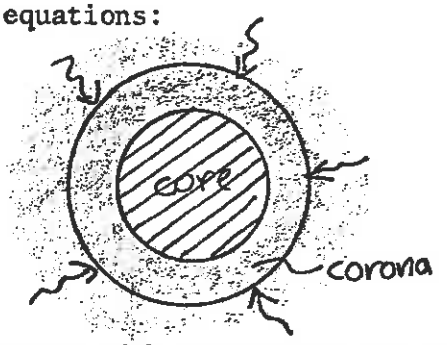

$$\frac{dT_{corona}}{dt} = Q(t) - \frac{\lambda_0}{T_{corona}^{3/2}}\left(T_{corona} - T_{core}\right)$$

$$\frac{dT_{core}}{dt} = \frac{\lambda_0}{T_{corona}^{3/2}}\left(T_{corona} - T_{core}\right)$$

Hwere Q(t) represents the effective heat source seen by the corona:

$$Q(t) = \text{(driver energy deposition rate)} \times \text{(probability of heat transfer into core)}$$

$$= \frac{Q_0(t)}{T_{corona}^{3/2}}\, P(T_{corona})$$

We expect that the heat transfer probability P is a decreasing function of the corona temperature

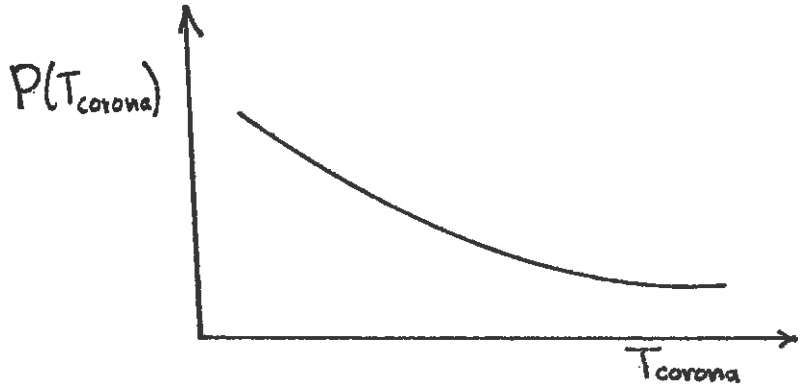

When these equations are solved, they reveal that if the driver energy increases too rapidly ($Q_o(t)$), then the core and corona temperatures will decouple:

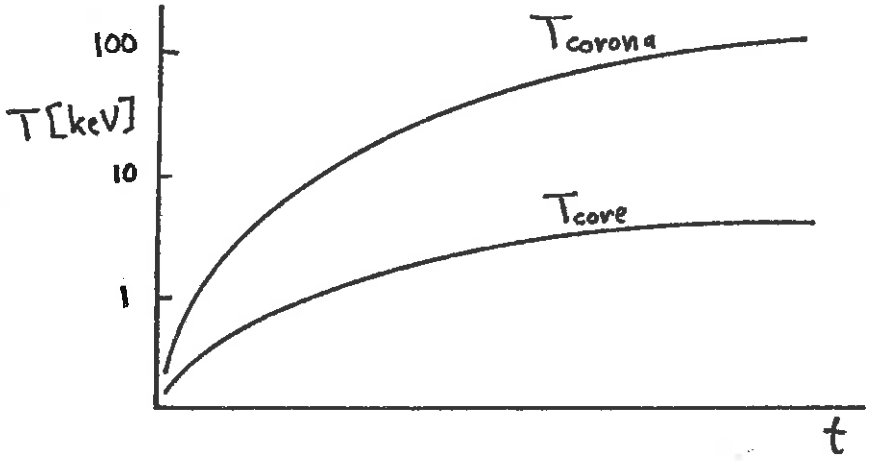

That is, if the corona is heated too rapidly, it will tend to decouple thermally from the pellet core, and further energy deposition merely heats up the corona to very high temperatures without affecting the core (burning the fuzz off of the peach). This effect becomes more pronounced for longer wavelength light in the case of laser drivers since the critical surface is at lower densities.

Thermal Flux Limiters

Recall that Fourier's law gives the heat flux as

$$\underset{\sim}{q}_e = -\kappa_e \underset{\sim}{\nabla} T_e$$

But in a plasma, the thermal conductivity $\kappa_e \sim T_e^{5/2}$. Hence for large temperatures, the thermal conductivity becomes very large and Fourier's law will predict too large a heat flux.

Actually, in these instances, Fourier's law is breaking down because the electron mean free path is becoming larger than the temperature gradient, i.e.

$$\left|\frac{T}{\nabla T}\right| \sim \text{mfp} \sim 3.81 \times 10^{12} \frac{T_e^2}{N_e}$$

If we calculate the electron mean free path for typical densities and temperatures we find

		N_e			
	λ_{ei}	10^{19}	10^{21}	10^{23}	10^{25}
T_e	10^2	10	1	-	-
	10^3	1000	10	.1	-
	10^4	10^5	1000	10	.1

where λ_{ei} is in microns

By way of comparison, computer code calculations indicate that for typical pellet conditions, the comparison between temperature gradient scales and electron mean free paths are:

$N_e = 10^{22}$, $T_e = 5$ keV, $\left|T/\nabla T\right| \sim 10\,\mu m$ (mfp $\sim 25\,\mu m$)

$N_e = 10^{21}$, $T_e = 5$ keV, $\left|T/\nabla T\right| \sim 100\,\mu m$ (mfp $\sim 250\,\mu m$)

Hence Fourier's law is clearly invalid for these situations.

This situation is particularly serious in hydrodynamic computer calculations since the unrealistically high thermal fluxes will lead to rubbish.

In practice, it is customary to artifically limit the thermal flux to a maximum value which corresponds to free particle flow. That is, one chooses a thermal flux which interpolates between the Fourier's law and streaming limits:

$$q = \frac{1}{\frac{1}{q_{FL}} + \frac{1}{q_{streaming}}}$$

To calculate the free streaming limit, we can simply estimate the flux of particles across a plane surface (assume an isotropic distribution of particles), and then multiply this by the mean kinetic energy per particle:

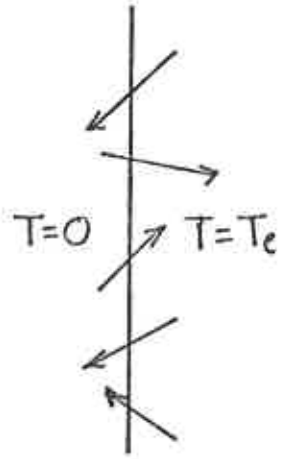

$$q_{streaming} = \overline{KE}\ \phi/4$$

$$= \left(\frac{1}{2} m \overline{v^2}\right) N_e \bar{v}/4$$

$$= \left(\frac{3}{2} kT_e\right)(N_e)\frac{1}{4}\left(\frac{kT_e}{m}\right)^{1/2}$$

In many computer codes, one simply uses a flux limiting form:

$$q_e = \frac{1}{\frac{1}{\kappa_e |\nabla T_e|} + \frac{2}{N_e \bar{v}_e}}$$

(It should be noted that this interpolation form has been around in gas dynamics circles for many years where it is referred to as "Sherman's universal relation". Interestingly enough, it can be derived more rigorously from kinetic theory arguments for linear heat flow problems.)

Strange Going-Ons in the Corona Region

A variety of unusual physical phenomena have been observed in the corona region of laser-irradiated pellets. Perhaps the single most important feature in many of the present experiments is the appearance of superthermal or high energy electrons generated by the light absorption process at the critical surface.

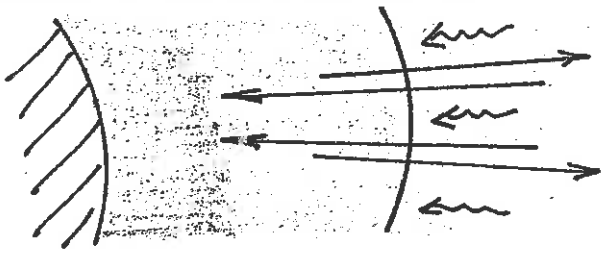

More precisely, it is found that when the incident light intensity exceeds some critical value, a significant fraction of the absorbed energy appears to go into the production of fast electrons. As these electrons blow off into the vacuum, they accelerate fast ions.

If we characterize the fast fast or hot electrons by an effective temperature T_H, then the measurement of X-ray spectra and fast ions suggests that the hot electron temperature is from 10 to 20 times that of the background electron temperature (typically 1-10 keV). The presence of superthermal electrons is particularly important, since their long mean free path allows them to penetrate into the target, causing an exploding pusher behavior and perhaps even preheating the target core.

A second important phenomenon is an inhibition of electron thermal conduction. More precisely, it is found that the actual value of the thermal flux in the corona region is almost an order or magnitude smaller than that predicted by classical physics (Fourier's law). It has been suggested that this effect might be explained by either the generation of ion turbulence in the corona region, or by the presence of strong magnetic fields produced by density and temperature gradients. In this section we will discuss these important processes.

Superthermal Electron Production and Transport: Evidence of the production of superthermal electrons in laser irradiated plasmas comes from several sources. A primary source has been the analysis of X-ray emission from targers. As we will indicate in a later chapter, the continuum or bremsstrahlung emission from these targets can be used to infer their temperatures. However detailed X-ray measurements have revealed that the X-ray emission can be characterized by not one, but rather two temperatures:

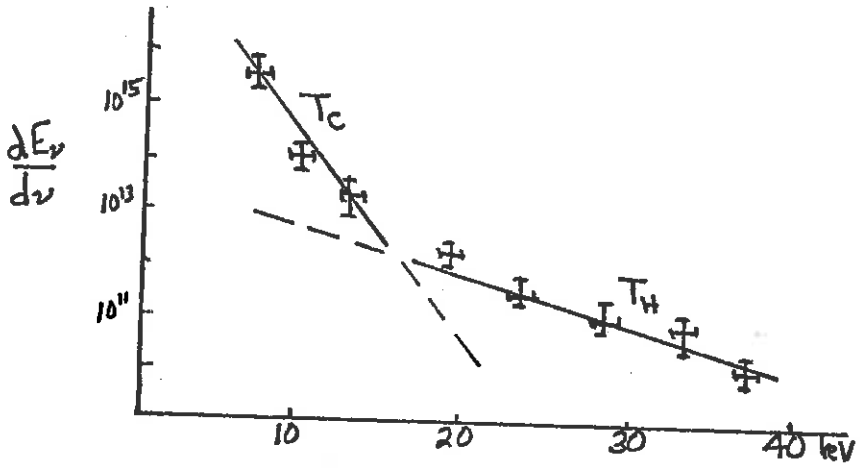

The slope of the X-ray measurements suggests that the temperature of the hot component is some 10 to 20 times that of the cold component.

One can also measure the fast ions that are accelerated in the space charge field set up by the freely expanding electrons leaving the low density corona. More recent experiments have attempted to measure the hot electron energies directly.

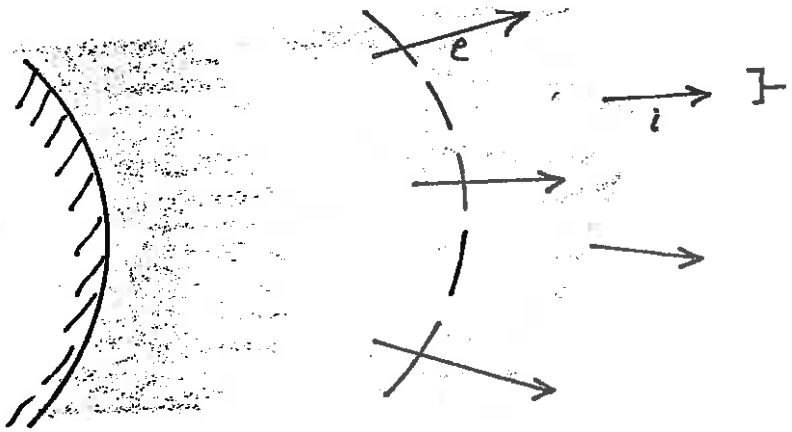

It is now felt that these fast electrons are generated as a result of a wavebreaking process induced by resonance absorption. As we will demonstrate in the next chapter, resonance absorption is a process in which light incident obliquely to a plasma density gradient can excite and drive electron plasma oscillations. The energy coupled into the

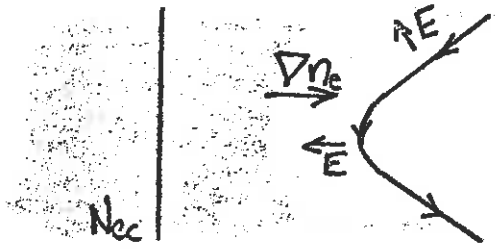

plasma oscillations then can dissipate through damping mechanisms to appear as thermal energy of heated electrons.

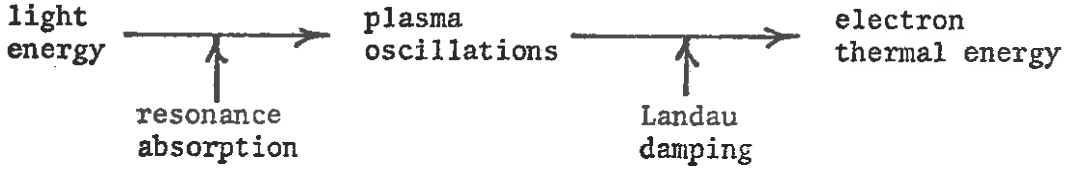

If the incident light intensity is strong enough, the electron plasma waves will be driven sufficiently strongly that electrons can be accelerated to high velocity through one wave period. At this point wave breaking occurs in which electrons are accelerated out of the thermal distribution and to very high velocities--that is, superthermal electrons are produced. A detailed analysis of the wavebreaking process indicates that these appear as very fast electrons moving outwards, away from the denser regions of the target.

The transport of these superthermal electrons is a particularly complex process because of their exceptionally long mean free paths. If we recall that the mean free path of electrons go as

$$\lambda \sim \frac{m_e^2}{4\pi e^4 \ln\Lambda} \frac{v^4}{n_e}$$

then we can tabulate mean free path versus density as:

density	10^{21}	10^{23}	10^{25}	10^{27}
mfp (100 keV)	10^7	10^5	10^3	$10\,\mu m$

Hence, except for the very dense compressed core, these superthermal

electrons see a relatively transparent plasma. They will tend to bounce off the space charge potential on the outer regions of the corona, being heated hotter and hotter until they strike the core. At this point they can penetrate ahead of the shock wave, causing preheating of the pellet fuel.

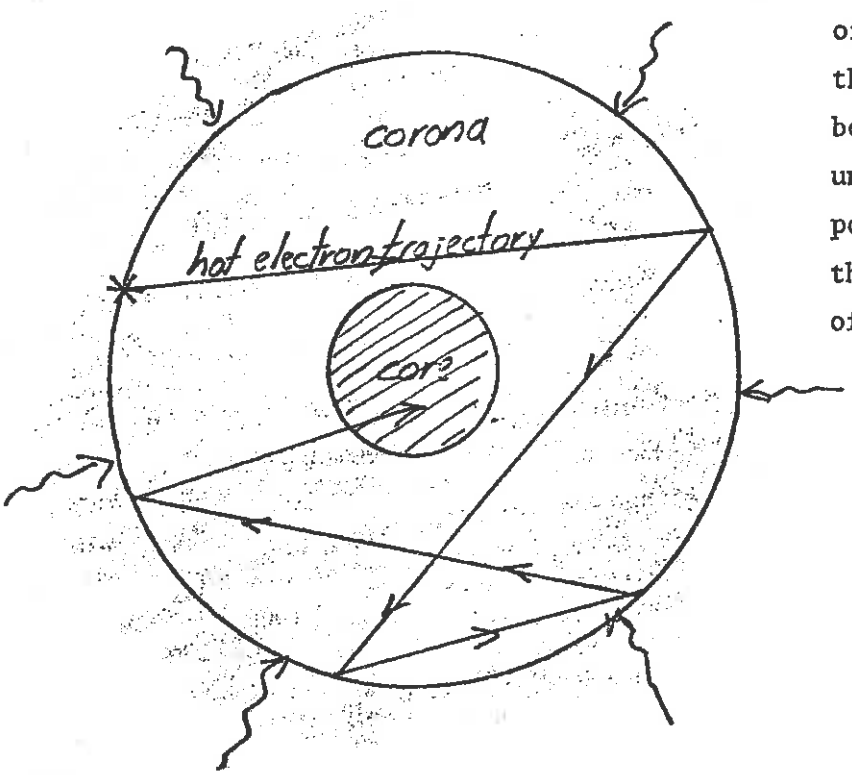

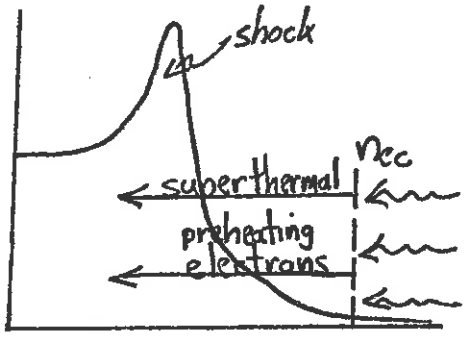

An accurate description of this phenomenon would solve some type of transport or kinetic equation for the electron motion, such as a Fokker-Planck equation:

$$\frac{\partial f}{\partial t} + \underline{v} \cdot \frac{\partial f}{\partial \underline{r}} + \underline{a} \cdot \frac{\partial f}{\partial \underline{v}} = \frac{\partial}{\partial \underline{v}} \cdot \left[\underline{\underline{G}} \cdot \frac{\partial}{\partial \underline{v}} + \underline{H} \right] f + S$$

However in most computer codes based on hydrodynamic analysis, the hot electrons are handled using multigroup diffusion theory (including the effects of electric fields). To handle the long mean free paths, a flux limiting procedure is implemented in which the particle current is taken to be

$$\underline{J} = -\left[\frac{v}{\frac{3}{\lambda} + \frac{1}{|\mu| n} \left| \frac{\partial n}{\partial r} \right|} \right] \frac{\partial n}{\partial r}$$

where

$$\frac{1}{|\bar{\mu}|} = 1 + 3e^{-\frac{\Delta}{2}\frac{1}{n}\left|\frac{\partial n}{\partial r}\right|}$$

More sophisticated pellet designs attempt to include a layer of high-Z material (such as gold) to shield the core of the pellet from preheating by hot electrons:

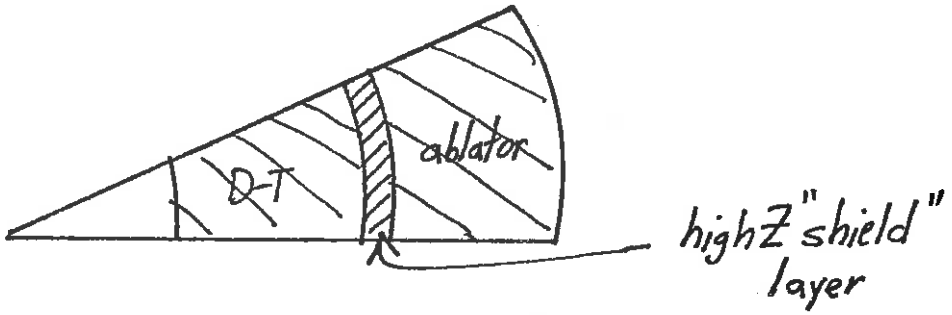

Thermal Conduction Inhibition: A second phenomenon of some concern is the apparent inhibition of thermal conduction in the pellet corona region, limiting the thermal flux to values one to two orders of magnitude below its classical value.

The evidence of this inhibition was provided first by a number of foil-irradiation experiments performed at Los Alamos. Thin foils were illuminated from one side with intense laser light:

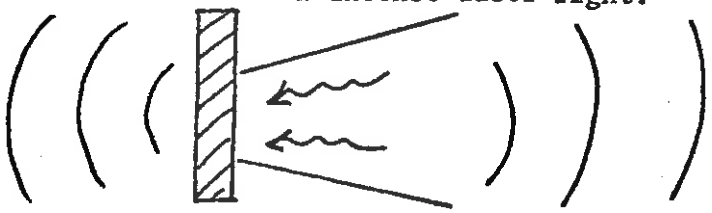

The foils were thin enough that classical thermal conduction was expected to be sufficiently strong to transport energy quickly through the foil and yield a symmetric pattern of fast ion blowoff on either side. In fact, however, a strongly asymmetric ion blowoff pattern was observed that could be explained by reducing the heat flux to roughly 3% of its classical value:

$$q \sim 0.03\, q_{classical}$$

A variety of other experiments including X-ray measurements have since supported the presence of some inhibition mechanism.

What might be causing the inhibition? Mechanisms range from the buildup of electric fields due to a return current of cold electrons, to ion turbulence due to a two-stream instability, to the presence of strong magnetic fields caused by density and temperature gradients in the corona region.

One simple mechanism might be the presence of plasma turbulence close to the critical surface. It is now well established that intense laser light can drive the natural modes of the plasma unstable (parametric coupling processes) and into a turbulent state in which all transport coefficients assume anomalous values.

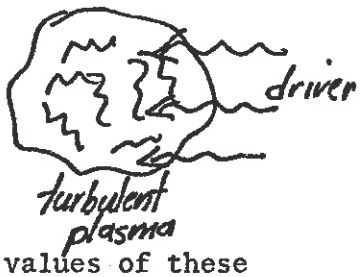

Early calculations suggested that the anomalous values of these transport coefficients would scale as

$$\alpha^{anom} \sim \left(\frac{\omega_{pi}}{\nu_{ei}}\right) \alpha^{clas}$$

That is, apparently the electron-ion collision frequency would be enhanced to an anomalous value more characteristic of the ion plasma frequency:

$$\nu_{ei} \rightarrow \omega_{pi}$$

Since the electron thermal conductivity scales as

$$\kappa_e \sim \frac{5 n_e k^2 T_e}{m_e \nu_{ei}}$$

this estimate would suggest that in a turbulent region:

$$\kappa_e^{anom} \sim \left(\frac{\nu_{ei}}{\omega_{pi}}\right) \kappa_e^{clas}$$

This estimate would yields a reduction in the electron conductivity by roughly 100, thereby inhibiting thermal conduction out of the turbulent zone. When such anomalous values of thermal conductivity are patched

into a laser-plasma hydrodynamics calculation, one finds density and temperature profiles as shown below:

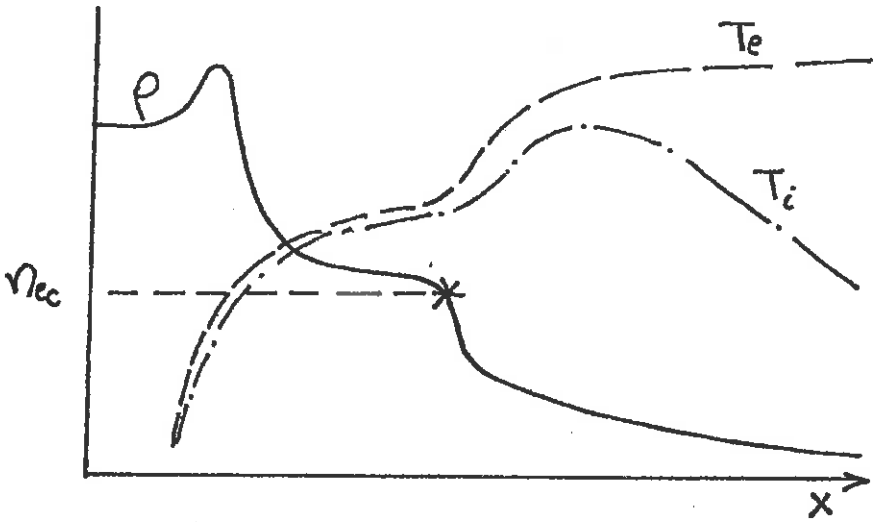

This indicates that the conduction inhibition leads to trapping of absorbed energy in the turbulent region, causing high ion temperatures (and hence thermal velocities) and strong blowoff just beyond the critical surface. The problem with this simple argument is that it applies to the vicinity of the critical surface and not to the overdense regions of the corona where the thermal flux inhibition is thought to occur.

However there is another mechanism which could lead to turbulence in this region as well. We noted earlier that there is a counterflow of cold elections to balance the hot electron flow. There is also a flow of ions due to the plasma blowoff.

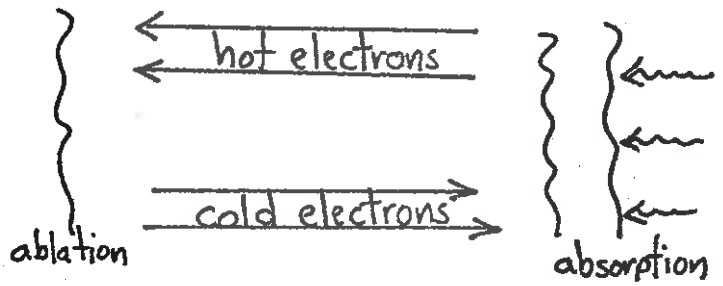

Since the ion distribution is at rest in a frame of reference moving with the plasma blowoff or flow, while the electron distribution is skewed (to yield a thermal flux), there is a displacement of the maxima of each distribution. This is a condition suitable for the presence

of a two-stream instability (when $T_e >> T_i$). The instability results in the formation of ion turbulence. The electrons would then scatter off of the turbulent ion fluctuations, thereby effectively increasing the electron-ion collision frequency ν_{ei}. Calculations at Los Alamos suggest that this process can be modeled by limiting the thermal flux characterizing free particle flow by

$$q_e|_{max} = \alpha (n_e)\left(\frac{3}{2} kT_e\right)\left(\frac{kT_e}{m_e}\right)^{1/2}$$

where the parameter α assumes values

$$0.03 < \alpha < 0.1$$

--a rather severe inhibition of thermal conduction.

A third mechanism that might lead to thermal flux inhibition involves the presence of magnetic fields. The large thermal and density gradients induced in the plasma corona can generate currents and hence spontaneous magnetic fields of some strength. If we ignore the Hall effect and thermoelectric terms, we can write

$$\frac{\partial \underset{\sim}{B}}{\partial t} = \underset{\sim}{\nabla} \times \left[\underset{\sim}{v} \times \underset{\sim}{B} + \frac{c}{e n_e} \underset{\sim}{\nabla} (n_e kT_e)\right]$$

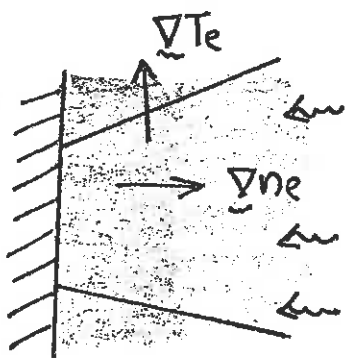

If the electron density and blowoff velocity are parallel to the incident laser beam, we find in the steady state that

$$B = \frac{c}{e} \frac{kT_e}{v} \frac{1}{H}$$

where H is the scale height of the electron temperature gradient perpendicular to the radial direction:

$$H = T_e / |\nabla T_e|$$

As a rough model, we can take

$$B = 10^4 \, T_e(\text{eV})/H(\mu\text{m})$$

For example, at T_e = 1 keV, H = 20 μm, we find a spontaneous field of B = 500 kgauss.

To determine the effect of this field on the thermal conduction, we can use the form of Braginskii for the transport coefficients:

$$\kappa_e = \frac{\kappa_e(B=0)}{1 + (\Omega_{ce}/\nu_{ei})^2}$$

where Ω_{ce} is the electron cyclotron frequency. In our previous example, if $N_e = 10^{22}$, then

$$\nu_{ei} = 3.4 \times 10^{12}, \quad \Omega_{ce} = 8.8 \times 10^{12}, \quad 1 + (\Omega_{ce}/\nu_{ei})^2 \sim 7$$

Hence the B-field reduces the thermal conductivity by a factor of 7.

Actually, a more correct analysis would use a thermal flux:

$$\underset{\sim}{q}_e = -\frac{\kappa_e}{1+(\Omega_e^2/\nu_{ei}^2)} \underset{\sim}{\nabla} T_e - \frac{\kappa_e(\Omega_e/\nu_{ei})}{1+\Omega_e^2/\nu_{ei}^2} \hat{B} \times \nabla T_e$$

But the important result is that the presence of a very strong magnetic field can significantly inhibit electron thermal conduction.

4.3. SUPERTHERMAL PARTICLE TRANSPORT

CHAPTER 5

DRIVER ENERGY DEPOSITION

We now turn our attention to the absorption of the incident driver beam energy in the plasma corona surrounding the fuel pellet. The details of this energy absorption process will depend sensitively on the type of driver:

laser beams; light absorption in plasmas
charged particle beams: slowing down of charged particles in a plasma
other: hypervelocity particles, imploding liners.

5.1. LASER LIGHT ABSORPTION IN PLASMAS

Laser light can interact in a variety of ways with a plasma. The simplest form of interaction is inverse bremsstrahlung or collisional absorption of the incident light. We recall that bremsstrahlung corresponds to radiation (photons) emitted when a charged particle is decelerated, for example, an electron emitting a photon in a collision with an ion:

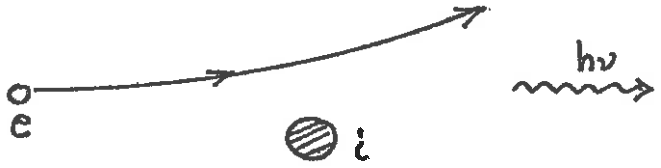

Inverse bremsstrahlung occurs when an incident photon is absorbed by an electron in the field of an ion.

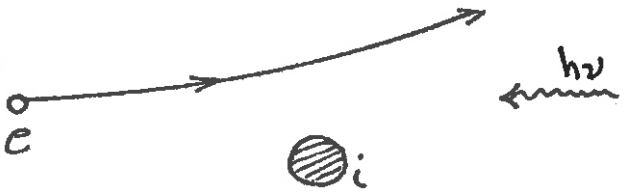

A simpler way to think of inverse bremsstrahlung is to consider the motion of an electron in the oscillating electric field of an incident electromagnetic wave (the incident light beam). As the electrons oscillate in this field, they collide with ions, thereby converting the directed energy of the oscillation into the random energy of thermal motion. In this way, the incident light energy eventually appears as increased electron temperature.

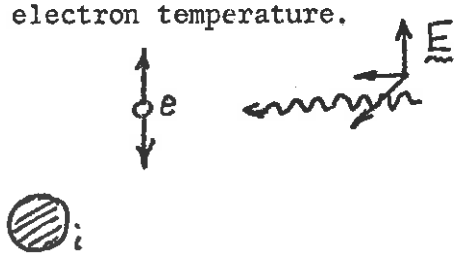

Since this process depends on electron-ion collisions, we might expect that the strength of the absorption goes as the electron-ion collision frequency:

$$\kappa \sim \nu_{ei} \sim \frac{1}{T_e^{3/2}}$$

But we know that $\nu_{ei} \sim T_e^{3/2}$. Hence as the plasma temperature increases, the collisional or inverse bremsstrahlung process becomes less effective. For example, for 1.06 μm light, $T_e \sim 1$ keV, $Z \sim 3$, the absorption length κ^{-1} is roughly 100 μm. Furthermore, we will show that for large beam intensities ($> 10^{14}$ W/cm^2), the absorption also becomes intensity dependent and falls as

$$\kappa \sim \frac{1}{I^{3/2}}$$

Thus, for high temperature plasmas and high intensity light, the classical absorption mechanism becomes quite ineffective.

Fortunately there are other absorption mechanisms involving the coupling of the incident light into waves in the plasma:

More specifically, the oscillation of the electrons in the electric field of the incident light across a variation in the plasma density drives a charge density fluctuation

$$\delta n_e = n_e(\underset{\sim}{x}+\underset{\sim}{x}_{osc}) - n_e(\underset{\sim}{x}) \sim \underset{\sim}{x}_{osc} \cdot \underset{\sim}{\nabla} n_e$$

where $\underset{\sim}{x}_o = eE_L/m\omega_o^2$ is the "quiver distance" of the oscillating electron. If the incident light frequency ω_o is comparable to the electron plasma frequency, then this coupling can resonantly drive electron plasma waves.

There are two sources of the plasma density gradient leading to this coupling:

(i) the plasma blowoff: This leads to the resonance absorption process.

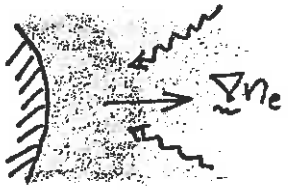

(ii) density fluctuations from other plasma waves such as ion acoustic waves: This leads to parametric excitation.

In this section we will discuss both classical and collective light absorption processes in plasmas. However it is appropriate to first discuss the various mechanisms in which intense light can interact with matter.

Interaction of Intense Laser Radiation with Matter

The electromagnetic energy density at the focal spot of a high powered pulsed laser reaches incredible magnitudes. By way or orientation, consider the focal spot of a 1,000 joule Nd glass laser which delivers this energy in a pulse of 10^{-10} second duration on a focal spot of area 10^{-4} cm^2. Then some parameters characterizing this focal spot are given below:

focused intensity:	10^{18} W/cm^2
energy density:	3×10^6 joules/cm^3
photon density:	3×10^{25} photons/cm^3
E_{rms} :	10^{10} volts/cm
B_{rms} :	50 Megagauss
average kinetic energy of electron oscillating in laser field :	5 keV

The energy density at the focal spot is well above the energy density of electron binding to an atomic nucleus of 4×10^5 joules/cm^3 (although well below the nuclear energy densities of 10^{11} joules/cm^3).

Needless to say, if this very intense laser light is focused upon a solid, rather major transformations will occur. Not only will the solid be vaporized, but it will be ionized as well, producing a very high density plasma which will continue to absorb the incident laser light. The very rapid temperature increase at the surfaceof the solid will cause the laser-produced plasma to blow off towards the laser beam. This, in turn, will drive a very intense hydrodynamic shock wave into the solid.

Heating without Phase Change: For sufficiently low light intensities, $I \sim 10^7$ W/cm^2, the incident laser light will merely heat the target surface without melting or vaporizing it. The incident light will be absorbed (and partially reflected) within a skin depth of the surface. This absorbed energy will then be transferred into the interior of the target by thermal conduction, i.e., as described by

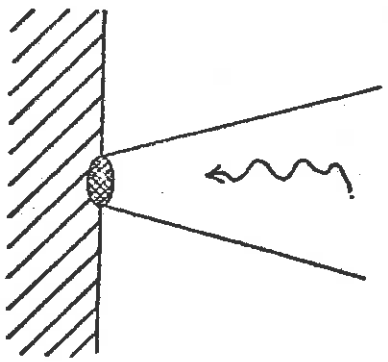

$$\rho c_v \frac{\partial T}{\partial t} = \kappa \nabla^2 T(\underline{r},t) + S(\underline{r},t)$$

This equation can easily be solved for the temperature distribution in the heated material, as shown on the next page for the case of laser heating of a copper surface.

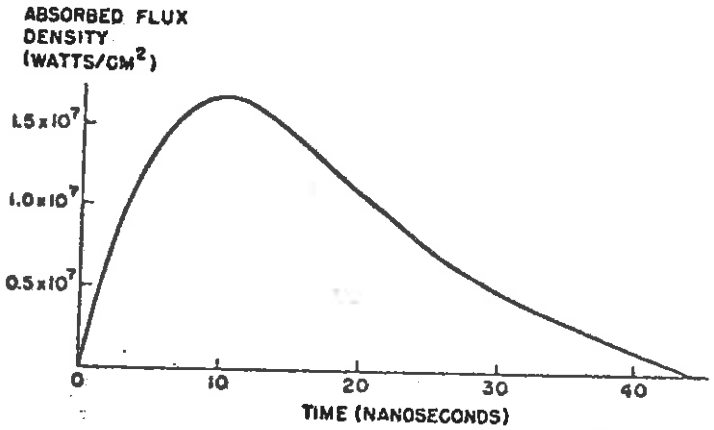

Laser pulse shape used for calculation. [From J. F. Ready, *J. Appl. Phys.* 36,

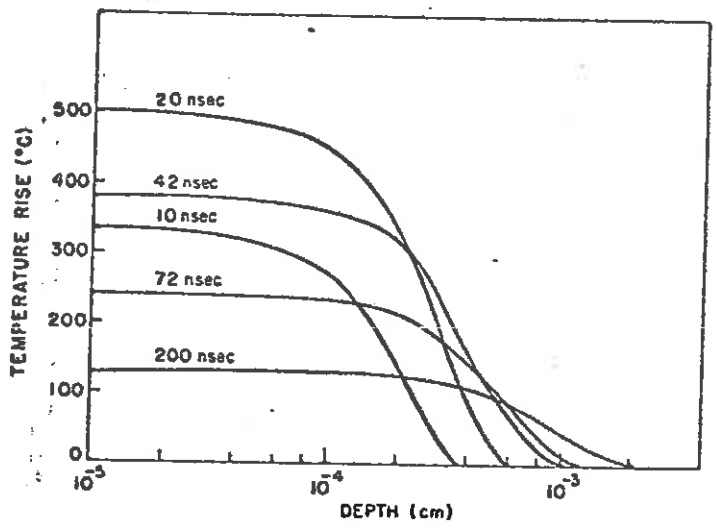

Calculated temperature rise as a function of depth, with time as a parameter, caused by absorption of a *Q*-switched laser pulse in copper. [From J. F. Ready, *J. Appl. Phys.* 36, 462 (1965).]

Laser Induced Melting and Evaporation: For somewhat higher intensities, $I \sim 10^6 - 10^9$ W/cm^2, the incident laser energy will actually melt or evaporate the solid surface. One usually finds vaporization of the surface as opposed to melting. The mechanism for vaporization depends on the laser light intensity (the pulse width).

For longer pulses at lower intensities, $I \sim 10^6 - 10^7$ W/cm^2, the laser light produces deep, narrow holes in the surface. There is very little "blowoff" of the vapor produced at the surface. Typically, a 10 joule pulse delivered in a millisecond will produce a crater of about 1 mm in depth.

For higher intensity but shorter pulses, $I \sim 10^9$ W/cm^2, only a small amount of the target material is vaporized. However this vapor cloud or blowoff can interact with the incident laser light, absorbing the light and shielding the surface. Since higher intensities produce high pressures which drive the vapor away from the surface at high velocities, the back reaction from the blowoff drives strong shock waves into the solid target itself. By way of an example, a 10 joule pulse delivered in 30 ns will only ablate $\sim$1-3 microns of surface material.

Laser Induced Ionization and Gas Breakdown: It has been known for some time that sufficiently intense laser light can ionize materials. In particular, the focal spot of a large pulsed laser is capable of creating a "spark" in air--that is, producing gas breakdown. The threshold of this phenomenon is usually around $I \sim 10^{11}$ W/cm^2.

There appear to be two essential processes involved in such breakdown phenomena: the production of an initial ionization and then the subsequent growth of this ionization. The second process is easy to understand as an avalance mechanism. If there are free electrons in the gas, they will be rapidly accelerated to high energies by the electric field of the incident laser light. In a very short time they will have achieved sufficiently high energy to ionize other atoms and produce more free electrons--and so on in a cascading ionization process.

The initial or "priming" ionization is more difficult to understand, since the photons present in the incident laser beam have energies $h\nu$ many

times less than the ionization potential of most atoms. For example, it would take the simultaneous absorption of 43 CO_2 laser photons to ionize a lithium atom. Such very high order multiphoton processes are very improbable. Nevertheless, in the very high photon densities of the laser focal spot, such a mechanism may be significant. Other explanations for the initial ionization include the presence of impurities, and also a distortion of the atomic electron energy levels in the very high intensity laser electric field which effectively lowers the ionization potential.

Needless to say, the calculation of the laser light threshold at which ionization occurs in a gas is rather complicated, and experimental verification is difficult. Fortunately at the very high intensities used in most applications ($> 10^{12}$ W/cm^2), the ionization of the target material can be regarded as instantaneous--regardless of the actual mechanism involved. Hence one usually considers the interaction of very high intensity laser light to be with a dense, low temperature ($\sim$5 eV) plasma--that is, a fully ionized gas at solid-state densities.

Classical Analysis of Laser Light Absorption in Plasmas

The classical mechanism for laser light absorption in plasmas is inverse bremsstrahlung or free-free absorption in which a photon is absorbed by a free electron in the field of an ion. However a more intuitive description of the absorption process would be to recognize that the incident electric field of the laser light will oscillate free electrons (the ions will also oscillate, but their motion can be neglected because of their much larger mass). This directed energy of electron motion will be randomized and hence converted into heat energy by electron collisions with ions. In other words, the incident laser electric field will drive electron currents, and the resistivity represented by electron-ion collisions will lead to "joule heating" in the plasma.

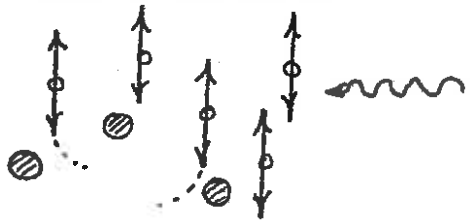

This process can be analyzed more qualitatively as follows: The propagation of a plane polarized electromagnetic wave in a medium can be described by Maxwell's equations (taking the propagation vector along the z-axis and the electric field vector along the x-axis):

$$\frac{\partial E}{\partial z} = \frac{\partial B}{\partial t}$$

$$\frac{\partial B}{\partial z} = \mu J + \frac{1}{c^2}\frac{\partial E}{\partial t}$$

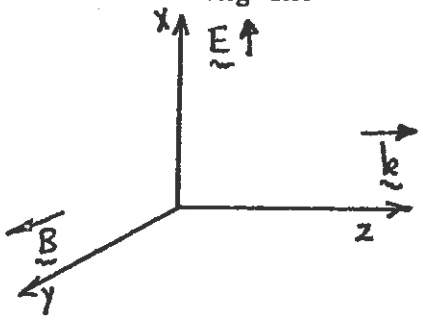

Here J represents the current induced by the electromagnetic wave in the x direction. This current can be calculated if we consider the motion of an electron in the electric field as described by its equation of motion:

$$m\frac{d^2\underset{\sim}{r}}{dt^2} + m\nu_{ei}\frac{d\underset{\sim}{r}}{dt} = -e\underset{\sim}{E}$$

or for the x coordinate of the velocity, u,

$$m\frac{du}{dt} + m\nu_{ei}u = -eE \qquad (*)$$

Here ν_{ei} is the "electron-ion collision frequency" which has been introduced as a phenomenological friction term in this equation. The induced current density can then be calculated in terms of u as

$$J = n_e e u$$

To solve these equations, we seek a solution in the form of a plane wave:

$$\underset{\sim}{E} = E\hat{e}_x e^{i(kz+\omega t)}$$

Then we can solve (*) for the electron motion

$$u = \frac{eE}{m}\left(\frac{i\omega - \nu_{ei}}{\omega^2 + \nu_{ei}^2}\right)e^{i(kz+\omega t)}$$

and hence for the current density

$$J = \left(\frac{e^2 n_e}{\epsilon_o m}\right)\left(\frac{i\omega - \nu_{ei}}{\omega^2 + \nu_{ei}^2}\right)\epsilon_o E e^{i(kz+\omega t)}$$

where it is convenient to define the plasma frequency

$$\omega_p^2 \equiv \frac{e^2 n_e}{\epsilon_o m}$$

If we substitute this current into the field equations, we arrive at a relation between the propagation wave number k and the laser light frequency ω --that is, a dispersion relation for the laser light propagation in the plasma:

$$\left(\frac{kc}{\omega}\right)^2 = 1 - \left(\frac{\omega_p^2}{\omega^2 + \nu_{ei}^2}\right)\left(1 + i\,\frac{\nu_{ei}}{\omega}\right)$$

Since k will be complex in general, the incident light will be attenuated as it propagates. In particular, the index of refraction n_i is given by

$$n_i \equiv \mathrm{Re}\left\{\frac{kc}{\omega}\right\} = \left[\frac{\beta}{2} + \frac{1}{2}\sqrt{\beta^2 + (1-\beta)^2(\nu_{ei}/\omega)^2}\,\right]^{1/2}$$

while the energy absorption coefficient is given by

$$\kappa \equiv 2\,\mathrm{Im}\{k\} = 2\frac{\omega}{c}\left[-\frac{\beta}{2} + \frac{1}{2}\sqrt{\beta^2 + (1-\beta)^2(\nu_{ei}/\omega)^2}\,\right]^{1/2}$$

where

$$\beta = 1 - \frac{\omega_p^2}{\omega^2 + \nu_{ei}^2}$$

Light Propagation in Plasmas: Before continuing, notice something very important. If $\nu_{ei} << \omega$, the index of refraction is given by

$$n_i = \sqrt{1 - (\omega_p/\omega)^2}$$

In particular, notice that when $\omega < \omega_p$, n_i is imaginary. This means

that light cannot propagate in a plasma when $\omega < \omega_p$. In most plasmas, one finds a density gradient as shown

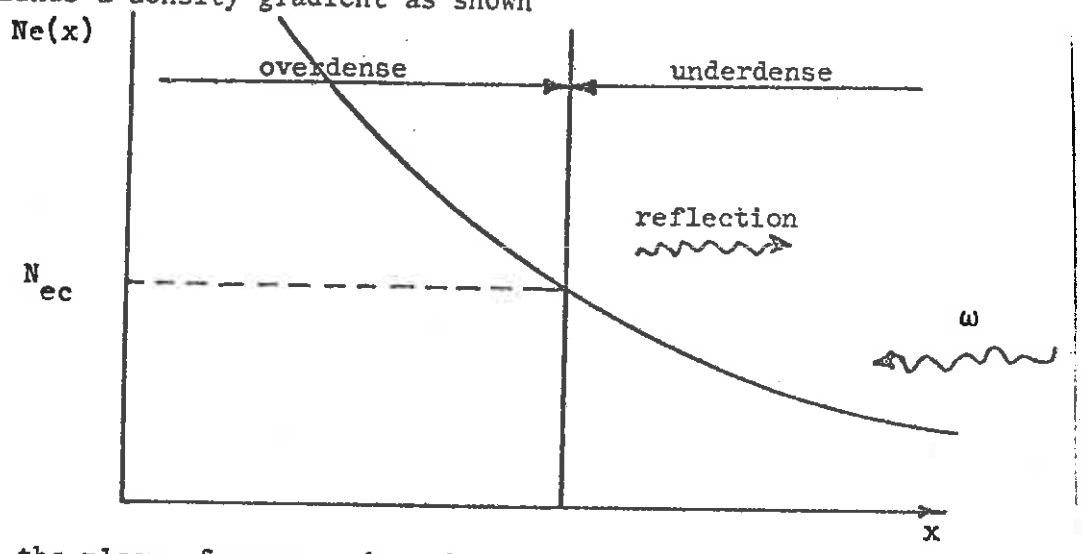

Since the plasma frequency depends on the density,

$$\omega_p = \sqrt{\frac{e^2 n_e}{\epsilon_o m}}$$

the incident laser light from the lower density ("underdense") region can only propagate up to the critical density N_{ec}, defined as that plasma density for which $\omega = \omega_p$. At this point the light will be reflected. From a more physical point of view, in the underdense region where the light frequency exceeds the plasma frequency, the electron inertia is sufficient to keep the material current and the light propagates unaffected. In the overdense region where the light frequency is less than the plasma frequency, the material current will oppose the displacement current in the light field and the wave cannot propagate.

We will see in a moment that most light absorption in a plasma occurs at or near the critical density, defined more explicitly as

$$n_{ec} \equiv \frac{\epsilon_o m \omega_o^2}{e^2}$$

We have tabulated the critical density N_{ec} as well as several other parameters characterizing laser light of different wavelengths.

We should also note that since the index of refraction n_i is less than one, the light will be refracted away from regions of higher density.

Laser Type	$\lambda_0(\mu m)$	$h\nu$ (eV)	ρ_c (g/cm^3)	N_{ec} (cm^{-3})
hypothetical	0.17	6.2	12.8×10^{-2}	3.9×10^{22}
"	0.20	7.3	9.3×10^{-2}	2.8×10^{22}
"	0.23	5.4	7.2×10^{-2}	2.2×10^{22}
2nd harmonic Nd	0.5	2.5	1.5×10^{-2}	4.5×10^{21}
Nd	1.06	1.17	3.3×10^{-3}	10^{21}
2nd harmonic CO_2	5.0	0.25	1.5×10^{-4}	4.5×10^{19}
CO_2	10.6	0.117	3.3×10^{-5}	10^{19}

Another important parameter which characterizes the plasmas response to the incident laser light is the "quiver velocity" with which the electrons oscillate in the light's electric field:

$$u_0 = \frac{e}{m} E_n \left(\frac{i\omega - \nu_{ei}}{\omega^2 + \nu_{ei}^2} \right)$$

We have plotted this versus laser light intensity for Nd and CO_2 wavelengths.

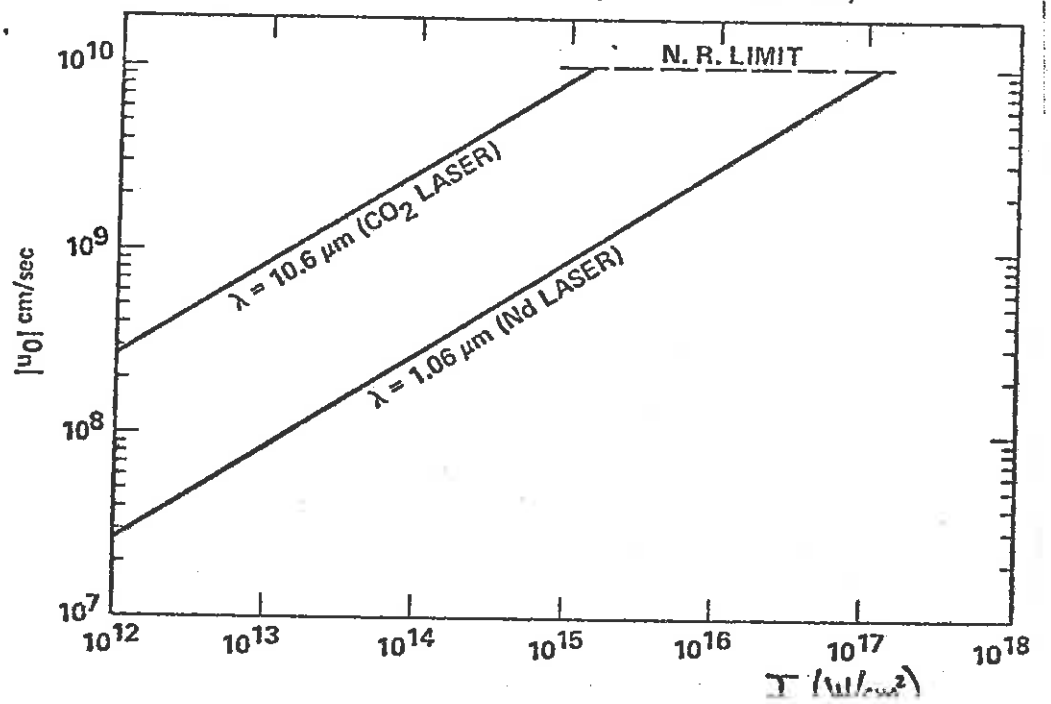

Classical Absorption: The usual situation in a plasma is

(i) $\nu_{ei} << \omega_0$ (dilute)

(ii) $\omega_p < \omega_0$ (underdense)

Then we can simplify our dispersion relation as

$$\left(\frac{kc}{\omega}\right)^2 \simeq 1 - \frac{\omega_p^2}{\omega^2}\left(1 - i\frac{\nu_{ei}}{\omega}\right) = 1 - \frac{\omega_p^2}{\omega^2} + \frac{\omega_p^2}{\omega^2} i\frac{\nu_{ei}}{\omega}$$

$$\therefore \quad \frac{kc}{\omega} \simeq \left(1 - \frac{\omega_p^2}{\omega^2}\right)^{1/2}\left[1 + \frac{1}{2} i \frac{(\omega_p^2/\omega^2)(\nu_{ei}/\omega)}{1 - \omega_p^2/\omega^2}\right]$$

Hence the absorption coefficient can be written approximately as

$$\kappa = 2\,\mathrm{Im}\{k\} \simeq \left(\frac{\omega_p}{\omega}\right)^2 \frac{\nu_{ei}/c}{\sqrt{1-\omega_p^2/\omega^2}} = \left(\frac{\omega_p}{\omega}\right)^2 \frac{\nu_{ei}}{n_i c}$$

If we now substitute in an explicit form for the electron-ion collision frequency, we can write the absorption coefficient characterizing inverse bremsstrahlung as

$$\kappa = \frac{(Ze^3)^2 N_e N_i}{3\epsilon_0^3 c\omega^2 (2\pi m k T)^{3/2}} \frac{\ln\Lambda}{n_i}$$

Let us examine this expression in more detail. For fixed plasma density N_e and temperature T_e, it appears that $\kappa \sim 1/\omega_0^2 \sim \lambda_0^2$, and hence we might expect that longer wavelength radiation is absorbed more effectively. However this is a misleading comparison since most absorption will occur near the critical density N_{ec} corresponding to a plasma frequency $\omega_p = \omega_0$. It is therefore more illuminating to rewrite the absorption coefficient in an alternative form

$$\kappa \simeq \frac{\phi^2}{\sqrt{1-\phi^2}} \kappa_{0c}$$

where $\phi = N_e/N_{ec}$ and κ_{0c} is the absorption coefficient characterizing the critical density,

$$\kappa_{0c} \equiv \frac{1}{c}\nu_{ei}(N_e = N_{ec})$$

Actually, ν_{oc} is the most appropriate measure of the effective absorption coefficient for a given wavelength light. Since the collision frequency behaves as

$$\nu_{ei} \sim \frac{N_e}{T_e^{3/2}}$$

it becomes apparent that $\nu_{oc} \sim \omega_o^2$. Hence the effective absorption length decreases rapidly as the wavelength of the laser light decreases (see the Figure on the next page).

The thickness of the plasma cloud surrounding the targer is characterized by its "scale height" H, that is, H essentially characterizes the plasma density gradient. For an exponential density profile, H would appear as the e-folding length:

$$N_e(x) = N_{ec}\, e^{-(x-x_c)/H}$$

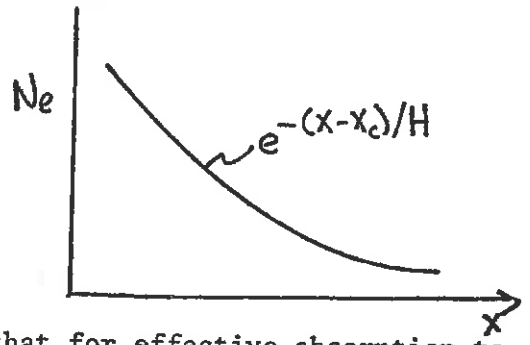

It should therefore be apparent that for effective absorption to occur, one must have a plasma scale height H comparable to the absorption length $l_{oc} = \frac{1}{\nu_{oc}}$ at critical density. More precisely, Kidder has shown that the scale height corresponding to an optical thickness of unity is

$$H_c = \frac{3}{8} l_{oc}$$

If we estimate the time necessary to blowoff a plasma to this scale height by assuming isothermal expansion of the plasma surface into a vacuum, then we find

$$\tau_{abs} = \frac{H_c}{c_s} = \frac{3 l_{oc}}{8 c_s}$$

where $c_s = (ZkT_e/m_i)^{1/2}$ is the isothermal speed of sound in the plasma. We have plotted these times for various wavelengths in Figure . These calculations suggest that one would not expect classical absorp-

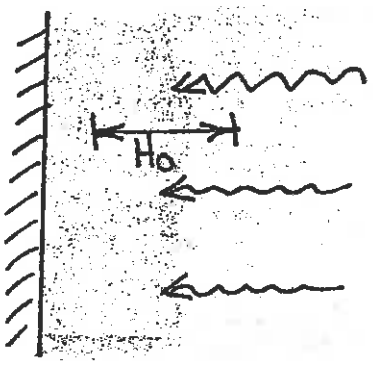

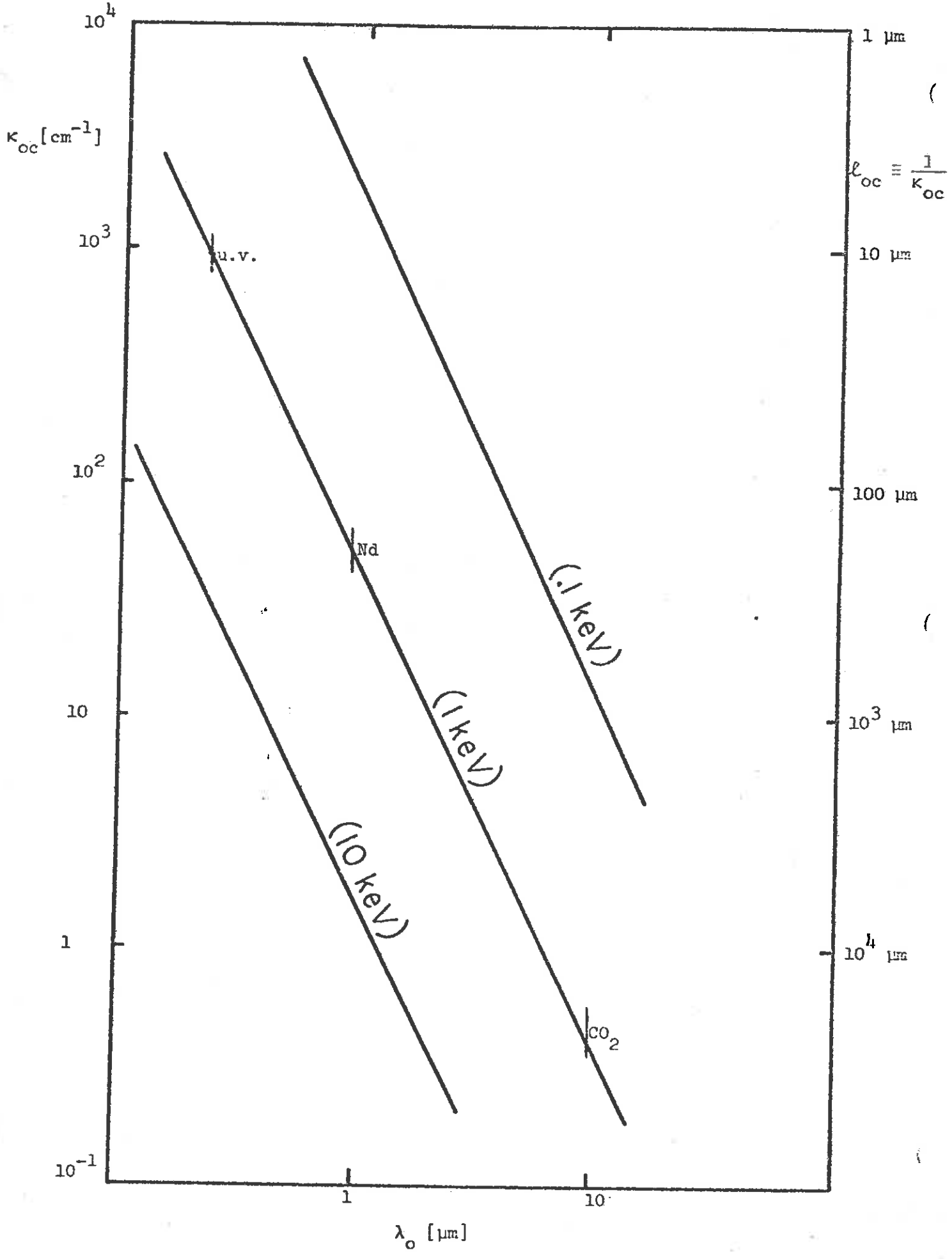
10^4
10^3
10^2
10
1
10^{-1}
κ_{oc} [cm^{-1}]
1 μm
10 μm
100 μm
10^3 μm
10^4 μm
$\ell_{oc} \equiv \frac{1}{\kappa_{oc}}$
u.v.
Nd
CO_2
(.1 keV)
(1 keV)
(10 keV)
1
10
λ_o [μm]

tion to play a significant role for 4 ns pulses for wavelengths $\lambda_0 > 4\ \mu m$ (e.g., for CO_2 wavelengths). These expectations are conformed by numerical calculations in which a 4 ns pulse is incident on a slab target. In Figure we have plotted the percentage of the incident beam energy which is absorbed by the target versus wavelength. It is evident that classical absorption is negligible for $\lambda_0 > 5\ \mu m$--indeed, it has dropped off appreciably even for Nd wavelengths ($1.06\ \mu m$). By way of contrast, the absorption is quite strong for short wavelengths (e.g., a uv laser).

Nonlinear Bremsstrahlung: There are many modifications that can arise in this simple picture of absorption in plasmas. For sufficiently low temperatures, bound-bound and bound-free absorption can occur. At higher intensities, the strong electric field of the light will distort the distribution of electron thermal velocities, hence modifying the collision frequency ν_{ei} and leading to a dependence of the absorption coefficient κ upon the light intensity I ("nonlinear bremsstrahlung"). This occurs at light intensities at which the energy of oscillation of the electrons in the light beam electric field is comparable to their thermal energy.

If we define the "quivering energy" of the electrons in the light field as

$$Q.E. = \frac{1}{2}\frac{e^2 E_{rms}^2}{m\omega^2} = \frac{1}{2}\frac{e^2}{m\omega^2}\left(\frac{8\pi}{c} I\right) \sim \frac{I}{\omega^2}$$

then nonlinear bremsstrahlung occurs when

$$Q.E. \sim kT_e$$

For still higher intensities there will be relativistic corrections to κ which occur when

$$Q.E. \sim m_e c^2$$

The threshold intensities for these effects can be calculated as shown below:

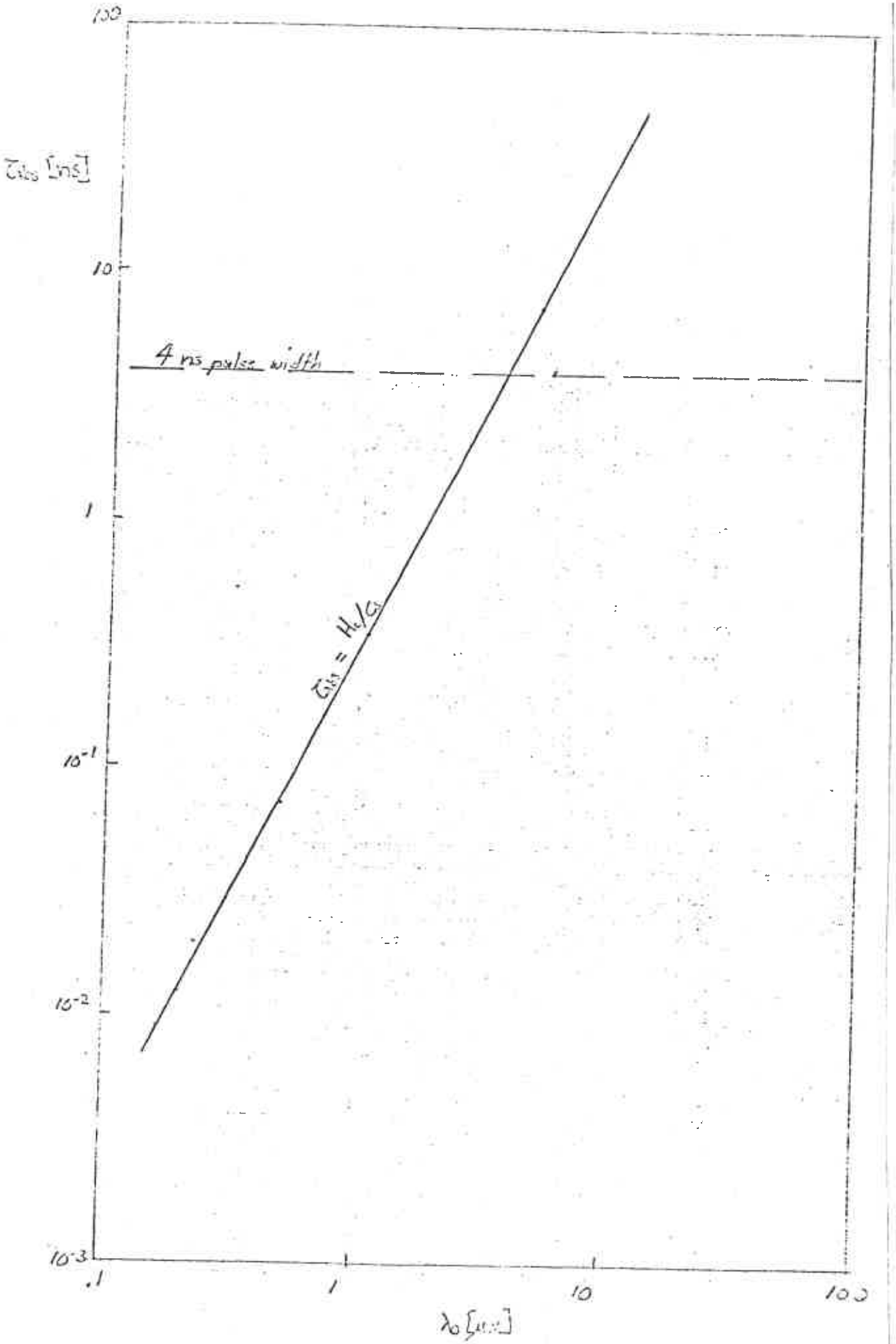
100
10
1
10^{-1}
10^{-2}
10^{-3}
.1
1
10
100
τ_{abs} [ns]
λ_0 [μm]
4 ns pulse width
$\tau_{abs} = H_c/G$

Model Problem:

deuterium:

$\rho_o = .2\ g/cm^3$

$[N_{eo} = .6 \times 10^{22}\ cm^{-3}]$

$T_{eo} = T_{io} = 5\ eV$

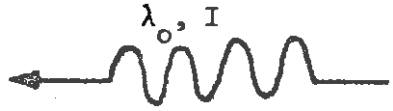

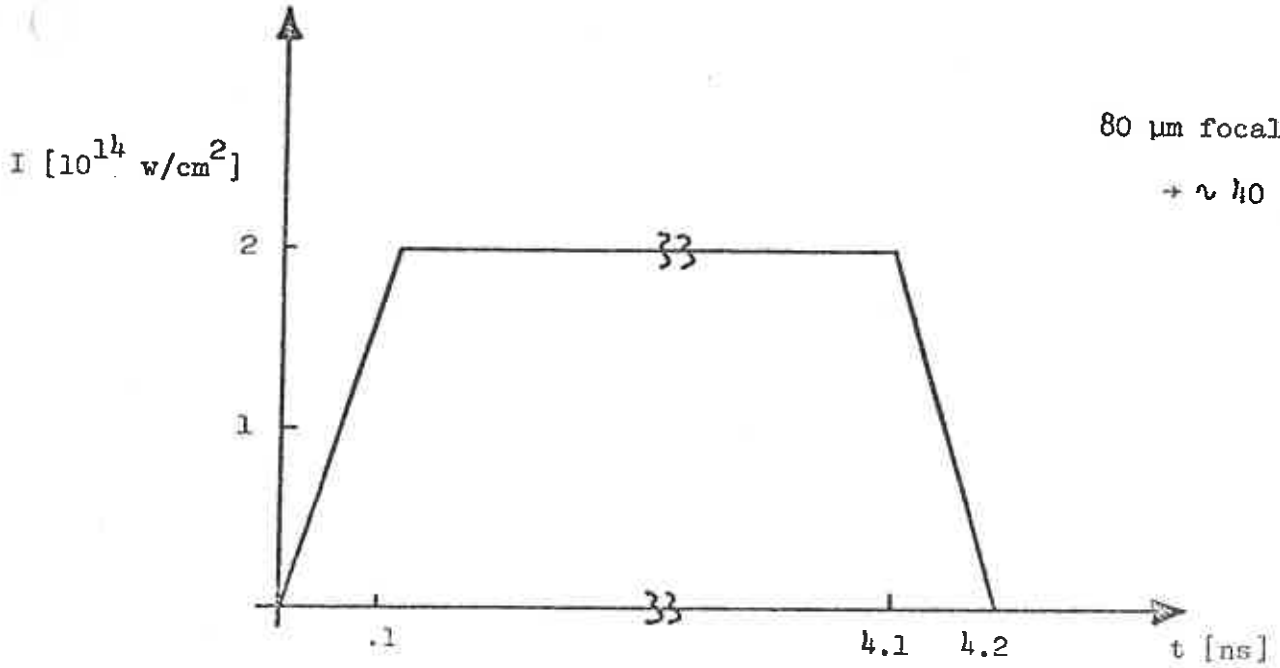

80 μm focal spot

→ ∿ 40 j

λ_o = 1.06 μm

t = 2.64 ns

classical absorption (45% absorbed)

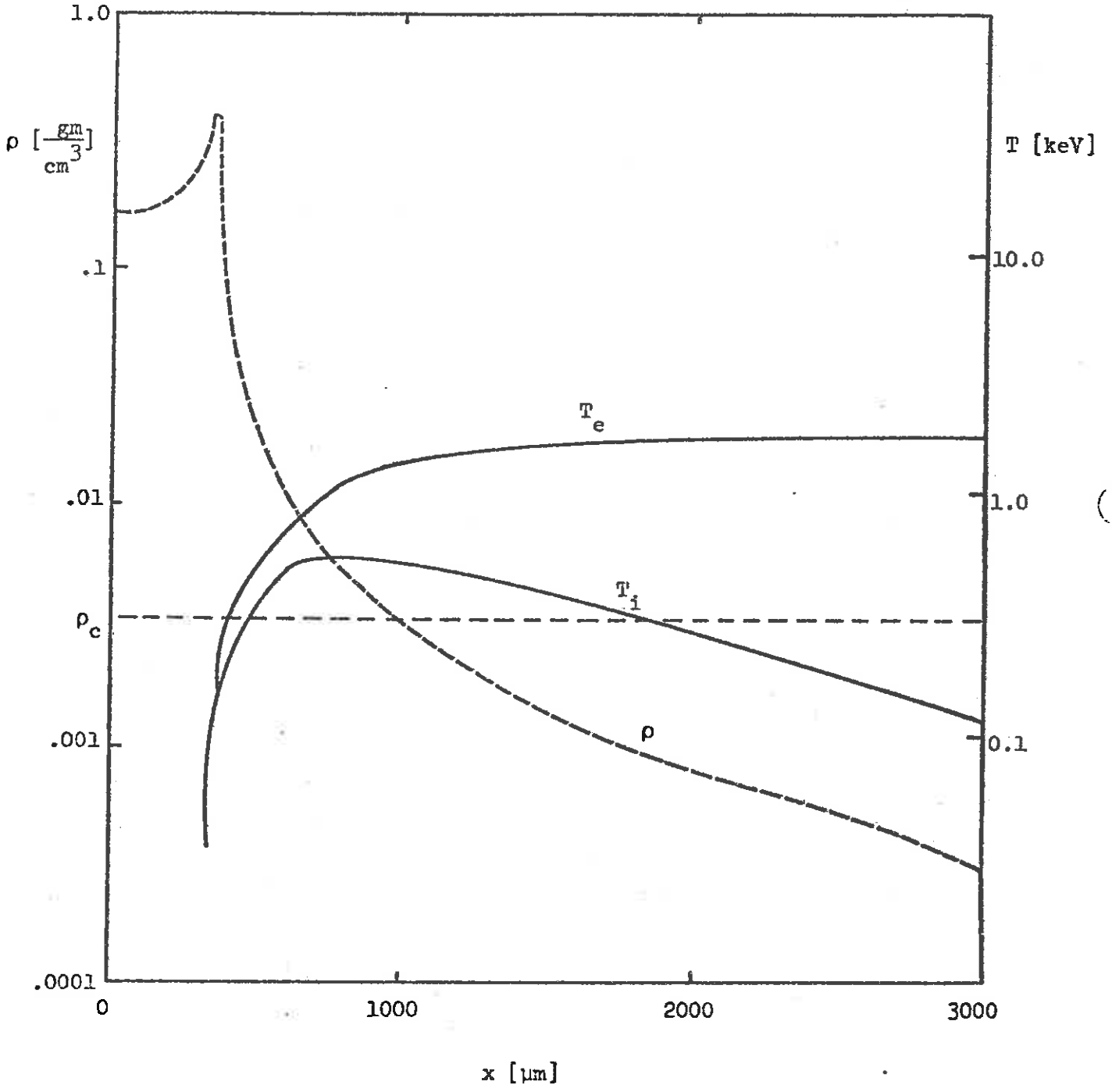

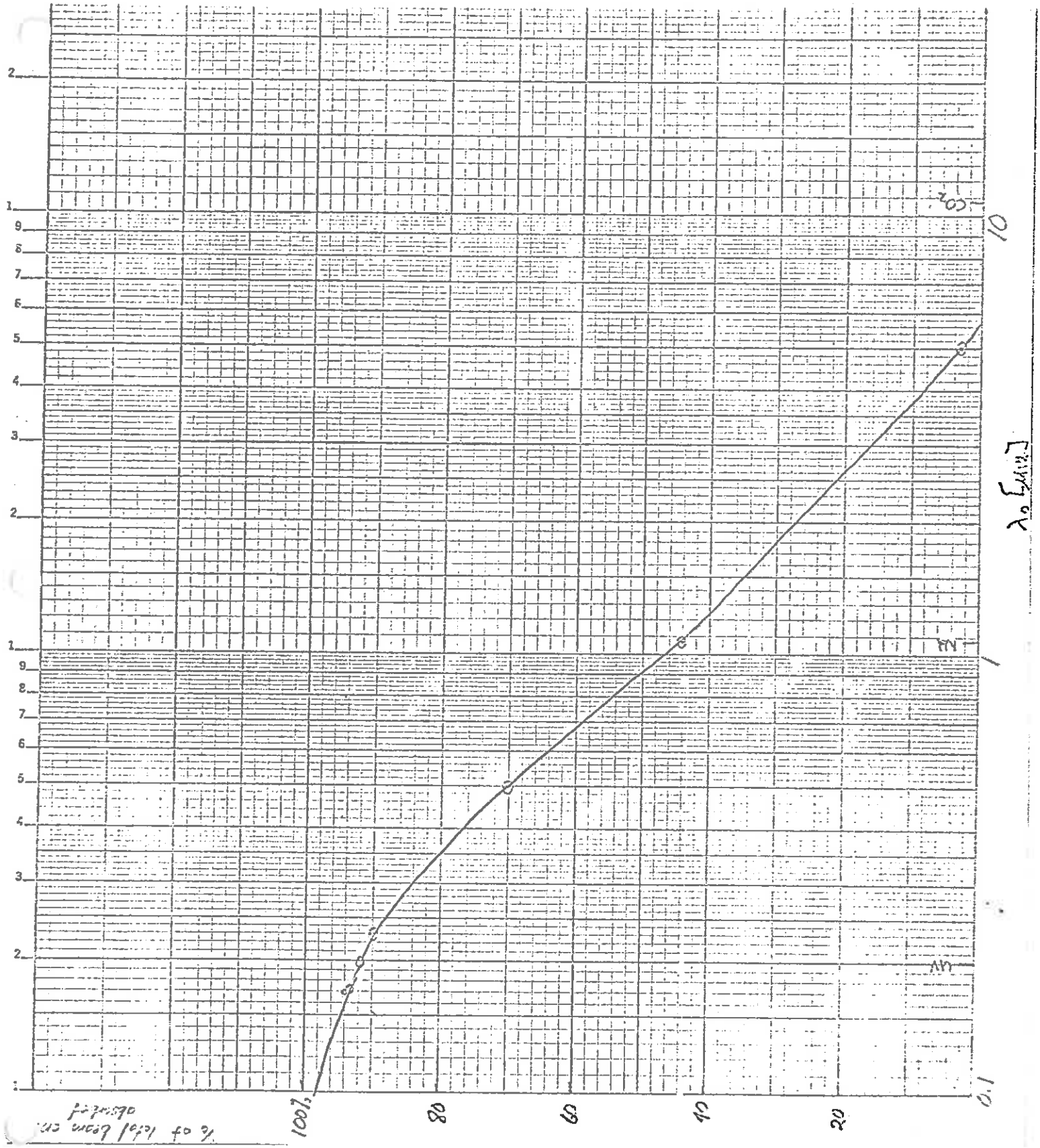
2
1
9
8
7
6
5
4
3
2
1
9
8
7
6
5
4
3
2
1
100
80
60
40
20
10
0.1
CO2
UV
λ0 [nm]

Laser type	Nonlinear Bremsstrahlung	Relativistic
Nd (1.06 μm)	10^{16} W/cm^2	10^{18}
CO_2 (10.6 μm)	10^{14}	10^{16}

Although the detailed calculation of the effect of intense light on the electron distribution function $f_e(v)$ and hence the collision frequency is cumbersome, a crude estimate for very intense light can be obtained by replacing

$$kT_e = m v_{th}^2 \rightarrow m u^2 = \frac{e^2 E_0^2}{m\omega^2}$$

in our earlier expression for the absorption coefficient so that

$$\kappa \rightarrow \frac{N_e N_i Z^2 e^3 \omega}{6\pi\epsilon_0^3 E_0^3 c \sqrt{2\pi}}$$

Notice, in particular, that this suggests that for large intensity I,

$$\kappa \sim \frac{1}{E_0^3} \sim \frac{1}{I^{3/2}}$$

A more thorough calculation yields the form of the absorption coefficient as

$$\kappa = \frac{(Ze^3)^2 N_e N_i}{3\epsilon_0^3 c\omega^2 (2\pi m k T)^{3/2}} \left(\frac{\ln\Lambda}{n_i}\right) F(\alpha)$$

where $F(\alpha)$ is a high intensity correction factor to account for nonlinear bremsstrahlung which takes the form:

$$F(\alpha) = \frac{3}{4\alpha}\left[\sqrt{\frac{\pi}{\alpha}}\,\mathrm{erf}\sqrt{\alpha} - 2e^{-\alpha}\right]$$

where

$$\alpha = \frac{I}{I_{NL}} = \frac{I}{2cn_i N_{ec} kT_e}$$

Although there is little doubt that such effects can be present, direct experimental evidence is scant because of the presence of a variety of other processes that set in at lower beam intensities. In any event, the strong temperature dependence of the inverse bremsstrahlung process, $\kappa \sim T_e^{-3/2}$, implies that this will not be a strong absorption mechanism in the higher temperature plasmas characteristic of laser fusion targets.

Resonance Absorption

When light is incident on an inhomogeneous plasma, electrostatic waves are generated whenever light has a component of the electric field $\underset{\sim}{E}$ along the density gradient $\underset{\sim}{\nabla} n$. In particular, when p-polarized light (with $\underset{\sim}{E}$ parallel to the plane of incidence) is incident obliquely on the density gradient, then the component of the light E field parallel

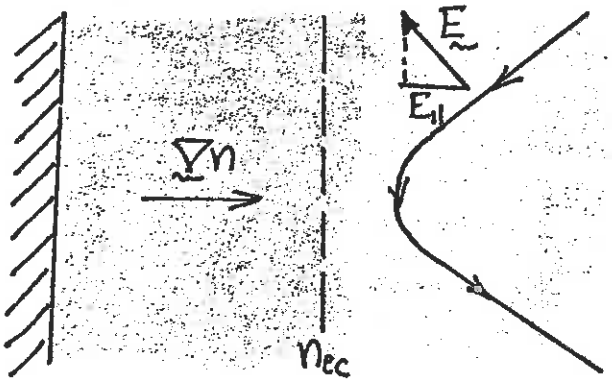

to the plasma density gradient can drive electron plasma waves. Near the critical density, the electric field becomes very large and will resonantly excite these waves. Hence one finds an energy transfer mechanism from the light into the waves, and eventually through the damping of the waves into the electron temperature:

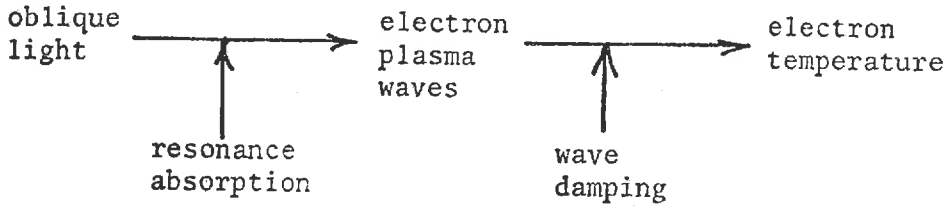

(Note that if the light is s-polarized, with E out of the plane of incidence, there will be no coupling to the plasma waves.) This process is known as resonance absorption. It is now felt that this is the dominant mechanism involved in the absorption of laser light in laser fusion applications.

A Simple Model of Resonance Absorption (Kruer): Consider a nonuniform plasma driven by a uniform electric field of strength E_d, frequency We can combine Maxwell's equations

$$\nabla \cdot \underset{\sim}{E} = 4\pi\rho \,, \quad \frac{\partial \rho}{\partial t} + \nabla \cdot \underset{\sim}{J} = 0$$

to find

$$\nabla \cdot \left(4\pi \underset{\sim}{J} + \frac{\partial \underset{\sim}{E}}{\partial t}\right) = 0$$

or

$$\frac{\partial \underset{\sim}{E}}{\partial t} + 4\pi \underset{\sim}{J} = \left\langle \frac{\partial \underset{\sim}{E}}{\partial t} + 4\pi \underset{\sim}{J} \right\rangle$$

where the average represents the spatially independent component. We neglect ion motion and linearize to write

$$J = -e n_0(z) u$$

where u is the oscillation velocity. If we differentiate with respect to time and use the linearized equation of motion, we find

$$\frac{\partial^2 E}{\partial t^2} + \omega_{pe}^2(z) E + \nu_{ei} \frac{\partial E}{\partial t} = -\left[\omega_{pe}^2(z) - \langle \omega_{pe}^2(z) \rangle\right] E_d \cos \omega_0 t$$

Next, we take a field $E \sim e^{i\omega_0 t}$ to find a response

$$E = \frac{\omega_{pe}^2(z)\, E_d}{\omega_0^2 - \omega_{pe}^2(z) + i\nu_{ei}\omega_0}$$

If we assume a linear density gradient

$$n(z) = n_{ec}\, z/L$$

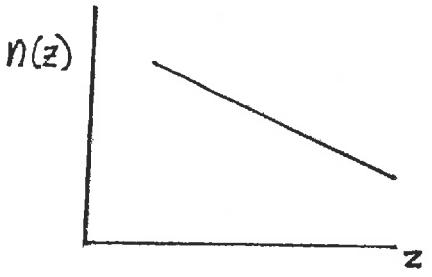

we can compute the power absorbed from the driver field:

$$I_{abs} = \int \frac{2k_i |E|^2}{8\pi} dz = \frac{\omega_0 L E_d^2}{8}$$

Notice in particular that the collision frequency cancels out. That is, the amount of resonance absorption is independent of the detailed damping mechanism. (This is a bit similar to resonance absorption in neutron capture, since the area under the resonance remains unchanged.)

Oblique Incidence: In the more realistic case, the light is incident obliquely upon the plasma density gradient as shown below:

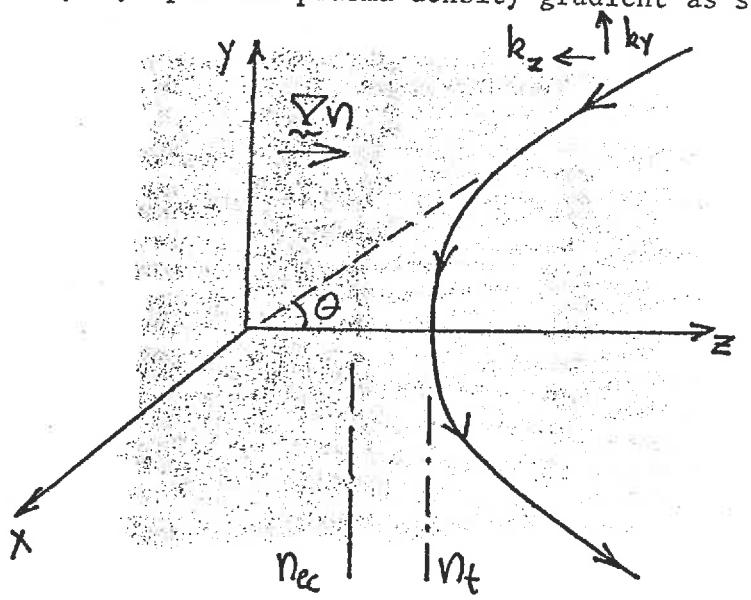

The dispersion relation characterizing the light wave is

$$\omega_0^2 = \omega_{pe}^2 + \omega_0^2 \sin^2\theta + k_z^2 c^2$$

The maximum distance of penetration occurs where $k_z = 0$ or

$$n_t = n_{ec} \cos^2\theta$$

For p-polarized light (in the y-z plane), there is a component of the electric field vector, $E_{\parallel}$, along the density gradient. To analyze this, we need to compute this component and then use it for E_d in our earlier modeled problem result. Kruer shows that the component of the electric field which drives the resonant process is

$$E_d = E_{\parallel} \sim \frac{E_0}{\left(\frac{\omega_0 H}{c}\right)^{1/6}} \sin\theta \exp\left[-\frac{2}{3}\frac{\omega_0 H}{c}\sin^3\theta\right]$$

where H is the scale height, assuming a linear density gradient proportional to (1 - z/H). He computes the fractional absorption as

$$f = \frac{1}{2}\phi^2(\tau) \quad , \quad \tau \equiv (k_0 H)^{1/3}\sin\theta$$

where the function $\phi(\tau)$ is given approximately by

$$\phi(\tau) \cong 2.31\,\tau e^{-2/3\tau^3}$$

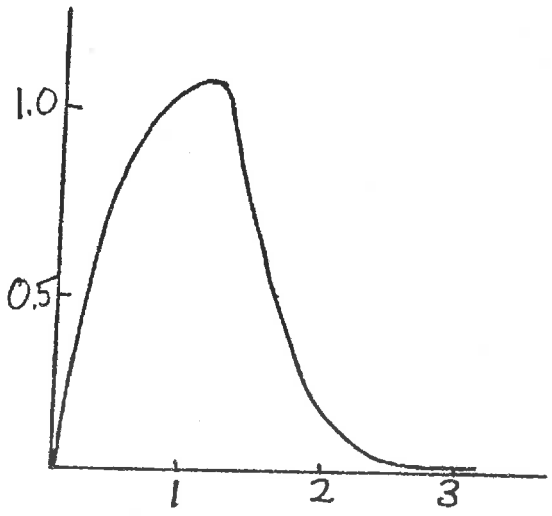

Notice in particular that the resonance abosrption vanishes at $\theta = 0$ (corresponding to normal incidence), since there is no component $E_{\parallel}$.

Furthermore, the resonance absorption is very small for large θ, since the light is turned too far from the critical density n_{ec}.

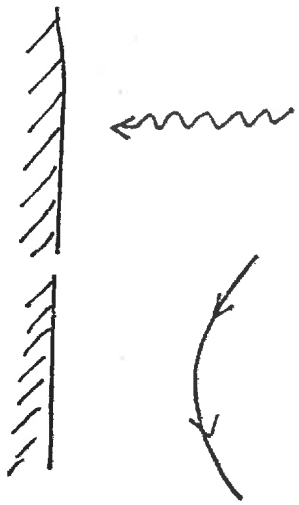

The range of angles, $\Delta\theta$, for which there is appreciable absorption depends on the scale height.

$H >> \lambda_o$ absorption only for narrow range $\Delta\theta$

$H \lesssim 10\lambda_o$ absorption for broad range $\Delta\theta$

More precisely, the dependence of the absorption fraction on the scale height is indicated below:

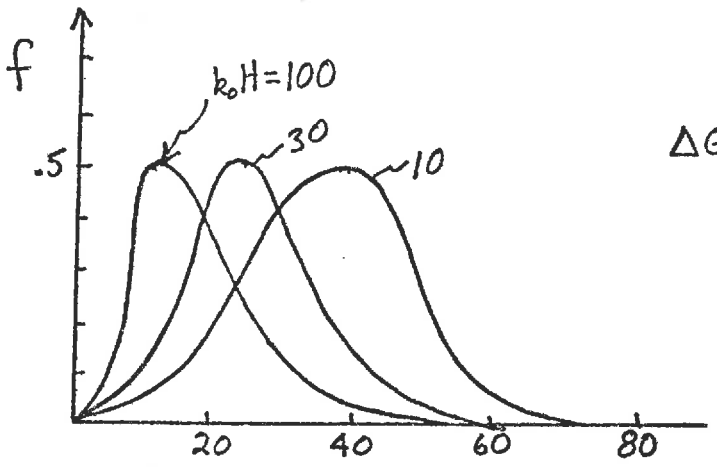

Nonlinear Effects: Although the resonance absorption process is basically linear, there are some nonlinear effects that become important at high light intensity. Two dimensional plasma simulations have shown that the resonantly driven wave field grows to sufficient intensity that electrons can be accelerated through in one oscillation period. This phenomenon is known as "wavebreaking". It leads to electron trapping by the localized oscillating field and the production of very high energy, i.e., superthermal, electrons.

A second nonlinear effect of some importance is the effect of the incident light on the plasma density gradient. The ponderomotive force exerted by the beam (the light pressure) can dam up the plasma flow, thereby steepening the density profile and reducing the scale height. We have noted that this can have a significant effect on the range of angles over which significant absorption will occur.

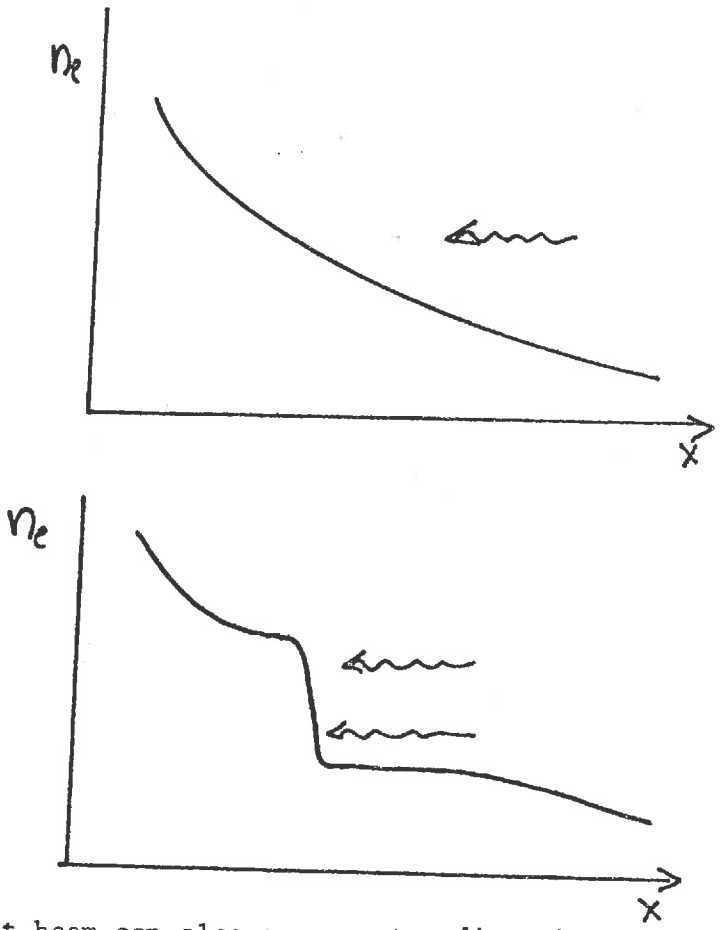

The incident beam can also cause a two-dimensional "rippling" of the critical surface.

Parametric Processes in Plasmas

The incident laser light can interact with the normal modes or waves in a plasma in a second way. The incident light wave can couple together the natural modes or waves in the plasma in such a way as to drive them unstable. These instabilities will then grow until they saturate in a turbulent state. This turbulent state of the plasma will then be characterized by enhanced values of transport coefficients such as those characterizing absorption, heat and charge conduction, and electron-ion energy transfer.

For example, the incident light can couple together electrostatic modes such as electron plasma waves and ion acoustic waves in such a way as to lead to enhanced absorption of the incident light in the vicinity of the critical surface. The light can also couple into electromagnetic modes and excite instabilities which lead to an enhanced reflectivity of the plasma.

These phenomena are examples of a parametric excitation process. More precisely, parametric excitation involves the amplification of the oscillation of a natural mode of a system due to a periodic modulation of a parameter which characterizes the system. Perhaps the most common example of this is the child on a swing. The natural frequency of the oscillating motion of the swing is determined by the mass and the length of the rope. But the child can influence this motion by kicking his feet in such a way as to change his center of mass--that is, he can change the effective length of the swing and hence the frequency of the swing in a periodic fashion. If he kicks at a frequency just double that of the natural frequency of oscillation, then he can amplify the motion of the swing. In this case, the parametric excitation appears through a modulation of the frequency parameter.

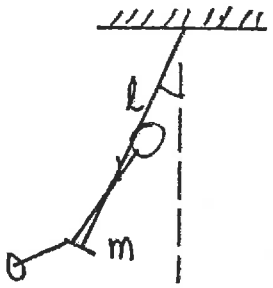

$$\frac{d^2\theta}{dt^2} + \Omega^2\theta = 0$$

$$\Omega^2 = \frac{m}{\ell}(1+\epsilon\cos\omega t)$$

In a plasma, there are a variety of different natural modes such as electron plasma waves and ion acoustic waves, which depend on parameters such as density and temperature. Since these latter parameters can be

modified--indeed, modulated--by the electromagnetic field of the incident light wave, it is not surprising to find that parametric excitation can play an important role in the interaction of laser light with plasmas. A variety of different coupling processes can occur involving both electrostatic and electromagnetic modes. These are indicated schematically below:

Electrostatic modes:

Decay mode

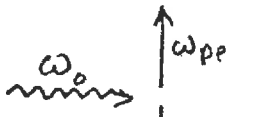

Oscillating two stream

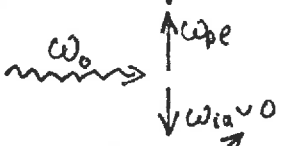

Jackson-Goldman

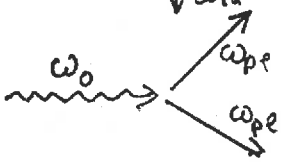

Electromagnetic modes:

Stimulated Raman scattering

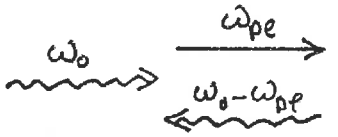

Stimulated Brillouin scattering

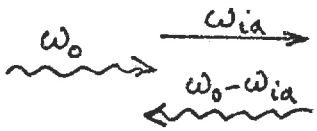

These are all examples of 3-wave processes in which the coupling involves three waves. There are also 4-wave and higher order processes which can occur, but which are usually of secondary importance in laser-plasma interactions.

The most general type of 3-wave interaction process can be represented schematically as shown:

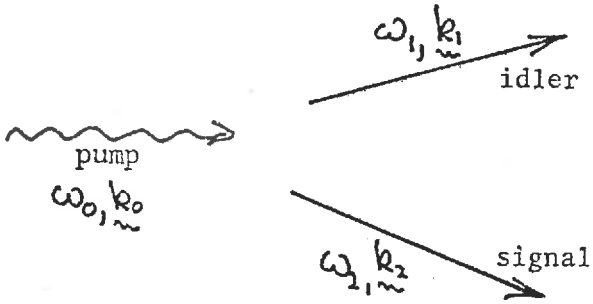

where we have employed the usual terminology of parametric amplifiers in electrical engineering by referring to the driving force (e.g., the incident light wave) as the "pump", the lower frequency natural mode (e.g., an ion acoustic wave) as the "idler", and the higher frequency natural model (e.g., an electron plasma wave) as the "signal". Such parametric processes are characterized by several general properties:

(i) A matching or "resonance" condition among frequency and wave numbers must be obeyed for strong coupling:

$$\omega_0 \sim \omega_1 + \omega_2$$

$$\underset{\sim}{k}_0 \sim \underset{\sim}{k}_1 + \underset{\sim}{k}_2$$

(ii) Since all natural modes of oscillation are damped, the driver or pump amplitude must exceed a certain threshold intensity to drive the modes unstable. These modes will then grow in amplitude with a certain growth rate as they absorb energy from the pump.

(iii) The final frequency of the amplified oscillation is determined by the pump frequency rather than the natural frequency of the modes. This is referred to as "frequency locking".

The general approach to analyzing parametric coupling plasmas in laser-plasma interactions is to first recast the equations characterizing the modes of the plasma into a form in which the parametric excitation is explicit. These equations are then analyzed in the linear limit to determine the thresholds on the pump amplitude for the onset of instabilities, and the growth rates of these instabilities. The more complex analysis of the nonlinear evolution of the parametrically driven modes and their eventual saturation in a turbulent state requires the use of plasma simulation codes.

Single Mode Analysis: To be more explicit, consider the case of a single mode parametric process, that is, in which both the idler and the signal are the same mode. The oscillator amplitude X(t) satisfies

$$\frac{d^2X}{dt^2} + 2\Gamma\frac{dX}{dt} + (\Omega^2 + \Gamma^2)X(t) = 0$$

where

$\Omega \equiv$ frequency of oscillation

$\Gamma \equiv$ damping coefficient

The parametric excitation is introduced as a modulation in the frequency:

$$\Omega^2 = \Omega_0^2(1 - 2\epsilon\cos\omega t)$$

where we will refer to Ω_0 as the natural frequency of the system in the absence of the modulation.

If we use a variable substitution

$$X(t) = e^{-\Gamma t}Y(t)$$

we find

$$\frac{d^2Y}{dt^2} + \Omega_0^2(1 - 2\epsilon\cos\omega t)Y(t) = 0$$

--a differential equation with periodic coefficients. This is a special case of Hill's equation known as the Mathieu equation. A theorem due to Floquet indicates that the solution to this equation will have a periodic form

$$Y\left(t + \frac{2\pi}{\omega}\right) = e^{i\mu}Y(t)$$

The usual approach to the analysis of such parametric processes involves perturbation theory. If we assume:

(i) weak pump (linearization): $\epsilon \ll 1$

(ii) small damping: $\Gamma/\Omega_0 \ll 1$

we can simplify the analysis considerably. We begin by introducing a Fourier transform:

$$X(t) = \frac{1}{2\pi}\int d\omega\, e^{-i\omega t}X(\omega)$$

If we now transform the differential equation, we find

$$D(\omega)X(\omega) = \epsilon\Omega_o^2\left[X(\omega-\omega_o)+X(\omega+\omega_o)\right]$$

where $D(\omega)$ is a dispersion relation

$$D(\omega) = -\omega^2 - 2i\Gamma\omega + (\Omega_o^2+\Gamma^2)$$

which would characterize the natural oscillation of the system. We can now study two cases suggested by Floquet's theorem:

Case 1: $\omega_o \cong 2\Omega_o$

If we look at frequencies $\omega \sim \Omega_o$, then

$$\omega - \omega_o \sim -\Omega_o$$

and is resonant with the natural oscillation frequency Ω_o. But

$$\omega + \omega_o \sim 3\Omega_o$$

which is off-resonance. Hence we can neglect $X(\omega+\omega_o)$ as an off-resonance term and consider only the coupling of $X(\omega)$ and $X(\omega-\omega_o)$:

$$D(\omega)X(\omega) = \epsilon\Omega_o^2 X(\omega-\omega_o)$$

In a similar fashion, we find that $X(\omega-\omega_o)$ satisfies

$$D(\omega-\omega_o)X(\omega-\omega_o) = \epsilon\Omega_o^2 X(\omega)$$

where we have neglected $X(\omega-2\omega_o) \sim X(-3\Omega_o)$ as off-resonance.

Combining these, we find the dispersion relation

$$D(\omega)D(\omega-\omega_o) = \epsilon^2\Omega_o^4$$

Now recall

$$D(\omega) = -\omega^2 - 2i\Gamma\omega + (\Omega_o^2+\Gamma^2)$$
$$= -(\omega+\Omega_o+i\Gamma)(\omega-\Omega_o+i\Gamma)$$

If we use the fact that $\omega \sim \Omega_0$ and $\Gamma/\Omega_0 << 1$, we can simplify this to

$$D(\omega) \sim -2\Omega_0(\omega - \Omega_0 + i\Gamma)$$

Similarly

$$D(\omega-\omega_0) \sim 2\Omega_0(\omega - \omega_0 + \Omega_0 + i\Gamma)$$

Thus our dispersion relation becomes

$$(\omega-\Omega_0+i\Gamma)(\omega-\Omega_0-\Delta+i\Gamma) + \epsilon^2\frac{\Omega_0^2}{4} = 0$$

where we have introduced

$$\Delta \equiv \omega_0 - 2\Omega_0 \quad \text{=frequency mismatch}$$

Let us now write

$$\omega = (\Omega_0 + x) + iy$$

Here, y positive would imply an instability in the mode. If we separate real and imaginary parts,

$$x(x-\Delta) - (y+\Gamma)^2 + \epsilon^2\Omega_0^2/4 = 0$$

$$(2x-\Delta)(y+\Gamma) = 0$$

we can identify two different types of solutions:

(i) $y = -\Gamma \Rightarrow$ damped oscillation with frequency $x = \frac{1}{2}\left[\Delta \pm \sqrt{\Delta^2 - \epsilon^2\Omega_0^2}\right]$

This makes sense only when $\Delta^2 \gtrsim \epsilon^2\Omega_0^2$. But $\Delta = \omega_0 - 2\Omega_0$
Hence we require

$$(\omega_0 - 2\Omega_0)^2 \gtrsim \epsilon^2\Omega_0^2$$

that is, ϵ sufficiently small or frequency mismatch Δ sufficiently large.

(ii) $x = \Delta/2$ Now we find

$$\mathrm{Re}\,\omega = x + \Omega_0 = \omega_0/2$$

Notice that this is a "frequency-locked" situation since it does not depend on the natural frequency. We also find

$$y = -\Gamma \pm \tfrac{1}{2}\sqrt{\epsilon^2\Omega_0^2 - \Delta^2} \qquad (*)$$

which makes sense in the region

$$\epsilon^2\Omega_0^2 > \Delta^2 \quad \text{or} \quad \epsilon^2\Omega_0^2 > (\omega_0 - 2\Omega_0)^2$$

From our expression for y we see that one of the modes is less damped than the natural oscillation (the other mode is more heavily damped). The less damped mode becomes unstable when

$$\epsilon^2\Omega_0^2 - \Delta^2 > 4\Gamma$$

or

$$\epsilon^2 > \frac{\Delta^2 + 4\Gamma^2}{\Omega_0^2}$$

Thus we have a threshold condition on the pump intensity for instability. Notice that for zero frequency mismatch, we have the minimum threshold.

This is the simplest example of a parametrically excited instability. The maximum growth rate y_{max} of the instability is obtained when $\Delta = 0$. The corresponding threshold is found by setting y = 0 in (*)

$$\epsilon_{min} = 2\Gamma/\Omega_0$$

Also

$$y_{max} = -\Gamma + \frac{\epsilon}{2\Omega_0}$$

We can repeat this analysis for the case $\omega_0 \cong \Omega_0$. Once again one finds two types of solution--one damped and one "frequency locked" with an oscillation frequency no longer dependent on the natural frequency but rather on the frequency mismatch.

Coupled Mode Parametric Excitation: The situation of more direct interest to 3-wave processes is the coupling of two natural modes by a pump mode, as described by

$$\frac{d^2X}{dt^2} + 2\Gamma_1 \frac{dX}{dt} + (\omega_1^2+\Gamma_1^2)X(t) = \lambda Z(t) Y(t)$$

$$\frac{d^2Y}{dt^2} + 2\Gamma_2 \frac{dY}{dt} + (\omega_2^2+\Gamma_2^2)Y(t) = \mu Z(t) X(t)$$

where the pump is given by

$$Z(t) = 2 Z_0 \cos \omega_0 t.$$

It is customary to assume, without loss of generality, that $\omega_1 << \omega_2$.

The analysis of these coupled oscillators was first given by Nishikawa (J. Phys. Soc. Japan 24, 916 (1968) and applied to analyze the interaction of electromagnetic waves with plasmas. The perturbation analysis of this problem, while quite similar to that of our previous single mode example, is cumbersome, and so we will only discuss results here. For the frequency matching condition

$$\omega_0 \sim \omega_1 + \omega_2$$

we can again Fourier transform to find the dispersion relation

$$D_1(\omega) = \lambda\mu Z_0^2 \left[\frac{1}{D_1(\omega+\omega_0)} + \frac{1}{D_2(\omega-\omega_0)} \right]$$

where

$$D_s(\omega) \equiv -\omega^2 - 2i\Gamma_s\omega + (\omega_s^2+\Gamma_s^2) \; ; \quad s = 1, 2$$

A perturbation analysis of this dispersion relation indicates two classes of solutions. Both cases can be driven unstable, but in one of these cases there is a nonoscillatory solution.

Application to Electrostatic Waves in Plasmas: To apply these results to the parametric excitation of electrostatic waves in a plasma by an incident laser beam, one must first transform the relevant equations describing the laser-plasma interaction into the form of the coupled parametric oscillators. One typically assumes that the laser beam is represented by a uniform electric field oscillating at a frequency comparable (but greater than) the plasma frequency. The dynamics of the plasma are represented by the coupled hydrodynamics equations:

$$\frac{\partial n_\sigma}{\partial t} + \underline{u}_\sigma \cdot \frac{\partial n_\sigma}{\partial \underline{r}} + n_\sigma \frac{\partial}{\partial \underline{r}} \cdot \underline{u}_\sigma = 0$$

$$n_\sigma \left[\frac{\partial \underline{u}_\sigma}{\partial t} + \underline{u}_\sigma \cdot \frac{\partial \underline{u}_\sigma}{\partial \underline{r}} \right] + \frac{1}{m_\sigma} \frac{\partial p_\sigma}{\partial \underline{r}} = \frac{e_\sigma}{m_\sigma} n_\sigma \underline{E} - \nu_\sigma n_\sigma \underline{u}_\sigma$$

$$\frac{\partial}{\partial \underline{r}} \cdot \underline{E} = 4\pi \sum_\sigma e_\sigma n_\sigma \qquad \sigma = e, i$$

These equations are then linearized about a spatially homogeneous part (oscillating with the applied field), and averaged over the high frequency motion of the electrons. The resulting set of equations then takes a form

$$\frac{\partial n_e}{\partial t^2} + \nu_e \frac{\partial n_e}{\partial t} + \omega^2(k)\, n_e(t) = \frac{ie}{m_e} \underline{k} \cdot \underline{E}_0\, n_i(t)$$

$$\frac{\partial n_i}{\partial t^2} + \nu_i \frac{\partial n_i}{\partial t} + \omega_{ia}^2(k)\, n_i(t) = -\frac{ie}{m_i} \underline{k} \cdot \underline{E}_0\, n_e(t)$$

which is identical to that of the coupled oscillator problem, and the results of the analysis of that problem can be applied directly.

More specifically, the dispersion relation for 3-wave parametric coupling of electrostatic waves becomes

$$(\omega^2 + i\nu_i\omega - \omega_{ia}^2) = \tfrac{1}{4}\omega_{pi}^2 \omega_{pe}^2 k^2 d_0^2 \left[\frac{1}{(\omega-\omega_0)^2 - \omega_k^2 + i\nu_e(\omega-\omega_0)} + \frac{1}{(\omega+\omega_0)^2 - \omega_k^2 + i\nu_e(\omega+\omega_0)} \right]$$

where

$d_0 \equiv \dfrac{eE_0}{m\omega_0^2}$ electron "quiver" displacement

$\omega_k^2 = \omega_{pe}^2 + \dfrac{\gamma_e k_B T_e}{m_e} k^2$ electron plasma wave frequency

$$\omega_{ia} = \left(\frac{k_B T_e}{m_i}\right)^{\frac{1}{2}} k$$ ion-acoustic wave frequency

Several assumptions have been made in deriving this dispersion relation:

(i) weak pump: $kd_0 << 1$

(ii) near critical density: $\omega_0 \sim \omega_R$

If we confine our attention to low frequency modes, $\omega << \omega_0$, and solve the dispersion relation for $\omega = \omega_r + i\gamma$, we can determine the threshold for instability by setting $\gamma = 0$. There are two cases:

(i) Decay mode instability: $\omega_r >> \nu_e$, $\omega_0 \sim \omega_r + \omega_R$

Then we find

$$\nu_i \omega_{ia} \nu_e \omega_R \sim \frac{1}{4} \omega_{pi}^2 \omega_{pe}^2 k^2 d_0^2$$

If we note that the light intensity is given by

$$I = \frac{1}{2} c n_i \epsilon_0 E_0^2$$

we can compute the threshold for the parametric decay mode instability as

$$I_{DM} = 4 c n_i N_e (k_B T_e) \left(\frac{\nu_e}{\omega_{pe}}\right)\left(\frac{\nu_i}{\omega_{ia}}\right) = 2\left(\frac{\nu_e}{\omega_{pe}}\right)\left(\frac{\nu_i}{\omega_{ia}}\right) I_{th}$$

where we have defined the laser light intensity at which the quiver energy is equal to the thermal energy as

$$I_{th} = 2 n_i c N_e (k_B T_e)$$

(ii) Oscillating two-stream instability: $\omega_r = 0$, $\gamma = 0$

Then

$$-\omega_{ia}^2 \sim \frac{1}{4} \omega_{pi}^2 \omega_{pe}^2 k^2 d_0^2 \left[\frac{2(\omega_0^2 - \omega_R^2)}{(\omega_0^2 \omega_R^2)^2 + \nu_e^2 \omega_0^2}\right]$$

(Note that this implies that we must have $\omega_0 < \omega_R$.) The minimum threshold occurs at

$$\omega_0^2 - \omega_R^2 = \nu_e \omega_0$$

Then $$\omega_{ia}^2 \nu_e \omega_o = \frac{1}{4}\omega_{pi}^2 \omega_{pe}^2 k^2 \delta_o^2$$

which yields

$$I_{2S} = 2\left(\frac{\nu_e}{\omega_{pe}}\right) I_{th}$$

Notice that these thresholds depend on the damping of the waves. For the ion-acoustic wave, one can write

$$\frac{\nu_i}{\omega_{ia}} \simeq \sqrt{\frac{m_e}{M_i}} + \left(\frac{T_e}{T_i}\right)^{3/2} \exp\left(-\frac{1}{2}\frac{T_e}{T_i}\right)$$

while for the electron plasma wave

$$\frac{\nu_k}{\omega_{pe}} = \frac{\nu_{ei}}{\omega_{pe}} + \sqrt{\frac{\pi}{8}}\,(k_{max}\lambda_D)^{-3} \exp\left(-1/2\,(k_{max}\lambda_D)^2\right)$$

Here, k_{max} is the wave number of the fastest growing ion acoustic mode and is given by

$$k_{max}\lambda_D = \left[\frac{2}{3}\left(\frac{\omega_o}{\omega_{pe}} - 1\right) + \left(\frac{1.7}{3}\right)^2 \frac{m_e}{M_i}\right]^{1/2} - \left(\frac{1.7}{3}\right)\sqrt{\frac{m_e}{M_i}}$$

Several comments are of interest:

(i) For the case of equal electron and ion temperatures, $T_e = T_i$, we find $\nu_i/\omega_{ia} \sim .6$. In this case:

$$I_{2S} \sim I_{DM}$$

(ii) In the case more typical of laser fusion plasmas, $T_e >> T_i$. Then

$$\frac{\nu_i}{\omega_{ia}} \sim \sqrt{\frac{m_i}{M_e}} << 1$$

and we find

$$I_{2S} >> I_{DM}$$

(iii) For $k/k_D << 1$ ($\lambda_o >> \lambda_D$), one can ignore Landau damping of the electron plasmas waves to find

$$\frac{\nu_e}{\omega_R} \sim \frac{\nu_{ei}}{\omega_{pe}} << 1 \qquad [\sim 10^{-3}]$$

Then the threshold for the decay mode instability becomes quite low;

$$I_{DM} \sim 10^{-3}\, I_{th}$$

One can also use these dispersion relations to calculate growth rates:

Decay mode: $$\gamma_{max} = \frac{\sqrt{3}}{2}\omega_{pe}\left[\frac{1}{4}\frac{m_e}{M_i}(kd_0)^2\right]^{1/3}$$

Two-stream: $$\gamma_{max} = \frac{1}{2}\omega_{pe}\left[\frac{m_e}{M_i}(kd_0)^2\right]^{1/3}$$

Notice that in both cases, the growth rates scale as

$$\gamma_{max} \sim I^{1/3}$$

The implications of these results are important. Consider laser light incident upon a density gradient as shown:

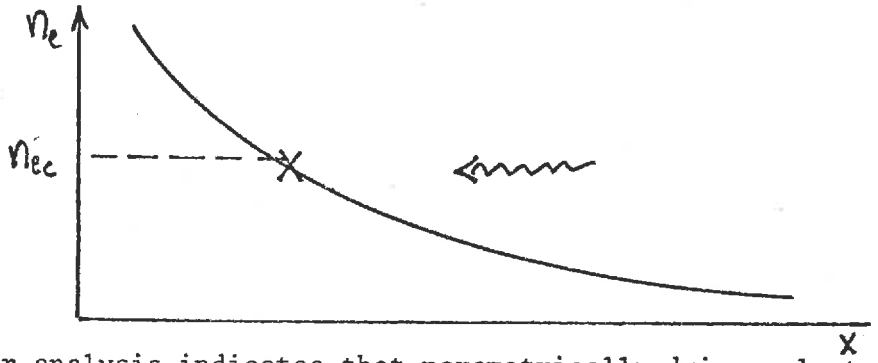

Our analysis indicates that parametrically driven electrostatic instability will occur near the critical surface. The minimum threshold for the excitation of these instabilities occurs for $T_e >> T_i$ and for $n_e \sim n_{ec}$. Then the damping is collision in nature and we find that the decay mode instability has the lowest threshold which scales as

$$I_{DM} \sim \frac{n_{ec}^{3/2}}{T_e^{1/2}} << I_{2S}$$

A brief table of the minimum thresholds for various types of parametric instabilities and laser wavelengths is given on the next page, along with a sketch showing where each could appear on the plasma density profile.

Stimulated Scattering Processes: The incident light wave can also parametrically excite electromagnetic modes of the plasma leading to a stimulated scattering of the light back out of the plasma. Of most interest are:

Stimulated Brillouin scattering; $\omega_0 \rightarrow \omega_{ia}$, $\omega_0 - \omega_{ia}$

Stimulated Raman scattering: $\omega_0 \rightarrow \omega_{pe}$, $\omega_0 - \omega_{pe}$

The frequency matching conditions imply that these processes can occur in the underdense region if there is a large scale height in the blowoff plasma:

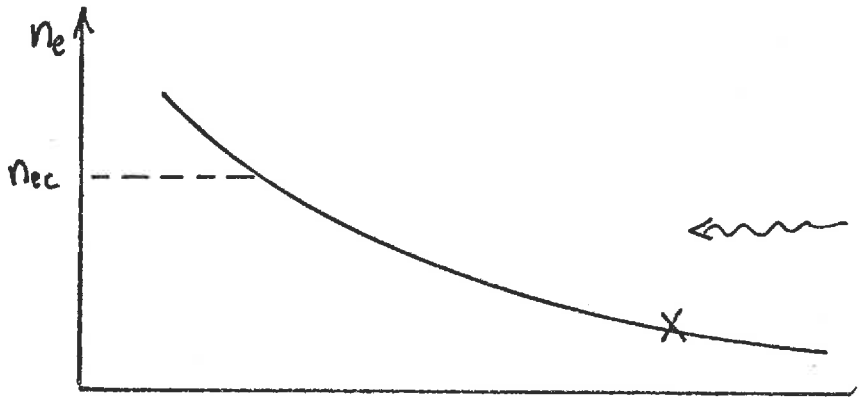

This is particularly serious since stimulated scattering processes can scatter back the incident light before it can penetrate into the critical surface where the most effective absorption (resonance or parametric) can occur. Brillouin scattering is the most serious, since the frequency matching condition $\omega_0 \sim \omega_{scat} + \omega_{ia}$ allows it to occur over a large region of the underdense plasma. Plasma simulations and experiments have indicated that nearly all of the energy of the incident light can be transferred to the scattered wave if conditions are right.

Several remedies have been proposed to circumvent this process. For example, one can avoid building up a large scale height plasma corona surrounding the target. An alternative approach is to modulate the frequency of the incident light (e.g., generating a random frequency by passing the light through a filter before focusing it on the target) in such a way as to increase the effective threshold intensity for the stimulated Brillouin process.

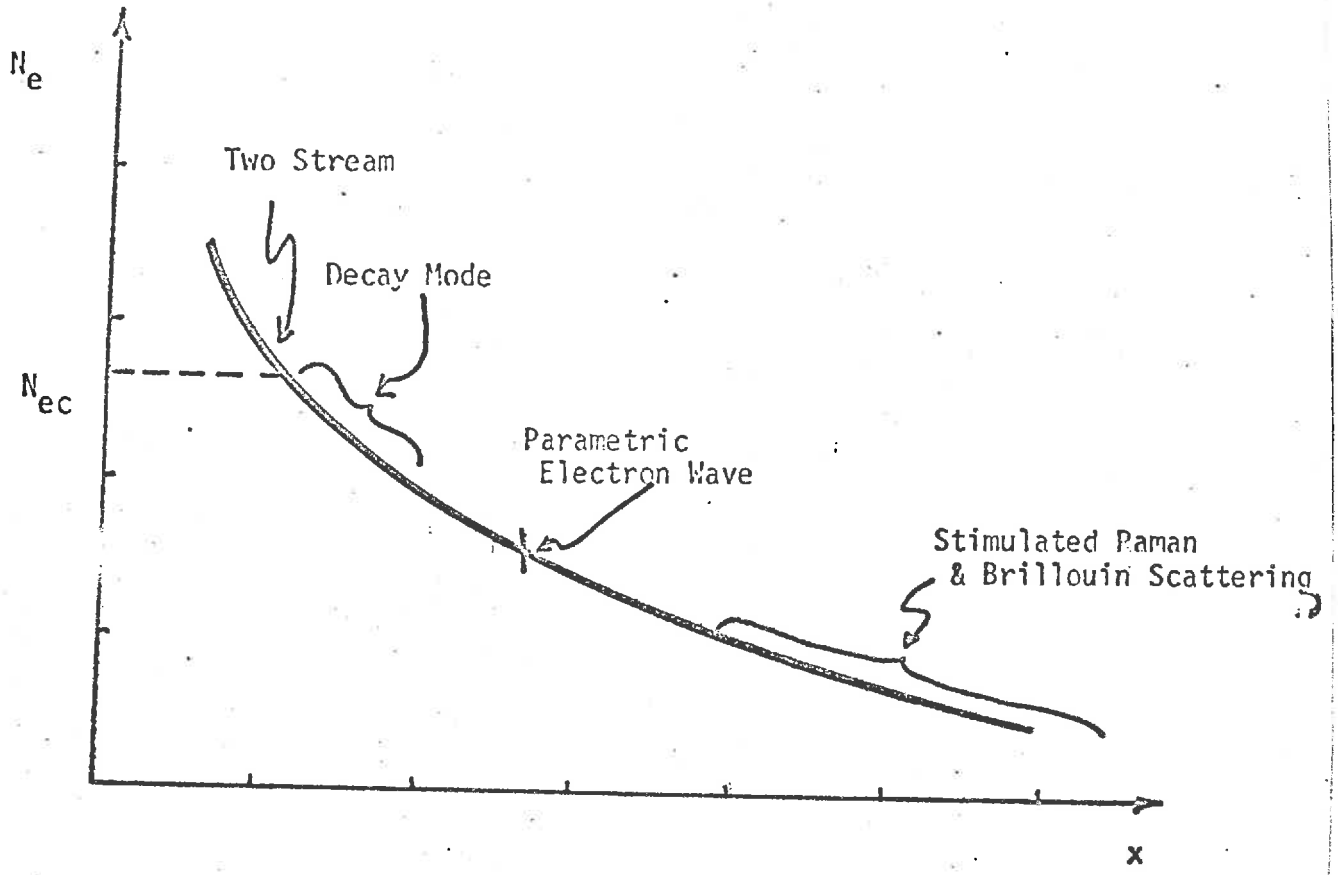

DENSITY WINDOWS FOR ANOMALOUS ABSORPTION

I $\left[\frac{\text{watts}}{\text{cm}^2}\right]$	$N_e=10^{21}$ $T_e=1$ keV	$N_e=10^{19}$ $T_e=1$ keV	$N_e=10^{19}$ $T_e=100$eV	$N_e=10^{19}$ $T_e=10\text{eV}=T_i$	
$I_{NL} \sim I_{th}$ (nonlinear brem.)	10^{16}	10^{14}	10^{13}	10^{12}	
I_{rel} (relativistic)	5×10^{18}	5×10^{16}	5×10^{16}	5×10^{16}	
I_{DM} (mode)	1.5×10^{12}	1.5×10^{9}	5×10^{9}	3.6×10^{10}	lower estimate (at $N_e=.9N_{ec}$)
	5×10^{14}	5×10^{12}	5×10^{11}	1.2×10^{11}	upper estimate (at $N_e=.7N_{ec}$)
I_{2s} (2 stream)	1.2×10^{13}	1.2×10^{10}	4×10^{10}	2.1×10^{11}	
I_{2e} (Jackson-Dubois)	10^{16}	10^{14}	10^{13}	10^{12}	
$I_{S.B.}$ (stim. Brillouin)	4.7×10^{11}	4.7×10^{8}	1.5×10^{9}	1.1×10^{10}	estimated at $N_e=.1N_{ec}$
$I_{S.R.}$ (stim. Raman)	10^{14}	10^{9}	10^{12}	10^{15}	estimated at $N_e=.1N_{ec}$

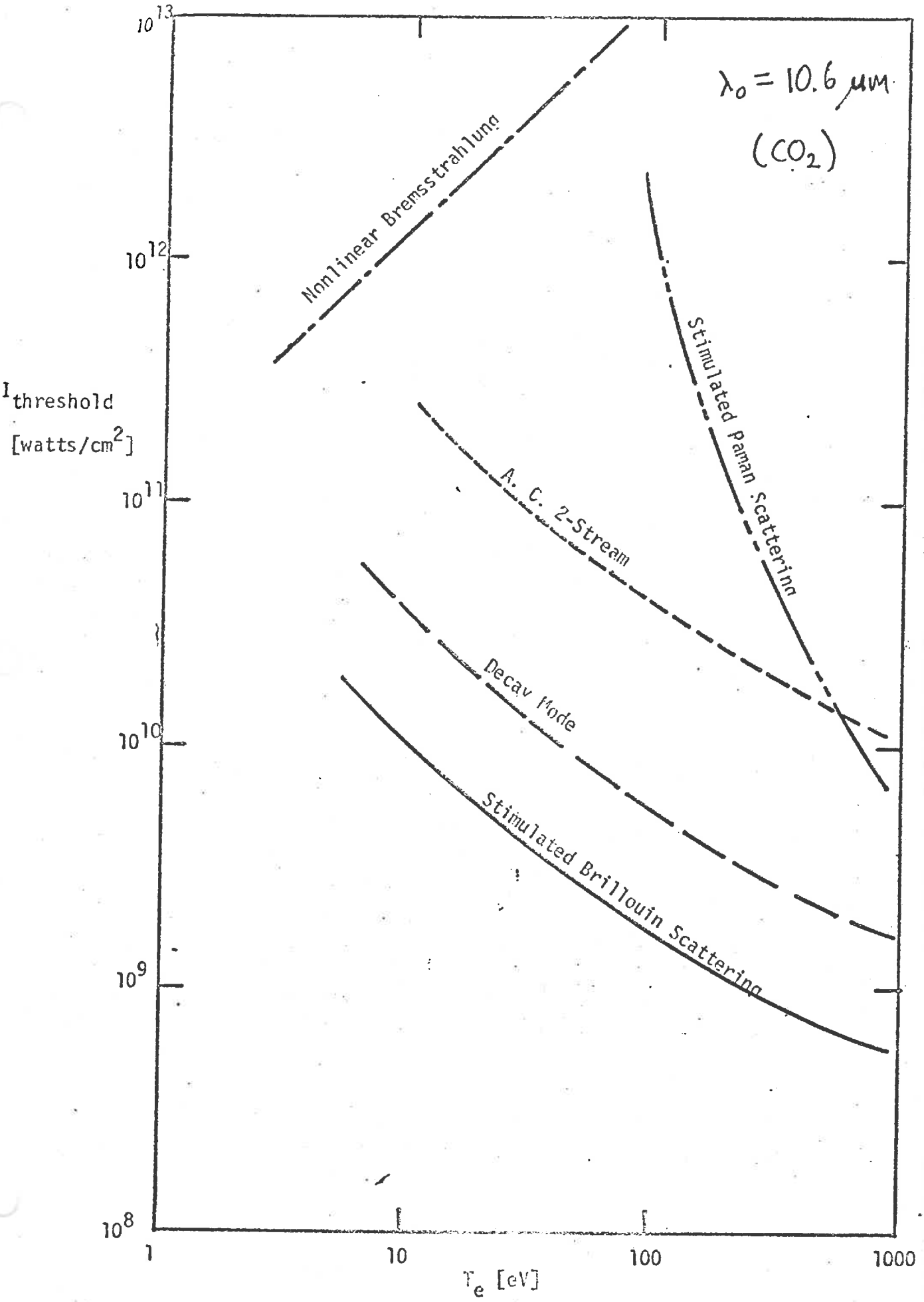
$\lambda_o = 10.6\ \mu m$
(CO_2)
Nonlinear Bremsstrahlung
Stimulated Raman Scattering
A. C. Z-Stream
Decay Mode
Stimulated Brillouin Scattering
$I_{threshold}$ [watts/cm^2]
10^{13}
10^{12}
10^{11}
10^{10}
10^9
10^8
1
10
100
1000
T_e [eV]

5.2. CHARGED PARTICLE BEAM ENERGY DEPOSITION

Electron Energy Deposition

When electron beam drivers are used in inertial confinement fusion, the incident electron beam deposits its energy in the electrons in the outer regions of the target. These hot electrons then equilibrate with the ions in the target:

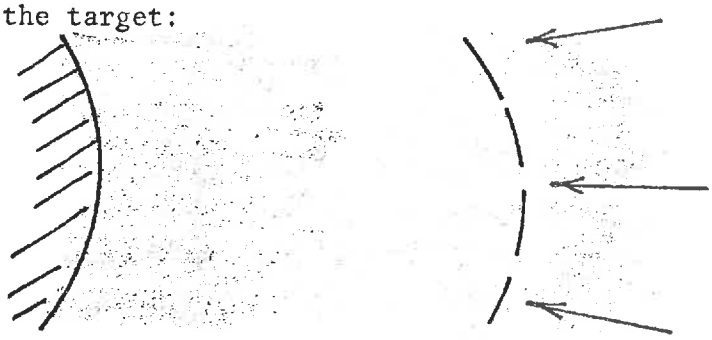

Several energy absorption mechanisms are of interest:

(i) collisional absorption

(ii) modifications due to beam magnetic fields

(iii) anomalous energy deposition due to collective (beam-plasma) effects.

Classical (collisional)

At low target temperatures and low beam current, electron energy loss is primarily through binary collisions with target electrons. As the target becomes a plasma, one must account for: (i) changes due to electron shielding at close range, and (ii) excitation of plasma waves (Cerenkov radiation).

More precisely, the possible interactions of an electron beam of energy $E \sim 1$ MeV incident upon a target can be tabulated for both low and high Z targets as shown below. Here we have ranked the various energy deposition mechanisms in order of importance and given crude estimates of their fractional contribution to the overall beam energy deposition.

mechanism	low Z target	high Z target
ionization	highest (1)	2nd (0.5)
elastic backscatter by nucleus	2nd (0,1)	highest (1)
inelastic scattering by atomic electrons	3rd (0,1)	3rd (0,1)
bremsstrahlung	lowest (~0)	lowest (0.01)

One can write the energy deposition formula as;

$$\frac{dE}{dx} = \left.\frac{dE}{dx}\right|_{\text{ionization}} + \left.\frac{dE}{dx}\right|_{\substack{\text{scattering}\\(\text{electrons})}} + \left.\frac{dE}{dx}\right|_{\text{bremsstrahlung}}$$

where

$$\left.\frac{dE}{dx}\right|_{\text{ionization}} = 4\pi r_0^2 \frac{m_0c^2}{\beta} NZ\left[\ln\beta\left(\frac{E+m_0c^2}{I}\right)\left(\frac{E}{m_0c^2}\right)^{1/2} - \frac{1}{2}\beta^2\right]$$

$$\left.\frac{dE}{dx}\right|_{\text{scattering}} = 4\pi r_0^2 \frac{m_0c^2}{\beta} NZ\left[\ln\left(\frac{m_0c\lambda_D\sqrt{\gamma-1}}{2\hbar}\right) + \frac{1}{4}\ln\beta^2\frac{m_0c^2}{kT}\right]$$

$$\left.\frac{dE}{dx}\right|_{\text{bremsstrahlung}} = 4\pi r_0^2 (E+m_0c^2) 4Z^2\left[\ln 2\left(\frac{E+m_0c^2}{m_0c^2}\right) - \frac{1}{3}\right]$$

Here $m_0c^2 = 0.511$ MeV, $\beta = v/c$, $4\pi r_0^2 = 10^{-24}$ cm^2

In particular, for relativistic electrons slowing down in a 1 keV plasma, one finds

$$\frac{dE}{dx} \sim 2.5\rho\frac{Z}{A} \text{ MeV/cm}$$

For solid density, dE/dx $\sim$ 1 MeV cm^2/g. Hence the range of a 1 MeV electron in solid density DT is several centimeters. But the pellet is of the order of millimeters in diameter. Hence classical absorption is insufficient to absorb the driver beam energy.

Magnetic Field Effects: The magnetic field established by the beam can alter electron trajectories--if it can penetrate the target:

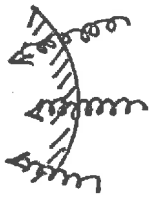

In the Mgauss fields of the beam one finds a Larmor radius of 0.01 to 0.1 mm. Hence electrons can be turned around and trapped in a layer of the order of the Larmor radius. But first the magnetic field of the beam must penetrate the target. This takes some time. In a time τ, one can estimate the penetration distance of magnetic field diffusion into the target as

$$\delta \sim 10^6 (\tau \ln N)^{1/2} T^{-3/4}$$

For example, if $\tau \sim 10^{-10}$, then the penetration distance is only 10^{-4} cm--far too short.

If anomalous resistivity is present (due to plasma turbulence), the penetration distance becomes larger. There is some hope that a two-stream instability induced by the return current in the target will have this effect. This has been observed experimentally, but it does not appear to be a strong effect. In fact, the coupling of the incident electron beam appears to be only 3 to 5 times that of the classical coupling.

Anomalous Effects: As in the laser-plasma interaction, there is some hope that the incident electron beam will excite plasma waves which will interact with the beam electrons, leading to more efficient energy absorption in the outer layers of the target:

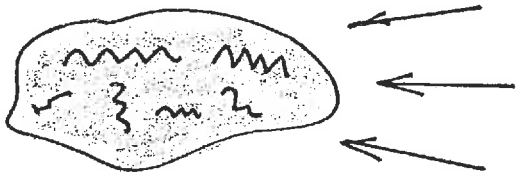

Unfortunately these beam plasma interactions are still not adequately understood.

High-Z absorption Targets: One remedy to the absorption problem is to use a layer of high Z material such as gold to shorten the energy deposition range. Unfortunately, this leads to a new problem since the bremsstrahlung generated by an electron beam incident upon a high Z tartet is appreciable:

Fraction of incident energy converted into Bremsstrahlung

Z	1	3	29	79
1 MeV	.001	.002	.027	.082
10 MeV	.01	.02	.16	.33

The importance of this is apparent when the mean free path of the bremsstrahlung radiation is noted:

bremsstrahlung mfp

material	0.1 MeV	1 MeV
Al	2.2 cm	6 cm
Pb	0,17	1.25
DT	35	96

Hence it is apparent that the bremsstrahlung produced during beam absorption in the high Z shell can penetrate into the target, preheating the inner shell and the fuel:

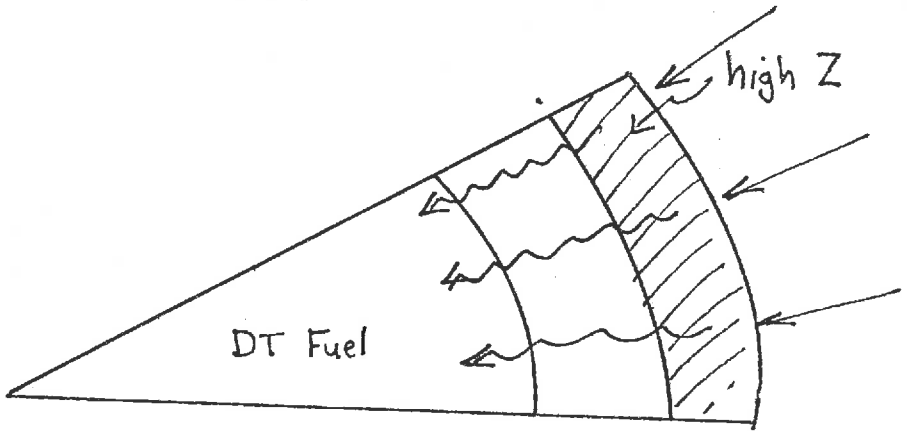

More detailed calculations indicate that for a 5 MJ beam input

Electron energy	1 MeV	10 MeV
% bremsstrahlung	8%	33%
T_{fuel}	eV	10s of eV

Several possible "cures" to the bremsstrahlung preheat problem have been proposed:

(i) using multi Z layered targets

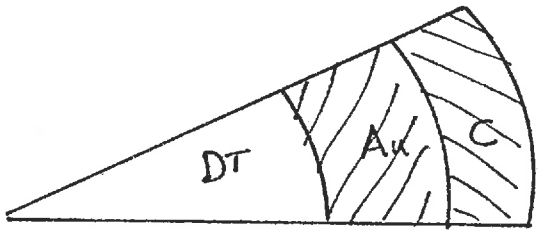

(ii) attempting to shorten the electron range, taking advantage of target designs which facilitate diffusion of the beam magnetic field

(iii) developing target designs which produce internal magnetic fields (see Chapter 8)

Summary: There appear to be many problems with electron beam driver energy absorption:

(i) long electron energy deposition range (implying the necessity of massive targets)
(ii) bremsstrahlung preheating (implying inefficient compression)
(iii) the relatively long pulse width of the driver beam

Light Ion Beams

The classical energy loss of a fast ion in a plasma is given by

$$\frac{dE}{dx} = \frac{8\pi e^4 n_i Z^2 \ln\Lambda}{m_i u_i^2} y^2 G(y) \left[1 - \frac{m_e}{M} \frac{\phi'(y)}{2y\,G(y)}\right]$$

where

$$y = u_i^2 / 2v_{th}^2$$

$$2y^2 G(y) = \phi(y) - y\,\phi'(y)$$

$$\phi(y) = \mathrm{erf}(y)$$

Only the electrons are effective at slowing down the ion. For plasma temperatures of roughly 1 keV and deuterium ions of incident energy 1 MeV, one finds

$$\frac{dE}{dx} \sim \frac{4\pi\sqrt{m_e}}{3\sqrt{2}} e^4 n_e Z^2 (\ln\Lambda) \frac{u_i}{(kT_e)^{3/2}}$$

$$\sim 3.8 \times 10^6 \frac{\sqrt{E}}{T_e^{3/2}} \rho$$

Hence, once again we find a relatively long range.

There is yet another common problem with both electrons and light ions--the absence of a critical density. We recall that in the case of light absorption, most of the absorption occurred in the neighborhood of the critical surface of the plasma where the plasma frequency was equal to the light frequency. However there is no analog to the critical density characterizing electron and ion penetration. Hence the energy deposition will occur over a large region of the target:

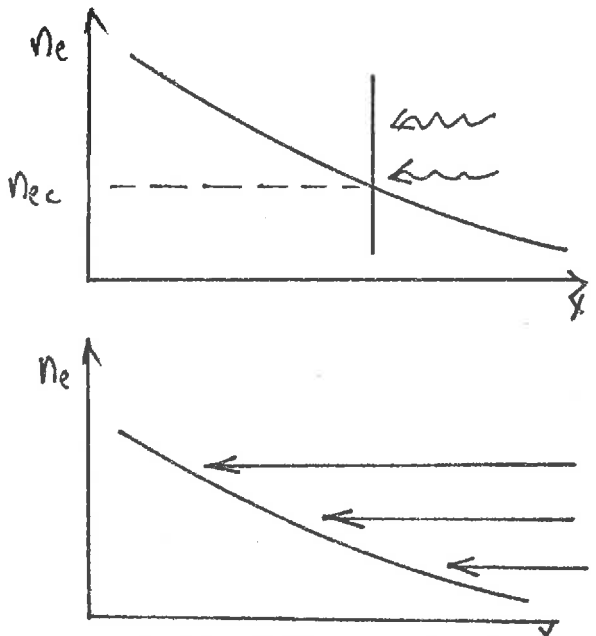

The importance of this difference is that pellet compression by electrons and light ions becomes very sensitive to pulse shape. If the incident beam energy is too large or the pulse is too long, the implosion will occur prematurely, before all of the beam energy is absorbed. In the opposite case, the implosion will occur too late. It is very difficult to synchronize the implosion process.

There is a second serious problem. Ions will deposit most of their energy at the cold temperature front, causing a heating wave to penetrate in preheating the fuel and reducing compression.

Heavy Ion Beams

The slowing down of heavy ions is well described by classical theory, although the stopping power decreases somewhat with increasing plasma temperature. In this case the incident beam ions heat target electrons, and then these electrons transfer their energy to target ions:

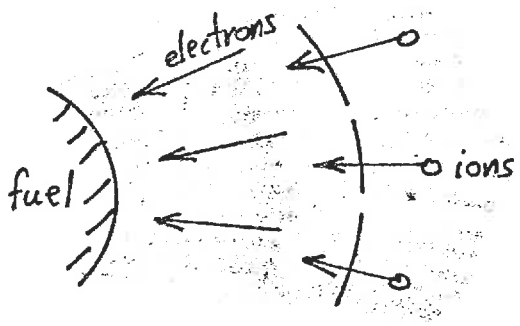

The range of heavy ions scales as

$$\text{Range} \sim \frac{A}{Z^2}\left(\frac{E}{A}\right)^{1.8}$$

Hence even for high energy ions, e.g., 10^3 MeV, the range is well under 0.1 mm. Although nonclassical (collective) effects may be present, these are not expected to degrade the absorption process.

Hence the big advantage of heavy ion beams is that they are readily absorbed in very short distances by classical mechanisms. One is not forced to depend on anomalous processes to facilitate the energy absorption in the target.

CHAPTER 6

COMPUTER SIMULATION*

Introduction

The successful development of the laser-driven fusion concept of the controlled thermonuclear reactor[1-3] depends on understanding many time-dependent coupled nonlinear processes typically represented by the plasma hydrodynamics equations and various other transport (Boltzmann or Fokker-Planck) equations. It is the carefully programmed coupling of laser light into the underdense plasma, conversion of the energy to an electron thermal conduction wave, and finally, conversion of thermal electron energy to hydrodynamic motion that sets the stage for the spherical implosion process that ultimately leads to very high adiabatic compressions (Fig. 1). As the spherical shock waves converge to the pellet center with a velocity in excess of 3×10^7 cm/s, they shock heat the central region of the compressed pellet to 4 to 10 keV and thermonuclear burning results. This burning self-heats the central region to over 20 keV, and a supersonic burn wave propagates outward from the pellet center, heating the surrounding, cold, adiabatically compressed plasma by redeposition of charged particle deuterium-tritium (DT) and deuterium-deuterium (DD) reaction products. As the surrounding plasma heats, it begins to burn, thus driving the burn wave (Fig. 2) (Ref. 4).

The success of this scenario depends sensitively upon many details of the implosion and energy transport process. During the implosion process, the plasma can be divided into three spatial regions, as shown in Fig. 1. The outermost region is bordered by the outer edge of the plasma and the critical density surface where the electron plasma frequency is equal to the laser light frequency, 10^{21} cm^{-3} for 1.06-μm radiation and 10^{19} cm^{-3} for 10.6-μm radiation. In this region, laser light is absorbed or reflected from the plasma, with most of the action taking place

[1]J. NUCKOLLS, L. WOOD, A. THIESSEN, and G. ZIMMERMAN, *Nature*, **239**, 139 (1972).

[2]J. CLARKE, H. FISHER, and R. MASON, *Phys. Rev. Lett.*, 30, 89 (1973).

[3]K. BRUECKNER and S. JORNA, *Rev. Mod. Phys.*, **46**, 325 (1974).

[4]G. FRALEY, E. LINNEBUR, R. MASON, and R. MORSE, *Phys. Fluids*, **17**, 474 (1974).

*Much of this chapter is taken from a review paper: G. Moses, Nuc. Sci. Eng. 64, 49 (1977)

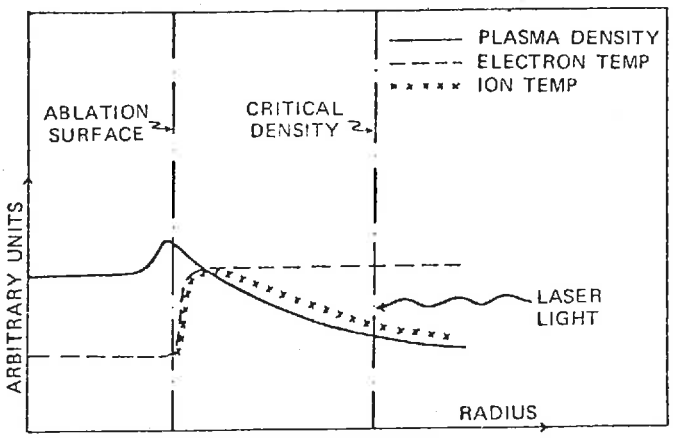

Fig. 1. Plasma density and electron and ion temperature profiles during the implosion of a spherical target.

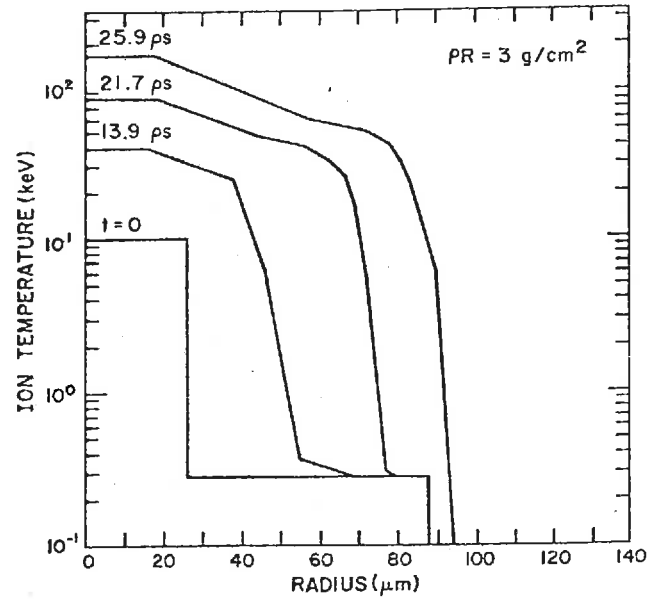

Fig. 2. Temperature profiles at different times during the propagating burn of a compressed pellet core.

near the critical density surface. Laser light absorption is typically characterized as classical (or inverse bremsstrahlung) absorption and anomalous absorption. Anomalous absorption can result from many different wave-wave couplings, with the most popular being resonant absorption, a coupling of the laser electric field with electron plasma waves.[5] This requires non-normal incidence of laser light on the electron density gradient in this outer, or corona, region near the critical density surface. Since this electron density gradient also refracts laser light, there will be an optimum angle at which resonant absorption is maximized (Fig. 3) (Ref. 6). In actual practice, this resonant absorption process cannot be self-consistently determined within a laser fusion hydrodynamics calculation, since the time and spatial scales are far too small. Instead, the results of numerical plasma simulations and experiments are used to provide a recipe for determining the amount of energy absorbed through resonant absorption. The resonant absorption process also leaves its energy with very few, very energetic electrons.[7] These so-called suprathermal electrons may be 10 to 100 times hotter than the thermal background plasma and consequently possess mean-free-paths (mfp) that are very long in comparison with the gradients in the thermal plasma. In the corona region, these suprathermal electrons are presumed to give rise to fast ions that are observed in laser-plasma experiments.[8] Those hot electrons streaming inward from the critical density surface can stream ahead of the

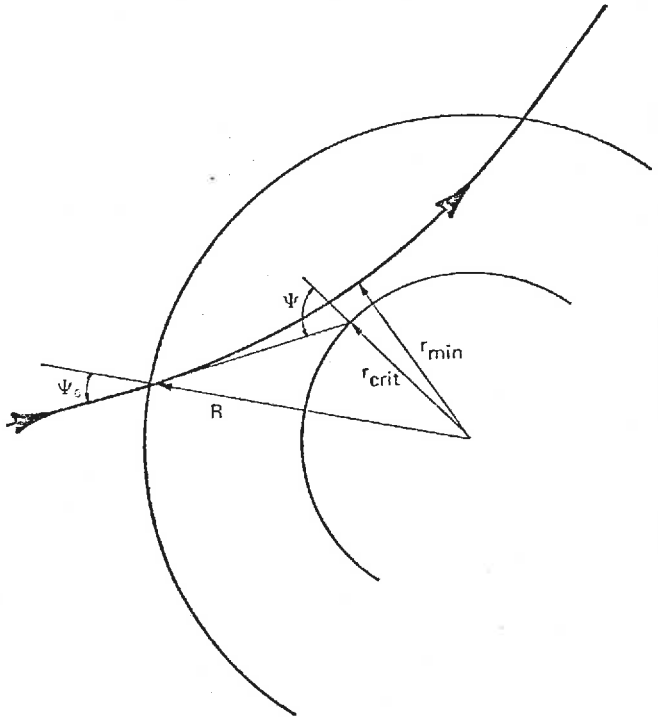

Fig. 3. Path of light ray at oblique incidence to the radial density gradient of a spherical pellet.

[5] J. FRIEDBERG, R. MITCHELL, R. MORSE, and L. RUDSINSKI, *Phys. Rev. Lett.*, **28**, 795 (1972).

[6] J. HOWARD, "Classical Energy Deposition and Refraction in Spherical and Planar Laser Fusion Targets," UWFDM-188, University of Wisconsin (1976); also submitted to *Nucl. Fusion*.

[7] R. MORSE and C. NIELSON, *Phys. Fluids*, **16**, 909 (1973).

[8] T. TAN, G. McCALL, A. WILLIAMS, D. GIOVANIELLI, and R. GODWIN, *Bull. Am. Phys. Soc.*, **21**, 1047 (1976).

ablation front and preheat the compressing pellet core (Fig. 1). This results in a degradation of the implosion process.[9] Therefore, it is very important to correctly treat these suprathermal electrons, with regard to both their origin and their transport, if a hydrodynamics code is to properly model the behavior of current experiments or predict the ultimate success of laser fusion.

In addition to this nonhydrodynamic coupling of laser energy into the plasma electrons, there is also a contribution to the hydrodynamic pressure due to the presence of laser radiation near the critical density. This so-called ponderomotive force, due to the intense radiation field, can significantly alter the electron density gradient profile near the critical density surface and, thus, can affect both classical and resonant absorption processes.[8] This makes the job of properly modeling the coupling of laser light into the plasma even more difficult. To date, no laser fusion hydrodynamics code can consistently predict the amount of laser energy deposited into the plasma. Typically, the amount of energy deposited is determined by a prescription that comes from the particular experiment being modeled, and the remainder of the simulation is performed under this assumption.

The second region of interest is bordered by the critical density surface on the outside and the ablation front on the inside. This region has a fluid velocity in the positive (outward) direction. However, the dominant energy flow is inward via the thermal electron conduction process and suprathermal electron streaming. Thus, the transport of energy is most important in this region, underscoring the fact that laser fusion calculations should not be considered as hydrodynamic calculations in the classical sense. Generally, a hydrodynamics problem is one where mass flow is an equally dominant process. In this middle region, however, the energy flow is an equally dominant process with thermal conduction and transport of nonthermal energy no longer representing a first-order effect. Later we see that for this reason the use of standard procedures for computing transport coefficients leads to erroneous results in hydrodynamics calculations and that *ad hoc* fix ups must be made to the equations to ensure plausible results.

The sensitivity of the implosion process to uncertainties in the electron thermal conduction process is displayed in Fig. 4, where thermal conductivity was scaled up and down from its nominal value while all other parameters, including the laser input pulse shape, were held fixed. These results are for a solid DT ball and a

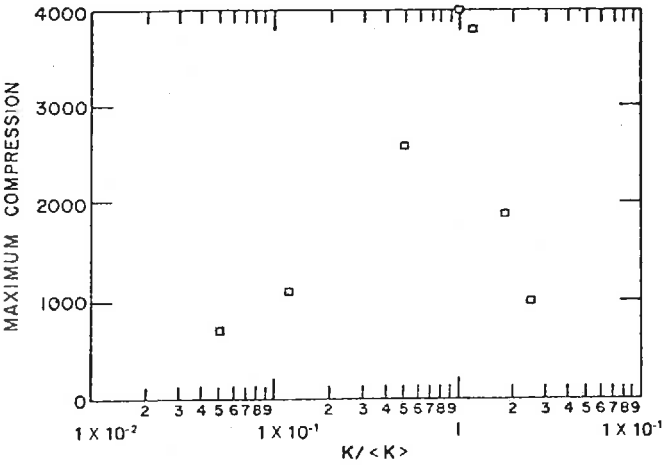

Fig. 4. Results of hydrodynamic simulations showing the dependence of the maximum compression of the pellet core on the ratio of the electron thermal conductivity to its nominal value.

60-kJ laser pulse with an optimum power law shape. The maximum compression of the pellet core was reduced by over an order of magnitude for changes in K_e within the uncertainty of its correct value.

Important reductions of K_e can result from both plasma instabilities and locally intense self-generated magnetic fields. Ion acoustic instabilities[10] are the result of the strong electron stream representing the thermal conduction and the counter streaming cold electron return current that is trying to maintain charge neutrality. These instabilities can lead to an increase in the electron-ion collision frequency and, thus, reduce thermal conduction. Again, these transport coefficient computations cannot be done in a self-consistent fashion within a hydrodynamic calculation, but must be approximated by using a prescription such as ratios of electron and ion temperatures and the magnitude of the electron heat flux. Self-generated magnetic fields can result from thermoelectric currents that are produced in an inhomogeneous plasma.[11] One typical situation is nonparallel density and temperature gradients, $\nabla n \times \nabla T$, that are the result of nonuniform laser illumination and/or the development of two-dimensional flow during the implosion process. Two-dimensional flow can result from a nonsymmetric target configuration such as a ball-on-disc target, or from the development of fluid instabilities during a symmetric implosion. In either

[9] J. LINDL, *Nucl. Fusion*, **14**, 511 (1974).

[10] R. MALONE, R. McCRORY, and R. MORSE, *Phys. Rev. Lett.*, **34**, 721 (1975).

[11] J. STAMPER and J. DAWSON, *Phys. Rev. Lett.*, **26**, 1012 (1971).

case, the thermal transport coefficient transverse to the magnetic field lines is reduced by the factor $(1 + \omega^2\tau^2)^{-1}$, where ω is the electron-cyclotron frequency and τ is the electron-ion collision frequency.[12] The point here is that a two-dimensional hydrodynamic treatment is necessary to predict this important effect, even for a presumably symmetric implosion. This is of great significance because two-dimensional calculations are extremely expensive, and accurate treatment of the transport processes, which are important in addition to the hydrodynamics, is prohibitively expensive in two dimensions.

The third region of interest is that part of the pellet within the ablation surface. In this dense, cold plasma, hydrodynamics is presumably an accurate model. However, care must be taken to properly evaluate the associated plasma equations-of-state. At high compressions, cold electrons behave as Fermions, and their properties must be treated accordingly. The other hydrodynamic effect of interest is fluid instability. Conditions at the ablation front can correspond to Rayleigh-Taylor instability conditions, and growth rates can be fast enough to destroy the isentropic implosion necessary to the success of laser fusion. Again, this necessitates the use of more than a one-dimensional treatment of the hydrodynamic flow. Perturbation techniques as well as fully two-dimensional calculations were used to study this problem.[13-16]

For all three of these regions, radiation emission, absorption, and transport also must be considered. High-energy photons created in the laser absorption region can stream inward to preheat the pellet core just as the suprathermal electrons. More importantly, in the current experiments, radiation is one of the principal diagnostic tools. The spectrum is used to determine electron temperature, suprathermal electron temperature, and the number of suprathermal electrons.[17] The spatial distribution of x rays provides information regarding the compression of glass microballoon pellets. X-ray line emission was used to diagnose the presence of suprathermal electron preheat of compressed DT fuel.[18]

In addition to the three spatial regions discussed, there is a final stage of the laser fusion process that involves burning the compressed core. Ignition of the central hot "microcore" causes the burn process to progress more rapidly than the implosion process itself. In fact, it can be decoupled from the implosion process for a nonmarginal burn, i.e., a burn that results in pellet gains near 100. This process again involves the transport of nonthermal particles, the charged particle fusion reaction products. These particles slow down in the dense pellet core, giving up their energy to bootstrap heat the core to optimum burn temperatures. In current laser fusion experiments, a negligible amount of charged particle energy is redeposited in the DT fuel. Many of the particles escape, however, and they can be used as a diagnostic to determine the temperature of the burning fuel. In this case, charged particle transport must be done to predict the amount of energy loss and spectrum broadening that results from interactions with the surrounding glass shell, so that experimental results can be translated into DT ion temperatures.

The preceding discussion was an attempt to very briefly summarize the laser fusion problem and to highlight some of the more important physics that must be considered when modeling laser fusion plasmas. It was meant to show that classical hydrodynamics in itself is not nearly enough to model these plasmas; this directly translates into increased computing costs. The actual solution of the hydrodynamics equations represents only a small fraction of the computing cost. Complicated prescriptions for transport coefficients must be computed many times, for almost all coefficients are nonlinear and/or time dependent. Time- and energy-dependent transport calculations must be done. These are considerably more time consuming than the hydrodynamics equations, since energy is typically represented in a multigroup structure. Due to the strong coupling between the energy, space, and time variables associated with charged particle slowing down, as many as 100 energy groups are needed to treat the transport problem.

---

[12] S. BRAGINSKII, *Review of Plasma Physics*, Vol. 1, p. 205, Consultants Bureau, New York (1965).

[13] J. SHIOU, E. GOLDMAN, and C. WENG, *Phys Rev. Lett.*, **32**, 352 (1974).

[14] D. HENDERSON and R. MORSE, *Phys. Rev. Lett.*, **32**, 355 (1974).

[15] D. HENDERSON, R. McCRORY, and R. MORSE, *Phys. Rev. Lett.*, **33**, 205 (1974).

[16] J. LINDL and W. MEAD, *Phys. Rev. Lett.*, **34**, 1273 (1975).

[17] K. BRUECKNER, *Nucl. Fusion*, **16**, 357 (1976); see also, M. STROSCIO, "Theoretical Results Relating Experimental X-Ray Spectra to the Number and Total Energy of Suprathermal Electrons in Laser-Heated Plasmas," LA-6465-MS, Los Alamos Scientific Laboratory (1976).

6.2. HYDRODYNAMIC CODES

Basic Model

Essentially all inertial confinement plasma hydrodynamics codes use a two-temperature, one-fluid model of the plasma. In this model, electrons and ions are assumed to flow as one fluid, implying no charge separation (at least on the scale of interest). However, each species maintains its own characteristic temperature due to weak energy coupling between the two populations. Radiation can be included as either a third temperature equation, assuming a local Planck distribution, or as an energy-dependent treatment of the photon distribution function. We will consider only the treatment of the electrons and ions here, since the radiation is most typically treated in an energy-dependent fashion.

Hence the basic equations of the two-temperature, one-fluid model of a plasma take the form:

$$\frac{\partial \rho}{\partial t} + \underset{\sim}{\nabla} \cdot \rho \underset{\sim}{u} = 0$$

$$\rho \left(\frac{\partial}{\partial t} + \underset{\sim}{u} \cdot \underset{\sim}{\nabla} \right) \underset{\sim}{u} = -\underset{\sim}{\nabla} p$$

$$\rho C_{ve} \left(\frac{\partial}{\partial t} + \underset{\sim}{u} \cdot \underset{\sim}{\nabla} \right) T_e = \underset{\sim}{\nabla} \cdot \kappa_e \underset{\sim}{\nabla} T_e - p_e \left(\underset{\sim}{\nabla} \cdot \underset{\sim}{u} \right) - \omega_{ei} (T_e - T_i) + S_e$$

$$\rho C_{vi} \left(\frac{\partial}{\partial t} + \underset{\sim}{u} \cdot \underset{\sim}{\nabla} \right) T_i = \underset{\sim}{\nabla} \cdot \kappa_i \underset{\sim}{\nabla} T_i - p_i \left(\underset{\sim}{\nabla} \cdot \underset{\sim}{u} \right) + \omega_{ei} (T_e - T_i) + S_i$$

Lagrangian Coordinates

When we write the hydrodynamics equations in terms of $(\underset{\sim}{r},t)$, we are using an Eulerian description in terms of a fixed coordinated frame. For example, the Eulerian form of the equations of continuity and motion are

$$\frac{\partial \rho}{\partial t} + \underset{\sim}{\nabla}\cdot\rho\underset{\sim}{u} = 0$$

$$\frac{\partial \underset{\sim}{u}}{\partial t} + \underset{\sim}{u}\cdot\underset{\sim}{\nabla}\,\underset{\sim}{u} = -\frac{1}{\rho}\underset{\sim}{\nabla}\,p$$

However when the fluid is rapidly expanding or contracting or reactions are occurring, it is useful to move to a reference frame that moves with the local flow velocity of the fluid. Such a frame is known as the Lagrangian description.

EXAMPLE: Plane flow

Consider a fluid particle at position x and the coordinate of a reference particle at x_1. The mass (per unit area) between x and x_1 is given by

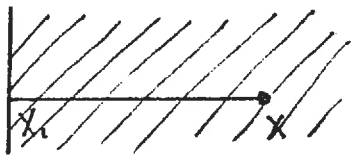

$$m = \int_{x_1}^{x} \rho(x')\,dx'$$

[Note that "m" just labels which particle we are considering--namely that particle which has a certain mass between it and x_1.] Hence we we treat m as a variable, we find

$$dm = \rho\,dx$$

The fluid mass separating one particle from another is therefore taken as an appropriate Lagrangian variable.

To convert the hydrodynamics equations describing plane fluid flow to Lagrangian form, we first write their Eulerian form as:

$$\frac{\partial \rho}{\partial t} + \frac{\partial}{\partial x}(\rho u) = \frac{\partial \rho}{\partial t} + u\frac{\partial \rho}{\partial x} + \rho\frac{\partial u}{\partial x} = 0$$

or $$\frac{D\rho}{Dt} + \rho \frac{\partial u}{\partial x} = 0$$

where we have introduced the substantial derivative (in the reference frame of the flow)

$$\frac{D}{Dt} \equiv \frac{\partial}{\partial t} + u \frac{\partial}{\partial x}$$

If we now make a variable substitution

$$dm = \rho dx$$

we find

$$\frac{1}{\rho^2} \frac{D\rho}{Dt} + \frac{\partial u}{\partial m} = 0$$

or defining the specific volume

$$V = \frac{1}{\rho}$$

we find

$$\frac{DV}{Dt} = \frac{\partial u}{\partial m}$$

But in Lagranian coordinates moving with the flow

$$\frac{D}{Dt} \rightarrow \frac{\partial}{\partial t}$$

Hence the continuity equation in Lagrangian coordinates becomes

$$\frac{\partial V}{\partial t} = \frac{\partial u}{\partial m}$$

where we now regard $V = V(m,t)$

$u = u(m,t)$

Thus in one-dimensional plane flow, we find

Eulerian	Lagrangian
$\frac{D\rho}{Dt} = -\rho \frac{\partial u}{\partial x}$	$\frac{\partial V}{\partial t} = \frac{\partial u}{\partial m}$
$\frac{Du}{Dt} = -\frac{1}{\rho} \frac{\partial p}{\partial x}$	$\frac{\partial u}{\partial t} = -\frac{\partial p}{\partial m}$

Suppose we have solved for V(m,t) and u(m,t). Then to get back to Eulerian form, $\rho(x,t)$ and u(x,t), we first integrate

$$dx = V(m,t)\,dm$$

to find

$$x(m,t) = \int_0^m V(m',t)\,dm' + x_1(t)$$

We can then use this to find $\rho(x,t) = [V(x,t)]^{-1}$ and u(x,t).

EXAMPLE: Spherical geometry

We now define our Lagrangian mass coordinate by

$$dm = \rho\, 4\pi r^2 dr$$

Then the Lagrangian form of the hydrodynamics equations becomes

$$\frac{\partial V}{\partial t} = \frac{\partial}{\partial m}\left(4\pi r^2 u\right)$$

$$\frac{\partial u}{\partial t} = -4\pi r^2 \frac{\partial p}{\partial m}$$

Frequently one omits the 4π factor and defines the dependent variables per steradian. Then the Lagrangian form of the hydrodynamics equations become

$$\frac{\partial V}{\partial t} = \frac{\partial}{\partial m}\left(r^2 u\right)$$

$$\frac{\partial u}{\partial t} = -r^2 \frac{\partial p}{\partial m}$$

The most general Lagrangian form is

$$\frac{\partial V}{\partial t} = V \underset{\sim}{\nabla} \cdot \underset{\sim}{u}$$

$$\frac{\partial u}{\partial t} = -V \underset{\sim}{\nabla} p$$

However it should be noted at this point that Lagrangian coordinates are of most use for 1-D geometries, since in 2-D and 3-D they lead to some complications in defining an appropriate numerical mesh. (We will return to discuss this in more detail later in this section.)

The general Lagrangian form of the hydrodynamics equations for 1-D symmetry is

$$\frac{\partial V}{\partial t} = \frac{\partial}{\partial m}\left(r^{\delta-1} u\right)$$

$$\frac{\partial u}{\partial t} = -r^{\delta-1} \frac{\partial p}{\partial m}$$

where

$$\delta = \begin{cases} 1 & \text{plane (mass/unit area)} \\ 2 & \text{cylindrical (mass/unit length-radian)} \\ 3 & \text{spherical (mass/steradian)} \end{cases}$$

We will write the general Lagrangian form of the two-temperature, one-fluid plasma model as

$$\frac{\partial \underset{\sim}{u}}{\partial t} = -\frac{1}{\rho} \underset{\sim}{\nabla} p$$

$$\rho C_{ve} \frac{\partial T_e}{\partial t} = \underset{\sim}{\nabla} \cdot \kappa_e \underset{\sim}{\nabla} T_e - p_e (\underset{\sim}{\nabla} \cdot \underset{\sim}{u}) - \omega_{ei}(T_e - T_i) - p_{eT} \dot{V} T_e + S_e$$

$$\rho C_{vi} \frac{\partial T_i}{\partial t} = \underset{\sim}{\nabla} \cdot \kappa_i \underset{\sim}{\nabla} T_i - p_i (\underset{\sim}{\nabla} \cdot \underset{\sim}{u}) + \omega_{ei}(T_e - T_i) - p_{iT} \dot{V} T_i + S_i$$

Numerical Solution of the Hydrodynamics Equations

To be explicit, let us consider the Lagrangian form of the hydrodynamics equations in 1-D spherical geometry:

$$\frac{\partial V}{\partial t} = \frac{\partial}{\partial m}\left(r^2 u\right)$$

$$\frac{\partial u}{\partial t} = -r^2 \frac{\partial}{\partial m} p$$

These equations are hyperbolic and therefore have a characteristic propagation speed. Furthermore they admit discontinuous solutions (shock waves) that can create difficulties for finite difference schemes. Hence we need some tricks to handle their numerical solution.

Artificial Viscosity (von Neumann "q"):

It is difficult to handle shock waves described by the inviscid hydrodynamics equations numerically, since a step discontinuity arises. Hence von Neumann proposed that one introduce a phony or artificial viscosity, which he labeled by "q", to spread out the shock over a few zones of the numerical mesh:

Notice that this does not affect the results on either side of the shock, since these are determined by the conservation laws as manifested in the Rankine-Hugoniot relations.

The von Neumann q must be chosen very carefully to yield a constand thickness for all shocks. This requires quadratic terms in velocity gradients (equivalent to using a small viscosity for weak shocks and a large viscosity for strong shocks):

We can therefore define:

$$q = \frac{1}{V}\left[b\,\Delta m\,\frac{\partial u}{\partial m}\right]^2 , \quad \frac{\partial V}{\partial t} < 0 \quad \text{compression}$$

$$= 0 , \quad \frac{\partial V}{\partial t} \geq 0 \quad \text{expansion}$$

where one usually chooses $b = \sqrt{2}$.

Then we implement the artificial viscosity by replacing the pressure p in the hydrodynamic equations by p + q in

$$\frac{\partial V}{\partial t} = \frac{\partial}{\partial m}\left(r^2 u\right)$$

$$\frac{\partial u}{\partial t} = -r^2 \frac{\partial}{\partial m}\left(p+q\right)$$

In summary, then the artificial viscosity is chosen so that it dissipates energy in a shock to a few surrounding finite difference zones while preserving the Hugoniot relations across the shock. This preserves the essential features of the shock while reducing the gradients across the shock to values that allow the treatment by finite difference methods. [A useful hint in analyzing data generated by hydrodynamic codes is to print out the value of "q" along with other hydrodynamic variables. Then one can easily determine those regions where shock waves are occurring by noting where q is nonzero. Furthermore, the strength of the shock is given by the size of q.]

Differencing Schemes:

These equations are both coupled and nonlinear, since $K_e \sim T_e^{5/2}$, $\omega_{ei} \sim T_e^{-3/2}$, etc.[20] They are usually solved using standard finite difference techniques.[21] Equation (1) is hyperbolic and has a characteristic propagation speed. It also admits discontinuous solutions (shocks) that create great difficulties for general finite difference schemes. Because of these properties, this equation is usually solved using an explicit differencing technique,

$$\frac{u^{n+1/2} - u^{n-1/2}}{\Delta t^n} = -\frac{1}{\rho^n}\nabla(P^n + q^{n-1/2}) , \qquad (4)$$

where

$$q^{n-1/2}(r) = q_{vn} \quad \text{for} \quad \dot{V} < 0 \quad \text{(compression)}$$
$$q^{n-1/2}(r) = 0 \quad \text{for} \quad \dot{V} > 0 \quad \text{(expansion)} . \qquad (5)$$

The spatial differencing was not specified here, since it varies depending on whether the equation is solved in one or two dimensions. This equation requires a stability condition given by the Courant condition,

$$\frac{C_s \Delta t}{\Delta X} < 1 , \qquad (6)$$

where C_s is the sound speed in the plasma. Of course, this condition says that a disturbance cannot be allowed to propagate across a finite difference zone in less than one time step.

[20] L. SPITZER, *Physics of Fully Ionized Gases*, 2nd ed., John Wiley and Sons, Inc., Publishers, New York (1962); see also, S. BRAGINSKII, *Review of Plasma Physics*, Vol. 1, p. 205, Consultants Bureau, New York (1965).

[21] R. RICHTMYER and K. MORTON, *Difference Methods for Initial Value Problems*, 2nd ed., Wiley-Interscience Publishers, Inc., New York (1967).

[22] J. Von NEUMANN and R. RICHTMYER, *J. Appl. Phys.*, **21**, 232 (1950).

Let us consider the case of a simple 1-D spherical geometry by way of illustration. We begin by breaking up the Lagrangian grid into J zones. That is, we discretize the variable m. (It is common to choose equal increments in m--that is, equal mass zoning.) Notice that the radius of each zone, $r_j(t)$, is actually a function of time. In simple codes one might pick about 30 zones.

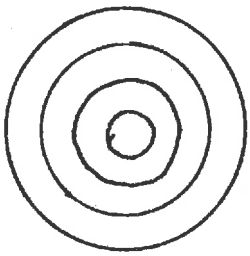

We now discretize such that

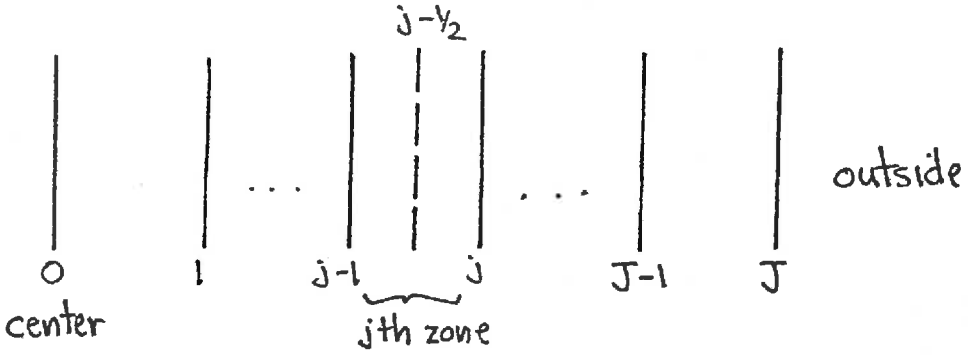

We also discretize the time variable

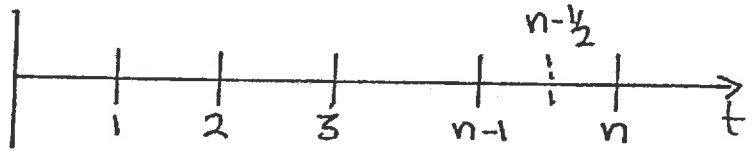

Here we will use the standard notation

$$u(m_j, t_n) = u_j^n$$

If we use an explicit differencing scheme, we can write

$$\frac{u_j^{n+\frac{1}{2}} - u_j^{n-\frac{1}{2}}}{\Delta t^n} = -(r_j^n)^2 \left[\frac{(p_{j+\frac{1}{2}}^n - p_{j-\frac{1}{2}}^n)}{\Delta m_j} + \frac{(q_{j+\frac{1}{2}}^n - q_{j-\frac{1}{2}}^n)}{\Delta m_j} \right]$$

where

$$\Delta t^n = \frac{1}{2}(\Delta t^{n+\frac{1}{2}} + \Delta t^{n-\frac{1}{2}})$$

$$\Delta m_j = \frac{1}{2}(\Delta m_{j+\frac{1}{2}} + \Delta m_{j-\frac{1}{2}})$$

Here

$$q_{j-1/2} = \frac{1}{V_{j-1/2}} \left[b \Delta m \left(\frac{u_j - u_{j-1}}{\Delta m} \right) \right]^2$$

Next, for r_j^n we use

$$\Delta r_{j-1/2}^{n+1} - \Delta r_{j-1/2}^{n} = (u_j^{n+1/2} - u_{j-1}^{n+1/2}) \Delta t^{n+1/2}$$

where $\Delta r_{j-1/2}^{n}$ is the zone thickness between j and j - 1 at time t_n:

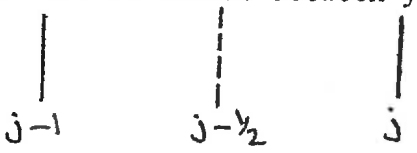

Also

$$r_j^{n+1} - r_j^n = u_j^{n+1/2} \Delta t^{n+1/2}$$

gives the change in the location of the jth zone as a function of time.

The continuity equation can be bypassed by calculating

$$V_{j-1/2}^{n+1/2} = \frac{\Delta r_{j-1/2}^{n+1}}{\Delta m_{j-1/2}} \left[r_j^{n+1} r_{j-1}^{n+1} + \frac{1}{3} (\Delta r_{j-1/2}^{n+1})^2 \right]$$

We also need to use:

$$V_{j-1/2}^{n+1/2} = \frac{1}{2} (V_{j-1/2}^{n+1} + V_{j-1/2}^{n})$$

$$\dot{V}_{j-1/2}^{n+1/2} = \frac{1}{\Delta t^{n+1/2}} (V_{j-1/2}^{n+1} - V_{j-1/2}^{n})$$

Temperature Equations (Heat Conduction): The coupled temperature equations are parabolic, which should imply that they have an infinite propagation speed. However, due to nonlinear thermal conductivity, they exhibit a behavior similar to that of a wave equation and, in fact, do have a finite propagation speed. Nevertheless, they are typically solved using an implicit differencing technique, since their characteristic time scale is usually much less than the equation of motion, and hence an explicit scheme would impose a much stricter

time step constraint. They need not be solved simultaneously, since their coupling is weak.

To be more precise, consider the simple heat conduction equation

$$\frac{\partial T}{\partial t} = \kappa \frac{\partial^2 T}{\partial x^2}$$

An explicit numerical solution scheme would discretize this as

$$\frac{T_j^{n+1} - T_j^n}{\Delta t} = \kappa \left[\frac{T_{j+1}^n - 2T_j^n + T_{j-1}^n}{(\Delta x)^2} \right]$$

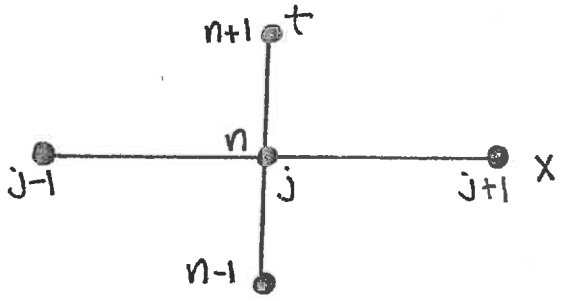

Here we note that the spatial derivative is evaluated at the earlier time step t_n. Since all T^n are known, we can solve explicitly for T_j^{n+1}. Stability problems arise if $\kappa \Delta t/(\Delta x)^2 > \frac{1}{2}$.

An alternative and more satisfactory approach is to use the Crank-Nicholson differencing scheme

$$\frac{T_j^{n+1} - T_j^n}{\Delta t} = \kappa \, \frac{1}{2} \left[\frac{(T_{j+1}^n - 2T_j^n + T_{j-1}^n)}{(\Delta x)^2} + \frac{(T_{j+1}^{n+1} - 2T_j^{n+1} + T_{j-1}^{n+1})}{(\Delta x)^2} \right]$$

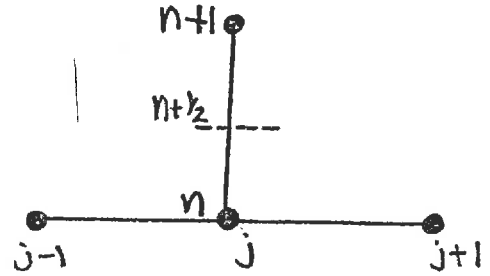

This is now a stable difference scheme. But T_{j+1}^{n+1}, T_j^{n+1}, and T_{j-1}^{n+1} on the right hand side are not known. Hence we must solve this equation implicitly (in this case, this corresponds to a linear tridiagonal system of equations for the T_j^{n+1}).

Although this is a straightforward scheme for linear problems, it does present problems when we have a nonlinear conduction problem:

$$\frac{\partial T}{\partial t} = \frac{\partial}{\partial x} \kappa(T) \frac{\partial T}{\partial x}$$

Then we must use either extrapolation or iteration techniques.

The finite difference equations for each equation are

$$\frac{T^{n+1} - T^n}{\Delta t^{n-1/2}} = \nabla \cdot K^n \nabla[\theta T^n + (1 - \theta)T^{n+1}] + \ldots , \qquad (7)$$

where, again, specific spatial differencing was not included. Parameter θ is taken as $\frac{1}{2}$, for if the equations were linear, which they are not, and Δt and ΔX were equal, which they are not, this value would give a second-order accurate differencing scheme. In light of nonlinearities and the nonconstant time and space steps, this can at best be considered an imperfect solution. The nonlinear thermal conductivity was shown with an explicit evaluation

$$K^n = K[T^n(r)] \qquad (8)$$

in Eq. (7), which is an approximation difficult to improve on in a two-dimensional calculation. In a one-dimensional calculation, several other possibilities exist. Past temperatures at each mesh point can be saved and used to extrapolate ahead in time to evaluate K at $n + \frac{1}{2}$,

$$\tilde{K}^{n+1/2} \equiv K(\tilde{T}^{n+1/2}) \quad , \quad \tilde{T}^{n+1/2} \equiv F(T^{n-2}, T^{n-1}, T^n) \quad , \qquad (9)$$

or the temperature equations can be iterated by reevaluating the nonlinear coefficients until the temperatures converge pointwise. However, even in one dimension, each of these methods has drawbacks. Experience has shown that neither is as stable as the single explicit evaluation method, and they often require more stringent conditions on the time step than the explicit evaluation. Furthermore, an "uninteresting" part of the plasma is usually the source of the smaller time step. In laser fusion calculations, the plasma electrons usually increase in temperature due to thermal conduction from a source of heat. This is a stable process for these two schemes; however, when electrons decrease in temperature, it is often because of an expansion of the plasma. The strong thermal conduction continually "feeds" these loss zones and an instability results.

For linear diffusion equations, the Crank-Nicholson ($\theta = \frac{1}{2}$) differencing scheme ensures unconditional stability. However, this is not the case for nonlinear equations where no rigorous estimate of the stability condition can be made. Experience has shown that a time step constrained to ensure

$$\max(\Delta T/T) < \tfrac{1}{4} \qquad (10)$$

usually provides stable solutions, but values as small as $\frac{1}{10}$ were necessary for some calculations. Quite often it is this *ad hoc* stability condition that sets the time step in the hydrodynamics calculation rather than the Courant condition.

EXAMPLE: Consider the temperature equations for a 1-D spherical code (in Lagrangian form)

$$c_i \frac{\partial T_i}{\partial t} + T_i P_T \frac{\partial V}{\partial t} = \frac{\partial}{\partial m}\left(\kappa_i r^2 \frac{\partial T_i}{\partial r}\right) - \omega_{ei}(T_i - T_e) + S_i$$

$$c_e \frac{\partial T_e}{\partial t} + T_e P_T \frac{\partial V}{\partial t} = \frac{\partial}{\partial m}\left(\kappa_e r^2 \frac{\partial T_e}{\partial r}\right) + \omega_{ei}(T_i - T_e) + S_e$$

It is most convenient to use matrix notation to write the finite difference form of these equations as

$$\underbrace{\begin{pmatrix} C_i & 0 \\ 0 & C_e \end{pmatrix}}_{\underline{\underline{\alpha}}} \frac{\Delta m}{\Delta t}\left[\underline{T}^{n+1}_{j-1/2} - \underline{T}^{n}_{j-1/2}\right] = \underbrace{\begin{pmatrix} S_{i\,j-1/2} - q_{j-1/2}\dot{V}_{j-1/2} \\ S_{e\,j-1/2} \end{pmatrix}}_{\underline{\beta}} \frac{\Delta m}{\Delta t}$$

$$+\tfrac{1}{2}\underbrace{\begin{pmatrix} K_i & 0 \\ 0 & K_e \end{pmatrix}}_{\underline{\underline{a}}} \frac{r^2}{\Delta r}\Big|_j \left[\left(\underline{T}^{n+1}_{j+1/2} + \underline{T}^{n}_{j+1/2}\right) - \left(\underline{T}^{n+1}_{j-1/2} + \underline{T}^{n}_{j-1/2}\right)\right]$$

$$-\tfrac{1}{2}\begin{pmatrix} K_i & 0 \\ 0 & K_e \end{pmatrix} \frac{r^2}{\Delta r}\Big|_{j-1} \left[\left(\underline{T}^{n+1}_{j-1/2} + \underline{T}^{n}_{j-1/2}\right) - \left(\underline{T}^{n+1}_{j-3/2} + \underline{T}^{n}_{j-3/2}\right)\right]$$

$$-\tfrac{1}{2}\underbrace{\begin{pmatrix} P_{r_i} & 0 \\ 0 & P_{r_e} \end{pmatrix}}_{\underline{\underline{\gamma}}} \dot{V}\,\Delta m_{j-1/2} \left[\underline{T}^{n+1}_{j-1/2} + \underline{T}^{n}_{j-1/2}\right]$$

$$-\underbrace{\begin{pmatrix} \omega_{ei} & -\omega_{ei} \\ -\omega_{ei} & \omega_{ei}+\omega_r \end{pmatrix}}_{\underline{\underline{\omega}}} \Delta m_{j-1/2} \left[\underline{T}^{n+1}_{j-1/2} + \underline{T}^{n}_{j-1/2}\right]$$

or in more abstract form

$$\underline{\underline{A}} \cdot \underline{T}^{n+1}_{j-1/2} = \underline{\underline{a}}_j \cdot \underline{T}^{n+1}_{j+1/2} + \underline{\underline{a}}_{j-1} \cdot \underline{T}^{n+1}_{j-3/2} + \underline{B}_{j-1/2}$$

where

$$\underline{\underline{A}}_{j-1/2} = \underline{\underline{\alpha}}_{j-1/2} + \underline{\underline{\omega}}_{j-1/2} + \underline{\underline{\gamma}}_{j-1/2} + \underline{\underline{a}}_j + \underline{\underline{a}}_{j-1}$$

$$\underline{B}_{j-1/2} = \underline{\beta}_{j-1/2} + \underline{\underline{a}}_j \cdot \left(\underline{T}^{n}_{j+1/2} - \underline{T}^{n}_{j-1/2}\right) - \underline{\underline{a}}_{j-1} \cdot \left(\underline{T}^{n}_{j+1/2} - \underline{T}^{n}_{j-1/2}\right)$$
$$- \underline{\underline{\gamma}}_{j-1/2} \cdot \underline{T}^{n}_{j-1/2} - \underline{\underline{\omega}}_{j-1/2} \cdot \underline{T}^{n}_{j-1/2} + \underline{\underline{\alpha}}_{j-1/2} \cdot \underline{T}^{n}_{j-1/2}$$

We can now solve for

$$\underline{T}_{j-1/2} = \underline{\underline{C}}_{j-1/2} \cdot \underline{T}_{j+1/2} + \underline{D}_{j-1/2}$$

where

$$\underline{\underline{C}}_{j-1/2} = \underline{\underline{K}}^{-1}_{j-1/2} \cdot \underline{\underline{a}}_j \,, \qquad \underline{D}_{j-1/2} = \underline{\underline{K}}^{-1}_{j-1/2} \cdot \underline{E}_{j-1/2}$$

The basic approach is then to take $\underline{\underline{C}}_{-1/2} = 0$ and $\underline{D}_{-1/2} = \underline{T}^{n}_{-1/2}$ to evaluate $\underline{\underline{C}}_j$ and $\underline{D}_j$. Then one can calculate $\underline{T}_{j-1/2}$ from each $\underline{T}_{j+1/2}$ by using the boundary condition in the outermost zone, $\underline{T}_{J-1/2}$. One usually considers the innermost boundary to be fixed and thermally insulated.

Some Comments on 2-D Lagrangian Codes:

In addition to these stability and accuracy problems, solution of the hydrodynamics equations encounters difficulties as a result of the use of Lagrangian zoning. In one dimension, this presents no problem, but in two dimensions it becomes a very significant problem. Since the mesh is embedded in the fluid, it distorts as the fluid motion evolves. This may not be a problem in two dimensions if the motion is well behaved. However, shear flows can often develop and this is troublesome. Vortices also cannot be handled by Lagrangian coordinates. Figure 5 demonstrates

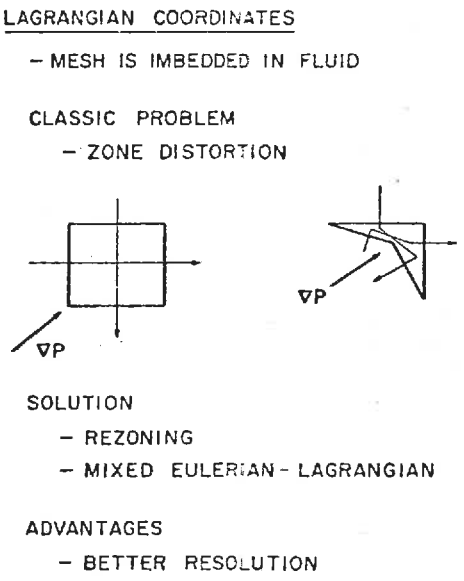

Fig. 5. A schematic diagram of the problems created by the distortions of two-dimensional Lagrangian finite difference zones.

the problem with a very simple example of a strong force pushing diagonally on the corner of a quadrilateral zone. If the other mesh points of the zone remain fixed, the zone develops a concave boundary and becomes a "banana zone." The temperature equations are usually solved in two dimensions by making two "sweeps" through the mesh, one along the k-index lines and then along the l-index lines, while holding the diffusion in the respective transverse direction fixed during each sweep (Fig. 6a). The problems of a banana zone become clear when the sweep path through the zone is indicated as in Fig. 5. Such badly distorted zones also demand very small time steps to maintain stability.

Many different "fix ups" were devised to minimize or correct this zone distortion problem. A more sophisticated generalization of the artificial viscosity can be added to the code that will mitigate zone distortion while maintaining the conservation properties of the fluid. When shear flow can be identified *a priori*, use of "slide lines" may be helpful. As shown in Fig. 6b, specified k or l lines are allowed to decouple and slide against one another. This idea is conceptually simple; however, in practice it is an extremely complex bookkeeping task to implement. A somewhat different approach involves stopping the calculation once zones have distorted sufficiently, and rezoning the problem before continuing. This is commonly done with most large two-dimensional codes, and sophisticated computer graphics programs have been developed to allow the user to automatically reposition mesh points with a light pen. Here again, we attempt to maintain conservation laws. Another method of computation, known as mixed Eulerian-Lagrangian, can also alleviate the zone distortion problem somewhat.

Despite all these drawbacks, there are, nevertheless, good reasons for using Lagrangian coordinates. One property they have is that when the mass of fluid originally falls within the borders of a zone, it remains within that zone throughout the calculation. This mass is, in fact, used as an independent variable rather than r, so equal mass zoning is usually desired. This is very important when materials with very different properties are adjacent to one another as in the case of a DT-filled glass microballoon. In a Eulerian calculation, the mesh remains fixed and the fluid flows through it, so that as time progresses, zones near the original DT-glass interface contain both glass and DT. Very fine Eulerian zoning would be necessary near the interface to maintain spatial resolution; the average properties of the DT-glass mixture would be difficult to determine. There is no mixing in Lagrangian coordinates, and hence no averaging must be done. Since mesh points

follow the fluid in a Lagrangian calculation, there tend to be more mesh points in steep density gradients and fewer points where the gradient is small, just as there should be to maintain good resolution. These considerations most often outweigh the disadvantages of zone distortion.

The other independent variable is the time step, Δt, which was mentioned above in the discussion of stability. Time steps must be computed by the hydrodynamics code because the characteristic time scale may vary by orders of magnitude throughout the course of a calculation. While the implosion process occurs in nanoseconds (10^{-9} s), the thermonuclear burn phase is through a few picoseconds (10^{-12} s) after ignition.

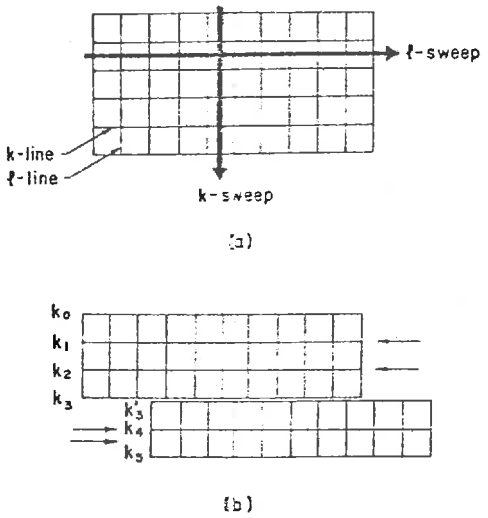

Fig. 6. A schematic of the two-dimensional zoning showing the use of slide lines.

WAZER: An Example of a Laser-Fusion Plasma Hydrodynamics Code

The earliest plasma hydrodynamics code designed for inertial confinement fusion studies was the WAZER code developed at LLL. We will summarize the essential features of this code since it is typical of many of the codes in use today. The code describes the hydrodynamic behavior of a single-fluid, two-temperature plasma in 1-D geometry (planar, cylindrical, or spherical). Specific processes included in the code include:

(i) heat flow due to thermal diffusion

(ii) heat exchange between electrons and ions

(iii) heat loss from the electrons as radiation

(iv) hydrodynamic effects of all energy transformations

(v) addition of energy through absorption of laser light

(vi) production of energy by thermonuclear reactions

(vii) gain or loss of energy by heat conduction across one boundary or by work done on or by the system at the boundary

Hydrodynamic equations; The 1-D hydrodynamic equations in Lagrangian coordinates used in the code are;

$$\frac{\partial V}{\partial t} = \frac{\partial}{\partial m}\left(r^2 u\right)$$

$$\frac{\partial u}{\partial t} = -r^2 \frac{\partial p}{\partial m}$$

Heat Transfer: The temperature equations for the electrons and ions are taken as:

$$c_i \frac{\partial T_i}{\partial t} + T_i P_{T_i} \frac{\partial V}{\partial t} = \frac{\partial}{\partial m}\left(\kappa_i r^2 \frac{\partial T_i}{\partial r}\right) - 2\omega_{ei}(T_i - T_e) + S_i$$

$$c_e \frac{\partial T_e}{\partial t} + T_e P_T \frac{\partial V}{\partial t} = \frac{\partial}{\partial m}\left(\kappa_e r^2 \frac{\partial T_e}{\partial r}\right) - 2\omega_{ei}(T_e - T_i) + S_e$$

where the thermal conductivities are given by

$$\kappa_i = \frac{40\left(\frac{2}{\pi}\right)^{3/2} k\,(kT_e)^{5/2}}{\sqrt{m_i}\,(Ze)^4 \ln\Lambda_i} = \kappa_i(V, T_i)$$

$$\kappa_e = \frac{40\left(\frac{2}{\pi}\right)^{3/2} k(kT_e)^{5/2}}{\sqrt{m_e}\,e^4 \ln\Lambda\,(Z + 3.47 + 0.26\ln Z)} = \kappa_e(V, T_e)$$

and the electron-ion energy exchange coefficient is

$$\omega_{ei} = \frac{\sqrt{2\pi/k}\;\left(N_e Z e^2\right)^2 V \ln\Lambda}{m_i m_e \left[\left(T_e/m_e\right) + \left(T_i/m_i\right)\right]^{3/2}}$$

Radiation: Heat loss through bremsstrahlung is modeled by a sink term in the electron temperature equation;

$$S_{rad} = 2\omega_r T_e$$

where

$$\omega_r = \left[\frac{2^5 N_i Z^3 e^6 V}{3h m c^3}\right]\left(\frac{2\pi k}{m_e T_e}\right)^{1/2} = \omega_r(V, T_e)$$

The code does not explicitly treat the transport or reabsorption of radiation.

Equation of State: A variety of equation of state models can be used. However in simple forms of the code it is common to use an ideal gas model:

$$p = NkT$$

$$e = \frac{3}{2} NkTV$$

$$p_T = Nk$$

$$c = \frac{\partial e}{\partial T} = \frac{3}{2} Nk V$$

Absorption of Laser Light: If ϕ is the photon flux, then the energy source term due to laser light energy absorption which appears in the electron temperature equation is

$$S_e = \kappa V \phi$$

where κ is the light absorption coefficient. We can break the light flux into two components, an inward-directed component ψ^- and an outward-directed component ψ^+

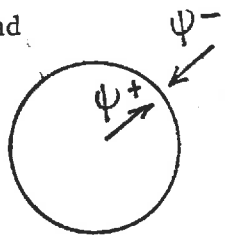

$$\phi = \frac{1}{r^2} (\psi^+ + \psi^-)$$

The light flux enters the system from the outer boundary such that.

$$\psi^-(r_{max}) = \Phi(t)$$

It then passes through the zones of the plasma as governed by

$$\frac{d\psi^-}{dr} = \kappa \psi^-$$

When it reaches the critical surface (or the origin of an underdense spherical plasma), it is reflected and propagates back outward as

governed by:

$$\frac{d\psi^+}{dr} = -\kappa \psi^+$$

The light absorption coefficient can be modeled in several ways, If only classical (inverse bremsstrahlung) absorption is present, we would take:

$$\kappa_{IB} = A N_e N_i Z^2 \left(\frac{I_o}{\hbar\omega}\right)^{7/2} \frac{F(\hbar\omega/kT_e)}{\sqrt{1-(\omega_p/\omega)^2}} = \kappa_{IB}(V, T_e)$$

However it is more common to model the absorption assuming an anomalous process such as resonance absorption or parametric excitation occurs in the neighborhood of the critical surface, Typically one simply assumes that a certain fraction of the incident laser light is dumped into the first overdense zone.

Thermonuclear reactions: In a DT fueled pellet, one solves the rate equations

$$\frac{\partial N_T}{\partial t} = -\langle v\sigma_{DT}\rangle N_T N_D + \frac{1}{4}\langle v\sigma_{DD}\rangle N_D^2$$

$$\frac{\partial N_D}{\partial t} = -\langle v\sigma_{DD}\rangle N_D^2 - \langle v\sigma_{DT}\rangle N_T D_D$$

A variety of options can be used to describe the fusion energy release. In very dilute implosions, one can simply assume that the alphas and neutrons carry off the energy, However in dense implosions one usually assumes that the alphas deposit their energy immediately as

$$S_{DT} = (3.6\,MeV)\langle v\sigma_{DT}\rangle N_D N_T V$$

The partitioning of the alpha energy deposition between electrons and ions can be modeled by

$$S_i = \frac{T_e S_{DT}}{32 + T_e} + \frac{T_e S_{DD}}{120 + T_e}$$

$$S_e = \frac{32 S_{DT}}{32 + T_e} + \frac{120 S_{DD}}{120 + T_e}$$

Other Features;

(i) Most such codes contain the capability to calculate total energy balances as a check on the accuracy of the code.

(ii) The time steps used in the code are usually variable. They are restricted by the Courant condition which demands that $\Delta x/\Delta t$ should not exceed the rate at which a disturbance would be propagated through the medium hydrodynamically. They are frequently also determined by demanding that the fractional density or temperature change of any zone in a given time step be less than some limit.

A flow diagram for the code calculations is given below.

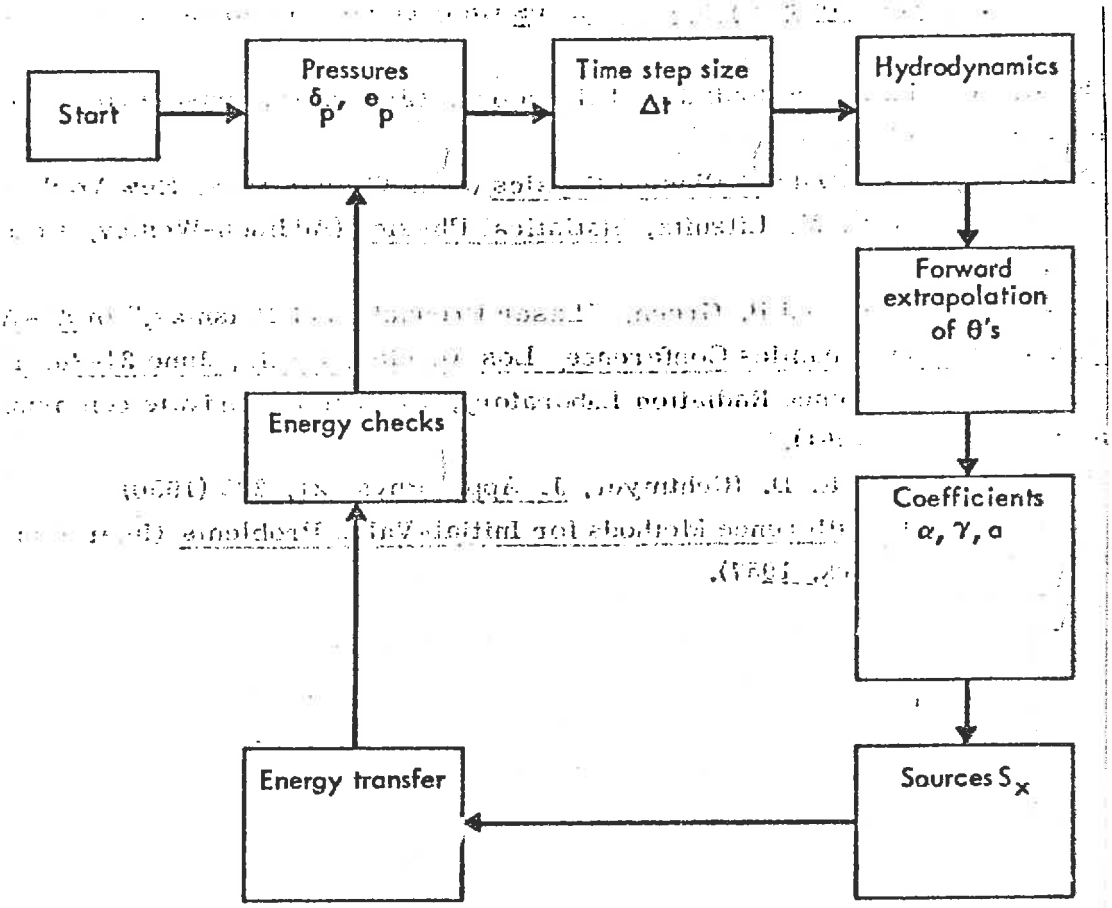

6.2. PARTICLE TRANSPORT

In addition to plasma hydrodynamics, several transport processes should be considered when modeling laser fusion plasmas. These include radiative transfer, suprathermal electron transport, and charged particle fusion reaction product transport. Reaction neutron product transport might also be important for very high density pellets. Each of these particles possesses an mfp that is considerably longer than the characteristic scale length of the hydrodynamic background plasma, at least in parts of the plasma. This behavior rules out the possibility of treating these species within the hydrodynamic framework. These particles are treated as separate species that interact with the plasma fluid through gain and loss terms in the temperature equations and through a momentum source term in the equation-of-motion.

With many particles "created" and "destroyed" by thermonuclear reactions and heating of thermal electrons up into the suprathermal distribution, the continuity equation must also have a gain and loss term,

$$\frac{\partial \rho}{\partial t} + \nabla \cdot \rho = G - L \ . \qquad (11)$$

In practice, in Lagrangian coordinates, mass is automatically conserved by the zones so this gain and loss computation is really a matter of bookkeeping.

The transport of radiation is not discussed in detail, except to point out some of the standard methods of solution. If the radiation mfp is short enough, the distribution function can be assumed to be the local thermal Planckian distribution and the radiation can be characterized by its own temperature and temperature diffusion equation. This treatment is consistent with the hydrodynamic treatment of the plasma fluid. The transport equation itself also can be directly solved using S_N or Monte Carlo techniques. These can be very expensive to use in a time-dependent problem and are used only in special cases. The transport equation can be expanded in angular moments to produce a diffusion equation or the P_N equations. The multigroup diffusion equation must be flux limited to account for long mfp's or the P_1 equations can be solved for the frequency-dependent energy density and energy flux, the so-called Variable Eddington method.[24]

More peculiar to laser fusion, however, are the transport of suprathermal electrons and charged particle reaction products. Suprathermal electrons play a significant role in the pellet implosion process, since they are created by laser light absorption near the critical density in the underdense corona region of the plasma and stream inward carrying their energy into the dense plasma core. With energies in excess of 100 keV, they may not be stopped until they stream through the ablation front into the cold adiabatically compressed plasma ahead of the front. This heats up the cold plasma, resulting in nonadiabaticity and a degradation of the implosion. To remedy this situation, pellets are designed with high-Z material surrounding the DT fuel that serves both as a tamper/pusher to enhance the implosion and as a shield against the suprathermal electrons and high-frequency x rays. Reaction product charged particles are principally ${}_1T^3$, ${}_2He^3$, ${}_1H^1$, and ${}_2He^4$ from the reactions

$${}_1D^2 + {}_1T^3 \rightarrow {}_2He^4\,(3.5\ \text{MeV}) + {}_0n^1\,(14.1\ \text{MeV}) \qquad (12)$$

and

$${}_1D^2 + {}_1D^2 \rightarrow \begin{cases} {}_2He^3\,(0.82\ \text{MeV}) + {}_0n^1\,(2.45\ \text{MeV}) \\ {}_1T^3\,(1.01\ \text{MeV}) + {}_1H^1\,(3.02\ \text{MeV}) \ . \end{cases} \qquad (13)$$

The temperature of the burning DT plasma is typically 4 to 100 keV, so each of the reaction products is nonthermal.

The method that has received the greatest use to date for the transport of these nonthermal particles in a laser fusion hydrodynamics code is multigroup flux-limited diffusion theory. This method is used in LASNEX, a two-dimensional Lagrangian hydrodynamics code written at Lawrence Livermore Laboratory.[19] Flux-limited diffusion uses a diffusion equation to model transport with a flux-corrected diffusion coefficient to account for long mfp situations. The slowing down is done in a multigroup structure, so the equations look like[25]

$$\frac{\partial N_g}{\partial t} - \nabla \cdot D_g \nabla N_g + L_g N_g = S_g \ , \qquad g = 1, \ldots, G \ , \qquad (14)$$

[24] P. CAMPBELL, *Int. J. Heat Mass Transfer*, **12**, 497 (1969).

[25] E. CORMAN, W. LOEWE, G. COOPER, and A. WINSLOW, *Nucl. Fusion*, **15**, 377 (1975).

where $N_g(r,t)$ is the density of particles with energies between E_g and E_{g-1} in d^3r at time t, and L_g is some slowing down operator that removes and adds particles from energy group g. Several questions concerning the applicability of these equations to charged particle transport must be answered:

1. How should the transport cross section in the diffusion coefficient be defined?
2. How should the slowing down operator be defined?
3. How good is the diffusion approximation and how does flux limiting help?
4. How good is the multigroup structure for this type of slowing down problem?

The answers to the first two questions come from the Fokker-Planck equation. This equation describes the evolution of the charged particle distribution function, $f_\alpha(r,v,t)$, where α denotes the particular species of particle being transported. The equation takes the form

$$\frac{\partial f_\alpha}{\partial t} + v \cdot \frac{\partial f_\alpha}{\partial r} + \frac{F_\alpha}{m_\alpha} \cdot \frac{\partial f_\alpha}{\partial v} = \left(\frac{\delta f_\alpha}{\delta t}\right)_c \quad , \qquad (15)$$

where

$$F_\alpha = q_\alpha(E + v \times B)$$

and

$$\left(\frac{\delta f_\alpha}{\delta t}\right)_c = \frac{\partial}{\partial v} \cdot \left(\mathrm{K} \cdot \frac{\partial f_\alpha}{\partial v} - L f_\alpha\right) \quad , \qquad (16)$$

where K and L are the velocity space diffusion and drag terms. Due to the long range of the Coulomb potential, charged particles slow down through many small angle scattering events. The right side of this equation models this process and is significantly different from the corresponding term in neutron transport. Solution of the Fokker-Planck equation in an infinite medium yields several characteristic transport times (or lengths) of interest. The first is the time (or length) that a fast particle takes to deflect through a 90-deg angle, which we call τ_D. For ions streaming through a thermal plasma, this is

$$\tau_D = \frac{(m/2)^{1/2} E^{3/2}}{2\pi Z^2 e^4 \ln \Lambda_I \sum_i Z_i^2 n_i} \quad , \qquad (17)$$

where m, E, and Z are the mass, energy, and charge of the fast particle and Z_i and n_i are the charge and density of the i'th ionic species. Using this time, a macroscopic transport cross section can be defined as

$$\Sigma_{tr} = \frac{1}{v\tau_D} \quad , \qquad (18)$$

and the multigroup diffusion coefficient is given as

$$D_g = \frac{v_g}{3\Sigma_{tr_g}} = \frac{v_g}{3/(v_g \tau_{Dg})} \quad . \qquad (19)$$

Time τ_D is obtained from the Fokker-Planck equation by considering the K term in the collision model. This term changes the distribution function by relaxing it toward isotropy.

The slowing down of particles depends on both the K and L terms in the Fokker-Planck equation. For fast ion transport at high energy, the L term dominates and is due to interactions with electrons, but as the fast ion slows down, the K term dominates and slowing is due to larger angle collisions with thermal ions. In Fig. 7, dv/ds is plotted for the thermal electron and ion contributions as a function of fast particle velocity. The domination of the electrons at high energy and ions at low energy is clearly seen.

If we let

$$\frac{dv}{dt} = v \frac{dv}{ds} \quad , \qquad (20)$$

and define

$$\tau_g = v_g/(dv_g/dt) \quad , \qquad (21)$$

then the slowing down operator can be expressed as

$$L_g = N_g/\tau_g - N_{g-1}/\tau_{g-1} \quad , \qquad (22)$$

and the multigroup diffusion equations are written as

$$\frac{\partial N_g}{\partial t} - \nabla \cdot D_g \nabla N_g + N_g/\tau_g - N_{g-1}/\tau_{g-1} = S_g \quad ,$$

$$g = 1, \ldots, G \quad , \qquad (23)$$

where we assume particles can only scatter into group g from the next higher energy group. When particles reach thermal energies, they are added back into the hydrodynamic thermal plasma.

The answer to the third question is, of course, that diffusion theory is not a very good transport approximation. However, it is partially corrected by flux limiting. Recall that the diffusion

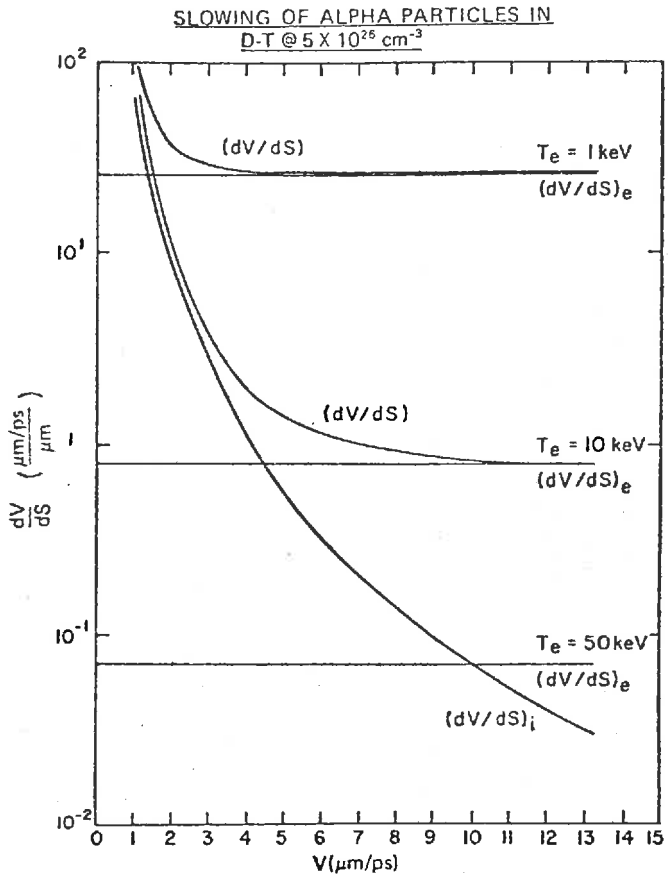

Fig. 7. A plot of *dv/ds* versus the velocity of a fast alpha particle slowing down in a DT plasma, for electron temperature of 1, 10, and 50 keV.

equation is obtained from the particle continuity equation,

$$\frac{\partial N}{\partial t} + \nabla \cdot Q + LN = S \quad , \tag{24}$$

by using the transport law

$$Q \simeq -D\nabla N \quad . \tag{25}$$

In the free streaming limit,

$$Q = vN \quad , \tag{26}$$

and this is the maximum flux that could arise.

In the situation where

$$N/(\nabla N) < \lambda_{\text{mfp}} \quad , \tag{27}$$

(that is, in the transport regime), the magnitude of the flux would be overestimated if Fick's Law expression,

$$|Q| = D\nabla N \quad , \tag{28}$$

were used since $D\nabla N > vN$. This unphysical problem can be avoided by redefining the transport law as

$$Q = \frac{-D\nabla N}{1 + \left|\dfrac{\tilde{D}\nabla N}{Q_{\max}}\right|} = -\tilde{D}\nabla N \quad , \tag{29}$$

where $Q_{\max}$ is chosen in some appropriate way to correspond to the flux in the free streaming limit.

The expression, $\tilde{D}\nabla N$, is designated in this way because the gradient operator does not enter the difference equations in an active manner. This whole expression is simply estimated from values of D and N from the previous time step, and the flux-limited diffusion coefficient $\tilde{D}$ is computed using this estimate. This *ad hoc* diffusion coefficient ensures physically plausible transport of the particles when diffusion theory holds

$$\frac{\tilde{D}\nabla N}{Q_{\max}} \ll 1 \quad , \tag{30}$$

so

$$Q = -D\nabla N \quad . \tag{31}$$

When the mfp is very long,

$$\frac{\tilde{D}\nabla N}{Q_{\max}} \gg 1 \quad , \tag{32}$$

and

$$Q = Q_{\max}\left(\frac{-D\nabla N}{|\tilde{D}\nabla N|}\right) \tag{33}$$

where the quantity in parentheses is a unit vector.

The accurate slowing down of charged particles by multigroup methods can be a problem. This is a continuous slowing down process with a strong coupling between the energy, space, and time variables. This can result in a great deal of numerical diffusion in energy space, with as many as 100 groups required to give reasonable accuracy.

The multigroup equations also are of only first-order accuracy in the energy variable and usually are of only first-order accuracy in time as well, since a fully implicit differencing scheme must be used to allow the hydrodynamic time step to be used:

$$\frac{N_g^{n+1} - N_g^n}{\Delta t^{n+1/2}} = \nabla \cdot D_g \nabla N_g^{n+1} - N_g^{n+1}/\tau_g + N_{g-1}^{n+1}/\tau_{g-1} + S_g^{n+1/2} \quad . \tag{34}$$

Of course, this is a general scheme that can be used to model almost any kind of particle transport. It produces reasonably good results for nondiffusive problems and is very straightforward to implement numerically, even in two dimensions. It embodies the essentials of most transport problems and should give reasonable answers for integrated quantities, such as total reaction rates. However, care should be taken when interpreting detailed results of the flux-limited diffusion treatment of transport-dominated problems. Over less than 1 mfp, as shown next, flux-limited diffusion can entirely miss details for certain types of problems.

An alternative approach to charged particle transport is to use techniques that are specifically adapted to the behavior of the particular charged particles. In Fig. 8, borrowed from Winsor's paper,[26] we see that the ion beam streaming through a background plasma has less dispersion in velocity space than the electron beam. The electron beam becomes much more isotropic as it slows down due to large-angle scattering; however, the ion beam simply slows down without much scattering out of the beam trajectory, $v_{\parallel}$. The electron behavior tends to reinforce the applicability of flux-limited diffusion theory as a description of electron transport, for that treatment demands that the distribution function be nearly isotropic. In the case of thermonuclear reaction products, however, ion beam results indicate that isotropy is not reached until near the end of the particle path to thermalization. This behavior can be used to great advantage in modeling the reaction product transport, for it says that a simple straight line trajectory will be a good approximation. This is the basic assumption used in the time-dependent particle tracking algorithm.

In a one-dimensional Lagrangian hydrodynamic treatment, the spherical plasma is divided into

[26] N. K. WINSOR, *Nucl. Sci. Eng.*, 64, 33 (1977).

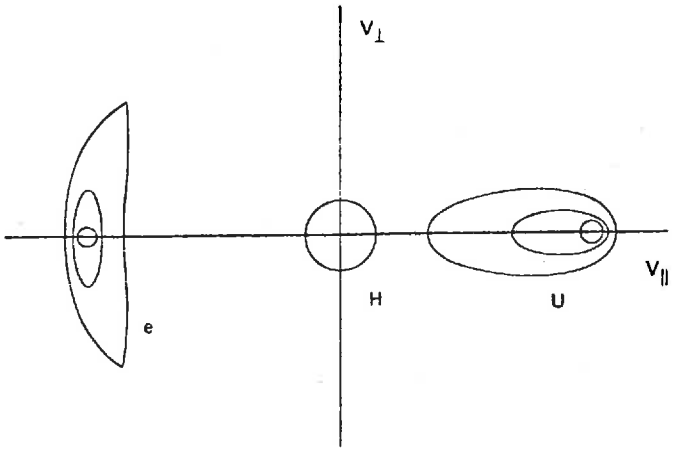

Fig. 8. A plot of velocity space at different times for beams of electrons and ions in a hydrogen background plasma.

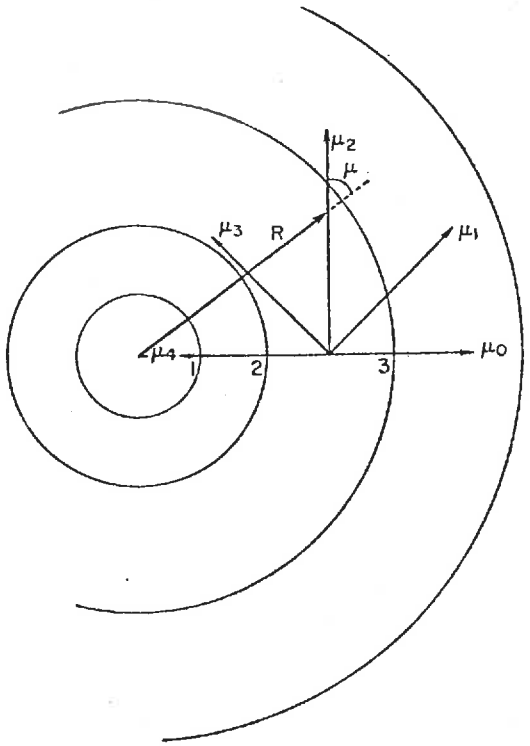

Fig. 9. A schematic diagram of the time-dependent particle tracking method in a spherical plasma.

concentric shells or "zones" and the plasma behavior is represented by the finite difference solution to the equations for density, fluid velocity, and electron and ion temperature, as discussed in Sec. II. To model the charged particle fusion reaction products ($_1T^3$, $_2He^3$, $_1H^1$, $_2He^4$), we assume that those created in each zone stream along a finite number of rays that originate in the center of the zone (Fig. 9). As they stream, they experience the Coulomb drag force represented by the L terms in the Fokker-Planck equation, Eq. (15), and a range-energy relation can be expressed in the following form[27]:

$$-\frac{dv}{ds} = A + B/v^3 = K(v)$$

$$A = A_0(Z^2/m)(\ln \Lambda_e) n_e/T_e^{3/2}$$

$$B = B_0(Z^2/m)(\ln \Lambda_i) \sum_i (Z_i^2 n_i/\rho) \quad , \qquad (35)$$

where A is due to scattering on thermal electrons and B is for thermal ions. This is the expression plotted in Fig. 7. The straight line trajectory is valid during most of the slowing down process; however, near the end, the fast particle loses its energy in large-angle collisions with thermal ions. In the transport of fusion reaction products, it is the energy redeposition back into the thermal electrons and ions that is of greatest importance. Near the end of a reaction product trajectory, it has very little energy remaining; hence, the error in redeposition is small. Equation (35) is solved along a ray as it passes from one zone boundary to the next by integrating along its exact path length,[27]

$$\Delta s = \int_{v_0-\Delta v}^{v_0} g(v)dv \quad , \qquad (36)$$

where Δs is the distance across the zone along the particle trajectory, v_0 is the particle velocity on entering the zone, Δv is the velocity loss in crossing the zone, and

$$g(v) = [K(v)]^{-1} \quad . \qquad (37)$$

The A and B terms are evaluated using the temperature and density of the zone. Equation (36) is an integral equation for Δv and can be solved using a Taylor expansion

$$g(v) \simeq g(v_0) + (v - v_0)g'(v_0) = g_0 + (v - v_0)g_0' \quad . \qquad (38)$$

Substitution into Eq. (36) yields

$$\Delta s \simeq g_0 \Delta v - \tfrac{1}{2} g_0'(\Delta v)^2 \quad . \qquad (39)$$

This expression can be inverted and solved to second order for Δv as

$$\Delta v = \Delta s/[g_0(1 - \tfrac{1}{2} g_0'/g_0^2 \Delta s)] \quad , \qquad (40)$$

or equivalently

$$\Delta v = K(v_0)\Delta s/[1 + \tfrac{1}{2} K'(v_0)\Delta s] \quad . \qquad (41)$$

[27]H. BRYSK, "Reaction Product Transport in a Fusion Pellet," KMSF U275, KMS Fusion, Inc. (1975).

This procedure is accurate for $\Delta v/v_0 \ll 1$; however, should $\Delta v/v_0 \geq 1$, then the particles have thermalized within the zone so again the error to energy redeposition is not serious. Only the partition of energy to the electrons and ions is important. The total energy lost in a zone is simply

$$\Delta E = \tfrac{1}{2} m[v_0^2 - (v_0 - \Delta v)^2] N \ , \qquad (42)$$

where N is the number of ions streaming along a given ray. The fraction of this energy going to the electrons is

$$\Delta E^{(e)} = A(\Delta s/\Delta v)\, \Delta E \ . \qquad (43)$$

Should the particles slow to thermal energy in the zone, i.e., if $\Delta v/v_0 \sim 1$, then the fraction of energy going to electrons can be obtained from the results of an infinite medium calculation, tabulated as a function of electron temperature. Then the loss to ions in either case is

$$\Delta E^{(i)} = \Delta E - \Delta E^{(e)} \ . \qquad (44)$$

In addition to energy redeposition, the nonthermal ions also impart momentum to the zone

$$m \Delta v N \cos\alpha = M \Delta u \ , \qquad (45)$$

where M is the zone mass, m is the nonthermal mass, and α is the angle between the trajectory of the ions and the outward radial direction. The algorithm to compute the energy redeposition from the reaction product ions would involve a computation for each reaction product, in each finite difference zone, and along each straight line ray originating in that zone. This computation would track the ion trajectories from creation to thermalization or escape, and would tally the amount of energy and momentum deposited in each zone along their path. This algorithm must be executed for each reaction product that is transported from each finite difference zone along each straight line ray and for each past time level that was remembered.

To advance the solution to the hydrodynamics equations by one time step, reaction rate equations must be solved for each zone and the particles produced on this time step divided among the different rays. Then three nested loops must be executed to determine the amount of energy and momentum deposited in each zone. This information can then be used as a source term in the hydrodynamic equations. This algorithm is very simple and is straightforward to implement in a hydrodynamics computer code. It does not use any finite difference methods and suffers from no numerical instabilities.

The particle tracking algorithm discussed thus far assumed an "adiabatic" approximation to the time dependence of slowing down.[27] Specifically, a slowing down calculation is done for each time step in the hydrodynamics calculation. Fast ions are "forced" to thermalize or escape the plasma during the time step on which they are created. This is, of course, an assumption that must be tested for its validity. A 3.5-MeV alpha particle has an initial velocity of 13 μm/ps. If this particle were born near the hot center of an otherwise cold pellet core, it may need to travel 15 μm before it is slowed appreciably by the surrounding cold plasma. Assuming no energy loss in the hot central "microcore," this particle requires 1.15 ps to reach the cold plasma, a time that is easily greater than typical time steps in a thermonuclear burn-hydrodynamics computation. In such calculations, time steps often are as short as 0.01 ps, so we see that the "adiabatic" approximation is not necessarily a good one; however, the only real proof is to compare it to a fully time-dependent calculation. The particle tracking method can be made time dependent at the sacrifice of its attractive simplicity. To do this, we note that a "bunch" of particles (for example, alphas) created at position $r_{j-1/2}$ at time $t^{n+1/2}$ and traveling along a ray in direction μ_m can be totally characterized by four numbers: the number of particles in the bunch, N; the position of this bunch of particles, R; the direction of these particles with respect to the radius vector to position R, μ; and the velocity of the particles, V. These are displayed in Fig. 9. Particles can now be "tracked" from their origin or birth place to the position they reach after time Δt, the hydrodynamic time step. At this time, their new position, direction, velocity, and number can be "remembered" until the next time step. Such an algorithm requires that the energy-time relationship also be integrated along the rays:

$$-\frac{dv}{dt} = -\frac{v dv}{ds} = Av + B/v^2 = J(v) \ . \qquad (46)$$

In exact analog to the solution of Eq. (36), Eq. (47) can be integrated to give

$$\Delta v = J_0 \Delta t/(1 + \tfrac{1}{2} J_0' \Delta t) \ . \qquad (47)$$

In addition to these relations, we must also know the distance traveled in a time Δt and the time taken to move a distance Δs. These are given by

$$\Delta t_{\Delta s} = (\Delta v/J_0) + \tfrac{1}{2} J_0'(\Delta v/J_0)^2 \qquad (48)$$

and

$$\Delta s_{\Delta t} = (\Delta v/K_0) + \tfrac{1}{2} K_0'(\Delta v/K_0)^2 \ . \qquad (49)$$

The algorithm to compute the time-dependent transport is considerably more complicated than in the time-independent case and is shown in Fig. 10. This algorithm must be executed for each reaction product that is transported from

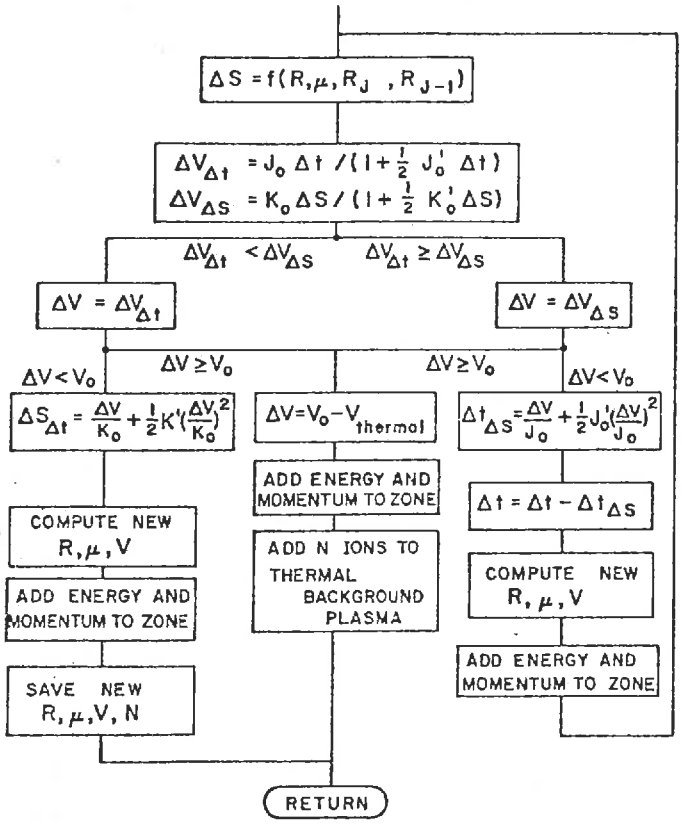

Fig. 10. A block diagram of the algorithm that must be executed to implement the time-dependent particle tracking method in a hydrodynamics code.

each finite difference zone along each straight line ray and for each past time level that was remembered. This algorithm involves remembering the positions, directions, and velocities of particles created on previous time steps that are still streaming. Saving all this information requires N_s words of computer memory, where

$$N_s = N_Z \times (N_A^+ N_T^+ + N_A^- N_T^-) \times N_p \times 4 \ ,$$

and where

N_Z = number of zones

N_A^+ = number of directions with $\mu > 0$

N_A^- = number of directions with $\mu \leq 0$

N_T^+ = number of time steps to remember particles starting in a $\mu > 0$ direction

N_T^- = number of time steps to remember particles starting in a $\mu \leq 0$ direction

N_p = number of different kinds of particles to be tracked.

The number of time steps necessary to follow particles starting in an outward direction is less than the number required for inward-directed particles, and provision is made to optimize the amount of necessary storage by utilizing this fact. Also, with such a scheme there is always the possibility that a group of particles that were remembered for $N_T^{\pm}$ future time steps will have neither thermalized nor escaped the plasma. In such a case, these particles are forced to thermalize or escape by using the adiabatic approach previously discussed. In practice, enough storage can usually be provided to minimize the effects of this problem. The advantage of this time-dependent particle tracking (TDPT) algorithm is the good treatment of the slowing down process and energy redeposition at a very reasonable cost. The disadvantage is the rather complex logic required to execute the algorithm necessitating very careful programming.

The first test of the TDPT algorithm is really a test of the accuracy of the slowing down treatment. In this test the energy redeposition to electrons and ions as a function of position from a point source of 3.5-MeV alphas is computed using TDPT, Monte Carlo, and flux-limited 100-group diffusion theory. The results shown in Fig. 11

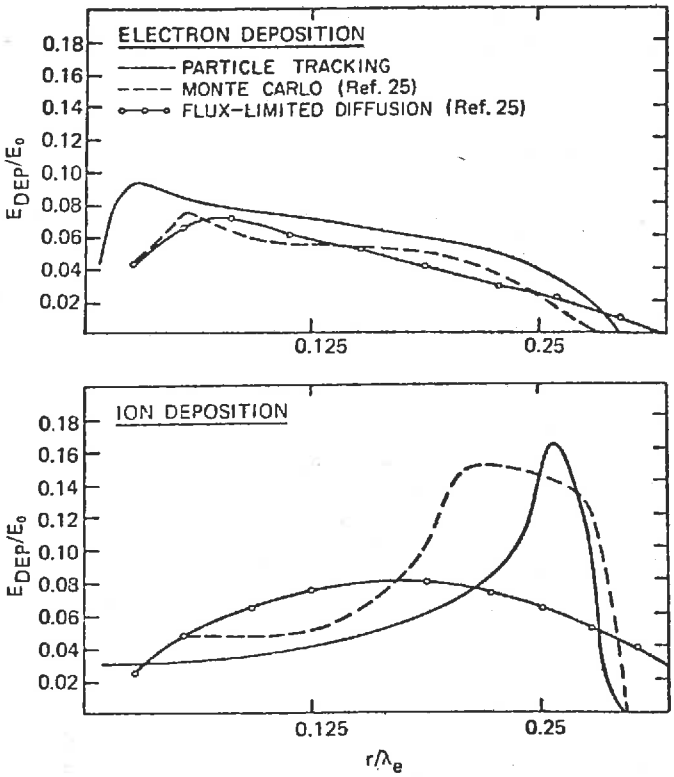

Fig. 11. Plots of the fraction of alpha particle energy deposited in electrons and ions as a function of the distance traveled by the alpha particle measured in units of its mfp to a collision with an electron.

indicate that the TDPT algorithm reproduces the most accurate Monte Carlo results better than flux-limited diffusion theory. Since the behavior displayed in Fig. 11 occurs in a distance that is <1 mfp for a collision between an alpha particle and an electron, we would expect that a transport theory treatment is necessary to describe it. This is in fact the case. Flux-limited diffusion theory, even with 100 groups, is unable to even qualitatively reproduce the ion redeposition results. Time-dependent particle tracking reproduces the Monte Carlo results remarkably well considering the electron temperature in this example was chosen to be 50 keV. At such electron temperatures, the straight line approximation to the fast ion trajectory is not necessarily good; however, the "Bragg peak" in the redeposition to the thermal ions is predicted by the TDPT method with nearly the correct amplitude and position from the origin. The straight line approximation forces the peak to be a little further from the origin and also narrower than the Monte Carlo result because no backscatter is allowed.

The second test of the TDPT method involves sensitivity of integrated burn results to changes in important parameters in the TDPT model. The results to be studied are the total number of 14-MeV neutrons produced and the total number of alpha particles escaping from a 3 g/cm^2 pellet core. These are computed using simulations with varying values of initial directions, of the number of remembered time steps, and of the minimum allowable time step. The results shown in Fig. 12 indicate that the total number of neutrons produced from DT reactions is insensitive to the variation of these parameters. The worst deviation is when only one time level is remembered, which is equivalent to the adiabatic approximation. Even here the deviation is not great. The number of escaping alpha particles is rather insensitive to these parameters also, except for the case of the adiabatic approximation. Here the number of

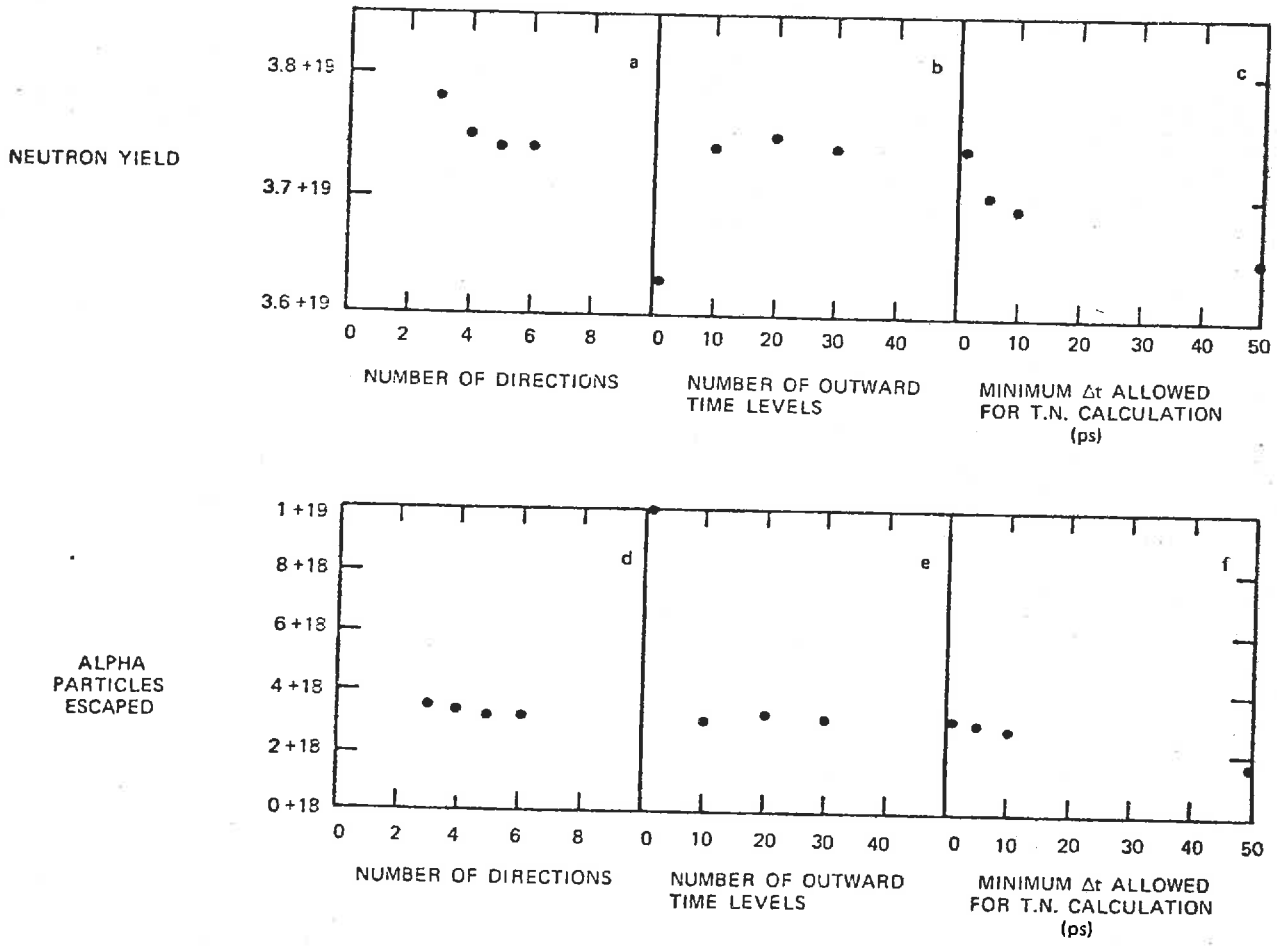

Fig. 12. The neutron yield and number of escaping alpha particles are plotted as functions of varying parameters needed to implement the time-dependent particle tracking method.

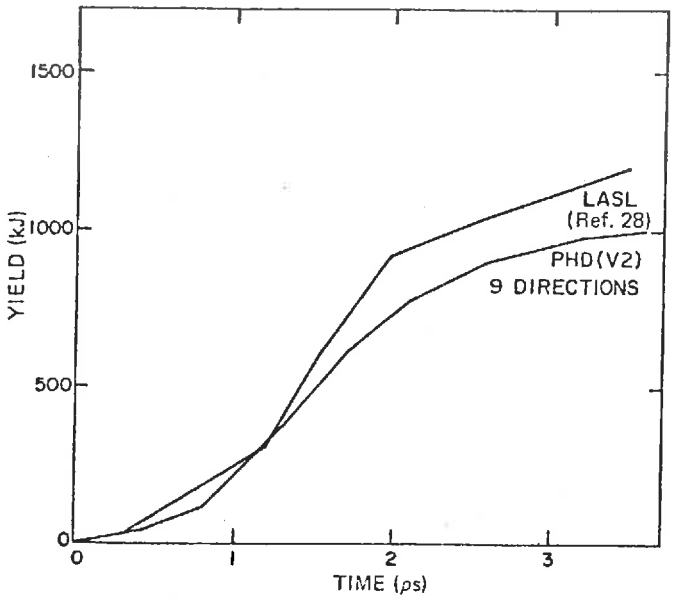

Fig. 13. The total thermonuclear yield plotted as a function of time for the S_N treatment of the reaction product transport and the TDPT method.

escaping particles is grossly overestimated; however, as noted earlier, the yield is about the same as other more exact time-dependent problems. These calculations are for a pellet core with a 1-mg mass and a 3 g/cm^2 density-radius product. Therefore, the yield of a nonmarginal pellet core is insensitive to the parameters used in the TDPT transport method. However, the number of escaping particles can be affected, so care must be taken if escaping charged particle spectra are to be computed.

The final result is a comparison with a full thermonuclear burn-hydrodynamics calculation. In this case, the TDPT result is within ~15% of the final yield of the comparison calculation, shown in Fig. 13. This indicates that the TDPT method coupled to a hydrodynamics code, PHD-II, gives results comparable to discrete-ordinates transport of the charged particles.

The discussion in this section centered on two different transport methods. One presumes diffusion and corrects for streaming, while the other presumes streaming and must correct for large-angle scattering. From Fokker-Planck studies of the detailed behavior of charged particles, it would seem that flux-limited diffusion is most applicable to the suprathermal electron transport, while time-dependent particle tracking does very well for nonthermal ion transport.

[28]G. FRALEY et al., *Phys. Fluids*, **17**, 479 (1975).

IV. SUMMARY

Laser fusion hydrodynamics and transport is a relatively new field that has room for much more development. This is apparent from the very few laser fusion codes that exist today. The most notable and complete code is the LASNEX code[24] with two-dimensional Lagrangian hydrodynamics and flux-limited diffusive transport. Another two-dimensional code with a sophisticated treatment of magnetic fields and radiative processes is the CYLAZR code,[29] a Eulerian code written at the Naval Research Laboratory. Each of the principle laboratories involved with laser fusion research also has its own one-dimensional code.

As more experiments are being undertaken, it becomes increasingly apparent that so-called anomalous effects are not just a first-order correction to the classical hydrodynamics problem, but are, in fact, dominating the results. Modeling these processes requires the treatment of particle distribution functions that may be far from equilibrium. Flux-limited multigroup diffusion is a first attempt to include these effects in a hydrodynamics code; however, the necessity for coefficient adjustments to obtain good agreement with experiment and the sensitivity of results to numerical parameters such as zoning, time steps, and differencing techniques raises doubts about the ability of these simple models to provide good insight into laser plasma dynamics. Detailed treatment of particle distribution functions and numerical schemes designed for accuracy rather than expediency imply a great increase in computer time for codes that already use large amounts of it. One solution must be to implement these codes with numerical algorithms that are optimal on the new generation of vector processing machines (TI-ASC, CDC-STAR, CRAY-I, etc.). Another partial solution may be to develop more codes or large modular codes that accurately treat very specific problems. While this may seem inefficient, it must be recognized that a code that is designed with enough generality to solve any kind of problem will probably embody too many oversimplifications to do the best job on any specific problem. The nonlinear equations we have discussed require careful consideration of both physics and numerical methods if large inaccuracies are to be avoided. The present codes are very valuable, though, and must continue to be used to point out sensitive and insensitive processes as a guideline for further development.

[29]D. COLOMBANT, K. WHITNEY, D. TIDMAN, N. WINSOR, and J. DAVIS, *Phys. Fluids*, **18**, 1687 (1975).

6.3. PLASMA SIMULATION (PARTICLE CODES)

Plasma physics is an inherently nonlinear phenomenon. Hence a major role is played by plasma simulation codes in which the equations of motion for the particles (ions and electrons) comprising the plasma are integrated directly. In this sense, particle simulation codes represent a microscopic simulation of the plasma dynamics. The basic approach can be understood by the following schematic:

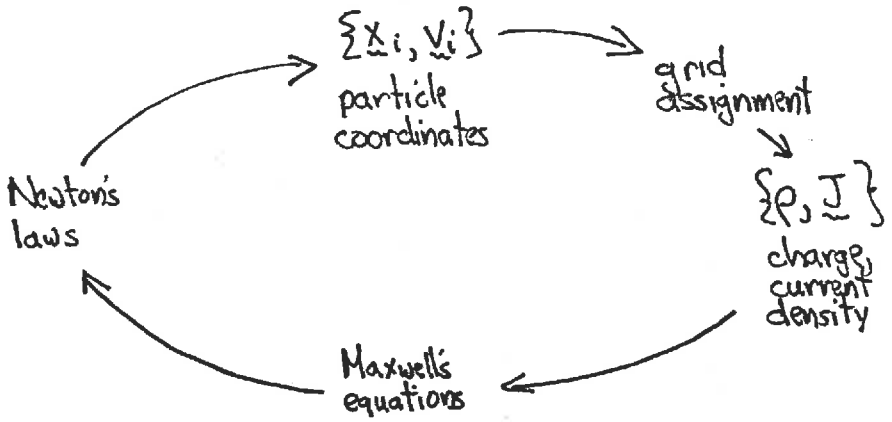

The coordinates of the particles are used to determine a macroscopic charge and current density. These are then used in Maxwell's equations to determine the corresponding electric and magnetic fields. These fields determine the forces acting on the particles, and the corresponding equations of motion are then integrated with these forces to determine the coordinates at the next time step.

There are several difficulties, however. The dynamics of the plasma occur on a time scale of the plasma frequency, hence very small time steps must be taken. Furthermore, the long range interaction implies that many particles interact simultaneously. For example, the effective range of interaction is determined by the Debye length, and in a typical fusion plasma there are perhaps 10^5 to 10^6 particles in a Debye sphere. Therefore one cannot simply solve the equation of motion for each

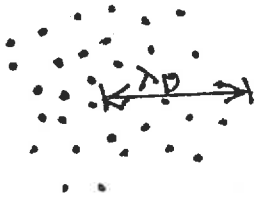

particle

$$m \frac{d^2 \underset{\sim}{r}}{dt^2} = \underset{\sim}{F}_i$$

Rather one must average or smear out the detailed structure over a relatively coarse grid (on the scale of the Debye length rather than the interparticle spacing). This is done by calculating the electromagnetic field on a coarse grid and using each "computer particle" to represent many plasma particles.

To be more precise, consider an electrostatic simulation code in which Maxwell's equations reduce to

$$\underset{\sim}{\nabla} \cdot \underset{\sim}{E} = 4\pi\rho$$

To assign the particle, consider a grid as shown:

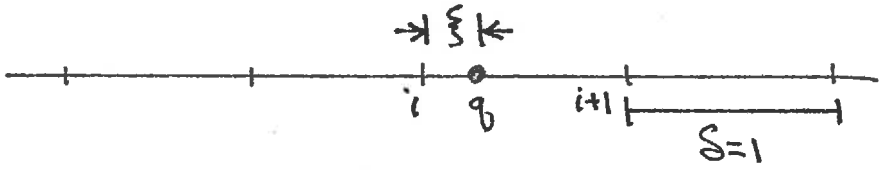

There are two schemes in use to assign charge to the grid:

(i) Nearest grid point (NGP): $p(i) = q$

(ii) Particle in cell (PIC): one interpolates as

$$p(i) = q(1 - \xi)$$

$$p(i+1) = q\xi$$

Next one solves for the electric field using this charge density (where one can either finite difference Poisson's equation directly or use fast Fourier transform methods).

One then maps the field from the grid to the particles; for example, in the PIC scheme a linear interpolation is used so that the force on the particle is

$$F = q\left[(1-\xi)E(i) + \xi E(i+1)\right]$$

The particle positions and velocities are then updated by a leap-frog algorithm (defining position and velocity one-half time step apart to achieve a second order accuracy).

Particle codes are far more complex when the full set of Maxwell's equations are used. Frequently multipole expansions of the radiation field are used.

How good are the plasma simulation? One interest comparison is with the solutions of the Vlasov equation for simple modeled problems:

$$\frac{\partial f}{\partial t} + v\frac{\partial f}{\partial x} - \frac{e}{m}E\frac{\partial f}{\partial v} = 0$$

$$\frac{\partial E}{\partial x} = -4\pi e\left[\int dv f - n_0\right]$$

since $n\lambda_D^3 \to \infty$ in this model. Kruer has compared the nonlinear behavior of large amplitude electron plasma waves with those described by particle codes, with the results as shown on the next page. The agreement with experiment is also quite good.

The state of the art of these codes can be summarized as:

2-D, electromagnetic, relativistic codes
40,000 grid points
single cell $\sim$ 2-3 λ_D
simulated plasma of size $\sim$ 400 x 400 λ_{De}
6 x 6 λ_0 (light wavelength)
5-10 particles per Debye square $\Rightarrow \sim 10^6$ particles
2500 time steps $\Rightarrow$ 20 hours on a CDC-7600

The general approach is to use particle codes to determine how microscopic turbulence affects the local plasma properties, such as energy absorption rates and transport coefficients. This information is then used to adjust the macroscopic description of the plasma in hydrodynamic codes.

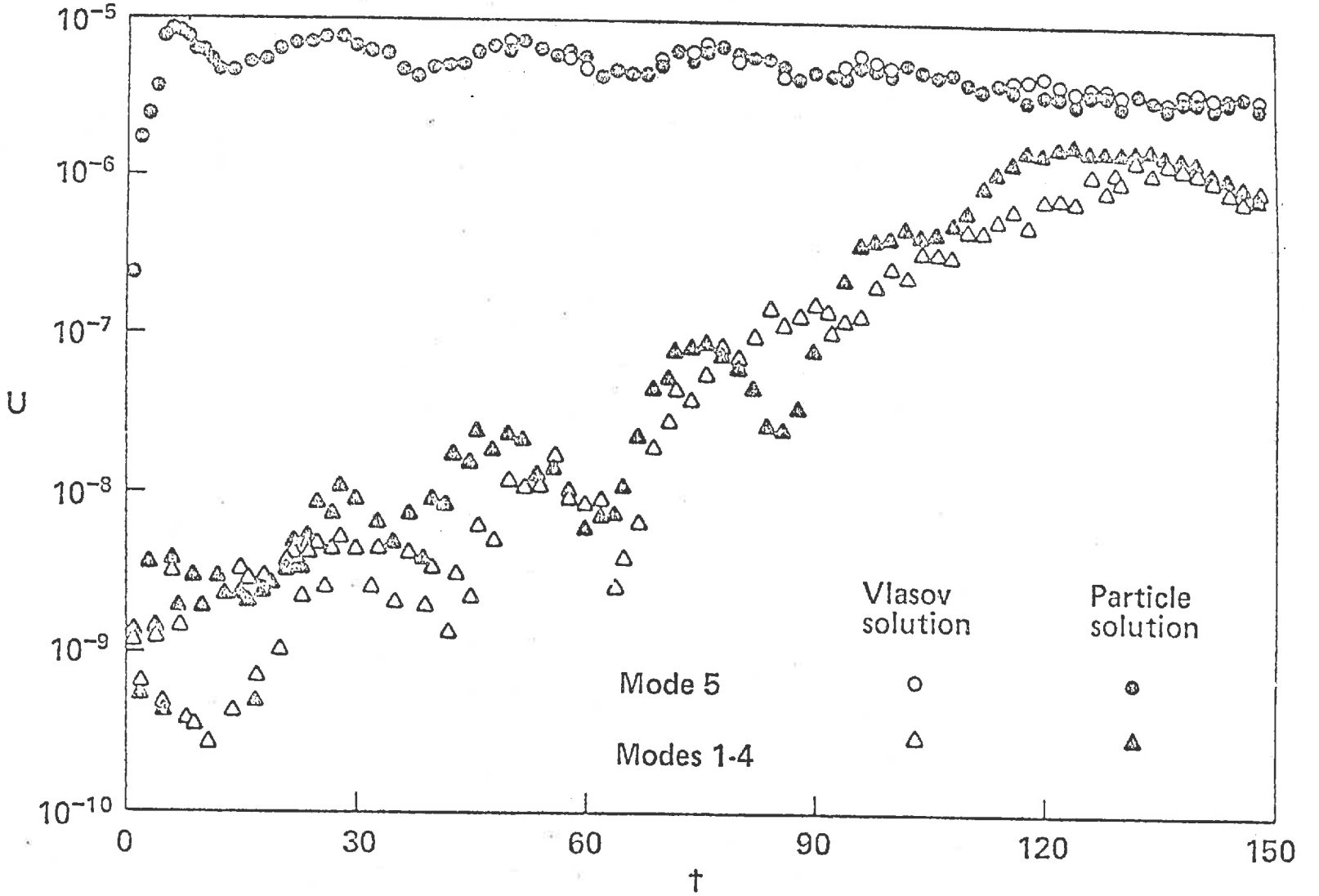
10^{-5}
10^{-6}
10^{-7}
10^{-8}
10^{-9}
10^{-10}
U
0
30
60
90
120
150
t
Vlasov solution
Particle solution
Mode 5
Modes 1-4

CHAPTER 7

DRIVER DEVELOPMENT I: LASERS

A laser is simply a device which can convert electrical (or chemical or gasdynamic) energy into light energy. But the light it generates is "coherent" (in phase) and hence can be transmitted very long distances (e.g., to the moon) and focussed to very tiny spots. To introduce the basic concepts involved in laser operation, consider the interaction of light with a very simple system: a single atom which can exist in one of only two possible energy states. Incident light photons with a frequency ν_{12} such that $h\nu_{12} = E_2 - E_1$ can interact with the atom in one of three ways: absorption, spontaneous emission, and stimulated emission. If we now consider a system of many such two-state atoms,

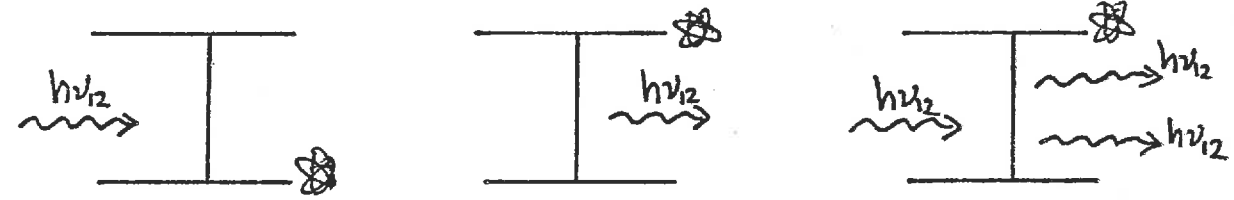

most of which are in their ground state, then it is evident that a photon of frequency ν_{12} incident upon the system would be absorbed. Suppose, however, that most of the atoms were in their excited state, E_2. Then one could induce a growing cascade of photons of frequency ν_{12} using the stimulated emission process. That is, one could achieve light amplification by stimulated emission of radiation.

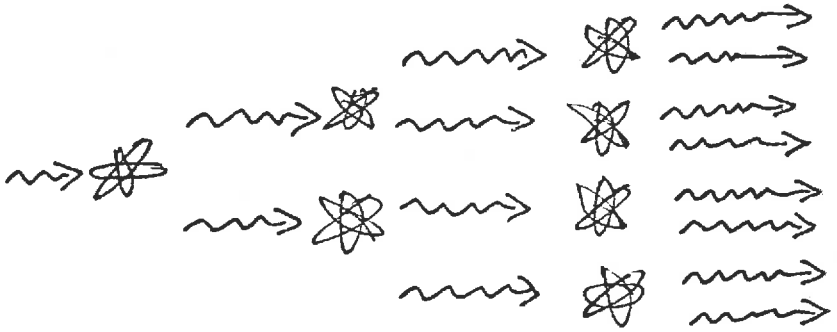

Under normal circumstances there will be many more atoms in the lower energy state (usually the ratio of population densities goes as the Boltzmann factor, $\exp[-(E_2-E_1)/kT]$). Hence we must somehow achieve a "population inversion", that is, prepare the medium so that more atoms are in the upper state, so that an incident photon will stimulate the emission of other photons rather than being absorbed. A variety of excitation mechanisms can be used, including irradiating the medium with intense light at another frequency, using electrical discharges, or using chemical reactions.

Most high energy laser facilities designed for laser fusion research utilize large, neodymium glass lasers which emit infrared light at a wavelength of 1.06 μm. These lasers are pumped by flash-lamps. To date these lasers have been restricted in size by glass damage considerations to energies less than 1,000 joules per beam. Several laboratories, both in the United States and abroad, have large, multibeam Nd glass lasers in the 10,000 joule range.

To achieve the high efficiencies (in conversion of electrical energy into light energy), it will probably be necessary to use gas lasers. Of most interest have been CO_2 lasers which emit light at 10.6 μm. However a large variety of other types of gas lasers are being studied as possible candidates for the "brand-X" laser most suitable for inertial confinement fusion applications.

In this chapter we will begin by summarizing the essential physics of laser operation. We will then continue on to discuss both solid state and gas lasers, concluding with a summary of the present status of laser development.

7.1. AN INTRODUCTION TO ATOMIC SPECTROSCOPY

I. INTRODUCTION

Since laser action essentially involves the collective de-excitation of a number of excited atoms or molecules contained in a resonant cavity, it should be apparent that a study of the various excited states (or "energy levels") available to atoms and molecules is of central concern to our understanding of laser operation. Hence we will begin our study of laser physics with a brief introduction to atomic and molecular "spectroscopy"--i.e., that branch of physics concerned with the emission and absorption of electromagnetic radiation (light) by atomic systems.

Of course, atomic spectroscopy is an enormously broad and diverse subject, and indeed, can be regarded as one of the cornerstones of modern physics. We will avoid a detailed study of the techniques necessary to calculate the energy levels available to atomic and molecular systems, since this would require the development of some background in quantum mechanics. Instead, we will be concerned with the physical phenomena involved in determining atomic level spacing, introducing spectroscopic notation, and indicating how one obtains and utilizes spectroscopic information in practical laser applications.

II. ATOMIC STRUCTURE AND THE ONE-ELECTRON ATOM

A. Energy Levels and Quantum States

It is a well-known consequence of quantum mechanics that atomic systems (atoms, ions, molecules, nuclei,...) can only be found in certain time-independent states, each of which corresponds to a definite value of energy. For example, the hydrogen atom (the simplest of atomic systems, being composed of only one electron and one proton) can exist only in the discrete states corresponding to the values of energy (or <u>energy levels</u>) as shown on the next page. Such atomic states can be labeled by giving the <u>quantum numbers</u> characterizing the state. In the case of hydrogen, four such numbers are necessary to characterize the state of this one-electron system:

principal quantum number: n

orbital angular momentum quantum number: ℓ

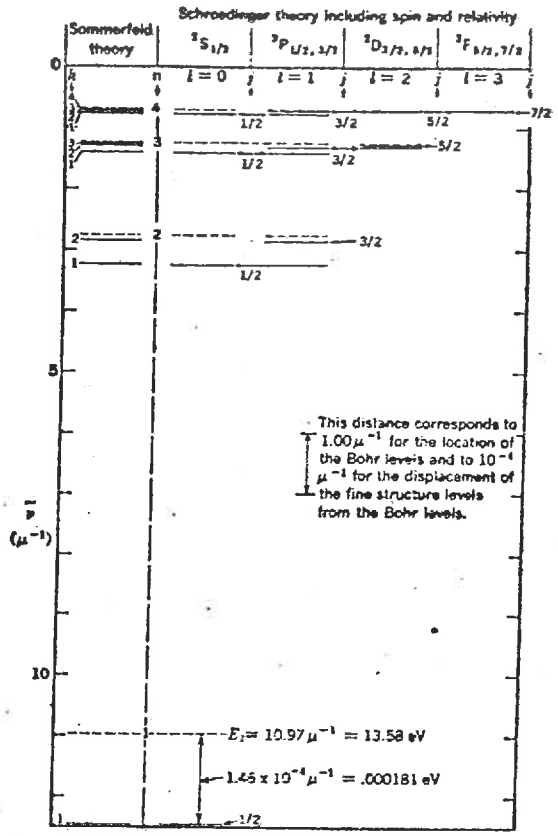

FIG. 5-6. Term diagrams for atomic hydrogen, showing fine structure. On this diagram the dashed lines represent the unperturbed energy levels as given by the Bohr formula 5-3(38). The fine structure of these levels is shown by the short solid lines, the scale representing the energy shifts being 10,000 times magnified with respect to that of the Bohr levels. The quantum numbers defining the various levels are given, both for the Schroedinger theory and for the old quantum theory, and the conventional spectroscopic designations of the terms are indicated along the top.

magnetic orbital quantum number: m_ℓ

magnetic spin quantum number: m_s

Frequently, two or more states will have the same energy. Such an energy level is then said to be degenerate, and the number of states with this energy is called the multiplicity of the level.

The atomic system may change from one state to another--i.e., make a transition among its possible energy levels--but only with an accompanying emission or absorption of the energy difference between the two levels involved as electromagnetic radiation (or by collisions with other atomic particles). The frequency of the emitted or absorbed quantum of electromagnetic radiation (the photon) is given by

$$h\nu = E_2 - E_1 = \hbar\omega$$

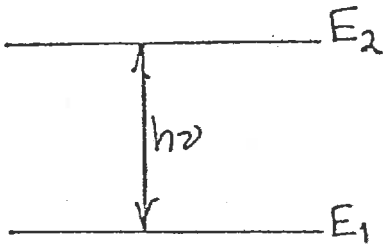

The lowest energy level available to an atomic system is known as its ground state, while all higher levels are referred to as excited states. Note that the absorption of a photon corresponds to an excitation of

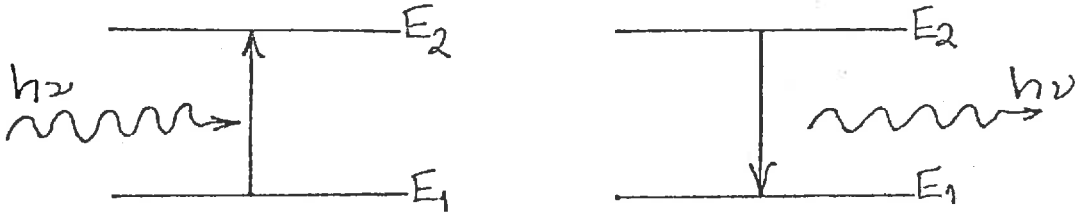

the system, whereas emission corresponds to a de-excitation. Hence by measuring the frequency of the light emitted or absorbed by an atomic system, one can study its energy level structure.

B. The Energy Levels of the Hydrogen Atom

The energy levels available to simple atomic systems can be calculated directly by using the well-known laws of quantum mechanics. For the simple hydrogen atom, this amounts in the lowest approximation to solving the time-independent Schrödinger equation

$$-\frac{\hbar^2}{2m}\nabla^2\psi - \frac{e^2}{4\pi\epsilon_0 r}\psi(\vec{r}) = E\,\psi(\vec{r}) \qquad \text{(I-2)}$$

to determine the allowable energy levels E. Although we will not be directly concerned with the calculation of atomic energy levels, it is useful to briefly review how such levels are determined for this very simple atom.

The Schrödinger equation (I-2) has nontrivial solutions only for values of E such that

$$E = -\frac{me^4}{32\pi^2\epsilon_0^2\hbar^2}\left(\frac{1}{n^2}\right) \equiv E_n \,, \quad n = 1, 2, 3, \ldots \qquad \text{(I-3)}$$

The corresponding solutions (or wavefunctions) can be written as

$$\psi_{n\ell m}(\vec{r}) = R_{n\ell}(r)\, Y_{\ell m_\ell}(\theta,\phi), \quad \begin{matrix} n = 1,2,3,\cdots \\ \ell = 0,1,\ldots,n-1 \\ -\ell \le m_\ell \le \ell \end{matrix} \qquad \text{(I-4)}$$

where $R_{n\ell}(r)$ are related to the associated Laguerre polynomials, and $Y_{\ell m_\ell}(\theta,\phi)$ are the spherical harmonic functions. Each wavefunction represents a different state of the system. These discrete levels of negative energy correspond to states in which the electron is bound to the proton. (There is also a continuum of states corresponding to all $E > 0$ which describe a free or ionized electron.) Notice that these energy levels have a very high degeneracy of multiplicity n^2, since there is no dependence of E_n upon ℓ or m_ℓ.

Actually, this analysis omits several important effects, even for the simple hydrogen atom. In particular, we have thus far ignored the fact that the electron has an intrinsic angular momentum--a spin s of magnitude $\hbar/2$. Associated with such a spin is a magnetic dipole moment

$$\vec{\mu} = -\frac{e}{mc}\vec{S} \qquad \text{(I-5)}$$

This magnetic moment will interact with any magnetic fields that are present, such as:

(i) external fields (Zeeman effect)

(ii) fields resulting from the motion of any other electrons in the atom

(iii) the magnetic moment of the nucleus

(iv) the magnetic field arising from the motion of the electron through the nuclear Coulomb field

Such interactions will correspond to additional terms in the Schrödinger equation(I-2) and hence to shifts in the allowable energy levels. Since these shifts are usually small, they are referred to as fine structure effects and include:

Spin-orbit interactions: The magnetic field seen by the electron moving through the nuclear Coulomb field is given by

$$\vec{B} = -\frac{1}{c^2}\vec{v}\times\vec{E} = \frac{\ell}{mec^2 r}\frac{dV}{dr} \quad . \qquad \text{(I-6)}$$

Hence the energy of orientation of the magnetic dipole moment of the electron in this field is

$$H_{larmor} = -\vec{\mu}\cdot\vec{B} = \frac{\vec{s}\cdot\vec{\ell}}{m^2c^2 r}\frac{dV}{dr} \quad . \qquad \text{(I-7)}$$

There is yet another spin-orbit effect however, due to the relativistic time dilation between the rest frames of the electron and the nucleus--so-called "Thomas precession." This gives rise to a reduction in the classical Larmor precession frequency predicted above which reduces H_{larmor} by a factor of 2 yielding a total spin-orbit interaction of

$$H_{\vec{s}\cdot\vec{\ell}} = \frac{1}{2}\frac{e^2}{4\pi\epsilon_0 m^2c^2 r^3}\vec{s}\cdot\vec{\ell} \qquad \text{(I-8)}$$

Relativistic Corrections: Yet another effect is due to the relativistic motion of the electron. We can account for this by expanding the relativistic classical Hamiltonian as

$$H = \sqrt{p^2c^2+m^2c^4} - mc^2 + V \cong \frac{p^2}{2m} - \frac{p^4}{8m^3c^2} + \cdots + V \qquad \text{(I-9)}$$

This gives rise to yet another correction term in (I-2) of the form

$$H_{rel}\,\psi = -\frac{\hbar^4}{8m^3c^2}\nabla^4\psi \quad . \qquad \text{(I-10)}$$

Hyperfine structure: An even higher order effect involves the interaction between the electron spin and the magnetic moment of the atomic nucleus itself. This leads to additional--but very small--terms in (I-2).

One can quantitatively account for these fine structure effects by using the methods of perturbation theory to calculate the corresponding energy shifts

$$E_n \rightarrow E_n + \Delta E_{\vec{s}\cdot\vec{\ell}} + \Delta E_{rel} + \Delta E_{hyperfine} \tag{I-11}$$

For the hydrogen atom, such a calculation yields

$$\Delta E_{\vec{s}\cdot\vec{\ell}} = \begin{cases} \dfrac{|E_n|\alpha^2}{n(2\ell+1)(\ell+1)} & \text{for } j = \ell + \tfrac{1}{2} \\ -\dfrac{|E_n|\alpha^2}{n\ell(2\ell+1)} & \text{for } j = \ell - \tfrac{1}{2},\ \ell \neq 0, \end{cases} \tag{I-12}$$

where j is a new quantum number characterizing the total angular momentum of orbital plus spin angular momentum, $\vec{j} = \vec{\ell} + \vec{s}$, while

$$\alpha = \frac{e^2}{\hbar c} = \frac{1}{137.0377} \tag{I-13}$$

is the so-called <u>fine structure constant</u>.

Furthermore

$$\Delta E_{rel} = \frac{|E_n|\alpha^2}{4n^2}\left[3 - \frac{4n}{\ell+\tfrac{1}{2}}\right] \tag{I-14}$$

(We will not treat the nuclear hyperfine corrections here.)

Notice that when these fine-structure corrections have been included, the energy levels depend upon three quantum numbers, n, l, j, and hence part of the degeneracy in the original levels (I-3) has been removed. This corresponds to a splitting of the original levels into several new levels, each slightly displaced from each other (by a separation of $O(\alpha^2)$). There is still a degeneracy of multiplicity 2 corresponding to m_j.

C. Spectroscopic Notation

The standard classification scheme used in atomic spectroscopy to identify these energy levels begins by specifying their orbital angular momentum. Unfortunately, history has left us with a rather nonsensical notation

ℓ	0	1	2	3	4	5	6	
letter	s	p	d	f	g	h	i	

where the letters were originally used to denote the observed character of the corresponding spectral lines (sharp, principal, diffuse, fine).

Such a terminology is applied to all of the energy levels corresponding to a given value of n such as

$$1s,\ 2s,\ 3s,\ \ldots,\ ns$$

Most of these levels are still degenerate. One denotes the multiplicity of this degeneracy by a preceding superscript, and the corresponding total angular momentum quantum number j of the level by a following subscript:

$$(\text{multiplicity})\,(\ell)_j$$

The multiplicity is equal to the number of different j values which can be formed from a given ℓ and s. For a one-electron atom such as hydrogen, s = 1/2, and hence the multiplicity is always 2.

For a many-electron atom, a very similar spectroscopic notation is used. In this case, one adds up the various angular momenta for all of the electrons, i.e. $\vec{L} = \sum \vec{\ell}_i$, $\vec{S} = \sum \vec{s}_i$, $\vec{J} = \sum \vec{j}_i$. Then the multiplicity is given by either 2S+1 or 2L+1, whichever is smaller. Since it is most often the case that S is smaller than L so that the multiplicity is equal to 2S+1, the preceding superscript has come to be <u>always</u> associated with the value of S:

$$(2S+1)(L)_J \qquad \text{(I-15)}$$

(Notice that this implies that if S > L, then 2S+1 is <u>not</u> the true multiplicity of the level.)

EXAMPLE:

	$^1S_0$	$^3D_2$	$^4P_{5/2}$
L	0	2	1
S	0	1	3/2
J	0	2	5/2
multiplicity	1	3	3

Note that a multiplicity of 1 is referred to as a "singlet" state, 2 as a "doublet," 3 as a "triplet," and so on.

D. Radiative Transitions and Selection Rules

We have seen that when an atom makes a transition between two energy states, a photon is absorbed or emitted with a corresponding frequency $h\upsilon = E_2 - E_1$. Hence by knowing the energy level structure, we can predict the frequencies (or wavelengths) of emitted or absorbed radiation. Possible transitions are most frequently depicted on a term diagram (sometimes called a Grotrian diagram). An example is shown below:

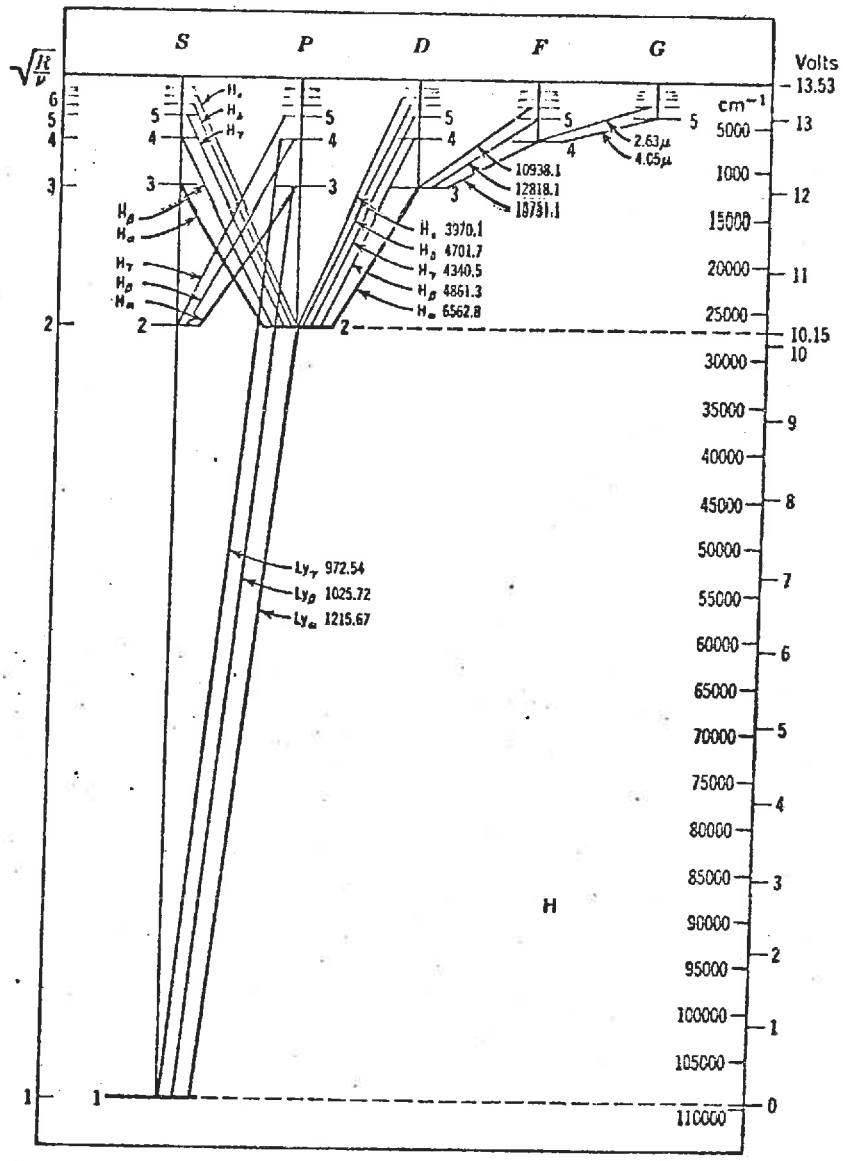

Grotrian diagram for hydrogen

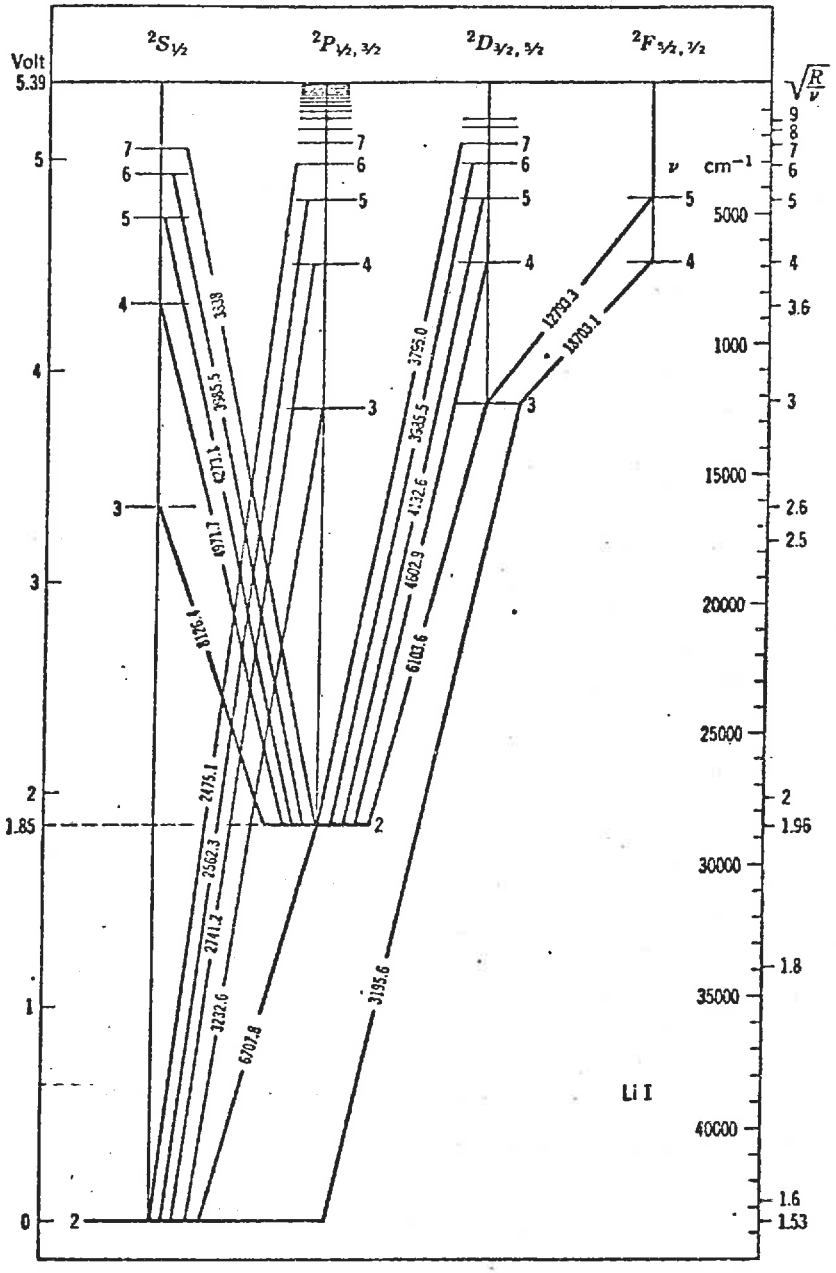

Grotrian diagram for lithium, Li I

The probability for a radiative transition to occur between two states is related to the wavefunctions associated with these states. The principal mechanism of interest in atomic and molecular spectroscopy involves electric dipole radiation. Classically, the electric dipole moment of a distribution of charges e_i with position vectors $\underline{r}_i$ would be given by

$$\vec{\mu} \equiv \sum_i e_i \vec{r}_i \quad . \tag{I-16}$$

The quantum mechanical analogie is given in terms of so-called "matrix elements" involving the wavefunctions of the two states involved:

$$\vec{\mu}_{1\to 2} \equiv e \int d^3r \; \psi_2^*(\vec{r}) \, \vec{r} \, \psi_1(\vec{r}) \quad . \tag{I-17}$$

The rate of transitions between the states is then given in terms of these matrix elements by

$$W_{1\to 2} = \frac{2}{3} \frac{\omega^4}{\pi \epsilon_0 c^3} \left| \vec{\mu}_{1\to 2} \right|^2 , \quad \omega = \frac{E_2 - E_1}{\hbar} \quad . \tag{I-18}$$

Frequently, the symmetry properties of the wavefunctions involved will lead to a zero matrix element. These are referred to as <u>forbidden</u> transitions--in the sense that a transition between such states cannot occur as a result of the interaction of the electric dipole moment of the atom with the radiation field. The transitions which yield a non-zero matrix element are referred to as <u>allowed</u> and can be specified by various <u>selection rules</u>. For example, for the one-electron atom, the selection rules for transitions are:

$$\Delta l = \pm 1$$
$$\Delta s = 0$$
$$\Delta j = \pm 1 \text{ or } 0 \quad (\text{but } j=0 \not\to j=0)$$
$$\Delta m_j = \pm 1 \text{ or } 0 \quad (\text{but } m_j = 0 \not\to m_j = 0 \text{ if } \Delta j = 0)$$

When electric dipole transitions are forbidden for two states, there is still a possibility that secondary mechanisms (e.g., electric quadrapole radiation) will cause a transition, but the transitions rates

for such secondary processes are generally several orders of magnitude lower than the rates for permitted dipole transitions.

III. THE MANY ELECTRON ATOM

Let us now consider the more interesting (and much more complicated) case of a many electron atom. The electrons will now interact not only with the nucleus, but as well with each other. However in the lowest order approximation, one can ignore the interactions between the electrons, and hence analyze the system as one would a one-electron atom. Note, however, that the Pauli exclusion principle implies that only one electron can occupy each state. This implies that the atomic electrons will occupy each of the energy levels such that

$n = 1, \quad \ell = 0, \quad m = 0, \quad m_s = \pm 1/2 \implies$ 2 electrons

$n = 2, \quad \ell = 0, \quad m = 0; \quad \ell = 1, \; m = -1,0,+1, \; m_s = \pm 1/2 \implies 8$ electrons

and so on. In earlier theories of atomic structure, each value of n corresponded to a "shell" of electrons with the notation:

Shell:	K	L	M	N	O
n	1	2	3	4	5
subshell	1s	2s 2p	3s 3p 3d	.....	.....
# of elec.	2	2 6	2 6 10	.....	.....

In this way, one can actually build up the periodic table of elements.

Unfortunately for our simple one-electron model (but fortunately for lasers), the interaction among electrons greatly complicates the actual energy levels of a many electron atom. Perhaps the most significant interaction is between angular momenta (both intrinsic spin and orbital angular momenta) of the various electrons. It is usually sufficient to consider only the coupling of so-called "valence" electrons, i.e., those electrons in the outermost unfilled subshell. There are essentially two different ways in which these angular momenta can then couple together:

Russell-Saunders of L-S Coupling: In this case, the interaction of the orbital angular momenta $\vec{\ell}_i$ of the individual electrons is so strong from one electron to another, that these momenta combine to give a resultant total orbital angular momentum

$$\vec{L} = \sum_i \vec{l}_i \qquad \text{(I-18)}$$

which is a constant of the motion. Similarly, the individual spins s_i combine to form a constant

$$\vec{S} = \sum_i \vec{s}_i \qquad \text{(I-19)}$$

If one now includes spin correlation energy (due to the Pauli exclusion principle) and residual electrostatic energy of repulsion among the electrons, one finds a line splitting as shown below for the example of a 4p and 4d valence electron:

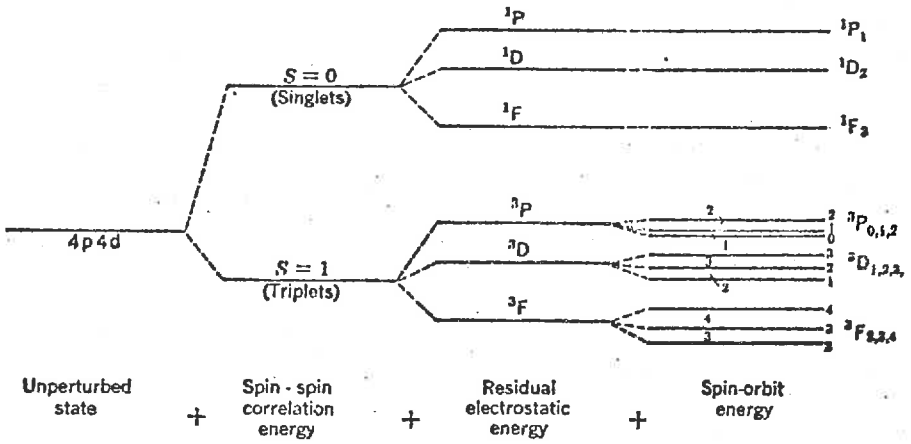

Schematic diagram illustrating the fine-structure splitting of a level corresponding to a 4p and a 4d valence electron. The Landé-interval rule is illustrated in the spacings of the triplet levels.

j-j Coupling: The reverse case is one in which there is considerable interaction between the orbital and spin angular momentum of the same electron. Then each $\vec{l}_i$ and $\vec{s}_i$ combine to form $\vec{j}_i = \vec{l}_i + \vec{s}_i$. The j_i's are then loosely coupled to each other. In this case, our previous example becomes

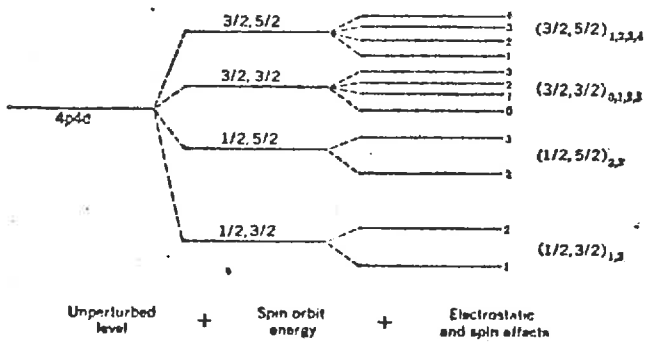

Schematic illustration of the fine structure of a pd configuration in *j-j* coupling.

Actually, L-S coupling prevails for most light elements. Pure j-j coupling occurs very seldom, and one frequently finds that the inner shell electrons obey L-S coupling while the outer electrons obey the j-j coupling scheme.

IV. SPECIFIC EXAMPLES

As we shall see in later lectures, laser action involves the collective de-excitation of excited states of atomic systems, with a corresponding emission of electromagnetic radiation. Such transitions can occur between the excited states of atoms, ions, or even molecules. To illustrate our brief introduction to atomic spectroscopy, it is appropriate to consicer examples of lasing transitions for both atomic and ionic systems:

Helium-Neon Laser: The first gas laser to be demonstrated experimentally (1961) involved transitions between various excited states in neutral neon (an "atomic" laser). (We will return later to the role played by the helium in this laser.) Many lasing transitions have been observed, but the three most important are shown below:

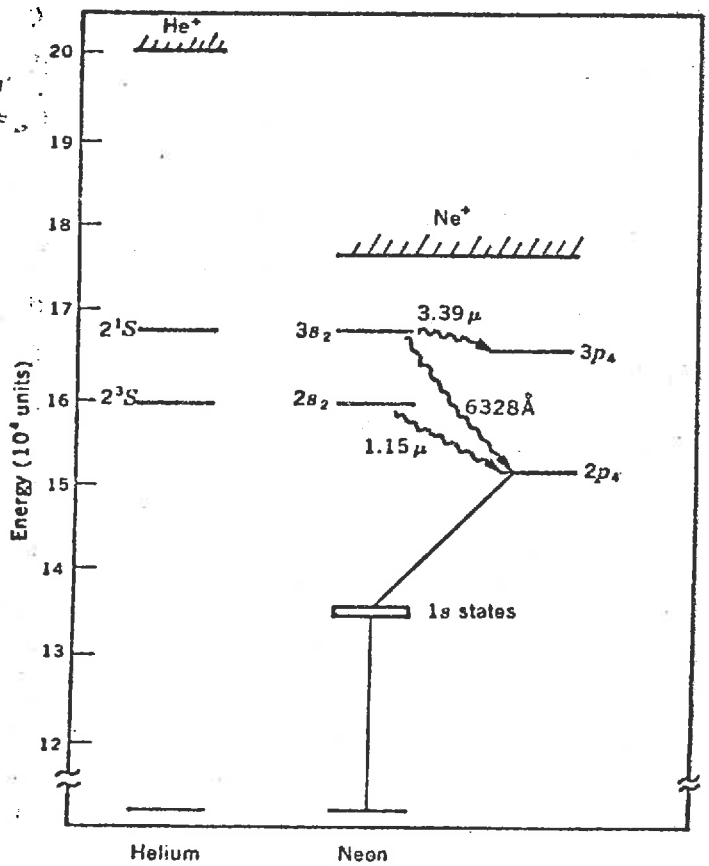

Energy-level diagram for the helium-neon laser.

$3s_2 \longrightarrow 2p_4$ $\quad \lambda = 6328$ Å $= \nu/c$

$2s_2 \longrightarrow 2p_2$ $\quad \lambda = 1.15$ microns

$3s_2 \longrightarrow 3p_4$ $\quad \lambda = 3.39$ microns

Argon Laser: One can also induce lasing transitions in ions (an "ionic" laser). In particular, transitions in singly ionized argon have been used:

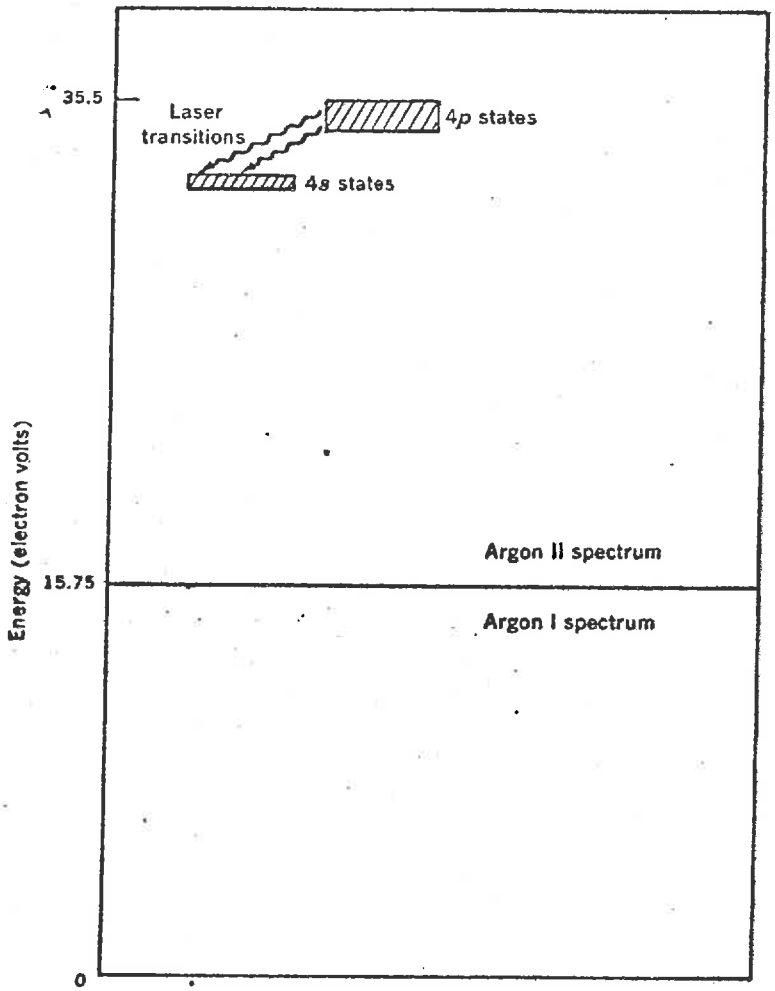

Energy-level diagram for the argon-ion laser.

$4p\,^2D_{5/2} \longrightarrow 4s^2\,P_{3/2}$ $\quad \lambda = 4880$ Å

$4p\,^2D_{5/2} \longrightarrow 4s^2\,P_{3/2}$ $\quad \lambda = 5145$ Å

There are a host of other atomic and ionic lasers. Indeed, it has occasionally been suggested that any material can be made to lase--if one is sufficiently clever (and able to invest enough money and energy).

We will continue on in later lectures to develop the theory of laser action and study specific laser types, but first we must develop one additional topic, that of molecular spectroscopy, which plays the key role in the study of molecular lasers such as the CO_2 gas laser.

7.2. MOLECULAR SPECTROSCOPY

I. INTRODUCTION

There has been a very considerable recent interest in molecular gas lasers which utilize transitions in molecules (such as CO or CO_2) to produce laser light at infrared wavelengths. The energy level spectra of molecular gases are considerable more complicated than those of atomic gases. In addition to the electronic energy levels which we studied in the previous lecture, a molecule can also have energy levels arising from the vibrational and rotational motion of the atoms in the molecule. Whereas the spacings of the electronic energy levels for molecules are comparable to those for atoms, the vibrational and rotational levels add a "fine structure" whose level spacing is typically smaller by factors of 20 and 500, respectively. A comparison of typical atomic vs. molecular spectra is shown on the next page. One should note in particular the difference in energy of the various levels, and the complexity of the molecular levels.

In this lecture we will briefly review some features of molecular energy levels, considering the simplest case of a diatomic molecule for convenience, and then analyze the molecular spectra of several gases of interest to laser technology (CO_2, H_2, and HCN) in more detail.

II. GENERAL FEATURES OF MOLECULAR SPECTRA

A. Electronic Energy Levels

Atoms are bound together into molecules by a rearrangement of their electrons which gives rise to an effective attractive potential between the atoms. The simplest type of such a chemical bond is the <u>covalent</u> bond in which an electron is "shared" between atoms (e.g., in O_2, H_2, and SiC). In other types of molecules (e.g., NaCl) electrons are exchanged from one atom to another resulting in <u>ionic</u> bonding (e.g., an attraction between Na^+ and Cl^-). The details of such chemical bonding is rather complicated, as are the calculations of the electronic energy levels for molecular systems. There are usually far fewer bound electronic states in molecules than in atoms, simply because for sufficiently large energies, the molecule disassociates (this can be seen in the figure on the following page).

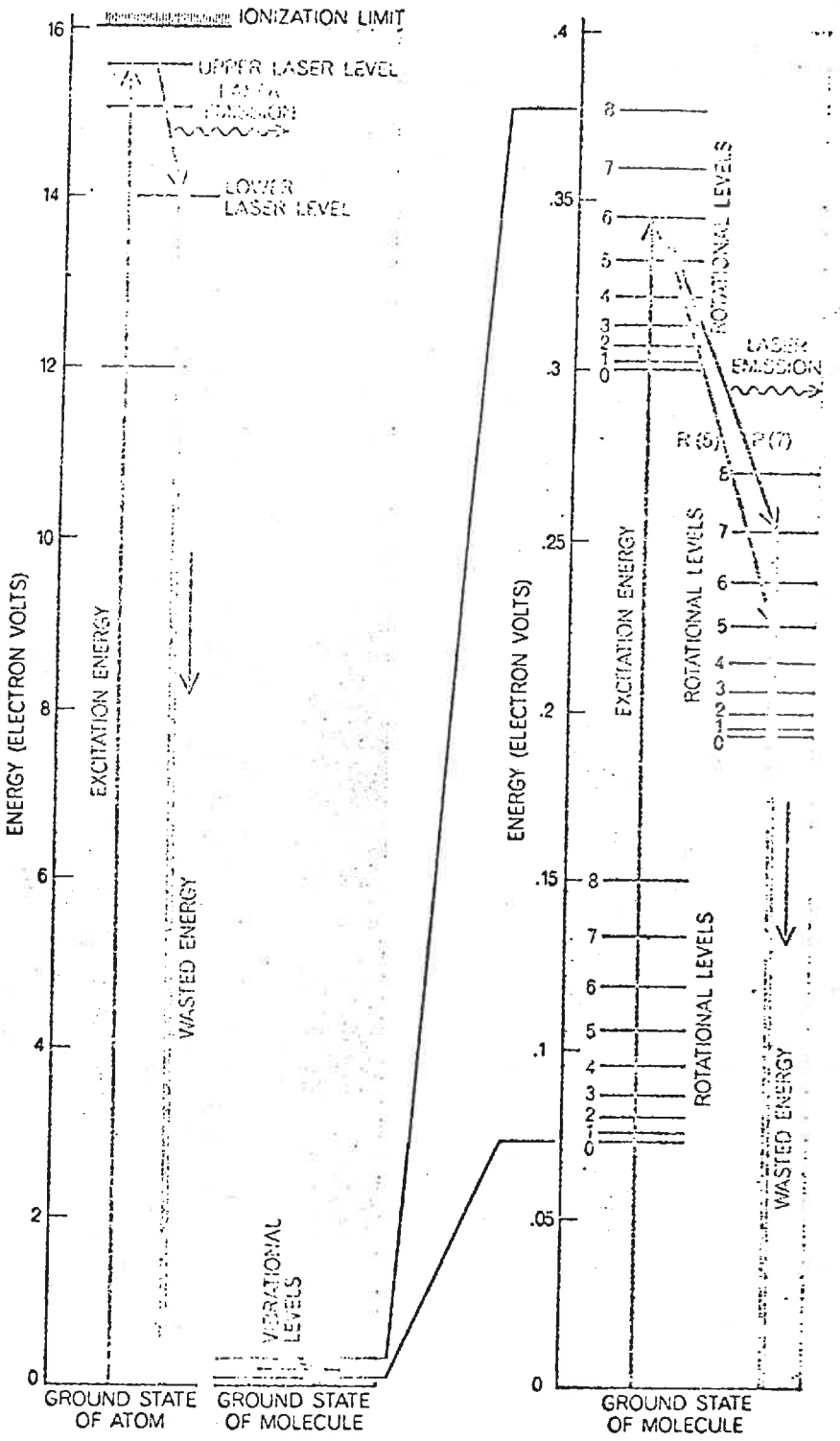

ENERGY-LEVEL DIAGRAMS of an atom and a molecule are compared. In an atom the electronic energy levels between which infrared transitions can occur are situated near the atomic ionization limit—far above the ground state of the atom. As a result the atom has to be excited to a very high energy in order to produce laser action, which in turn results in the emission of a photon with a comparatively small amount of energy. Thus the use of atomic gases wastes a great deal of energy and results in a low quantum efficiency. In a molecule, on the other hand, the vibrational levels of the electronic ground state are very close to the ground level of the molecule; hence the photon energy is a sizable fraction of the total energy needed to excite the molecule from the ground state to the upper laser level. This results in a much higher quantum efficiency. The enlargement at right shows that the vibrational levels of the molecule's electronic ground state are in turn composed of a number of rotational energy levels due to the rotation of the molecule. The number with each level indicates that level's rotational angular momentum in units of $h/2\pi$. Two of the allowed infrared transitions between the rotational levels belonging to two different vibrational levels are indicated.

We will be most concerned with the energy levels available to the molecule for a given electronic configuration. In this sense, then, one assigns to each electronic state n an effective interatomic potential energy $V_n(r)$, and then proceeds to analyze the energy levels of the atoms in such a potential. (Naturally if the electronic state changes, then $V_n(r)$ also changes, and this analysis must be repeated for the new effective potential.)

Examples of such effective electronic potentials are shown for several different diatomic systems as a function of atomic separation

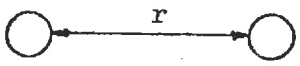

in the figure below. Incidently, these curves clearly reveal than NaCl must involve ionic bonding, while H_2 must have covalent bonding, since these yield the only bound states.

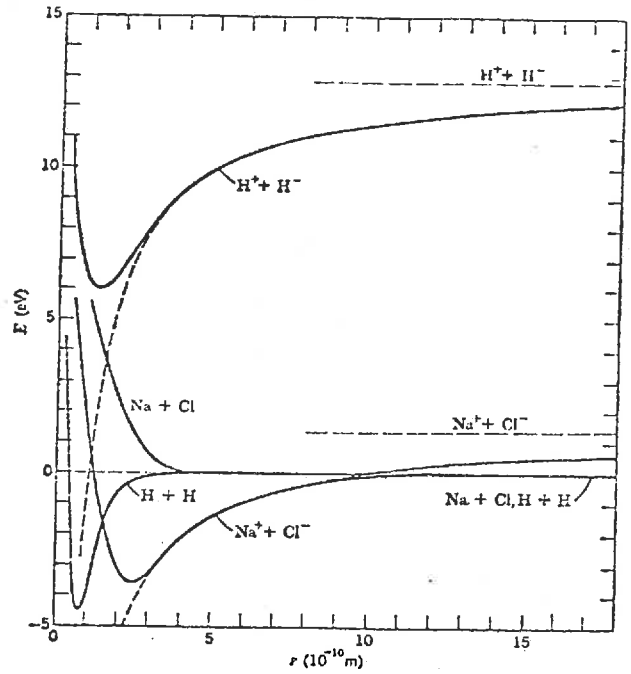

Interatomic potential-energy curves for the ionic molecule NaCl and the homopolar molecule H_2. The zero of energy corresponds to the neutral atoms situated at infinity.

B. Vibrational and Rotational Energy Levels

Since the effective potential has a minimum, it is possible for the atoms to vibrate or oscillate about their equilibrium positions. They may also rotate--that is, assume various values of angular momentum. In fact, one can write the energy levels of a diatomic molecule as

$$E_{nKv} = V_{no} + \frac{\hbar^2 K(K+1)}{2m_r r_K^2} + \hbar\omega_{nK}(v+\tfrac{1}{2}) \qquad \text{(II-1)}$$

where

n electronic quantum number

K rotational quantum number (similar to ℓ in atomic spectra)

v vibrational quantum number

Here also, $m_r = M_1M_2/(M_1 + M_2)$, the reduced mass of the diatomic system, r_K is the equilibrium separation of the atoms, and ω_{nK} is their vibration frequency. Note that all of these factors depend upon the electronic state n.

In practice, one finds

$$V_{no} >> \hbar\omega_{nK}(v+\tfrac{1}{2}) >> \frac{\hbar^2 K(K+1)}{2m_r r_K^2}. \qquad \text{(II-2)}$$

Hence the vibrational levels are imposed as fine structure upon the electronic levels, and the rotational levels as fine structure upon the vibrational levels. The energy levels are degenerate with respect to the z-component of the rotational angular momentum, M_K, with a multiplicity (2K+1).

C. Molecular Spectroscopy of Diatomic Molecules

Having thus isolated the various components of the molecular energy levels, we can now consider the various kinds of radiative transitions possible between these states:

Pure-Rotational Spectrum: The simplest kind of transition is one in which only the rotational quantum number changes. These are most common when the molecule is in its electronic and vibrational ground state. Since such radiative processes usually involve dipole transitions (at least for asymmetric molecules), the usual selection rules apply

$$\Delta K = +1 \quad \text{(absorption)}$$
$$= -1 \quad \text{(emission)}$$
$$\Delta M_K = \pm 1 \text{ or } 0$$

The corresponding frequencies are given by

$$\omega_K = \frac{E_{K+1} - E_K}{\hbar} = \frac{(K+1)\hbar}{m_r r_K^2} \qquad \text{(II-3)}$$

and lie in the far infrared ($\sim$ 1000 μm).

Vibrational-Rotational Spectrum: Next in complexity are transitions which involve a change in both the vibrational and rotational states of the molecule. The selection rules are then:

$$\Delta K = \pm 1$$
$$\Delta M_K = \pm 1 \text{ or } 0$$
$$\Delta v = +1 \quad \text{(absorption)}$$
$$= -1 \quad \text{(emission)}$$

Then the frequencies observed fall into two "branches," depending on the sign of ΔK (consider the ground electron state n = 0).

R-Branch:

$$\omega_{OKv} = \frac{E_{0,K+1,v+1} - E_{0,K,v}}{\hbar} \cong \omega_{oo} + \frac{(K+1)\hbar}{m_r r_K^2} - \frac{(v+1)\hbar\omega_{oo}^2}{2B_o} \qquad \begin{matrix} \Delta K = +1 \\ \Delta v = +1 \end{matrix}$$

P-Branch:

$$\omega_{OKv} = \frac{E_{0,K-1,v+1} - E_{0,K,v}}{\hbar} \cong \omega_{oo} - \frac{K\hbar}{m_r r_K^2} - \frac{(v+1)\hbar\omega_{oo}^2}{2B_o} \qquad \begin{matrix} \Delta K = -1 \\ \Delta v = +1 \\ K \neq 0 \end{matrix}$$

A typical example of a vibrational-rotational spectrum and the branch structure in an absorption spectrum are shown below

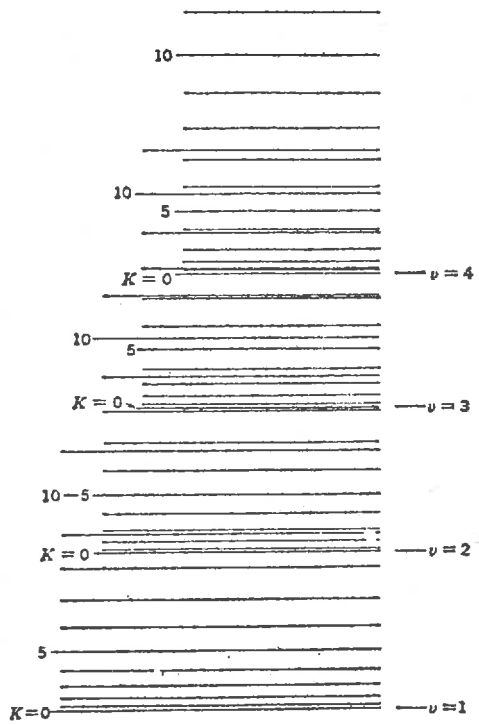

Schematic energy-level diagram of the vibration-rotation states of a diatomic molecule.

Such transitions are also in the infrared ($\sim$ 10 μm).

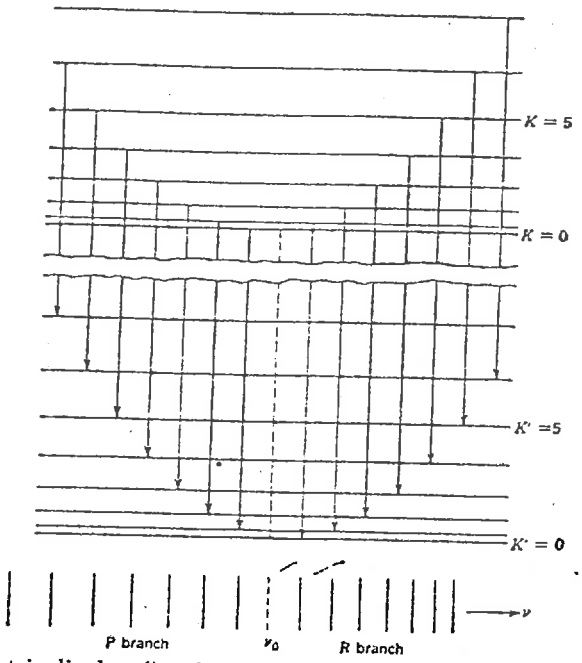

Electric-dipole vibration-rotation transitions between two vibrational states of a diatomic molecule. (Adapted by permission from Herzberg, "Spectra of Diatomic Molecules," copyright D. Van Nostrand Company, Inc., Princeton, N.J., 1950.)

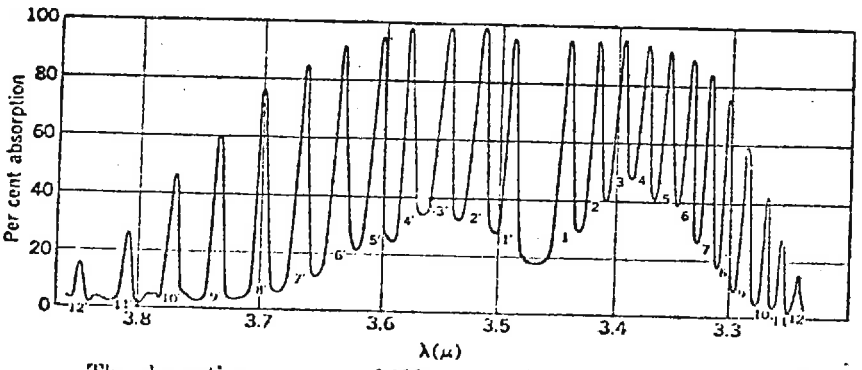

The absorption spectrum of HCl vapor in the near infrared. [After Imes, *Astrophys. J.*, 50, 251 (1919).]

Electronic Transitions: The most general transition of a molecule is one in which the electronic, vibrational, and rotational states all change. Because of the participation of the electronic state in the transition, there is no strict selection rule for the vibrational quantum number v.

The vibrational modes will impose a fine structure upon the electronic transitions, which in turn will be broken into broad bands by the rotational structure. Hence the spectra of even

diatomic molecules can become extremely complex. We will later discuss the H_2 laser which relies upon such electronic transitions.

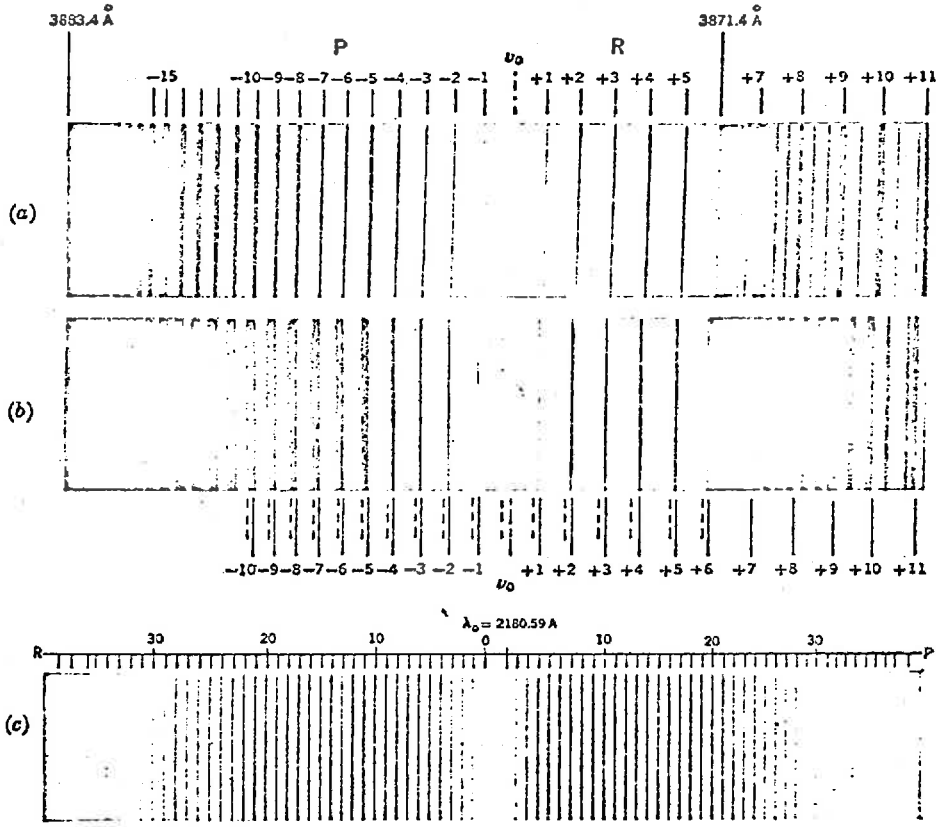

(*a*) Fine structure of the CN band 0.3883μ at low temperature and (*b*) at intermediate temperature. The dashed lines refer to the returning limb of the P-branch. (By permission from Herzberg, "Spectra of Diatomic Molecules," copyright D. Van Nostrand Company, Inc., Princeton, N.J., 1950.) (*c*) Structure of the 0-0 band of CN^+ at 0.2181μ. [After Douglas and Routly, *Astrophys. J.*, 119, 303 (1954).]

III. SPECIFIC EXAMPLES OF MOLECULAR SPECTROSCOPY

A. The CO_2 Laser

We now turn our attention to a specific molecule, CO_2, which is linear and symmetric as shown below:

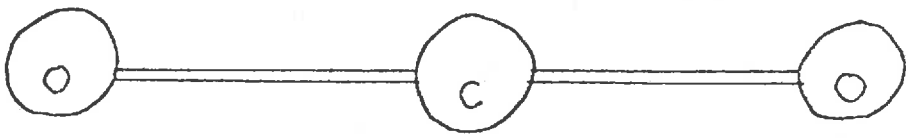

The transitions of most interest are vibrational-rotational transitions (in the electronic ground state). The band structure is revealed in the absorption spectra below

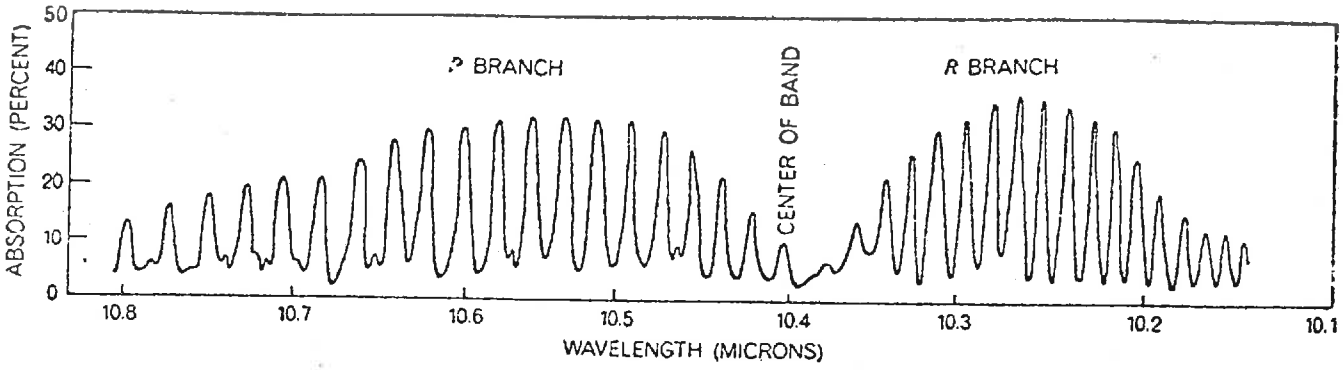

Again recall that the P-branch corresponds to an increase in angular momentum of $\Delta K = 1$, while the R-branch involves a decrease in angular momentum of $\Delta K = -1$. These states lie very close to the ground state. (We shall see later that this is a key reason for the very high efficiencies of molecular lasers.)

The vibrational motions of CO_2 are somewhat more complex than for diatomic molecules, since it has 3 degrees of freedom. These vibrational modes are shown schematically on the following page.

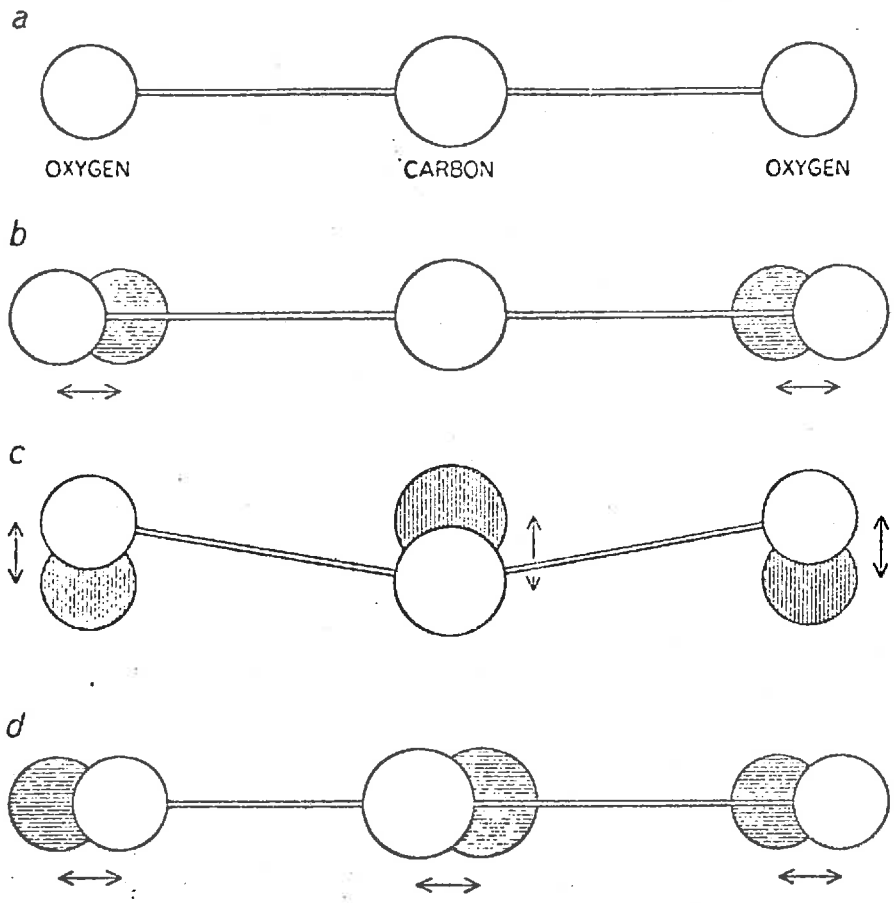

CARBON DIOXIDE MOLECULE (*a*) is linear and symmetric in configuration and has three degrees of vibrational freedom. In the symmetric stretch mode (*b*) the atoms of the molecule vibrate along the internuclear axis in a symmetric manner. In the bending mode (*c*) the oscillation of the atoms is perpendicular to the internuclear axis. In the asymmetric stretch mode (*d*) the atoms vibrate along the internuclear axis in an asymmetric manner. The vibrational state of the molecule is accordingly described by three quantum numbers, v_1, v_2 and v_3, and is usually written in the form $(v_1 v_2 v_3)$, where v_1 describes the number of vibrational quanta in the symmetric stretch mode, v_2 the number of vibrational quanta in the bending mode and v_3 the number of vibrational quanta in the asymmetric stretch mode.

Hence there are three vibrational quantum numbers, v_1, v_2, and v_3 which represent the number of quanta in each mode. The description of a given vibrational level is given by (v_1, v_2, v_3).

The vibtational levels of most interest are shown in the diagram on the next page. (The rotational levels have been omitted to keep the level diagram as simple as possible.) Note that the 001 → 100 transition corresponding to 10.6 micron radiation is of most interest in CO_2 laser applications.

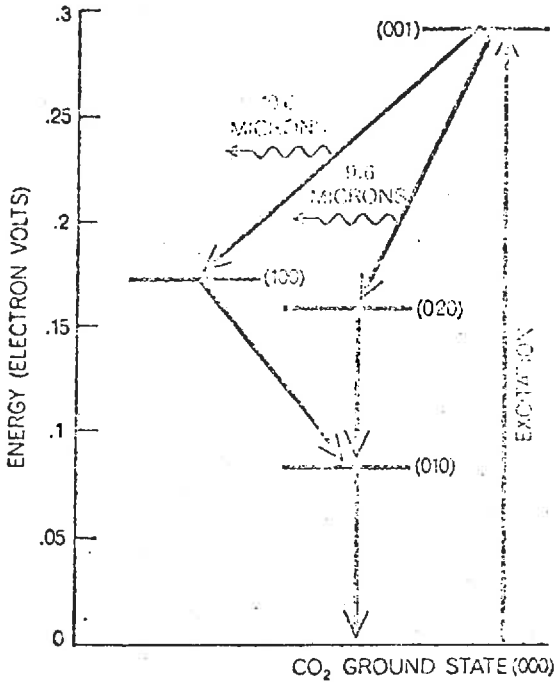

B. The HCN Laser

Very long wavelength laser radiation can be obtained from transitions in HCN as shown in the partial level diagram on the next page.

C. The H_2 Laser

At the other extreme, transitions between different electronic levels in molecular hydrogen can yield extremely short wavelength radiation in the ultraviolet (1600 Å). The transitions involved are shown on the next page. (Note that the upper level is not a bound molecular state in this case.)

PARTIAL HCN ENERGY LEVEL SCHEME

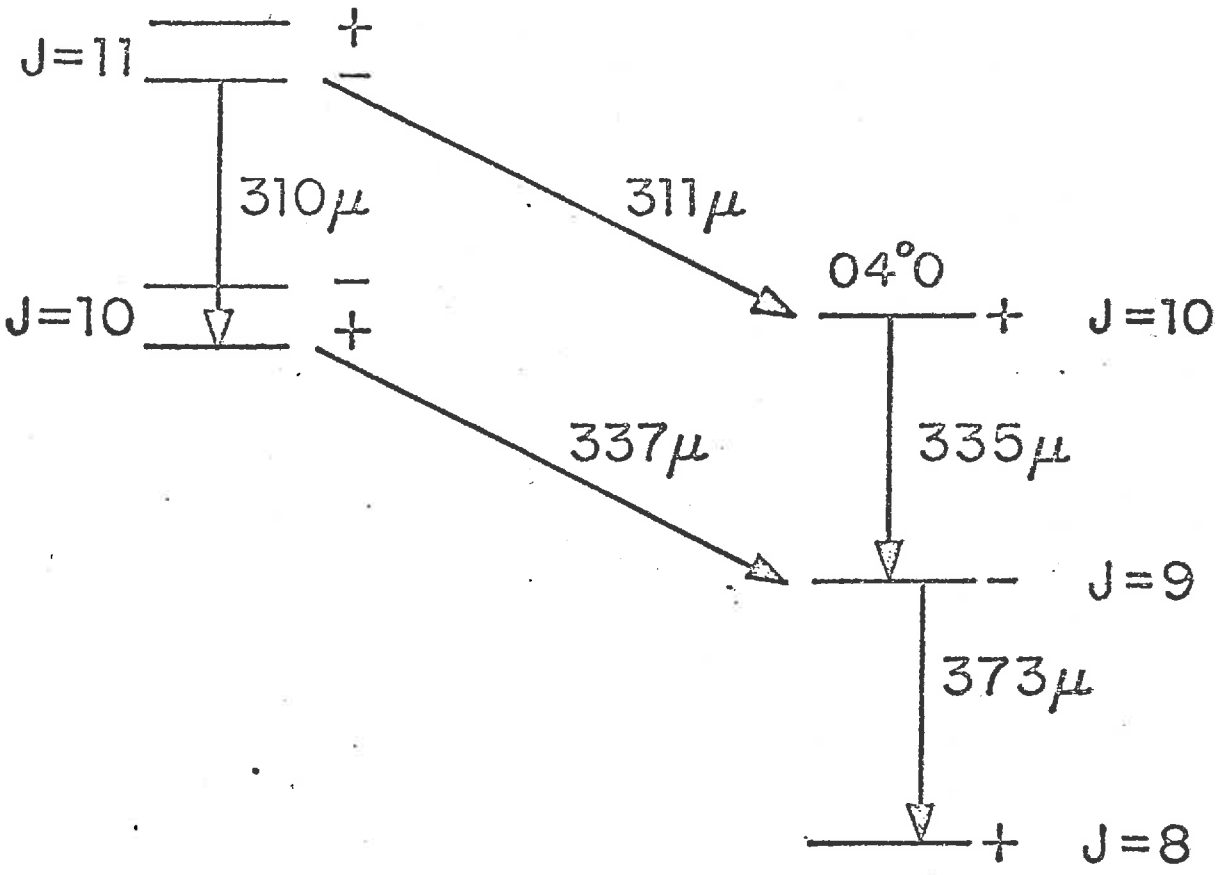

H_2 ENERGY LEVELS

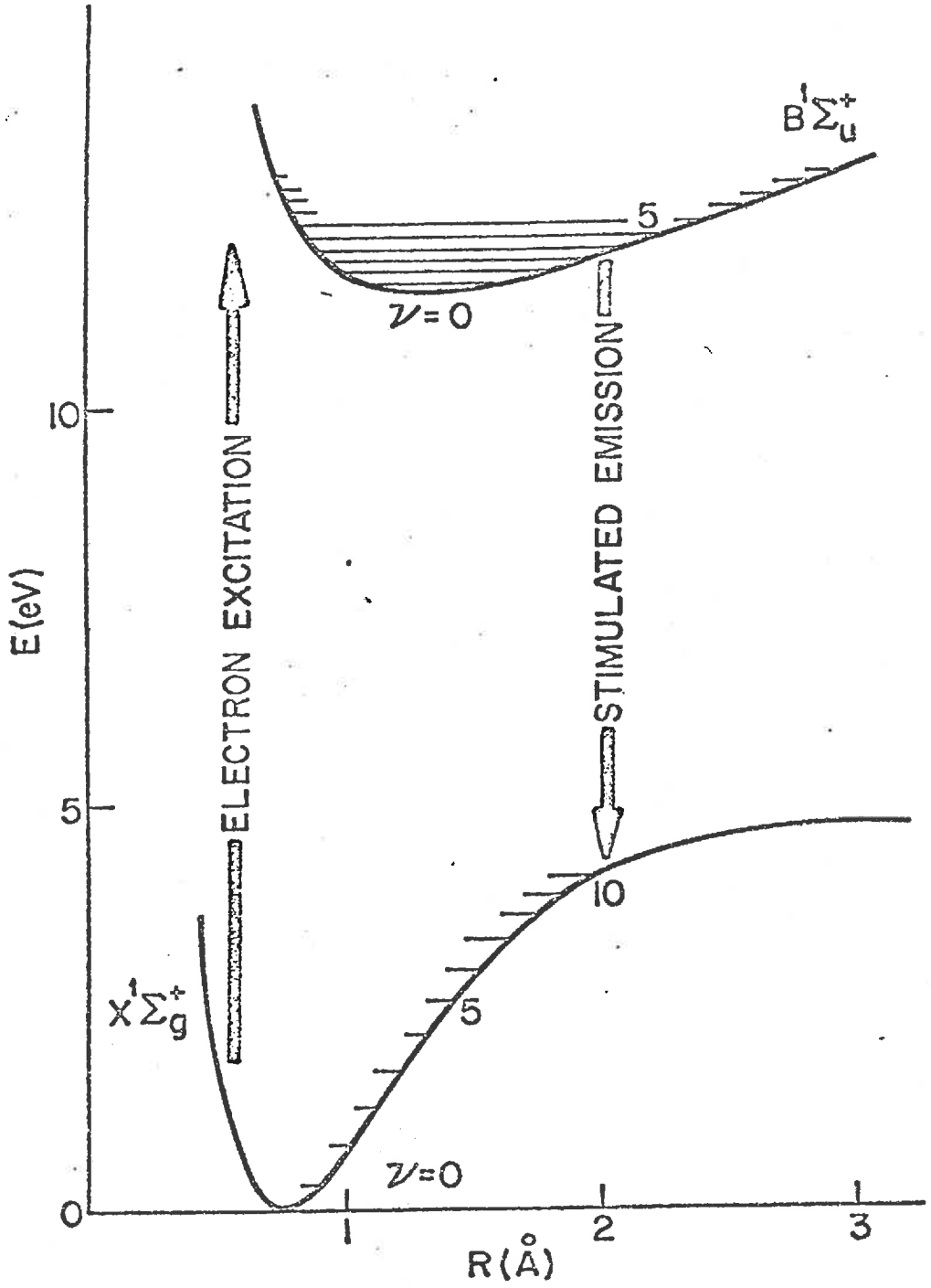

7.3. INTERACTION OF ELECTROMAGNETIC RADIATION WITH ATOMIC SYSTEMS

I. STIMULATED AND SPONTANEOUS EMISSION

Thus far we have studied the possible spectra of electromagnetic radiation emitted by atomic and molecular systems. In particular, an introduction to the available energy states of atoms and molecules was given. We now direct our attention towards the interaction of electromagnetic radiation with large numbers of atoms and molecules.

First, let us review very briefly the interaction of radiation with a single atom (or molecule) with two levels as shown. If the atom is initially in the state E_1, then it can be excited into the upper state E_2 by the absorption of a photon of energy

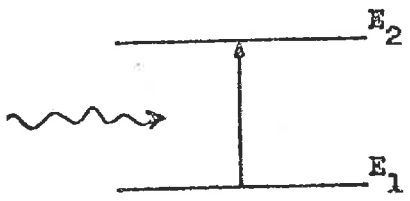

absorption

$$h\nu_{12} = E_1 - E_2$$

Similarly, if the atom is initially in the upper state E_2, it can spontaneously decay by emitting a photon.

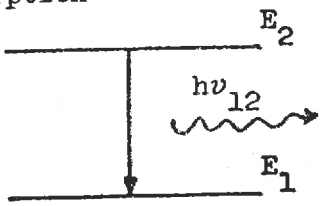

spontaneous emission

Suppose we denote the transition probability per unit time (i.e., rate) for such spontaneous emission of light as A_{21}.

There is yet another process for emission, however. An atom in an excited state can be stimulated to emit a photon if one subjects it to electromagnetic radiation of the same frequency as the energy level spacing. That is, there is a probability that an incident photon of energy $h\nu_{12}$ will stimulate the emission of yet another photon. These two photons emerge from the atom in phase. In this sense, stimulated emission can lead to a coherent amplification of light. This is in contrast to spontaneous emission in which the photons are emitted randomly.

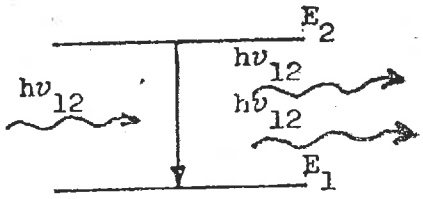

stimulated emission

The transition rate for stimulated emission must be proportional to the photon density or radiation density at frequency ν_{12}, u_{12}. Hence let us write the corresponding transition rate as $u_{\nu_{12}} B_{21}$. Note that the total decay rate from E_2 to E_1 is then

$$W_{2\to1} = A_{21} + u_{\nu_{12}} B_{21} \qquad \text{(III-1)}$$

In fact, B_{21} is closely related to the absorption transition rate which can be written as

$$W_{1\to2} = u_{\nu_{12}} B_{12} \qquad \text{(III-2)}$$

In general then, for two levels m and n one has the transition rates

$$W_{n\to m} = A_{nm} + u_\nu B_{nm} \qquad W_{m\to n} = u_\nu B_{mn} \qquad \text{(III-3)}$$

The rate constants A_{nm} and B_{nm} can be calculated in terms of the electric dipole matrix elements for the atom, as we have seen earlier in Lecture I. However there are two very useful relationships known as the Einstein relations:

$$g_n B_{nm} = g_m B_{mn} \qquad g_n = \text{multiplicity}$$

$$A_{nm} = \frac{8\pi h\nu^3}{c^3} B_{nm} \qquad \text{(III-4)}$$

(In a medium with index of refraction $\eta \neq 1$, this is modified as

$$A_{nm} = \frac{8\pi h\nu^3\eta^3}{c^3} B_{nm} \, , \quad)$$

Stimulated emission of radiation is the key phenomenon in lasers. For if one can prepare an "active medium" in which most of the atoms can be placed in an excited state, then electromagnetic radiation passing through them will stimulate a cascade of photons--each in phase with the others. Hence an enormous coherent amplification of light at this wavelength is possible.

But, of course, the first requirement is to develop a way to excite large numbers of atoms into the appropriate excited states. Most of our discussion in this lecture will be concerned with how one actually prepares such an "inversion" of excited state populations.

II. EQUILIBRIUM STATE POPULATIONS AND INVERSIONS

Consider a large number N_o of atoms in thermal equilibrium at a temperature T. Then if E_j is the energy of the jth state, the distribution

of atoms among the various states is given by the Boltzmann factor:

$$N_j' = N_0 \frac{e^{-E_j/kT}}{\sum_i e^{-E_i/kT}} \qquad \text{(III-5)}$$

If the jth level has multiplicity g_j, then the population or number of atoms in level j is

$$N_j = g_j N_j' = N_0 \frac{g_j e^{-E_j/kT}}{\sum_i e^{-E_i/kT}} \qquad \text{(III-6)}$$

In particular, the populations of any two levels, say E_2 E_1 and E_2, are related by

$$\frac{N_2}{g_2} = \frac{N_1}{g_1} e^{-(E_2-E_1)/kT} \qquad \text{(III-7)}$$

Hence in thermal equilibrium, the relative population in the upper state will be many times smaller than that of the lower state. If we were to irradiate such a collection of atoms with light of frequency ν_{12}, then obviously absorption would greatly overwhelm any stimulated emission, and light attenuation rather than amplification would result.

More quantitatively, let the incident light be of energy density u_ν and frequency ν_{12}. Then

$$\begin{aligned} \#\text{ of emissions/sec} &= (A_{21} + u_\nu B_{21})\, N_2 \\ \#\text{ or absorptions/sec} &= u_\nu B_{12}\, N_1 \end{aligned} \qquad \text{(III-8)}$$

Hence the net loss in coherent incident beam photons (remembering the spontaneous emission is incoherent) is given by

$$\#\text{ lost/sec} = (N_1 - N_2)\, u_\nu B_{21} \qquad \text{(III-9)}$$

implying attenuation if $N_1 > N_2$.

What we must obviously do is disturb the equilibrium distribution so that we preferentially populate the upper state in such a way that $N_2 > N_1$. Such a <u>population inversion</u> will amplify light:

$$\text{photon gain/sec} = (N_2 - N_1)\, u_\nu B_{21} \qquad \text{(III-10)}$$

Such an amplification or "negative absorption" is the objective of laser design.

III. EXCITATION MECHANISMS

How does one obtain such a population inversion? Obviously not by trying to directly excite atoms from E_1 to E_2 since this would require absorption from the beam one wishes to amplify. Instead additional levels must be introduced. The simplest scheme is a 3-level laser which was first applied in the ruby laser. The idea is to irradiate the lasing material (in this case, the chromium ions in ruby) with flash lamps to excite them into the upper state 3. Since the light from flash lamps is not monochromatic, only a small fraction of the incident photons will be absorbed to excite the atoms. For this reason, one wants the upper level to have as large a line width as possible, to cover a broad frequency range and hence "catch" as many of the flash lamp photons as possible. The atoms in the upper level 3 then decay very rapidly via fast radiationless transitions into the intermediate level 2 , which has a very narrow line width and a relatively long lifetime for spontaneous emission. Hence by using sufficiently intense flash lamp irradiation, one can prepare a population inversion in which the number of atoms in 2 exceeds that in 1 . The transition between 2 and 1 is then used as the lasing transition for stimulated emission.

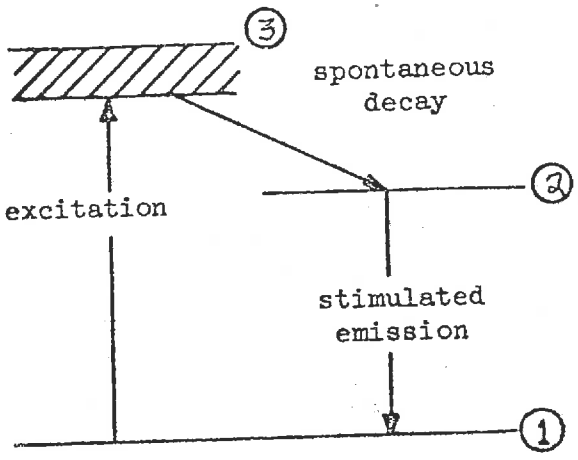

The three level laser is only one of a huge variety of level schemes used to excite atoms or molecules into suitable population inversions for light amplification by stimulated emission of radiation. Other excitation mechanisms used in gas lasers include:

(i) direct excitation by charged particle collisions: If one maintains an electrical discharge in the lasing media, then in elastic collisions between free electrons and atoms or ions can create excited states. Such excited states can then transfer energy to the upper lasing levels by collisions (see ii below). This combination of electron excitation and collisional energy transfer is the principal

mechanism used in lasers such as helium-neon or CO_2. We will return to discuss it in considerably more detail when we study specific laser systems.

(ii) excitation through resonant or near resonant energy transfer: The excitation present in a particular species can be selectively transferred to a particular state (or a narrow band of states) in another species by resonance collisions in which the relative energy between the colliding atoms or molecules is very close to the energy level spacing of their excited states.

(iii) excitation by gas dynamical processes: Rapid heating or cooling of a molecular gas can generate a population inversion (such as by expanding a gas through a nozzle). Such excitation mechanisms are currently being applied in extremely high power continuouous operation (cw) CO_2 lasers.

(iv) excitation by chemical processes: It is well known that in many chemical reactions the products are formed in excited states. Hence chemical reactions can be used to create population inversions of molecular gases. In practice, a rather considerable fraction of the available chemical reaction energy can be coupled to the radiation field. Examples of such chemical lasers include HF, HCl, and CO.

(v) excitation through the Penning effect: The Penning ionization process involves using the internal energy of an excited atom to cause the ionization of its collision partner during an encounter. This mechanism is operative in the helium-cadmium ionic laser.

It is apparent that regardless of the specific mechanisms used to excite atomic or molecular systems and achieve population inversions, the relative widths of energy levels and their lifetimes against spontaneous emission play very significant roles in achieving laser light amplification. Hence we now turn briefly to a discussion of spectral line widths and energy state lifetimes.

IV. SPECTRAL LINE BROADENING

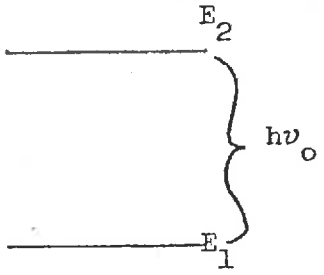

Suppose we consider light of frequency ν propagating in a medium in which there is an excited state at an energy $h\nu_o$ above the ground state. Then if $\nu = \nu_o$ we would expect to find appreciable absorption of the incident light, and attenuation of its intensity by

$$I(x) = I_o\, e^{-k(\nu_o)\, x} \qquad \text{(III-11)}$$

where $k(\nu)$ is an absorption coefficient for light at frequency ν. In our study of atomic energy levels, we have assumed the levels are of vanishing width so that only light of the proper frequency ν_o can be absorbed. If this were true, $k(\nu)$ would be nonzero only for $\nu = \nu_o$. In fact, however, an experimental measurement of $k(\nu)$ would reveal that it has the shape as shown, being peaked about ν_o. This corresponds to the fact that the excited state E_2 has a finite width, $h\Delta\nu$ (measured at half-maximum).

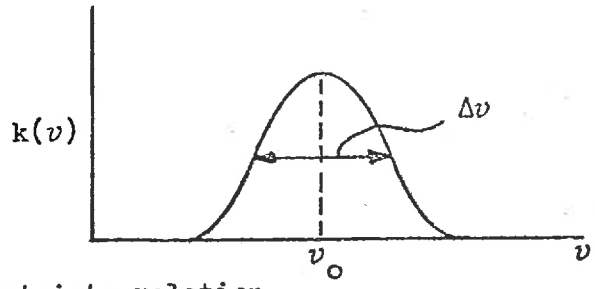

If one recalls the Heisenberg uncertainty relation

$$\Delta E \Delta t > h \quad , \qquad \text{(III-12)}$$

then a finite width ΔE implies a finite lifetime Δt to the excited state.

There are a number of physical processes responsible for such a broadening of the energy level. Of course, an isolated atom in an excited state will have a finite lifetime against spontaneous decay. But this "natural" line width is extremely small and can usually be ignored. The two major factors contributing to line broadening are the frequency variations resulting from the thermal motion of the atoms (Doppler broadening) and those resulting from the interruption of absorption or emission of radiation by atomic collisions (collision broadening).

Doppler broadening: Let's assume that the distribution of atomic velocities follows a Boltzmann distribution, so that the probability of an atom having a velocity whose z component lies between v_z and $v_z + dv_z$ is

$$P(v_z)\,dv_z = \sqrt{\frac{2M}{\pi kT}}\, e^{-Mv_z^2/2kT}\, dv_z \qquad \text{(III-13)}$$

Now this speed v_z will cause the true frequency ν_o to be Doppler shifted to an effective value

$$\nu' = \nu_o\left(1 + \frac{v_z}{c}\right) \qquad \text{(III-14)}$$

Hence the probability that an atom has a Doppler-shifted resonance frequency between ν' and $\nu' + d\nu'$ is

$$P(\nu')\,d\nu' = \frac{2}{\sqrt{\pi}\,\Delta\nu_D}\, e^{-\left(\frac{\nu'-\nu_o}{\Delta\nu_D}\right)^2} d\nu' \qquad \text{(III-15)}$$

where the Doppler width is $\Delta\nu_D \equiv \nu_o\sqrt{\frac{2kT}{Mc^2}}$

Hence this will lead to a Gaussian spectral line shape of width $\Delta\nu_D$.

Collision broadening: If an atom suffers a collision while it is radiating, the radiation is disrupted and a finite wavetrain will result. The phase of the radiation after the collision has no correlation with the phase before collision, and the emission appears to have a finite lifetime. Lorentz showed that when the frequency of collisions was small compared to the undisturbed frequency, the spectral line shape was

$$g(\nu) \cong \frac{\Delta\nu_c}{2\pi}\,\frac{1}{(\nu-\nu_o)^2 + \left(\frac{\Delta\nu_c}{2}\right)^2} \qquad \text{(III-16)}$$

(Lorentzian)

where this is normalized such that $\int_{-\infty}^{\infty} g(\nu)\,d\nu = 1$. Here the line width is

$$\Delta\nu_c = \frac{1}{\pi\tau} \qquad \text{(III-17)}$$

where τ is the mean time between collisions.

Collision broadening is sometimes referred to as "homogeneous" broadening in the sense that its effect is the same for all the atoms in the gas. The Doppler broadening is different due to the different velocities of the atoms, and hence is known as "inhomogeneous" broadening. The differences in these spectral line shapes are shown on the next page.

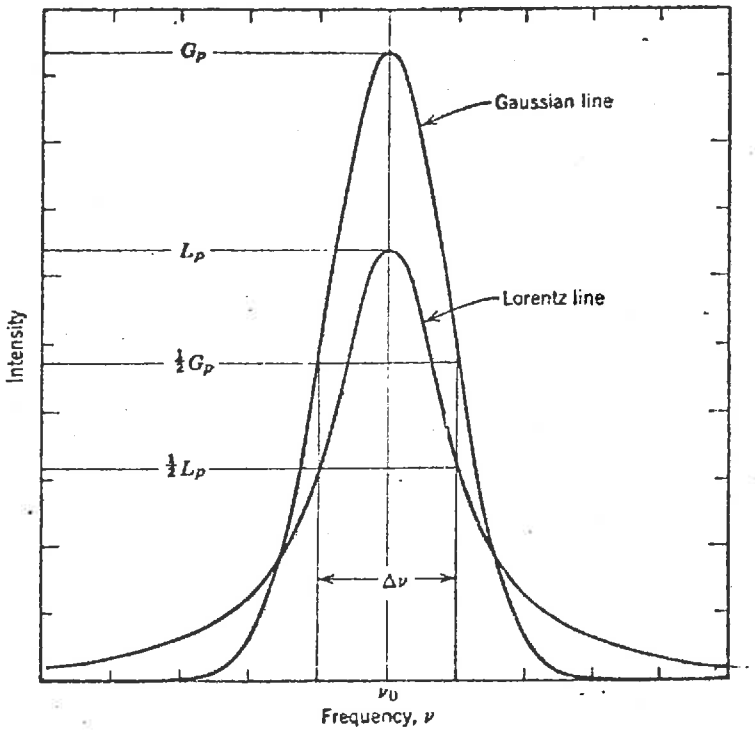

Gaussian and Lorentz lines of common linewidth. (G_p and L_p denote the peak intensities.)

We will use this information in the next lecture in which we determine the threshold for laser amplification, and outline how gain calculations are performed.

7.4. THEORY OF LASER ACTION

I. INTRODUCTION

Suppose we consider a beam of light propagating in a medium in which the atoms are assumed to have only two available energy levels.

Then the equation describing the beam intensity I_ν at any point x can be derived by considering the change in beam intensity in a frequency interval $d\nu$ due to absorption and stimulated emission over a distance dx:

$$d(I_\nu d\nu) = h\nu \left(B_{21}\, dN_{2\nu} - B_{12}\, dN_{1\nu}\right) I_\nu \frac{dx}{V} \qquad \text{(IV-1)}$$

where $v = c/\mu$ is the phase velocity of the light. If we rewrite this as

$$-\frac{1}{I_\nu}\frac{dI_\nu}{dx} d\nu = \frac{h\nu\eta}{c}\left(B_{12}\, dN_{1\nu} - B_{21}\, dN_{2\nu}\right) \equiv k_\nu d\nu, \qquad \text{(IV-2)}$$

then we can identify the absorption coefficient by integrating over the level widths as

$$\int k_\nu d\nu = \frac{h\nu_0\eta}{c}\left(B_{12}N_1 - B_{21}N_2\right). \qquad \text{(IV-3)}$$

If we now use the Einstein relations (lecture III),

$$g_1 B_{12} = g_2 B_{21}, \qquad B_{21} = \frac{c^3}{8\pi h\nu^3\eta^3} A_{21} \qquad \text{(IV-4)}$$

we can write

$$\int k_\nu d\nu = \frac{c^2 A_{21} g_2}{8\pi\nu^2\eta^2 g_1}\left(N_1 - \frac{g_1}{g_2}N_2\right) \equiv \kappa\left(N_1 - \frac{g_1}{g_2}N_2\right). \qquad \text{(IV-5)}$$

If the atoms are in thermal equilibrium, then we have seen that

$$\frac{g_1}{g_2} N_2 << N_1 \sim N_o$$

Hence we find

$$\int k_\nu d\nu = \kappa N_o \qquad \text{(IV-6)}$$

where κ can then be identified as the integrated absorption cross section per atom for the line of interest, while

$$\sigma_\nu = \frac{k_\nu}{N_o} \qquad \text{(IV-7)}$$

is the absorption cross section per atom.

When population inversion occurs such that

$$N_1 < \frac{g_1}{g_2} N_2$$

then the absorption coefficient k_ν becomes negative, corresponding to an exponential growth in intensity

$$I_\nu(x) = I_o e^{\alpha_\nu x}, \quad \alpha_\nu = -k_\nu \; . \qquad \text{(IV-8)}$$

We can calculate α_ν as before

$$\int \alpha_\nu d\nu = \kappa \left(\frac{g_1}{g_2} N_2 - N_1 \right) \qquad \text{(IV-9)}$$

(Equations (IV-6) or (IV-9) are known as the Füchtbauer-Ladenburg formulas.) If we define the <u>population inversion</u>

$$N = \frac{g_1}{g_2} N_2 - N_1 \qquad \text{(IV-10)}$$

and the relative population inversion

$$n = \frac{N}{N_o} = \frac{g_1}{g_2} \frac{N_2}{N_o} - \frac{N_1}{N_o} \qquad \text{(IV-11)}$$

then (IV-9) can be written as

$$\int \alpha_\nu d\nu = \kappa N_o n \; . \qquad \text{(IV-12)}$$

II. THRESHOLD CONDITIONS FOR LASER OSCILLATION

Consider now an aggregate of atoms in which a population inversion has been achieved such that

$$\frac{g_1}{g_2} N_2 > N_1 . \qquad \text{(IV-13)}$$

Hence a beam of frequency $\nu \sim \nu_{12}$ will grow in this medium according to the equation

$$I(x) = I_0 e^{\alpha_\nu x} , \quad \alpha_\nu = -k_\nu \qquad \text{(IV-14)}$$

Of course, in a laser oscillator, the beam must pass back and forth through the active medium many times in order to be amplified to appreciable intensities. To do this, one places the atomic "amplifiers" between two mirrors (one of which is only partially reflecting to allow some of the laser light to escape the "optical cavity"). For our present analysis, suppose each mirror has a reflectivity r and the mirror separation is a distance L (see below). If we consider only the parallel

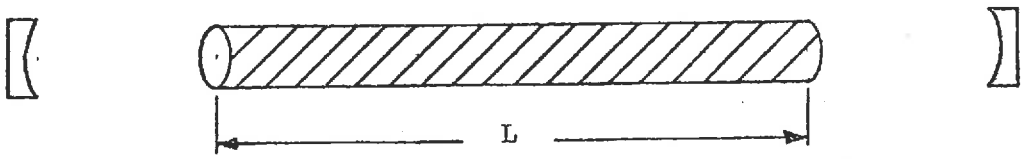

propagation of light, then upon each reflection, 1-r of the incident light energy is lost. Hence one complete pass yields an amplification of

$$F = r^2 e^{2\alpha_\nu L} \equiv e^{2(\alpha_\nu L - \gamma)} \qquad \text{(IV-15)}$$

To achieve net amplification, one requires F > 1. Hence the threshold condition on α_ν for laser amplification is

$$\alpha_\nu = \alpha_m \equiv \gamma/L . \qquad \text{(IV-16)}$$

Since α_ν will only be greater than or equal to α_m for a narrow range of frequencies, and since only modes with these frequencies will be amplified, the resultant laser output will have a line width much narrower than the atomic linewidth characterizing the lasing transition.

III. RATE EQUATIONS

We can study the dynamic behavior of a laser by writing down the rate equations describing its various state populations. For convenience, consider the 3-level laser as shown on the right, where

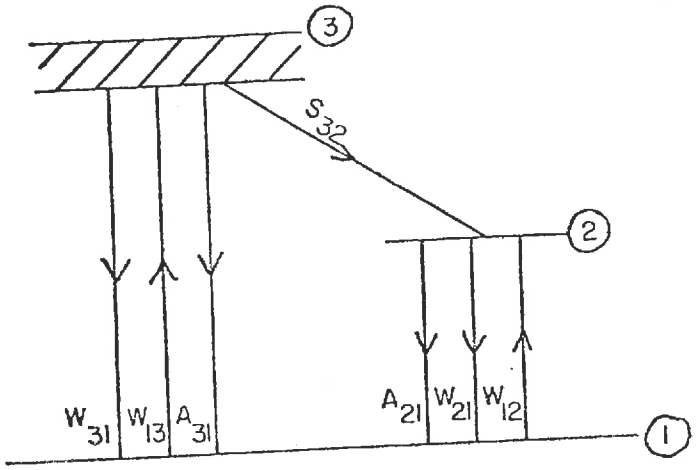

$W = u_\nu B$ = stimulated emission rate

A = spontaneous emission rate

S_{32} = rate for radiationless transition from 3 to 2

Then we can immediately write down the corresponding rate equations:

$$\frac{dN_3}{dt} = W_{13}N_1 - (W_{31} + A_{31} + S_{32})N_3$$

$$\frac{dN_2}{dt} = W_{12}N_1 - (W_{21} + A_{21})N_2 + S_{32}N_3 \qquad \text{(IV-17)}$$

$$N_0 = N_1 + N_2 + N_3$$

These equations describe the time dependent state populations for the 3-level system, but of particular interest is the equilibrium or steady state situation in which:

$$W_{13} N_1 - (W_{31} + A_{31} + S_{32}) N_3 = 0$$

$$W_{12} N_1 - (W_{21} + A_{21}) N_2 + S_{32} N_3 = 0 \qquad \text{(IV-18)}$$

$$N_0 = N_1 + N_2 + N_3$$

We can simplify these equations as follows: First note that A_{31}, the spontaneous emission rate from the upper level, will be small and can be neglected. Furthermore, Einstein's relations imply

$$W_{13} = W_{31} \qquad\qquad W_{21} = W_{12}$$

If we furthermore assume that the radiationless relaxation between levels is very fast, then $S_{32} >> W_{13}$, and we can solve (IV-18) for

$$\frac{N_2 - N_1}{N_0} = \frac{W_{13} - A_{21}}{W_{13} + A_{21} + 2W_{12}} \qquad \text{(IV-19)}$$

Notice in this equation that W_{13} is proportional to the excitation or "pumping" energy while W_{21} is proportional to the laser light output. Hence we can directly calculate the minimum value of W_{13} required to achieve the threshold condition:

$$W_{13} = A_{21} + (W_{13} + A_{21} + 2W_{12}) \frac{\alpha_m}{\kappa N_0} \qquad \text{(IV-20)}$$

It is similarly of interest to calculate the minimum value pumping power required to achieve negative absorption such that $W_{13} = A_{21}$. If n photons/sec of frequency ν_{pump} are incident, then the incident power is

$$P = n h \nu_{pump} \qquad \text{(IV-21)}$$

and furthermore

$$W_{13} = u_{pump} B_{13} = \frac{1}{c}(n B_{13} h \nu_{pump} \eta) \equiv n \sigma_{pump} \qquad \text{(IV-22)}$$

Hence to achieve negative absorption:

$$P > P_{min} \equiv \frac{A_{21} h \nu_{pump}}{\sigma_{pump}} \qquad \text{(IV-23)}$$

IV. INTERACTION WITH AN OPTICAL CAVITY

As we have seen, the laser consists of a large number of atomic amplifiers placed between two mirrors which form an optical cavity. A variety of electromagnetic modes of oscillation in this cavity are possible. Because the length of a laser is $\sim 10^5$-10^6 wavelengths, and the amplification occurs over a finite frequency range, usually a number of laser modes will be amplified simultaneously.

One can characterize the ability of the laser to amplify a given mode by the cavity quality factor

$$Q = \frac{2\pi\nu_0 E}{P_d} \qquad \text{(IV-24)}$$

where E is the energy, and P_d the rate at which the mode energy is dissipated in the cavity. In this sense, the linewidth of the cavity is given by

$$\Delta\nu = \frac{\nu_0}{Q} \qquad \text{(IV-25)}$$

As the laser oscillations build up, certain modes (those falling within the amplification line width with the highest Q) will be preferentially excited. The presence of the optical cavity (the mirrors) is essentially to the growth of oscillations, since a given wave must pass back and forth through the amplifying medium many times.

This feature can be used to pulse the laser output. If a shutter is placed in front of one of the mirrors, then oscillation growth is inhibited, and as the pumping continues, a larger and larger population inversion will build up since little stimulated emission depletion occurs. If the shutter is then suddenly removed (e.g., by using a Kerr cell), the oscillations build up extremely rapidly, leading to a laser pulse which dies out when the excited state populations have been depleted. Such pulsing amounts to artificially suppressing the Q of the cavity to allow the large amounts of energy to be stored in the population inversion, and then releasing this energy as laser light by "Q-switching" the optical cavity. Pulse widths of 10^{-8} to 10^{-7} can be achieved in this manner.

7.5. INTRODUCTORY THEORY OF GAS LASERS

I. INTRODUCTION

The spectroscopy of gas atoms is much simpler than that of atoms bound in solids, since the former interact only via collisions. For this reason there are no excited states with broad widths--that is, no broad absorption bands such as one finds in solids which are capable of absorbing polychromatic photons. Hence excitation of gas lasers by means of flash lamps is impossible. Instead one must rely on excitation by electron impact and transfer of excitation by resonant atomic collisions.

As atoms are excited into higher energy states and then cascade down to lower energy levels by nonradiative (collisional) transitions, a nonequilibrium situation will be set up in which states of longer lifetimes accumulate a larger number of atoms. Such an accumulation is particularly prevalent for those states for which radiative transitions are forbidden by selection rules (so-called "metastable" states). We will see that such metastable states play a key role in influencing the competition between excitation and decay rates of the energy levels necessary for successful population inversion.

The most convenient excitation mechanism is that by inelastic electron atom collisions in an electrical discharge. In such a discharge, electrons are accelerated and suffer inelastic collisions with atoms, thereby exciting them to higher energy states. Such electron collisions can be used to directly achieve a population inversion, but more frequently the electron excitation is redistributed by means of resonant atomic collisions. Frequently a second gas with energy levels near to the lasing gas is introduced into the discharge to facilitate this energy transfer.

II. THE HELIUM-NEON LASER

As an example, consider the Helium-Neon laser in which transitions occur as shown on the next page:

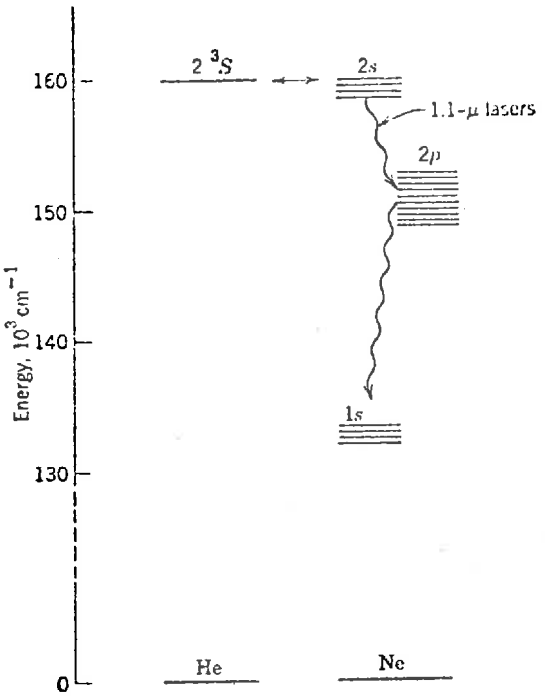

Energy levels of He and Ne involved in the cycle of the 1.1-μ laser.

The 2^3S state of He is metastable (direct radiative transitions to the singlet ground state are forbidden) and can be populated by an electric discharge in which He atoms are excited by electron collisions and cascade down to the 2^3S state. The He atoms in the 2^3S state then suffer resonant collisions with the ground state neon atoms, thereby exciting them up to one of their 2s states. Radiative transitions from 2s to 2p are allowed in neon. Since the 2p levels are not populated by He-Ne collisions, a population inversion is possible and hence lasing can occur between the 2s and 2p states (with a wavelength of 1.15 microns). Transitions from 2p to the lower s levels are quite rapid, hence implying a population inversion can be maintained during lasing between 2s and 2p.

It is important to note that it is actually the excited metastable state helium atoms which pump the neon atoms into a population inversion. In this sense, the helium atoms act as a funnel to convey the broad band of electron excitation into a few sets of neon levels. Of course some Ne atoms will also be excited into both 2p and 2s states directly by electron collisions, hence reducing the population inversion. For this reason, the neon density is kept considerable below the helium density.

There is yet another effect characteristic of gas lasers. If the neon 1s level population becomes too high, photons emitted by a 2p → 1s transition from one neon atom can excite another neon atom in a 1s state. This process is known as radiation trapping and has the effect of increasing the lifetime of the 2p state, hence reducing the population inversion.

Many other types of noble gas transitions have been used (both electronic and ionic) in laser applications. We have discussed the helium-neon laser only because of its simplicity and its historical interest as the first gas laser.

III. THE CO_2 LASER

Currently there is very considerable interest in the development of molecular gas lasers capable of delivering high output powers with high efficiency in the infrared wavelengths. Of particular interest are the CO_2 and CO molecular lasers, because of their output wavelengths of 10.6 and 5 microns, respectively, which fall in the atmospheric transmission windows, and because they possess remarkable potential for efficiently producing extremely high output powers (either pulsed or cw).

A. Excitation Mechanisms

As we have seen, the CO_2 laser utilizes transitions between different vibrational-rotational levels in the CO_2 molecule (see below):

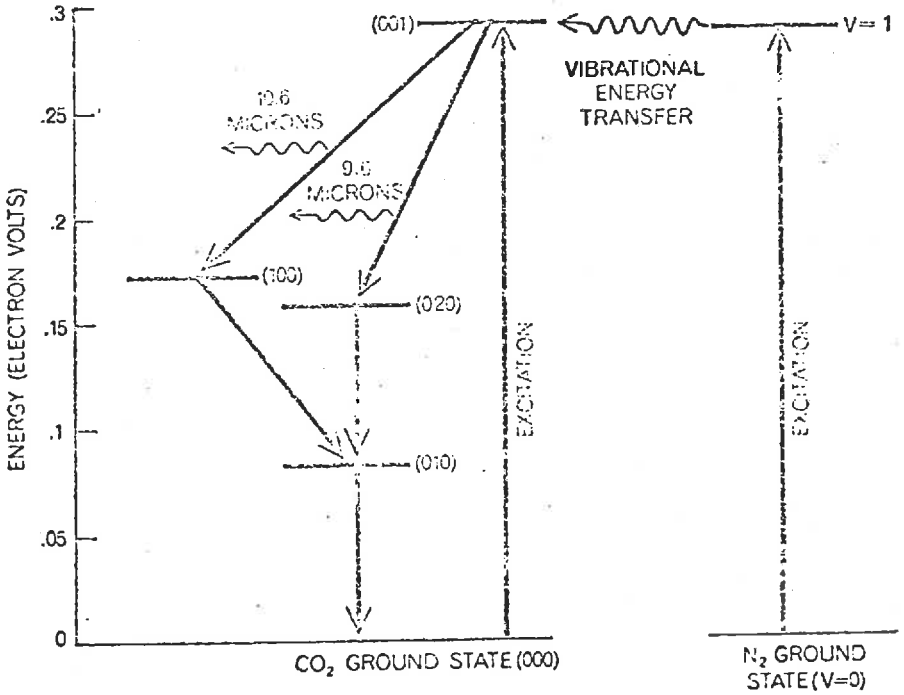

In particular, transitions between the (001) asymmetric stretch vibrational mode and the (100) symmetric stretch mode yield laser light at 10.6 microns wavelength. However, even though the CO_2 laser involves molecular transitions, its excitation and population inversion mechanisms are very similar to those of the He-Ne laser (which utilizes electronic transitions).

In the CO_2 laser, nitrogen N_2 plays the role of the energy transfer species by being excited into higher vibrational levels by electron collision in a discharge, and then transferring this energy into CO_2 vibrational levels by resonant collisions. Since nitrogen N_2 is a diatomic molecule, it has only one degree of vibrational freedom. Furthermore, since N_2 is homonuclear, its excited vibrational states (in the ground electronic state) cannot decay radiatively (there is no electric dipole moment). Hence these states are extremely long lived--i.e., metastable. The higher N_2 vibrational levels $N_2(v)$ are almost equally spaced. Hence resonant collisions between the N_2 molecules will tend to cascade the more highly excited $N_2(v)$ molecules into the $N_2(1)$ states.

These $N_2(1)$ molecules, in turn, will transfer their energy of excitation to the CO_2 molecules in a resonant collision exciting the $CO_2(001)$ state. Since the higher $CO_2(00v_3)$ levels are also evenly spaced, resonant collisions will enhance the population of the $CO_2(001)$ level via cascading down from upper vibrational levels.

Once having emitted a 10.6 photon in the $CO_2(001) \rightarrow CO_2(100)$ transition, the molecules must still cascade down through the (010) level to the ground state. Again the transition from (100) to (010) occurs via resonant collisions, but this time with (020) molecules. The final transition from (010) to the ground state is nonresonant and involves the conversion of the excitation energy into kinetic energy via collisions. Sometimes He gas is introduced to facilitate this final transition--again via resonant collisions.

B. Quantum Efficiency

At this point, some mention should be made of the very high "efficiency" of the CO_2 laser. The normal definition of efficiency would be

$$\frac{\text{output power of laser beam}}{\text{input power of electrical discharge}} \equiv \text{working efficiency}$$

But there is a more inherent limitation on efficiency which is directly attributable to the quantum transitions which occur in pumping and lasing. One defines

$$\frac{\text{energy emitted in lasing transition}}{\text{excitation energy}} \equiv \text{quantum efficiency}$$

In the case of CO_2, the energy of excitation to the CO_2(001) level is $\sim$.3 eV, while the lasing transition is $\sim$.12 eV. This corresponds to a quantum efficiency of 40%. The remaining 60% of the excitation energy is wasted in the transitions from (100) to the ground state and ultimately appears as thermal energy of the gas.

The electrical-discharge-resonant-collision mechanism of pumping the CO_2 states can be made very efficient, and in practice one can design the CO_2 laser such that the working efficiency approaches the quantum efficiency. This is in very sharp contrast to high power solid state lasers (such as Nd glass) which typically operate at a 0.1% working efficiency, primarily due to the inefficiency of pumping using black body radiation (i.e., flash lamps).

C. Single Mode Operation

One further point should be discussed. We have seen that the vibrational levels have a detailed fine structure (the P and R branches) due to rotational energy states (see below):

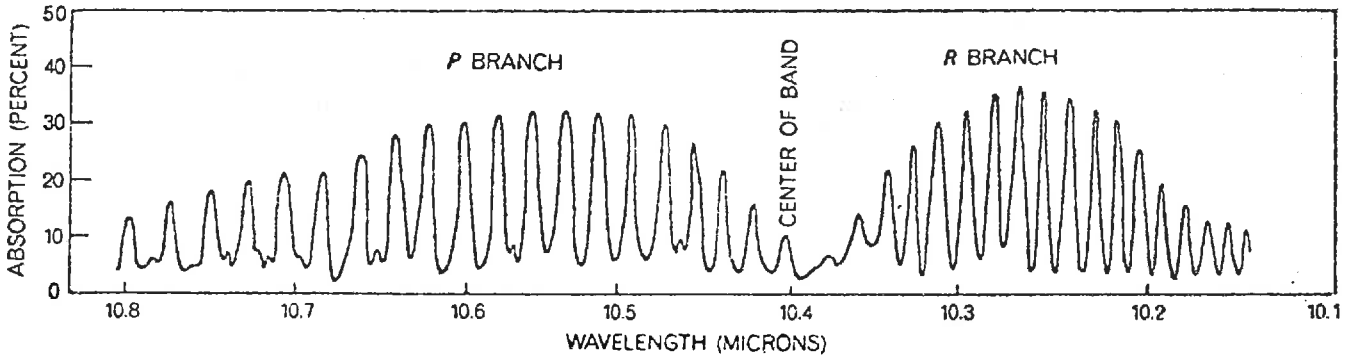

In practice the lasing can be made to occur from a single P-branch transition, P(20) at 10.5915 microns, by exploiting some subtle competitions between P and R branch transitions.

This arises because the spacing between rotational levels, unlike the vibrational levels, is much less than the kinetic energy of the molecule (typically $\sim$.025 eV). Hence the population density of a given

rotational level is closely coupled to other levels via collisions ("rotational thermalization") which in turn gives rise to a Boltzmann distribution of populations among the levels ($\exp(-E_j/kT)$)

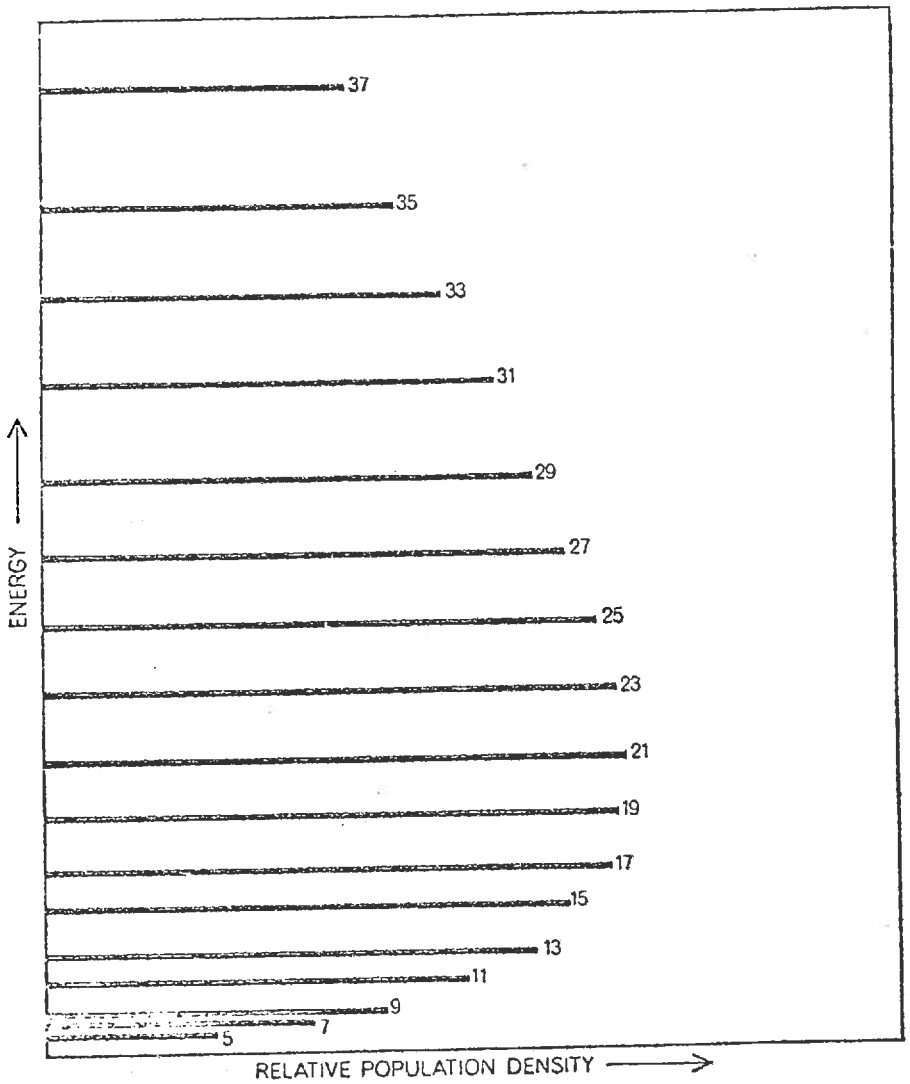

The rotational transition with the highest gain (say P(20)) will start oscillating first. But thermalizing collisions will transfer other molecules into the P(20) upper level even as stimulated emission drains them out. Hence the population density of all the other levels decreases, and the P(20) transition will dominate, yielding a monochromatic output.

D. Pulsed Mode Operation

We have seen earlier that by controlling the characteristics of the laser optical cavity (Q-switching), a laser can be pulsed thereby yielding enormous powers. By using nonlinear optical devices such as bleachable dyes, one can shorten even the Q-switched pulses by mode-locking

to achieve even higher powers (some present day Nd glass lasers can achieve 10^{15} watts). Gas lasers such as the CO_2 laser can also be operated in a pulsed mode, but Q-switching is unnecessary if one instead pulses the pumping electrical discharge ("gain switching") and uses an atmospheric pressure (or higher) gas in the laser.

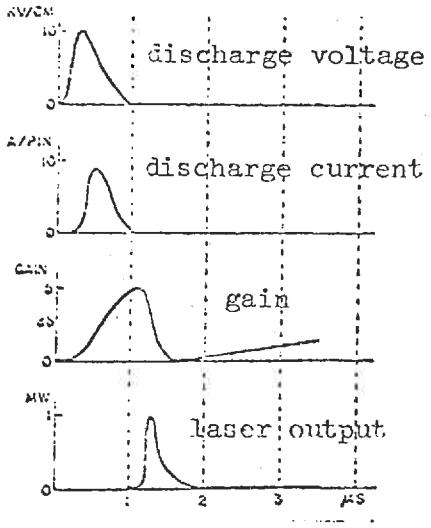

If the discharge is pulsed in a time less than 1 μsec, the laser gain will reach its maximum near the end of the discharge. But it will take some time for the dominant mode of the optical cavity to build up to a power sufficient to deplete the excited levels (typically about 40 round trips in the cavity corresponding to about 300 nsec). Hence the gain (e.g. the population inversion) will reach a large value before the laser field becomes sufficiently strong to rapidly depopulate the upper lasing level--without the necessity for Q-switching. This gain switching technique is capable of generating pulses of widths 100-200 nsec.

Even shorter pulses can be generated by mode-locking the laser. However this requires that a number of modes be simultaneously amplified in the laser oscillator. Since gas lasers are characterized by their very narrow bandwidth ($\sim$ 3-4 GHz in atmospheric pressure CO_2), this is very difficult to accomplish at atmospheric pressures or lower. However by going to higher pressures, say greater than 10 atmospheres, collisional broadening will cause the rotational lines of the P branch to broaden and overlap, giving an amplification band of nearly 10^3 GHz. Hence with this large bandwidth, many modes will be available for mode-locking, and in principle, pulses as short as 10^{-12} sec should be possible.

IV. THE CO LASER

Yet another molecular gas laser with a great potential for high power operation is the CO laser. Unlike CO_2, CO is diatomic and hence has only one ladder of energy levels, corresponding to a single vibrational mode. Lower laser levels of a given transition can serve as the upper level of a subsequent transition, thus permitting the vibrational energy

to be extracted as coherent radiation through several pairs of levels for which the populations are sufficiently inverted. Any molecule reaching a terminal laser level can be re-excited by resonant collisions, and hence the absence of lasing on the lower levels will not limit efficiency. This is in sharp contrast to the CO_2 laser in which the energy of the CO_2(010) level is dissipated as heat energy through "vibrational-translation" collisional relaxation. Such vibrational-translation relaxation times for the lower CO states are quite long by comparison. Instead the resonant "vibration-vibration" exchange collisions will dominate the molecular kinetics, hence re-exciting the lower energy states. For this reason, the quantum efficiency of the CO laser is nearly 100%. (To date, 50% working efficiency has been achieved.)

The primary excitation mechanism is again electron inelastic collisions which excite vibrational states in a N_2, CO_2 mixture, with the N_2 transferring its excitation to CO vibrational states via resonant collisions. Many more vibrational levels are involved in the CO system than in the CO_2 case, and hence the molecular kinetics are much more complicated.

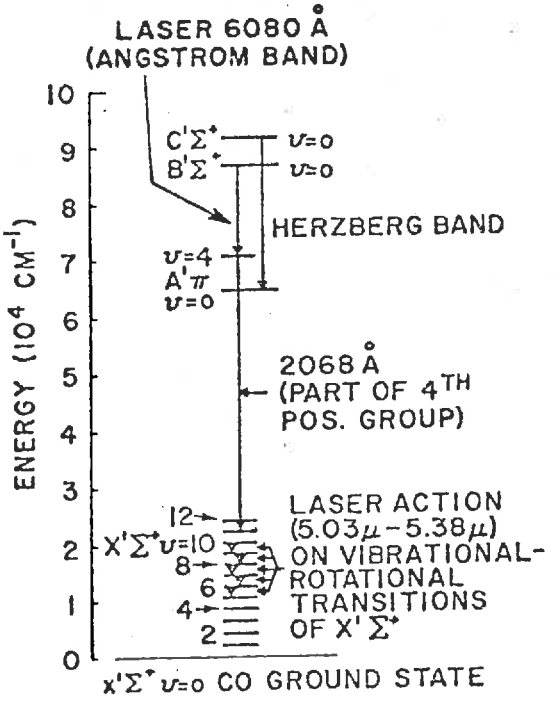

Partial energy level diagram of CO, showing the electronic laser transitions belonging to the Ångström band, and vibrational-rotational laser transitions belonging to the $X^1\Sigma^+$ ground electronic state. (Rotational levels have been left out for simplicity.)

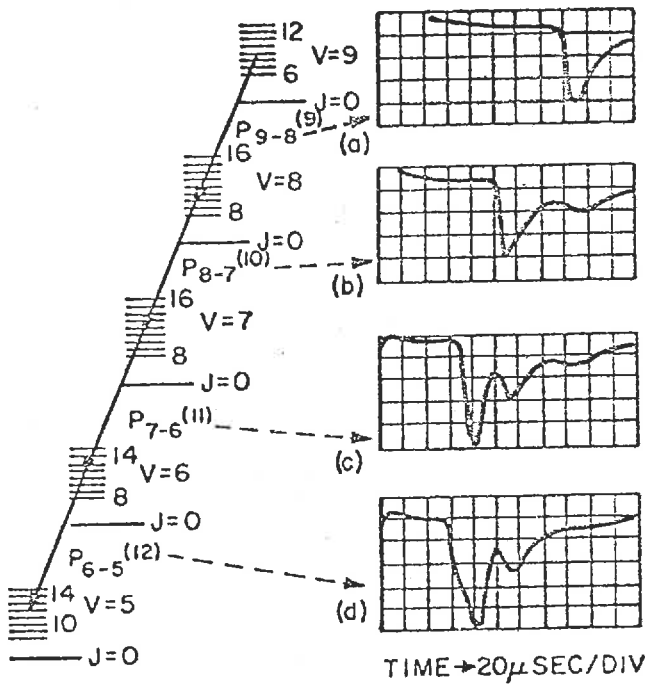

Typical cascade laser power outputs for the vibrational-rotational transitions of CO($X^1\Sigma^+$ electronic ground state). (a) $P_{9\text{-}8}(9)$ at 5.26310μ; (b) $P_{8\text{-}7}(10)$ at 5.20345μm; (c) $P_{7\text{-}6}(11)$ at 5.14530μm; and (d) $P_{6\text{-}5}(12)$ at 5.08845μm. (Energy level diagram at the left showing pertinent vibrational-rotational levels is not to scale.)

7.6. CO_2 LASERS

The relevant energy levels in the CO_2-N_2 mixture are shown below

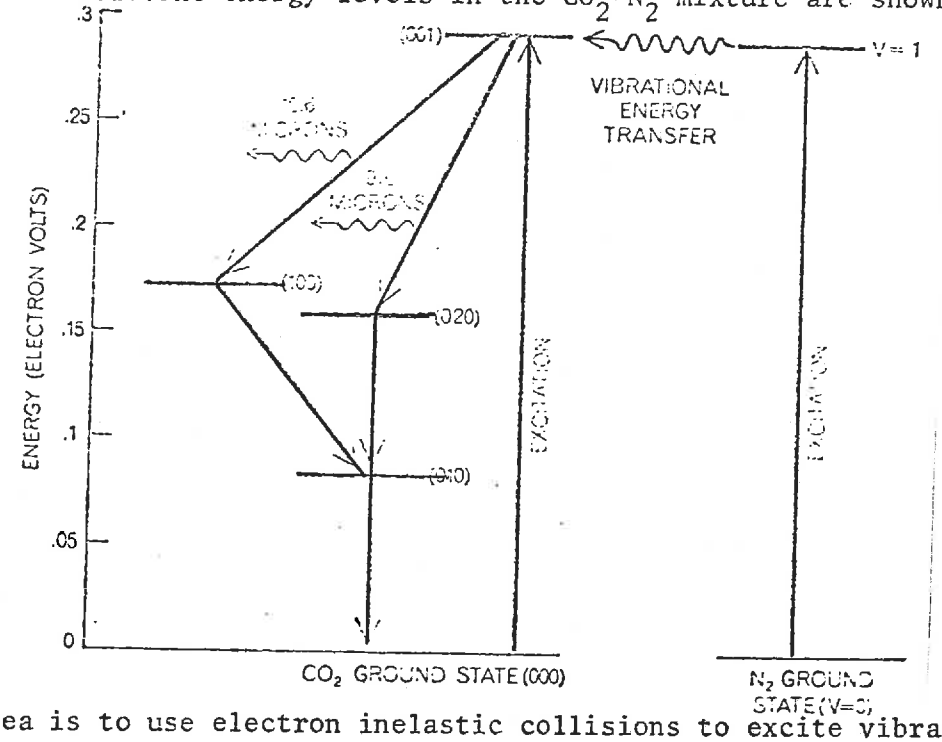

The idea is to use electron inelastic collisions to excite vibrational states of CO_2 and N_2, and then rely on the long lifetime of the (001) CO_2 state and the vibrational excitation exchange occurring in collisions between N_2 and CO_2 to populate the CO_2 (001) state, thereby creating a population inversion with the CO_2(100) and CO_2(020) states. Lasing action will then occur either from

$$CO_2\ (100) \xrightarrow{10.6\ \mu m} CO_2\ (100)$$

or

$$CO_2\ (100) \xrightarrow{9.6\ \mu m} CO_2\ (020)$$

Of course, the maintenance of the population inversion relies upon the ability of the lower lasing states to rapidly depopulate in vibrational-translational collisions with either CO_2(000) or He atoms. In general, the ability of these states to depopulate will diminish as the temperature of the lasing gas rises. Usually, after about a 300 ^{o}C temperature rise, the population inversion can no longer be maintained, and the lasing action ceases (a "temperature bottleneck").

We will now examine in more detail several of the processes occurring in this laser.

The Laser Plasma

Of course, since electrons will pump the laser via inelastic scattering, we must produce a plasma in the mixture of CO_2, N_2, and He. There are several mechanisms for doing this:

Axial discharge lasers: Here, two electrodes are inserted into the gas, and a low pressure discharge is established:

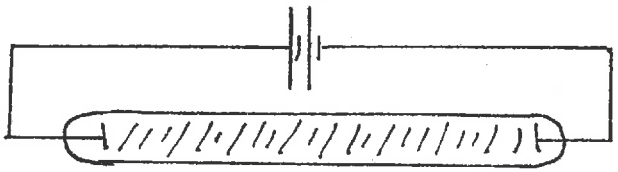

TEA (transversely excited atmospheric pressure) lasers: The electrodes are now arranged such that the discharge occurs across the laser:

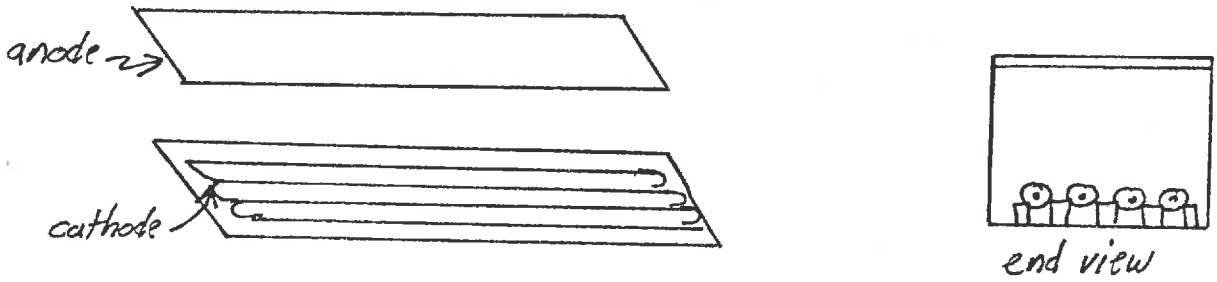

Both of these types of lasers use the applied electric field to both

(i) produce the electron plasma via Townsend avalanche

(ii) accelerate the electrons, hence "pumping" the inelastic excitation of the vibrational states of the gas.

Unfortunately, this dual role severely limits the control one has over the electron energy distribution, and hence over the pumping efficiency.

An alternative scheme is to separate the ionization and electron acceleration features, say by using incident UV light or high energy electrons to establish the laser plasma, and then use an applied drift or "sustainer" field to pump the inelastic collisions. The most popular of such approaches is the so-called E-beam laser:

E-Beam Lasers: In this approach, a high energy electron beam (~250 keV) is used to ionize the laser gas mixture. Such lasers can be operated at atmospheric or higher pressures (~10 atm):

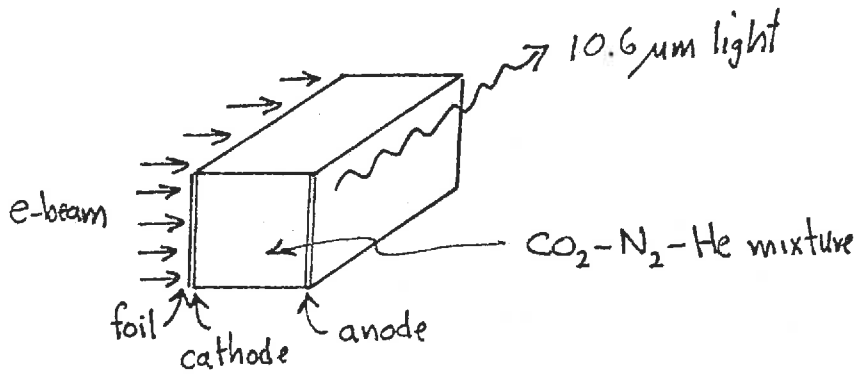

The incident or primary E-beam ionizes the laser gas mixture, producing a secondary electron density of $\sim 10^{13}$ cm^{-3}. The electron density is primarily limited by electron-ion recombination--that is, by a rate equation of the form

$$\frac{dn_e}{dt} = -\alpha n_e^2(t) + S_e(t)$$

where $S_e(t)$ is the volumetric rate of electron-ion pair production by the primary beam. The resultant current density produced in the cavity by the applied sustainer field is

$$J_d = n_e e v_d$$

where v_d is the electron drift velocity in the applied field. The power which is dissipated in electron collisions in the cavity is then simply

$$P = E_d J_d$$

where E_d is the sustainer field.

To proceed further, one must study the rate equations describing the populations of each of the molecular energy levels of interest:

$$\frac{dN_i}{dt} = \sum_j \lambda_{ij} N_j(t) + S_i$$

where λ_{ij} is the relaxation rate of each level, and S_i is the source term representing level excitation. In practice, one allocates the dissipated power P among the various levels and then solves the rate equations for the level populations $N_i(t)$.

Finally one can use our earlier results to write the laser gain as

$$g = f_x \frac{\sigma(T)}{P} \left[N_{001}(t) - N_{100}(t) \right]$$

where $\sigma(T)$ is the stimulated emission cross section while f_x is a mixture-dependent term to account for rotational relaxation.

Typically, one finds drift current and laser output power time profiles as shown below:

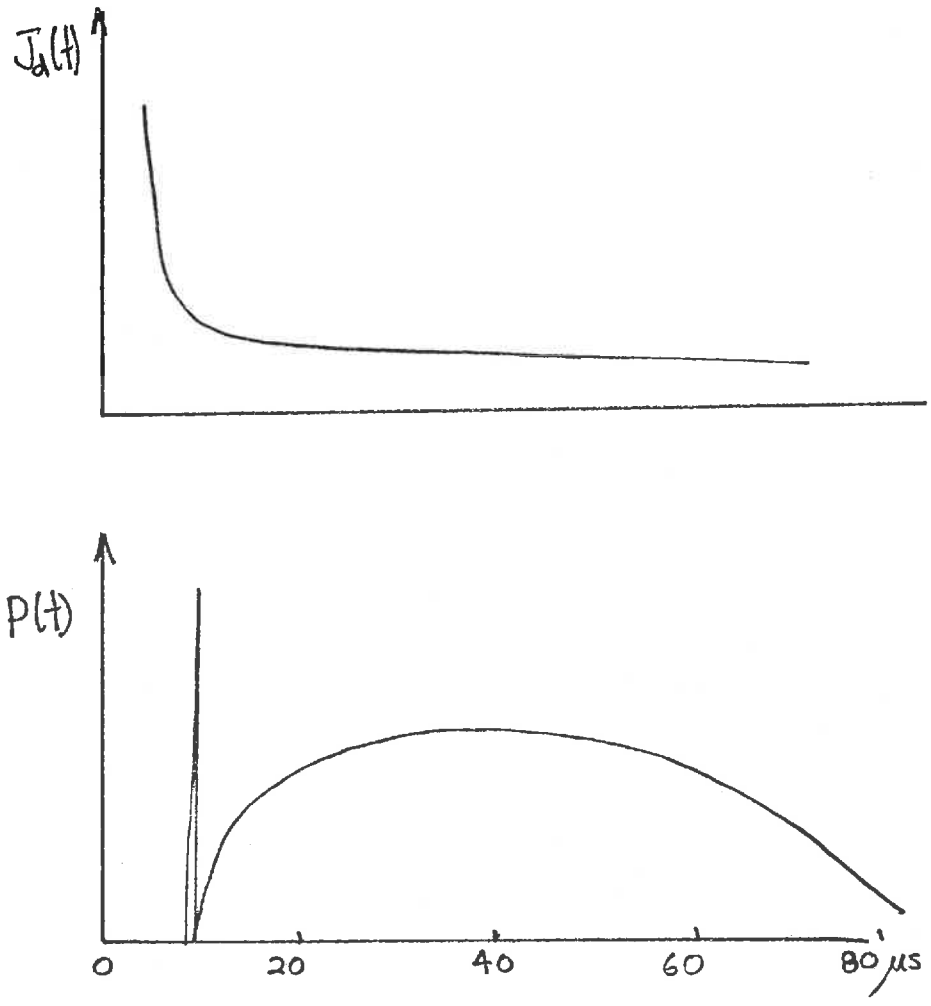

Los Alamos CO_2 Laser Systems

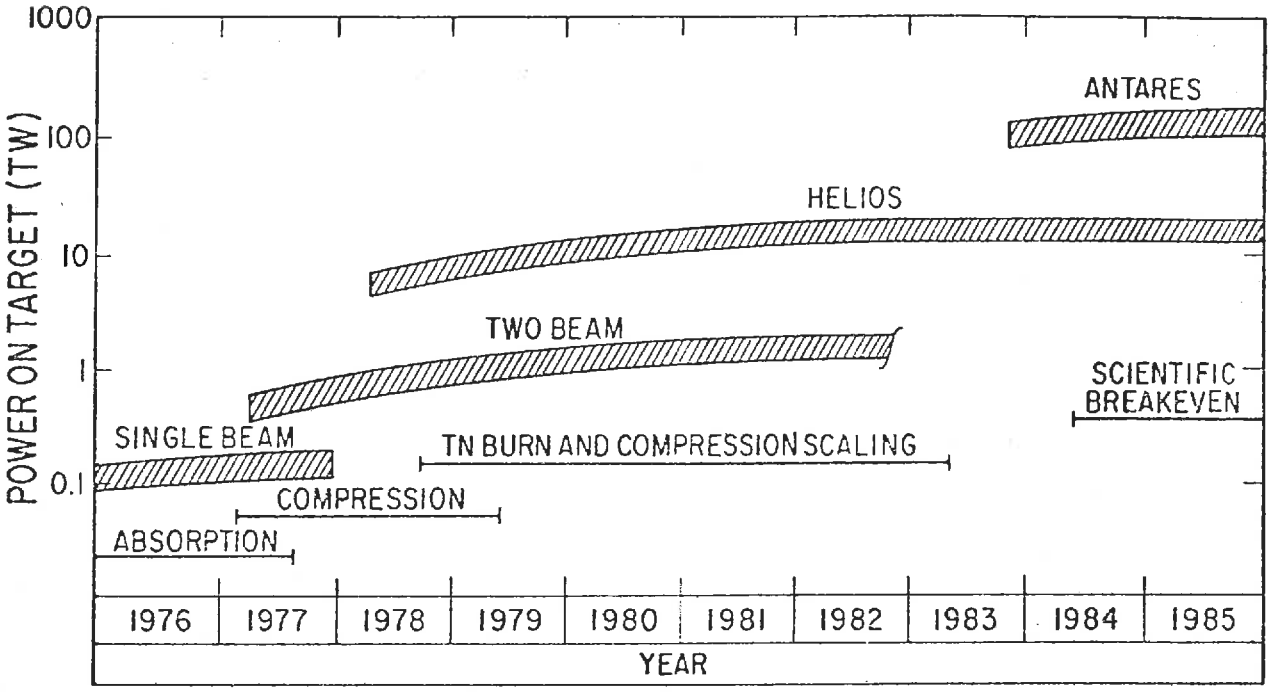

LASL is completing and operating several increasingly energetic CO_2 laser systems in the power range of 0.4- to 200-TW. In 1973, target absorption experiments at a wavelength of 10.6 micrometers began with a Single-Beam System at energy levels up to 100 J, power levels of 0.2 TW, and with on-target intensities of 7×10^{14} W/cm^2. Since October 1976, the Two-Beam System has been used in flat-foil and spherical target experiments. Beginning in January 1977, measurable quantities (3×10^5) of 14-MeV fusion neutrons were produced in experiments by compressing and heating deuterium-tritium pellets with the Two-Beam System (the first time for CO_2 lasers). In July of 1978, after exceeding its design energy goal, Helios began experiments to develop a scientific breakeven target for Antares. For future scientific breakeven experiments, the 100- to 200- TW (100 kJ in 1 ns, or 50 kJ in 0.25 ns) Antares Laser System will be used. A prototype of a sector of one of the six Antares laser power amplifiers has been developed and tested successfully.

Two-Beam CO_2 Laser System

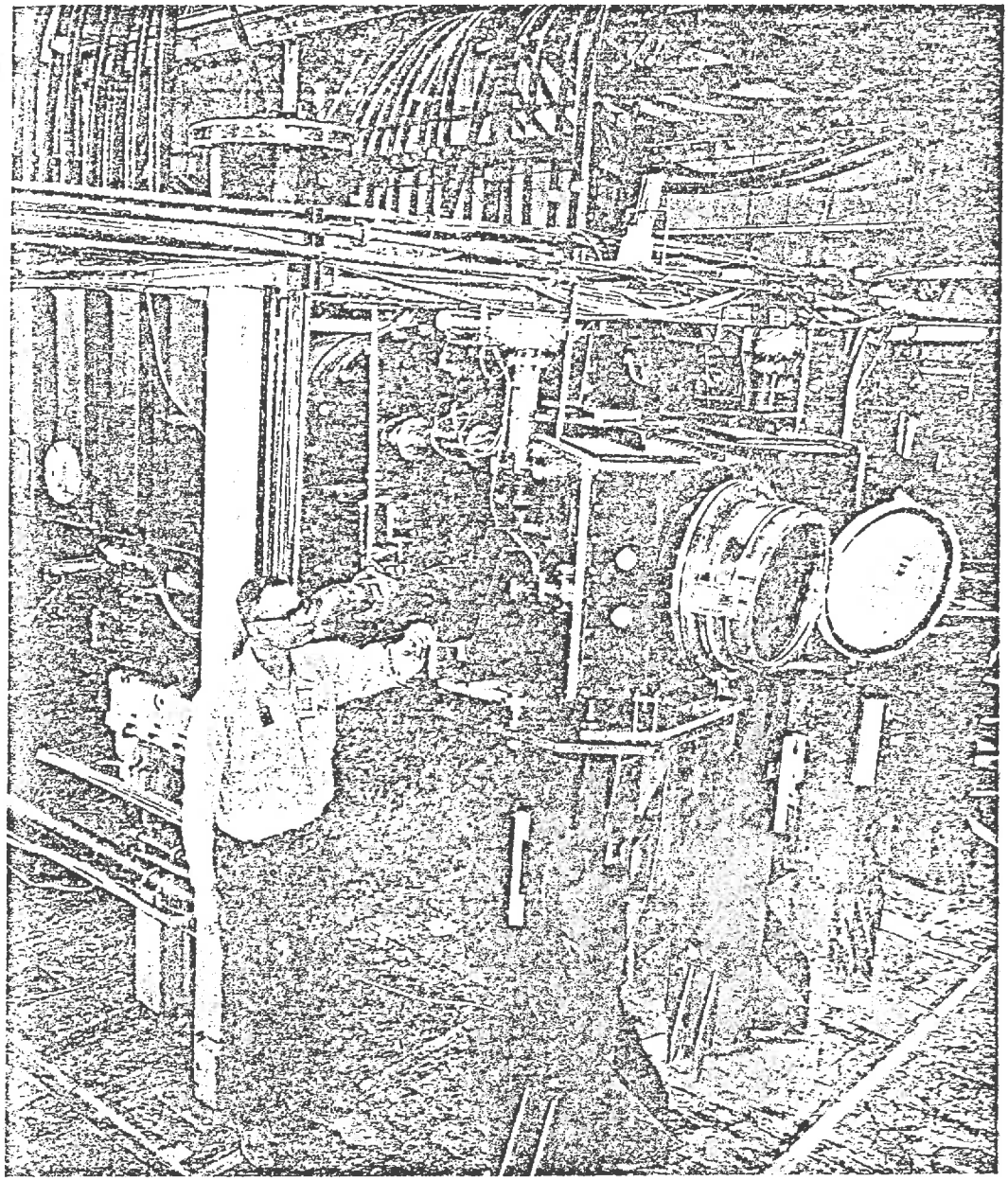

The Two-Beam System was originally intended only as a prototype for the Helios System because it included two major innovations. First, an electron-beam gun chamber at the center of the machine serves two amplifier regions, with a significant saving in cost and complexity over earlier amplifiers having only one amplifier region. Second, the system was made even more compact by using three-pass amplification — each pulse traverses the amplifier three times, the first two providing the amplification required for the pulse to extract most of the amplifier's energy on the third pass.

This photograph shows the Two-Beam System's twin power amplifier exit ends. Thick polycrystalline salt flats 30 cm in diameter and polished to high optical quality, serve as the nearly lossless transmitting windows for the two nanosecond-pulse laser beams. The windows are mounted in circular metal rings and attached to structures that are supported by pedestals. Master oscillator pulses enter at the rear of the amplifier chambers and after three passes through the two-meter-long carbon dioxide gain medium, exit through the salt windows. It was on this system that the first thermonuclear fusion reactions ever produced by a CO_2 laser were observed in early 1977.

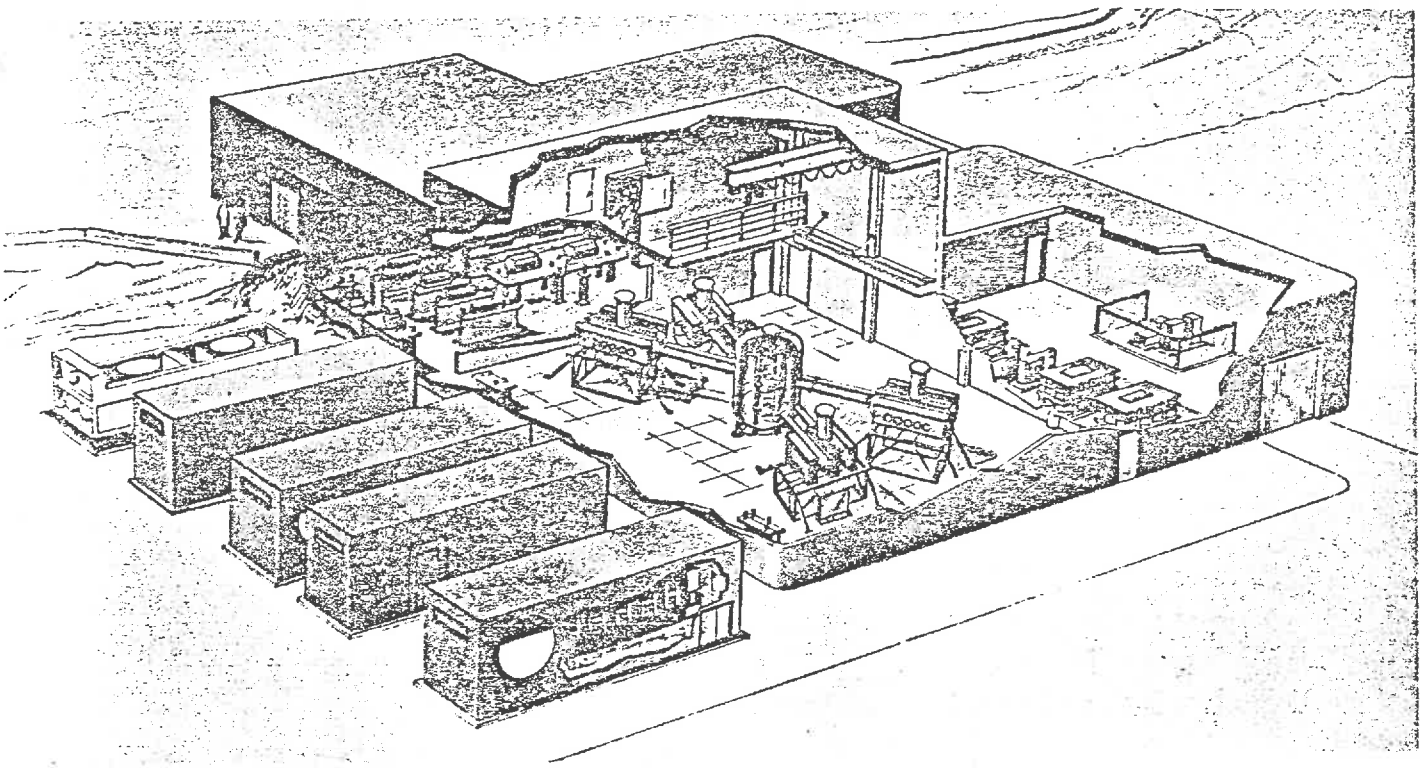

Helios CO_2 Laser Fusion Laboratory

The 10-kJ Helios System completed construction and successful testing in April 1978. It consists of four dual-beam amplifier modules that can irradiate targets simultaneously and symmetrically at power levels in excess of 10 TW. The targets are positioned at the center of an optical space frame that carries the beam focusing optics. The entire assembly is enclosed in an evacuated steel target chamber. A room housing the master oscillator and chain of intermediate amplifiers is adjacent to the power amplifier and target experiments area. Controls for charging the supplies (four brown rectangular boxes) for the power amplifiers, and the supplies (four grey objects in the right-hand room) for the electron-guns, as well as for system triggering, are located in a second-floor room above the master oscillator. All system controls, system check-out operations and operating performance data are managed by computer.

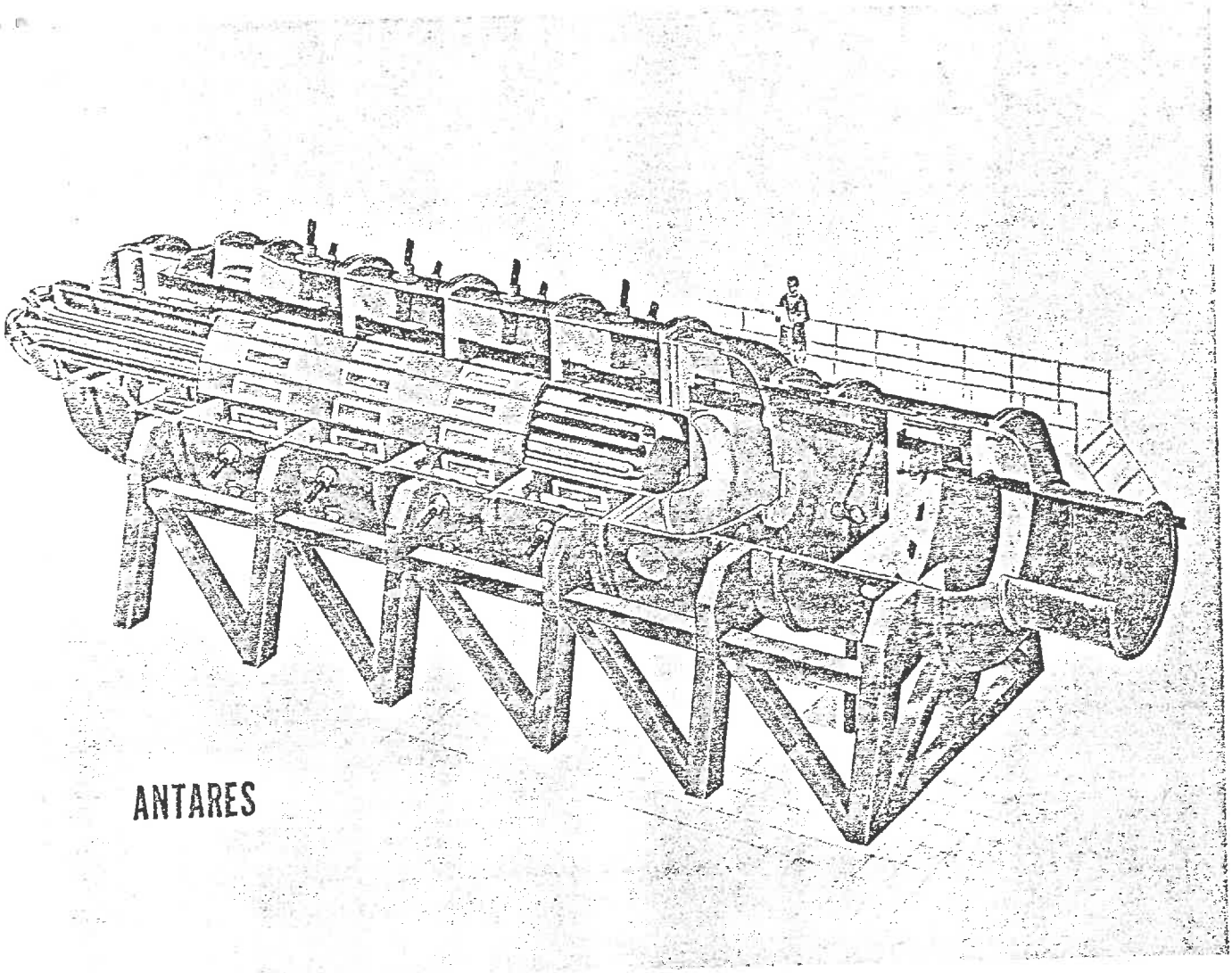

Antares Power Amplifier Module

Six of these power amplifier modules will amplify the laser pulses in Antares. The central cylinder in the module contains an electron beam source, which controls the laser gas electrical discharge. Twelve beams will be amplified by each module, each beam passing twice through the gain medium. A typical beam path is shown in red. The beam enters the CO_2/N_2-filled amplifier section from the right, then reflects from a mirror on the left for a second amplification pass. The resulting high-power laser pulses exit the amplifier to the right, entering evacuated beam tubes for transport to the target chamber. The exterior coaxial cables conduct the 550-kV, 800-kA electrical pumping pulse that excites the laser gas.

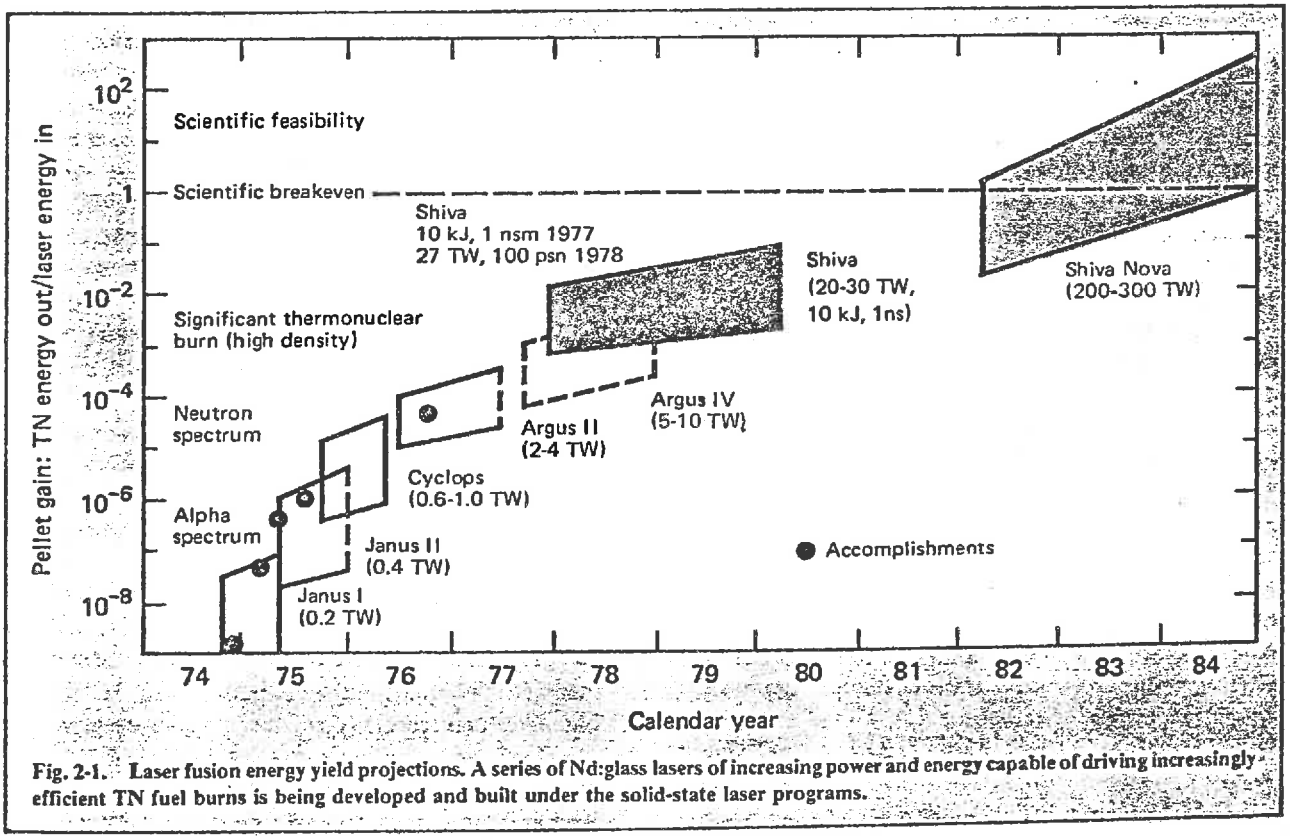

Fig. 2-1. Laser fusion energy yield projections. A series of Nd:glass lasers of increasing power and energy capable of driving increasingly efficient TN fuel burns is being developed and built under the solid-state laser programs.

Fig. 2-6. View of the Shiva laser from the exit aperture back toward the oscillator and beam-splitter arrays.

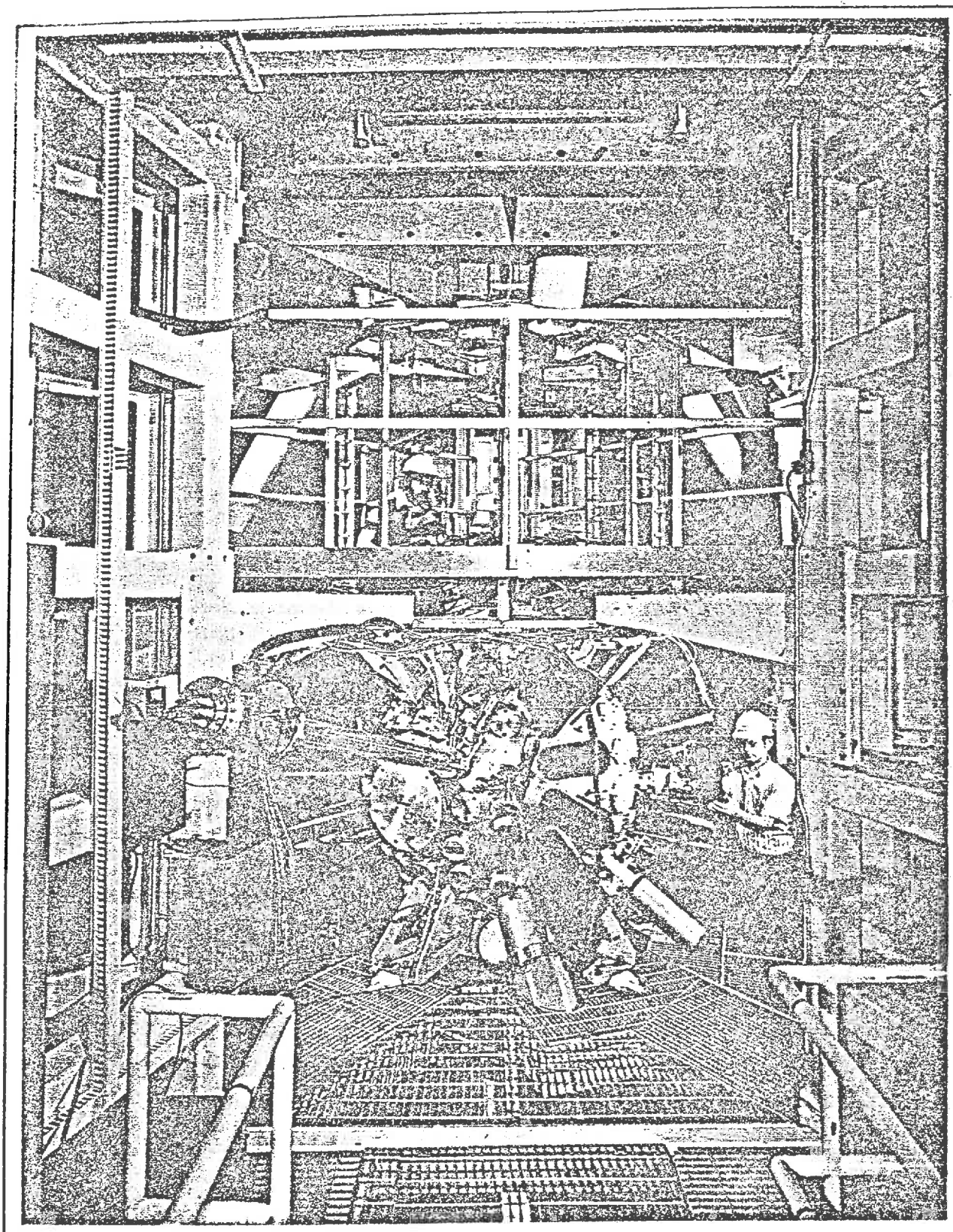

Fig. 2-62. The Shiva target chamber, rigidly supported in the spaceframe. Laser beams enter from above and below through plenums to eliminate air currents and to preserve cleanliness. The numerous black cylinders are energy-balance modules, each containing an ion calorimeter, an x-ray calorimeter, a light calorimeter, a photodiode, and a Faraday cup. The blue pipe in the left foreground contains a seven-channel x-ray detector that uses K-edge filters and PIN photodiodes to separate energy bands. The technician on the right is adjusting an x-ray microscope, which uses cylindrical Kirkpatrick-Baez imaging mirrors.

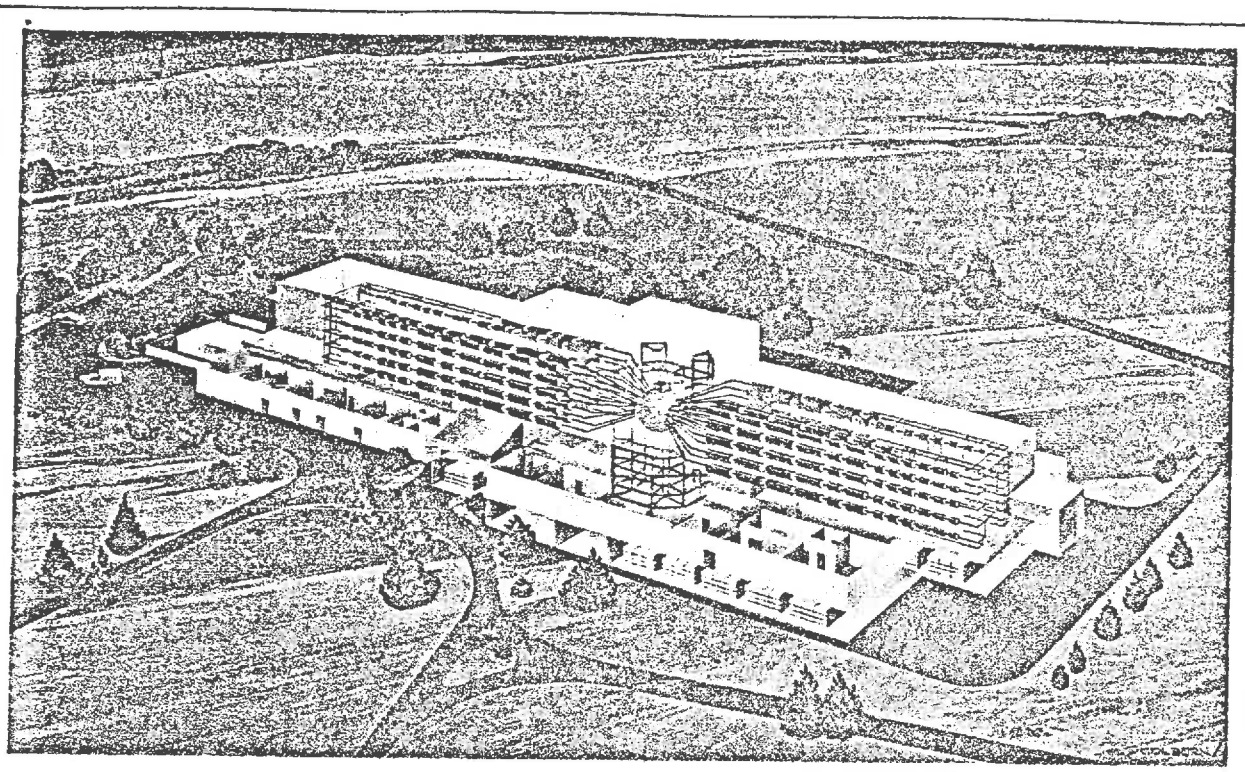

Fig. 1-2. Nova laboratory facility. The current high-energy laser facility, which houses the Shiva laser, is on the left; the laboratory addition with the new target room and Nova laser bay is on the right.

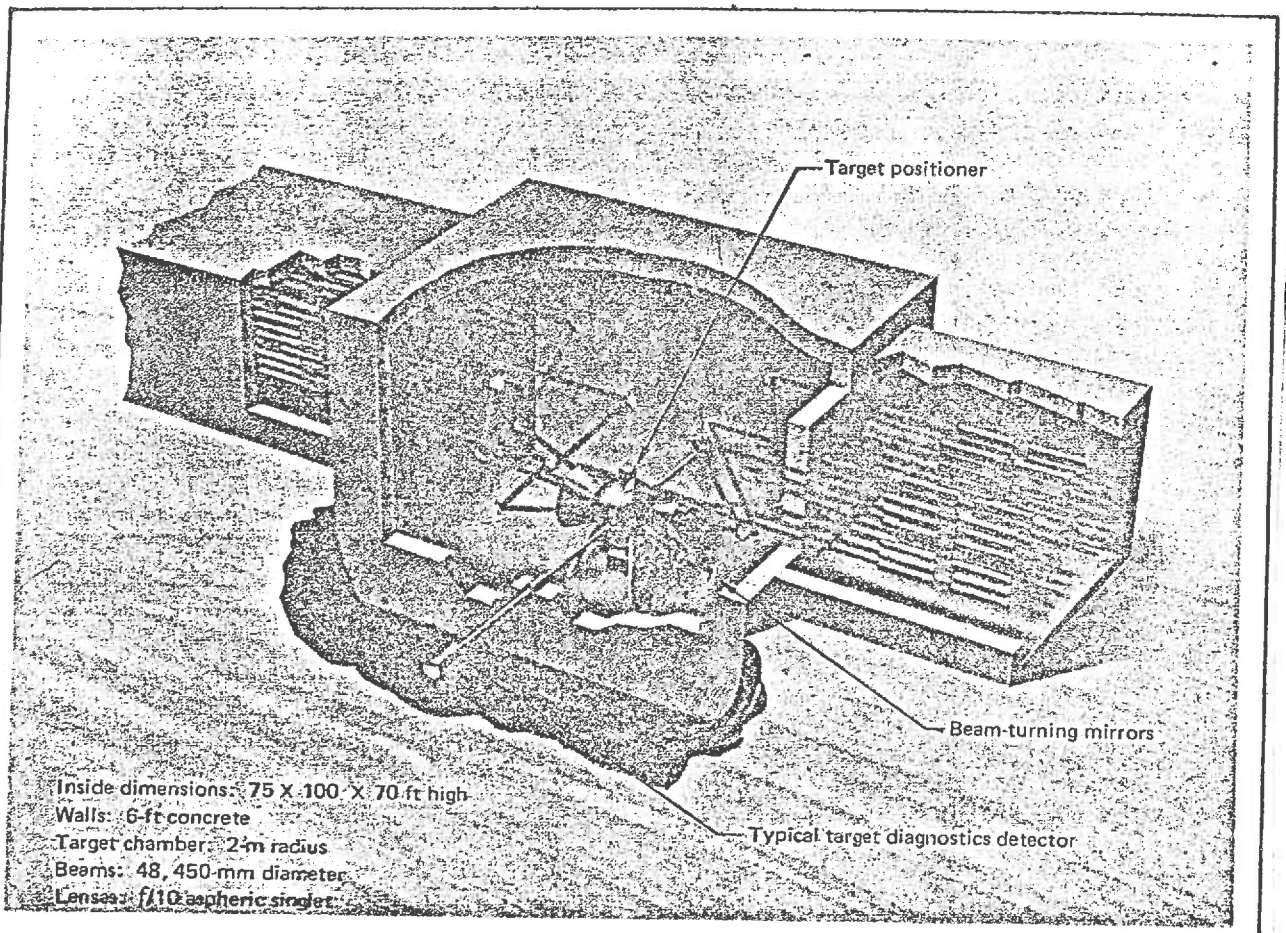

Fig. 2-104. Nova target-chamber area.

7.7. ADVANCED LASER DEVELOPMENT

A rough estimate of the potential of the lasers presently used in laser fusion research is given in the table below:

Property	CO_2	Nd:Solid	I	CO	HF
Wavelength	10.6 μ	1.06 μ	1.32 μ	5 μ	2.5 μ
Efficiency	5%	0.1%	0.5%	50%	3.3% chemical 180% electrical
Energy density	15 J/ℓ (3 atm)	500 J/ℓ	30 J/ℓ	100 J/ℓ (100 torr)	96 J/ℓ
Small-signal gain	0.045- 0.055 cm^{-1}	0.04- 0.08 cm^{-1}			
Pulsewidth	≥ 1 ns	≥ 20 ps	0.6 ns		
Demonstrated energy output	20 J (1 ns)	350 J (1 ns)	15 J (1 ns)	200 J (100 μs)	2.3 kJ (35 ns) 0.8 kJ (6 ns)
Scalability	Partially defined	Defined to 10^4 J			
Wavelength conversion	Not demonstrated	0.265-1.9 μ (≥ 40% eff)	Similar to ND:glass		
Average power capability	High (flow)	Very low	High (flow)	High (flow)	High

This should be compared with the requirements for a laser-driven ICF reactor:

Property	Value range
Laser wavelength	250-2000 nm
Pulse energy	1-3 MJ
Pulse duration	5-10 ns
Peak power	200 TW
Pulse-repetition rate	A few hertz
Average power	10 MW
Overall efficiency	≥1%

It should be apparent from this comparison that advanced types of lasers will be required to achieve these goals. The goal of any such laser system is to convert low quality conventionally stored energy (e.g., chemical fuels) to high quality energy stored in excited atomic or molecular states for extraction as laser light. There are essentially two ways that one can approach this goal:

(i) to begin with a statistical distribution (e.g., a Maxwell-Boltzmann distribution) of states and rely on energy transfer cross sections to select out only those high energy states in the tail of the distribution.

(ii) begin with a narrow distribution of states above the upper lasing level and rely on energy transfer kinetics to accomplish efficient energy down conversion

An example of the first process would be electrical discharges. Here we start with a statistical distribution of mostly low energy electrons and rely on favorable electron excitation cross sections to produce a nonthermal distribution in the radiating atom or molecule. But the trick here is to tailor the electron distribution to pump the desired state while avoiding losses into lower states. The combination of the large number of low energy electrons and the much larger cross section means that the excited state density must be low.

Hence to achieve large energy density we must use the second approach and "pump from the top" using electron beam excitation, photolytic process, or the conversion of chemical bond energy. All advanced laser types rely on this latter approach.

Of particular interest are the class of so-called "excimer" lasers in which a bound molecular state is formed from the association of a ground state atom and an excited state of the same or similar atom. This state can then radiate to the unbound ground state formed from the repulsive action of the two closed shell atoms. Of particular interest are rare gas lasers.

The rare gas excitation process is as follows:

1.) Ionization and excitation of the atoms by the high energy electron beam (with about 75% of the excited states appearing as ions).

2.) Formation of the molecular ion R^+ by three-body reactions:

$$R^+ + 2R \rightarrow R_2^+ + R$$

3.) Dissociative recombination of the molecular ion:

$$R_2^+ + e \rightarrow R^{**} + R$$

4.) Collisional deactivation of the highly excited states of the rare gas R^{**} into the lowest metastable R^* of the rare gas system.

5.) Three-body reactions involving R^*, $R^* + 2R \rightarrow R_2^* + R$, produce the excited excimers R_2^* which can now radiate.

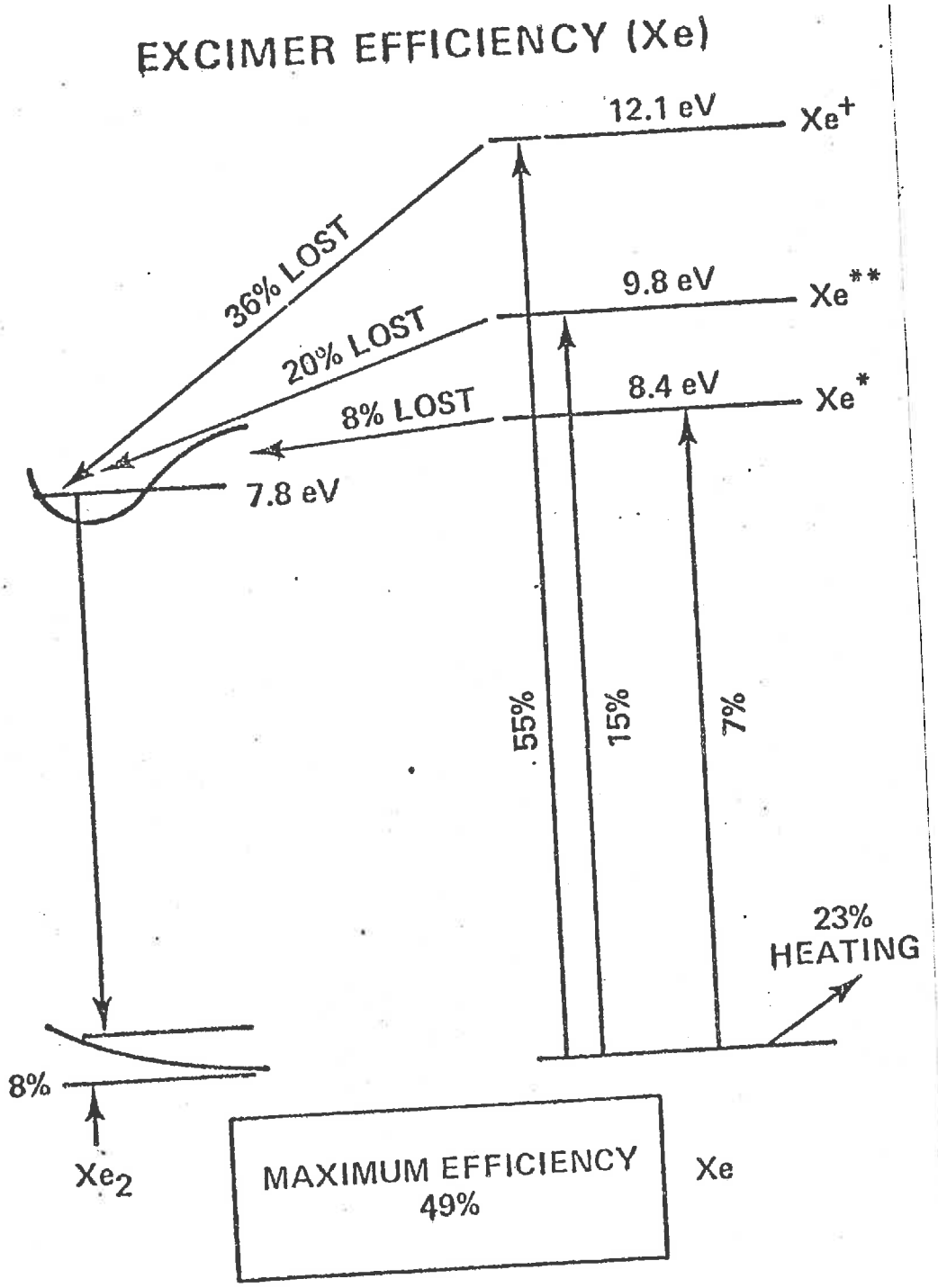
EXCIMER EFFICIENCY (Xe)
12.1 eV
Xe+
36% LOST
9.8 eV
Xe**
20% LOST
8.4 eV
Xe*
8% LOST
7.8 eV
55%
15%
7%
23%
HEATING
8%
Xe2
MAXIMUM EFFICIENCY
49%
Xe

Modeling and experimental results indicate that approximately 50% of the initial electron energy deposited in the gas appears in the excited metastable and excimer species, At pressures of 1 atm this reaction sequence occurs very rapidly, within 10 to 100 ns.

There are four classes of lasers being studied as potential ICF advanced drivers. These are listed in the table below

Potential laser systems for fusion applications.

Generic species concept	Active species	Pump source	Medium type
Photolytic group VI atoms	Sulfur (S), selenium (Se)	E-beam-driven rare gas excimers (Kr_2^*, Xe_2^*)	Storage
Rare-earth molecular vapors	Tb-A1-C1, $TbThd_3$	E-beam-driven rare gas monohalide excimer (KrF)	Storage
Rare-earth solid-state hybrids	Tm^{3+}: glass, crystal	E-beam-driven rare gas monohalide excimer (XeF)	Storage
Raman stacker/compressors	Methane (CH_4)	E-beam-driven rare gas monohalide excimer (KrF)	Nonstorage

These advanced laser types can be further distinguished by the time scale of their population inversion;

(i) In photolytic and rare earth lasers, the energy storing medium in which the population inversion occurs is stable for long periods of time in excess of several μs. Such lasers store energy for relatively long periods of time compared to energy extraction (lasing) times, Hence these lasers can be pumped for long times (comparable to storage time), However their effectiveness is limited since the pump species (photons or electrons) can easily deactivate the excited electronic states,

(ii) The rare earth and monohalide excimer lasers (such as KrF) are characterized by highly radiating media with a population inversion decay time of the order of ns. In order to pump these media for times longer than the required pulse length (10 ns) one must use sophisticated optical extraction techniques (e.g., angular multiplexing) or optical pulse compression techniques.

Photolytic Group VI Lasers

Photolytic lasers utilize an excimer laser such as Xe_2^+ to pump atomic transitions in Group VI elements such as O, S, or Se. For example, one scheme would be to use a xenon excimer pump laser to photolyze OCSe fuel. A diagram of this process is shown below:

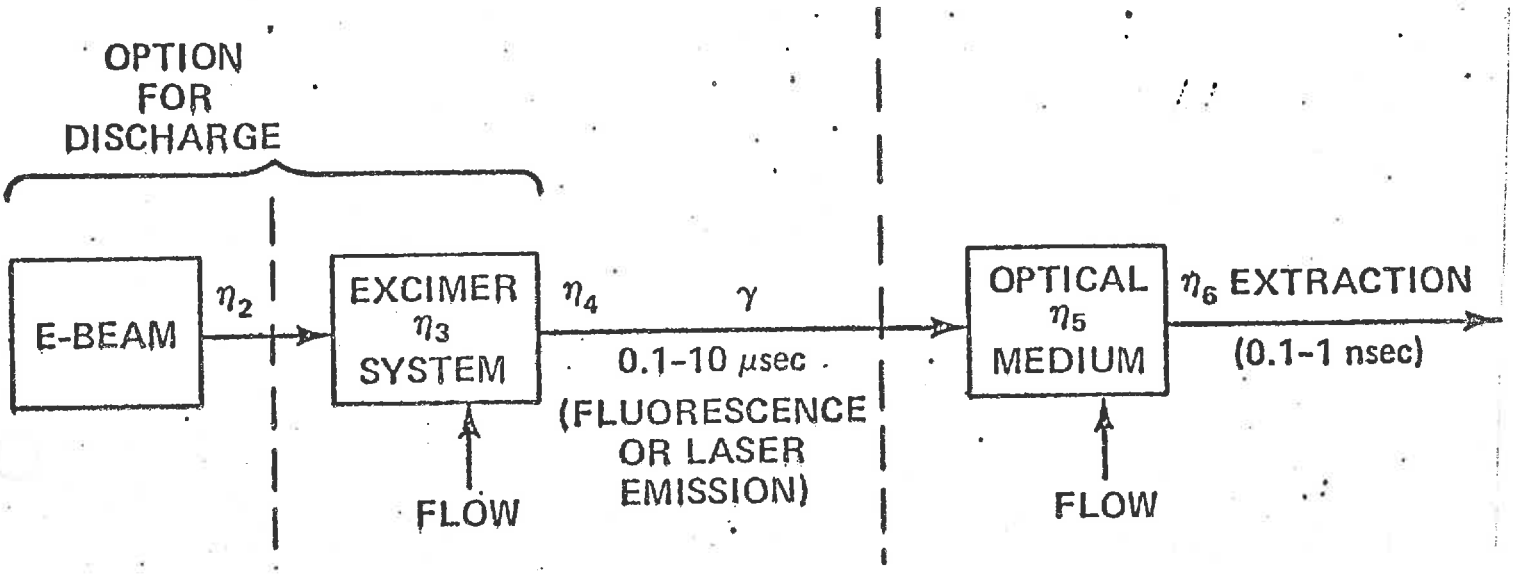

These storage lasers utilize the auroral ($^1S - {}^1D$) or transauroral ($^1S - {}^3P$) transitions of O, S, or Se:

S ($^1S - {}^1D$)	773 nm	Se ($^1S - {}^1D$)	777 nm
S ($^1S - {}^3P$)	459 nm	Se ($^1S - {}^3P$)	489 nm

The particular photolytic reactions that produce the population inversion are typified by

$$OCS + \gamma \rightarrow S(^1S) + CO \qquad 140 \text{ nm} < \gamma < 160 \text{ nm}$$

$$OCSe + \gamma \rightarrow Se(^1S) + CO \qquad 160 \text{ nm} < \gamma < 180 \text{ nm}$$

A schematic of a xenon excimer pumped LCSe laser is shown below:

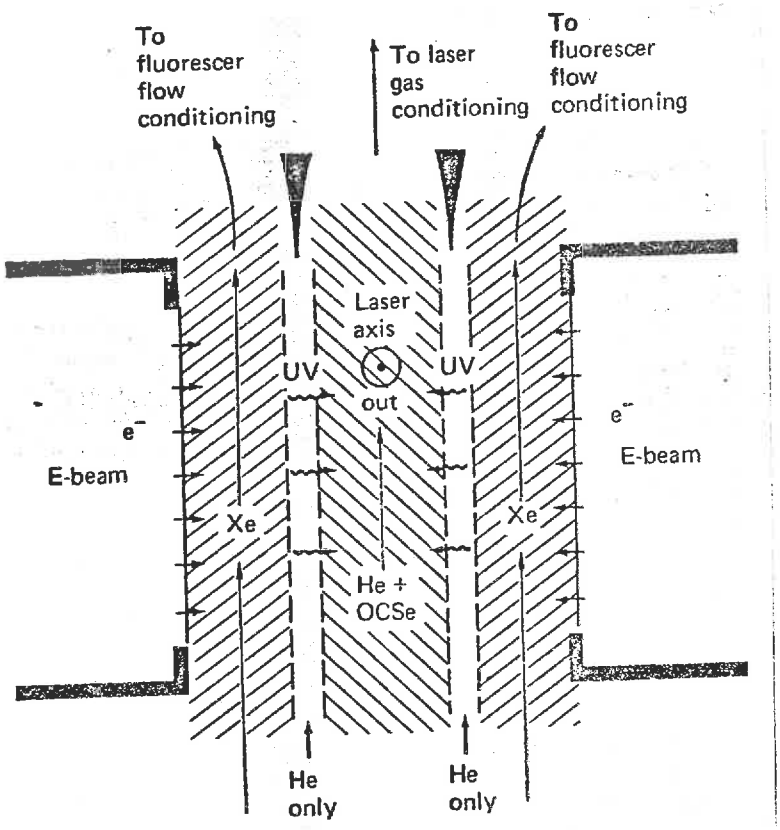

Metal Vapor Excimer Lasers:

These systems are storage lasers operating on bound-free transitions of excimers formed from lowest metastable states of metal atoms. The principal candidates under investigation are CdHg and Hg_2 lasers. Excitation is provided by an electron beam sustained discharge. Such discharges can efficiently pump metastable atomic states (with a possibility of an efficiency in excess of 10%).

(i) CdHg: This excimer is formed by $Cd(^3P)$ metastable and Hg ground state. It radiates at 470 nm. The operating conditions require 4×10^{17} cm^{-3} Cd and 4×10^{18} cm^{-3} Hg in a buffer gas at 10^{19} cm^{-3} at T $550^{o}C$.

(ii) Hg_2: This is a homonuclear excimer formed by $Hg(^3P)$ metastable and Hg ground state atoms. It radiates at 335 nm. It also requires operating conditions of 10^{19} cm^{-3} at $500^{o}C$.

Rare Gas Halide Lasers:

These are high gain excimer lasers whose upper levels are ion pair states. Examples include:

Ar F	193 nm
Kr F	249 nm
Xe F	353 nm

These lasers are excited by electron beams or electron beam sustained discharges. Since they are highly radiating (short storage), they must be accompanied by pulse compression or multiplexing to achieve desired pulse lengths.

One can use rare gas halide lasers to resonantly pump rare earth ions in a solid matrix. The long storate times of the excited ions then permits the rare gas halide pump times to be longer than several μs. A schematic of such a laser is shown below.

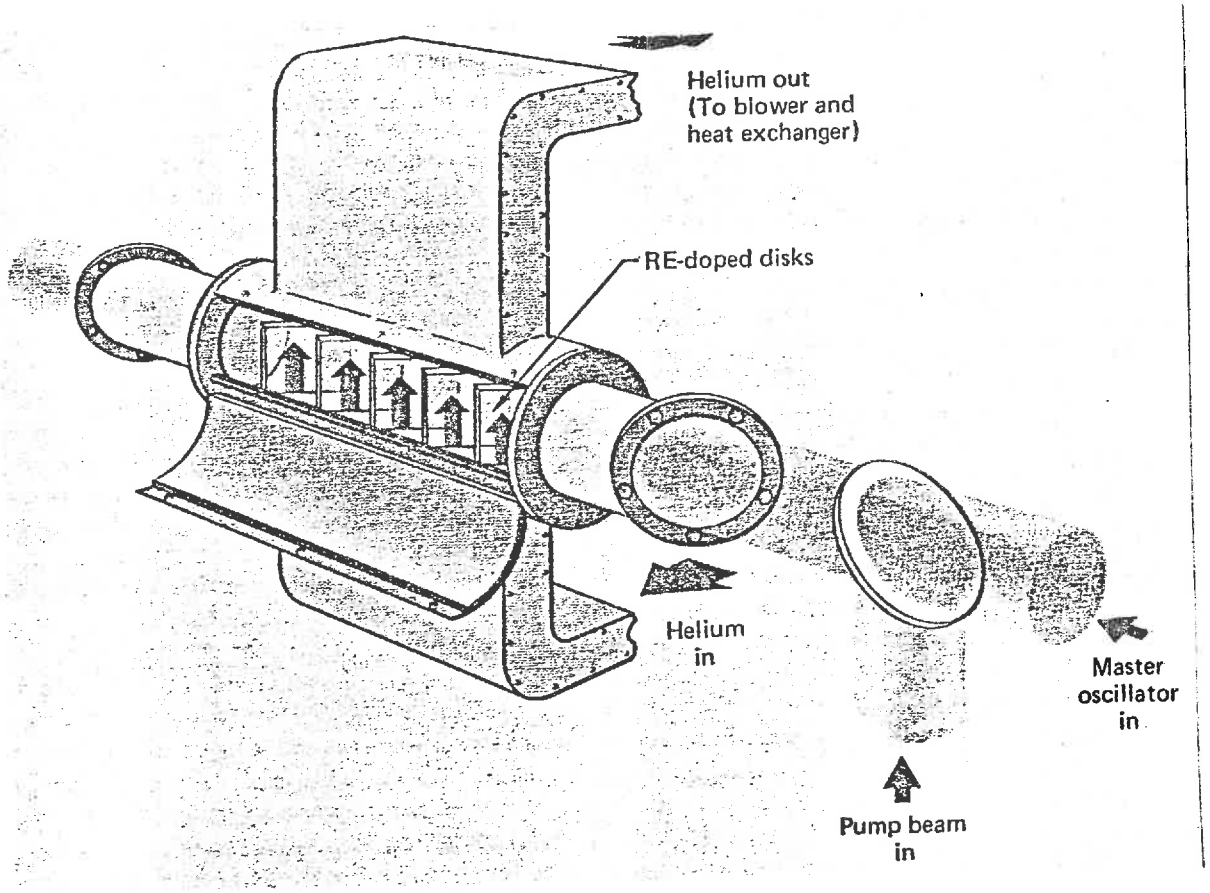

ADVANCED LASER CONCEPTS

Type	Pump	λ	Efficiency
Group VI Atomic	Optical	.48 μm	1-4%
Metal Vapor Excimers	Discharge	.33-.47 μm	10-15%
HF Channel	E-beam	2.7 μm	5-10%
Rare-Gas Halide and Conversion	Discharge	.25-.31 μm	5-10%
Resonantly Excited Solid State	Optical	.28-.45 μm	2-6%
Optically Pumped Storage	Optical	.27-.34 μm	1-7%

CHAPTER 8

DRIVER DEVELOPMENT II: PARTICLE BEAMS

We have noted that the rough requirements for ICF drivers correspond to an incident beam energy of 100 to 1000 kJ and a beam power of 100 to 1000 TW. Although this represents a significant challenge to high-powered laser development, charged particle beam accelerators seem capable of achieving such energies and powers with a mild extrapolation of existing technology. For example, we have compared in the table below the status of various proposed ICF drivers:

	lasers	electrons	light ions	heavy ions
particles	1-10 μm photons	1-10 MeV e^-	1-10 MeV p, α, Al^{+3}	1-50 GeV D-U
power	20 TW Shiva	10 TW Proto II	1 TW Gamble II	2 TW ISR
energy	10 kJ	200 kJ	70 kJ	6 MJ
seriously proposed	300 TW/300 kJ Nova	80 TW/500 kJ Angara 5	?	600 TW/10 MJ

The ability of charged particle accelerators to produce beams of the necessary energy and power with existing technology has motivated serious study of electron and ion beams as ICF drivers.

8.1 ELECTRON BEAM DRIVERS

One can distinguish between two classes of electron beam drivers. Most attention in the United States has been directed at the development of pulsed power technology which produces the beams in a diode device. In contrast the Soviet Union is developing a multiple beam approach in which the electron beams are produced and then transported over long

distances before focusing on the target.

8.1.1. Pulsed Power Diode Accelerators

Pulsed power accelerators have been used for many years as sources of intense X-rays. In these accelerators, a capacitor bank is used to store energy at high voltage. The capacitors are then discharged through switches into an insulated pulse-forming line to produce a short pulse of intense electromagnetic power. This power is propagated through a transmission line to a diode to produce an intense electron beam between a dense plasma which forms on the metal surface of the cathode and the anode. If the anode is formed from a thin foil, the intense electron beam can penetrate through the foil and propagate to a target as shown below:

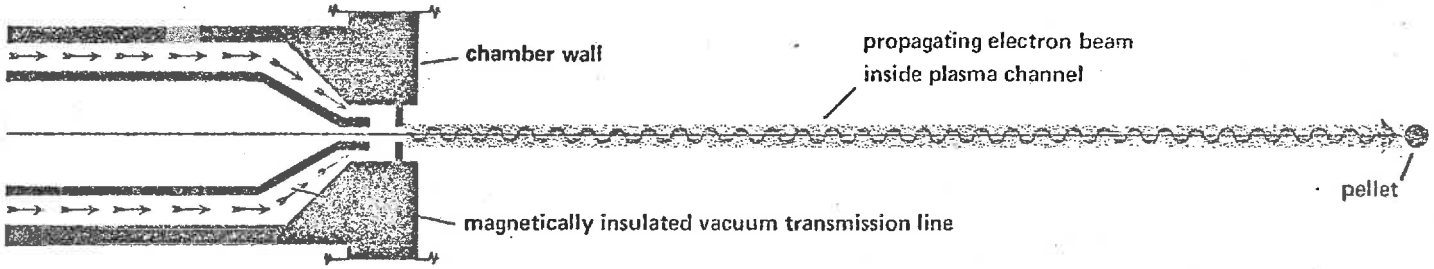

An example of such an electron beam accelerator is the Electron Beam Fusion Accelerator (which has recently been renamed the Particle Beam Fusion Accelerator) or EBFA (PBFA) under development at Sandia Laboratories. In this device (shown on the next page), 36 electron beams are produced in diodes driven by independent accelerator lines and then propagated the last 50 cm to a target along dense, magnetized plasma channels formed in air inside the target chamber. This accelerator is designed to achieve an intial power of 30 TW (by 1983) with a potential capability of 60 TW (in an upgrading scheduled for 1985). The key components of such diode accelerators are also indicated schematically.

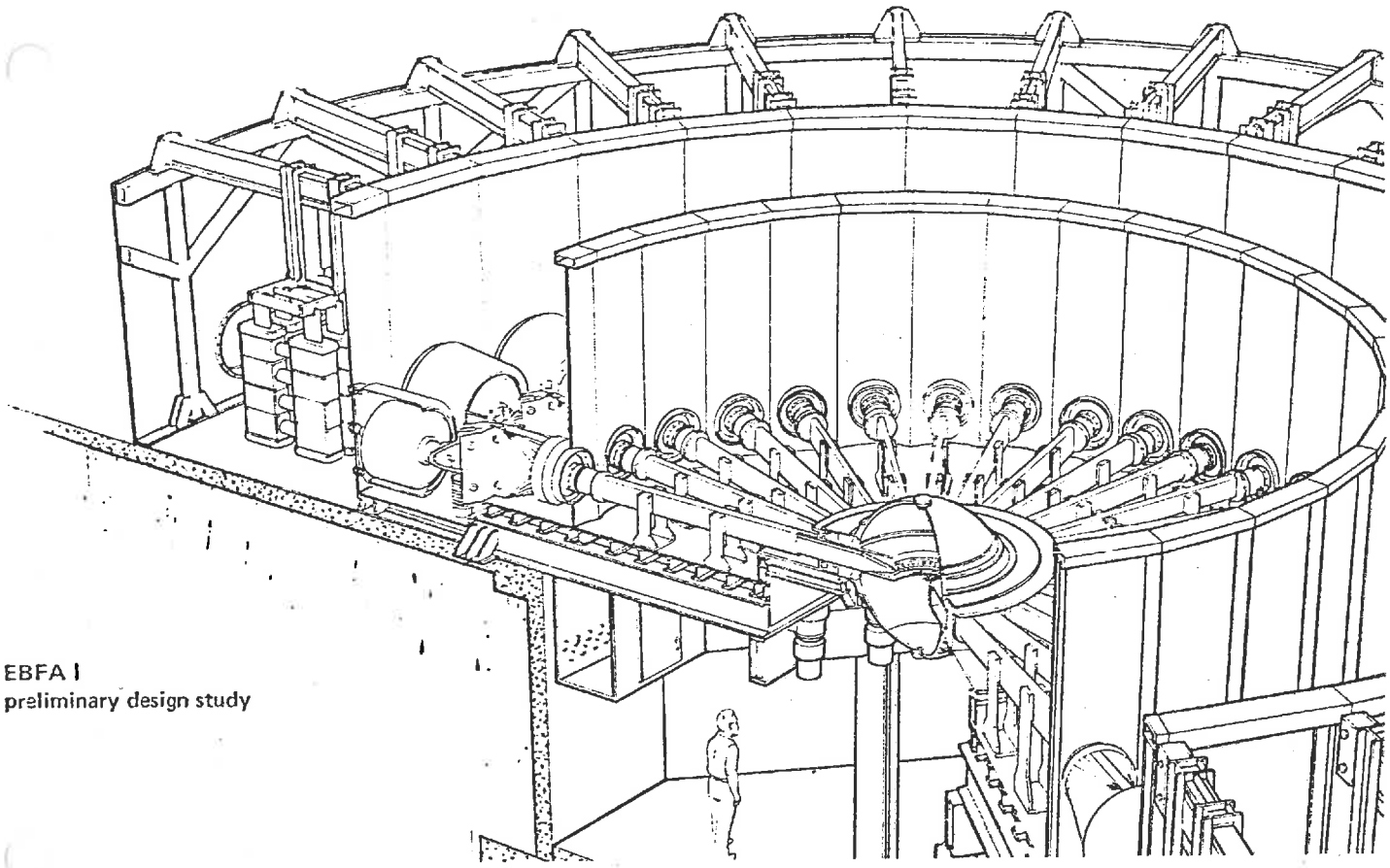

EBFA-I (PBFA-I) at Sandia Laboratories

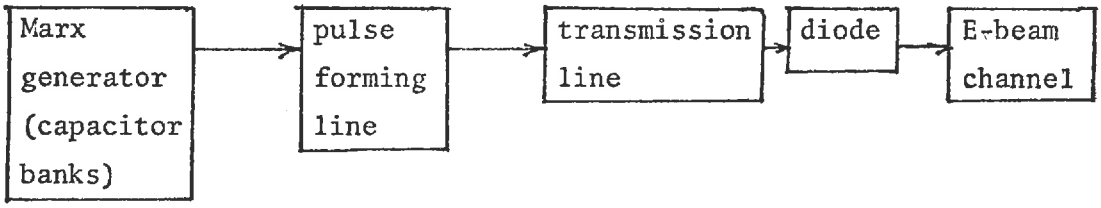

We will examine the design and function of each of these components in detail. However the general operation involves the discharge of energy from the Marx generator to a pulse-forming line where a short-duration, high power pulse is formed and then applied to the diode through a transmission line. An intense electromagnetic wave sweeps inward along the transmission line and emerges on apair of face-to-face particle accelerating diodes. One electrode, the cathode, is pulsed-

charged negatively with respect to the other electrode, the anode. When millions of volts are applied to the electrodes, the electric fields produced are sufficient to draw electrons out of the cathode material and into the vacuum. Electrons drawn from the cathode dissipate enough energy in both the cathode and anode to vaporize their surface layers and form plasmas. The cathode plasma becomes the electron source and the anode plasma provides a source of positive charge to neutralize the electrostatic field of the beam.

The basic components of a diode accelerator include:

Capacitive energy storage system: This is typically a Marx generator that functions as both a storage device and a voltage multiplier. The Marx generator charges capacitors in parallel and then discharges them in series to achieve a very high voltage. The rise time of the pulse produced by the Marx generator is too slow for accelerator applications, so one must next compress the pulse in time.

Pulse-forming Lines: A pulse forming network is used to compress the electrical energy into a short, fast pulse, roughly doubling the output voltage in the process. This can be either a single pulse line or a more complex transmission line developed by Blumlein (and illustrated on the next page).

Transmission line: The energy pulse then travels as an intense electromagnetic wave down a transmission line to a diode. The high-voltage insulation of the transmission line is of particular concern since it determines the maximum voltage pulse allowable.

Diode: The diode consists of a cathode and an anode foil separated by a short gap. When the high voltage pulse arrives at the cathode, its voltage causes intense field emission from the cathode tip which produces a plasma on the surface of the cathode and leads to the production of an intense stream of electrons moving toward the anode. At high energies the electrons can easily penetrate the anode foil and continue on to form a relativistic electron beam with beam currents of up to several Mamps. This process is shown on the next page.

The Blumlein principle

as applied to the Sandia Laboratories PROTO 1 Electron Beam Accelerator

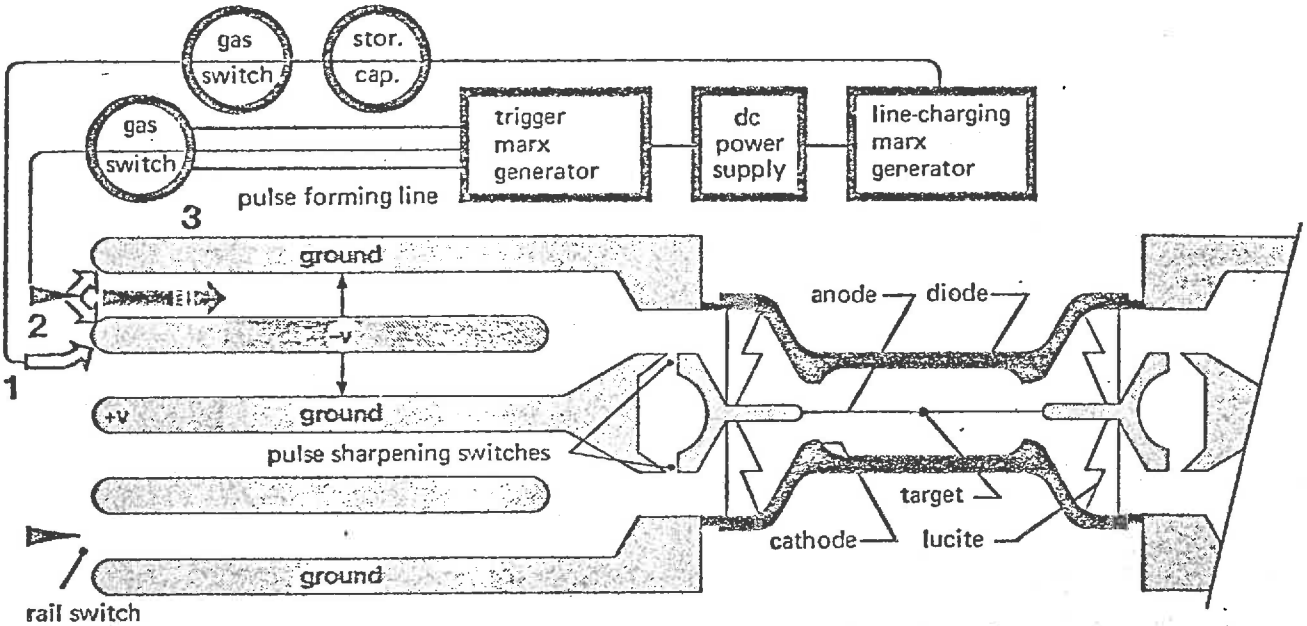

1. The center transmission line is charged (shown for one Blumlein).
2. A high voltage pulse is applied to the trigger electrodes.
3. The trigger switch pulse initiates an electro-magnetic wave which traverses the length of the transmission line three times.

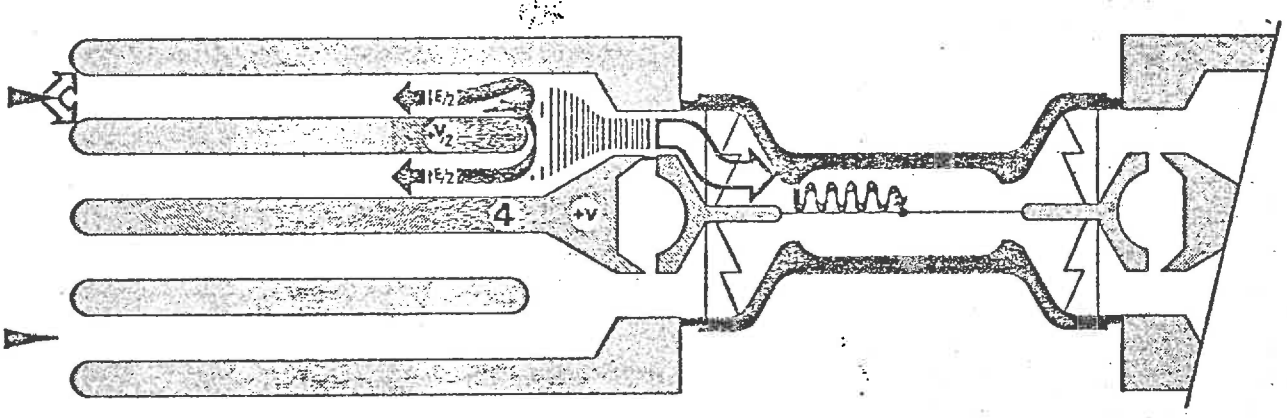

4. At the end of the first traverse the wave is reflected back and energy begins to flow into the diode.
5. All of the stored energy is released into the diode as the wave makes the second and third traverse.

6. The 2 trillion watt Electron Beam is deposited in the fusion target in 24 billionths of a second.

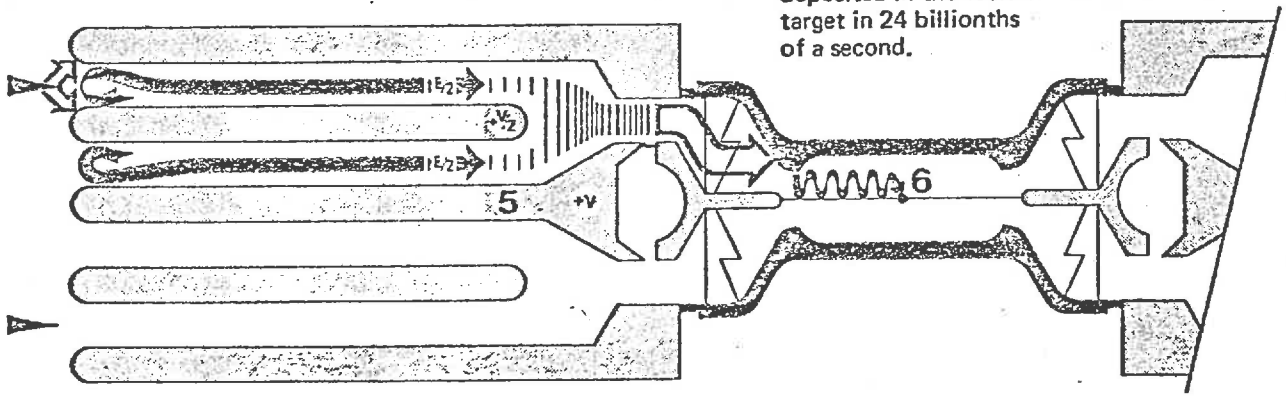

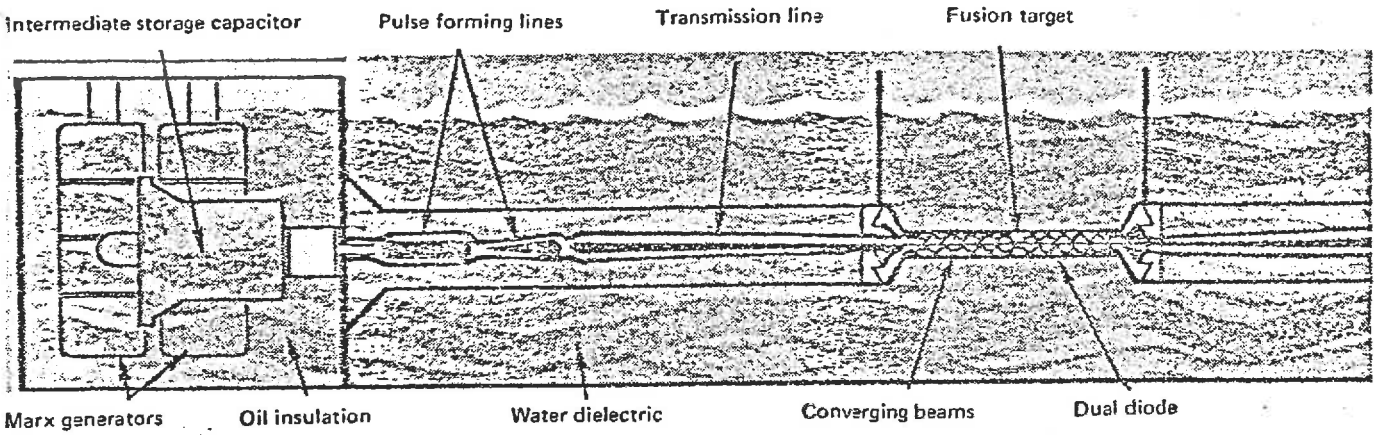

Schematic of the accelerator elements used in the power compression process.

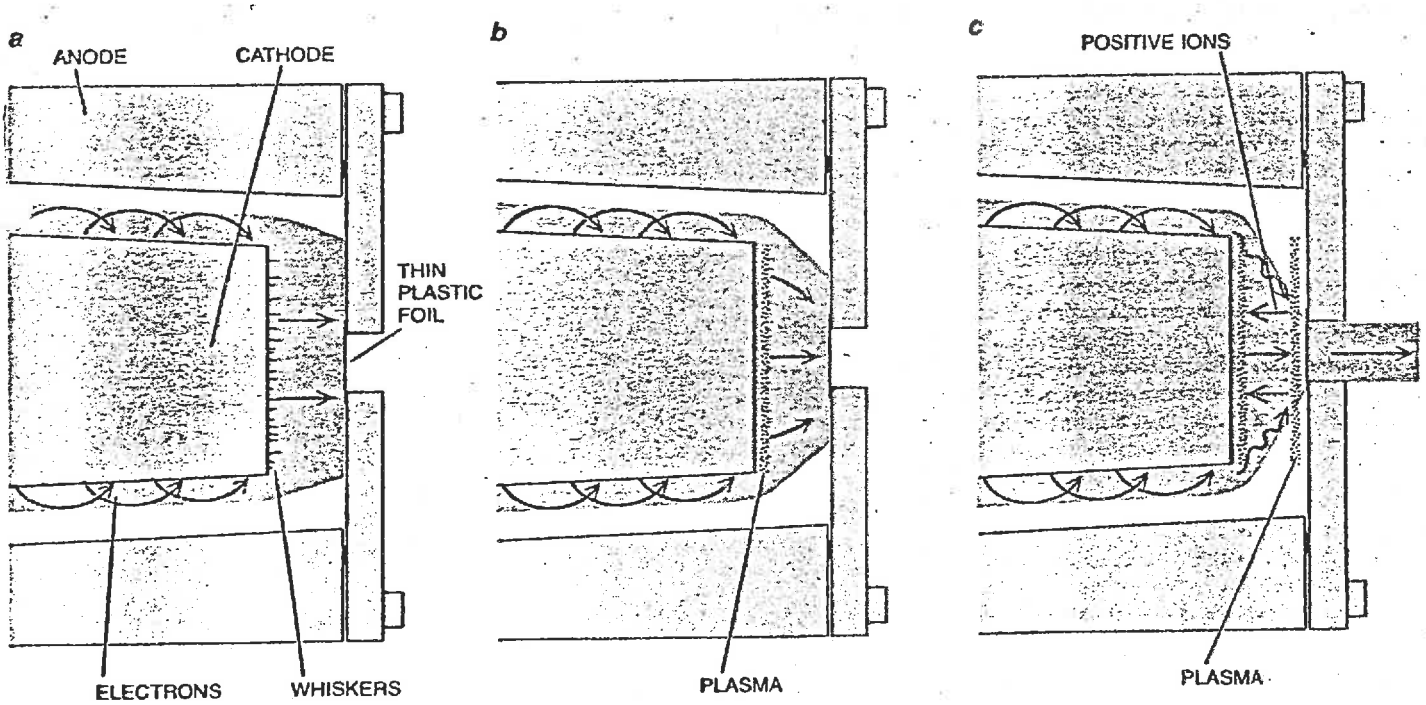

SELF-FOCUSING EFFECT will enable the electrons flowing along the cathode of a magnetically insulated transmission line to focus onto the anode at the axis where the magnetic field drops to zero. The effect is strongly influenced by the formation of a plasma layer (*black stippling*) on the face of both the cathode and the anode. Initially the electrons are emitted from microscopic surface protrusions ("whiskers") on the cathode and are accelerated to the anode in a relatively unfocused beam (*a*). The explosion of the heated whiskers forms a plasma (a hot gas of charged particles) on the surface of the cathode, intensifying the flow of electrons across the gap between the cathode and the anode. The electron flow heats the surface of the anode, forming another plasma layer there (*b*). The reverse flow of positively charged ions (*black arrows*) from the anode plasma to the cathode plasma helps to neutralize the self-repulsive force of the electrons, thereby sharpening the focus of the electron beam as it passes into the reaction chamber through a small hole in the face of the anode (*c*).

History of Pulsed Power Electron Accelerators

The Department of Defense has developed a number of pulsed power electron accelerators to use as intense X-ray sources for nuclear weapons simulation. These culminated in the gigantic Aurora accelerator at Harry Diamond Laboratories which produces a 20 TW beam of 12 MeV electrons. This sequence of accelerators is shown on the next two pages.

More recently Sandia has developed a sequence of electron beam diode accelerators specifically for ICF driver applications. These accelerators are shown on the following pages. The Proto I accelerator achieved a peak power of 2 TW in 24 ns using oil insulated transmission lines. The Proto II accelerator used water insulated lines to achieve 8 TW. Early next year the Electron Beam Fusion Accelerator (EBFA-I) will go into operation at a design power of 40 TW. This accelerator makes use of a new concept known as magnetically insulated transmission lines. Subsequent modification of this facility could increase its power to 100 TW, roughly the level needed for breakeven target experiments.

Transmission of Intense Electromagnetic Waves

A major question concerns the propagation of intense electromagnetic energy. At energy levels of 1 MJ and power levels of 10^{14} watts, electrical breakdown of insulating materials becomes a major concern. Early accelerators such as Proto I used oil insulators, but this material is both expensive to use in the large quantities required-- and also creates quite a mess if a tank rupture occurs. On the microsecond times scales of pulsed power technology, water is an excellent insulator (with a dielectric constant roughly 30 times that of oil), and this was the insulating material used in Proto II. However even this will eventually break down at high power levels.

Therefore advanced diode accelerators have developed the concept of "magnetic insulation" in which the self-magnetic field of the pulse inhibits breakdown directly. This can be most easily seen in the diagrams on the following page. At low power levels, electrons will be emitted at fields of $E \gtrsim 2 \times 10^5$ V/cm and lead to breakdown:

ELECTRON BEAM ACCELERATORS

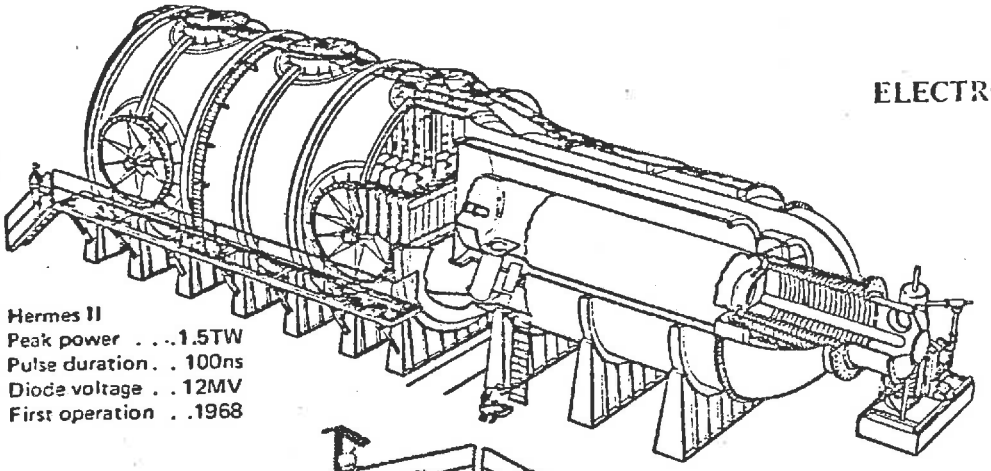

Hermes II
Peak power 1.5TW
Pulse duration . . 100ns
Diode voltage . . 12MV
First operation . .1968

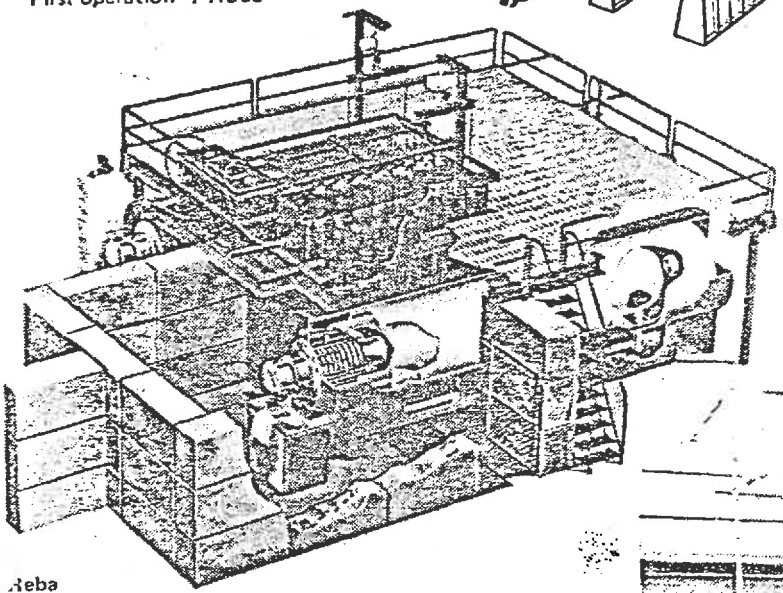

Aeba
Peak power . . .0.2TW
Pulse duration . . .80ns
Diode voltage . . .3MV
First operation . .1970

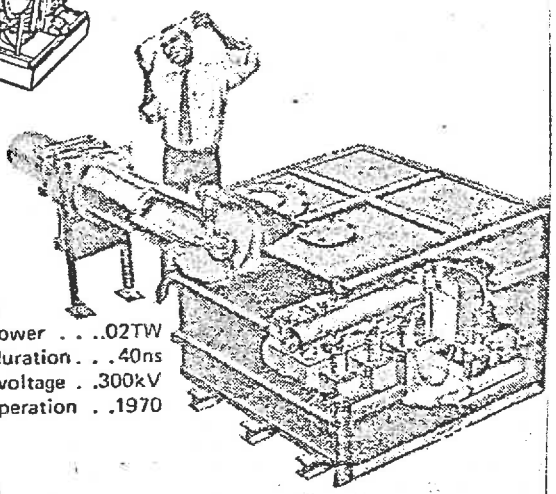

Nereus
Peak power 02TW
Pulse duration . . . 40ns
Diode voltage . .300kV
First operation . .1970

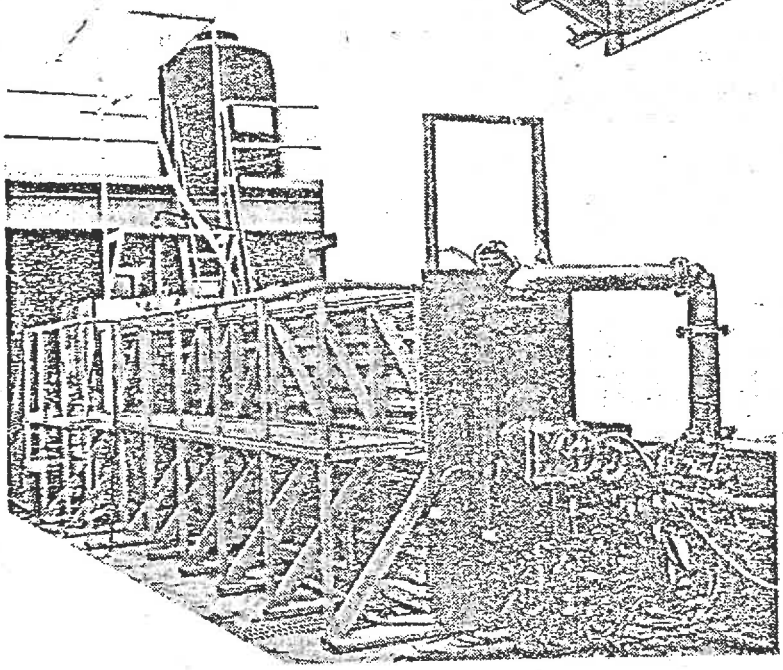

Slim
Peak power . . .0.1TW
Pulse duration . . .80ns
Diode voltage . .300kV
First operation . .1971

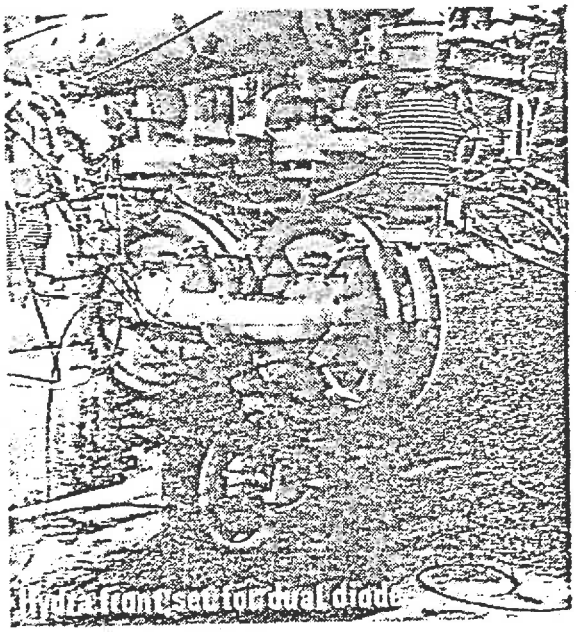

Hydra front section for dual diode

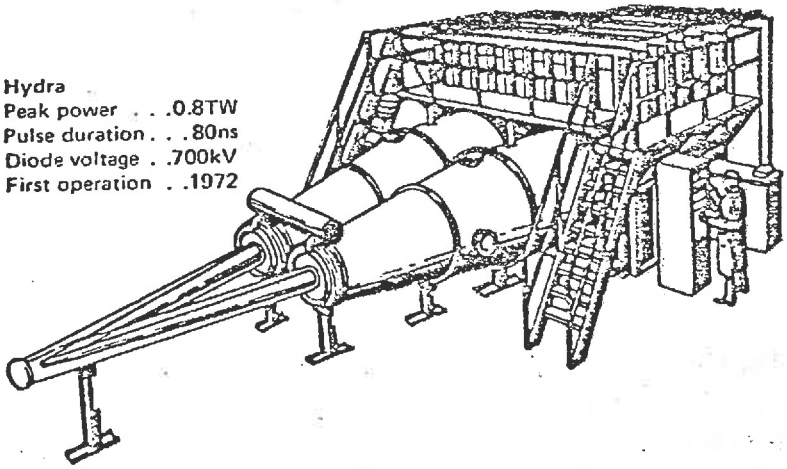

Hydra
Peak power . . .0.8TW
Pulse duration . . .80ns
Diode voltage . .700kV
First operation . .1972

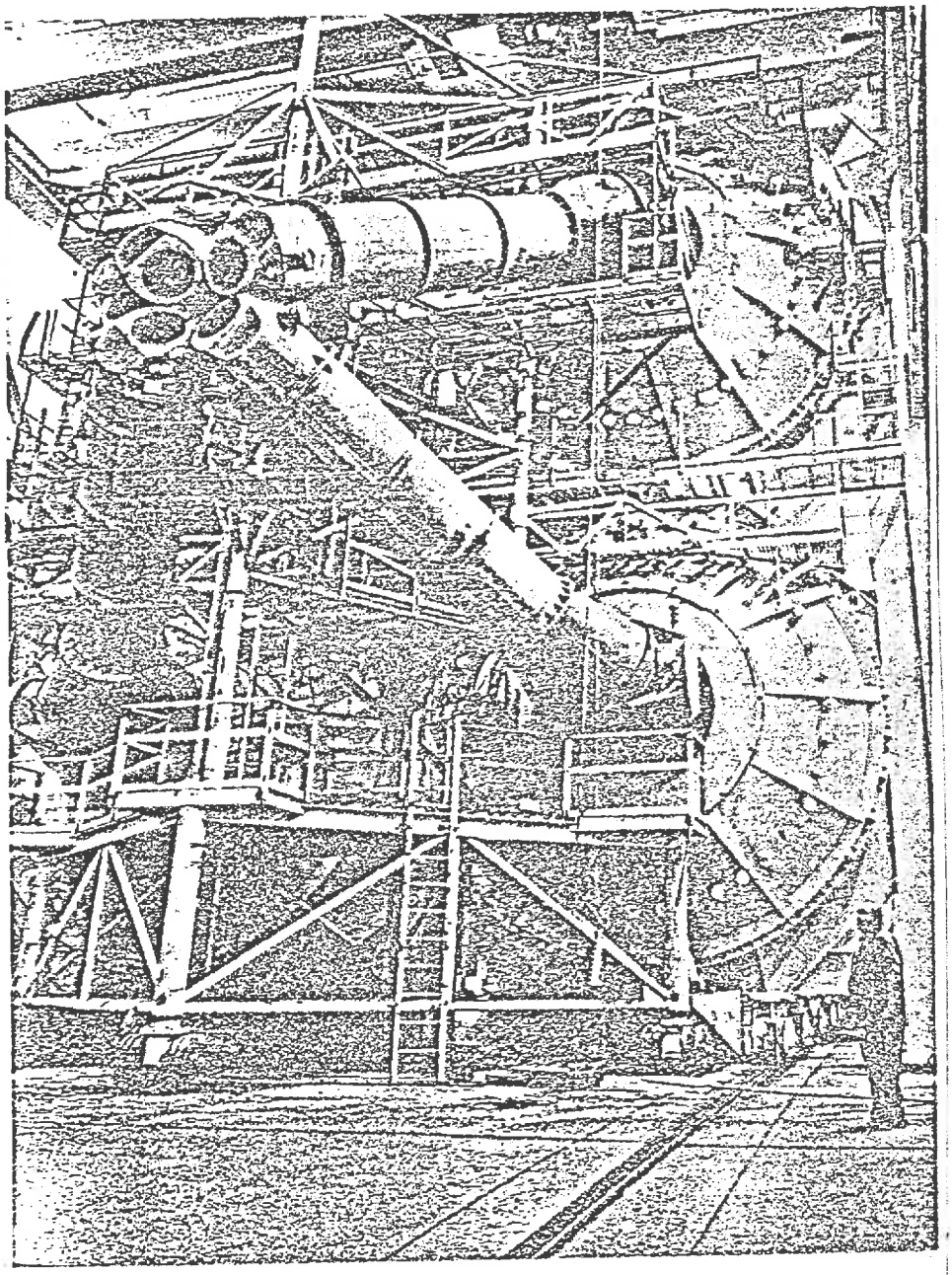

"AURORA," the most powerful electron accelerator in existence, was built for the Department of Defense by the Physics International Company to test the survivability of intercontinental ballistic missiles against simulated bursts of radiation from antimissile warheads. The four-beam, 20-trillion-watt device was photographed at the Army's Harry Diamond Laboratory near Washington, D.C. The accelerator operates at an electric potential of more than 10 million volts and generates electron pulses lasting 100 billionths of a second. Although Aurora is not suitable for fusion experiments, it demonstrates potential of pulsed-power technology.

PARTICLE BEAM FUSION ACCELERATORS

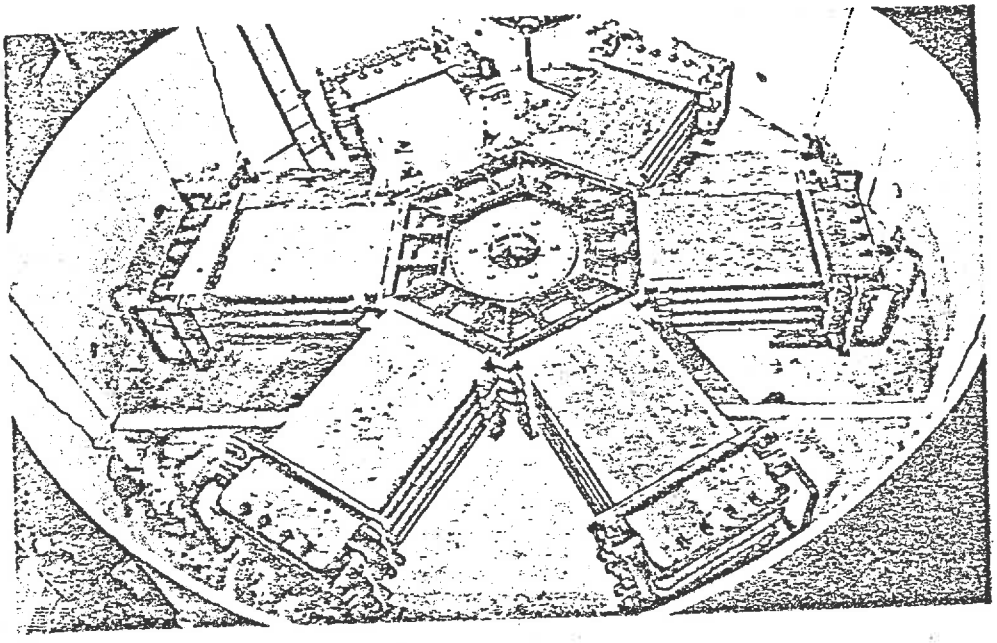

Proto I
Peak power 2TW
Pulse duration. 24ns
Diode voltage 3MV
First operation 1975

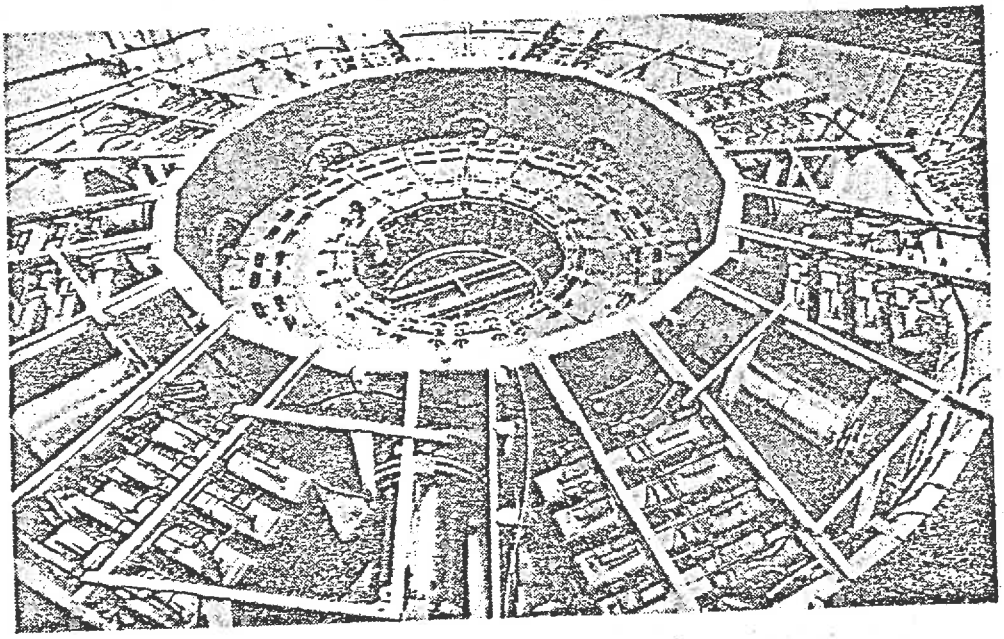

Proto II
Peak power 8TW
Pulse duration. 24ns
Diode voltage 1.5MV
First operation 1977

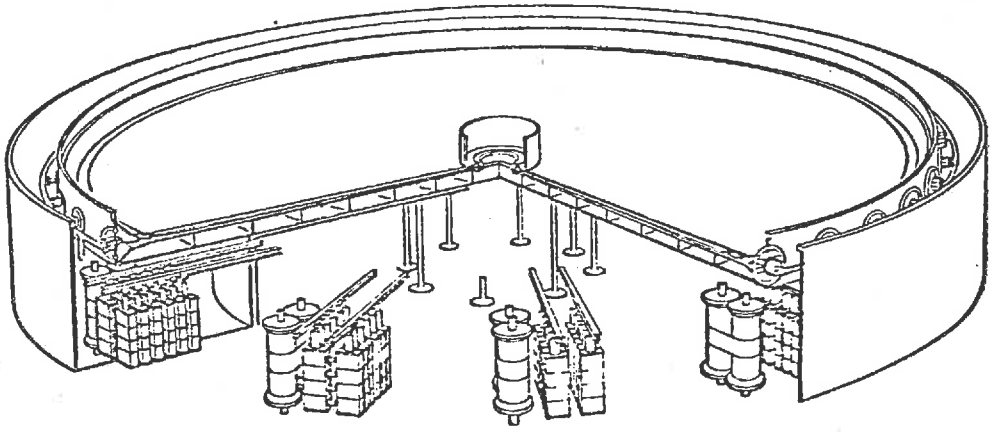

EBFA
Peak power 40TW
Pulse duration. 24ns
Diode voltage . . . 2.3MV
First operation 1979

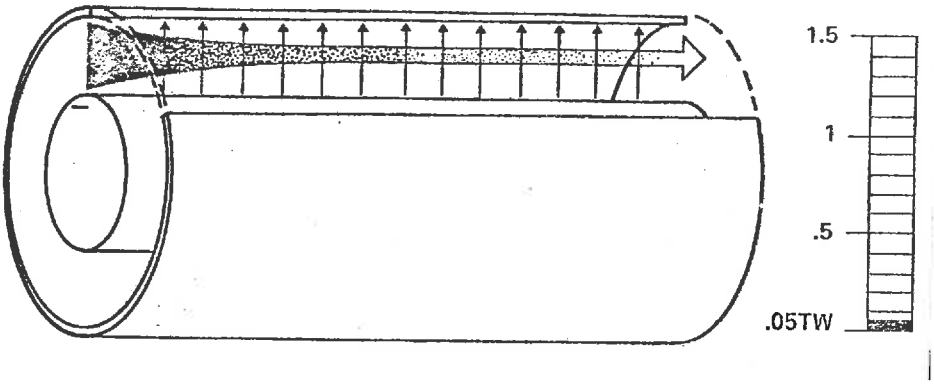

At very high power levels, the transverse magnetic field of the propagating electromagnetic wave deflects the electron orbits, The electrons are bent back to the cathode without losing power:

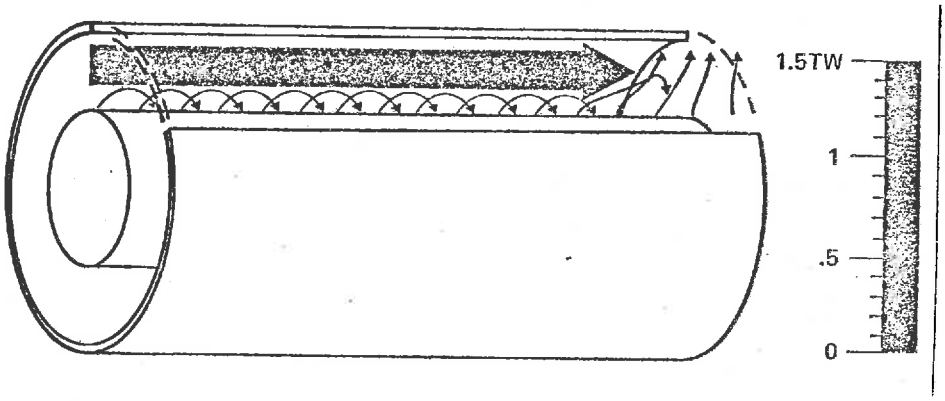

This magnetically insulated transmission line scheme has been verified both by experiments as well as with 2-D simulation codes which yield electron trajectories such as that shown below:

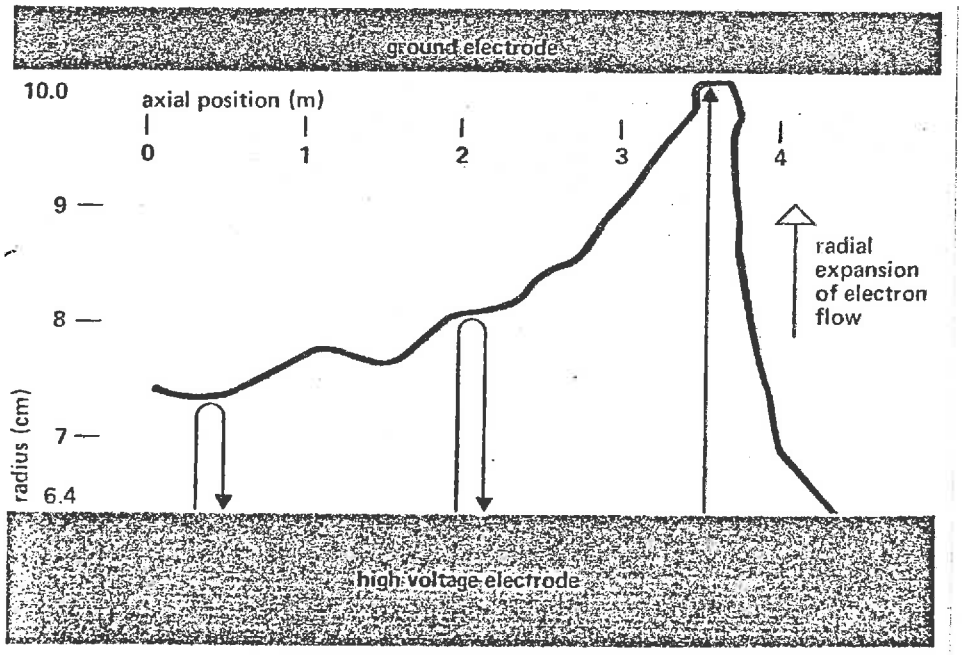

Diode Physics

The diode consists of a cathode and an anode foil separated by a short gap:

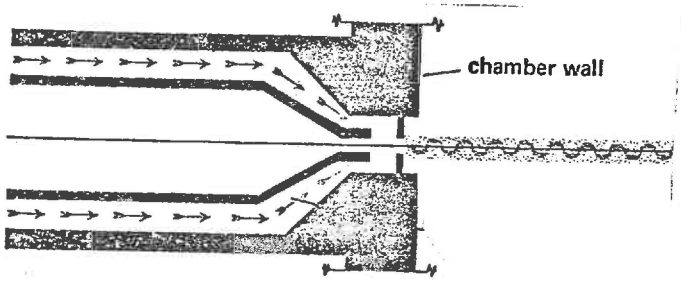

The pulsed potential applied across the diode causes intense field emission from the cathode tip to produce a high current stream of MeV electrons moving toward the anode. These high energy electrons can easily penetrate the anode foil to form a relativistic electron beam. More precisely, the field emission first occurs from metal whiskers on the cathode. The intense currents explode these whiskers, producing a plasma on the cathode surface. The electrons pulled from this plasma then bombard the anode surface, producing a second plasma. When these plasmas collide, the voltage drops across the diode.

Early theories of diode current flow usually assumed that the electrons traveled along smooth, noncrossing trajectories from cathode to anode. But experiments have indicated that electron trajectories are quite complex. In fact, experiments suggest that the high current electron beam behaves more like a gas than like a bundle of particles following parallel paths to the target. Hence in early accelerator designs, targets were occasionally placed at the anode plane to receive symmetric illumination on one hemisphere. A double diode design was developed to achieve full illumination of the targets (see next page).

Beam Propagation

In any fusion application, one must provide standoff separation between the imploded target and the beam injector. Hence one must propagate the electron beam away from the diode and focus it on a target some distance away.

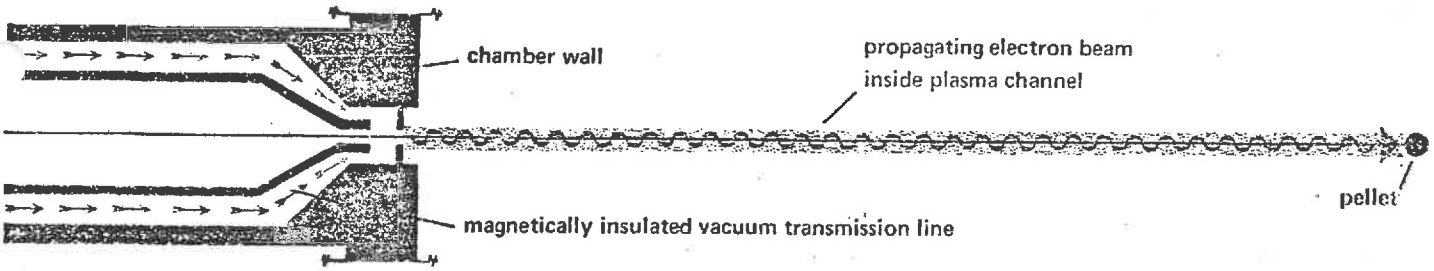

If the electron beam propagates into a vacuum, mutual repulsion will cause beam spreading and defocusing:

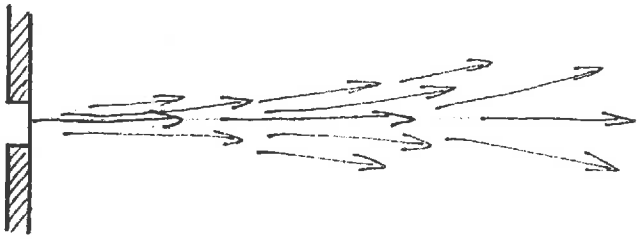

However by allowing the beam to propagate through a low pressure gas (air), ion production will neutralize the space charge of the beam and permit it to propagate.

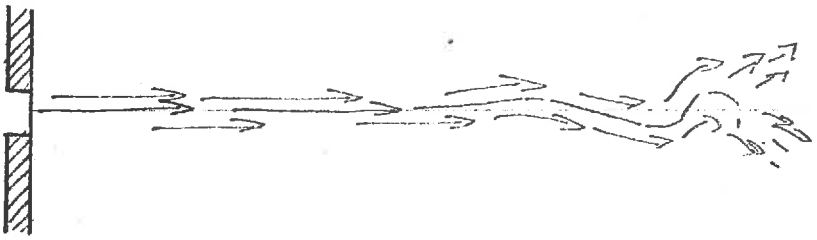

The beam propagation will also generate a strong magnetic field which can pinch down the beam radius, If the beam current is too high, instabilities will develop and the beam will not propagate.

However by allowing the beam to propagate through a plasma channel, the return current will allow currents in excess of this critical limit (although the net current is still below the limit). The propagation of a relativistic electron beam in a plasma channel produced by a wire-driven discharge in air is shown below:

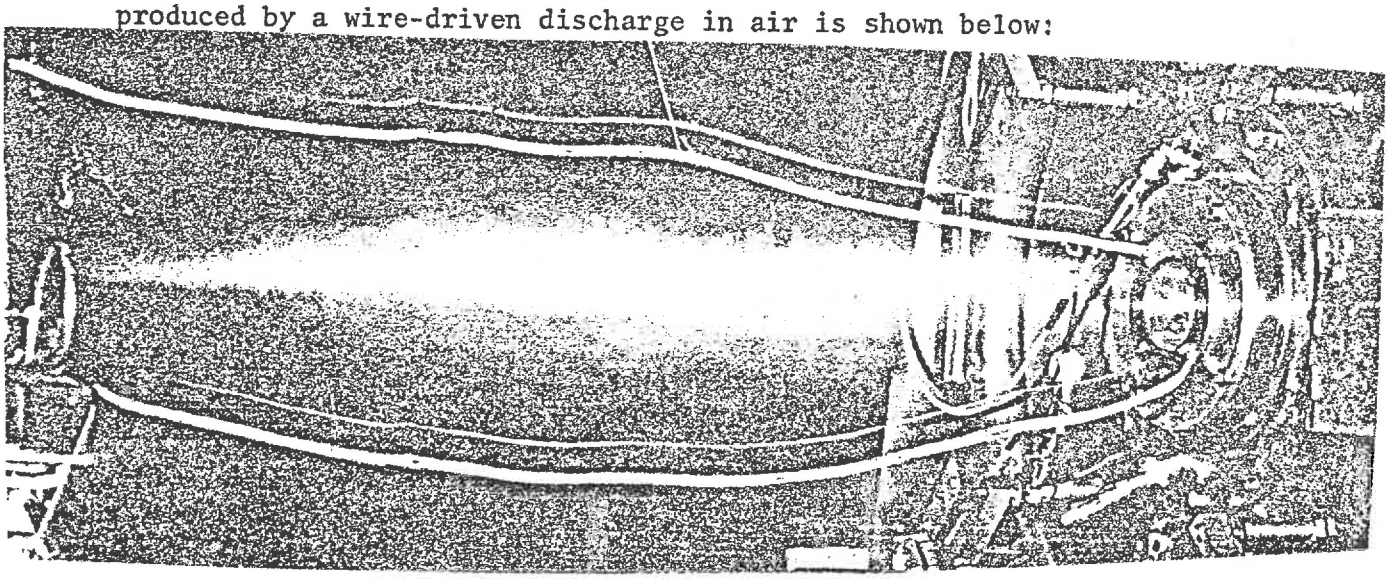

Of course, in a fusion device, wires could not be used to produce the plasma channel in the blast chamber. Instead it is proposed to use a laser to breakdown the chamber gas and produce the beam propagation channels.

Electron Beam Accelerator Development

As we have noted earlier, the Sandia Laboratories have developed a series of electron beam diode accelerators for fusion applications:

Proto I: The Proto I accelerator was a 2 TW machine utilizing oil insulated transmission lines as shown below:

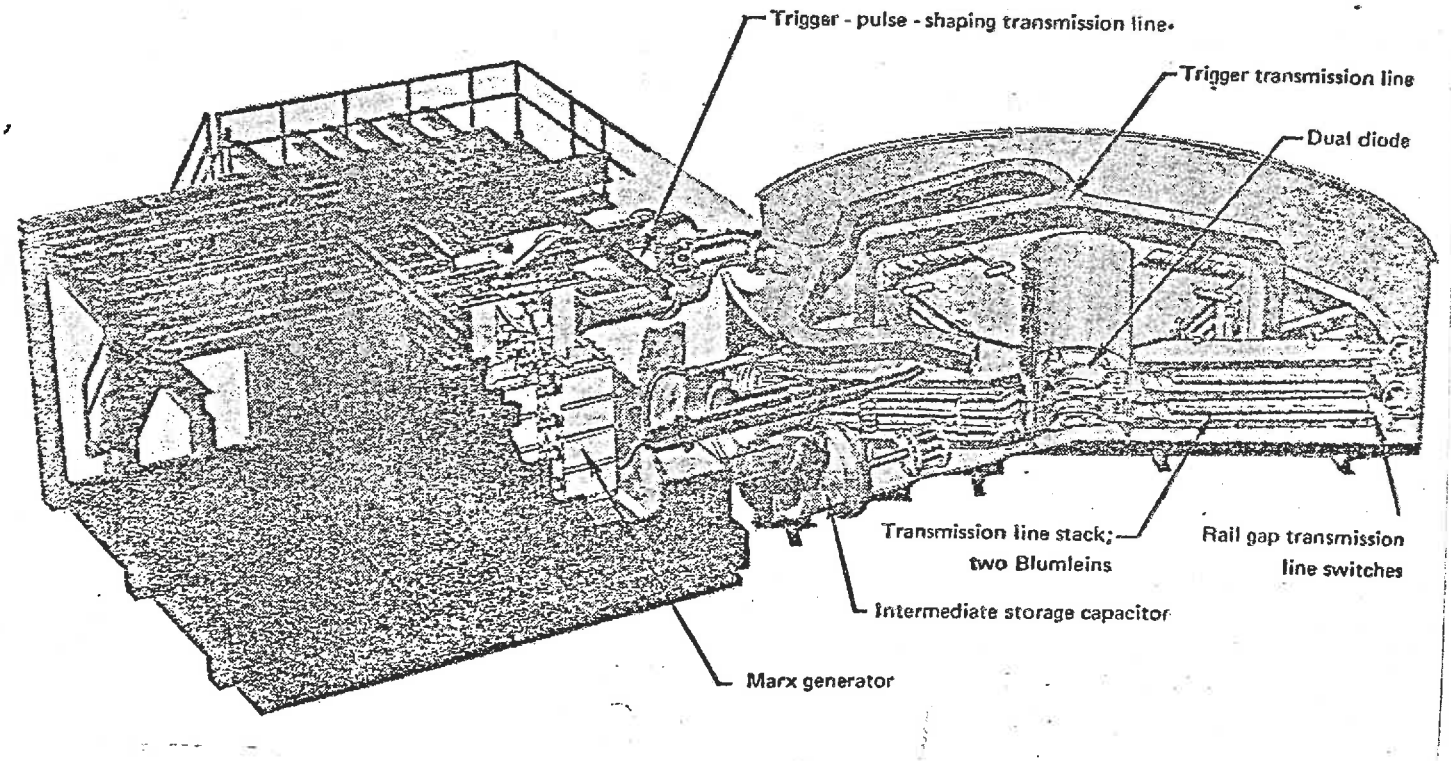

One particularly interesting aspect of this machine was the use of a double diode with the pellet mounted on the anode so that it received electron beam fluence from both sides. In this configuration beam propagation was not necessary.

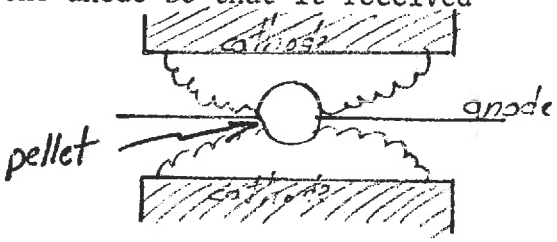

Proto II: The Proto II accelerator produces roughly 100 kJ of beam energy in a double diode at a voltage of 1.5 MV and a peak current of 6 MA in a 24 ns pulse. Eight Marx generators charge 16 intermediate storage capacitors. These capacitors then charge the first set of pulse-forming lines in 240 ns. This set then self-switches through 16 current carrying channels to charge the second set of pulse forming lines in 70 ns. The second set of lines switches through 200 channels to launch an electromagnetic wave down the water-insulated, converging transmission lines toward the diode. This accelerator is shown below.

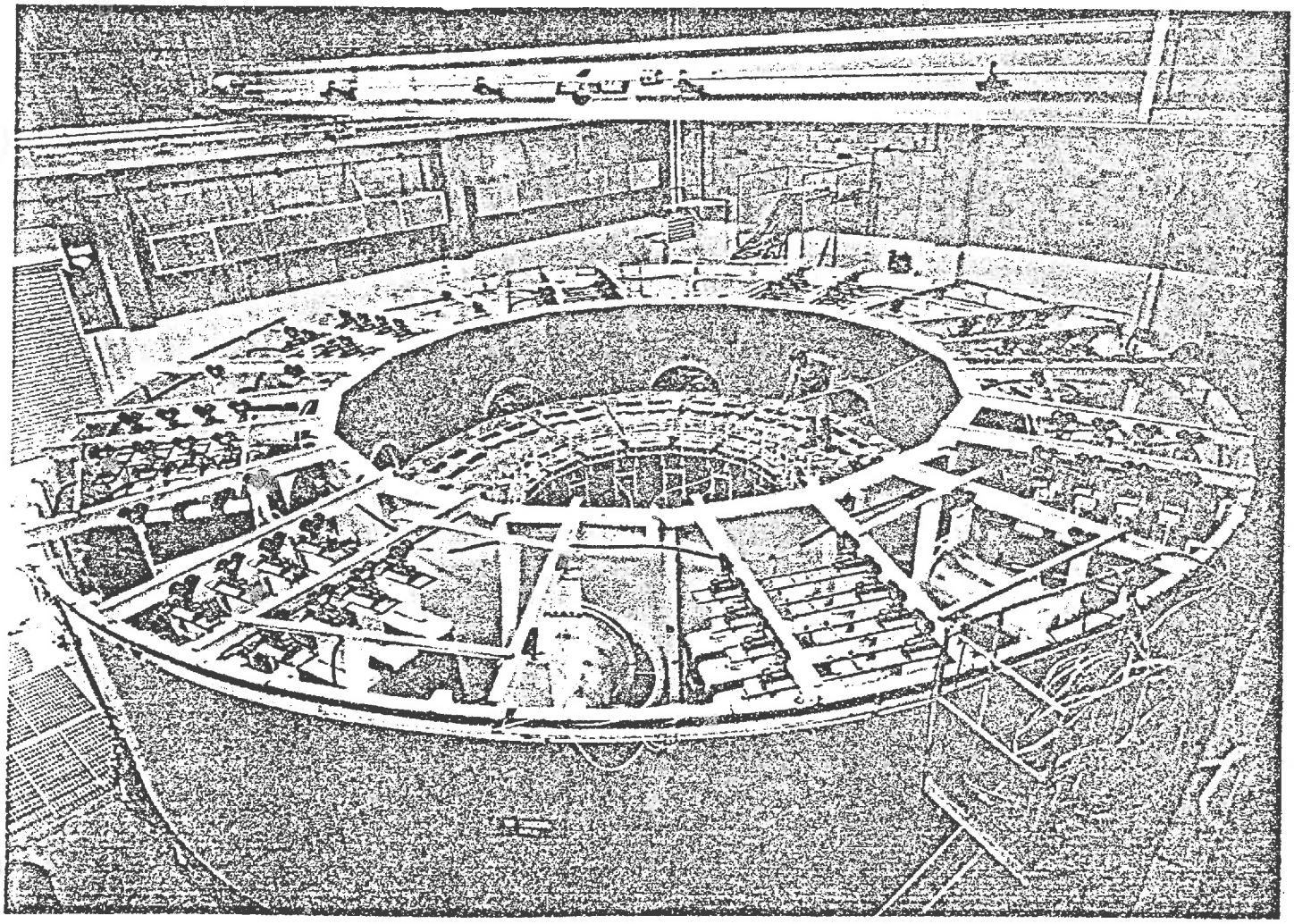

Particle Beam Fusion Accelerator (Formerly known as EBFA): Sandia is presently bring on line a 30 TW machine which produces 1 MJ of electron beam energy through 36 accelerator lines, This machine makes use of the magnetic insulation principle. Schematic cross sections of both phases of this machine are compared below:

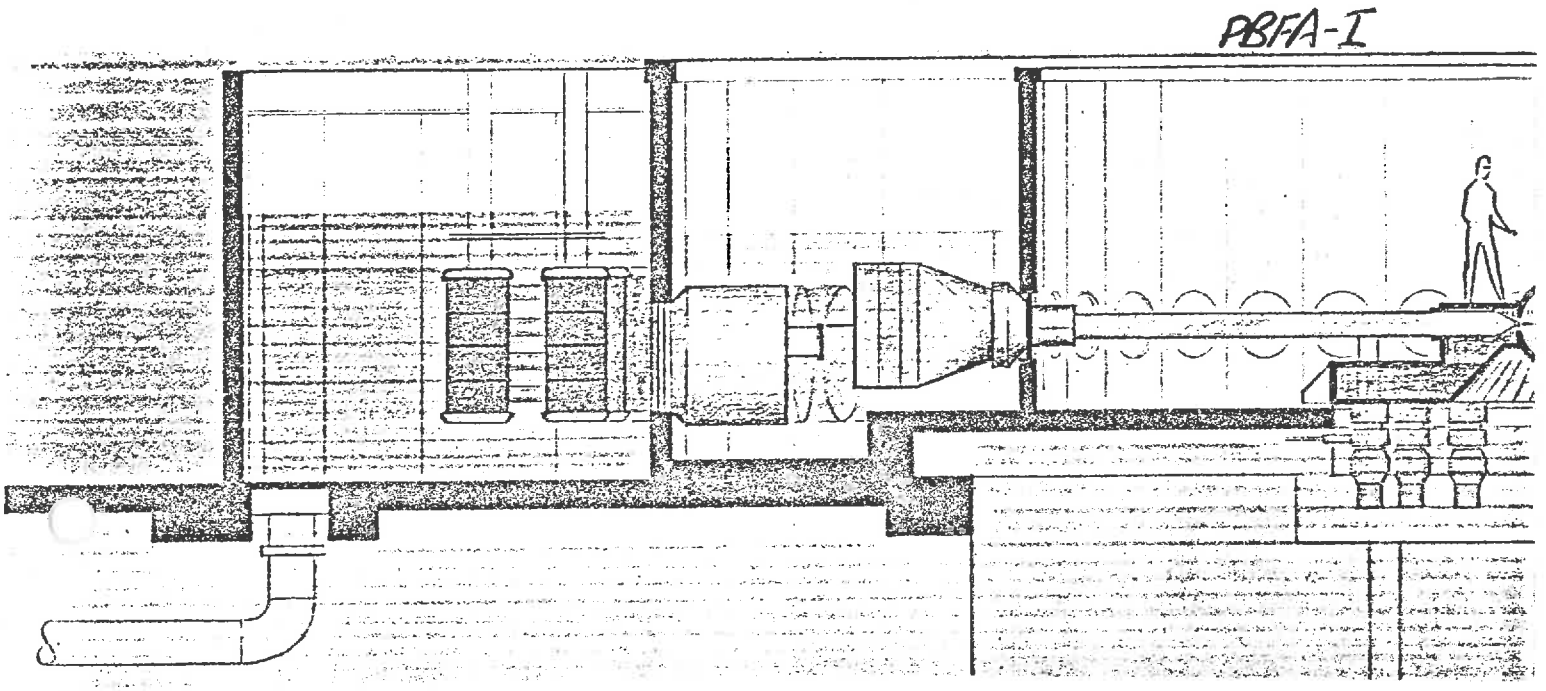

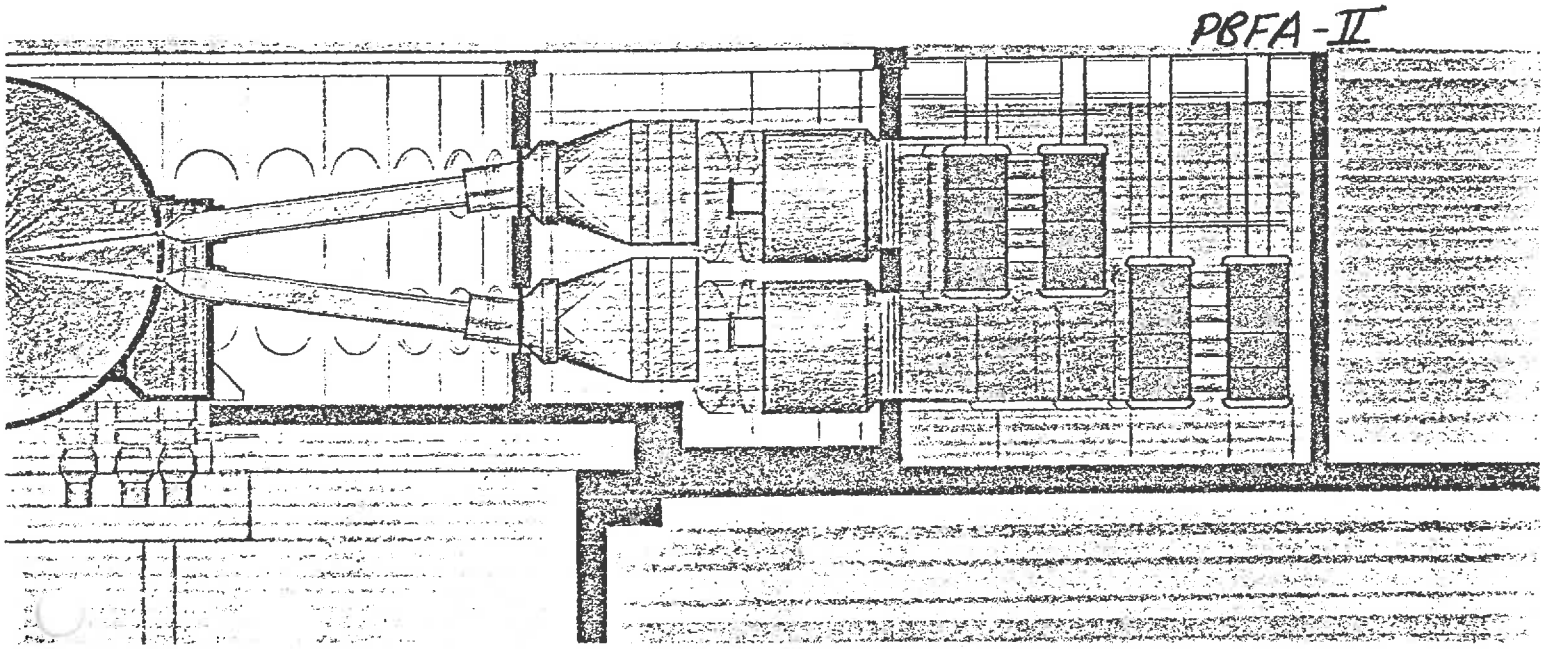

The capability of the PBFA machines are compared with the Shiva, Nova, and Antares laser systems below:

	SANDIA		LLL		LASL
	EBFA I	EBFA II	SHIVA	NOVA	Antares
peak power TW	30	60	1	250	100
pellet energy, kJ	1000	2000	15	250	100
pulse width, ns	40	40	.1	1	1
cost/joule, $	8	7	1000	300	300
energy efficiency	25%	25%	.06%	.2%	1.8%
operational date	1980	1984	1977	1984	1983

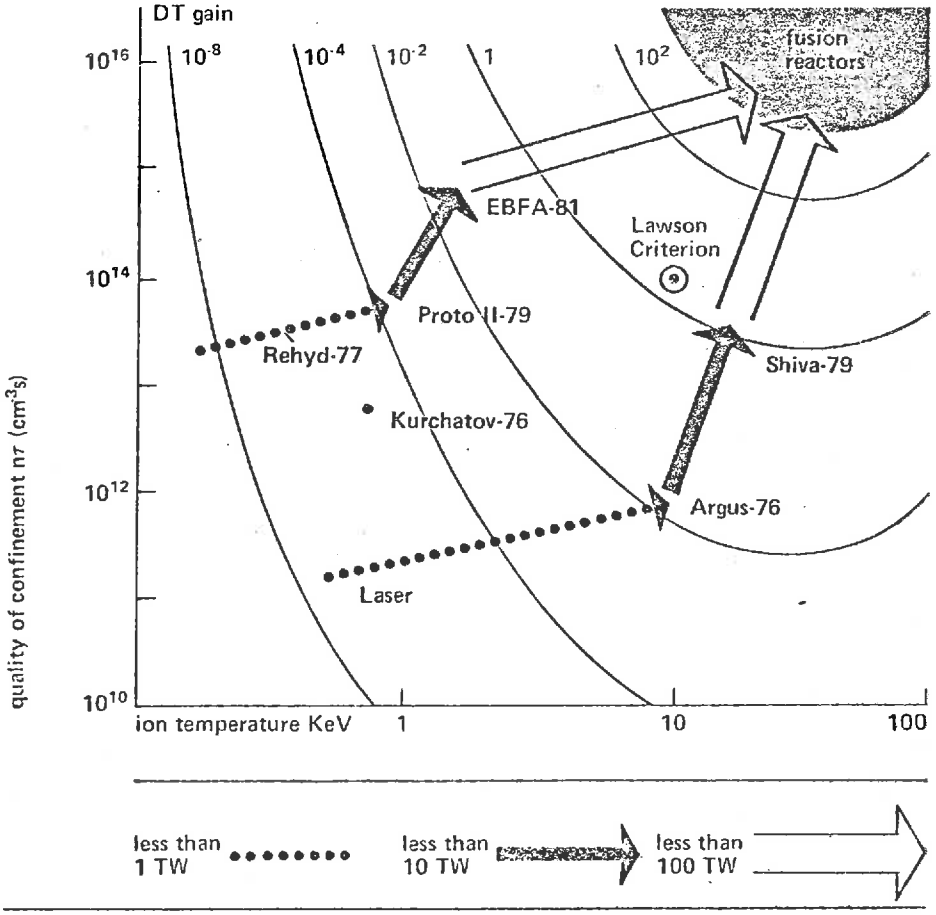

8.1.2. Beam Accelerators

In contrast to pulsed-power diode devices, the Soviet Union is developing a series of large accelerators utilizing multiple beams with beam transport and focusing at large distances from the beam generator. This approach is compared schematically with the diode focusing method using in the Proto I and Proto II accelerators below

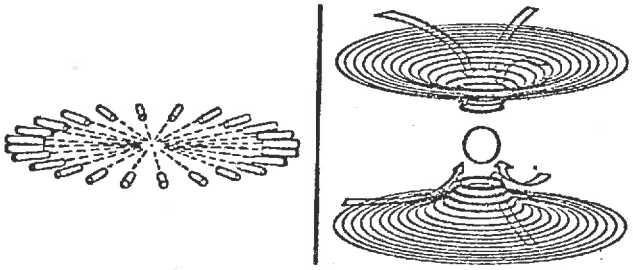

(although the PBFA will also propagate beams). The Angara V accelerator being developed at the Kurchatov Institute in Moscow will produce 100 TW in a 50 ns pulse (5 MJ) through 48 beams. A Russian schematic of a reactor based on such a device is shown below:

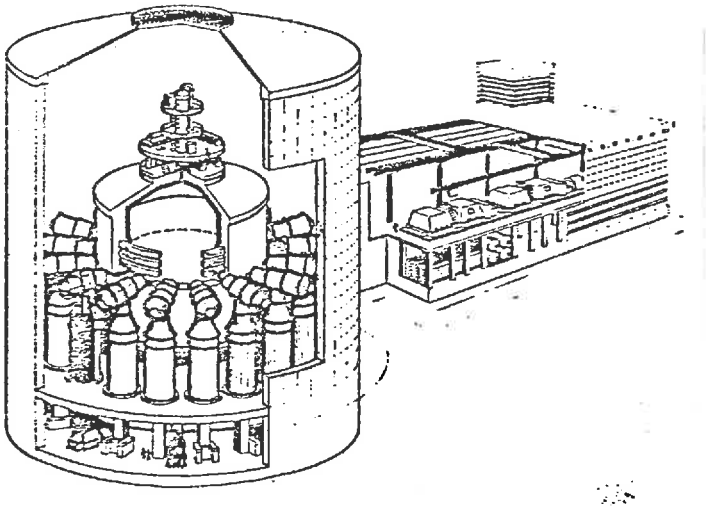

Soviet multiple-beam scheme for fusion target implosion.

8.2. LIGHT ION BEAMS

Pulsed power diode accelerators can produce intense ion beams as well as electron beams. In fact, in many instances high-energy ions can be found traveling along with the electron beams even when such devices are operated in the electron beam mode. This occurs because if the electron current density is high enough (greater than several kA/cm^2), then the anode material and anode surface contaminants are strongly heated and turned into a plasma sheet before the end of the pulse. The diode's electric field then pulls positively charged ions from this anode plasma and accelerates them to the cathode, thereby producing a very power ion beam.

Hence to produce ion beams for use as fusion drivers, we first reverse the polarity of the diode. Then we must suppress the electron flow. This latter action is necessary since in normal diode behavior, the small mass of the electrons compared to the ions causes the majority of the current to be carried by this species. For example, if the ions were protons, then the proton current (and therefore the proton beam power) would be only about 2% that of the electron beam.

There are several mechanisms to suppress the electron flow:

(i) Use of magnetic fields to reflect back the electrons: One can place a magnetic field screen across the diode as shown below:

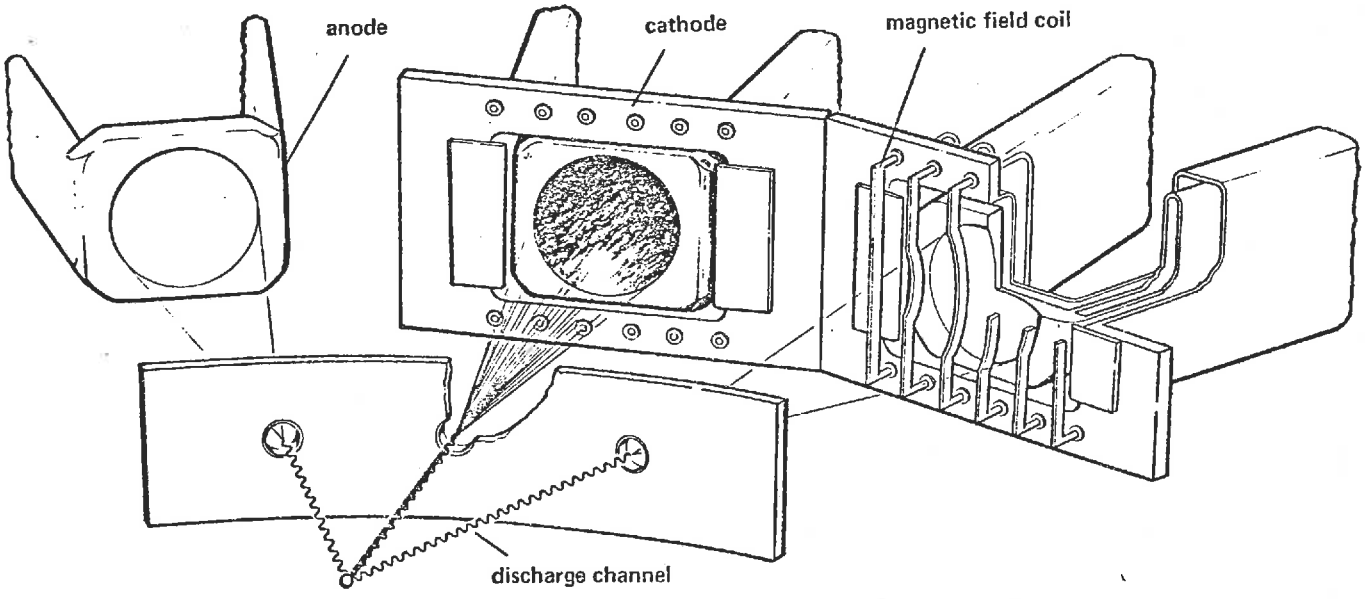

The magnetic grid converts the diode into essentially a reflex triode in which the electrons are reflected back and forth, establishing a space charge field and inhibiting electron current flow:

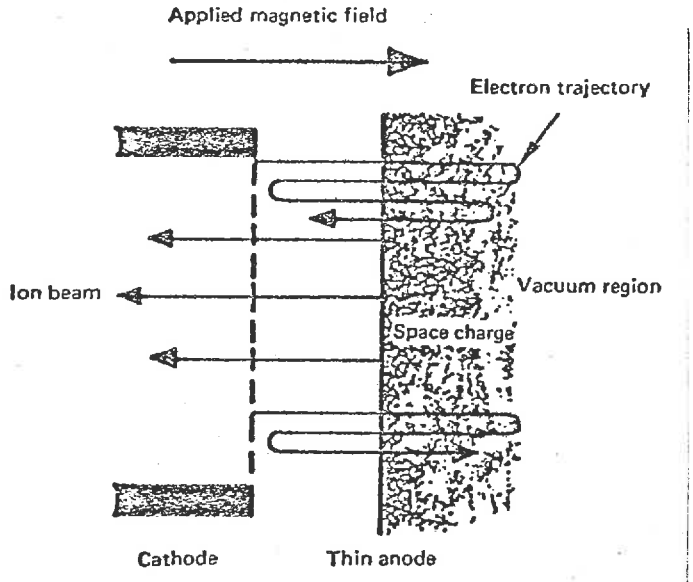

(ii) One can also use the self-generated magnetic fields of the high current in the diode to limit the flow of electrons:

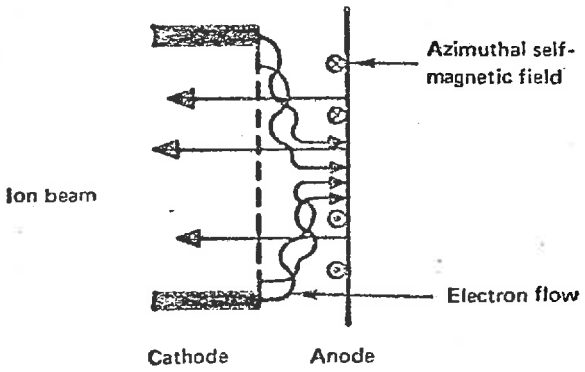

High current electron beams tend to be focused by their self-magnetic fields. But this process is ineffective with the much heavier ions. Hence geometric focusing is used by shaping the anodes and cathodes as shown below:

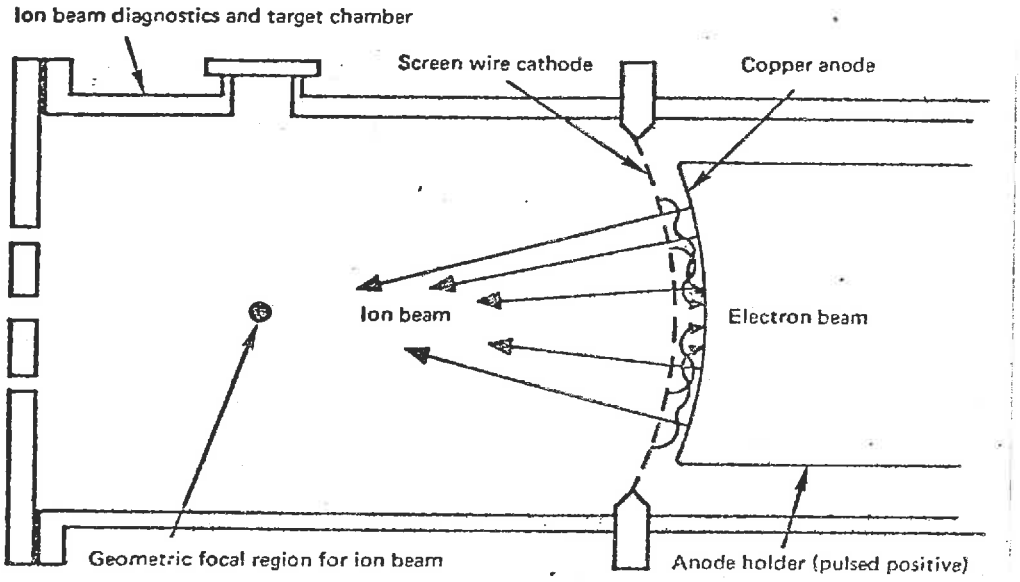

If the ions are created so that they are directed toward the target, they can pass through a cathode grid or thin foil and coast balistically to the target. To prevent the space charge of the beam from producing divergence, it must be neutralized by picking up low energy electrons from the cathode plasma.

The Sandia accelerators (Proto I, Proto II, and PBFA) can be used in the ion mode. Multiple ion beams can be generated at the end of magnetically insulated transmission lines and geometrically focused over a distance of abut 1 meter. These focused beams can then be transported to the target in plasma discharge channels.

One can use beam bunching methods to compress the time pulse shape of the ions since they are relatively slow moving (compared to electrons). Hence if the accelerating voltage is increased over the period of the pulse, the faster ions at the end of the pulse can be made to overtake the slower ions injected at earlier times.

8.3. HEAVY ION BEAM FUSION

One of the more attractive approaches to ICF is to use heavy ion beams. Conceptual designs based on the mature accelerator technology developed for high energy physics suggest that suitable drivers can be built for ICF applications with only a modest extrapolation. That is, heavy ions can be acclerated to high energies and focused on small targets using essentially conventional accelerator methods. And, as we saw in Chapter 6, the energy deposition by heavy ions is ideally suited to ICF targets.

More specifically, the advantages of heavy ion beam fusion include:

(i) The classical ranges of heavy ions are quite short (see the Figure on the next page). Hence ions can be accelerated to very high energies (in the GeV range) and still be effectively absorbed in the outer layers of the target. This allows one to utilize lower currents of high energy particles to achieve the same energy deposition. For example, to achieve the same beam energy intensities with light ions and heavy ions (of the same range), one finds

$$\text{light ions} \sim 1 \text{ MeV} \Rightarrow 10^9 \text{ amps}$$

$$\text{heavy ions} \sim 100 \text{ GeV} \Rightarrow 10 \text{ kamp}$$

Since accelerators are generally current-rather than voltage-limited, this implies that the accelerator requirements are eased with heavier ions.

(ii) Purely classical energy deposition is adequate for high gain targets. For example, 10 GeV uranium ions will stop in 5 mil of Au. Furthermore, heavy ions do not produce appreciable bremsstrahlung during slowing down, thereby avoiding preheating problems.

(iii) Heavy ion drivers would make use of a highly developed technology which allows a realistic estimate of cost, reliability, and other performance characteristics. Indeed, most components of a heavy

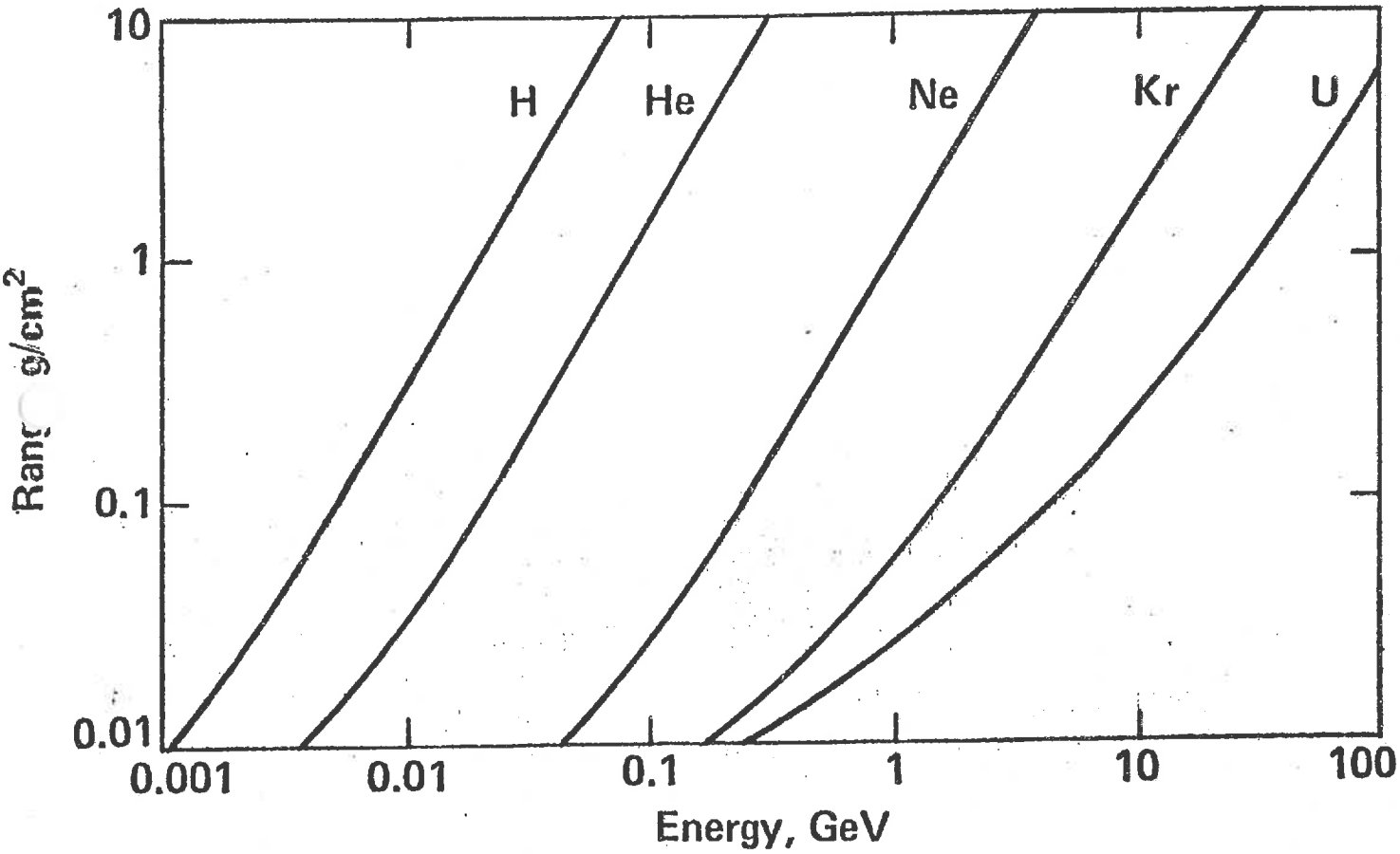
10
1
0.1
0.01
Range, g/cm²
H
He
Ne
Kr
U
0.001
0.01
0.1
1
10
100
Energy, GeV

ion fusion reaction can be analyzed without further experimental data.

(iv) Operation of heavy ion accelerators at low currents and high voltages allows power to be delivered to the beam in successive, physically separated stages, thereby greatly easing the task of power concentration. One can utilize the well-developed technology of beam storage rings. For example, the Intersecting Storage Rings (ISR) at CERN can hold two beams with 2 MJ of energy each. A larger storage ring machine ISABELLE at Brookhaven would have 20 MJ in each ring.

Against these advantages must be balanced the very real difficulty in developing accelerators that can produce intense currents of heavy ions. One particular difficulty is that even facilities designed for very modest experiments (at the 10 kJ level of Shiva, Helios, or EBFA) would cost in excess of $100 M. Hence heavy ion beam fusion may be blocked initially by the cost of its initial demonstration. Accelerator designers have had relatively little experience with ions as heavy as iodine (127) or uranium (238).

Possible Accelerator Configurations:

A variety of possible accelerator configurations have been proposed for heavy ion ICF drivers:

(i) full energy RF linac:

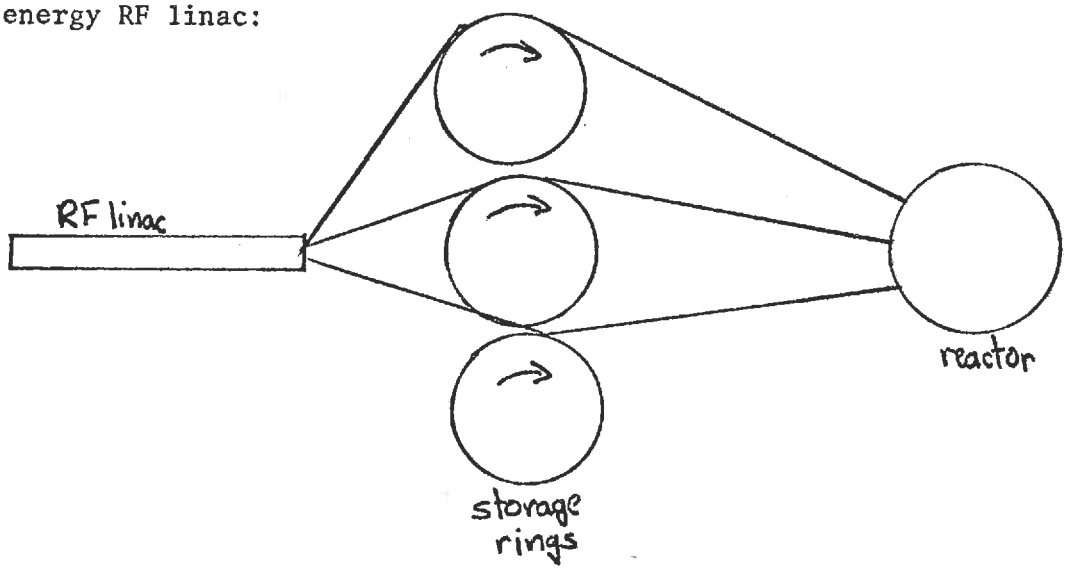

(ii) low charge state synchrotron system without external storage rings

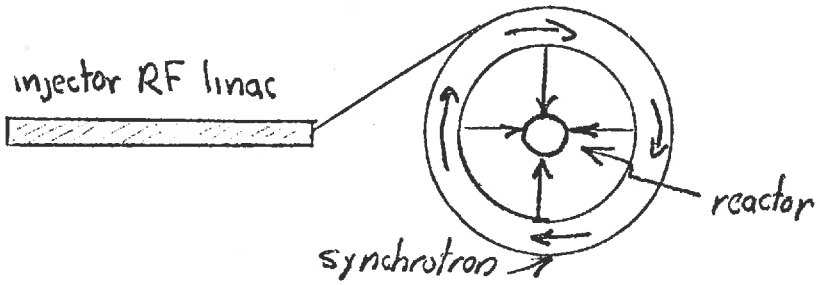

(iii) synchrotron system with storage rings

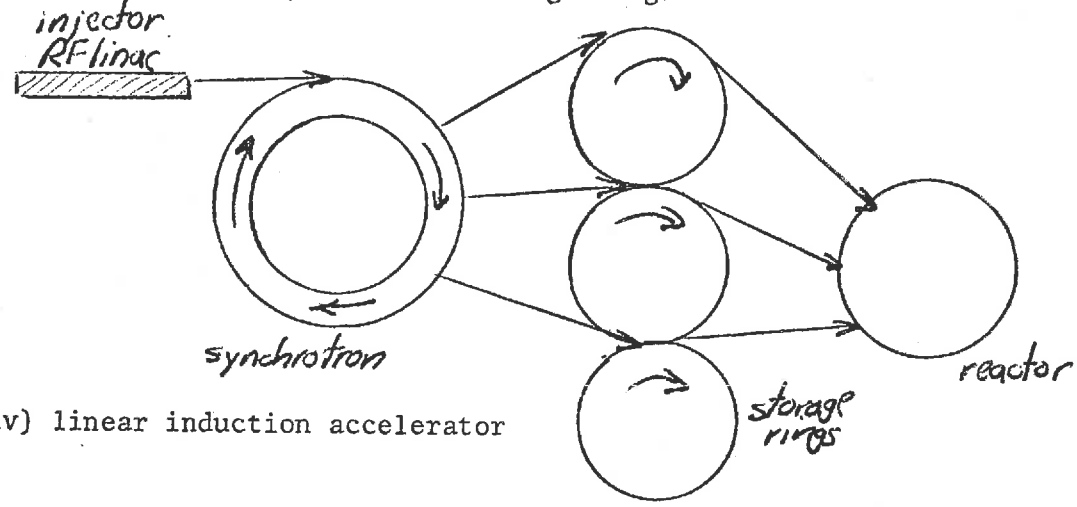

(iv) linear induction accelerator

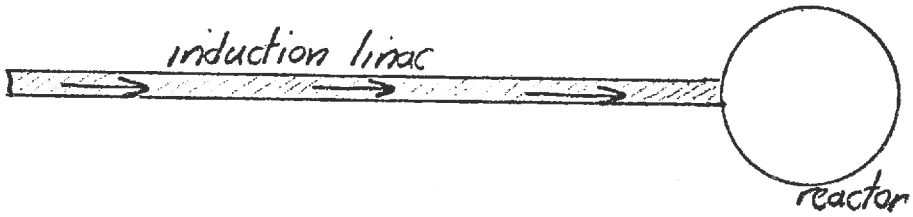

An earlier conceptual design of a heavy ion ICF reactor was the HEARTHFIRE concept developed at Argonne (for high energy accelerator and reactor for thermonuclear fusion with ion beams of relativistic energy). This proposal envisioned the acceleration of hydrogen iodide ions $(HI)^+$ using a 600 MeV linear accelerator followed by a 40 GeV synchrotron. It used 100 beam bunches in a small superconducing storage ring. The $(HI)^+$ was dissociated to I^+ before injection into the storage ring. The cumulative current of the subsequently stripped I^{+52} ions on the target would be 400,000 amps corresponding to 2,4 MJ.

Ion Sources

One needs sources with a high current but a small divergence in particle angles or speeds. For example, one requires 10 to 100 mA with an emittance of 0.1 π cm mrad.

Noble gases are possible species, with Xe being a particularly convenient choice (although Hg and Cs are also being examined). One can achieve higher charge states by stripping singly charged ions in foils or gases

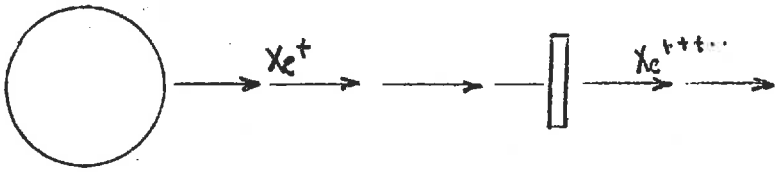

but this results in a loss of ions from the beam--although the current does not decrease.

To accelerate the ions to 1 MeV, one needs a d.c. accelerator such as a Cockroft-Walton or Dynamitron.

Acceleration to Full Energy

Here one needs final energies of up to 30 GeV. Several options are available:

(i) RF linac: This can load a storage ring in a few ms

(ii) synchrotron: This is much cheaper, but requires about 1 s to load a storage ring.

(iii) linear induction accelerator

(iv) collective-effect ion accelerators

As a rule, higher currents are tougher to achieve than high energies. Thus the accelerator designer would rather go to the highest possible energy.

However the maximum energy is limited by the range of the ions which scales as

$$\text{Range} \sim (E/A)^2$$

For example, if we desire a driver energy of 1-10 MJ, then the use of

ions with A $\gtrsim$ 100 would allow 20-40 GeV for a 1 mm radius pellet with an outer layer of high Z material.

Storage Rings

The amount of beam current that can be stored in a storage ring is limited by defocusing effects of electrostatic repulsion among particles--the "space charge limit". To achieve the maximum number of ions in the ring, one must minimize the ratio of charge to mass (Q/A). The ion energy stored in the ring scales as E^2.

The storage lifetime is limited by losses from ion collisions with both background gas and other ions. Ions may recombine with electrons when they strike other ions in the beam or the residual gases of the vacuum chamber in which the beam travels. The cross sections for heavy ion reactions with background gas atoms are unknown at GeV energies.

Bunching, Transport, and Focusing

The circulation time characteristic of storage rings is about 1000 ns. This must be compared with ICF target requirements of several tens of ns. Hence one must bunch the beam to achieve time compression of the ion pulse. One can either subdivide the beam in the storage ring or extract selectively.

Transport of the beam is also a problem, particularly at the kA current level. The power per beam line is limited to about 10 TW. The focusing of these heavy ion beams will also present a problem.

Beam Propagation in Target Chamber

Once the beams have been produced and focused in space and time, they must then be propagated through the target chamber to the fuel pellet. But space-charge effects can defocus the beam as it propagates through the chamber. Therefore most reactor designs have included a background gas pressure in the chamber of about 1 torr.

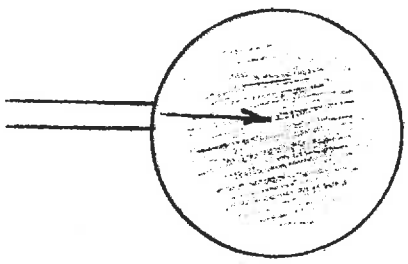

This background gas will charge-neutralize the beam. The conductivity of the plasma produced in the gas will also help to prevent beam instabilities (hose or two-stream).

Heavy Ion Beam Fusion Programs

The main United States effort in heavy ion fusion is being conducted at Lawrence Berkeley Laboratory, Argonne National Laboratory, and Brookhaven National Laboratory. BNL and ANL are concentrating on conventional linac and synchrotron technology, while LBL is developing a linear induction accelerator.

Aside from small scale component experiments and design studies, the heavy ion program is preparing detailed proposals for the construction of a heavy ion demonstration facility (HIDE) which will cost from $60 to $100 M.

EXAMPLE: An example of a larger breakeven facility is that proposed by Argonne. It would produce a 1 MJ, 100 TW beam of Xe^{+8} ions. These would be accelerated to 20 GeV in 8 parallel rapid cycling synchrotrons, each 40 m in radius. The synchrotrons would be driven by an injector linac producing 30 mA of Xe^{+8} at 4.4 GeV. Pulses from the synchrotrons would be accumulated for 1 s in 16 storage rings. A final fast compression of a factor of 50 would be accomplished before extraction into 24 beam lines and injection into a 5 m reaction chamber. This particular device is estimated to cost $250 M.

Some Final Comments

Although there is some concern that heavy ion beam fusion may have been oversold by high energy physicists looking about for some way to save large accelerators such as the ZGS at ANL and the AGS at BNL, there is no doubt that heavy ions do exhibit some attractive features for ICF applications. For example, recent target design studies performed with LASNEX at LLL indicate the heavy ion beam driver requirements as shown below:

Energy (MJ)	Power (TW)	Ion Energy (GeV)	Radius (mm)	t(ns)	Gain
1	100	5	2	20	8
3	150	10	2.5	40	30
10	300	10	4	70	120

Unfortunately, there has been a recent tendency for pellet designers to drop the desired incident ion energy (and thereby shorten the range), and this causes an increased in required beam current and hence increased demands on accelerator designs.

A brief summary of the advantages and problems faced by heavy ion beam fusion is given on the following page).

Some advantages and problems of heavy ion beam fusion

advantages

Short range allows high voltage, low current operation.

Accelerator efficiencies over 40 % available.

Fast pulse rate technology already well developed.

Accelerators have proven reliability and durability.

Costs of about 5 $/W(average beam power) and pellet gains of about 100 might give capital cost of accelerator around 160 $/$kW_e$.

problems

Selection of ion species, charge state, and energy. There is little experience with high-energy beams of heavy ions.

Selection of accelerator type. Again,little experience with heavy ion beams.

Beam losses by charge changing collisions. The required cross sections are not all known.

Source development. Heavy ion sources with high brightness and about 100 mA current are under development.

Injection into storage rings. Efficient heavy ion injection and filling both horizontal and vertical space need to be demonstrated.

Transport and Focussing. The ability to overcome space charge effects and to direct many beams over 5 meters onto a tiny target ($\sim$ 3 mm radius) must be developed.

CHAPTER 9

TARGET DESIGN AND FABRICATION

Detailed target designs depends sensitively upon driver type:

- lasers
- electron beams
- light ion beams
- heavy ion beams

and upon the intended application

- power production
- physics experiments
- space propulsion
- military applications

Target design is also very closely coupled to a number of other areas

- beam-target interaction physics
- target fabrication
- driver design
- combustion chamber (reactor) design
- systems studies

In this chapter we will consider some of the more general aspects of this particular concern of inertial confinement fusion. However we must note two caveats at the outset. Many of the detailed aspects of ICF target design are still heavily classified because of their apparent relationship to nuclear weapons physics. Furthermore, the resources and efforts of the target design groups at the nuclear weapons laboratories (Livermore and Los Alamos) are enormous. Therefore discussing target design and fabrication from "outside the fence" is a bit like scratching the tip of the iceberg.

However in the spirit of completeness, we will attempt a brief review of those aspects of target design which have been made available in the open literature.

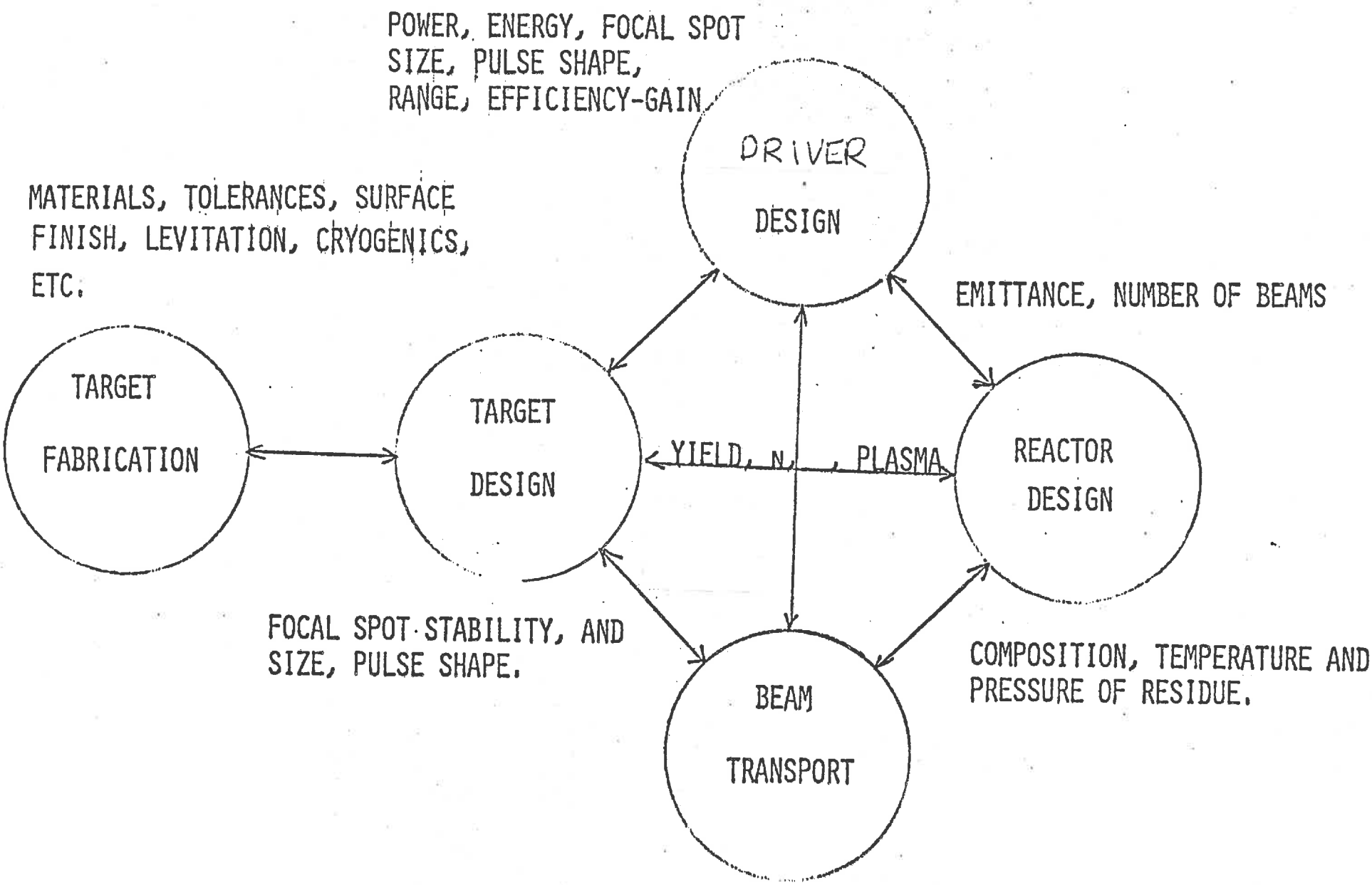
POWER, ENERGY, FOCAL SPOT SIZE, PULSE SHAPE, RANGE, EFFICIENCY-GAIN
DRIVER DESIGN
MATERIALS, TOLERANCES, SURFACE FINISH, LEVITATION, CRYOGENICS, ETC.
EMITTANCE, NUMBER OF BEAMS
TARGET FABRICATION
TARGET DESIGN
YIELD, N, , PLASMA
REACTOR DESIGN
FOCAL SPOT STABILITY, AND SIZE, PULSE SHAPE.
BEAM TRANSPORT
COMPOSITION, TEMPERATURE AND PRESSURE OF RESIDUE.

9.1. GENERAL TOOLS OF TARGET DESIGN

The primary design tool in target design studies is an inertial confinement fusion hydrodynamics code such as LASNEX. We have considered such codes in some detail in Chapter 6. However we have provided a simple schematic of the essential physics in the LASNEX code on the next page.

A variety of other more specialized codes are used in target design. These include:

(i) plasma simulation codes to study the microscopic behavior of energy deposition and transport mechanisms in plasmas

(ii) fluid instability codes to describe Rayleigh-Taylor instability growth

(iii) particle transport codes to describe the transport of superthermal particles

The complexity of these calculations should not be underestimated. For example, most pellet designs are composed of multi-layered shells of different materials and densities. Furthermore there is a strong dependence on the incident beam pulse shape, driver type (photons, electrons, or ions), number and location of beams, focal spot size and spatial distribution in beam, and wavelength, polarization, or energy spread.

By way of example, a single 1-D LASNEX run will require some 30 minutes of CDC 7600 time. Hence it is essential for the target designer to use simple estimates and back of the envelope calculations whenever possible. Target design contains a high degree of artistry and inspiration as well.

LASNEX Physics

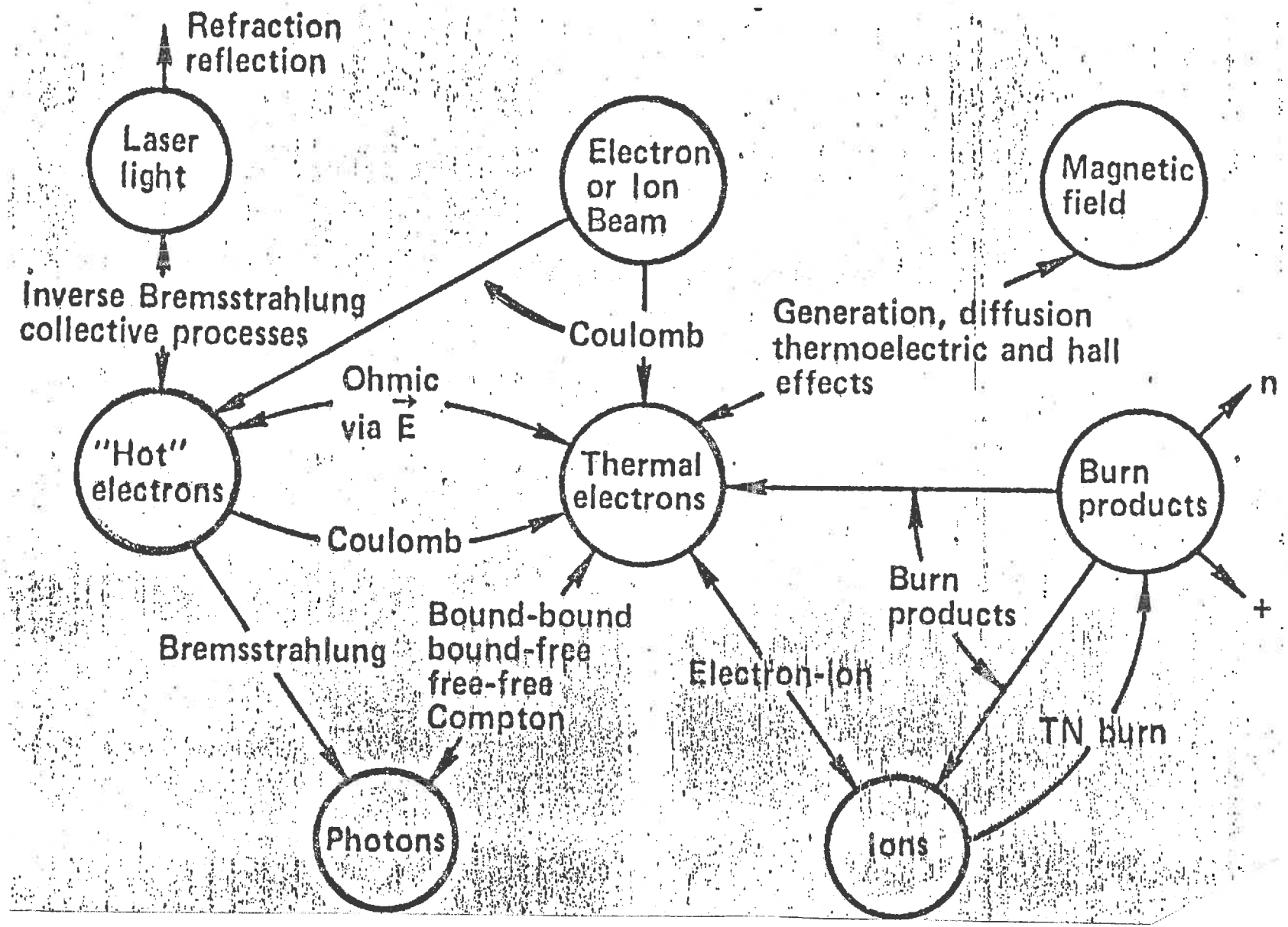

Some simple rules of thumb for pellet parameters:

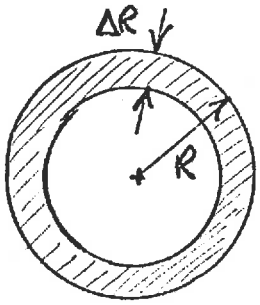

(i) The Taylor stability will limit the allowable aspect ratio $R/\Delta R$ of the target. That is, very thin-walled targets tend to be more susceptible to Taylor instabilities.

(ii) Generally, an absorbed energy $E \sim 1$ MJ and an incident power $P \sim 100$ TW are necessary for a gain $G \sim 200$. This will determine the necessary fuel mass since

$$1 \text{ mg DT} \quad \sim \quad 340 \text{ MJ}$$

(iii) We can estimate the required implosion velocity as roughly 4×10^7 cm/s

(iv) Implosion efficiency can be estimated using a simple rocket model:

Let

m = rocket mass

m_o = initial mass

v = rocket speed

v_o = exhaust speed

When we can solve Newton's law for

$$F = v_o \frac{dm}{dt} \Rightarrow v = v_o \ln \frac{m_o}{m}$$

Now the implosion efficiency can be calculated as

$$\text{Eff} = \frac{x \ln^2 x}{1-x}, \qquad x \equiv \frac{m}{m_o}$$

If one include thermal energy loss, then the efficiency is reduced to

$$\text{Eff} = \frac{x \ln^2 x}{2.5(1-x)}$$

For good efficiency, $x \sim 0.1$, we need

$$v \quad \sim \quad 2\, v_o$$

But using our earlier estimate of $v = 4 \times 10^7$ we find that the ablation velocity should be $v_1 \sim 2 \times 10^7$ cm/s.

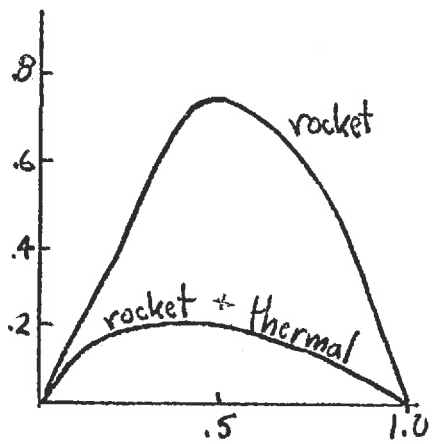

(v) One can multiply the implosion velocity by using multiple-shell targets. This works just like the collision of two billiard balls. That is, if the outer shell has a mass μ times greater than the inner shell, then the velocity multiplication of the inner shell which occurs when the outer shell collides with it is

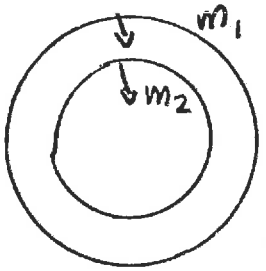

$\frac{m_1}{m_2} = \mu$

$$VM = \frac{2\mu}{1+\mu}$$

The implosion efficiency then becomes

$$Eff = \frac{4\mu^2}{(1+\mu)^2}$$

Major constraints on pellet design:

(i) Rayleigh-Taylor instability

When we try to compress a low density fuel (such as DT) with a high density tamper shell we can encounter a fluid instability known as the Rayleigh-Taylor instability. A good analogy to this process involves trying to float a layer of water on a layer of lighter fluid such as oil. If we are very careful, we can prepare two such fluid layers in a container. However the slightest disturbance will cause surface oscillations to grow until globs of oil begin to pass through the water to the surface because of the force of gravity. (This concept is used in artistic display models using various colored fluids of different density.) In the pellet implosion the acceleration force can cause the boundary between the heavier tamper shell and the lighter fuel to become unstable. A sequence of LASNEX computer code runs on the following pages illustrates this phenomenon. The Rayleigh-Taylor instability becomes more severe for high aspect ratio (thin walled) targets.

THREE POSSIBLE CASES OF RAYLEIGH-TAYLOR INSTABILITY

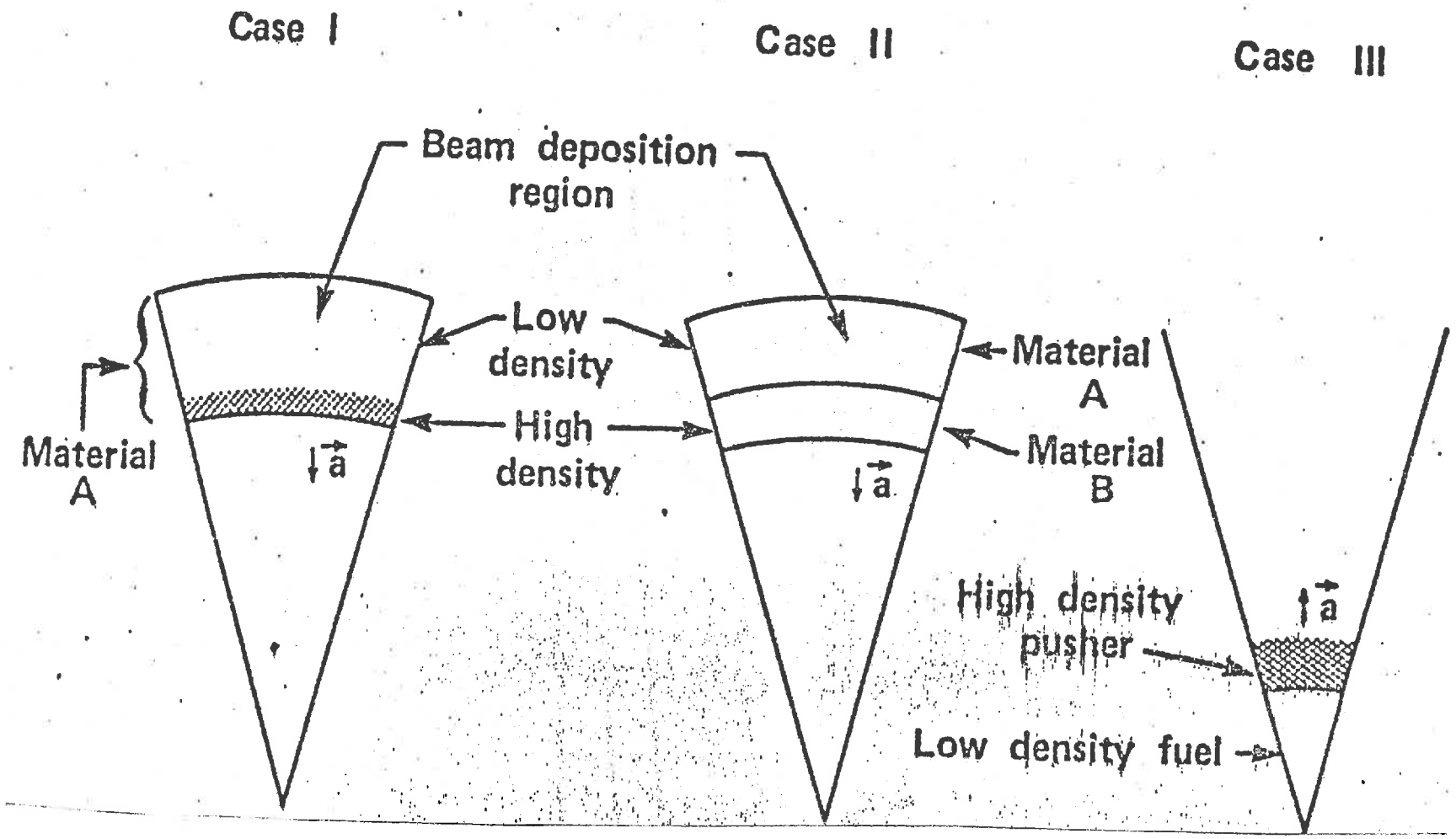

LAGRANGIAN MESH FOR A TYPICAL PROBLEM

Typically ~100 radial zones. The radial zone thickness must satisfy $k\delta r < 1$ at the unstable interface.

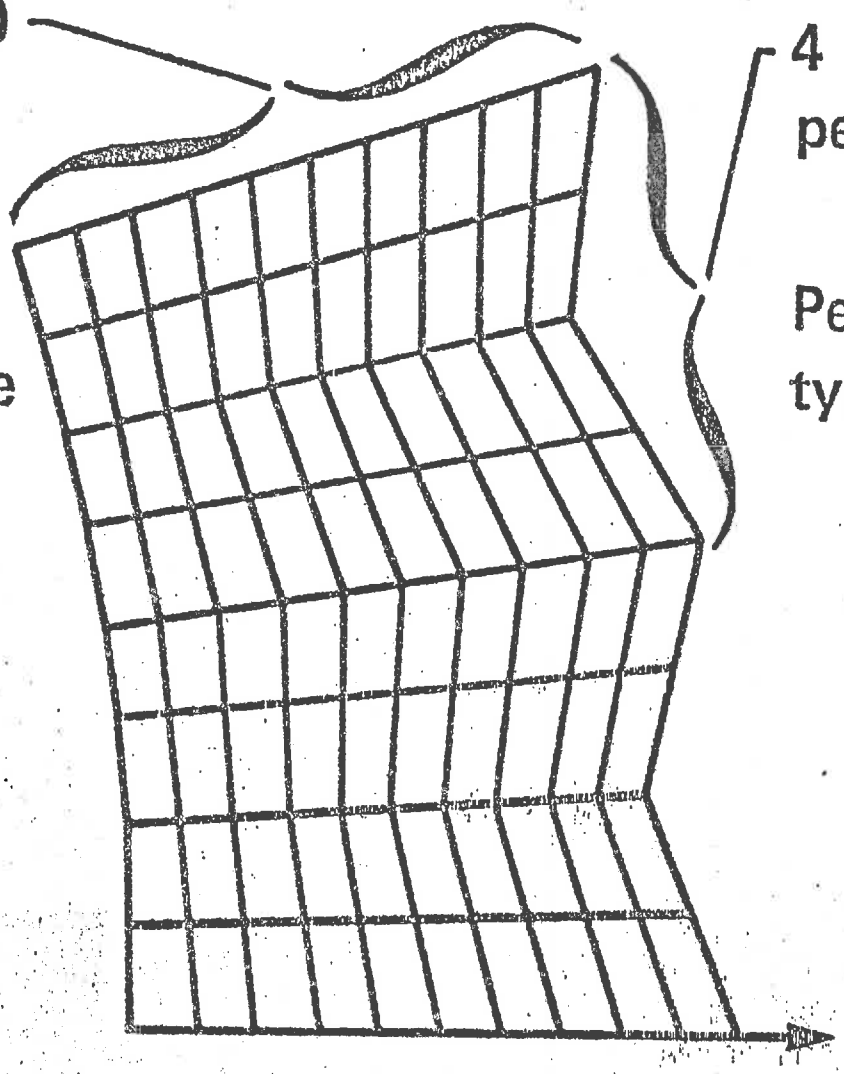

4 angular zones per wavelength

Perturbation is typically ~10 Å

Axis of rotation

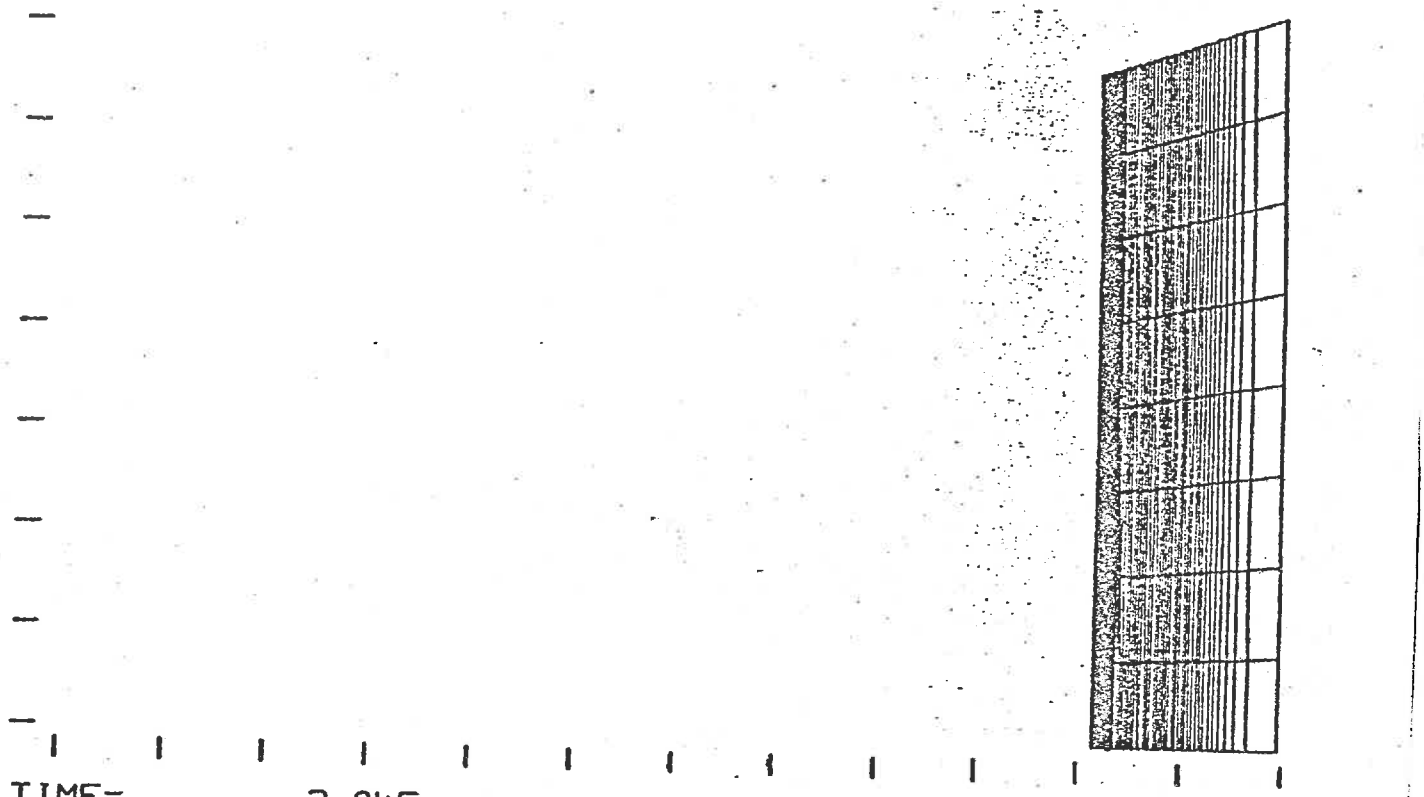

TIME= 2.045 ALPHA-5MEV CYCLE= 300.0
ZO= .050 ZMX= .110 DR/DZ= .20

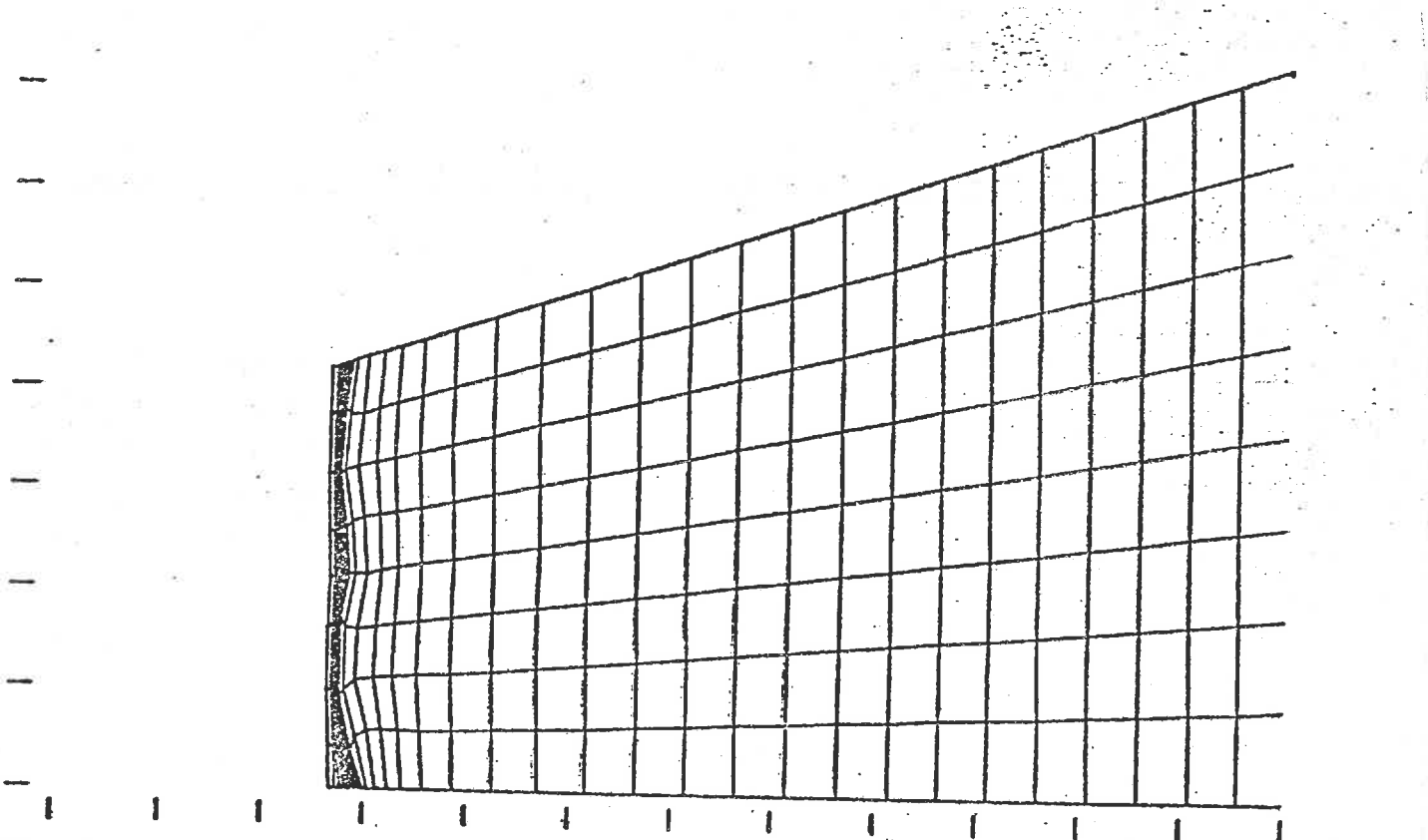

TIME= 6.861 ALPHA-5MEV CYCLE= 1550.0
ZO= .050 ZMX= .110 DR/DZ= .20

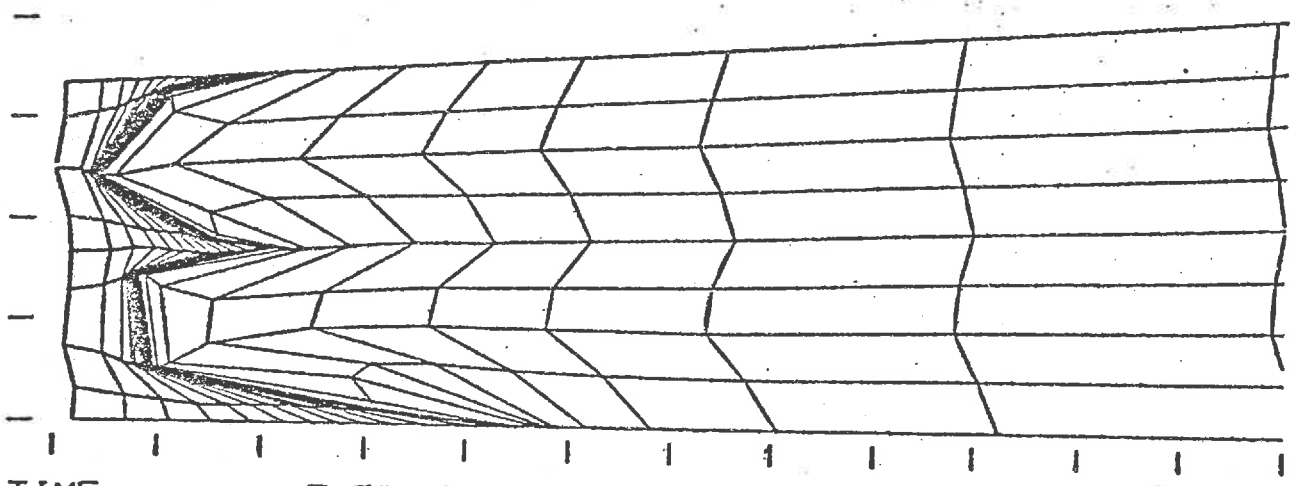
TIME= 7.591 ALPHA-5MEV CYCLE= 1725.0
ZO= .050 ZMX= .062 DR/DZ= 1.00

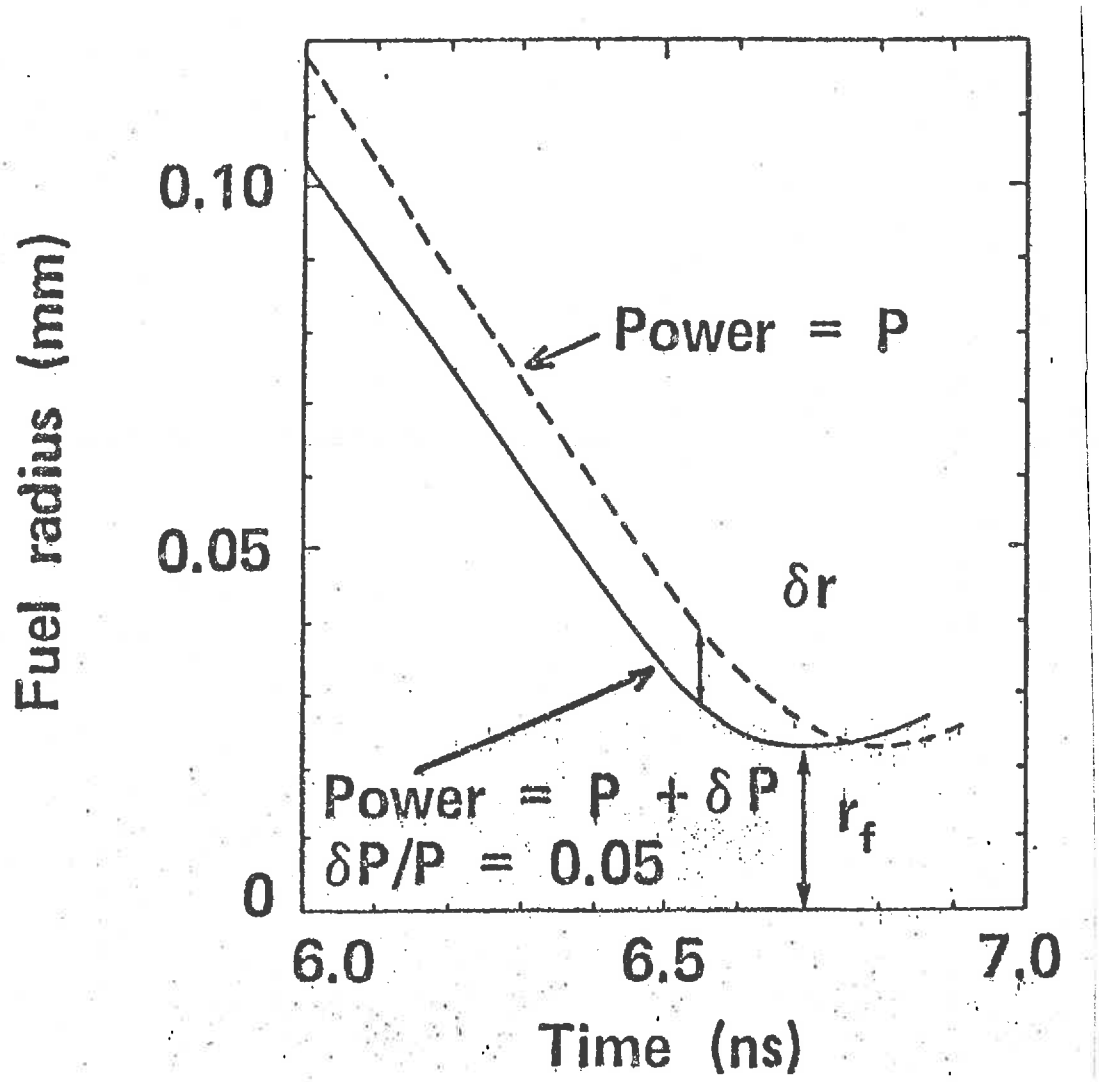
Fuel radius (mm)
0.10
0.05
0
Power = P
δr
Power = P + δP
δP/P = 0.05
r_f
6.0
6.5
7.0
Time (ns)

(ii) pre-heating considerations

We have noted that preheating of the fuel by superthermal electrons or bremsstrahlung radiation produced in the energy deposition region can significantly degrade pellet gain. Hence a variety of mechanisms are employed to reduce preheating, including the use of shielding materials and magnetic fields within the pellet.

(iii) economic constraints

For electrical power applications, one must utilize pellet designs which are compatible with economic constraints. For example, large central station power plants produce electricity for several cents per kWh. Their capital cost is roughly $1 per watt installed capacity.

Since 1 kWh is about 4 MJ, we will need about 10 MJ/kWh (accounting for the thermal cycle). If we allow 0.25¢ per kWh, this implies that 40 MJ can only cost 1¢. Put another way, 4000 MJ or 1 ton TNT-equivalent of fusion energy can only cost $1. (Another comparison is that 1 barrel of oil is roughly 1 ton TNT-equilivalent. Since oil presently sells for $20 to $30 per barrel, the constraints of this very low fuel cost are evident.)

9.2. LASER FUSION TARGETS

Thus far our discussion has been confined to a theoretical analysis of the implosion of either solid or DT shell targets. Many early studies of laser fusion assumed solid spheres of DT. Although such pellets would be easy to fabricate, they would require very high power levels in excess of 1000 TW for high gain. By using spherical shell targets, one can reduce the power requirements to the 100 TW level.

In most experimental work to date, the targets have been shells containing DT gas at high pressure. In the majority of applications, the fuel containing material has been glass. More recently, polymeric materials such as polyvinyl alcohol (PVA) has been used either as the primary fuel container or as a low-Z coating on the exterior of the glass shell or metal shell containers. These simple shell targets behave in an exploding pusher mode. That is, the incident laser light deposits energy so rapidly in the outer shell, that it explodes, half inward, half outward. The imploding shell half acts as a piston, driving a shock ahead of it into the DT fuel that compress and heat the fuel.

Target design parameters (dimensions, fill pressures) are determined by laser characteristics. The low power levels of existing lasers have limited target mass to less than μg, so that glass targets have typical diameters in the range of 50 μm to 300 μm with wall thicknesses from 0.5 μm to 5 μm.

Simple cryogenic exploding pusher targets have been developed in which the DT fill gas is liquefied into a layer coating the inside of the glass shell. This shell fuel geometry leads to an enhancement in neutron yields for the same laser power levels.

However such exploding pusher targets will never be able to achieve the gains required for high yields. This limitation is shown quite clearly on the graph plotting gain versus laser aperture size on the next page. It is apparent that high gains will require the implementation of pellets which utilize the isentropic implosion scheme discussed in Chapter 2.

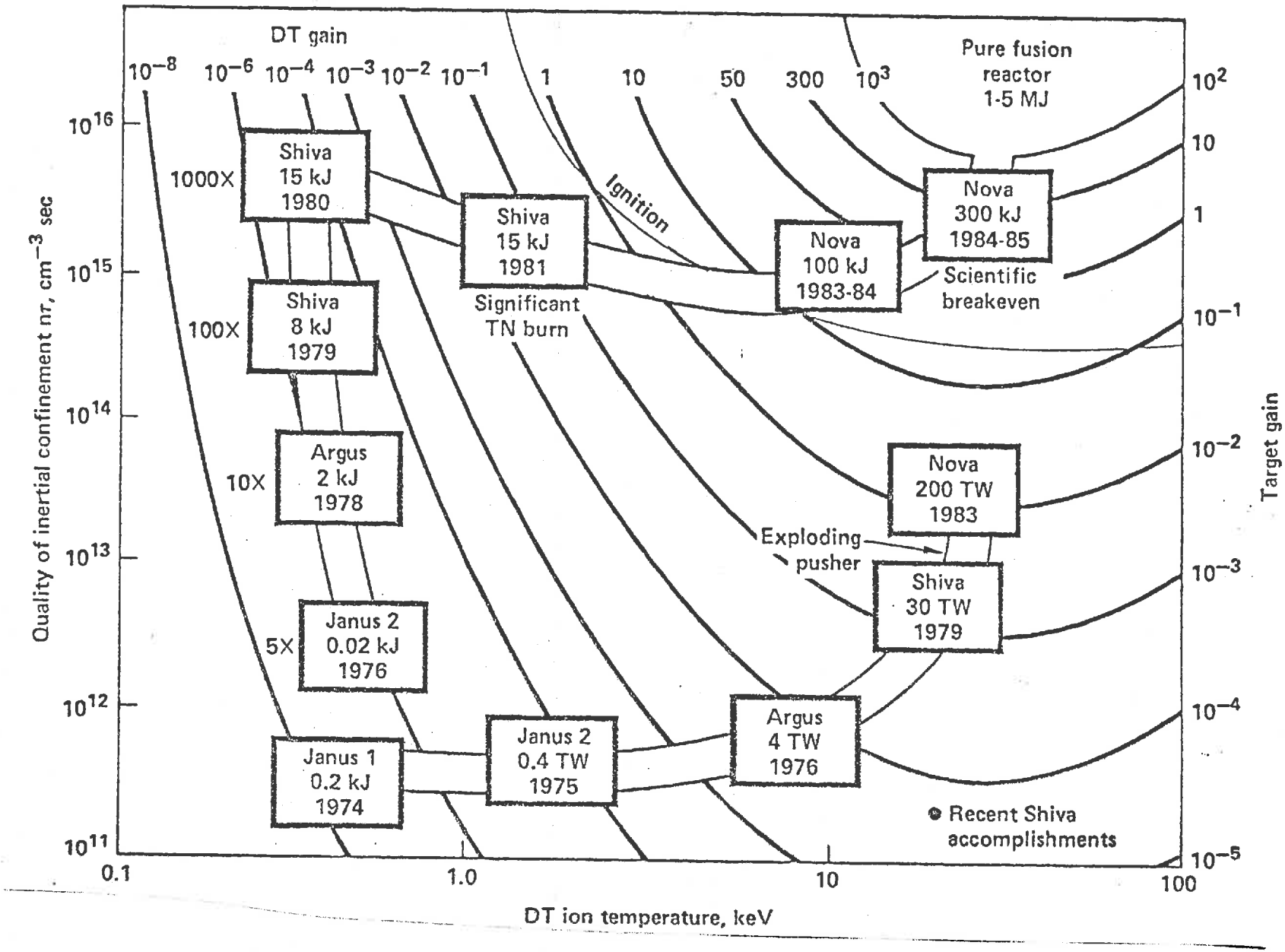
DT gain
10^{-8} 10^{-6} 10^{-4} 10^{-3} 10^{-2} 10^{-1} 1 10 50 300 10^3
Pure fusion reactor 1-5 MJ
Ignition
1000X
Shiva 15 kJ 1980
Shiva 15 kJ 1981
Significant TN burn
Nova 100 kJ 1983-84
Nova 300 kJ 1984-85
Scientific breakeven
100X
Shiva 8 kJ 1979
10X
Argus 2 kJ 1978
Nova 200 TW 1983
Exploding pusher
Shiva 30 TW 1979
5X
Janus 2 0.02 kJ 1976
Janus 1 0.2 kJ 1974
Janus 2 0.4 TW 1975
Argus 4 TW 1976
Recent Shiva accomplishments
Quality of inertial confinement $n\tau$, cm^{-3} sec
10^{16} 10^{15} 10^{14} 10^{13} 10^{12} 10^{11}
Target gain
10^2 10 1 10^{-1} 10^{-2} 10^{-3} 10^{-4} 10^{-5}
0.1 1.0 10 100
DT ion temperature, keV

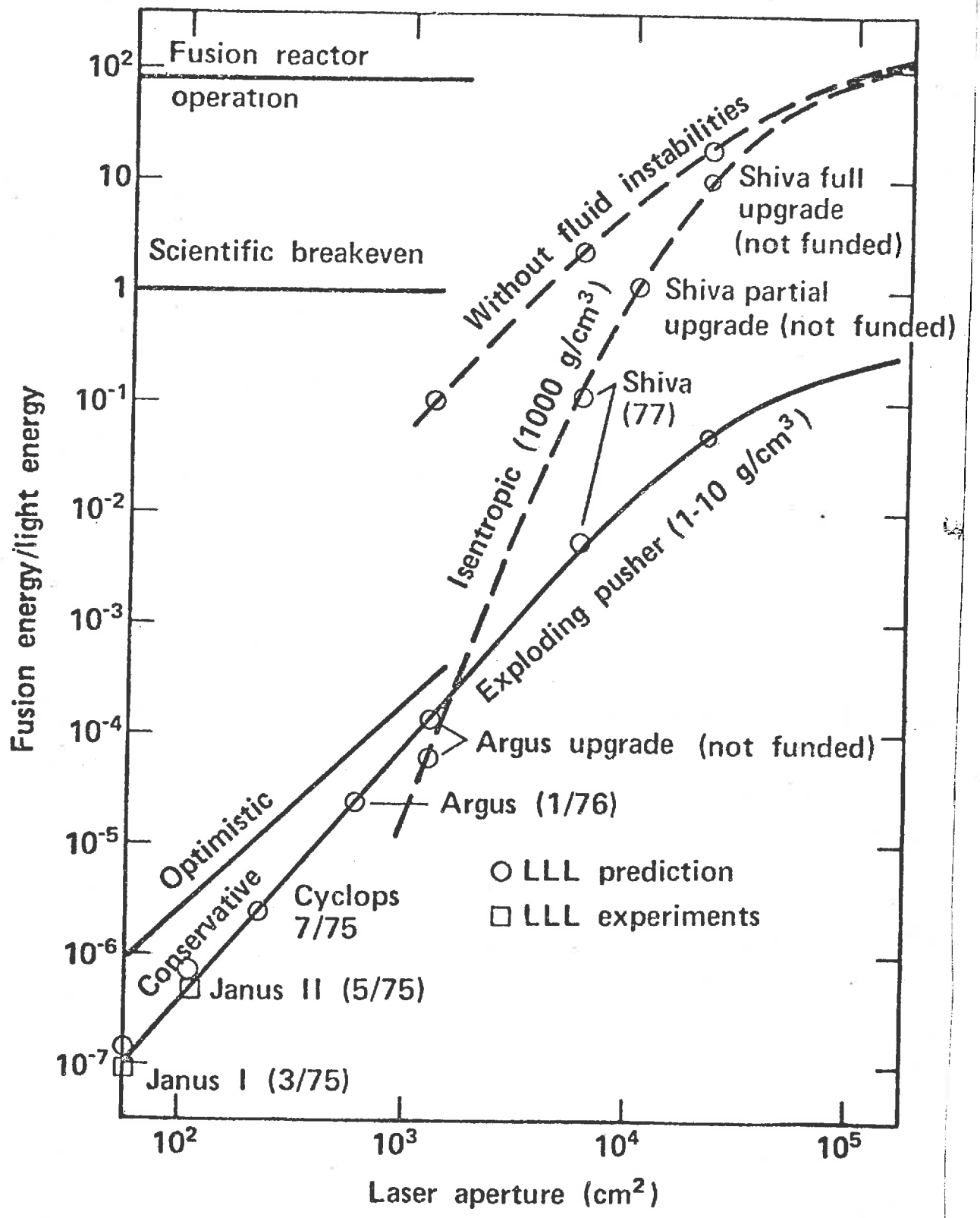
Fusion reactor operation
Scientific breakeven
Without fluid instabilities
Isentropic (1000 g/cm³)
Exploding pusher (1-10 g/cm³)
Shiva full upgrade (not funded)
Shiva partial upgrade (not funded)
Shiva (77)
Argus upgrade (not funded)
Argus (1/76)
Optimistic
Conservative
Cyclops 7/75
Janus II (5/75)
Janus I (3/75)
LLL prediction
LLL experiments
Fusion energy/light energy
Laser aperture (cm²)
10²
10
1
10⁻¹
10⁻²
10⁻³
10⁻⁴
10⁻⁵
10⁻⁶
10⁻⁷
10²
10³
10⁴
10⁵

Ablatively driven targets are generally coated with one or more layers of materials design to perform the functions of ablation, tamping, shielding the fuel core from preheat, or to increase laser light coupling to the fuel. The general goal is to design targets capable of high gains (G~100 to 1000) using incident laser beams characterized by power levels of roughly 100 TW and energies of roughly 1 MJ. A typical high gain target design is shown on the next page.

9.2.1. High Gain Target Designs

One can identify a variety of different target designs suitable for laser fusion:

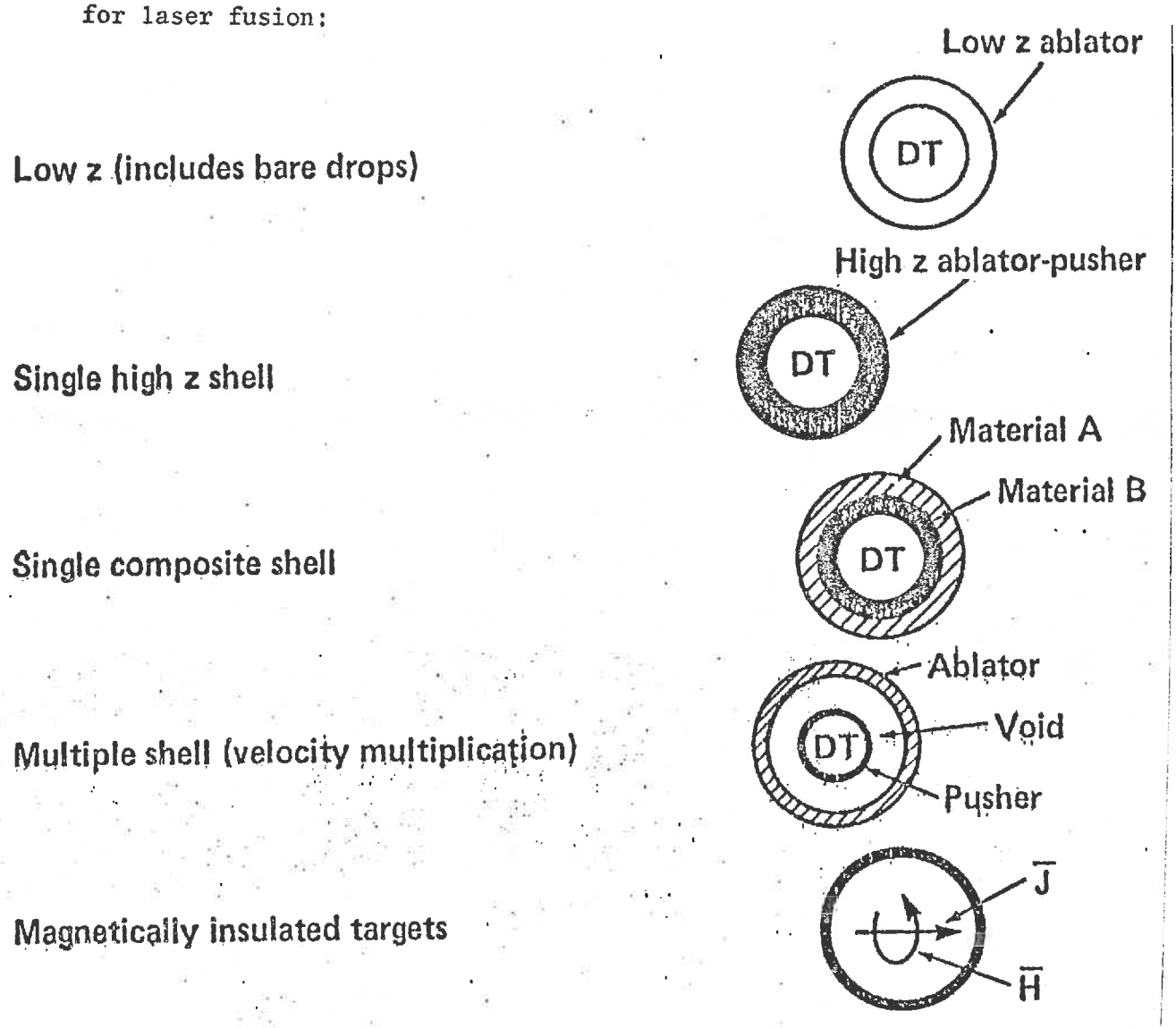

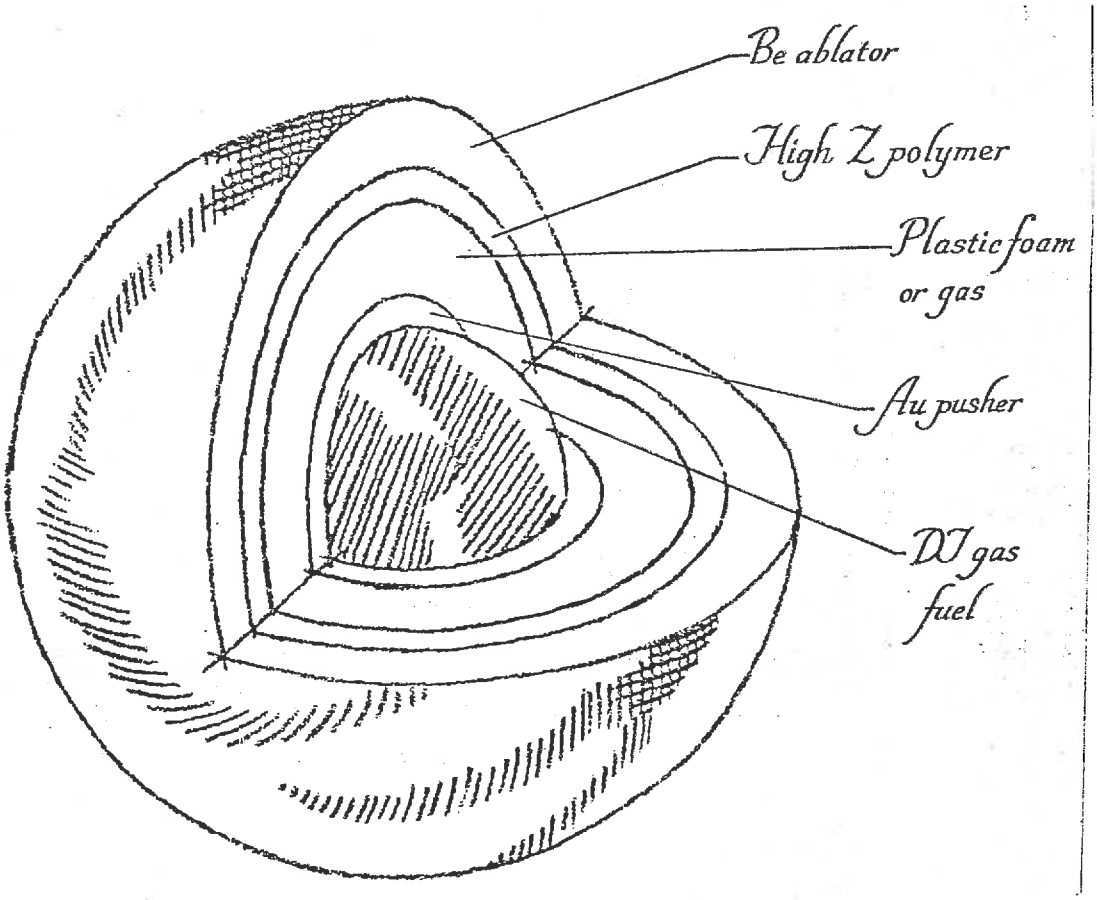
Be ablator
High Z polymer
Plastic foam
or gas
Au pusher
DT gas
fuel

Low Density Targets

To achieve high gains with low density targets, one must optimize the pellet implosion:

(i) symmetry: The central fuel core must be sufficiently symmetric to achieve high density and ignite efficiency. In a typical case, the radius of the fuel might decrease from 0.3 cm to of the order of 10^{-3} cm:

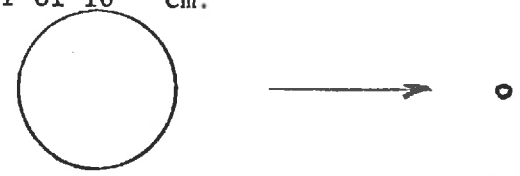

If we recognize that the radial variations $\Delta r \sim \Delta (vt)$, this implies that we need implosion accuracies better than 1%. Such implosion symmetry can be assisted using multiple beam illumination, electron transport in the target corona, and shimming (using nonspherical variations in the shell radius and thickness).

(ii) fluid instabilities: low density targets imply small aspect ratios, $R/\Delta R < 10$. The growth of fluid instabilities may be controlled by density gradients with scale heights comparable to the wavelenth of the most rapidly growing perturbations.

(iii) entropy: the entropy of the compressed core can be minimized by careful pulse shaping and avoiding preheat (perhaps by using a layer of high-Z material to shield from hot electron transport).

(iv) efficient absorption: we can use an outer layer of $Z \sim 5 - 10$ to enhance inverse bremsstrahlung absorption (although higher Z can lead to energy loss via bremsstrahlung).

Several target designs have been attempted to achieve high gains using low density shells with moderate aspect ratios. However computer simulations suggest that the required compression energy in these targets is considerably above that needed to obtain efficient ignition and high gain. The present view is that such low density targets cannot achieve high gains at moderate incident laser energy ($\sim$ 1 MJ).

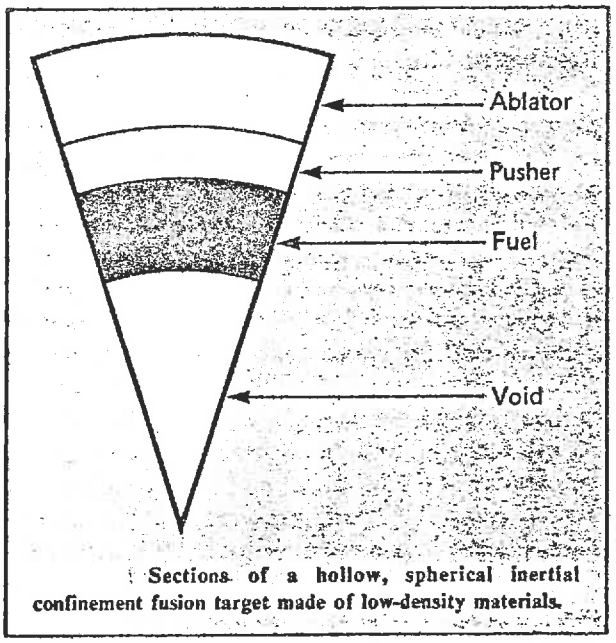

Sections of a hollow, spherical inertial confinement fusion target made of low-density materials.

Targets with Very Thin Shells

An alternative approach is to use very high aspect shells ($R/\Delta R \sim 100$) of high mass with densities ranging from 2 to 20 g/cm^3. The power requirements for such shells scale as

$$P \sim (m \rho \Delta R)^{1/2} v^3$$

Unfortunately, such high aspect shells are quite unstable to fluid instabilities. Furthermore, computer simulations suggest that such ultrathin shells have no significant advantage in gain or power requirements and only relieve slightly the requirements on pulse shaping. When coupled with the increased susceptibility to Taylor instability, such targets do not appear to be particularly attractive.

Targets with Central Ignitors

A particularly interesting target design involves placing the fuel in two different regions, a massive outer shell and a small inner shell or core. The massive outer shell is imploded at a velocity less than that necessary for ignition (roughly 1.4×10^7 cm/s) and compresses the low density gas or foam between the inner and outer pellet regions. This compressed region acts as a spring and subsequently implodes the inner pellet at a higher velocity (2×10^7 cm/s). The inner pellet implodes, ignites, and burns with a gain of about 50. The exploding inner pellet delivers 10 MJ of X-ray and ion debris onto the inner surface of the outer pellet, thereby igniting it. Burn then propagates through the more massive outer shell providing a total gain of as high as 500. Hence the inner pellet gain of 50 can be multiplied by 10

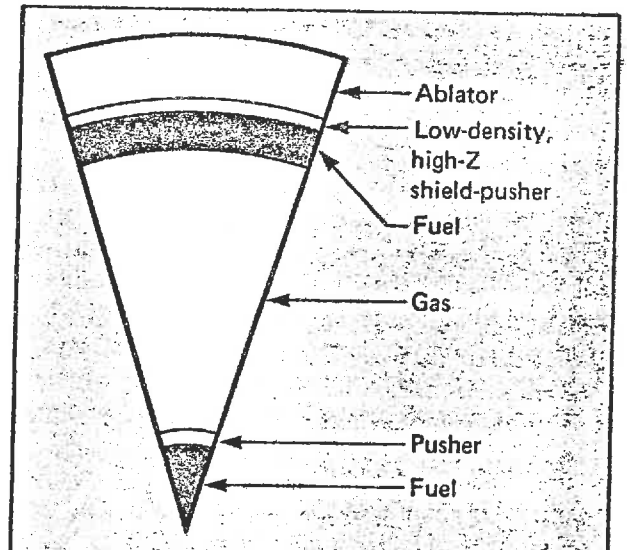

Fig. 4-13. Sector of a spherical inertial confinement fusion target having a central ignitor and an outer fuel layer. This target is capable of very high gains, and the required driving power is exceptionally low.

by propagating the burn into the outer pellet where large ρR is achieved by more DT mass rather than high compression. By using a central ignitor region, we can reduce the required implosion velocity by roughly a factor of two, thereby imploding roughly twice as much fuel for the same energy and increasing the gain.

Magnetically Insulated Targets

The essential idea here is to induce a strong magnetic field in the target (at a megagauss level) that will inhibit electron thermal conduction and fusion ion debri motion, thereby trapping fusion energy in the central fuel core and allowing more efficient burn:

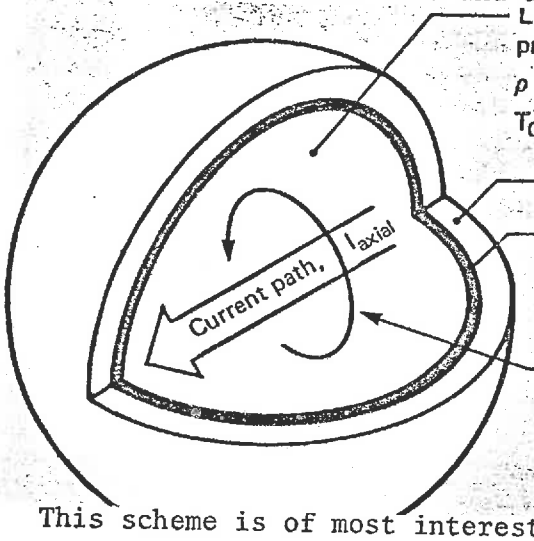

Conceptual view of magnetically insulated target. A frozen fuel layer surrounds a preheated low-density gas containing a magnetic field. The preheated gas is compressed to ignition conditions by the imploding pusher, and then propagates the burn to the frozen fuel layer for gains ~100.

This scheme is of most interest for charged particle beam fusion applications, and therefore we will return to consider it in more detail at a later point.

Nonablative Acceleration Methods

Here the essential idea is to replace the driver energy deposition by hypervelocity particle impact. Between 10 to 10^4 small pellets would be accelerated to high velocity (2×10^7 cm/s) using either electromagnetic or laser-driven ablation methods. These pellets would then be directed onto the surface of the fuel pellet. The hypervelocity pellets are vaporized by impact with the outer shell of the fuel pellet, and high velocity jets penetrate into the gas region of the target. This heats the gas to high temperature, thereby imploding a double-shelled

with a thick low density outer shell. Such a target is shown below:

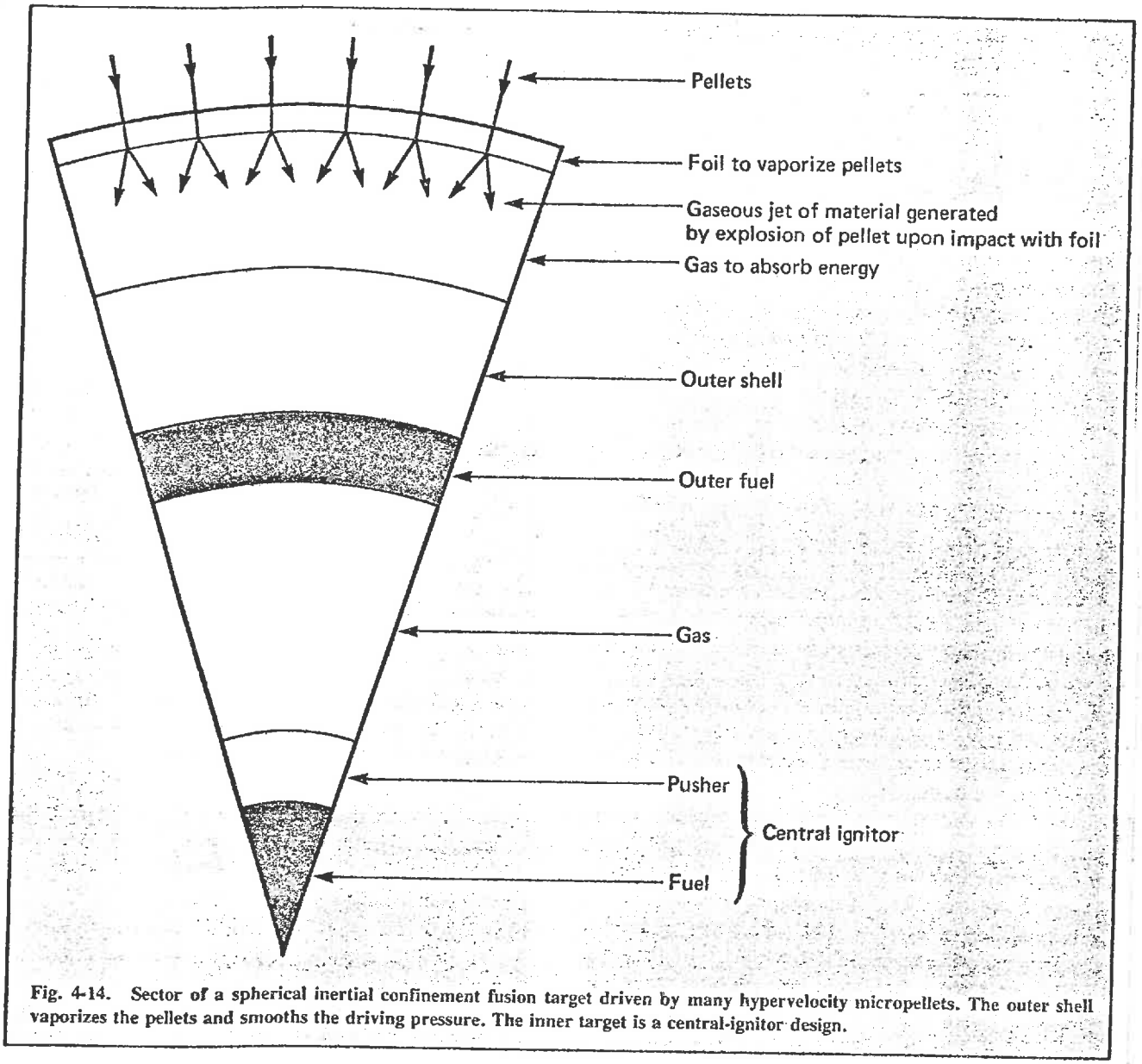

Fig. 4-14. Sector of a spherical inertial confinement fusion target driven by many hypervelocity micropellets. The outer shell vaporizes the pellets and smooths the driving pressure. The inner target is a central-ignitor design.

9.2.2. A Generic Target Design

Laser fusion targets can become quite complex as different layers are included to alleviate problems such as hydrodynamic instabilities, hot electron and hard X-ray preheat, fuel tamping, and efficient laser light-corona coupling. We have shown below the evolution in target design, progressing from simple exploding pusher glass microballoons containing a DT gas mixture, to ablator-mode targets with a teflon layer to serve as the ablator, to complex multi-layered targets with both gas and frozen (cryogenic) DT fuels.

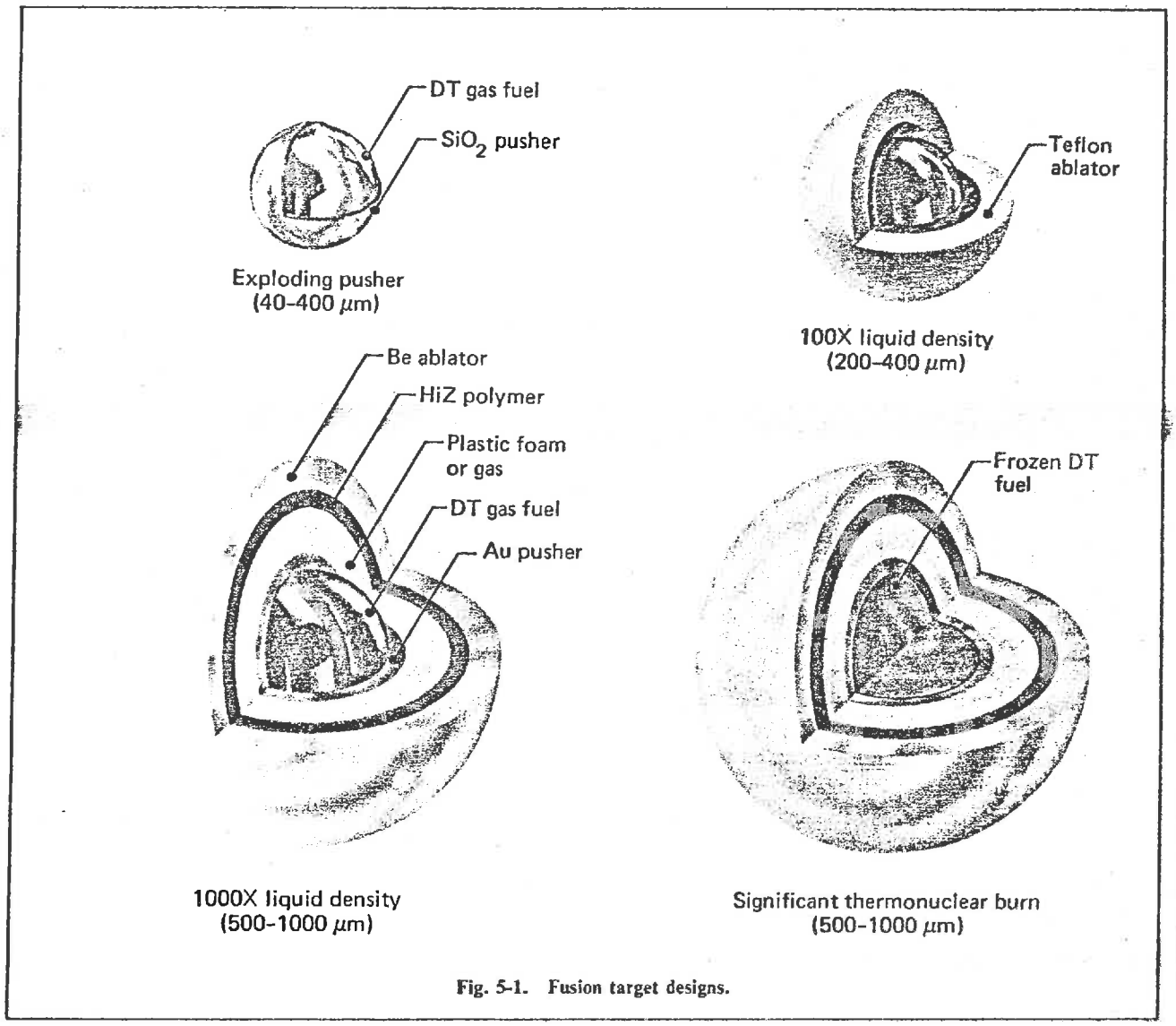

Fig. 5-1. Fusion target designs.

In their laser fusion reactor study, the University of Wisconsin group developed a generic pellet design consisting of 4 layers as shown on the next page. The first, or innermost layer, consists of the condensed fuel mixture, which has a total mass of 1 mg. The second layer is usually the structural capsule which serves to contain the fuel during processing and injection. It can be either glass or polyvinyl alcohol (PVA). If PVA capsules are used, a layer of Xe condensed between the DT and the PVA is probably required to protect the capsule from radiation damage. The third layer is made of high Z material (e.g., Hg) with a mass of perhaps 10 mg and is needed only when the Z of the structural shell is not sufficiently high to protect the fuel from preheat. The outermost layer is chosen to be a low Z low density ablator.

Actually, there are a variety of options for materials for each region of the pellet. Although silicate glasses and polyvinyl alcohol are the most promising candidates for container materials, iron and beryllium would also be possibilities. Other pellet materials are listed in the tables on the next two pages, along with estimates of possible masses.

9.2.3. Experience with Laser Fusion Targets

A variety of target designs have been used in laser fusion experiments in recent years. Of most interest are ablative target designs aimed at achieving high fuel compression. We have compared the target designs used in these high density experiments along with experimental results on the following pages.

LASER FUSION PELLETS

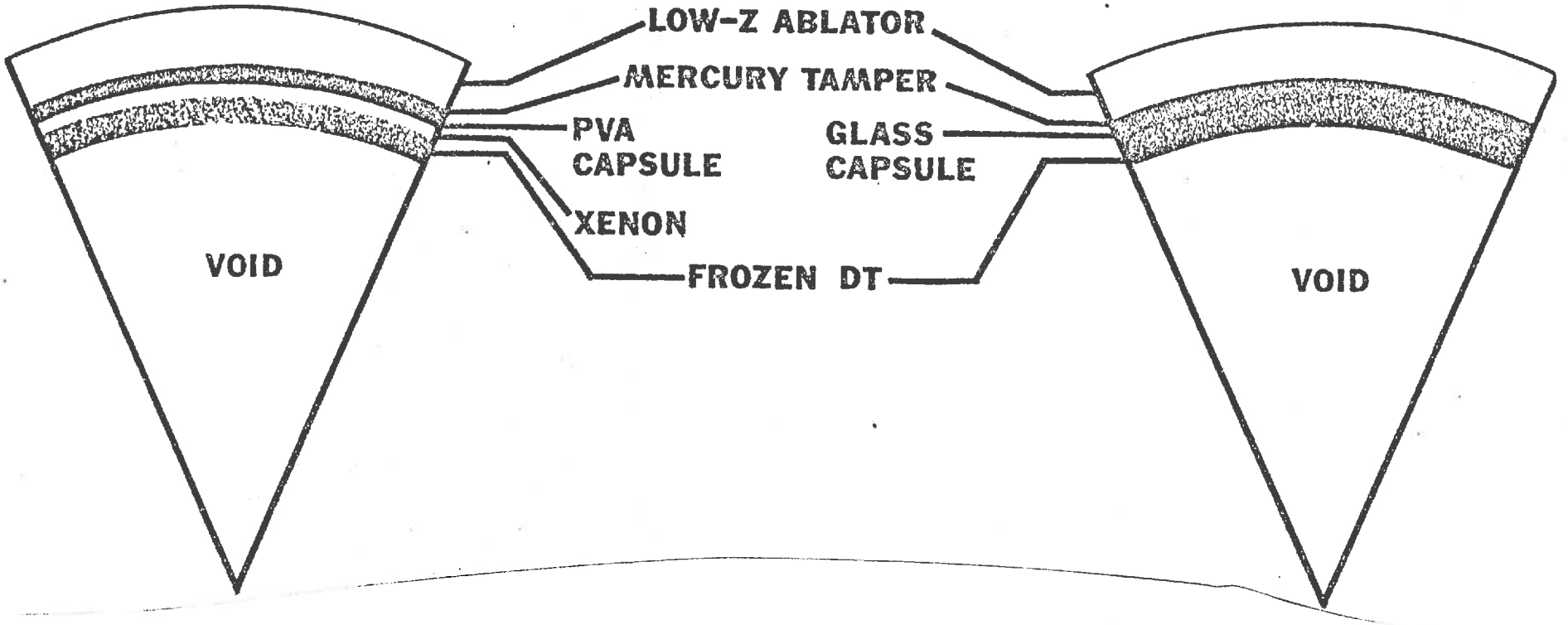

REACTOR PELLET MATERIALS

CONTAINER MATERIAL (pertinent properties)	SHELL (LAYER) MATERIAL LAYER NUMBER* 1	2	3
GLASS (H_2-permeability)	High Z[1] Materials	Glass	Low ρ, low Z[2] Materials
POLYMER (heavy atom-permeability)	Xe and High Z[1] Materials	PVA	Low ρ, low Z[2] Materials
HIGH Z CONTAINER	---	W-25 Re[3] 50 Mo-50 Re	Low ρ, low Z[2] Materials

(1) High Z coating materials - Ta, W, Pb, Hg, Pt, Au, Pd

(2) Low density, low Z layers - CH_2, $LiBH_4$ (foams); Be, B, B_4C, LiH or LiD (open structures)
H_2, D_2 (low density frost)

(3) Candidate high Z materials - tensile strengths > 2×10^5 psi
shell fabricability - unknown

*The layers are numbered in sequence starting with the innermost layer, which is next to the DT fuel layer

Mass of DT and Other Materials in Laser Fusion Pellet

I. Ball and Shell Target*

DT - 0.0388 μg

SiO_2 - 117.3 μg

Au - 10.46 μg

CH - 5.33 μg

H_2 - 0.1 μg

$$\frac{\text{OTHER mass}}{\text{DT mass}} = 3432$$

II. Vacuum Insulation Target**

DT - 0.83 μg

Au - 36 μg

CH - 154 μg

Ni - 2022 μg

$$\frac{\text{OTHER mass}}{\text{DT mass}} = 2659$$

III. Glass Microballoon Target***

DT - 1 ng

SiO_2 - 30 mg

$$\frac{\text{OTHER mass}}{\text{DT mass}} = 30$$

*"Laser Program Annual Report," UCRL-50021-75, p.

**R. Perkins, "The Laser-Fusion Program at LASL," LA-UR-77-174.

***G. Charatis et. al., Glass Microballoon Experiments, IAEA Tokyo Meeting, 1974.

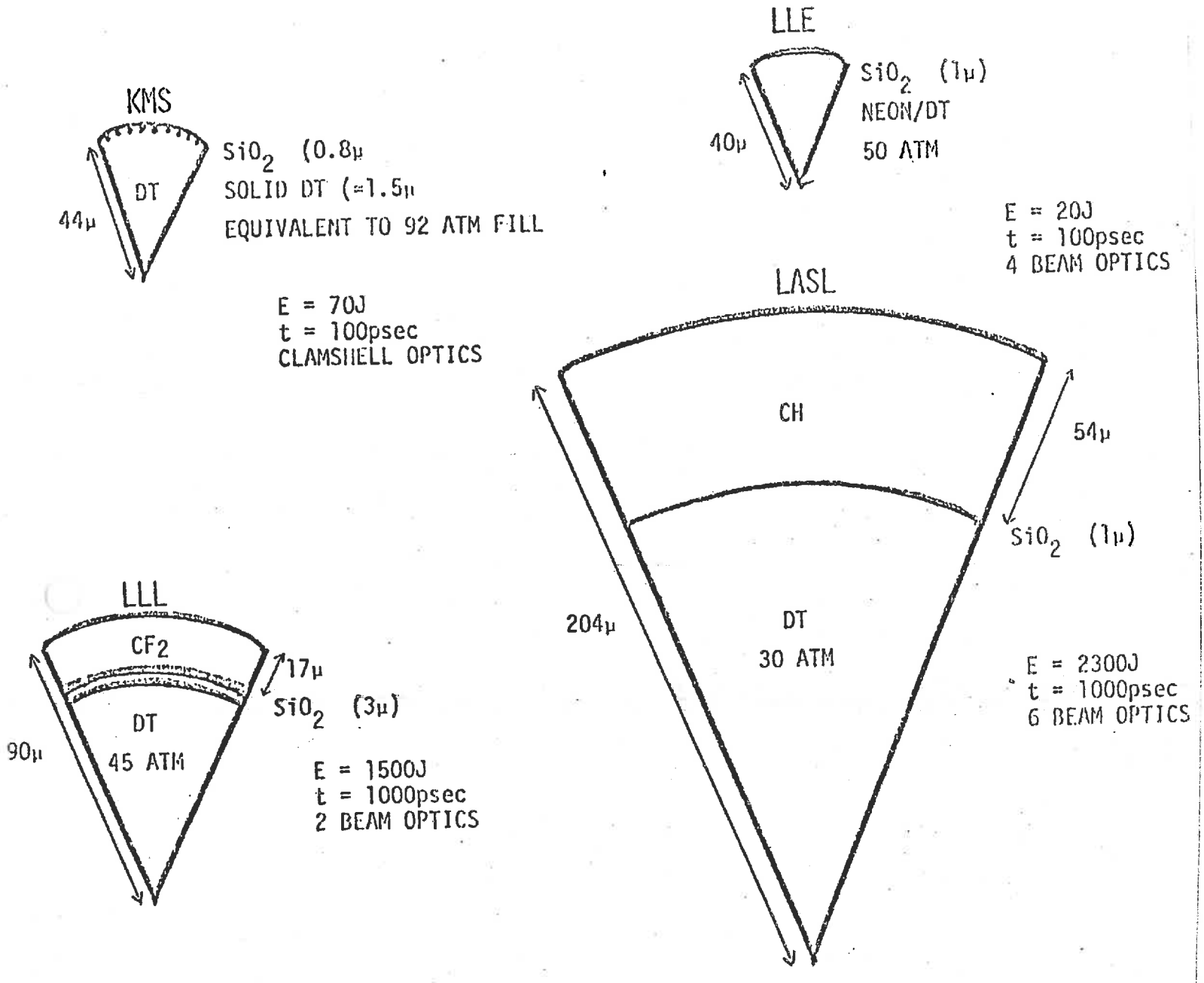

FIGURE 1. REPRESENTATIVE EXPERIMENTAL PELLETS

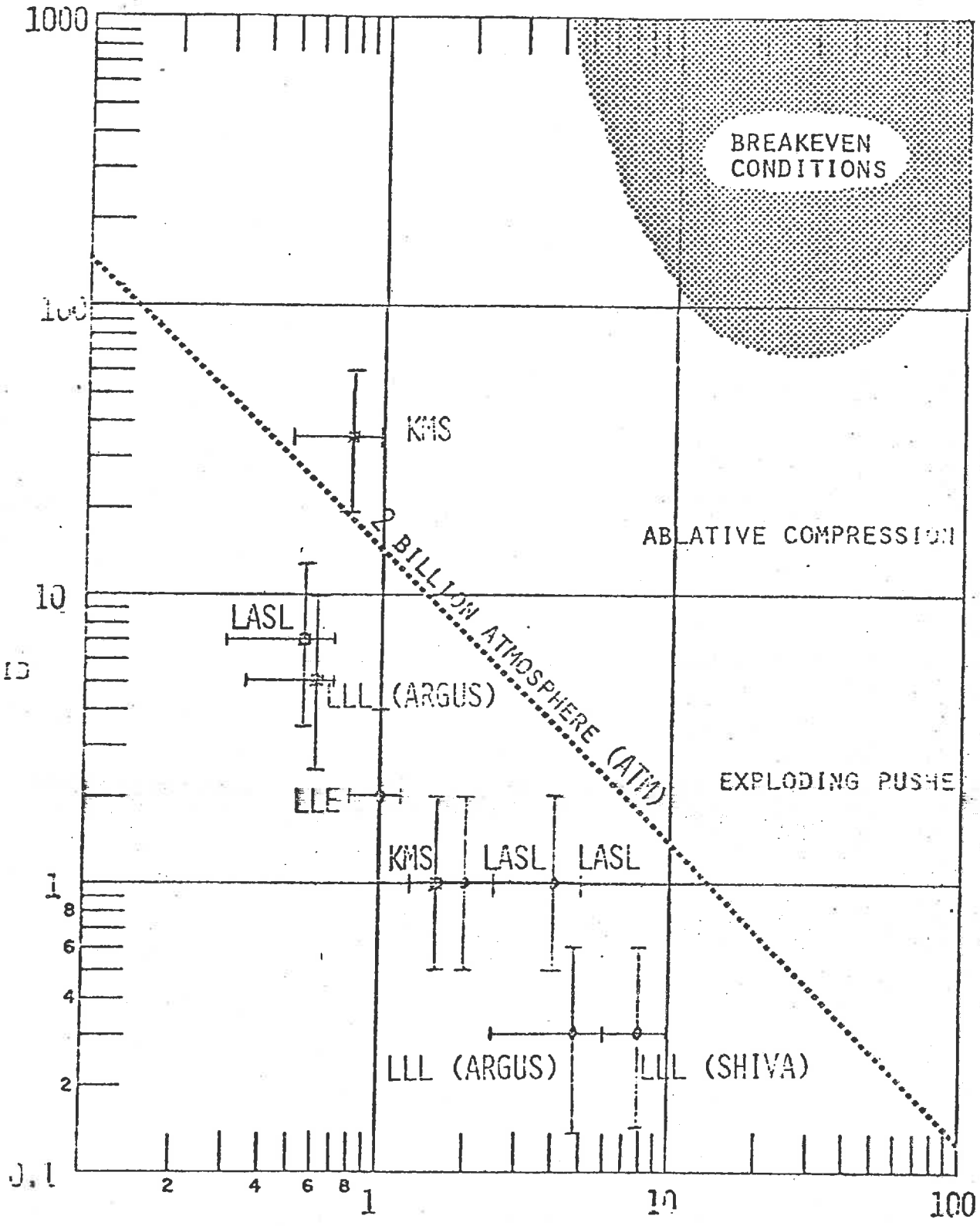

FIGURE 2. RECENT RESULTS

TABLE I. CURRENT RESULTS

LABORATORY	COMPRESSION [x LIQUID DENSITY] MOST PROBABLE		SPECULATIVE		HIGH DENSITY DIAGNOSTICS EMPLOYED	DIAGNOSTIC CONFIDENCE
	Exploding Pusher	Ablative Compression	Exp	Code		
LASL						
HELIOS 2300J/1000ps	1x [2]	7x [0.55]	7-20x	20-50x	Pinhole Yield Yield Delay	Code Correlation For All 3
LLL						
ARGUS 1500J/1000ps	0.3 [4.5]	5x [0.6]	5x	10-20x		Code Consistency
SHIVA 8500J/750ps	---		---	40x	Yield	
SHIVA 2000J/100ps	0.3x [8]		0.5x		X-Ray Microscope	
LLE						
DELTA, 20J/100ps	2x [0.2 neon] [1.0 DT]		1x	1x	Pinhole Yield Line Broadening	Pinhole Correlati with Line Broade
ZETA, 300J/100ps	1x [4.0]					
KMS						
70J/100ps	35x [2.5]		20-80x	NA	Pinhole Yield α Particle Spectrum	Consistency of 3 Diagnostics

[ ] = Temperature in Kev

FUEL DENSITY AT BURN TIME VERSUS NEUTRON YIELD

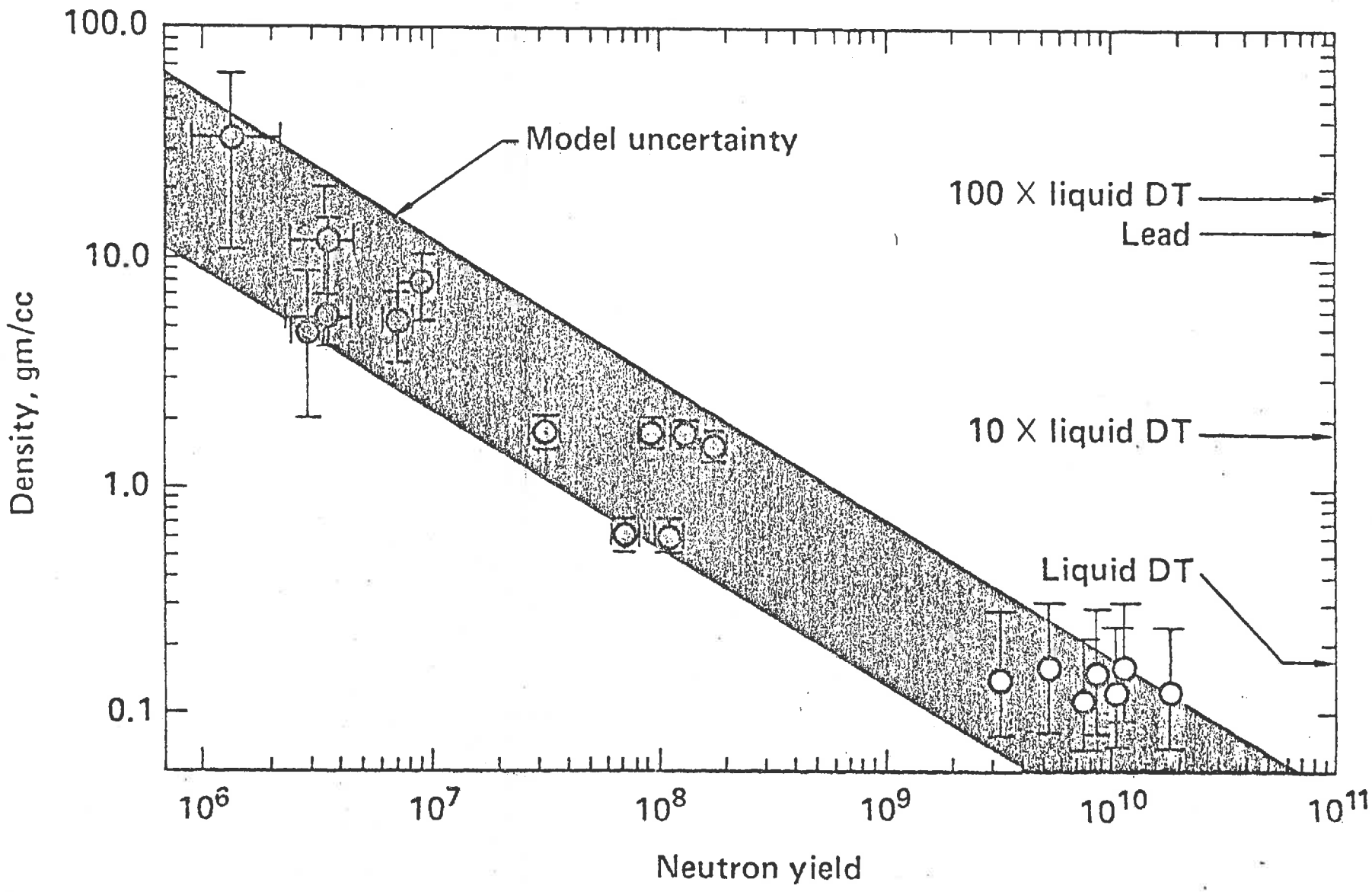

9.2.4. Some Conclusions Regarding Target Design

The general trend in target design is toward more non-fuel pellet material to alleviate problems such as hydrodynamic instabilities, preheat, and laser/plasma coupling. Extrapolated to reactor grade pellets with 1 mg of fuel, this trend implies from 10 to 1000 mg of non-fuel materials per pellet. Such large quantities per pellet imply that the handling and recovery equipment for non-fuel materials will be an important consideration in the fuel cycle of a laser fusion power plant. To minimize the complexity of the fuel cycle, it is desirable to have as few different materials in the pellet as possible.

Furthermore it is important to keep in mind that many nonfuel materials may react physically or chemically with reactor components. The interaction of nonfuel materials with the first wall and exhaust gas processing equipment is a problem unique to inertial confinement fusion and may prove as troublesome as the plasma impurity problem in magnetic confinement fusion approaches.

Detailed computer simulations of pellet designs have also suggested other important features. As a rule, pellet yields increase with incident driver energies. For example, a laser input energy of 10 MJ greatly increases the ease of designing a high gain pellet over that for a IMJ input energy, Since higher gains significantly reduce the recirculating energy fraction in a power plant for a driver of fixed efficiency, this scaling trend becomes quite important.

The burn dynamics of bare and tamped pellet cores is significantly different. In the case of a bare core the DT fuel becomes transparent and the radiation escapes. For tamped cores, radiation is trapped, thereby raising the temperature and pressure inside the core until it explodes. The X-ray spectra for tamped cores varies as a function of the ratio of tamper to fuel mass. For ratios between 1 and 10 the spectrum actually becomes harder because the fuel is burning at higher temperatures. For higher ratios the spectrum becomes softer due to down conversion in the higher Z materials. The fraction of total energy in X-rays is between 1 and 10% and peaks for mass ratios of about 10. The bare DT core has 1% of its yield in X-rays.

The charged particle and X-ray energy fractions and spectra depend upon the fuel and tamper density profiles at ignition. These spectra and fractions will have a major impact on reactor cavity design.

Burning DD in inertial confinement systems is very difficult because of the high values of ρR needed to support burn propagation. Input energies of 100 MJ appear to be necessary. However recycling of unburned tritium (a DD reaction product) into the pellets could reduce these requirements considerably. Burning p-^{11}B requires even greater values of ρR (500 g/cm^2) and a very high ignition temperature (300 keV). To achieve such ρR values requires unrealistic compressions or fuel masses that imply unrealistically large input energies and yields. Hydrodynamic implosions do not appear to be capable of generating the necessary ignition temperatures.

9.3. PARTICLE BEAM TARGETS

9.3.1. Electron Beam Targets

The long pulse width characteristic of relavistic electron beams (20-30 ns) imply that one must irradiate massive, low gain targets. The long energy deposition range of the electrons requires particular attention.

The most obvious approach would be to coat the target with a high Z material to more efficiently absorb the incident electron beam. Unfortunately, the incidence of high energy electrons on high Z materials generate high energy X-rays as bremsstrahlung, and these can penetrate into the center of the target causing substantial preheat.

An alternative is to induce an intense magnetic field in the target which traps the incident electrons while thermally isolating the fuel core of the target to allow high compressions. This concept is shown on the next page along with several methods to generate the 1 to 10 Mgauss fields required.

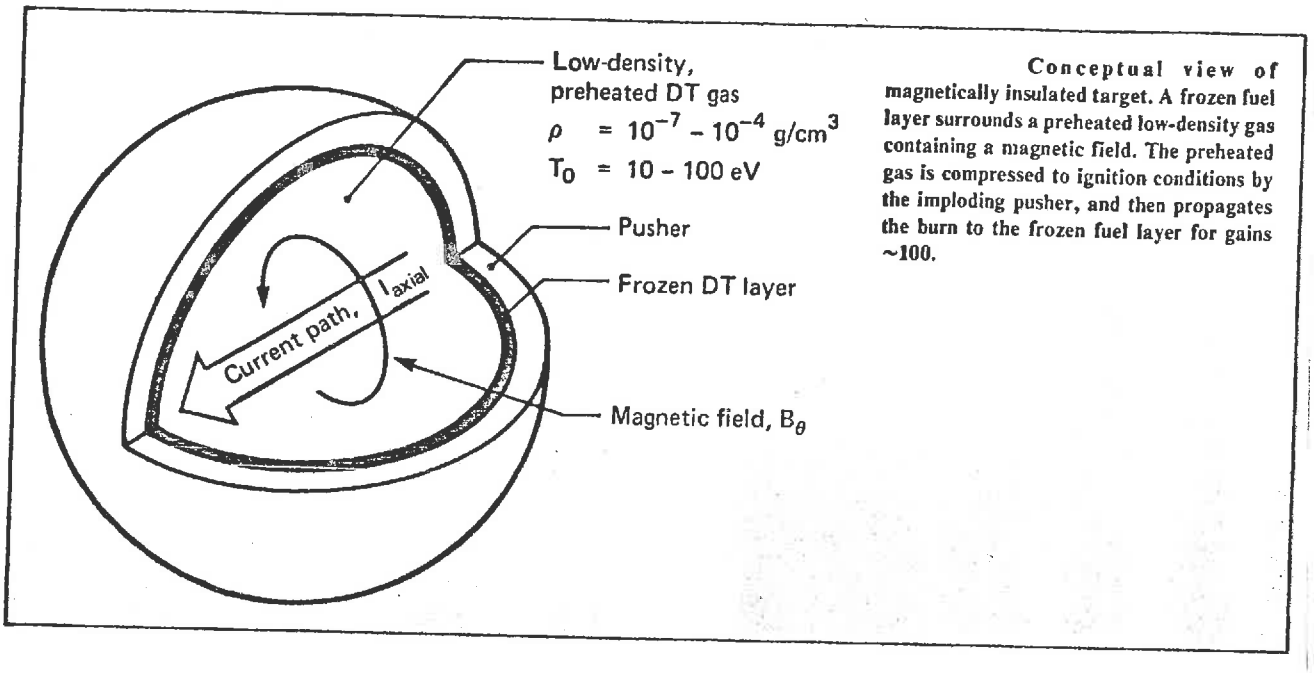

Conceptual view of magnetically insulated target. A frozen fuel layer surrounds a preheated low-density gas containing a magnetic field. The preheated gas is compressed to ignition conditions by the imploding pusher, and then propagates the burn to the frozen fuel layer for gains ~100.

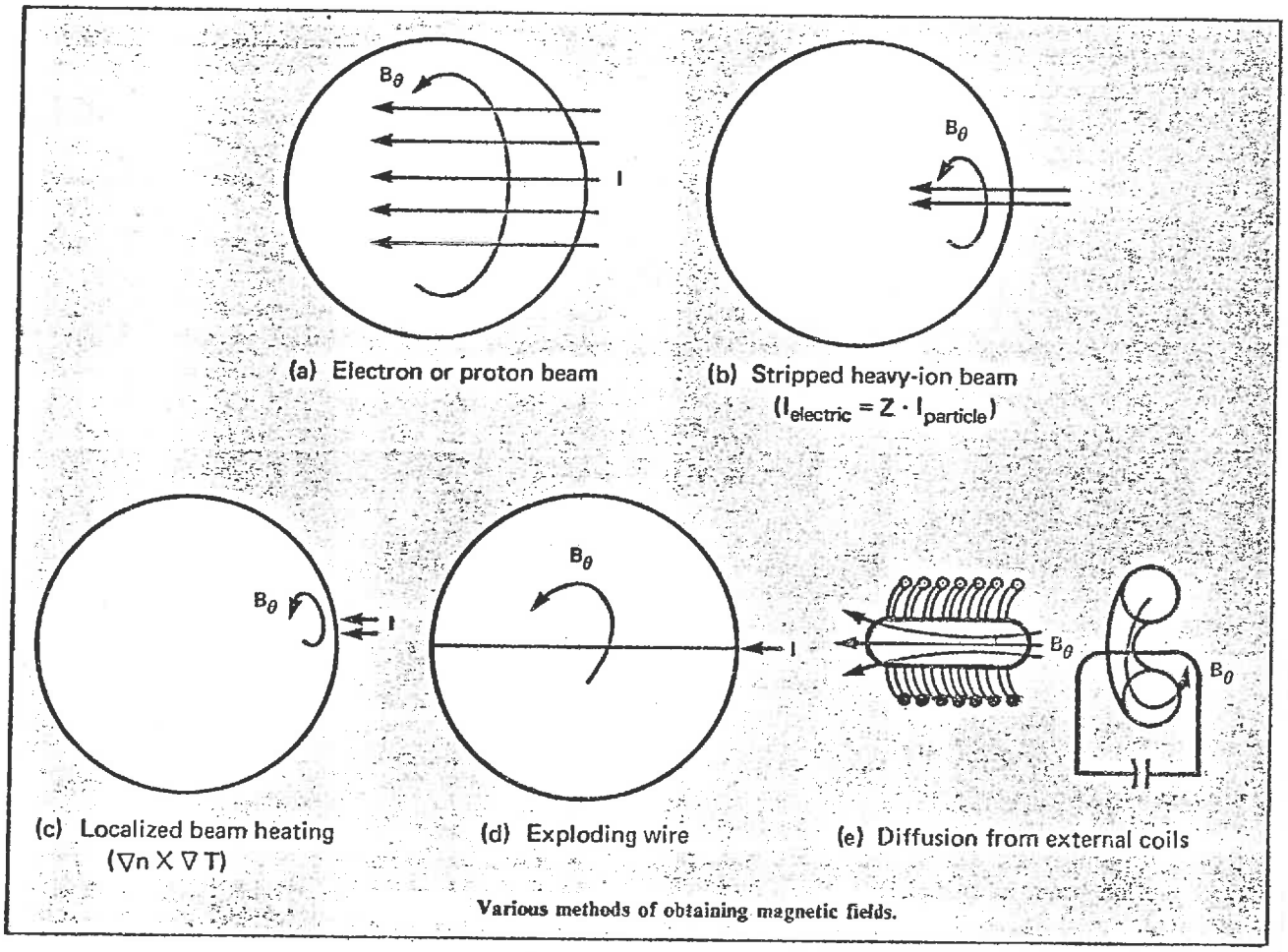

Various methods of obtaining magnetic fields.

Ion Beam Fusion Targets

Ion beam fusion targets utilize many of the same concepts as laser or electron beam fusion targets. However in this case, the massive ions do not generate appreciable bremsstrahlung and deposit their energy in a short range via classical mechanisms. Therefore the absorption region can be a high Z material such as Pb. The longer times characteristic of ion beam pulse widths imply somewhat larger pellets. We have compared ion beam versus electron beam fusion target designs below:

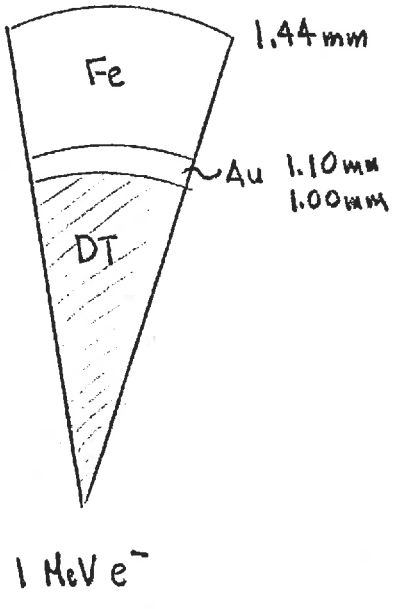

1 MeV e^-

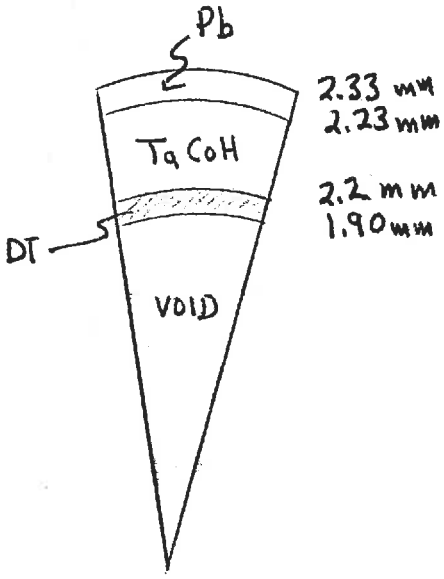

Heavy Ions

9.4. TARGET FABRICATION (quite incomplete)

Several steps will appear in most pellet-processing schemes:

(i) permeation: filling the pellet with DT gas by letting the gas diffuse through the container layer at high temperatures

(ii) final cryogenic processing immediately prior to injection to freeze the DT fuel gas

(iii) deposition technology to add on low-Z ablation layers or high Z layers.

The basic techniques such as radiographic inspection, cleaning, and floatation are well-established procedures. The technology to perform all the fabrication operations for any of the representative pellets is already in existence.

In going to practical designs for reactor applications, several aspects of pellet design must be kept in mind. The most likely approach to reactor-type pellet designs will be substitution of acceptable materials for experimentally convenient materials. For instance, a thin layer of gold is often used as a high-Z fast electron shield in current pellet designs. The mass of this gold is most often at least ten times the mass of the DT fuel. Extrapolated to reactor size pellets, when the DT mass is 1 mg, this represents a consumption of 720 grams of gold per hour. Such quantities of gold are available and affordable, but the efficiency of the recovery process will determind the fraction of gold that is unrecoverable. Should this fraction be too high, or should the cost of the equipment necessary to recover an acceptable fraction be too high, then the use of a substitute material such as mercury or lead must be considered.

Pellet storage must also be considered in design. Safety, shelf life and material properties of fabricated pellets, and energy costs for pellet fabrication and storage will also be important design factors. Cryogenic storage appears the most attractive method at the present time.

CHAPTER 11

APPLICATIONS

Inertial confinement fusion research has expanded quite rapidly along several fronts during the past decade. A primary goal has been to demonstrate scientific breakeven for ICF targets, i.e., to create that situation in which the fusion energy yield is equal to or greater than the incident driver energy. A summary of experimental programs (both achieved and under development) is provided on the next page. This status suggests that drivers capable of achieving breakeven should become available by the mid-1980s. Hence it is appropriate that we look beyond these breakeven experiments to identify possible applications of inertial confinement fusion.

We can identify three general classes of applications:

(i) power production

(ii) weapons applications

(iii) fundamental physics studies

Certainly the most significant application of ICF will be to the production of energy which can then be used for a variety of purposes such as the generation of electricity, the production of process heat or synthetic fuels, or propulsion. Unfortunately, it appears that this will also be the most difficult application to achieve. Nevertheless we will concern ourselves almost entirely with the energy production applications of ICF in this chapter.

On a shorter term basis, much (if not essentially all) of the funding for ICF research has been directed toward military applications. The environment created by the implosion and thermonuclear burn of a tiny ICF fuel pellet is similar in many respects to that of a thermonuclear weapon. Hence there has been considerable interest in using ICF targets to simulate on a microscopic scale weapons physics and effects.

Perhaps the most immediate application of ICF will be in basic physics studies. The imploded ICF pellet produces conditions of temperature and pressure which are quite unusual (at least on a terrestrial scale). ICF implosions can be used to study properties of

NEAR TERM EXPERIMENTAL DRIVERS FOR INERTIAL CONFINEMENT FUSION EXPERIMENTS

LABORATORY	DRIVER	POWER, TW	COMPLETION DATE	ANTICIPATED EXPERIMENTAL RESULTS
SANDIA-A	e-BEAM (PROTO-II)	7	1977	10^7 - 10^9 NEUTRONS
LLL	Nd: GLASS LASER (SHIVA)	10-40	1977	~10^{13} NEUTRONS
LASL	8-BEAM CO_2 LASER	10-20	1978	10^{10} - 10^{12} NEUTRONS
LLE-UR	Nd: GLASS LASER (OMEGA-10)	3-30	1979-80	USER FACILITY
SANDIA-A	e-BEAM (EBFA-I)	30 (1 MJ, 40 ns)	1980	10^{10} - 10^{13} NEUTRONS
KURCHATOV	e-BEAM (ANGARA V)	80 (5 MJ, 85 ns)	1982	G ~ 100
LLL	Nd: GLASS LASER (NOVA)	100-300	1983	10^{16} - 10^{19} NEUTRONS G ~ 1 - 100
LASL	CO_2 LASER (ANTARES)	100-200	1983	10^{16} - 10^{17} NEUTRONS G ~ 1 - 10
SANDIA-A	e-BEAM (EBFA-II)	60-80	1983-85	10^{15} - 10^{17} NEUTRONS G ~ 0.1 - 10

matter under extreme conditions, the interaction of intense radiation with matter, and aspects of low energy nuclear physics. Indeed, ICF presents us with a unique opportunity to study certain aspects of astrophysics such as steller interiors on a laboratory scale.

But, as we noted earlier, perhaps the most important application of ICF will be to the production of energy, whether directly through the conversion of fusion energy into electricity, or indirectly, by using the fusion energy or reaction products to produce synthetic chemical or nuclear fuels. We will examine each of the major applications of inertial confinement fusion to energy production in this chapter:

(i) electric power generation
(ii) fissile fuel production
(iii) process heat and synthetic fuel production
(iv) propulsion

11.1. INERTIAL CONFINEMENT FUSION REACTORS

Perhaps the central question concerns how we can capture the energy released in an ICF microexplosion and convert it into a useful form such as electrical power. As with all early generation fusion systems based on DT fuels, this energy will appear primarily as the kinetic energy of fast, 14 MeV neutrons. Therefore our goal is to burn the ICF fuel pellets using appropriate drivers (lasers or particle beams), confine the pellet microexplosion in a suitable blast chamber or reactor cavity, capture the kinetic energy of the fusion reaction products (primarily fast neutrons) as heat in a surrounding blanket, and then use this heat to perform useful work (e.g., driving a steam thermal cycle to produce electricity). Since most attention has been directed toward the study and design of laser driven ICF, we will confine our attention for the most part to a discussion of laser fusion power systems. A primitive schematic of such a system is given on the next page.

But, of course, a detailed design must address and answer a host of complex questions involving the fuel pellet design and fabrication,

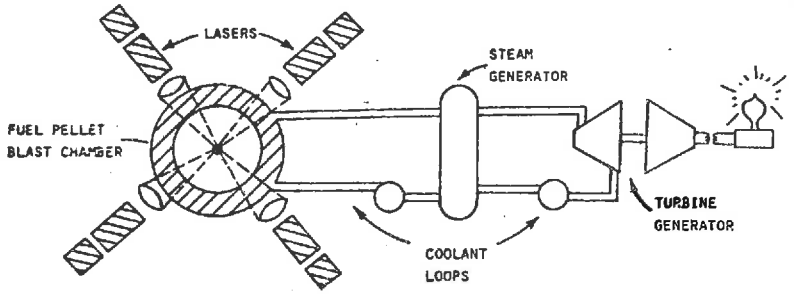

A simple schematic of a laser fusion reactor.

the driver, the blast chamber and blanket design, and the thermal cycle, Some of these questions are summarized below (as taken from the University of Wisconsin Solase design study):

1. Laser Pellet Studies: What range of pellet gain is required? What yield should one choose? What value of laser energy is appropriate? What are the spectra associated with various forms of pellet debris? What degree of target illumination uniformity is required and how many laser beams are needed? What do targets cost, how are they fabricated, and how are they delivered to a spot inside the chamber?

2. Laser Studies: What is the range of viable wavelengths? What is the laser energy? What is the laser pulse shape? How are beam lines designed and what are the problems with the last mirror? What repetition rate is required and how does this influence laser design, power supplies, and component lifetimes?

3. Optical Beam Train: How many last mirrors are there and how are they designed? How is the beam train integrated with the laser system? Do we combine beams? What is the shape and location of the last mirrors? How does the wavelength influence optics system design?

4. Cavity and Blanket Design: Is a protective liner for the first wall required? How does the liner or first wall respond to X-rays, ions, and reflected laser light? How does this response vary as the spectra and fraction of energy in each category change? How will we design the first wall? How will the blanket be designed to remove the heat and breed tritium?

5. Materials and Neutron Radiation Damage: Are there special rate effects in inertial confinement reactor systems? How does the damage vary with temperature? What structural material should one choose? What should one choose for the neutron wall loading? What are the dynamic stress problems and how should they be treated?

6. Tritium Systems and Power Cycle: What does the complete tritium cycle look like? How do we breed and recover tritium? How do we minimize leakage effects? How do we integrate the various forms of heat flow into an optimum power cycle? Is an intermediate loop needed?

It has become apparent that the successful application of inertial confinement fusion to the production of electrical power will require:

(i) a high-average-power driver with the required efficiency ($\gtrsim 1\%$) and reliability ($\gtrsim 70\%$),

(ii) a first wall able to withstand the effects of X-rays, debris, and neutrons from the ICF microexplosions,

(iii) structural materials that can withstand the cumulative damage effects of high-energy neutrons and cyclical stresses,

(iv) final beam focusing elements that can be protected or placed sufficiently far from microexplosions to prevent compromising the availability of the power plant.

2.1. Reactor Cavity (Blast Chamber)

The design of a chamber to contain the blast of the ICF micro-explosion would appear at first to be a challenge. A yield of 100 MJ of energy is equivalent to 48 pounts of TNT which might be expected to blow a well-constructed reactor cavity to bits with a repetition rate of typically 1 to 10 blasts per second. Fortunately, this is not the case because the force on the walls of the chamber due to such a blast is proportional to the square root of the debris mass. Thus for a pellet mass of 10^{-3} g, the fusion pellet debris produces less than 1/1000 the force of the debris from a chemical explosion.

However of far more significance is the radiation emitted by the microexplosion. This produces an extremely hostile environment which places severe demands on cavity structures.

2.1.1. Radiation

In general, four types of radiation will be emitted from a laser fusion pellet:

X-rays
charged particles (including alphas and pellet debris)
reflected laser light (photons)
fusion neutrons

Typical release fractions and energies for these products (except for reflected laser light) are shown in the table on the next page for both bare and structured pellets. For bare DT pellet cores, 80% of the yield is in the form of 14.1 MeV neutrons and 19% and 1% escapes as charged particles and X-ray energy. The charged particle energy is in two forms: nonthermal DT and DD reaction products that escape the pellet core before thermalizing and the blow-off plasma that results from the hydrodynamic disassembly of the pellet core. For a $\rho R \sim 3$ g/cm^2 and a 1 mg pellet core, 33% of the reaction product charged particles escape carrying 19% of the total charged particle energy. This corresponds to 668 keV deuterons, 1000 keV tritons, and 1330 keV alphas.

Although the 14.1 MeV neutrons initially constitute 80% of the fusion

Energy Release Mechanisms from Laser Fusion Pellets

Particle Type	Bare Pellet Frac. of Energy (%)	Bare Pellet Ave. Energy	Structured Pellet Frac. of Energy (%)	Structured Pellet Ave. Energy
X-rays	1	$\sim$ 4 keV	0.20-0.05	0.05-10 keV
γ-rays	0	--	0+	$\sim$1 MeV
Charged Particles	22	$\sim$50 keV	0.05-0.30	0.05-0.20 MeV
Neutrons	77	$\lesssim$14 MeV	0.70-0.65	$\sim$12 MeV

reaction energy, computations have shown that through collisions experienced while leaving the pellet, these neutrons will moderate and lose a substantial fraction of energy to the fuel. In fact, for a pellet of $\rho R \sim 5$, 60% of the 14.1 MeV neutrons will suffer a collision in the pellet, losing as much as .89 of their original energy in a single collision with a deuteron.

The X-ray spectrum for bare pellets is quite hard and nonthermal, but it can be approximated as an 8 keV black body spectrum. In structured pellets, more neutron energy is transferred to the particle debris via increased moderation. The energetic charged collision products will quickly radiate this additional energy away in the form of X-rays. Thus, up to 20% of the fusion energy can be released in the form of X-rays in complex pellets. In such pellets there is some production of MeV gammas due to the inelastic scattering of neutrons with pellet constituents.

Reflected laser light can also be significant in certain situations. For low yield targets, the reflected light energy may well exceed the energy of the reaction products. For short wavelength lasers with short pulses and high pellet reflectivity, the reflected laser light can cause excessive surface heating of the wall.

Although fast neutrons have large mean free paths in most wall materials (10 cm) and will pass easily to the reactor blanket, the other types of radiation will be totally absorbed by the first wall

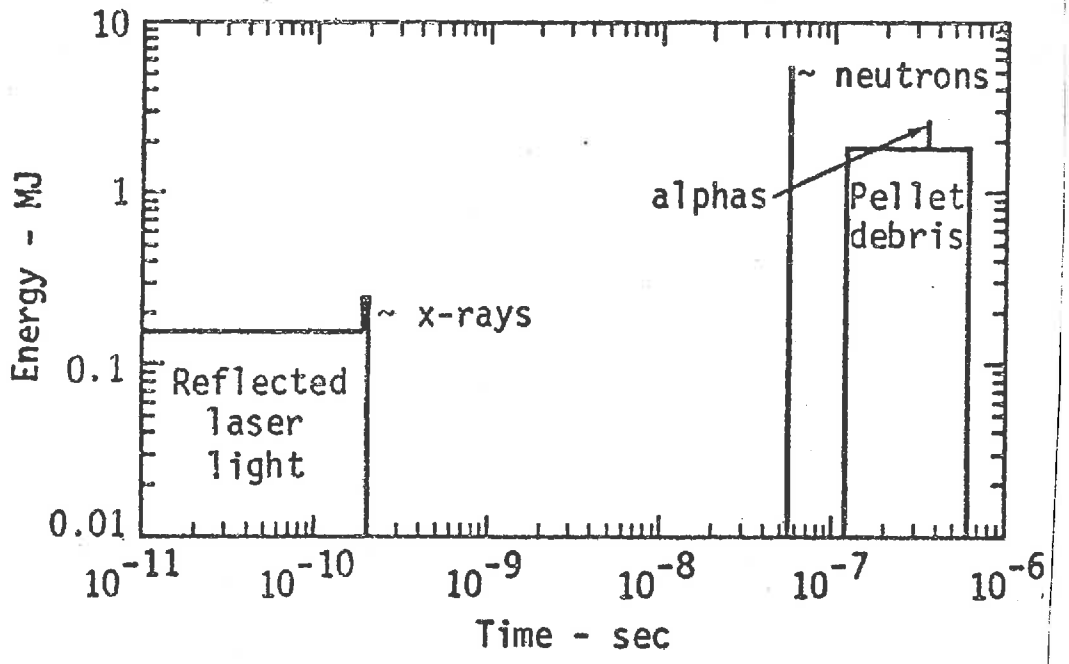
10
1
0.1
0.01
Energy - MJ
~ neutrons
alphas
Pellet debris
~ x-rays
Reflected laser light
10^{-11}
10^{-10}
10^{-9}
10^{-8}
10^{-7}
10^{-6}
Time - sec

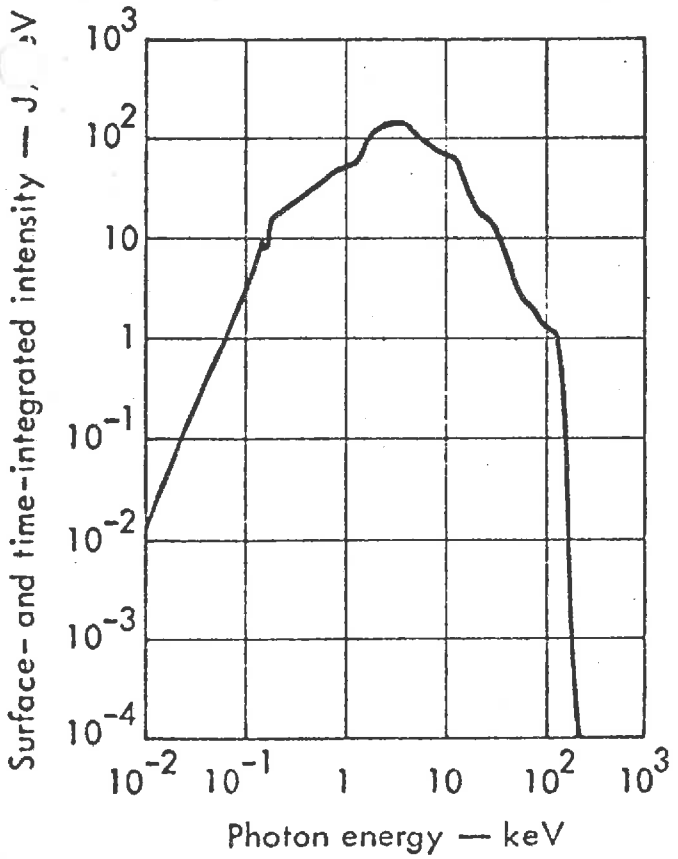
Surface- and time-integrated intensity — J, V
10^{3}
10^{2}
10
1
10^{-1}
10^{-2}
10^{-3}
10^{-4}
10^{-2}
10^{-1}
1
10
10^{2}
10^{3}
Photon energy — keV

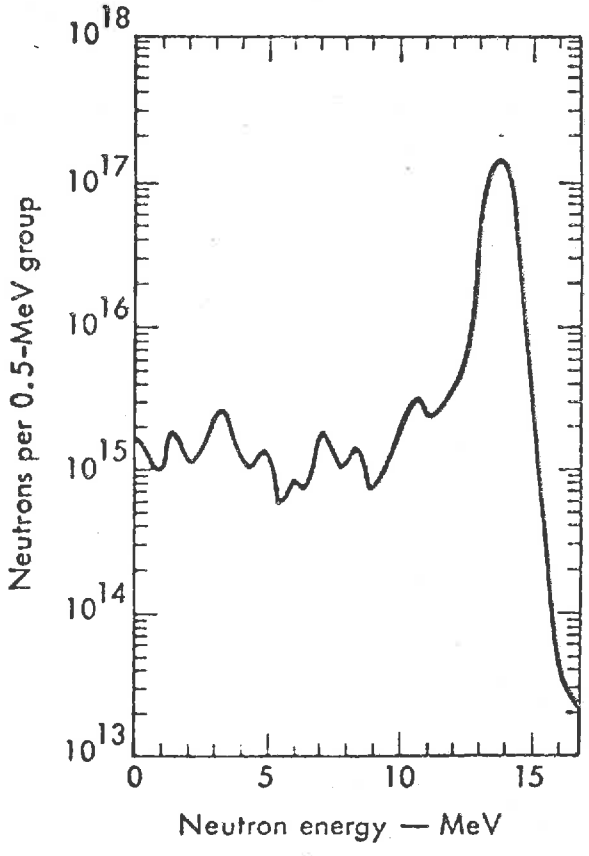
10^{18}
10^{17}
10^{16}
10^{15}
10^{14}
10^{13}
Neutrons per 0.5-MeV group
0
5
10
15
Neutron energy — MeV

11.1.2. Wall Load Mechanisms

The sudden deposition of the ICF burn product energy in the first wall will result in a stress due to thermal gradients in the material from nonuniform heating and conduction as well as inertial effects. One can distinguish among several different load mechanisms:

(i) pellet debris impact
(ii) blast wave reflection
(iii) evaporation recoil
(iv) blanket expansion
(v) thermal distortion

The principal source of energy deposition at the first wall will be due to the charged particles supplemented to a lesser extent by the reflected photons and X-rays.

The task of calculating the first wall response (i.e., the surface temperature rise and mechanical stress due to a pulse) is quite difficult. Because of the extreme conditions at the first wall surface, phase relations will play a large role. Furthermore, thermal relaxation time constants for first wall materials are often of the same order as the heat deposition times. More specifically, if τ_m is the mechanical relaxation and τ_T is the thermal relaxation time of the wall, we find that the deposition time spread of the neutrons, X-rays, and high energy alphas is

$$\tau < \tau_m << \tau_T$$

while that of the pellet debris is more typically much longer

$$\tau_m << \tau_T \sim \tau$$

The rapid energy deposition and short deposition range of charged particle debris and X-rays can cause severe damage to the surface of first wall materials. In fact, the Wisconsin group has concluded that an unprotected dry wall cavity design made from any reasonable material will not survive a microexplosion at economically reasonable wall loadings ($\gtrsim$ 1 MW/m^2) because of excessive thermal ablation and sputtering of the wall surface material. Both graphite and metallic first walls (Mo, Ta, SS) will experience large surface temperature excursions since the ions and soft X-rays deposition their energy in a

thin surface layer. Excessive ablation ($\sim$ 1 cm/year) will take place, Sputtering will also be significant ($\sim$ 1 cm/year) since damage occurs a elevated temperatures. (Sputtering yields increase sharply as the surface approaches the melting temperature.) By way of contrast, spallation of wall material does not appear to be a serious problem since there will be no thermoelastic stress wave from ion energy deposition (because of the spread in arrival time). Also, if the X-ray spectrum is harder than about a 1 keV black body, only small amplitude transient stresses will be generated.

Neutron damage to structural materials will also play an important role in cavity design. The primary neutron damage mechanisms are atomic displacements and gas production (primarily helium). Displacement damage is expressed as displacements per atom (dpa) and gas production is expressed as atom-parts-per-million (appm). The damage limits for 316 SS at an operating temperature of 500^{o} C are estimated to be 150 dpa and 500 appm helium. At a neutronic wall loading of 1 MW/m^2, an unprotected first wall of 316 SS would experience a displacement damage rate of $\sim$10 dpa per full power year, and the helium production rate would be $\sim$220 appm per full power year. A more detailed comparison of displacement rates and gas production for various reactor types is given in the table on the next page. We have also provided a table listing the various materials proposed for fusion reactors.

Anticipated Structural Materials Requirements for Fission and Fusion Reactors

Parameter	LMFBR	MCTR	LCTR
Temperature(°C)	300-600	300-500 (Steel) 500-1000 (refractory)	300-500 (Steel) 500-1000 (refractory)
Maximum Instantaneous Displacement Rate(dpa/s)	$\sim 10^{-6}$	$3\text{-}10 \cdot 10^{-7}$ (mirrors and tokamaks) $1\text{-}10 \cdot 10^{-5}$ (theta pinch)	$\sim$1-10
Average*Disp. Rate(dpa/yr)	$\sim$50	10-30	10-30
Helium Gas Prod.(appm/yr)	$\sim$10	200-600 (Steel) 25-150 (refractory)	200-500 (Steel) 25-150 (refractory)
Power Cycles Per Year	$\sim$10	$\sim$10 (mirror) 10^3-10^5 (tokamak) $3 \cdot 10^6$ (theta pinch)	10^7-10^9
Stress Level(MPa)	60-120	60-120	100-200
		Dedired Lifetime Conditions**	
Displacements Per Atom	100-150	300-1000	300-1000
Helium Product(appm)	20-30	6,000-20,000	6,000-20,000
$\Delta V/V_0$(%)	<5	<10	<10
Creep	<1	< 1	< 1

*PF = 70%
**30 year lifetime

Fusion Reactor Structural Materials

Aluminum (SAP):

Advantages:

- very low induced radioactivity

Disadvantages:

- very low operating temperature [<300°C] required to preserve strength and compatibility with lithium
- high gas production
- low modulus of elasticity

Titanium:

Advantages:

- very high strength/weight ratio in 400-500°C operating temperature range
- low swelling and creep
- lower long term radioactivity than steel
- large heat capacity and low thermal expansion
- very abundant

Disadvantages:

- temperature limited [<500°C]
- low thermal conductivity
- low modulus of elasticity

Stainless Steel:

Advantages:

- well known and abundant
- no drastically unacceptable properties
- long lifetime to high fluences at low temperatures

Disadvantages:

- low temperature operation [<500°C] required to preserve strength and lithium compatibility

Stainless Steel:

Disadvantages (Cont.):

- prolonged afterheat and significant radioactivity (possibly reduced if isotopic tailoring is utilized)
- large thermal expansion

Vanadium:

Advantages:

- high temperature operation (800°C)
- low induced radioactivity

Disadvantages:

- poor fabricability
- high short term afterheat
- possibly poor strength unless alloyed (i.e., V-20 Ti)
- possibly poor lithium compatibility

Molybdenum:

Advantages:

- high temperature operation (1000°C) and good strength
- low activity during operation
- low gas production
- good availability
- low hydrogen permeability
- large (n,2n) cross section

Disadvantages:

- poor fabricability
- low ductility
- very high long term radioactivity (possibly reduced if isotropic tailoring is utilized)

Niobium:

Advantages:

- high temperature operation (~1000°C) and good strength
- low gas production
- high ductility
- low afterheat

Disadvantages:

- highest long term radioactivity
- possibly limited supply

Graphite:

Advantages:

- very high temperature operation ($\gtrsim$2000°C)
- low induced radioactivity and afterheat
- well known and available
- possibly self annealing to radiation damage leading to 1-30 year lifetime

Disadvantages:

- poor strength and fabricability
- not compatible with lithium
- high helium production
- swelling and creep at moderate fluences ($\sim 4 \cdot 10^{22}$ n/cm^2)

11.1.3. Reactor Cavity Designs

X-ray and charged particle debris damage to first wall materials is a problem primarily associated with inertial confinement fusion systems. A variety of reactor cavity designs have been proposed to deal with this problem:

(i) dry wall, sacrificial liners
(ii) magnetically protected walls
(iii) wetted wall or fluid curtain
(iv) gas filled cavities

These approaches differ primarily in the way in which the inner surface of the first wall interacts with the X-rays and microexplosion debris. (These approaches are illustrated schematically on the next page.) In the dry wall approach a sacrificial metal or ceramic liner is placed between the fusion chamber and the blanket. This wall would then be replaced periodically. The magnetic protection concept uses a solenoid generated magnetic field to divert the pellet debris away from the sides of a cylindrical blanket and into conical collectors at top and bottom. The wetted wall approach feature a thin layer of liquid metal that covers the metal wall and protects it from the blistering and structural ablation that would otherwise occur from the microexplosion debris. The fluid curtain approach shields the first wall from X-rays netrons, and debris with a thick falling region of liquid metal (lithium) or solid pellets. The gas-filled cavity design fills the blast chamber with a buffer gas such as neon at less than 1 toor pressure, sufficient to protect the first wall from the ions and soft X-rays produced by the microexplosion.

In this section we will discuss each of these approaches.

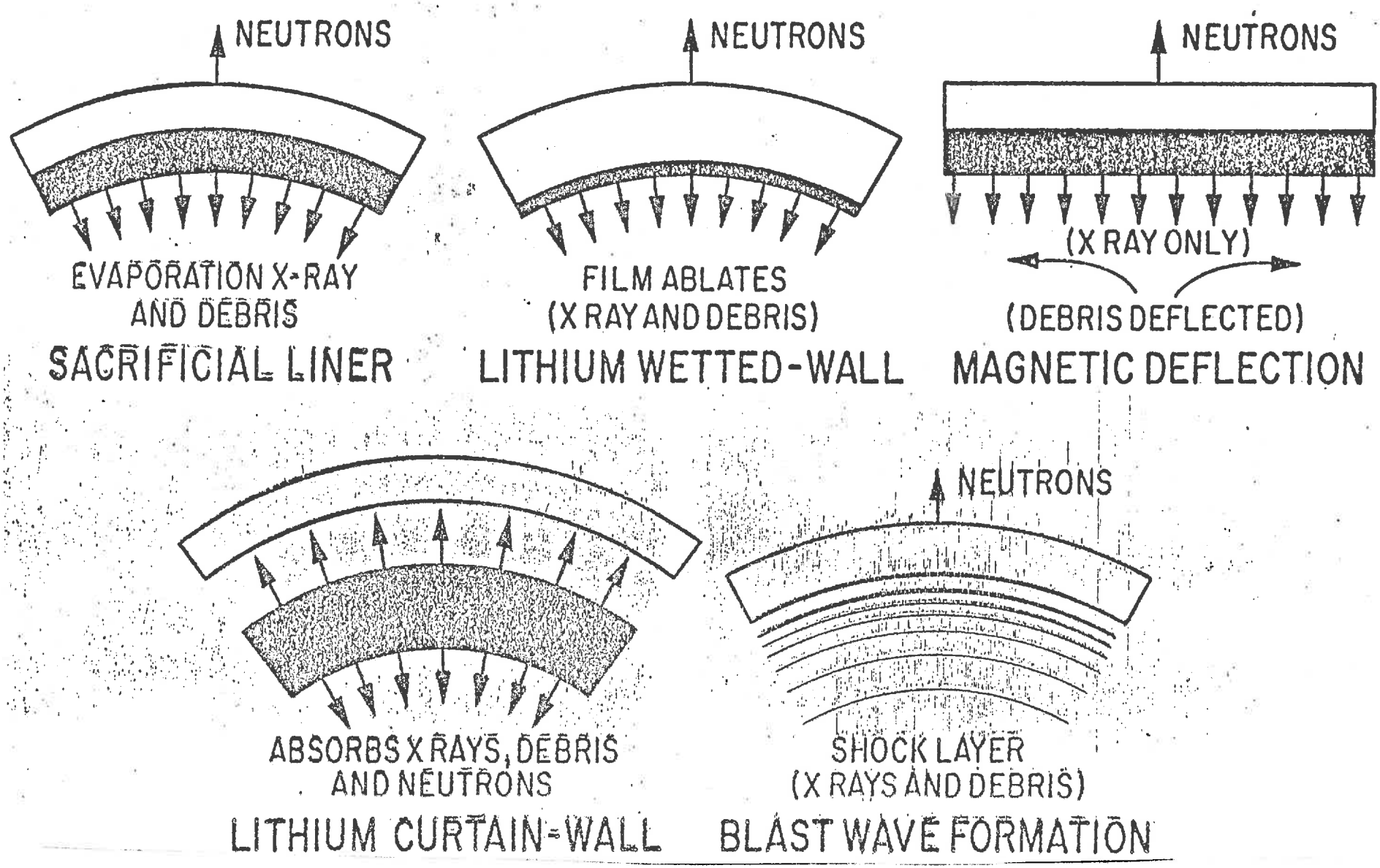
NEUTRONS
EVAPORATION X-RAY AND DEBRIS
SACRIFICIAL LINER
NEUTRONS
FILM ABLATES (X RAY AND DEBRIS)
LITHIUM WETTED-WALL
NEUTRONS
(X RAY ONLY)
(DEBRIS DEFLECTED)
MAGNETIC DEFLECTION
ABSORBS X RAYS, DEBRIS AND NEUTRONS
LITHIUM CURTAIN-WALL
NEUTRONS
SHOCK LAYER (X RAYS AND DEBRIS)
BLAST WAVE FORMATION

Dry Wall/Sacrificial Linear Designs

We have noted that an unprotected or dry wall would experience such extensive surface damage from fusion reaction debris that it would not constitute an acceptable design by itself. However it is proposed to place a sacrificial liner fabricated out of a material such as graphite which could protect the first wall. The sacrificial liner would experience thermal ablation and sputtering damage until it is reduced to a minimum design thickness. At this point it would be replaced. A graphite protected dry wall design is shown on the right (where the first wall is fabricated out of stainless steel and contains channels for coolant flow). Other dry wall concepts which have been investigated have specified unprotected niobium walls.

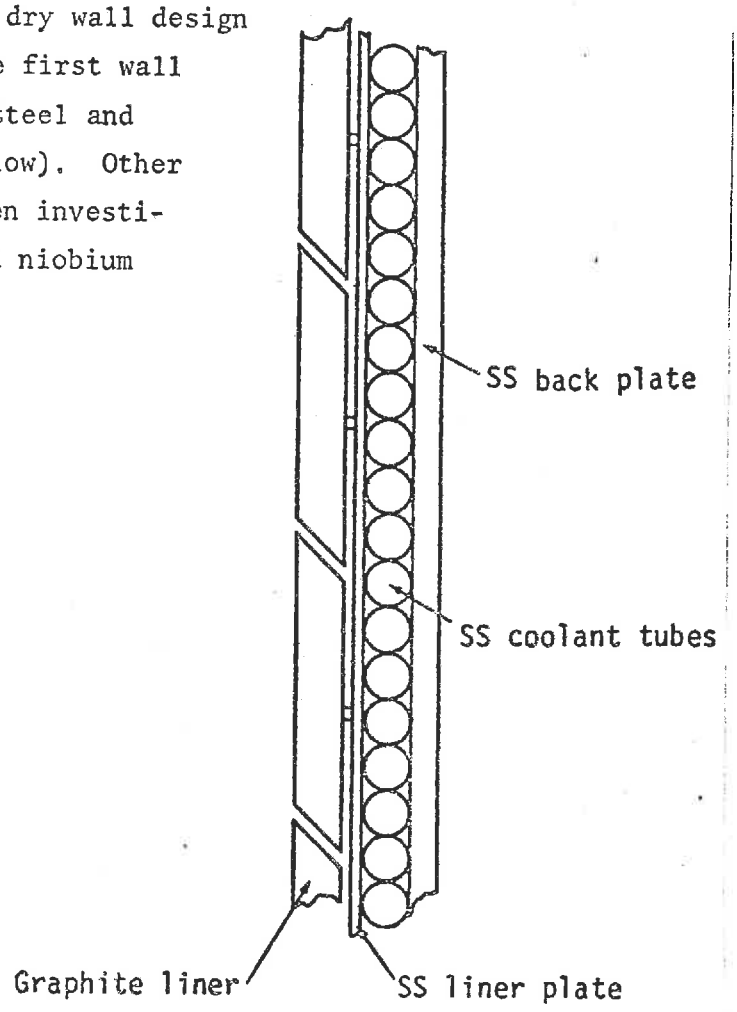

Magnetically Protected Wall Designs

This design utilizes an axial magnetic field produced by exterior coils to divert the charged particle debris out into conical energy sinks which are located on the ends of a cylindrical reactor cavity (see the Figure below). If this system works ideally, the graphite protected

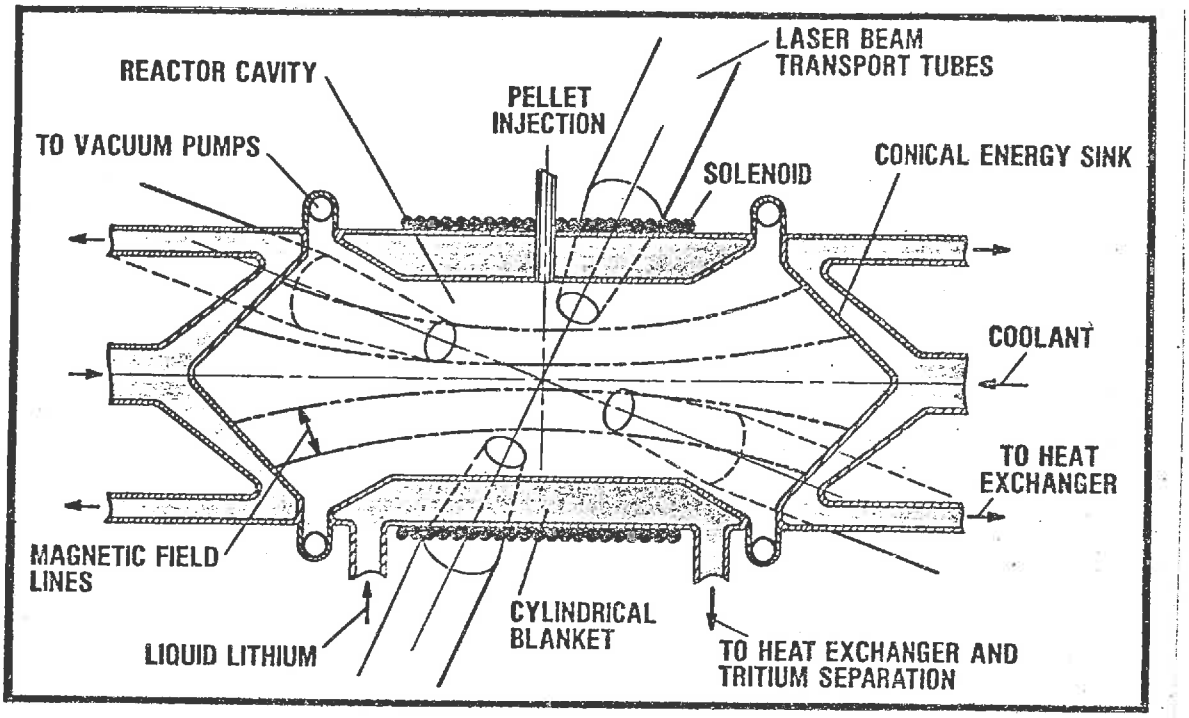

cylindrical first wall would see only the $\sim$ 1% X-ray yield plus the $\sim$ 0.1% reflected laser light flux. The energy sinks would be fabricated from refractory materials such as graphite and would be replaced periodically when radiation and material damage levels exceed operating tolerances. In principle, at least, the magnetically shielded first wall could be combined with direct conversion of the pellet debris kinetic energy into electricity (although this would only be attractive with advanced fuel schemes utilizing DD or p-^{11}B).

This approach suffers from several disadvantages: Although the alpha particles act as single particles and are quickly diverted to the sink cones, the slower debris plasma acts collectively in doing work against the magnetic field. Thus as the debris expands out the

ends of the cylinder it first excludes and then compresses the magnetic field between the plasma and the cavity wall. This can give rise to plasma instabilities which would cause particles to cross field lines and impact against the wall. Furthermore, magnetically shielded first walls present a disadvantage if liquid metal coolants are to be used because of the pumping power required to move the coolant across field lines. The blanket modules and the first wall would be more inaccessible than in the dry wall concepts.

Wetted Wall Designs

In wetted-wall designs (see next page), the cavity wall is formed by a porous refractory metal through which coolant lithium flows to form a protective coating for the first wall surface. This coating for the first wall will serve to absorb charged particles and reflected laser light while attenuating X-rays. Typically, the coating will be about 1 to 2 mm thick of which about 0.1 mm will be evaporated and ablated following each pulse. Because of this ablation, such cavities would be limited to about one repetition per second, the time delay associated with replenishing the protective layer and pumping the cavity back down to maximum pressures of 10^{17} atoms/cm^3. The major disadvantages of this design are the large vacuum pumping loads required due to the high vapor pressure of the lithium flow and the complex first-wall designs which must allow the coolant to migrate from reservoirs to cover the first wall liners.

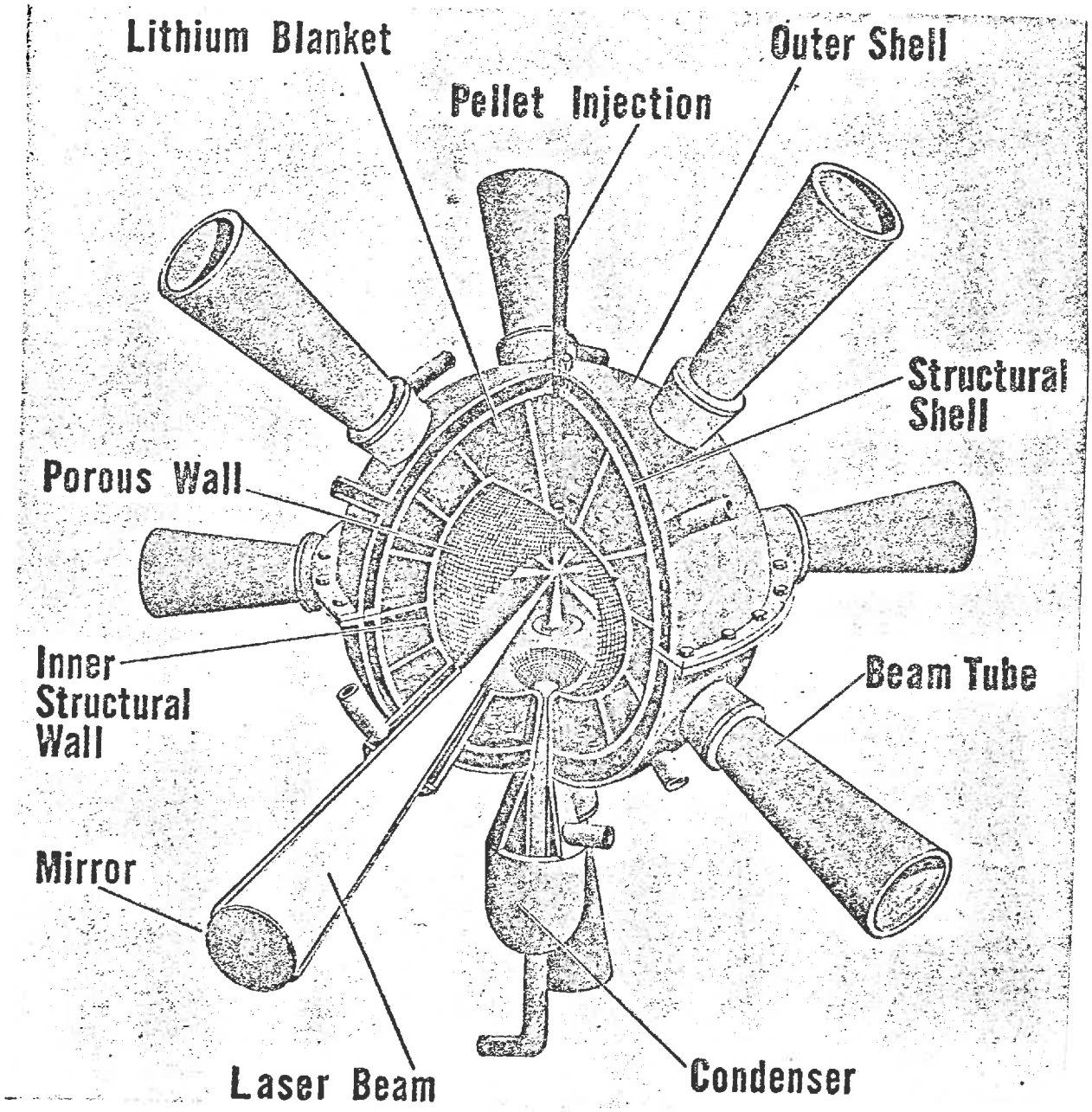
Lithium Blanket
Outer Shell
Pellet Injection
Structural Shell
Porous Wall
Inner Structural Wall
Beam Tube
Mirror
Laser Beam
Condenser

Lithium Curtain

This concept features a thick, continuously recyclable first wall of liquid lithium or small lithium pellets that protects the first structural wall from direct exposure to microexplosions. Each shot disassembles the "waterfall" of lithium, which is reestablished between each shot. The lithium is continuously pumped to the top of the vacuum chamber through a reservoir region separating the first structural wall from the pressure vessel. A small fraction of the lithium flow circulates as the primary coolant to the heat exchanger. The return flow from the heat exchangers is injected through a vortex generator to protect the top of the chamber.

The principal purpose of the fall is to reduce neutron damage in blanket structural materials, allowing them to survive for the useful life of the plant. Besides moderating neutrons, the fall also absorbs photons (X-rays and reflected laser light) and pellet debris (alpha particles, unburned fuel, and other pellet material). Because the fall is separated from the chamber wall, any shock wave produced in the fall will not be directly transmitted to the structural wall.

The falling lithium region contains enough lithium to significantly reduce neutron damage to the reactor structural materials from atomic displacements and gas production. Such a system could be operated at a wall loading of 4 MW/m^2 for the 30 year life of the plant without exceeding radiation damage limits. The liquid lithium waterfall concept also appears to yield excellent energy-conversion, energy-removal, and tritium breeding characteristics. Nearly 99% of the total energy is deposited directly in the primary lithium coolant. This essentially eliminates cyclical thermal stresses in the structural walls.

The principal disadvantages appear to be the mechanical complexity of the design and the limitations of allowable partial atmospheres in the cavity to allow laser beam propagation. In addition, pumping power to maintain the waterfall will add significantly to the recirculating power in the plant.

LIQUID LITHIUM "WATERFALL" CONCEPT

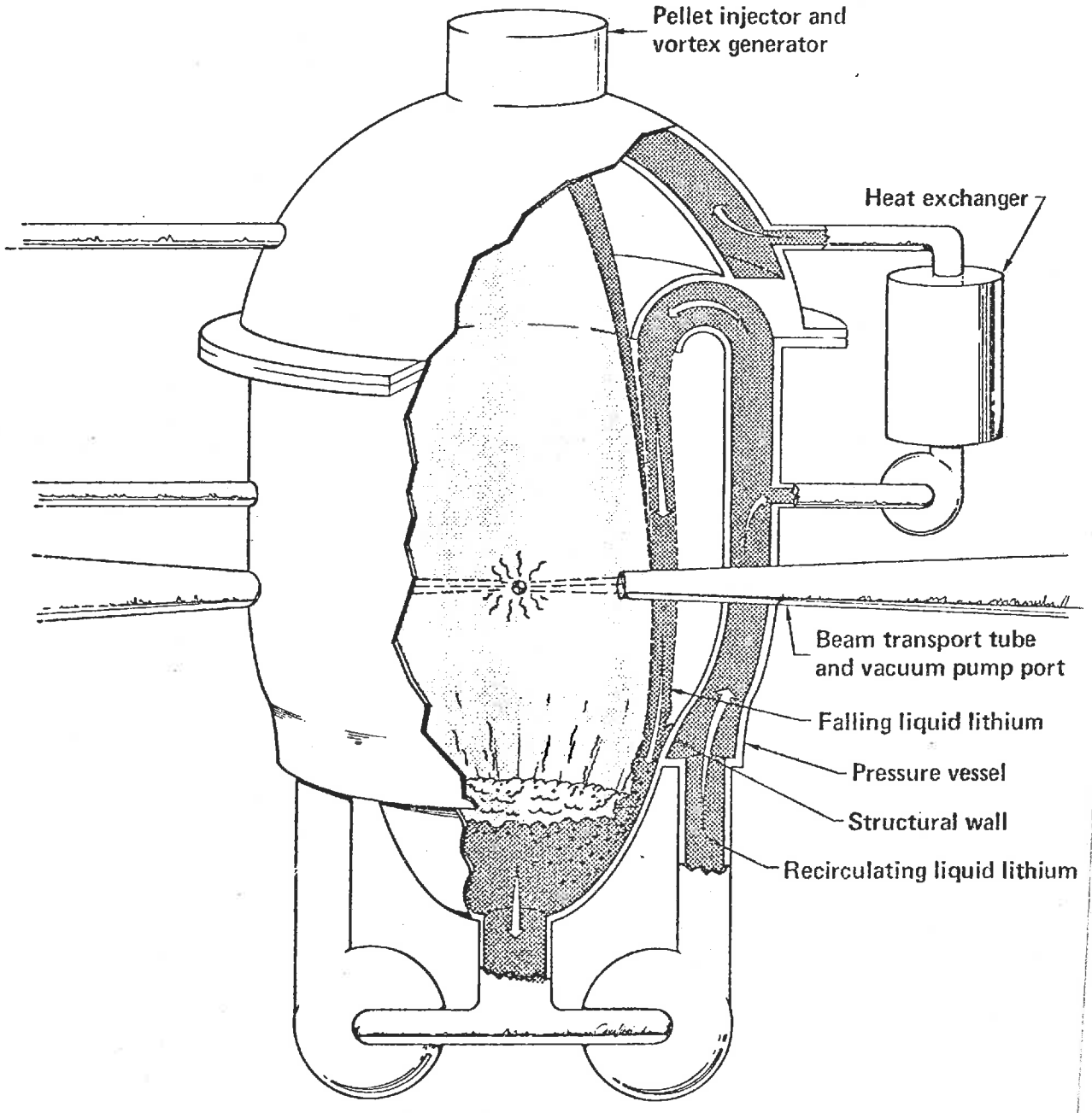

Gas-Filled Cavity Designs

In these designs, neon or xenon is included in the cavity at pressures of 0.5 to 1 torr to act as a buffer gas to prevent the charged particle debris from striking the first wall. The energy deposited in the gas is radiated to the front wall over a relatively long time period ($\sim$1 ms) so that surface heating and thermal ablation of the wall become insignificant. The maximum overpressure generated at the first wall is only $\sim$ 100 torr.

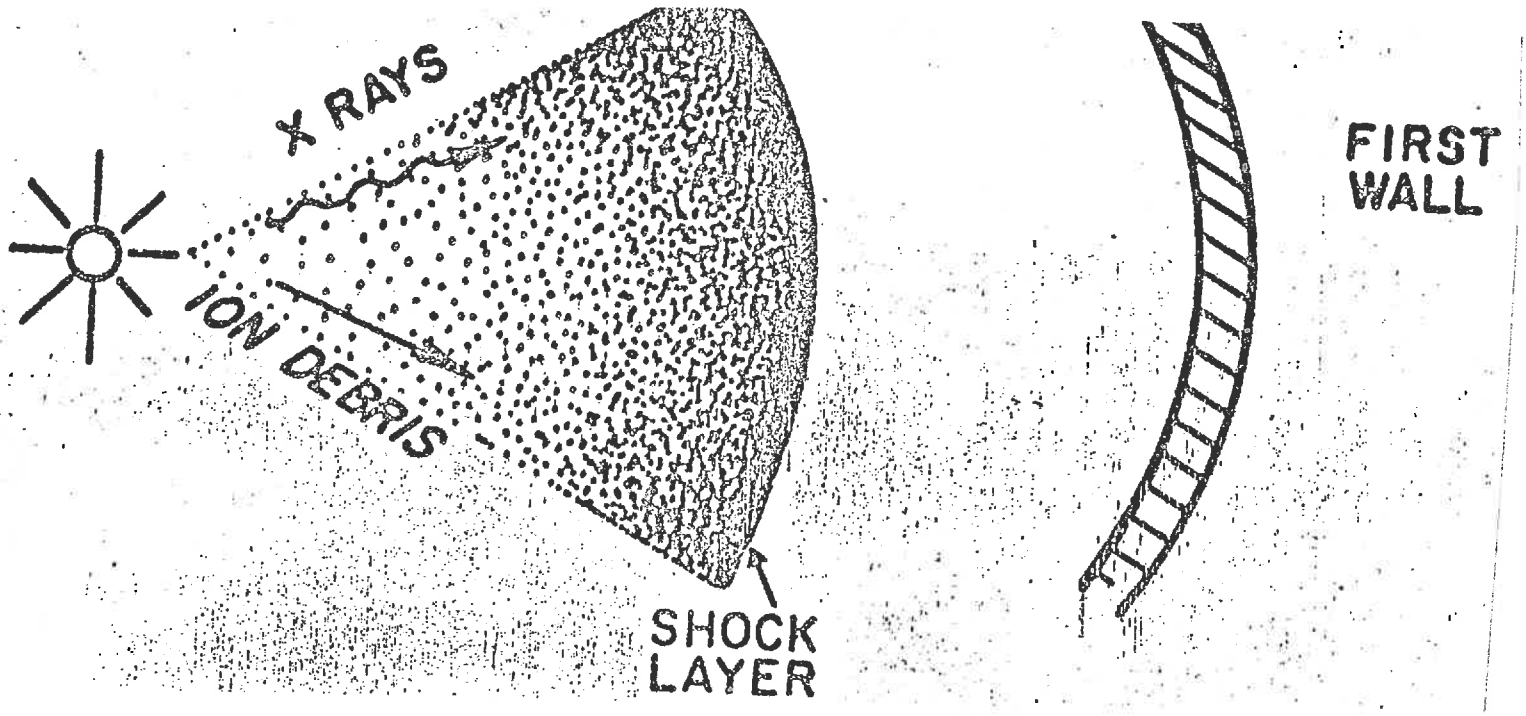

The primary concern in this design is to keep the gas density sufficiently low to avoid laser beam defocusing and attenuation. An example of this design concept is the Solase laser fusion reactor system illustrated on the next page.

THE SOLASE LASER FUSION REACTOR SYSTEM

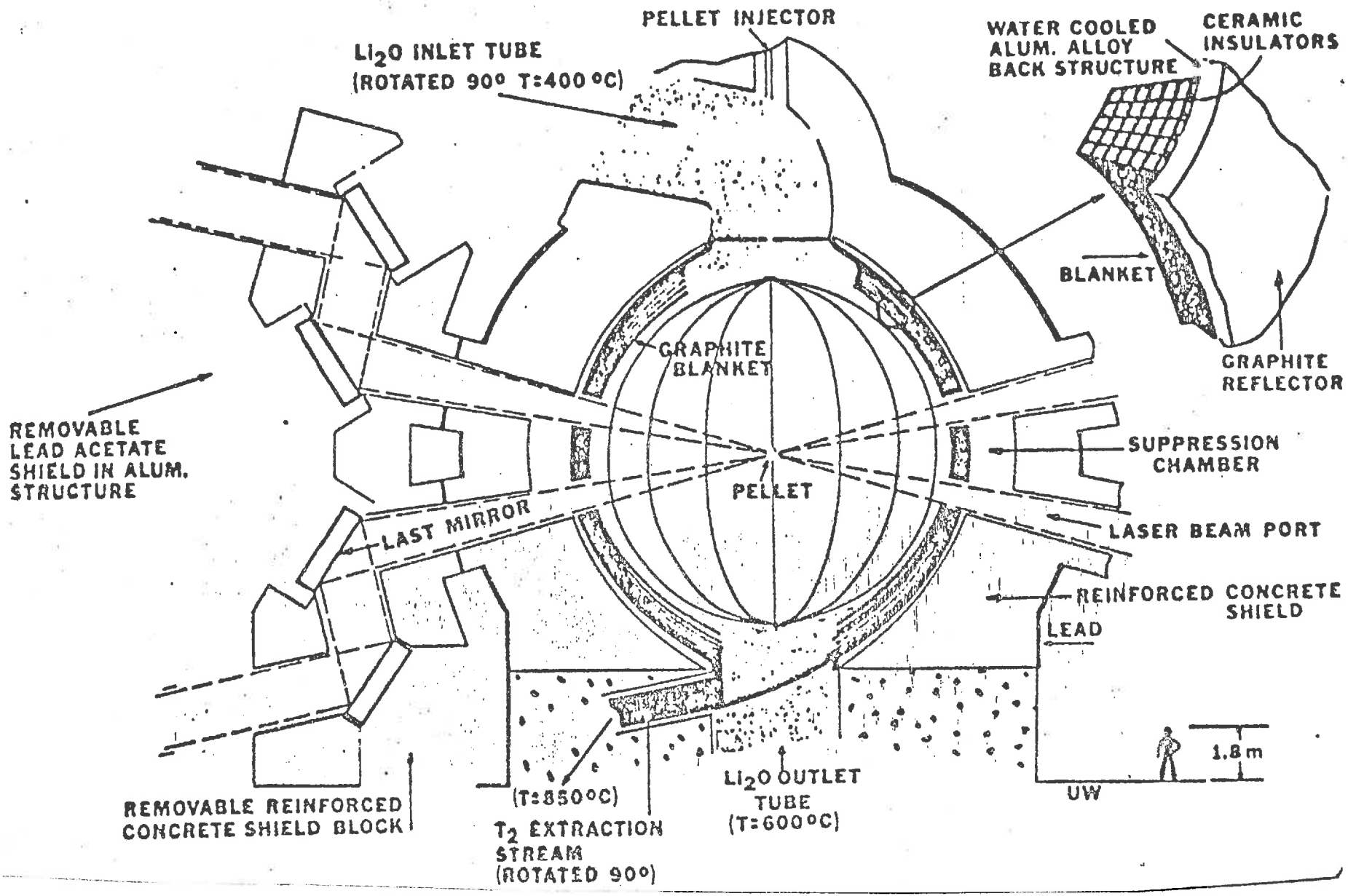

We have compared each of these reactor cavity designs below in the table:

	major design considerations				
	material loss		impulse		
	X-ray	Debris	Pellet output	Cavity phenomena	Rep-rate limit
Dry wall	X	X	X		
Sacrificial liner	X	X	X		
Magnetic shield	X		X		
Wetted wall				X	X
Lithium curtain				X	X
Gas fill				X	X

The present status of each design concept is given on the next page.

CURRENT STATUS

BARE METAL

- very large cavity diameters (10's meters)
- economically infeasible

SACRIFICIAL LINER

- frequent liner replacement
- probably not economic

MAGNETIC DEFLECTION

- periodic liner replacement (only from x-ray evaporation)
- further analysis required

GAS FILL

- protection from x rays and ion debris
- restoration of initial conditions uncertain
- further analysis required

WETTED WALL

- protection from x rays and ion debris
- significant wall impulse
- repetition rate limited to ~ 1 pps

THICK LITHIUM WALL

- protection from x rays and ion debris
- mitigation of structural radiation damage
- significant wall impulse
- restoration of initial conditions uncertain
- further analysis required

11.1.4. Blankets

The blanket system of the reactor must perform several functions;

(i) convert the fusion energy into thermal energy

(ii) provide for efficient removal of the thermal energy

(iii) breed enough tritium to replace that which was burned in the fusion reaction

(iv) maintain the required vacuum in the fusion chamber,

Perhaps the primary constrainton the design of most fusion reactor blankets is the requirement that tritium must be continually bred and processed from lithium. Since natural lithium is isotopically 7.4% ^{6}Li and 92.6% ^{7}Li, one can make use of two reactions:

$$^{7}Li + n\ (\ 2.5\ MeV) \longrightarrow {}^{4}He + {}^{3}T + n(slow)$$

$$^{6}Li + n(slow) \longrightarrow {}^{4}He + {}^{3}T + 4{,}8\ MeV$$

Note that the ^{7}Li reaction is a threshold reaction which is neutron conserving, and that the ^{6}Li reaction has a large thermal cross section and is exothermic. Thus, in a very ideal case, the best we can hope to do with a single 14.1 MeV fusion neutron and a pure lithium system is to cause a reaction first with ^{7}Li and have the resultant neutron absorbed in ^{6}Li. The result would be one surplus tritium atom (i.e., a breeding ratio of 2) and about 16.4 MeV (14,1 - 2,5 + 4,8).

In most designs, liquid lithium is used both as a breeding medium and as the blanket coolant. However other tritium breeding compounds which may prove compatible with fusion reactor designs are molten salts (Li_2Be_4 or flibe and LiF), ceramic compounds (Li_2O and Li_2C_2) and aluminum compounts (LiAl, LiAl O_2).

Liquid-Lithium Cooled Stainless Steel Manifold

The conventional approach requiring the least in sophisticated technology would be a cylindrical annulus of stainless steel into which vertical coolant channels have been drilled to form a manifold. The stainless steel manifold concept is comparible with either a dry or wetted first-wall approach. In the dry-wall approach, one could use

LIQUID LITHIUM COOLED STAINLESS STEEL MANIFOLD CONCEPT

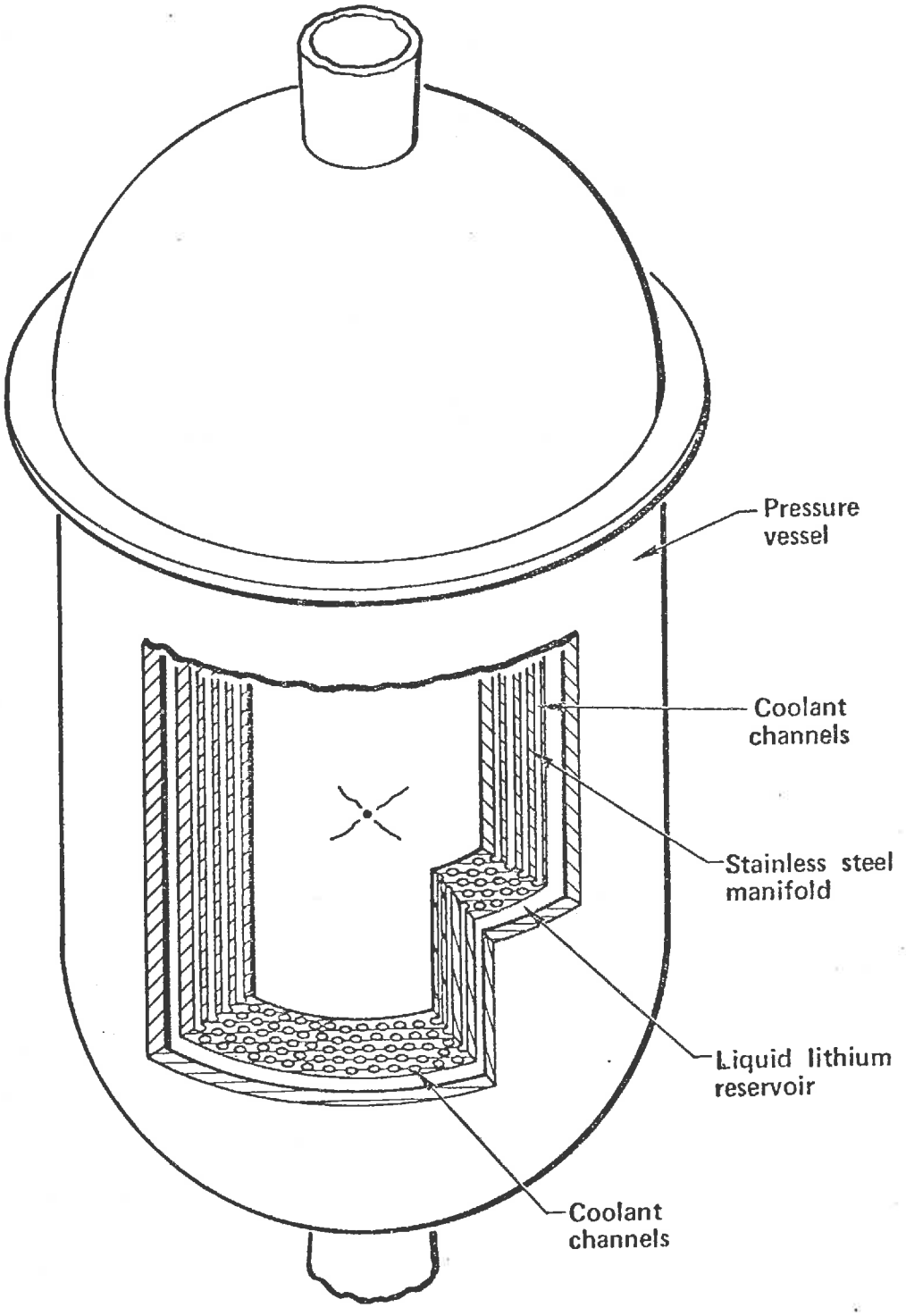

a graphite liner that is supported by stainless steel and cooled with liquid lithium. The graphiteliner might be designed for an operational lifetime of one year. In the wet-wall approach one could maintain a thin (3 mm) film of liquid lithium on the inner surface of the manifold. Tritium breeding considerations limit the thickness of a structural wall of solid stainless steel to less than 10 cm. The stainless steel manifold would operate at a neutronic first wall loading of about 1 to 2 MW/m^2, and this would require a relatively large chamber radius (10 to 15 m for a 4000 MWt system). For use with stainless steel, lithium temperatures must be limited to about 500^{o} C to avoid excessive corrosion.

Gas Cooled Graphite Manifold

A graphite manifold would be similar to the stainless steel manifold except that vertical coolant channels are drilled into an array of graphite blocks that make up the fusion chamber (see next page). One could adapt high temperature gas cooled fission reactor (HTGR) technology to design a vacuum vessel of reinforced, prestressed concrete. High pressure helium gas would then be pumped through the coolant channels, some or all of which are filled with pellets of a lithium ceramic. Tritium is removed from these channels by the gas coolant as it diffuses out of the lithium compound in which it is bred. The graphite manifold design is a reactor concept that exhibits low activation and low tritium inventories.

GAS COOLED GRAPHITE MANIFOLD CONCEPT

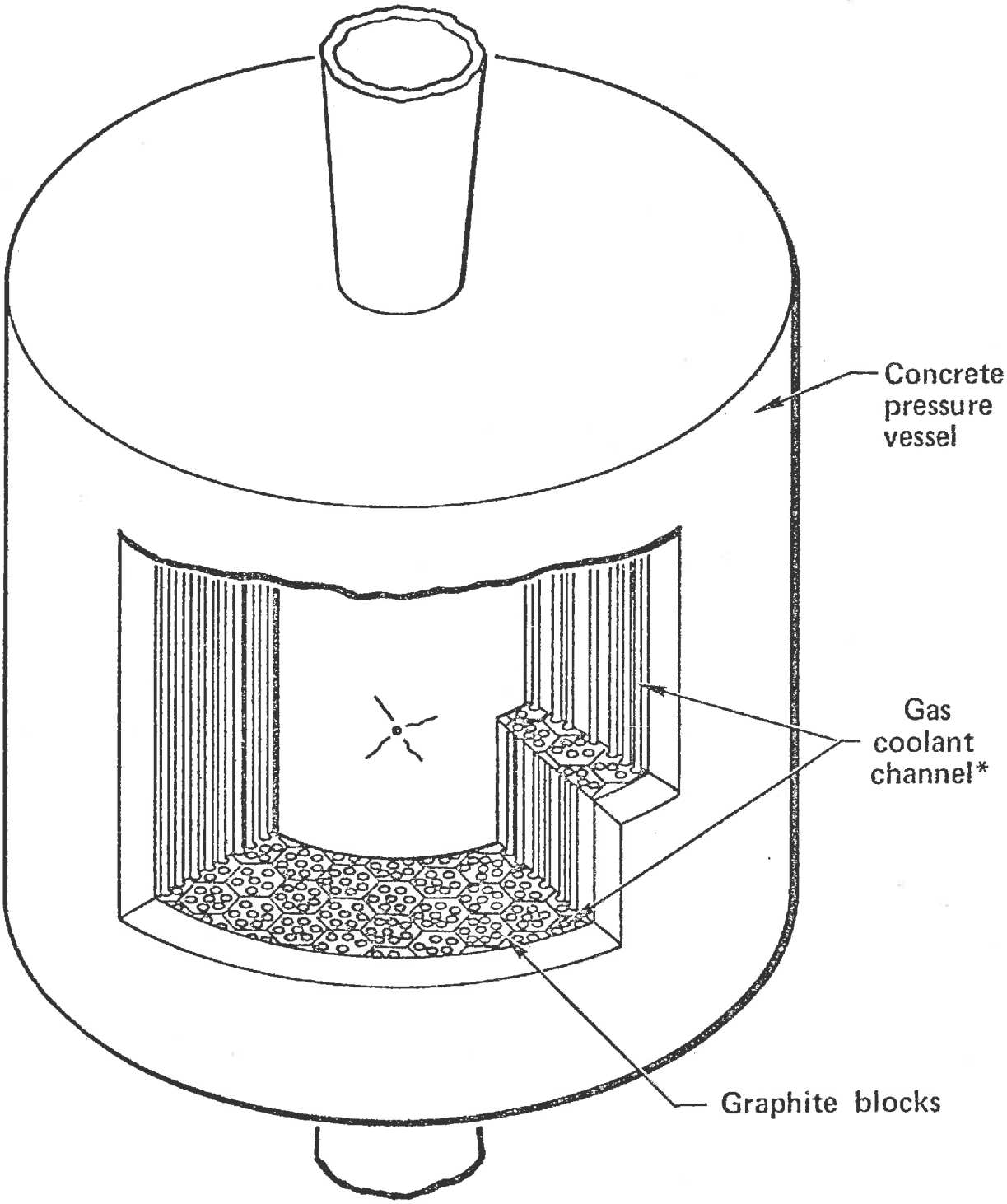

*Coolant channels filled with ceramic lithium

Fluidized Wall Concepts

Fluidized wall concepts provide protection to the first metallic wall from high energy neutrons in addition to the X-rays and debris. These concepts appear to be less dependent on materials development because radiation damage is significantly reduced. Designs using both a liquid lithium "waterfall" and a ceramic-lithium pellet fall have been proposed and studied (see figures on next two pages).

The principal feature of the ceramic-lithium pellet waterfall is a thick layer of falling solid ceramic-lithium pellets that shields the first structural wall from the microexplosion. The pellets are continuously recirculated to the top of the vacuum chamber through a reservoir region between the first wall and the pressure vessel. The pellets are either transported through heat exchangers or cooled by the flow of high-pressure helium gas in the reservoir region.

The liquid lithium waterfall concept features a thick continuous fall of liquid lithium that protects the first structural wall, allowing it to last for the useful life of the plant. By keeping the fall of the chamber wall shock waves generated in the fall are not directly transmitted to the structural wall. The majority of the fusion energy is thus deposited in the liquid lithium, which serves as the primary coolant, fertile material for tritium breeding, and first wall. Hence the system does not have to rely on conduction of heat through structural materials to remove thermal energy.

As one might expect, fluidized wall concepts have excellent tritium breeding characteristics. With no structural material between the fusion neutrons and the lithium fall, the design takes full advantage of the high-energy ^{7}Li (n,n'T) reaction.

FALLING BALLS CONCEPT

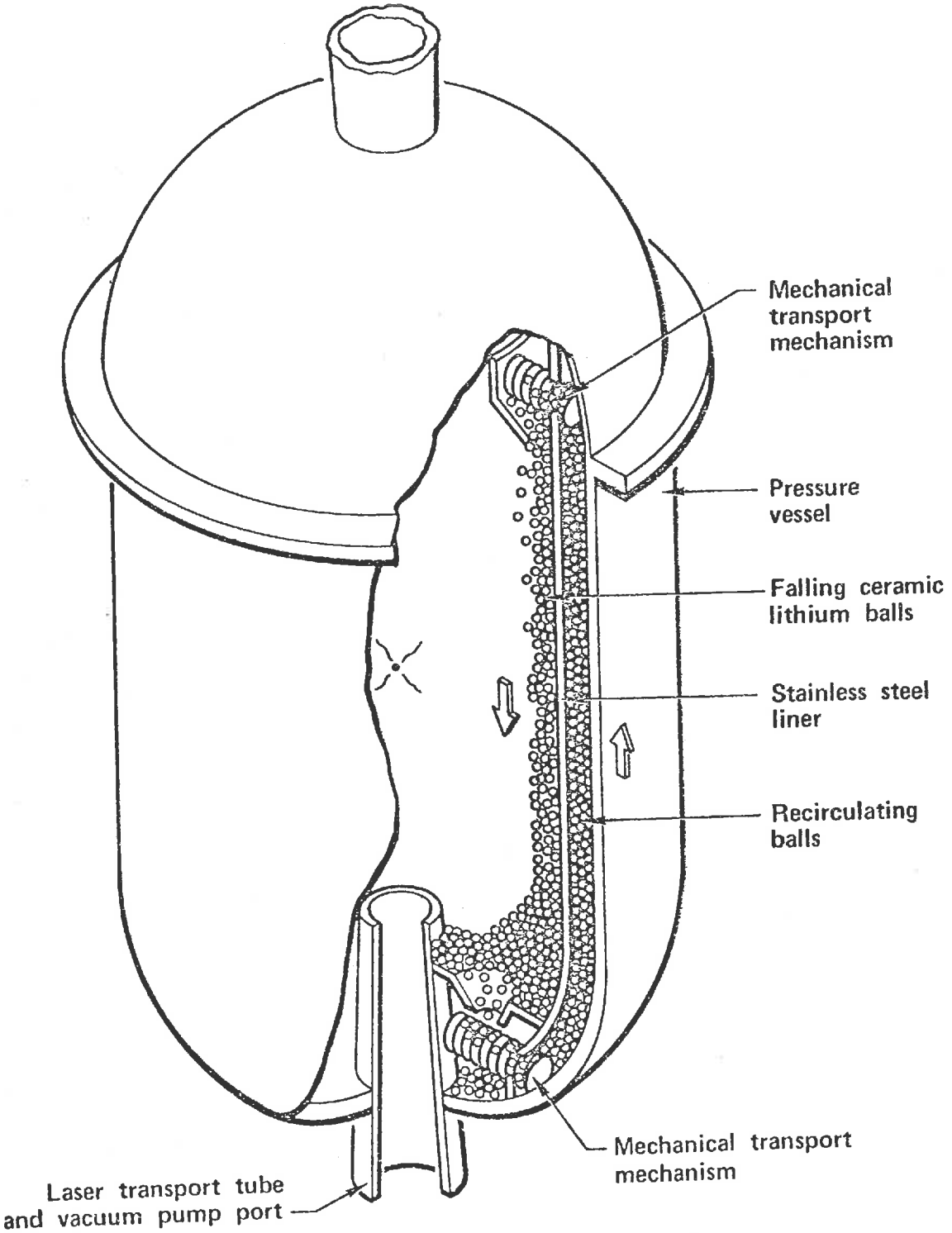

LIQUID LITHIUM "WATERFALL" CONCEPT

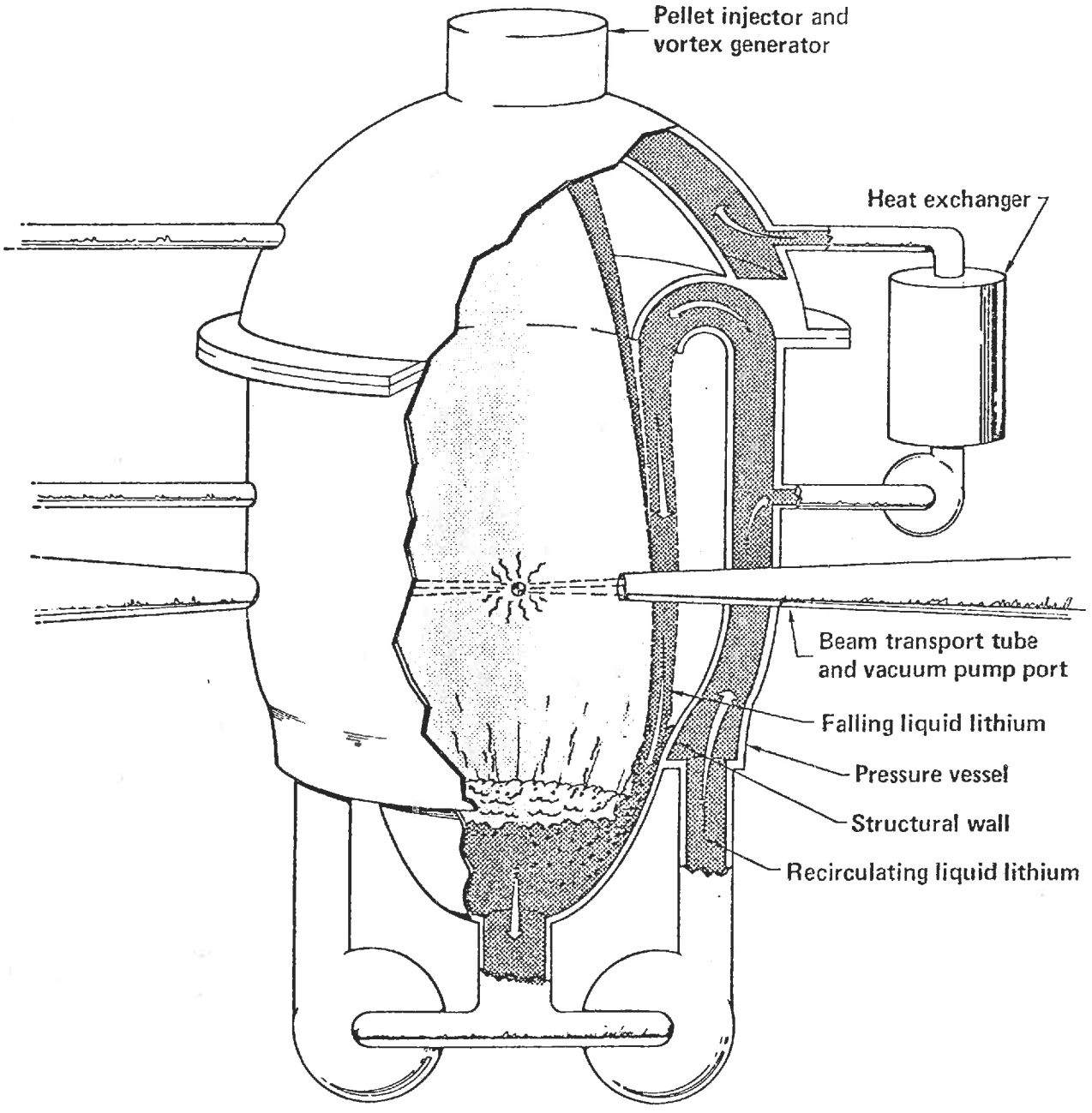

Gas-Filled Cavity Designs

The prototype gas filled cavity design is the Solase system studied at Wisconsin. The Solase blanket (see next page) is constructed primarily with graphite and either nuclear grade graphite or chopped-fiber type graphite composite. Lithium oxide particles, 100 to 200 μm in diameter, flow under gravity through the blanket and serve the dual purpose of tritium breeding and heat transfer. This design eliminates the need for metallic first walls and liners since the buffer gas attentuates the radiation to a level compatible with first wall thermal and mechanical tolerances. The estimated lifetime of the blanket structure at 5 MW/m^2 wall loading is approximately 1 year (corresponding to $\sim$ 30 dpa). Hence the design utilizes a blanket structure which can be periodically replaced in segments.

11.1.5. Target Injection

Injection of laser fusion targets into a power reactor chamber will be quite different from the static mounting procedures used in experimental research today. Electrostatic and pneumatic injection are the two injection modes of most interest. Electrostatic methods appear to be more susceptible to damage in the intense radiation and temperature environment of the reactor chamber. Hence most interest rests with pneumatic injection.

For example, one could inject the pellet with a pneumatically operated launching device which injects the pellet along a vertical trajectory. In the Wisconsin design, the pellet traverses a distance of about 12 m with a velocity of 480 m/s. The state of the art of pneumatic injection is quite well developed, with present high-precision air guns being able to deliver projectiles into an area of radius less than 0.7 mm at a distance of 12m with a generally horizontal trajectory.

SCHEMATIC OF GRAPHITE BLANKET SEGMENT FOR SOLASE

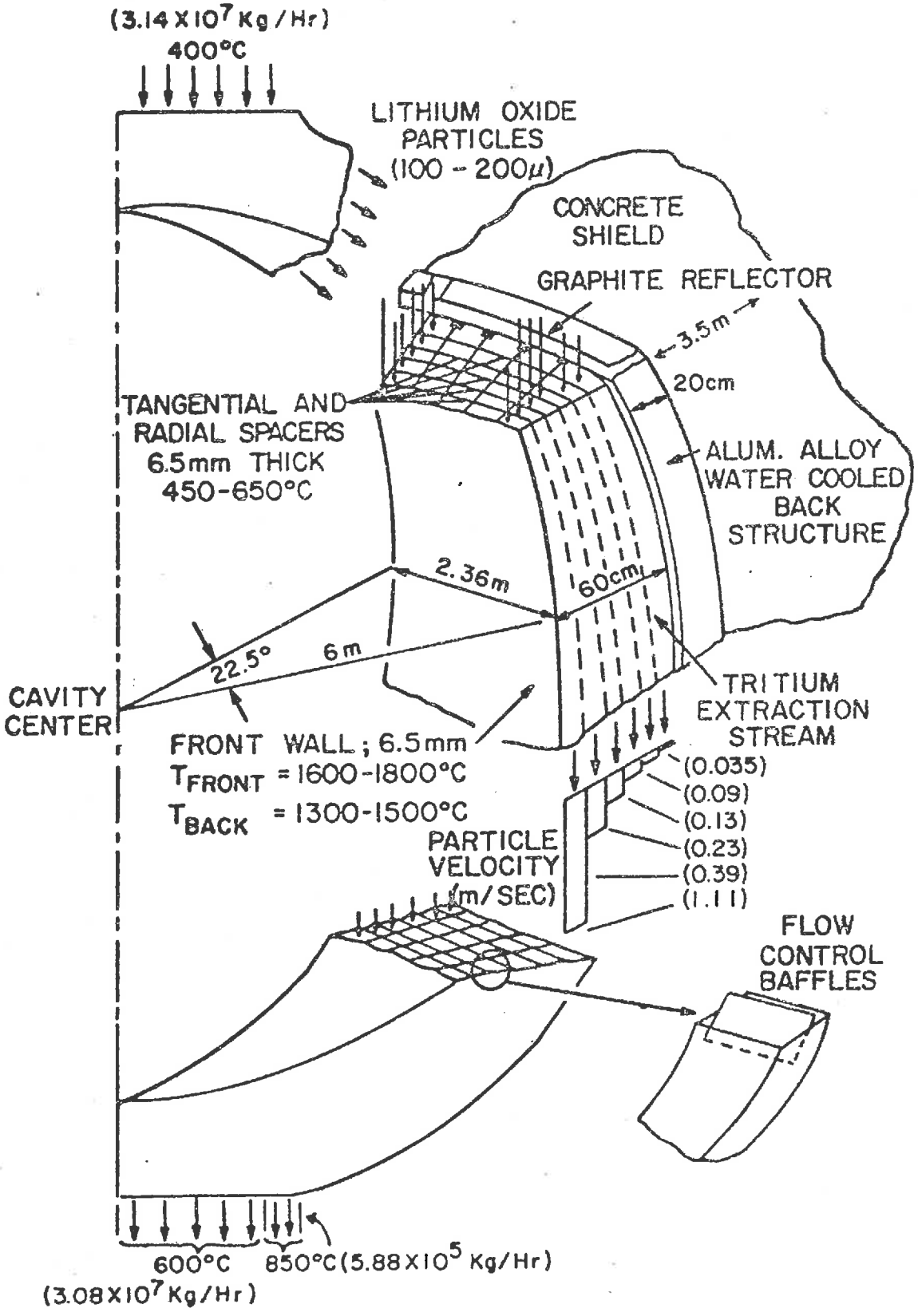

11.1.6. Driver Development

We have summarized the status of high power laser and charged particle beam driver development in Chapters 8 and 9. We suspect that driver development will be the most critical link in the achievement of ICF power generation systems. The complexity of developing reliable and efficient drivers with the required energy, power, and beam qualities necessary for ICF applications is formidable.

No presently known class of laser will obviously meet the requirements for laser fusion. However several lasers such as CO_2 and I can probably be scaled to meet minimum requirements for energy (1 to 4 MJ), power (100 to 1000 TW) and pulse width (1 to 10 ns). There are few lasers that have the potential to achieve an efficiency greater than 1 or 2%. If a power plant can be designed to operate with a laser of this efficiency, then the number of potential laser candidates increases substantially, and the chance of finding a suitable laser should also improve. Lasers with 1-2% efficiency demand pellet gain in the 500 to 1000 range.

The lifetime requirements for laser and power supply components must be about 10^9 shots. This is several orders of magnitude beyond the present state of the art and represents a serious challenge to successful laser fusion systems.

11.1.7. Beam Optics

An important facet of reactor design involves beam optics. To transport and focus intense laser beams into the target chamber, and to protect the necessary lenses and mirrors from the radiation produced in the microexplosion presents a major challenge. Of particular concern are the last mirrors of the optics chain since these mirrors will be in a direct line of sight to the microexplosion.

The Wisconsin study determined that uniform pellet illumination is not truly compatible with reactor requirements. They therefore used nonuniform illumination with six beams on each side to yield two-sided illumination (much as in the Shiva and Nova systems).

Surface damage to final mirror components by X-rays and pellet

debris is a significant problem. Large quantities of pellet debris on mirror surfaces cannot be tolerated. Physical, and more importantly, chemical reactions at the mirror surface will degrade beam optical quality. A method to protect the mirrors from the pellet debris is to flow a gas, such as xenon or neon, in front of the mirror surface (see diagram on the next page).

It is felt that neutron induced damage is not a serious problem. Neutron damage in a Cu on Al substrate mirror at 15 m from a 150 MJ yield pellet at the rate of 20 Hz is moderate, about 10^{-7} dpa/s, and the neutron heating is less than 10 W/cm^3. This provides little incentive to move the mirror farther than 15 m from the target. (Furthermore, removing the final optics to distances of 100 m or more seriously increase pointing errors.)

11.1.8. Fuel Pellets

Although detailed pellet designs are still highly speculative, one might well assume a generic pellet consisting of a frozen DT fuel encapsulated by a glass or polyvinyl alcohol shell. This shell is then surrounded by a high Z layer and a final low Z, low density ablative zone.

The fabrication of these targets involves three main processes: permeation filling, cryogenic processing, and deposition techniques. All techniques are widely used today and appear to be capable of meeting ICF target requirements.

Storage of fuel pellets will be required because the manufacturing process is a batch process and because a store is needed to allow plant operation in the event of a failure. The storage is likely to be at cryogenic temperatures to minimize the outdiffusion of the DT fuel. Furthermore, the total plant tritium inventory is highly sensitive to storage methods.

A particularly important aspect of ICF fuel design will be the compatibility of pellet materials with cavity walls. Pellet designs must avoid the use of reactive materials and minimize oxygen and hydrogen content.

SCHEME FOR PROTECTING LAST MIRROR FROM PELLET DEBRIS

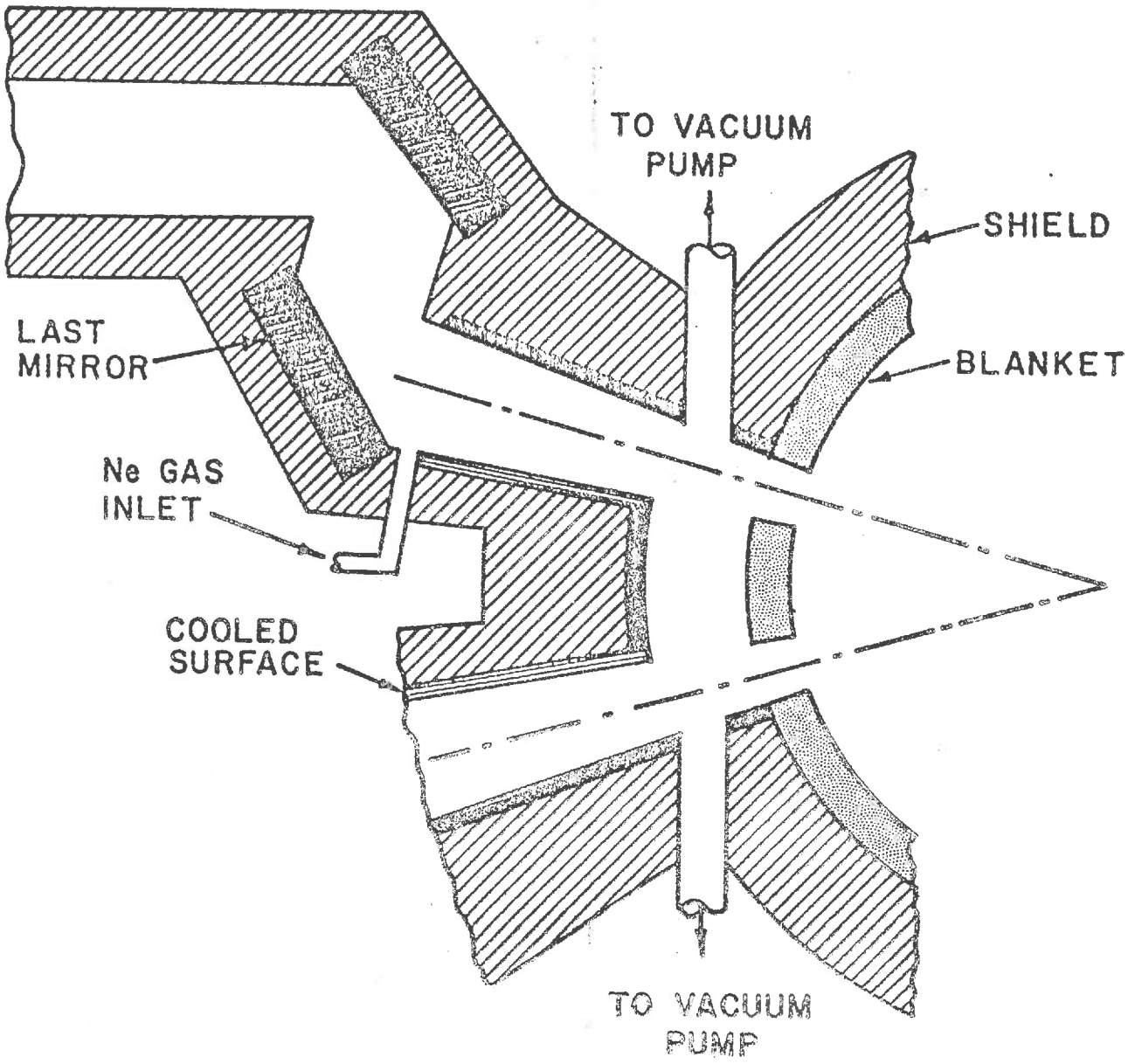

11.1.9. Balance of Plant

The design of ICF generating station will vary considerably with the different first wall protection schemes. For example, a LASL design based on the wetted wall cavity protection system would incorporate up to 26 reactor cavities (generating about 120 MWt each) with pairs of cavities served by common heat transfer loops, steam generators, and fuel processing systems. Two eight-beam laser systems would each have the capability to drive allof the cavities via a rotating mirror which would direct the beam to each cavity, respectively. Each laser would have a redundant partner to achieve high reliability.

An electric generation station based upon the magnetic protection concept is shown on the next page. Due to the output of each cavity (1249 MWt), this design is characterized by only four cavities which leads to a lesser degree of modularization and shared components than the wetted wall design. As in the previous concept, there would be a rotating mirror and a redundant laser system.

The use of such multiple cavities was briefly studied by the Wisconsin group. Although the primary motivation for such multiplicity was to increase the potential availability time of the reactor, they found that the most reliability-sensitive subsystem was the laser rather than the reactor chamber. Multiple lasers and power supplies, while not economically attractive, would be preferable to multiple cavities. Further the use of multiple cavities increases the complexity of the beam line system and reduces accessibility. Multiple cavities would appear to be necessary only if the time required to re-establish the chamber environment (e.g., due to vacuum pumping) becomes too long.

An alternative plant design of some interest is that based on the lithium waterfall reactor concept. The parameters characterizing this particular design, along with schematic diagrams of the plant, are given on the following pages.

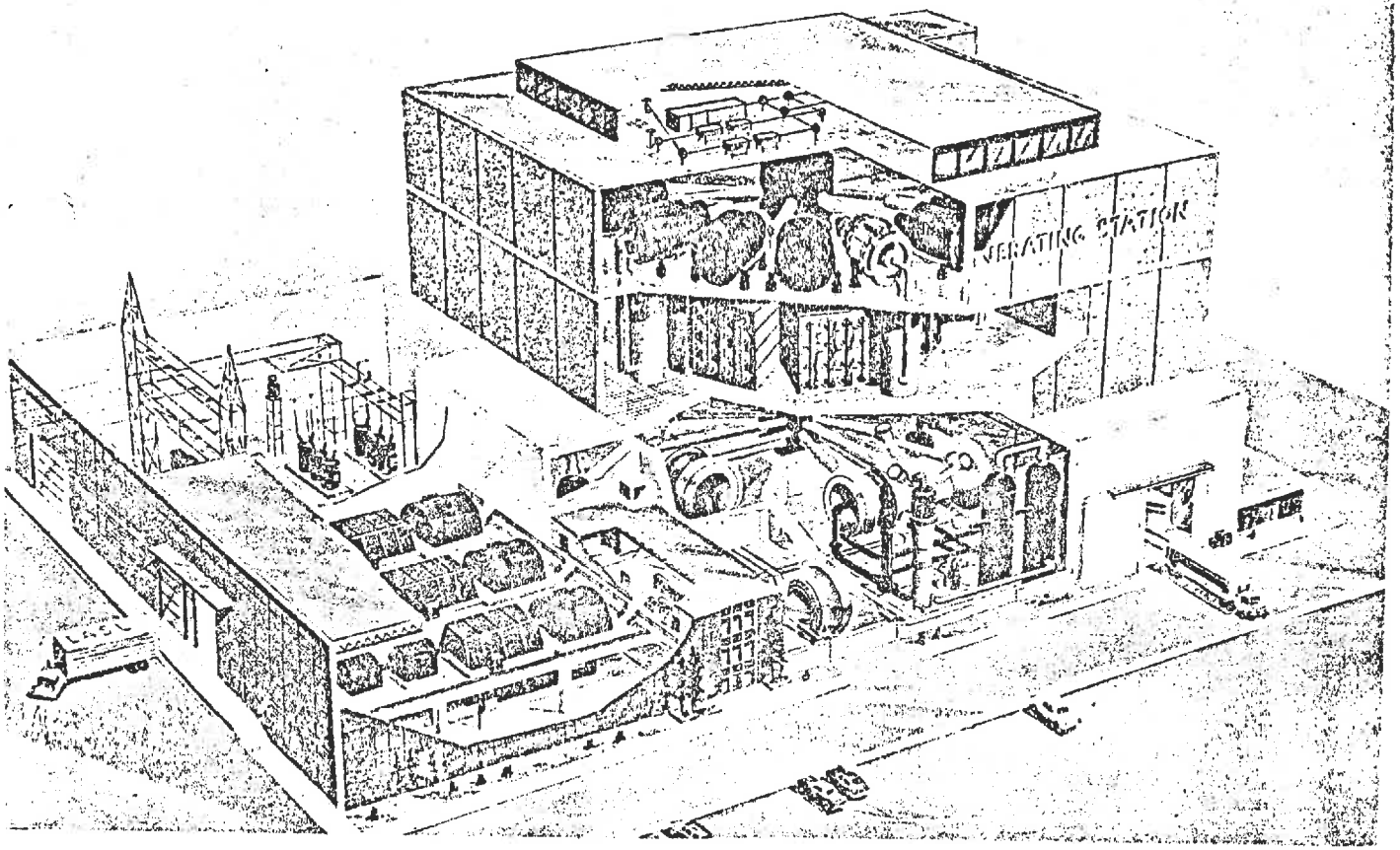
OPERATING STATION

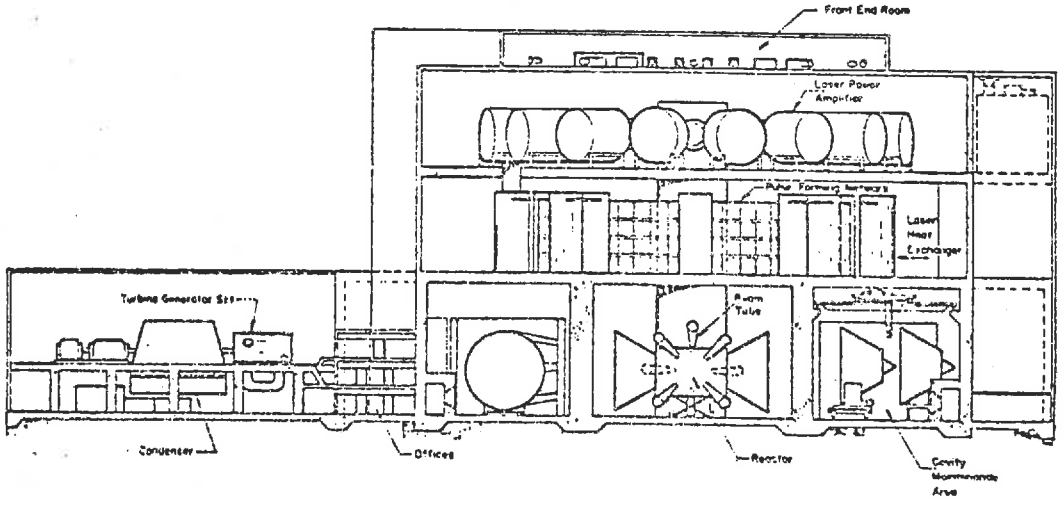
Front End Room
Laser Power Amplifier
Pulse Forming Network
Laser Heat Exchanger
Turbine Generator Set
Beam Tube
Condenser
Offices
Reactor
Cavity Maintenance Area

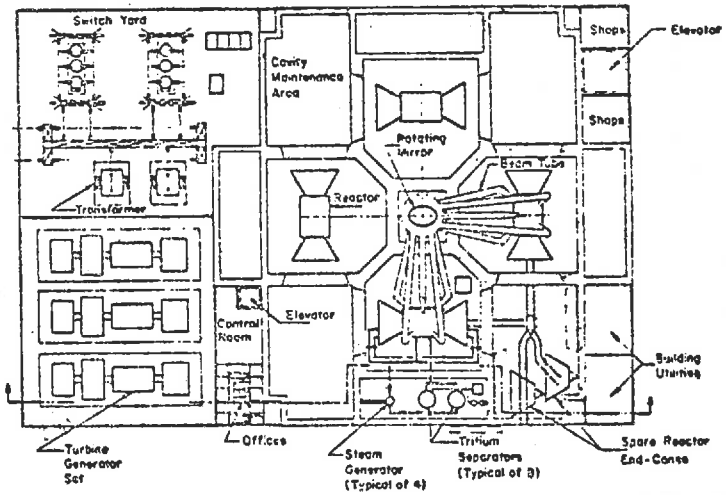
Switch Yard
Cavity Maintenance Area
Shops
Elevator
Shops
Rotating Mirror
Beam Tube
Transformer
Reactor
Control Room
Elevator
Building Utilities
Turbine Generator Set
Offices
Steam Generator (Typical of 4)
Tritium Separators (Typical of 3)
Spare Reactor End-Cones

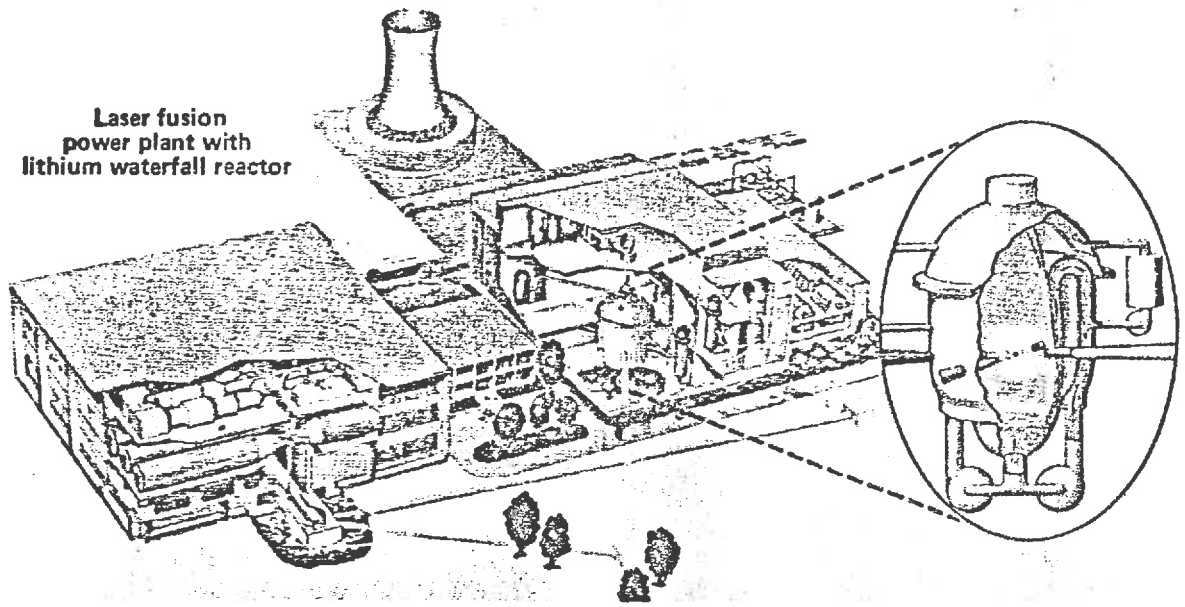

The LLL laser fusion electric power plant concept.

Overall performance

Thermal power	1160 MW_t
Thermonuclear power	1000 MW_t
Gross electrical power	460 MW_e
Net electrical power	380 MW_e
Thermal cycle efficiency	38%
Recirculating power fraction	17%
System efficiency	33%

Laser and pellet parameters

Laser energy	1 MJ
Pulse repetition rate	1.43 Hz
Laser power	1.43 MW
Pellet gain (Q)	700
Pellet yield	700 MJ
Laser system efficiency (η_L)	2%
Number of modules	10
Number of beams	4

Reactor parameters

Geometry	Cylindrical
Inner radius	4 m
Height	8 m
Lithium fall thickness	0.6 m
Equivalent first-structural-wall fusion neutron flux	4 MW/m^2
Tritium breeding ratio	1.7
Blanket energy multiplication	1.24
Reactor materials	
Structure	Stainless steel
Coolant	Lithium

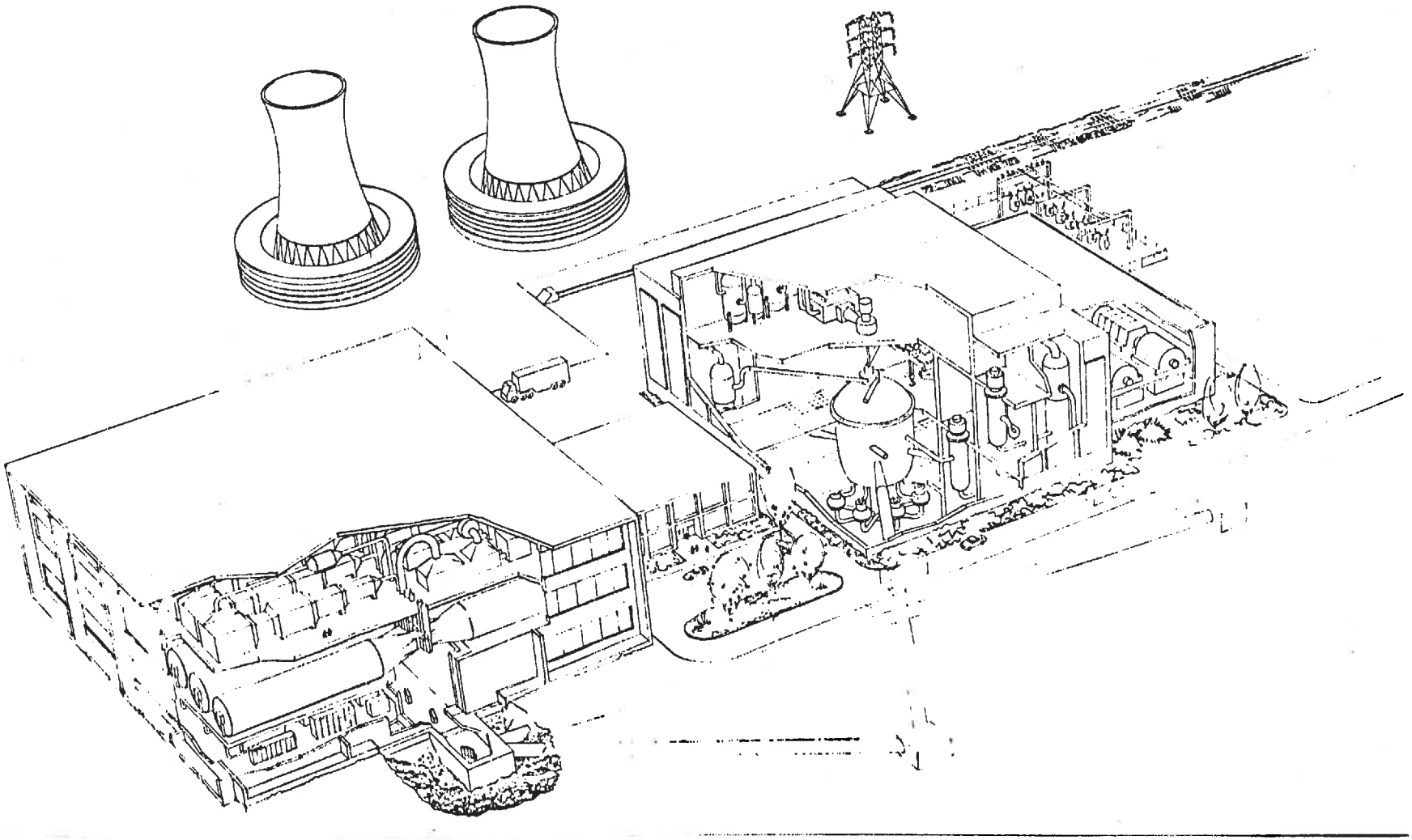

Nominal Reference System Parameters, 1000 MWe LCTR

	Dry Wall	Wet Wall	Magnetically Protected	Solase-I
Number of chambers	4	24	4	1
Pulse rate, Hz/chamber	7.2	1.2	7.2	30
Fusion energy gain (Qn_L)	6.5	6.5	6.5	10
Blanket gain, M	1.3	1.3	1.3	1.07
Tritium breeding ratio	1.2	1.2	1.2	1.24
Cavity shape	Sph.	Sph.	Cyl.	Cyl.
First wall radius, m	9.7	1.7	2.5	5.0
No. of laser beams/cavity	8	8	8	6
Laser energy into cavity/pulse, MJ	1	1	1	1

11.1.10. A Detailed Example: Solase

The Solase reactor designed by the University of Wisconsin Fusion Project is shown on the following pages. This reactor is designed to produce 1000 MWe at a net efficiency of 30% from laser driven ICF fuel pellets with a gain of 150. The laser energy on target is taken as 1 MJ, and 20 targets are imploded each second. The laser efficiency is assumed to be 6.7%, including multipassing of the next-to-last and last laser amplifier. The laser is designed, generically where possible, as a gas phase laser modeled after the CO_2 system but no laser wavelength is specified. The optimistic laser efficiency of 6.7% still implies relatively large power supply needs and the recirculating power fraction is 28%.

Thermonuclear burn dynamics calculations were performed to determine pellet debris spectra for cavity design analysis. A buffer gas of neon at 0.5 to 1 torr pressure is used to stop the ions. Multi-layered cryogenic targets produced in a batch process appear to have acceptable costs because tooling costs can be amortized over the lifetime of the plant and material costs are negligible. Target delivery is by pneumatic guns although trajectory diagnostic and correction techniques must be developed. The last mirrors are diamond turned copper on an aluminum structure located 15 m from the reactor cavity center with f number 7.5. Heating of the mirror surface is minor so long as the debris ions are stopped in the buffer gas.

The reactor cavity itself is a sphere 6 m in radius. It is constructed from graphite designed to guide the gravitational flow of lithium oxide (Li_2O) pellets serving as both the tritium breeding and heat transport medium. The breeding ratio is 1.33 and the maximum Li_2O flow velocity is only about 1 m/s. The neutron wall loading is 5 MW/m^2 so that Solase presents a reasonably comapct system given the net power produced. The blanket back structure is made from an aluminum alloy and the shield can be either concrete or lead acetate solution. Thus, the overall levels of neutron induced activity decay very rapidly following shutdown. It appears that limited hands-on maintenance is possible after just one week.

Parameters for the SOLASE Laser Fusion Reactor

CAVITY SHAPE	SPHERICAL
CAVITY RADIUS	6 m
14 MeV NEUTRON WALL LOADING	5 MW/m^2
THERMAL POWER	3340 MW
GROSS-ELECTRICAL POWER	1334 MW
NET ELECTRICAL POWER	1000 MW
RECIRCULATING POWER FRACTION	28%
NET PLANT THERMAL EFFICIENCY	30%
LASER TYPE	GAS PHASE
LASER ENERGY ON TARGET	1 MJ
LASER EFFICIENCY (WITH MULTIPASSING)	6.7%
NUMBER OF FINAL AMPLIFIERS	6
NUMBER OF FINAL BEAMS	12
ENERGY OUTPUT/AMPLIFIER PASS	45.8 kJ
PULSE WIDTH	1 ns
PULSE REPETITION RATE	20 Hz
PELLET YIELD AND GAIN	150 MJ
FRACTIONAL BURNUP OF FUEL	45%
INITIAL FUEL MASS	1 mg
GENERIC TARGET DESIGN	MULTILAYERED-CRYOGENIC

Parameters for the SOLASE Laser Fusion Reactor

TARGET ILLUMINATION	TWO SIDED
NUMBER OF FINAL MIRRORS	12
F/No. OF FINAL MIRROR	7.5
DISTANCE FROM LAST MIRROR TO PELLET	15 m
DIAMETER OF LAST MIRROR	3.5 m
COMPOSITION OF LAST MIRROR	Cu on Al
MANUFACTURING PROCEDURE	DIAMOND TURNING
FIRST WALL PROTECTION METHOD	Ne or Xe BUFFER GAS
BLANKET STRUCTURE	GRAPHITE COMPOSITE
BLANKET BREEDING AND HEAT TRANSPORT MEDIUM	LITHIUM OXIDE (Li_2O)
TRITIUM BREEDING RATIO	1.33
TOTAL ENERGY PER FUSION EVENT	18.6 MeV
TOTAL Li_2O FLOW RATE	3.12×10^7 kg/hr
AVERAGE Li_2O FLOW VELOCITY	0.7 m/s
Li_2O INLET TEMPERATURE	400°C
Li_2O OUTLET TEMPERATURE	600°C
TRITIUM INVENTORY	
GLASS ENCAPSULATION OF TARGET	24.7 kg
POLYMER ENCAPSULATION OF TARGET	10.9 kg
TOTAL REACTOR RADIOACTIVITY LEVEL 50 YEARS AFTER SHUTDOWN	3 Ci

THE SOLASE LASER FUSION REACTOR SYSTEM

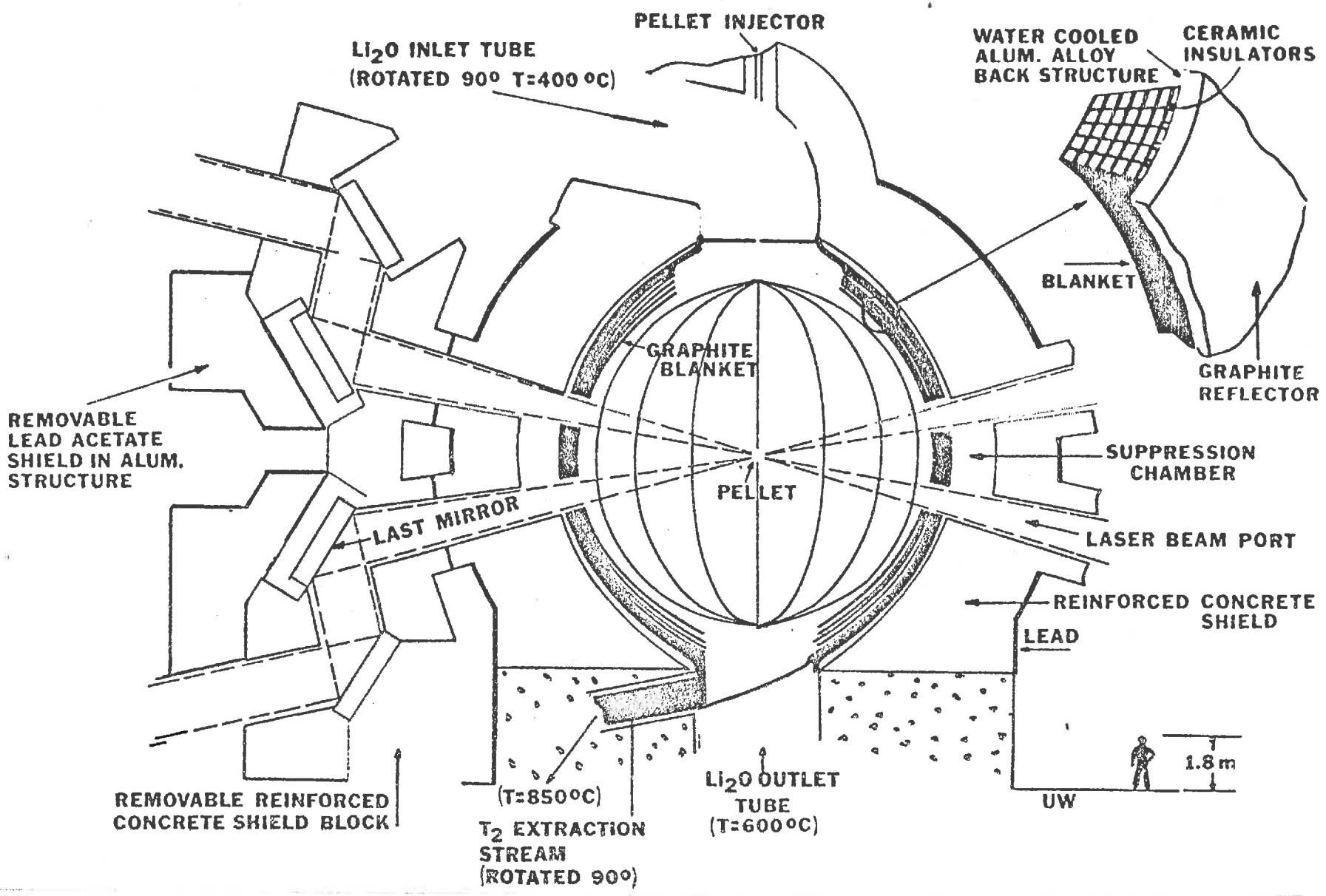

TOP VIEW OF SOLASE
A CONCEPTUAL LASER FUSION REACTOR POWER PLANT

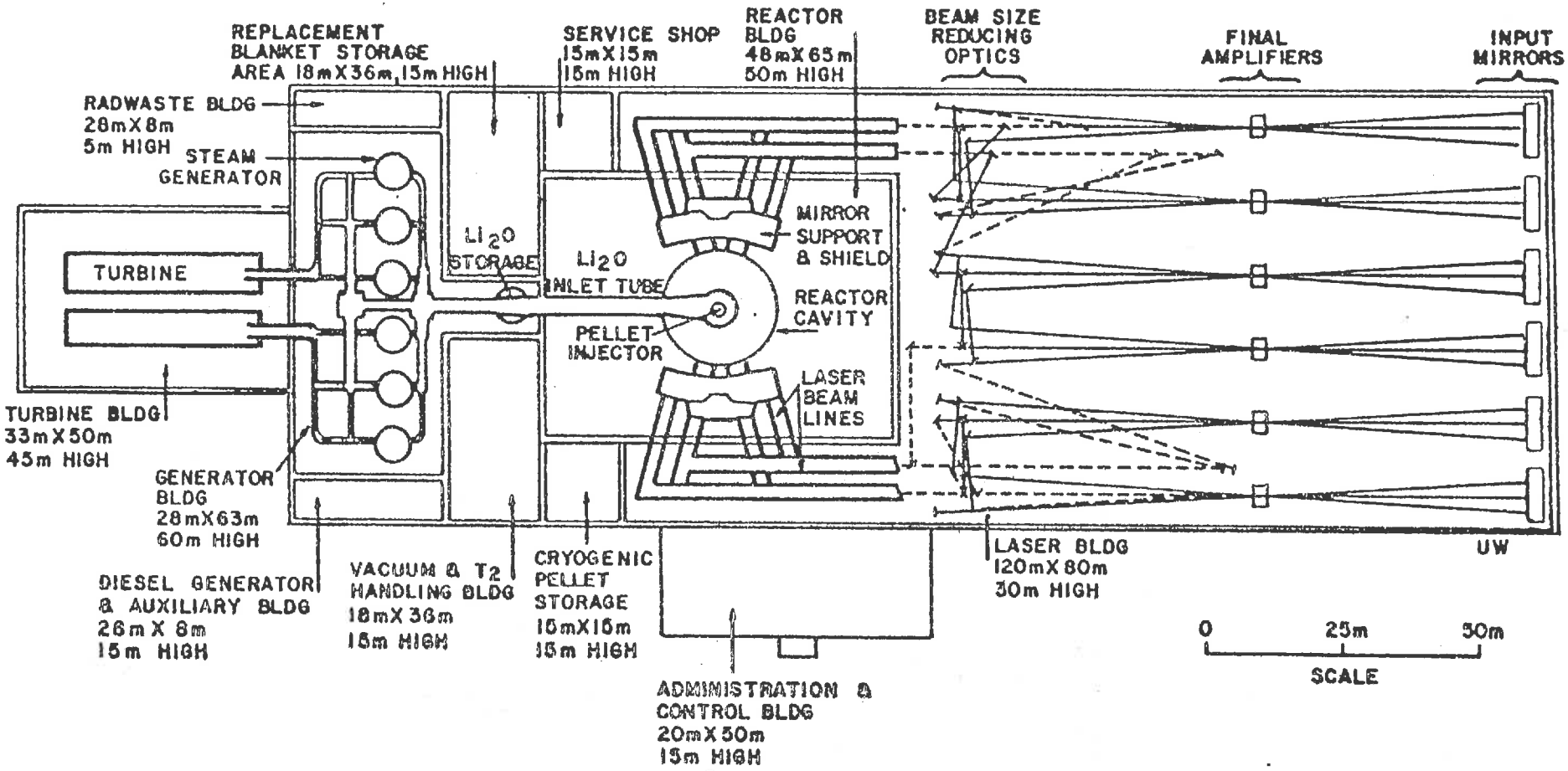

This spherical system is highly accessible from the outside provided that two-sided target illumination (six beams on each side) is acceptable. A procedure has been developed for annual blanket replacement that is simple and fast. The expected downtime to replace graphite blanket segments is two weeks. The design philosophy is that blanket maintenance per se will be avoided; after draining the Li_2O, the graphite will simply be discarded.

The laser system is designed as generacally as possible, but is modeled after the CO_2 laser where specificity is required.

In the steam power cycle, LI_2O transport heat directly to steam generators which then drive turbines producing 1334 MWe gross. The laser recirculating power requirement is 300 MWe and other internal plant power requirements lead to a new plant electrical output of 1000 MWe and a net thermal efficiency of 30%. The large recirculating laser power fraction appears typical of laser fusion systems unless gains much larger than 150 or laser efficiences much greater than 5 to 10% can be achieved.

11.1.11. Some Conclusions

As we have noted, laser driven fusion power plants will have a large recirculating power fraction (30% or so) unless very high gain targets ($\lesssim$ 500) or high efficiency lasers ($\sim$10-20%) can be developed. The development of targets with even modest gains ($\sim$ 100) and lasers with modest efficiencies ($\sim$ 1%) is highly uncertain at present. The development of power supplies and pulsed power switching with high reliability (10^8 - 10^9 shots) of modest costs is also a major concern.

The constraints of few beams and pellet physics have led to a variety of reactor cavity concepts. There appears to be no essential constraint on cavity geometry (except cavity diameter), unlike magnetic fusion systems. Furthermore, the background density of cavity fill and debris gas appears to be low enough to permit beam propagation.

Most reactor design considerations are dominated by protection of the first wall and the achievement of the high repitition rate.

Preliminary reactor design studies appear to rule out the use of dry or bare metal walls. The tendency is to move toward either fluid walls or sacrificial (replaceable) liners with limited life. The success and choice of a cavity design will strongly depend on pellet materials and output characteristics.

Another important issue specific to ICF applications has to do with security classification. The relationship of ICF to technical ideas and information related to thermonuclear weapons, if any, could severely impede the commercialization of this process due to extensive classification of pellet design ideas. It seems highly unlikely that ICF power generation could be developed for commercial implementation in the face of the present classification restrictions. No utility in its right mind would add the extra burden of classification to the already overwhelming hurdles it faces in power plant licensing and regulation.

11.2. HYBRID FUSION/FISSION SYSTEMS

Since a typical ICF power station will have a large laser system recirculating power fraction (about 30%) leading to a low net plant efficiency (about 28% assuming a 40% thermal efficiency), there is considerable incentive to find methods other than the direct conversion of thermal fusion energy to electricity which would improve the overall economics of such a system. One scheme involves including fissionable materials in the blanket of the reactor. Such designs, termed fusion/fission hybrid reactors, are actually subcritical fissionable assemblies which are driven by a fusion neutron source. Interest in hybrid systems has been motivated primarily by their potential to relax fusion energy gain criteria significantly and to breed substantial quantities of fissile material. The principal advantages of such a coupled system result from the fact that, taken separately, fission systems are inherently power rich (with 200 MeV per fission reaction) and neutron poor, while DT-burning fusion systems are comparatively power poor (with 17.6 MeV per fusion) and fast-neutron-rich. The term fast-neutron-rich should be emphasized because it is the 14.1 MeV neutrons from DT fusion that provide hybrid systems with the ability to generate substantial amounts of energy and fissile materials from fertile materials such as U-238 and Th-232, thereby operating with low fissile material inventories in a subcritical fashion. In a sense, the overall objective in a hybrid reactor design is to trade 14.1 MeV fusion neutrons for 200 MeV fission events; represented either by actual fissions in the blanket or by the conversion of fertile to fissile species. The combination of the above factors can effectively increase the energy output of a fusion device by up to two orders of magnitude.

In general hybrid systems can be separated into three categories:

(i) systems which produce fissile fuel but very little power

(ii) systems which produce fissile fuel and power (although perhaps only at a breakeven level)

(iii) systems which consume fissile fuel and produce power

Systems of the first type may find the earliest commercial application

as "fuel factories" for conventional fission plants. Although systems of the second type will be more efficient than those of the first type, they will require sophisticated technologies to effectively remove the heat generated in hybrid blankets which are not intrinsically well-suited to this purpose. Thus hybrids which produce significant power will probably not find application until a later developmetn stage, Because systems of the second type have been found to have the potential to increase the blanket energy gain by ten to one hundred fold, in addition to producing fissile fuel, it follows that systems of the third kind are probably not realistic, with the exception of specialized applications such as actinide transmutation as a radioactive waste disposal scheme.

The principal advantage of hybrid systems is that they have the potential to produce approximately 10 times more fissile material per unit of thermal energy than fission breeder reactors. In a pure fusion device, the neutron loading at the first wall will be restricted (at least in the near term) to values of less than 10 MW/m^2, thereby restricting power densities to less than 10 W/cm^3. However a properly optimized hybrid design could multiply the fusion energy density by a factor of 50 or more (i.e., 500 W/cm^3), making the device 50 times as energy efficienty while maintaining power densities which can, in principle, be accommodated by extensions of current fission reactor technology.

Several hybrid designs have been undertaken using a laser-fusion system as a driver. One such system studied by LLL and Bechtel is shown on the following page.

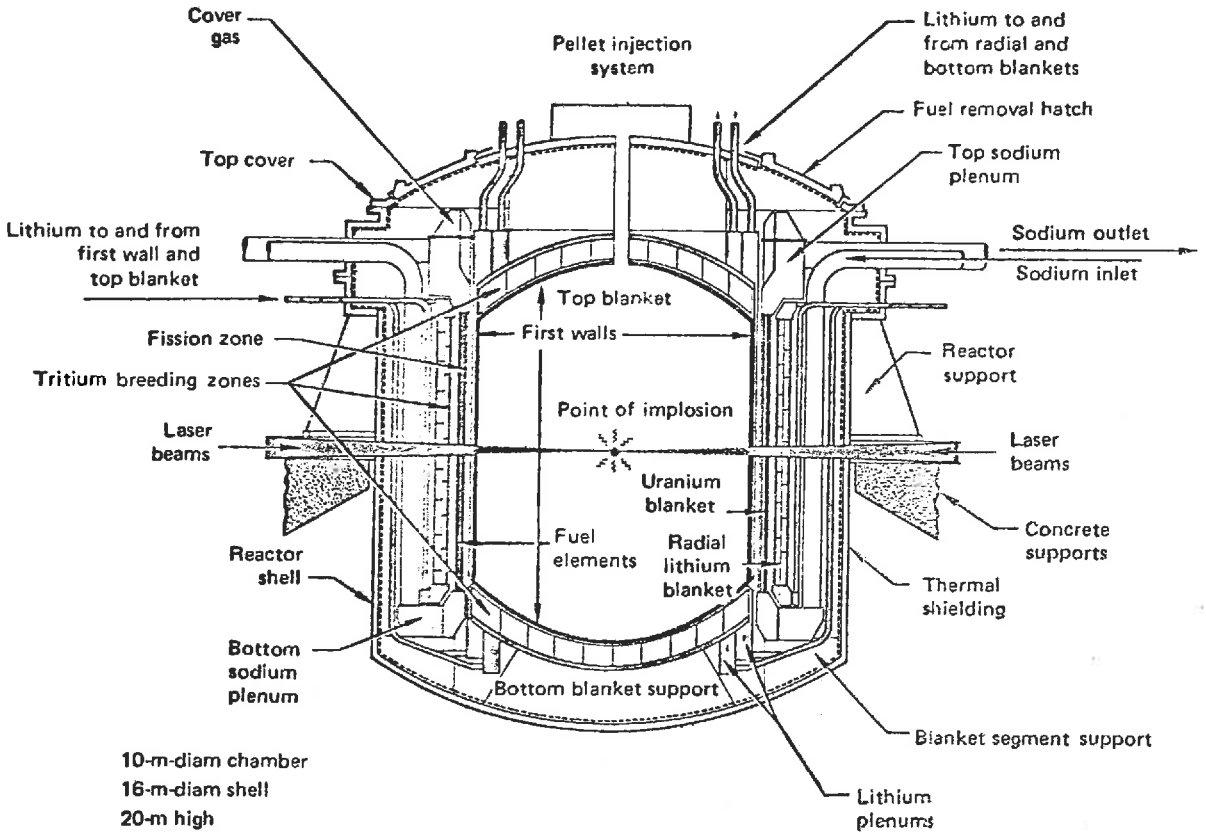

LLL/Bechtel 4000-MW$_t$ hybrid reactor.

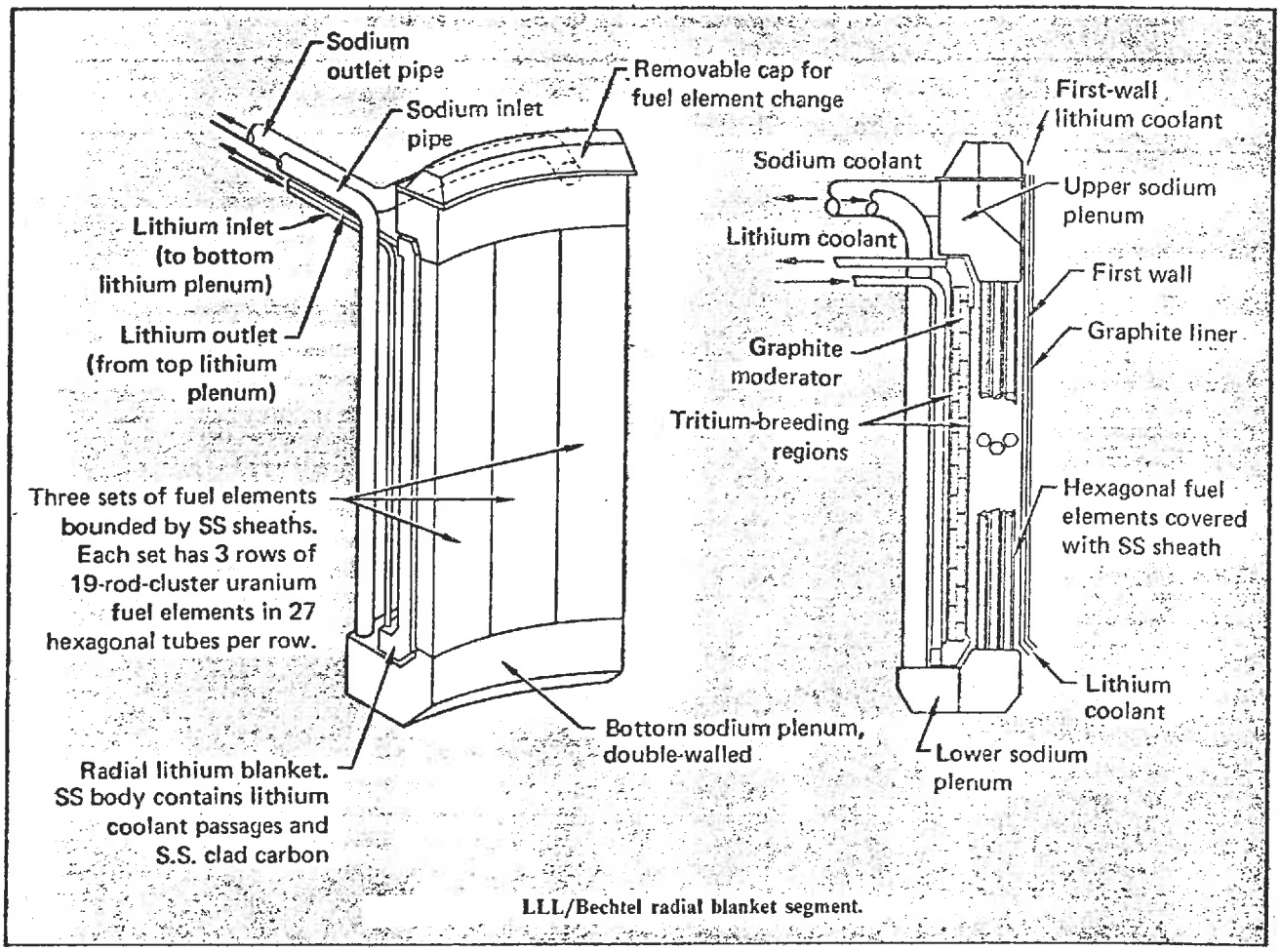

LLL/Bechtel radial blanket segment.

Actinide Burning

Introduction. The neutrons from DT-fusion systems can convert long-lived fission waste products (primarily actinides) to short-lived or stable isotopes. This method could serve as a mechanism to relax requirements for long-term geological storage of high-level radioactive wastes. Actinide half-lives are quite long, even in comparison to such geological phenomena as ice ages and earthquake fault movements. Storage of long-lived wastes is difficult because these events can render a disposal area unacceptable.

Laser Fusion-Driven Actinide Burner Study. At present, laser fusion appears to be capable of attaining a 5- to 10-MW/m^2 fusion neutron wall loading. In addition, the ability to utilize simple geometry makes the laser fusion reactor an attractive candidate for actinide burning. Recognizing these attributes, Berwald and Duderstadt (University of Michigan) have performed scoping studies [107] for an actinide burner adapted from a University of Wisconsin pure laser fusion reactor design. The goal was to identify a fusion-driven actinide burner system that could be expected to perform efficiently within the framework of anticipated fusion technology. Reasonable extrapolations in technologies that could be expected to develop during the same time frame as the fusion driver itself were utilized.

The laser fusion-driven actinide waste burner (LDAB) system investigated uses partitioned fission reactor generated actinide wastes dissolved in a molten tin alloy as fuel. A novel fuel processing concept based upon work by Anderson and Parlee [108] concerning the high-temperature precipitation of "actinide-nitrides" from a liquid tin solution is proposed. This concept will allow for fission product removal to be performed at high burnup within the device. Thus, the LDAB actinide transmutation process may represent less short-term hazards than solid fuel systems with a fixed fuel cycle period, because the need to refabricate and transport actinide wastes once charged to the system is eliminated.

The LDAB is a power producing hybrid reactor. With an equilibrium blanket energy multiplication of 30 in actinide fission regions about the axial midplane of a cylindrical cavity, a total system blanket energy multiplication of 12 is attained. This corresponds to a reduction in the laser system recirculating power fraction from 24% (pure fusion reactor) to 2.7%. The equilibrium neutron wall loading of 5.7 MW/m^2 represents an average flux of 6.4×10^{15} $n/cm^2 \cdot s$ in the fission regions. The overall system power is approximately 22,000 MW_{th} with an average fission power density of 287 W/cm^3 in the actinide fuel regions.

No attempt has been made to optimize this system, but potential performance seems impressive. In one possible fuel management scenario, the LDAB attains an effective equilibrium composition in 15 years. The equilibrium LDAB consumes 7.60 MT/yr of actinide waste corresponding to the waste output from 134 LWR's operating with full plutonium recycle (1000 MW_e, 33,000 $MW \cdot d/t$, 33% thermal efficiency, 75% capacity factor). With an actinide loading of 34 t, the mean life of an actinide atom in the system is only 4.5 yr.

If the 134 LWR's and one LDAB are evaluated as one system, the LDAB will produce 5.5% of the system power. If the cost of LDAB power generation is three times that of LWR power generation, then the system power generation costs will be 11% above the LWR power generation costs. If the LDAB burns LWR-uranium recycle waste instead of LWR-plutonium recycle waste, it might serve 420 reactors with only a 3.7% increment in power generation costs. As in the WFPS design study, the blanket thermal power could also be utilized for synthetic fuel production.

Although the LDAB has the potential to efficiently burn actinide wastes, process the wastes generated in a large system of commercial reactors, and reduce the short-term hazard caused by transporting and fabricating actinide fuels, its performance represents an optimistic goal. Its realization will require significant development in the fields of high-level waste partitioning, laser fusion and hybrid systems, fusion environment materials, and pyroprocessing. However, these results suggest that high-burnup solid-fuel hybrid blanket designs with considerably less technological risk might attain adequate performance as actinide burners. In particular, HTGR fuel pellets appear to have burnup capabilities in excess of 25%. [109]

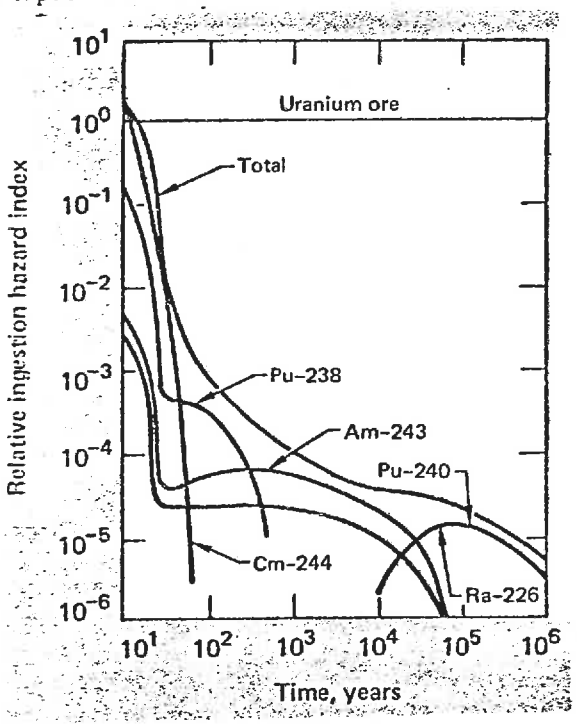

11.3. PROCESS HEAT AND SYNTHETIC FUEL PRODUCTION

Other applications of ICF reactors have been proposed. The temperatures in a laser fusion reactor blanket will be limited only by the properties of refractory materials in the blanket. Thus, temperatures above the HTGR limit of 1650°K can be achieved. Such temperatures are attractive for producing process heat for industrial applications. (Indeed, about 28% of the energy consumption in the United States is to generate process heat.) ICF reactors seem to be unique in this respect, since they do not suffer from the temperature limitations of magnetic fusion systems or fuel melting of fission reactors.

Los Alamos has designed several ICF blankets suitable for process heat production. Using two zone blankets, composed of pure carbon and a 90% carbon-10% boron carbide mixture, spherical ICF reactors have been designed that would supply from 20 to 100 MW of thermal power at about 2100°K. Examples of these designs are shown on the next few pages.

ICF reactors could also supply the energy necessary to produce synthetic fuels. A variety of approaches have been proposed, including thermochemical, electrolytic, and radiolytic processes.

The thermal energy for the ICF reactor could support a sequence of high-temperature chemical reactions in various hydrogen-producing thermochemical processes. While these thermochemical processes generally do not consume the chemical reactants, they often use large quantities of hazardous and corrosive chemicals. Practical energy conversion efficiencies range from 30% to 65%--that is, up to 65% of the fusion energy is recoverable as thermal energy by burning the hydrogen produced.

Such reactors could also generate electricity for subsequent electrolysis of water to produce hydrogen. For existing electrolysis plants, the combustion energy of the hydrogen produced is 60% to 100% of the electrical energy input. Hence if we assume a 40% plant thermal efficiency, we find that this scheme would produce hydrogen with an overall energy conversion efficiency of 24% to 40%.

Hydrogen production by radiolysis can be achieved in several ways. The penetrating neutron radiation of an ICF reactor could be utilized

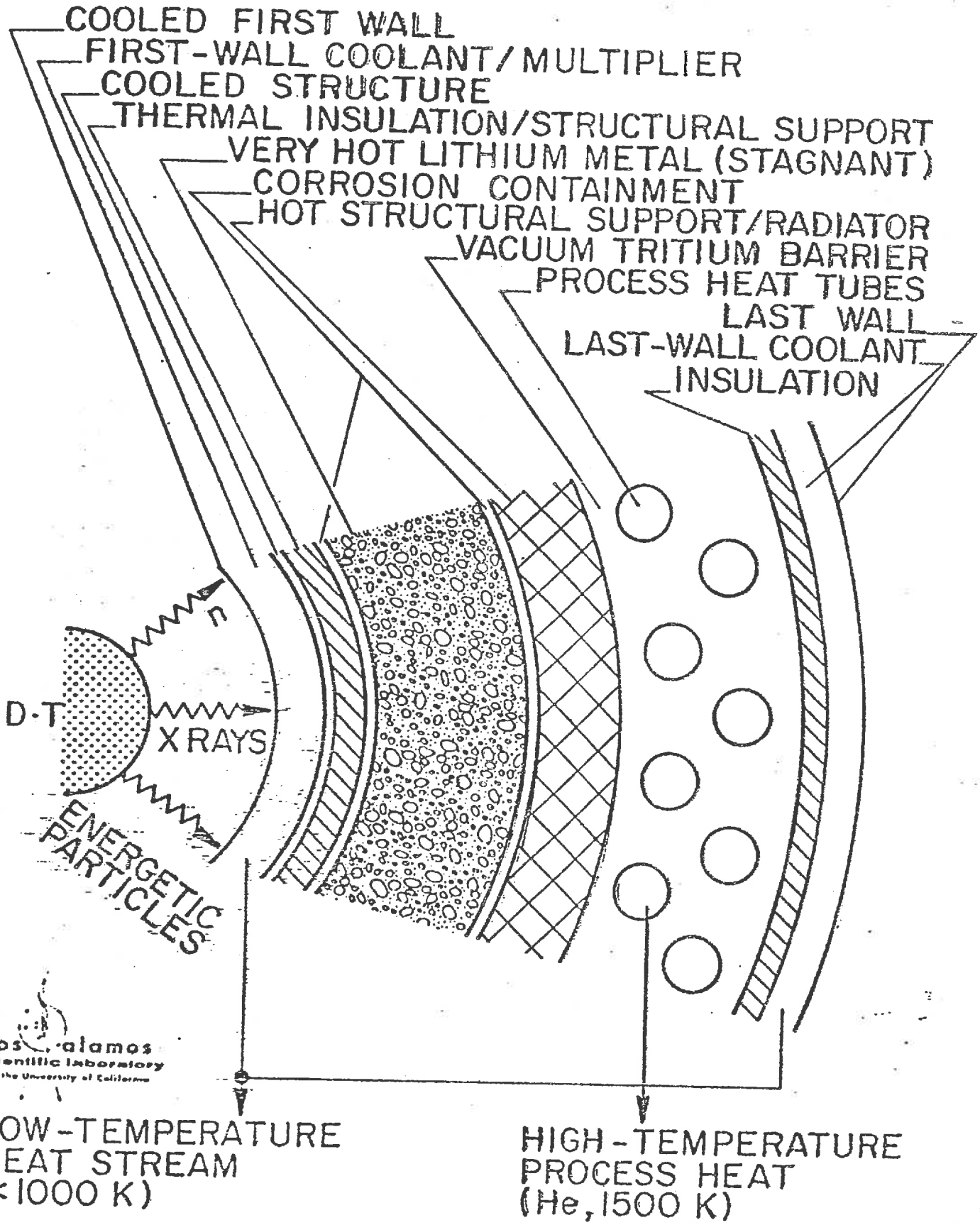

SIMPLE RADIATOR BLANKET

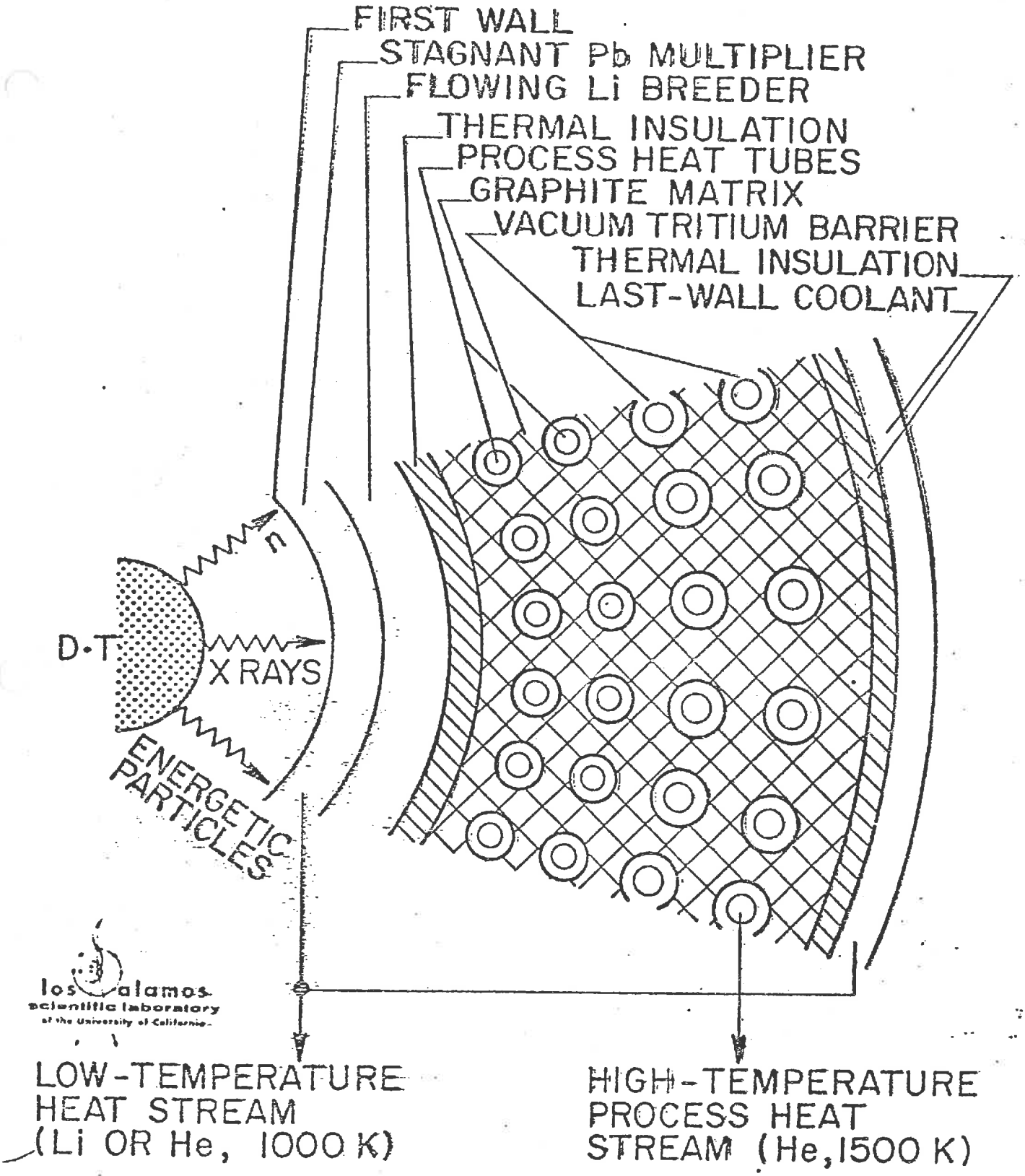

IMBEDDED RADIATOR BLANKET

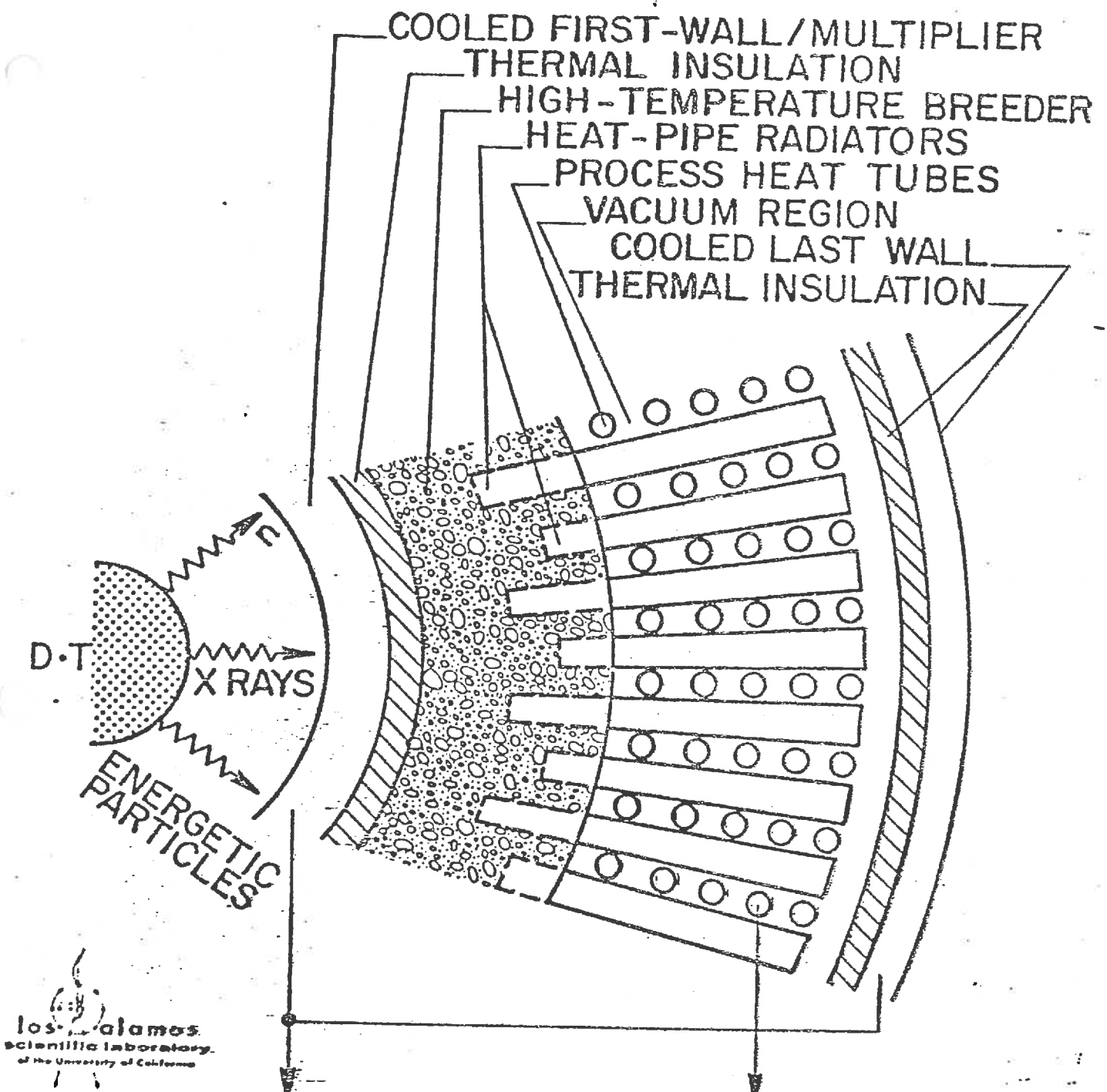

EXTENDED RADIATOR BLANKET

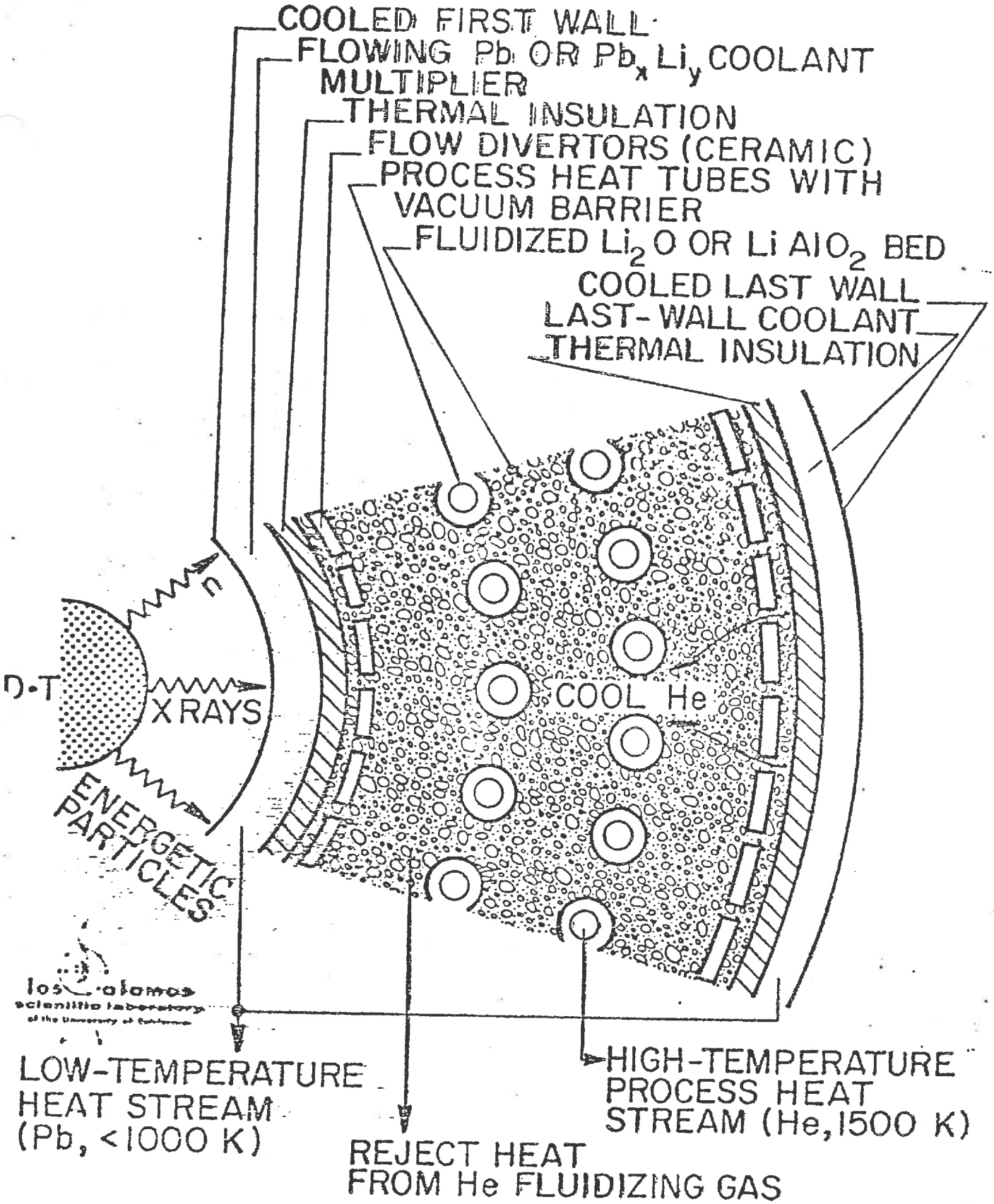

FLUIDIZED - BED BLANKET

by incorporating sufficient quantities of H_2O in the blanket regions surrounding the fusion vacuum chamber. In this sense, fusion reactors are quite attractive since they produce an intense fast neutron flux in a surrounding blanket region rather than in the core proper (as with a fission reactor).

A variety of synthetic fuel production schemes have been studied which use an ICF reactor as an energy or radiation source. Several of these are described schematically on the following pages. We have also provided a comparison of various methods for producing hydrogen below:

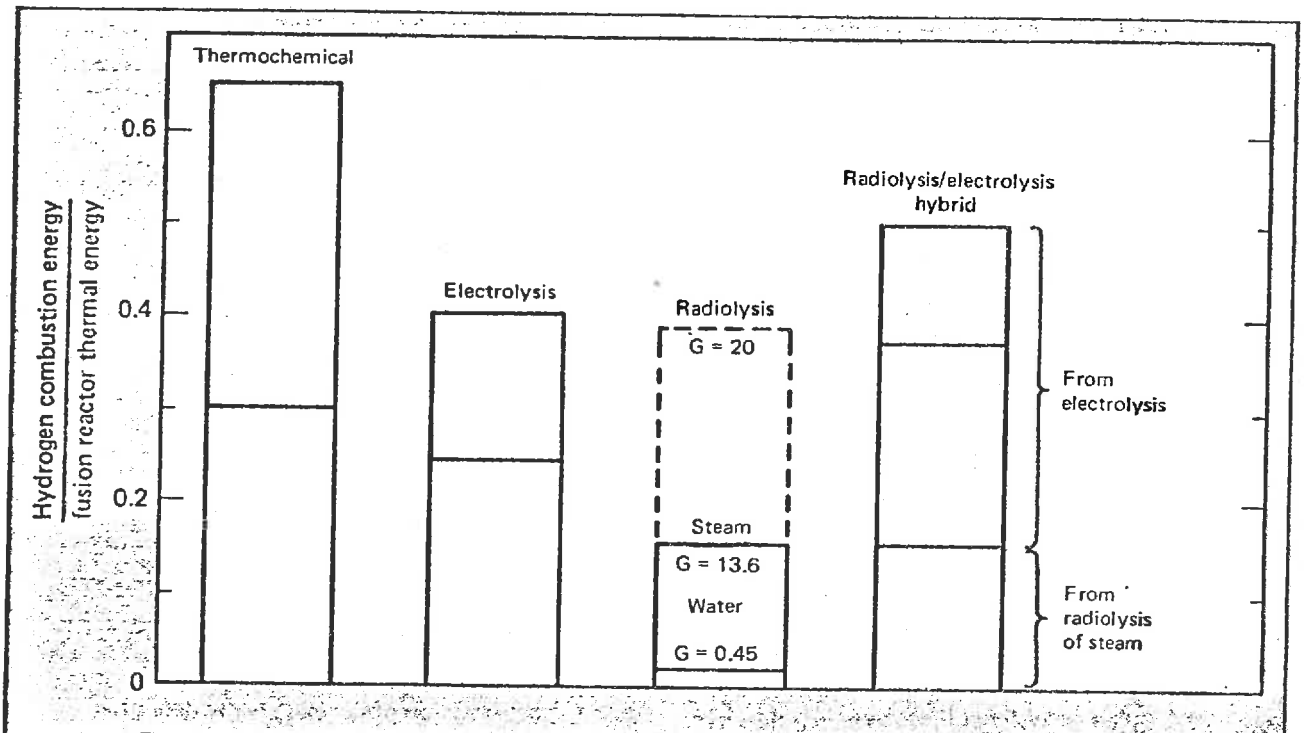

The combustion energy of hydrogen recoverable from one unit of fusion-reactor thermal energy. (The fraction of the neutron energy deposited in hydrogen processing regions is generously assumed to be 100% for radiolysis of water and 60% for radiolysis of steam. It is unlikely that a dedicated radiolysis hydrogen-production facility could ever prove practical unless a liquid medium with a higher G value is found. Therefore, a hypothetical G = 20, liquid medium system is shown.)

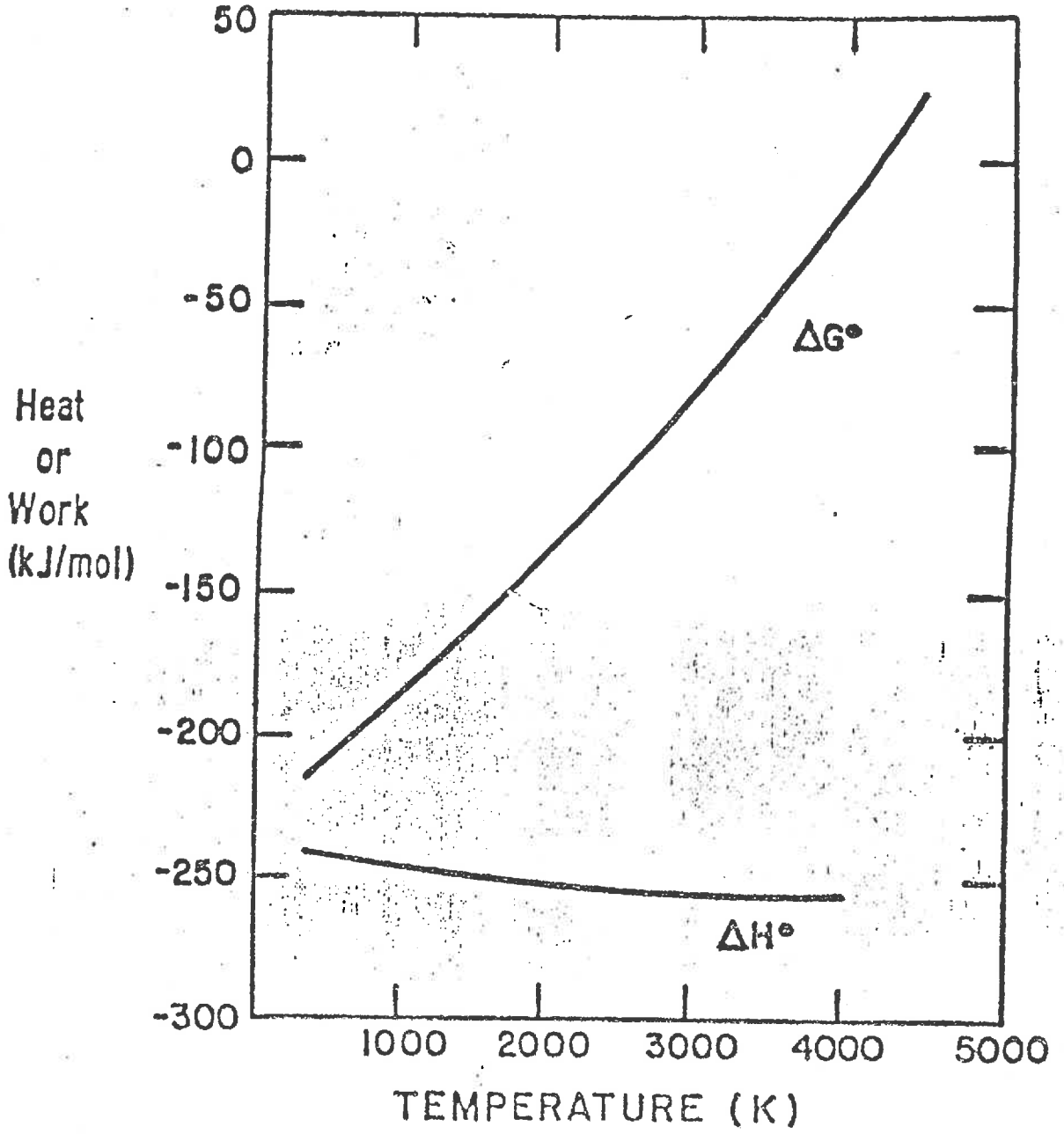

Water is our only available source of hydrogen and energy must be supplied for its decomposition.

THERMOCHEMICAL CYCLE USING HIGH TEMPERATURE THERMAL ENERGY PROMISES HIGH EFFICIENCY

LASER FUSION

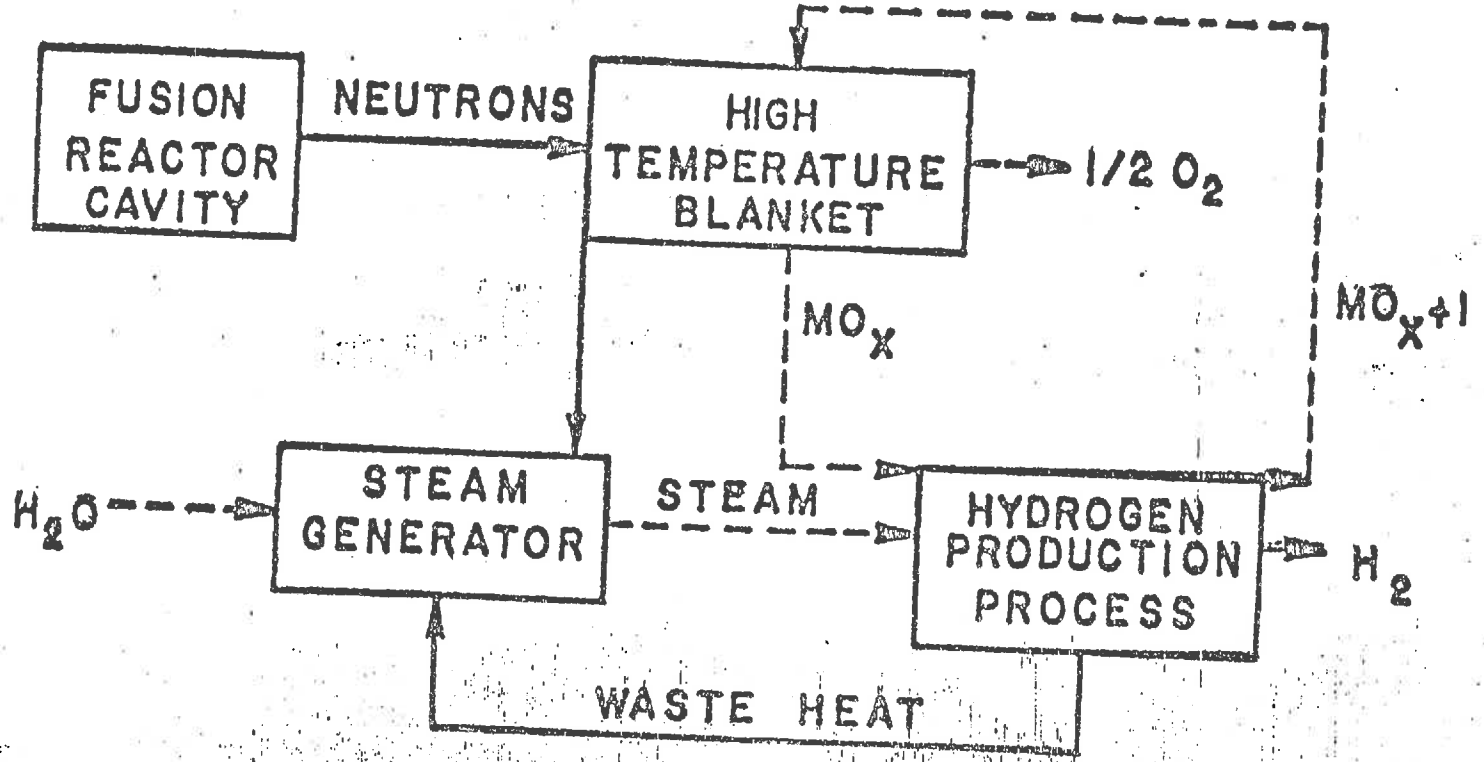

- At blanket temperatures > 1500 K, efficiencies > 50% expected
- Neutron energy deposition directly in reacting medium may be possible
- Neutron energy deposition in refractory material with thermal radiation to process tubes appears feasible.

HIGH-TEMPERATURE ELECTROLYSIS USES BOTH THERMAL AND ELECTRICAL ENERGY IN A FEASIBLE AND MORE EFFICIENT PROCESS

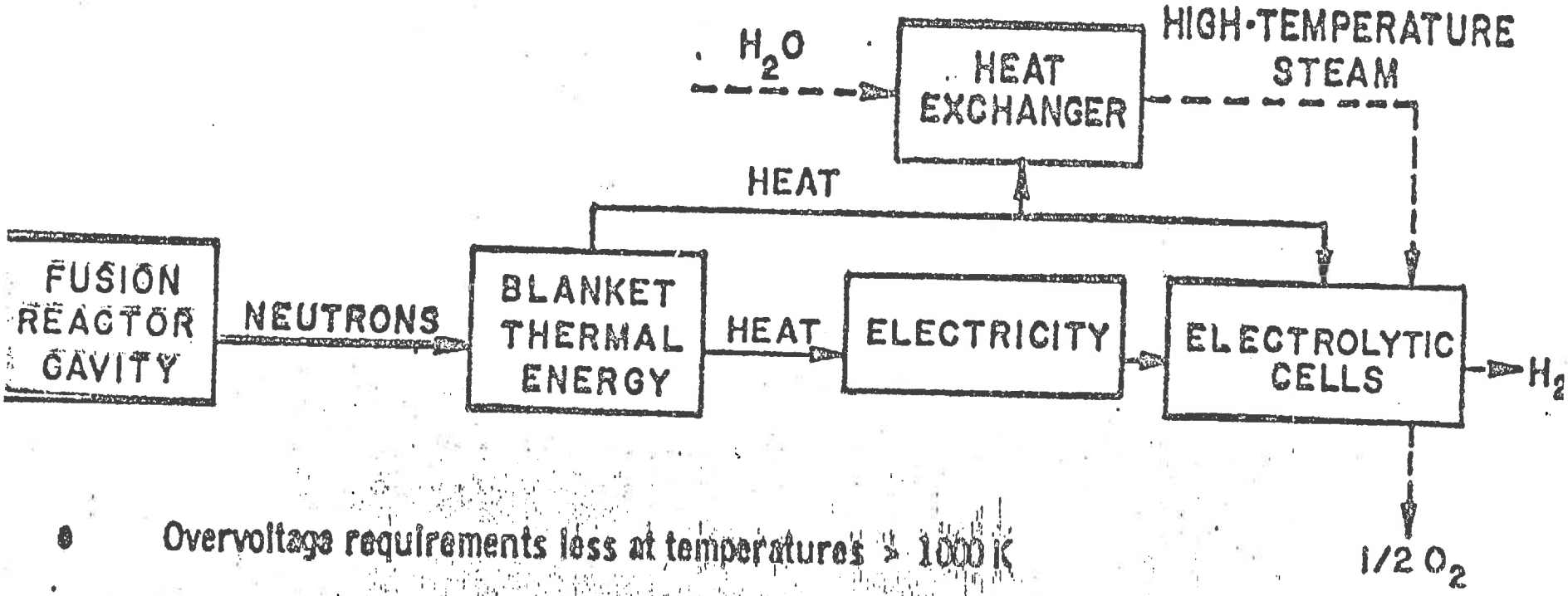

- Overvoltage requirements less at temperatures $\geq$ 1000 K
- Significant fraction of decomposition energy by heat ($\sim$ 40% at 1500 K)
- Technology for high-temperature electrolytes under development
- Cost of H_2 production less than room-temperature electrolysis

11.4. PROPULSION

ICF reactors have been proposed as energy sources for propulsion of marine vessels, aircraft, and space craft. Acutally, we can probably discard aircraft propulsion immediately since the power density of the overall ICF systems would be less than that of chemical jets or rockets. ICF ship propulsion would appear to be characterized by features very similar to that of nuclear fission propulsion, and therefore once again would not appear to present any significant advantages over existing technology.

On the other hand, the very high velocities of fusion reaction products (10^7 m/s) suggest that rockets using this debris as propellants would be characterized by very high specific impulses (exhaust velocity divided by the gravitational acceleration g). For example, ICF systems might make possible specific impulses as high as 10^6 m/s in contrast to that of chemical fuels with specific impulses of 450 s or less and fission rockets with 2000 s.

Two schemes have been proposed. The first would use the debris produced in an ICF microexplosion to collide with a pusher plate, thereby transferring some of its momentum to the spacecraft:

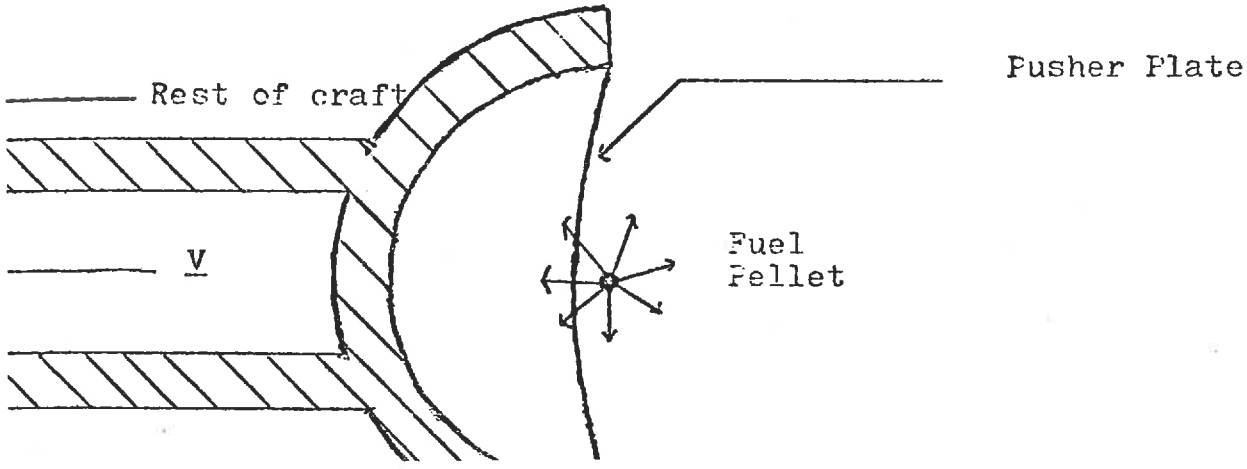

This particular approach is, in effect, a microscopic approach to the Orion project in which the explosions were originally intended to be fission or fusion bombs.

A more attractive option would be to implode the pellet in a magnetic mirror that is reflecting at one end and open at the other,

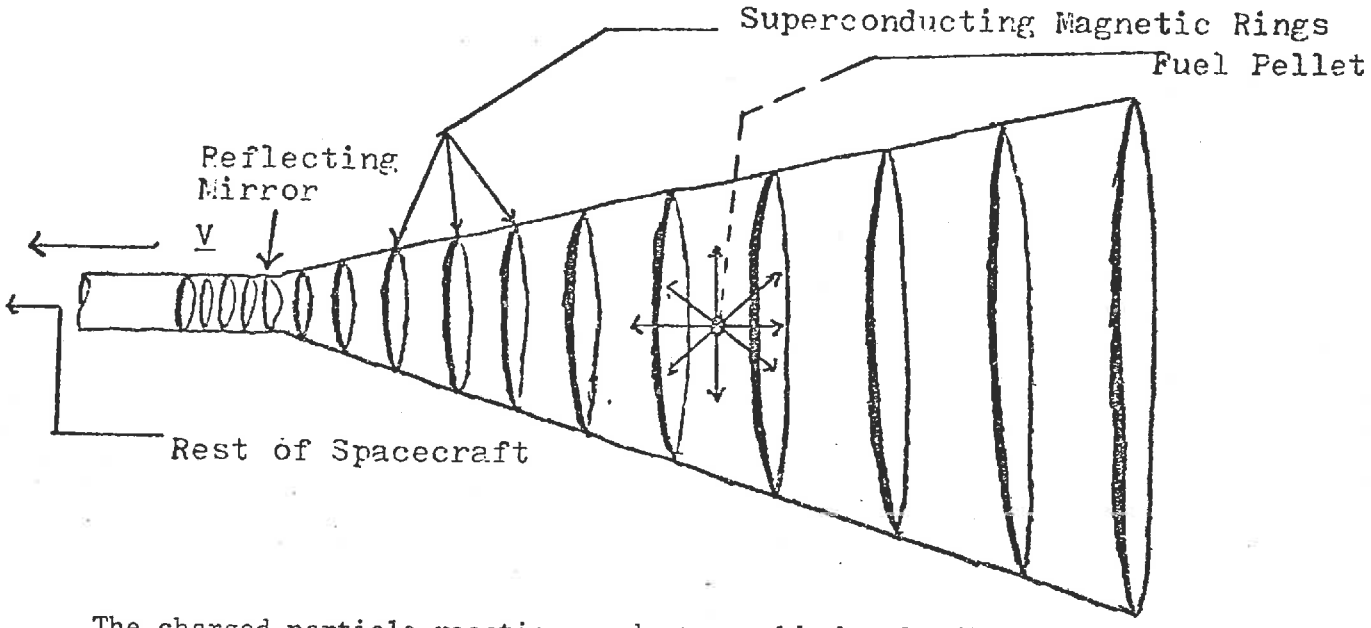

The charged particle reaction products would then be directed by the mirror field out the exhaust of the rocket. This latter approach would place a premium on fuels such as D-He^3 or p-B^{11} that produce primarily charged fusion products.

Such ICF propulsion systems would be best suited for deep space missions. For example, LLL has studied a laser fusion system using a 1 MJ laser pulse to produce a 260 MJ pellet yield which translates into 120 MJ producing thrust. For a pulse repetition frequency of 500 per second, this system would develop a thrust of 2.2 tons at a specific impulse of 5.5×10^5 s (an exhaust velocity of 6×10^6 m/s). For a spacecraft with a 300 ton propulsion system and a 200 ton deuterium fuel load, a payload of 100 tons can make a round trip to any point in the solar system in one year.

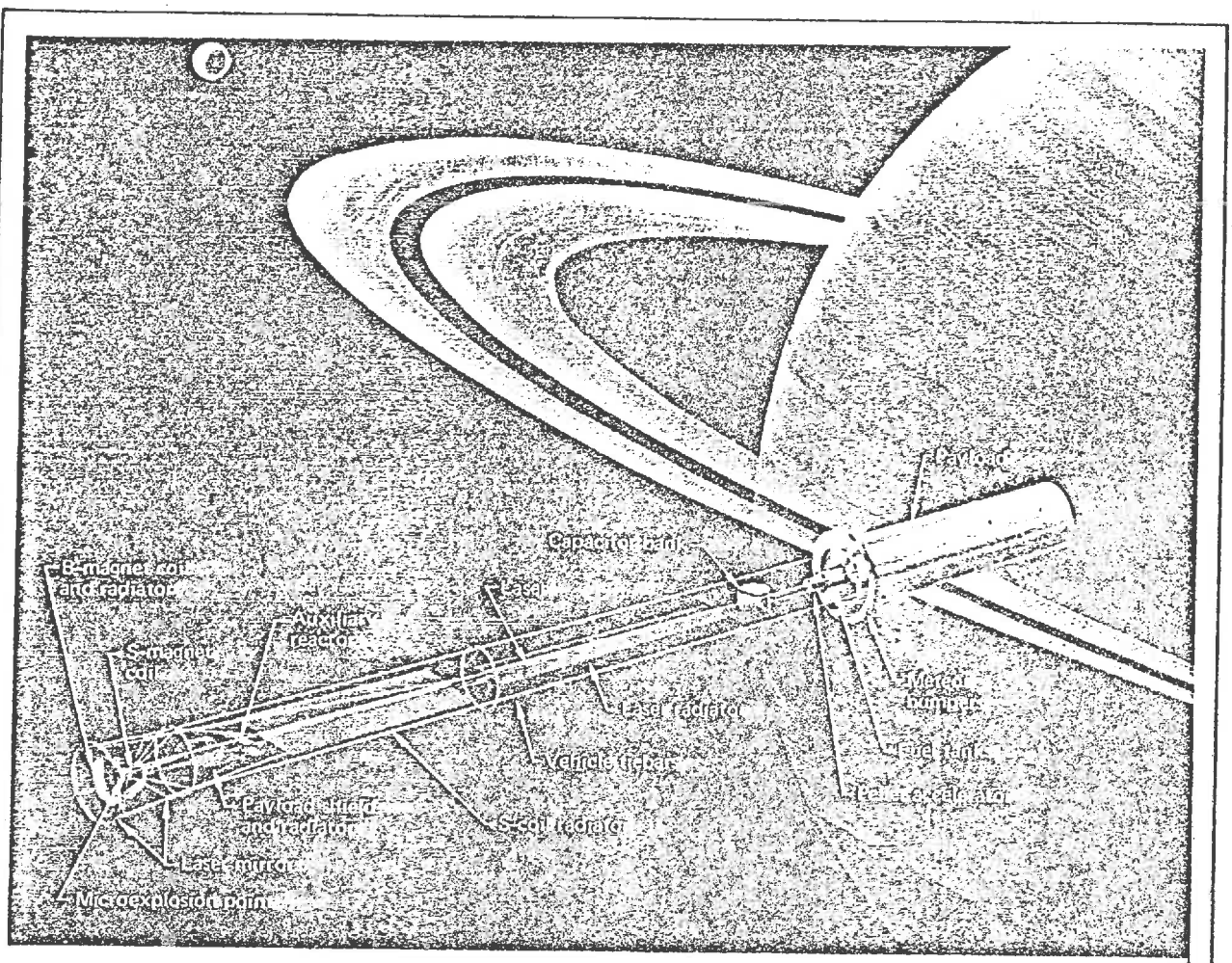

Laser fusion-powered extraterrestrial spacecraft.